Improvement of stable boundary layer flow simulation over complex terrain with fine resolution and new land cover treatment

Michiel de Bode

THÈSE

En vue de l'obtention du

DOCTORAT DE L'UNIVERSITÉ DE TOULOUSE

Délivré par l'Université Toulouse 3 - Paul Sabatier

Présentée et soutenue par

Michiel DE BODE

Le 18 février 2022

Amélioration de la représentation des écoulements de couche limite stable en terrain complexe avec simulation fine échelle et nouveau traitement de l'occupation de sols

---

Ecole doctorale : **SDU2E - Sciences de l'Univers, de l'Environnement et de l'Espace**

Spécialité : **Océan, Atmosphère, Climat**

Unité de recherche :
LAERO - Laboratoire d'Aérologie

Thèse dirigée par
Pierre DURAND et Thierry HEDDE

Jury

M. Stephan DE WEKKER, Rapporteur
M. Alain CLAPPIER, Rapporteur
Mme Chantal STAQUET, Examinatrice
M. Pierre ROUBIN, Examinateur
M. Pierre DURAND, Directeur de thèse
M. Thierry HEDDE, Co-directeur de thèse
M. Jean-Luc ATTIE, Président

Acknowledgements

Never did I ever expect that there would be a pandemic in the middle of my PhD. Nevertheless, I have thoroughly enjoyed the experience at this unique location with wonderful people. When we were allowed on the location the sunny walks between the canteen and the lab, learning more French and enjoying surrounding. Getting many questions if I was not cold in just a t-shirt. Altogether it has been an amazing three years in a spot I never thought I would go to. To make these three years as fantastic as they were, I need to thank some people who made it possible.

For the members of the jury I would like to say that I appreciate the time you have you dedicated to reading of my thesis, the interesting questions, comments, and details you have shared with me during the 'soutenance'. Sadly, due to Corona not everybody who wanted to be at the location could be present . Thank you Chantal STAQUET for being part of the jury. Thank you Jean-Luc for being chair during my defense and also for partaking in my comité de these together with Claire SARRAT, giving me good advices. Alain CLAPPIER and Stephan de Wekker thank you for reading my thesis over the Christmas holidays, that must have been a real chore seeing as it is has quite some pages. I would have liked to have discussed it with you in person. Merci à vous tous. Dank jullie Welf.

Les gens de LMTE, vous était formidable, vous m'avez aidé apprendre la langue Français plus rapide. Et je vais essayer de maintenir mon niveau. Je reviendra du temps en temps. En juillet pour ma pot de départ, ça prend une peu de retard, mais je sais combien vous aimez des pots. J'avais presque là pour vous aider avec les mots-crossées, il faut que je trouves une autre manier pour obtenir ce niveau. Mais aussi pour m'aider de comprendre la météo et autres modes de transport. A bientôt.

Pour commencer, je voudrais remercier mes encadrants, ils m'ont aidé et supporté. Thierry m'avait aidé avec beaucoup de bureaucratie de la France et le CEA. J'aurais bien voulu aller courrier avec lui dans une pause, mais le Covid était arrivé. Les discussion avec Thierry était joli parce qu'il avait toujours des nouvelles idées et perspectives différentes. Pierre Roubin était aussi en Cadarache et on avait beaucoup discuter dans les bus. Maintenant je sais beaucoup plus sur les trains modèle. Je devrais aussi remercier Wan pour cuisiner très bien et m'inviter pour des repas de midi et les petites devinettes sur les ingrédients des gâteaux. Et dernière mais pas le moindre, Pierre Durand. Il m'avait bien guidé et m'appris des choses de la turbulence et de la couche limite. Je n'étais pas si souvent à Toulouse que j'aurais voulu pour te rencontrer et discuter avec toi. En conclusion, c'était une plaisir d'avoir travaillé avec vous.

Dear friends that I made in Aix. You have made my stay in Aix much more fun. In the beginning it was hard to be completely new and know hardly anybody. You made me feel home, although it finding you all took some effort. If you every are in the Netherlands let me know and I will show you around.

Dan is er natuurlijk nog het stukje voor mijn vrienden en familie van thuis. Ik vind het fantastisch dat zo veel van jullie nog gekomen zijn in de anderhalve jaar dat we hebben mogen reizen. Helaas hadden we niet altijd een out tot onze beschikking dus is het vaak bij Aix en makkelijk bereikbare dingen gebleven, maar we hebben wel mijn vaste bakkerij en kraam op de markt leren kennen. Aan Hanna en Lisanne, fantastisch dat jullie langs geweest zijn, nu moet ik bij jullie langs, zo krijgen we een heel divers reispatroon. Matthijs, ik heb er erg van genoten dat je twee keer langs geweest bent. Het was een hele leuke manier om Will te introduceren, ik hoop dat we nog vaak samen op uitjes of vakantie kunnen gaan. De rest van de jaarclub, helaas heb ik jullie niet voorbij zien komen dus dat moeten we misschien maar een ander moment doen. Sophie, wat een weer had je uitgekozen om langs te komen. Hitte records, gelukkig was book in bar open om in een wat koelere plaats toch nog je werk te doen. Mapa wat fijn dat jullie ook regelmatig langs kwamen, samen dingen ontdekken in de omgeving maar ook de

nederlandse producten waren onmisbaar en vonden gretig aftrek bij de fransen in Aix. Marlot je bent een grote steun voor mij geweest, wat hebben we een hoop gereisd om elkaar te zien. Ik heb het leuk gevonden om bij jou op gesloten te zitten in je huis in Nederland. Net zo goed heb ik ook van onze reisjes naar Lille. Je hebt me gesteund als het moeilijk en me gemotiveerd weten te houden.

Abstract

This thesis is a contribution to the understanding of atmospheric valley flows under conditions of stable stratification. These conditions are pressing for air quality concerns because the mixing and dispersion of compounds emitted close to the ground level are strongly reduced. Furthermore, the topography plays a major role even at a local scale, making the flow simulation with numerical weather models difficult. The region studied as an application case is the Cadarache Valley (CV), in southeastern France that hosts a French atomic commission research center.

Previous work on the flows in this area was based on the KASCADE field campaigns and managed to establish a numerical simulation platform with the WRF model. Up to now, the model was able to forecast the flows in the Durance valley, but its smaller tributary valleys, such as the CV, remained unresolved, necessitating a statistical approach for their relevant but limited description. This thesis explores ways to improve flow descriptions in these smaller valleys, based on simulations as fine as 111 m horizontal resolution, as well as the improvement of the land cover (LC) representation in the WRF model.

The Corine Land Cover (CLC) dataset has proven to be an excellent representation of the land cover over Europe thanks to its large number of classes and its fine spatial resolution, but it is not yet fully compatible with WRF. To better integrate CLC into the model, I introduced a new table for land cover categories and developed a new aggregation method to prevent errors originating from the diversity in classes. Comparing this method with a conventional aggregation shows a mismatch that depends on the horizontal resolution of the simulation and reveals that both the new table parameters and the aggregation method bring an overall improvement of numerical simulations.

Then I started the building of a fine-resolution WRF simulation over the Cadarache region. An observation period of the second KASCADE campaign was simulated on five nested domains, with resolutions ranging from 9 to 0.111 km. This simulation shows a real improvement compared to the previously available 1 km simulations since the low-level wind in the CV now satisfactorily compares to the observations. However, further investigation shows that the stability within the CV is weaker in the simulation than in the observations, which relates to slope flows and an advected disturbance caused by a wrongly timed large-scale wind. Nonetheless, the model manages to simulate previously unresolved flows.

Further investigation was performed through the release of tracers from various locations in the simulation domain. The analysis of their plumes reveals the complexity of interactions between the different low-level winds within the region. As expected, the large Durance Valley flow dominates and forces the flows in the tributary valleys. However, this forcing varies throughout the night, making the local flows behave unexpectedly and sometimes take unforeseen routes.

Résumé

Cette thèse est une contribution à la compréhension des vents de vallée en condition de stratification stable. Ces conditions sont prégnantes pour la qualité de l'air car alors le mélange et la dispersion des composés émis près du sol sont fortement réduits. De plus, la topographie joue un rôle majeur même à l'échelle locale, rendant difficile la simulation des écoulements avec des modèles numériques météorologiques. Le site étudié comme cas d'application est la vallée de Cadarache (CV), dans le sud-est de la France, qui abrite un centre de recherche du Commissariat à l'énergie atomique.

Les travaux précédents sur l'aérologie de ce site étaient basés sur les campagnes de terrain KASCADE et ont permis d'établir une plateforme de simulation numérique avec le modèle WRF. Jusqu'à présent, ce modèle pouvait prévoir les écoulements dans la vallée de la Durance, mais ses vallées tributaires plus petites comme la vallée de Cadarache restaient non résolues, nécessitant une approche statistique pour leur description pertinente mais limitée. Cette thèse explore les moyens d'améliorer la description des écoulements dans ces petites vallées, en se basant sur des simulations aussi fines que 111 m de résolution horizontale, ainsi que l'amélioration de la représentation de l'occupation des sols dans le modèle WRF.

Corine Land Cover (CLC) s'est révélé être une excellente représentation de l'occupation des sols en Europe grâce à son grand nombre de classes et à sa résolution spatiale fine, mais il n'est pas encore totalement compatible avec WRF. Pour mieux intégrer CLC dans le modèle, j'ai introduit une nouvelle table de paramétrisation et développé une nouvelle méthode d'agrégation. La comparaison de cette méthode avec une agrégation conventionnelle montre un décalage fonction de la résolution horizontale et révèle que la méthode d'agrégation ainsi que la paramétrisation apportent une amélioration globale de la qualité des simulations numériques.

J'ai ensuite construit une simulation WRF à résolution fine sur la région de Cadarache. Une période de la campagne d'observation KASCADE 2017 a été simulée sur cinq domaines imbriqués, avec une résolution horizontale à 111 m. Cette simulation montre une réelle amélioration par rapport aux simulations à 1 km précédentes, puisque le vent à basse altitude dans la vallée de Cadarache est modélisé maintenant de manière satisfaisante par rapport aux observations. Cependant, une étude plus approfondie montre que la stabilité dans la vallée de Cadarache est plus faible dans la simulation que dans les observations, ce qui est lié aux vents de pente et à une perturbation advectée par un vent à grande échelle mal simulé. Néanmoins, le modèle parvient à simuler des écoulements non résolus auparavant.

Une étude plus approfondie a été réalisée en libérant des traceurs à différents endroits du domaine fin de simulation. L'analyse de leurs panaches révèle la complexité des interactions entre les différents vents de basse altitude dans la région. Comme prévu, le vent de la vallée de la Durance domine et force les écoulements des vallées tributaires. Cependant, ce forçage varie au cours de la nuit, ce qui fait que les écoulements locaux se comportent de manière inattendue et prennent parfois des routes imprévues.

General introduction

Everybody lives in the lower levels of the atmosphere, called the boundary layer (BL), with depths of a few hundred meter to a few kilometers. Pollutants are mostly released into the BL through various phenomena, such as pollen from plants, or gases such as NO_x from combustions, and CFC from accidental releases. To estimate the concentrations and effects of pollutants, it is important to know their source type and duration. For example, mobile sources affect larger areas than fixed sources. Similarly, an accidental source has a one-time release, while sporadic or continuous sources allow pollutants to build up over time. In the end, too high concentrations of pollutants such as fine particles harm our general health, giving rise to anything from mild issues with breathing to dangerous severe respiratory diseases and irregular heartbeat. All these pollutants have their own hazards, but they all spread through the atmosphere, and thus, the understanding and correct forecast of airflow is important.

Wind, also called airflow, influences the concentration of pollutants. Wind transports pollutants away from their sources, diminishing their concentration by moving released quantities and mixing air masses. Dilution along the vertical is strongest during the day when solar radiation causes instability by heating the earth's surface. Warm air rises and leads to large mixing structures in the BL (thermal mixing). These large structures mean that pollution is transported vertically and is spread in larger volumes, resulting in a reduced concentration close to the emission source. At night, the absence of solar radiation leads to stable conditions, reduced surface wind speeds, and less mixing in the BL, especially when synoptic winds are low. Therefore, nighttime conditions are more inclined to keep particles closer to their source and increase concentration because reduced vertical mixing limits transport to the faster, high-up winds.

Some types of terrain restrict transport even further. This is the case for complex terrain with many elevation differences, such as alpine valleys. Complex terrains can increase pollutant concentration by reducing thermal mixing through blocked solar irradiation, reducing airflow in the valleys because of mechanical obstacles, and reducing air volumes into which pollutants can spread. An illustration of trapped species in the bottom of the valleys during stable stratification conditions is shown in Figure 0.1, where fog visualizes stagnation. Another example, in the French Arve Alpine Valley, the topography causes the air to stagnate for several days and fine particle concentration often exceeds the regulatory health limit (Chemel et al., 2016). Such concerns are major motivations for field campaigns to investigate the exact flows and their origins. One such campaign is the Passy-15 (PACI et al., 2017). Some other recent field campaigns are MATERHORN (Fernando et al., 2015), COLPEX (Price et al., 2011), and NEWA-Perdigão (Wagner et al., 2019).

Another example of complex terrain is the Cadarache Valley (CV) in southeastern France, a small valley 1 – 2 km in width and 5 km in length. It ends in the middle section of the Durance Valley (DV), which spans 5 km at its widest point and 67 km in length. The reason that great interest was shown for many years in the CV flows is that this valley hosts a site of the atomic and alternative energy research institute CEA (Commissariat à l'énergie atomique et aux énergies alternatives). Here, the research laboratory LMTE (Laboratoire de Modélisation des Transfert dans l'Environnement) performs studies about the transport of chemicals and radionuclides in the soil, water, and atmosphere around the center. Knowledge about the transport of these substances is important to ensure population safety. Conventional methods for particle displacement in the region use Gaussian dispersion, which does not apply to the complex terrain. The LMTE started field campaigns in the region as part of their atmospheric research projects because many past studies focusing on stable night conditions demonstrate that local topography determines the airflow in these conditions.

Figure 0.1: Stable flows with fog channeled by mountain ridges in complex terrain. Photo thanks to the courtesy of T. Hedde. View of the Durance valley around the "Clue de Mirabeau". Picture taken from "Pic des Mouches" (43.5393°N, 5.6456°E, North azimuth. 8 dec. 2019 8 :16 CEST)

Extensive research started in 2012 with a first study of the flows in and above the CV during the field campaign of KASCADE-2013 (Duine et al., 2017). This data led to understanding the typical DV and CV flows during stable night conditions. With this dataset, a numerical weather prediction (NWP) model adapted to the DV was developed based on the LMTE operational weather forecast version of the WRF model (Kalverla et al., 2016), which is run daily in grid-nested mode with a kilometer resolution for the innermost domain around Cadarache. However, this evolution is not sufficient to resolve the winds inside the small CV. Instead, statistical methods were set up to determine in real-time the presence or absence of drainage winds into the CV (Duine et al., 2016).

The following study focused on the spatial variation within the CV with a second field campaign called KASCADE-2017. Its data were used to understand the different wind structures along the CV sidewalls and the thermal profile within the CV. Further work with statistical methods based on artificial neural networks allowed the determination of the wind speed and direction in the CV, either from observations above the valley (Dupuy et al. 2019) or from the coarse simulations (Dupuy et al. 2021).

A limitation of the methods above is that only one location has the wind information. Solving this lack of information in space requires more training locations for the statistical methods or a new NWP simulation with a horizontal resolution that allows the model to resolve the CV.

The primary focus of this thesis is contributing towards tools and knowledge needed to adapt the WRF model for the CV airflows. Additionally, the findings help the general understanding of airflows in small valleys and their interactions with their surroundings. Furthermore, the thesis contributes to knowledge on how to set-up an NWP model in complex terrain.

To improve the NWP model to the extent that it works for the CV, I investigate two possible and complementary ways. The first way is to refine the model resolution. Models predict weather on a given scale. Coarse models (with a poor resolution) predict weather parameters for large areas of land. The local surface variation, such as variation in elevation, is not accurately represented in such models. Fine models have a better resolution and contain a more detailed – and therefore more accurate –

description of the surface. Using a finer resolution can result in improved simulated parameters such as temperature. This, in turn improves the prediction of stratification-related airflows. The second way to improve the NWP model, as it has been set up by Duine (2015), is by enhancing land cover representation. In particular, realistic vegetation in the model is important because it influences exchange processes between earth and atmosphere, improving the prediction of atmospheric parameters.

In my thesis, I shall adapt the widely used NWP model called WRF. The adaptations aim to improve wind and temperature forecasting in a small valley. I formed several questions to direct my research:

- How does improved land cover representation affect the WRF model outputs in the Cadarache area and over a larger domain?
- How does the WRF model with a ~100 m horizontal resolution grid represent nocturnal Cadarache valley winds?
    - How is the interaction of the Cadarache and Durance valley winds simulated?
    - What are typical turbulent length scales of the Cadarache valley wind, and are parameterization schemes appropriate for these lengths?

I intend to answer these research questions by building upon the observational data from the two KASCADE campaigns.

This thesis contains five chapters that build upon each other. In the first chapter, I address theories, equations, and relations in order to create a basis for understanding the processes discussed in my research. I will focus on the nocturnal processes and valley flows. Chapter 2 describes the CV, surroundings, and previous measurement campaigns relevant to my current research. Additionally, it contains some preliminary analyses relevant to my work. Chapter 3 describes the effects of different land cover inputs on the WRF model skill, with special attention to the Corine Land Cover dataset, including an aggregation method I developed to estimate the best-suited land cover category at coarser resolutions. Further chapters are on fine-resolution runs. Chapter 4 details how simulations with a 111 m horizontal resolution allow the Cadarache valley flows to be represented. Chapter 5 then discusses local flows visualized using passive tracers released at various locations in the simulation domain. Finally, I conclude the thesis with a summary, primary findings, and recommendations for future works.

Introduction générale

Nous vivons tous dans les niveaux inférieurs de l'atmosphère appelés couche limite (CL), dont l'épaisseur profondeur varie de quelques centaines de mètres à quelques kilomètres. Les polluants sont le plus souvent libérés dans la CL par divers phénomènes, comme le pollen des plantes, les particules fines issues de la combustion, ou les gaz tels que les NOx lors des combustions lors les CFC des rejets accidentels. Pour estimer les concentrations et les effets des polluants, il est important de connaître leur type de source et sa durée. Par exemple, les sources mobiles affectent de plus grandes zones que les sources fixes. De même, une source accidentelle entraîne un rejet unique, tandis que les sources sporadiques ou continues permettent aux polluants de s'accumuler au fil du temps. En fin de compte, des concentrations trop élevées de polluants tels que les particules fines nuisent à notre santé générale, donnant lieu à des problèmes légers de respiration ou aussi dangereux que des maladies respiratoires graves et un rythme cardiaque irrégulier. Tous ces polluants présentent leurs propres dangers, mais ils se propagent tous dans l'atmosphère, d'où l'importance de comprendre et de prévoir correctement le flux d'air.

Le vent, également appelé écoulement, influence la concentration des polluants. Le vent peut transporter les polluants loin de leurs sources, diminuant leur concentration en déplaçant les quantités libérées et en mélangeant les masses d'air. La dilution le long de la verticale est la plus forte pendant la journée, lorsque le rayonnement solaire provoque une instabilité en chauffant la surface de la terre. L'air chaud s'élève et conduit à de grandes structures de mélange dans la CL (mélange thermique). Ces grandes structures font que la pollution est transportée verticalement et se répand dans de plus grands volumes, ce qui entraîne une concentration réduite. La nuit, l'absence de rayonnement solaire entraîne des conditions stables, une réduction de la vitesse des vents de surface et une diminution du mélange dans la CL, en particulier lorsque les vents synoptiques sont faibles. Par conséquent, les conditions nocturnes sont plus enclines à maintenir les particules plus près de leur source et à augmenter la concentration, car le mélange vertical réduit limite le transport vers vents d'altitude plus rapides.

Certains types de terrain restreignent encore plus le transport. C'est le cas des terrains complexes présentant de nombreuses différences d'altitude, comme les vallées alpines. Les terrains complexes peuvent augmenter la concentration de polluants en réduisant le mélange thermique par le blocage du rayonnement solaire, en réduisant le flux d'air dans les vallées en raison d'obstacles mécaniques, et en réduisant les volumes d'air dans lesquels les polluants peuvent se répandre. La figure 0.1 illustre les espèces piégées dans le fond des vallées dans des conditions de stratification stable, où la stagnation est visualisée par le brouillard. Autre exemple, dans la vallée alpine française de l'Arve, la topographie fait que l'air stagne pendant plusieurs jours et que la concentration en particules fines dépasse souvent une limite sanitaire (Chemel et al., 2016). De telles préoccupations ont motivé des campagnes de terrain pour étudier en détails les écoulements leurs origines. L'une d'elles est Passy-15 (PACI et al., 2017), une campagne de terrain qui s'inscrit dans une longue lignée d'études des écoulements en conditions stables. Parmi les plus récentes on peut mentionner MATERHORN (Fernando et al., 2015), COLPEX (Price et al., 2011), et NEWA-Perdigão (J. Wagner et al., 2019).

Un autre exemple de terrain complexe est la vallée de Cadarache (CV) dans le sud-est de la France, une petite vallée de 1 - 2 km de largeur et de 5 km de longueur. Elle se termine dans la section médiane de la vallée de la Durance (DV), qui s'étend sur 5 km à son point le plus large et a une longueur de 67 km. La raison pour laquelle un grand intérêt a été porté pendant de nombreuses années aux écoulements dans la CV est que cette vallée abrite un site du Commissariat à l'énergie atomique et aux énergies alternatives (CEA). Là, le laboratoire de recherche LMTE (Laboratoire de Modélisation des Transferts dans l'Environnement) réalise des études sur le transport de substances chimiques et de radionucléides dans le sol, l'eau et l'atmosphère autour du centre. La connaissance du transport de ces

substances est importante pour assurer la sécurité, car elles peuvent être dangereuses. Les méthodes conventionnelles d'estimation de la dispersion dans la région s'appuient sur des modèles de panaches gaussiens, qui ne sont pas adaptés au terrain complexe. Le LMTE a lancé des campagnes de terrain dans la région dans le cadre de ses projets de recherche sur l'atmosphère car une longue histoire de campagnes axées sur des conditions nocturnes stables démontre que la topographie locale détermine l'écoulement de l'air dans ces conditions.

Figure 0.1 : Écoulements stables avec brouillard canalisés par des crêtes montagneuses en terrain complexe. Par la grace de T. Hedde. Vue de la vallée de la Durance auprès la clue de Mirabeau pris du Pic de Mouches (43.5393°N, 5.6456°E, North azimuth. 8 dec. 2019 8 :16 CEST).

Des recherches approfondies ont commencé en 2012, avec une première étude des écoulements dans et au-dessus de la CV pendant la campagne de terrain de KASCADE-2013 (Duine et al., 2017). Ces données permettent de comprendre les écoulements typiques de la DV et de la CV dans des conditions nocturnes stables. Avec ce jeu de données, un modèle de prévision numérique du temps (PNT) adapté à la DV a été développé sur la base de la version de prévision météorologique opérationnelle du modèle WRF (Kalverla et al., 2016), qui est lancé quotidiennement au LMTE en mode *grid-nested* avec une résolution kilométrique pour le domaine le plus central autour de Cadarache. Cependant, ce modèle ne peut pas résoudre les vents à l'intérieur de la CV, car elle est trop étroite. En lieu et place, des méthodes statistiques ont été mises au point pour déterminer en temps réel la présence ou l'absence de vents de drainage dans la CV (Duine et al., 2016).

L'étude suivante s'est concentrée sur la variation spatiale au sein de la CV avec une deuxième campagne de terrain appelée KASCADE-2017. Ses données sont utilisées pour comprendre les différentes structures de vent le long des parois latérales de la CV et le profil thermique au sein de la CV. D'autres travaux avec des méthodes statistiques basées sur des réseaux neuronaux artificiels ont permis de déterminer la vitesse et la direction du vent dans la CV, soit à partir d'observations au-dessus de la vallée (Dupuy et al. 2019), soit à partir de simulations grossières (Dupuy et al. 2021).

Un problème avec les méthodes ci-dessus est qu'un seul paramètre est déterminé (le vent) et en un seul endroit. Pallier ce manque d'information à la fois sur les variables et dans l'espace nécessite des

ensembles de données et une formation pour les méthodes statistiques, ou une nouvelle simulation NWP avec une résolution horizontale qui permet au modèle de résoudre la CV.

L'objectif principal de cette thèse est de contribuer aux outils et aux connaissances nécessaires à l'adaptation du modèle WRF pour la CV. De plus, les résultats doivent aider à la compréhension générale des écoulements dans les petites vallées et de leurs interactions avec leur environnement. En outre, ce travail permet de mieux savoir comment mettre en place un modèle PNT dans un terrain complexe.

Pour améliorer le modèle PNT, afin qu'il fonctionne pour la CV, j'étudie deux moyens possibles. Le premier consiste à affiner la résolution du modèle. Les modèles prévoient le temps à une certaine échelle spatiale, qui peut être grossière ou fine. Les modèles grossiers (dont la résolution est faible) prévoient les paramètres météorologiques pour de vastes zones. La variation locale présente à la surface, telle que la variation du relief, n'est pas représentée avec précision dans ces modèles. Les modèles fins ont une meilleure résolution et contiennent une description plus détaillée - et donc plus précise - de la surface. L'utilisation d'une résolution plus fine peut permettre d'améliorer les paramètres simulés tels que la température. Ce qui, à son tour, améliore la prédiction des écoulements liés à la stratification. Deuxièmement, la version du modèle PNT, telle qu'elle a été mise en place par Duine (2015), pourrait être améliorée au niveau de la représentation de la couverture terrestre. En particulier, une végétation réaliste dans le modèle est importante car elle influence les processus d'échange entre la terre et l'atmosphère, améliorant ainsi la prédiction des paramètres atmosphériques.

Dans ma thèse, je vais adapter le modèle NWP largement utilisé appelé WRF. Les adaptations visent à améliorer la prévision du vent et de la température dans une petite vallée. J'ai formulé plusieurs questions pour orienter mes recherches :

- Comment l'amélioration de la représentation de l'occupation du sol affecte-t-elle les sorties du modèle WRF dans la région de Cadarache et sur un domaine plus large ?
- Comment le modèle WRF avec une grille de résolution horizontale de 100 m représente-t-il les vents nocturnes de la vallée de Cadarache ?
    - Comment est simulée l'interaction des vents de la vallée de Cadarache et de la vallée de la Durance ?
    - Quelles sont les échelles de longueur turbulentes typiques du vent de la vallée de Cadarache, et les schémas de paramétrage sont-ils appropriés pour ces longueurs ?

J'ai l'intention de répondre à ces questions de recherche en m'appuyant sur les données d'observation acquises lors des deux campagnes KASCADE.

Cette thèse contient six chapitres, qui s'appuient les uns sur les autres. Dans le premier chapitre, j'aborde les théories, équations et relations importantes afin de créer une base pour comprendre les processus abordés dans ma recherche. Je me concentrerai sur les processus nocturnes et les écoulements de vallée. Le chapitre 2 décrit la CV, l'environnement et les campagnes de mesure précédentes pertinentes pour ma recherche actuelle. En outre, il contient quelques analyses préliminaires pertinentes pour mon travail. Le chapitre 3 décrit les effets de différentes données de couverture du sol sur la performance du modèle WRF, avec une attention particulière portée à la base de données Corine Land Cover, avec une méthode d'agrégation que j'ai développée pour estimer la catégorie de couverture du sol la mieux adaptée à des résolutions plus grossières. Les chapitres suivants portent sur les simulations à résolution fine. Le chapitre 4 détaille comment des simulations avec une résolution horizontale de 111 m permettent de représenter les écoulements de la vallée de Cadarache. Le chapitre 5 traite ensuite des écoulements locaux visualisés à l'aide de traceurs passifs

relâchés à différents endroits de la simulation. Enfin, je conclus la thèse par un résumé, des principaux résultats et les recommandations pour les travaux futurs.

Chapter 1

Understanding the structure of the stable boundary layer flow in valleys and its simulation

In this chapter, I will explain basic principles within the atmosphere related to my research. I start with the broader topics such as different atmospheric layers and progress to more specific processes like stable boundary layers, soil-atmosphere interactions, topography influences, and thermal flows, because all these processes affect the nocturnal down-valley winds.

1.1 Atmosphere: basics, scales, and formulas.

This part will give a brief summary of the earth's atmosphere, starting with explanting typical processes and their spatial and temporal scales. This will be continued with the surface energy balance, turbulence, atmospheric stability, and conservation equations.

1.1.1 Different scales of the atmosphere

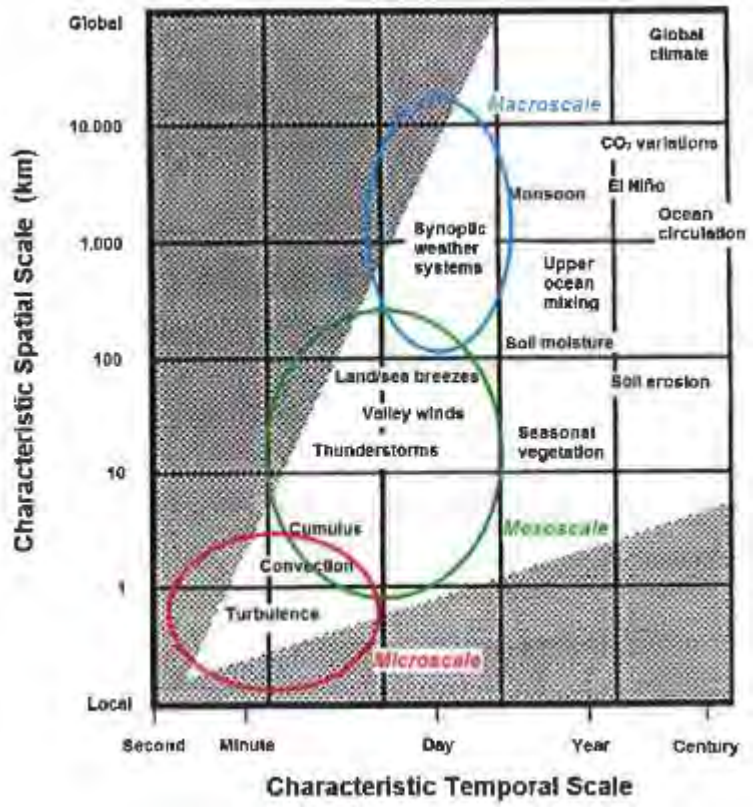

Figure 1.1: Typical length and time scales of atmospheric processes. Original from Holtslag (2003), adapted in Duine (2015).

The atmosphere surrounds the earth and contains phenomena with scales as large as the earth to scales smaller than a meter (see Figure 1.1). Similarly, processes can last a few seconds for turbulence or centuries for climate-related processes. In meteorology, atmospheric processes are divided into three classes: the macroscale, the mesoscale, and the microscale. Where macroscale processes last a few days to a few weeks, such as high- and low-pressure systems, mesoscale exist for a few hours to days, such as land-sea-breeze, thunderstorms, valley winds, and cellular convection. Lastly, microscale contains short-lived local processes such as turbulence or local (dry or moist) convection (Holtslag, 2003). Valley wind is a mesoscale phenomenon affected by both micro- and mesoscales. In short, we need knowledge on all scales to understand valley processes.

1.1.2 Atmospheric stability

Atmospheric stability is a leading parameter in vertical air movement. Simply put, hydrostatic atmospheric stability means heavy air going down and light air going up. However, directly measuring the density of air is a complicated task. Air is a compressible fluid and follows the ideal gas law described for dry air in eq. 1.1. It shows that temperature is a leading air density component.

$$p = \rho R_d T \qquad \textit{eq. 1.1}$$

Here p is the atmospheric pressure in Pa, ρ the air density in $\mathrm{kg\ m^{-3}}$, R_d is the gas constant for dry air (287 $\mathrm{J\ K^{-1}\ kg^{-1}}$) and T represents the absolute atmospheric temperature in Kelvin. Assuming a fixed mass in adiabatic conditions if the pressure decreases, temperature decreases. In the lower parts of the atmosphere, temperature decreases with height according to the so called lapse rate ($\Gamma_d \equiv -\frac{dT}{dz}$) with a theoretical neutral stability value of 9.8 K km^{-1} for dry air, while observed rates in the troposphere vary from 6 to 7 K km^{-1} depending on atmospheric conditions. This difference explains why an adiabatically descending air parcel becomes (on average) warmer than its environment and

why subsidence brings heat to the ground level. To facilitate the comparisons of air parcels density, potential temperature (eq. 1.2) introduces a temperature variable normalized to a standard pressure, according to the law of an isentropic process, thus removing the pressure-induced variation, and relating density (buoyancy) directly to temperature.

$$\theta = T \cdot \left(\frac{p_0}{p}\right)^{\frac{R_d}{C_p}} \qquad \textit{eq. 1.2}$$

Here, p_0 represents a reference pressure of 1000 hPa, a value close to sea level pressure. C_p is the specific heat of dry air at constant pressure (1004.7 $\mathrm{J\ kg^{-1}\ K^{-1}}$). The variable θ is a conserved variable for dry adiabatic processes.

Up to now, I have discussed dry processes. However, water vapor in the atmosphere, which takes up to 4 % of the volume (Hobbs, 2000) but averages around 0.25 %, has a lower density than dry air. To compensate for this buoyancy difference, I use virtual potential temperature θ_v (in Kelvin). It includes the water vapor effect on density but no liquid water effect:

$$\theta_v = \theta \cdot (1 + 0{,}61q) \qquad \textit{eq. 1.3}$$

In eq. 1.3, q is the specific humidity in kg kg^{-1}. Further specification for liquid water exists, but I will not include them since I investigate clear-sky nights without clouds.

In eq. 1.1, the pressure becomes constant when a potential temperature variable replaces the temperature variable, meaning that potential temperature directly relates to the density or buoyancy of the air. Based on buoyancy, three static stability states are distinguishable for air parcels in the atmosphere: unstable, neutral, and stable. Using θ_v, it describes them as follows (for atmospheric temperature, replace the pressure corrected lapse rate 0 with adiabatic lapse rate):

$$\frac{\partial \theta_v}{\partial z} < 0 \text{ Unstable layer}$$

$$\frac{\partial \theta_v}{\partial z} \approx 0 \text{ Neutral layer}$$

$$\frac{\partial \theta_v}{\partial z} > 0 \text{ Stable layer}$$

Atmospheric instability can be defined locally and non-locally. Figure 1.2 shows a situation in both absolute and potential temperature. In this situation, the stability across multiple layers can be determined locally or non-locally, on the most right and the second from the right profiles, respectively. For the local approach, we determine stability in a given layer independently from the situation in the neighboring layers. In Figure 1.2, the area closest to the surface is warm, and in the lowest part of the profile temperature increases with height, making it locally stable. This is followed by a strong unstable zone due to cooling with height. Next, the potential temperature is constant, making it a neutral layer and ending with stable sections of increasing temperature. On the other hand, the non-local approach represents natural conditions better and depicts typical atmospheric daytime conditions. Even though a layer has already become stable, a parcel from the surface may have enough buoyancy to penetrate the stable layer to a height with similar potential temperatures as at the surface.

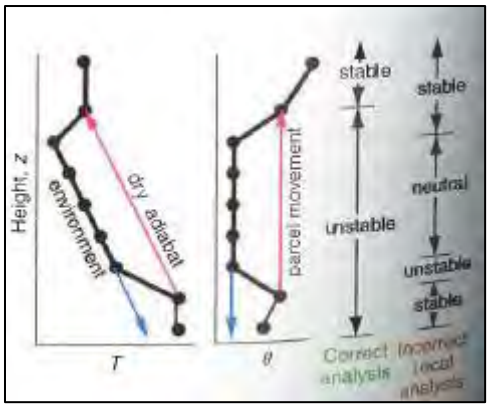

Figure 1.2: Difference between atmospheric temperature and potential temperature. The right part shows the different classifications of stable and unstable sections of a vertical profile. Original from Stull, 2000 and adapted by Wallace & Hobbs, 2006.

An air parcel may oscillate around its initial state in stable conditions, driven by gravity and Archimedes' push. This oscillation is called the buoyancy frequency or Brunt-Väisälä frequency, expressed in $\mathrm{rad\ s^{-1}}$.

$$N = \sqrt{\frac{g}{\theta_v}\frac{\partial \theta_v}{\partial z}} \qquad \textit{eq. 1.4}$$

Following eq. 1.4, for stable ($\frac{\partial \theta_v}{\partial z} = 3$ K km^{-1}) tropospheric conditions, $N \approx 1.6x10^{-3}s^{-1}$, meaning a period of about 10 min. While neutral indicates $N = 0$, meaning no return force, and after a perturbation, the parcel remains in neutral equilibrium at its new location. For unstable conditions ($\frac{\partial \theta_v}{\partial z} < 0$), disequilibrium force increases with time until a stable layer ($\frac{\partial \theta_v}{\partial z} > 0$) is reached.

1.1.3 Turbulence

As mentioned above, turbulence is a mixing mechanism consisting of irregular quasi-random motions and is mainly present in the lower parts of the atmosphere. It is vital to understand turbulence for boundary-layer processes because turbulence is often the main driving force in vertical and horizontal mixing of energy, vapor, and other quantities, such as pollutant concentrations. Its vertical eddies have lengths ranging from a few mm to the height of the boundary layer, with Turbulent Kinetic Energy (TKE) expressing their energy. Large eddies break down into smaller eddies until they dissipate through molecular viscosity (ϵ_d in eq. 1.5).

Turbulence has two origins, mechanical and thermal. Mechanical turbulence originates from wind shear, their ratio is quantified through the Richardson number, described with eq. 1.6 to eq. 1.8. Possible origins of shear are the frictional drag of winds at the surface or wind swirls in the wake of obstacles such as trees and buildings or meeting streams having different velocities or directions. A major contributor to mechanical turbulence is inertial turbulence, which causes small eddies to form along large eddies so that the smaller eddies get some inertial energy from the large eddies. Thermal (or buoyancy) turbulence results from convection (buoyant warm air rising and cold heavy air descending), causing vertical currents. It typically forms with temperature profiles resembling those in Figure 1.2. Note that during the evening transition, the thermal turbulence production can stop, however, the nocturnal mechanical turbulence production processes need time to start up, and therefore, in calm weather conditions, a drop in wind speeds and reduction of turbulence through the whole system is possible. Such intermediate stops are uncommon but occurred during the BLLAST

campaign (Lothon et al., 2014). Acevedo & Fitzjarrald, 2001 explain several forms of the evening transition in more detail.

Before further discussing turbulence, we need to understand the turbulent kinetic energy (TKE) budget and its behavior in the atmosphere. TKE is an interesting scalar as it is essential in boundary layers (section 1.2) and consists of several terms. The conservation equation format is applied to properly describe the TKE budget, whose layout is detailed in eq. 1.5. To do so, an explanation of the Reynolds decomposition is needed. Reynolds decomposition splits a flow (u) into the mean flow ($\overline{u}$) and the variation around mean flow (u'), reading as $u = \overline{u} + u'$ and is used in the expression of TKE per unit mass (e) as $\bar{e} = 0{,}5\ (\overline{u_i'^{\,2}})$, where the subscript i indicates Einstein summation notation, meaning that it is a summation over all three spatial coordinates x, y, and z (u, v, and w for wind). The TKE equation without simplifications, reads as:

$$\underbrace{\frac{\partial e}{\partial t}}_{storage} + \underbrace{\overline{U_i}\frac{\partial e}{\partial x_i}}_{advection} = \underbrace{\frac{g}{\theta_v}\left(\overline{w'\theta_v'}\right)}_{buoyancy} - \underbrace{\overline{u_i u_j}\frac{\partial u_i}{\partial x_j}}_{\substack{mechanical\\ production}} - \underbrace{\frac{\partial \overline{u_i' e'}}{\partial x_i}}_{\substack{turbulent\\ transport}} - \underbrace{\frac{1}{\bar{\rho}}\frac{\partial\left(\overline{w'p'}\right)}{\partial z}}_{redistribution} - \underbrace{\epsilon_d}_{dissipation} \qquad \textit{eq. 1.5}$$

The left-hand side first term represents the storage change over time and the second term describes the advection. First-term on the right-hand side is the buoyancy term and can produce or consume TKE, depending on the stability. The second term is the mechanical production of TKE by shear. As momentum decreases towards the surface, the minus sign combined with a negative gradient creates a positive term. The third term describes turbulent transport of TKE, largest in the vertical. The fourth term is the pressure correlation term, redistributing TKE through pressure fluctuations and is often associated with an oscillating nature. Lastly, a viscous dissipation term, i.e., converting turbulence into heat (note that this means it is technically not a conservation equation as the TKE amount decreases with time unless generated by a source of turbulence).

The mixing flow caused by turbulence is chaotic, contrary to the ordered laminar flow. The flux Richardson number (Ri_f; eq. 1.6) is the ratio between mechanically and thermally produced TKE and serves as an indicator for different flow types and stability types.

$$Ri_f = \frac{\frac{g}{\theta_v}\overline{w'\theta_v'}}{\overline{u'w'}\frac{\partial\overline{u}}{\partial z} + \overline{v'w'}\frac{\partial\overline{v}}{\partial z}} \qquad \textit{eq. 1.6}$$

The mechanical production term (denominator) is always negative, so the determination of the sign depends on the buoyancy term. When buoyancy creates turbulence, the term is negative ($Ri_f < 0$) and the atmosphere is unstable. With zero buoyancy, the atmosphere is neutral, and with turbulence suppression, the atmosphere is stable ($Ri_f > 0$).

When the fluxes are not computable, the Ri_f can be approximated with the gradients and is called the gradient Richardson number (Ri_g; eq. 1.7). Further approximations in assessing the gradients lead to the bulk Richardson number (Ri_B; eq. 1.8).

$$Ri_g = \frac{\frac{g}{\theta_v}\frac{\partial\theta_v}{\partial z}}{\left(\frac{\partial U}{\partial z}\right)^2 + \left(\frac{\partial V}{\partial z}\right)^2} \qquad \textit{eq. 1.7}$$

$$Ri_B = \frac{g\Delta\overline{\theta_v}\Delta z}{\overline{\theta_v}((\Delta\overline{u})^2+(\Delta\overline{v})^2)} \quad \textit{eq. 1.8}$$

In this formula, variables $\Delta\theta_v$ and ΔU are the difference of respectively virtual potential temperature, and wind speed between the top and bottom of the layer Δz. With the bulk Richardson approach and dry air assumption, θ can substitute for the virtual potential temperature. As mentioned before, the Ri number indicates the type of flow. Turbulent flows occur when values drop below a critical value of $Ri_c = 0.25$. However, a turbulent flow often stays turbulent until values are larger than 1.0. For values $0.25 \leq Ri \leq 1.0$, the presence or absence of turbulence depends on the flow history (Wallace & Hobbs, 2006). This area of uncertainty comes from the hysteresis effect and is described by McTaggart-Cowan & Zadra (2014). Generally, layers with $Ri < 0.25$ are called dynamically unstable and above 1.0 are called statically stable. Note that the uncertainty in the Richardson number is dependent on the bulk depth, the deeper the layer, the larger the uncertainty (Stull, 2009).

Circling back to the characteristics of turbulence, it consists of eddies with all different sizes, the TKE is often visualized with turbulence energy density spectra where the eddy wavelength is plotted versus the total amount of energy carried by all eddies with the same wavelength. Large eddies are few, but each holds a lot of energy compared to numerous small eddies with little energy individually. Note that synoptic movements also have wavelengths, at sizes much larger than the here discussed turbulence. Most studies use a 30-minute interval to avoid these synoptic signals in the turbulent spectra. To convert measurements in time to a plot with wavelengths requires the understanding of how turbulence behaves throughout time; the variations (u') of u vary through time with different frequencies caused by differently sized eddies. A Fourier transformation of the u' series converts the time variations to frequencies, readying it for application of Taylor's frozen turbulence hypothesis, which allows conversion of frequencies to lengths. Frozen turbulence assumes that the variations are small compared to the mean velocity ($\frac{u'}{\overline{U}} \ll 1$), meaning that spatial fluctuation can be considered as temporal fluctuations at a given point, also allowing the derivation of spatial series from temporal ones.

As illustrated in Figure 1.3, the turbulent spectra density shapes present three main sections: the energy-containing range, where new eddies form and most of the system energy resides; the Inertial subrange, where eddies breakdown and create smaller eddies following a -5/3 power relationship; and the dissipation range, where viscosity stress dissipates eddies turning kinetic energy into heat. We can quantify the spectrum with a few typical lengths. Commonly used scales are the peak wavelength, the wavelength range in spectra containing the most energy and the integral length, determining the transition from local isotropy to low wave-number domains (Kristensen et al., 1989).

These eddies carry air parcels in any direction, the up and down movements lead to vertical turbulent transport mechanisms (fluxes), see section 1.1.4.2. Solving the equations of turbulent fluxes requires an equation with a higher-order correlations to describe the flux, leaving more unknowns than equations; however, fluxes can be computed through covariances of fluctuations with other variables, which avoids solving the flux equation.

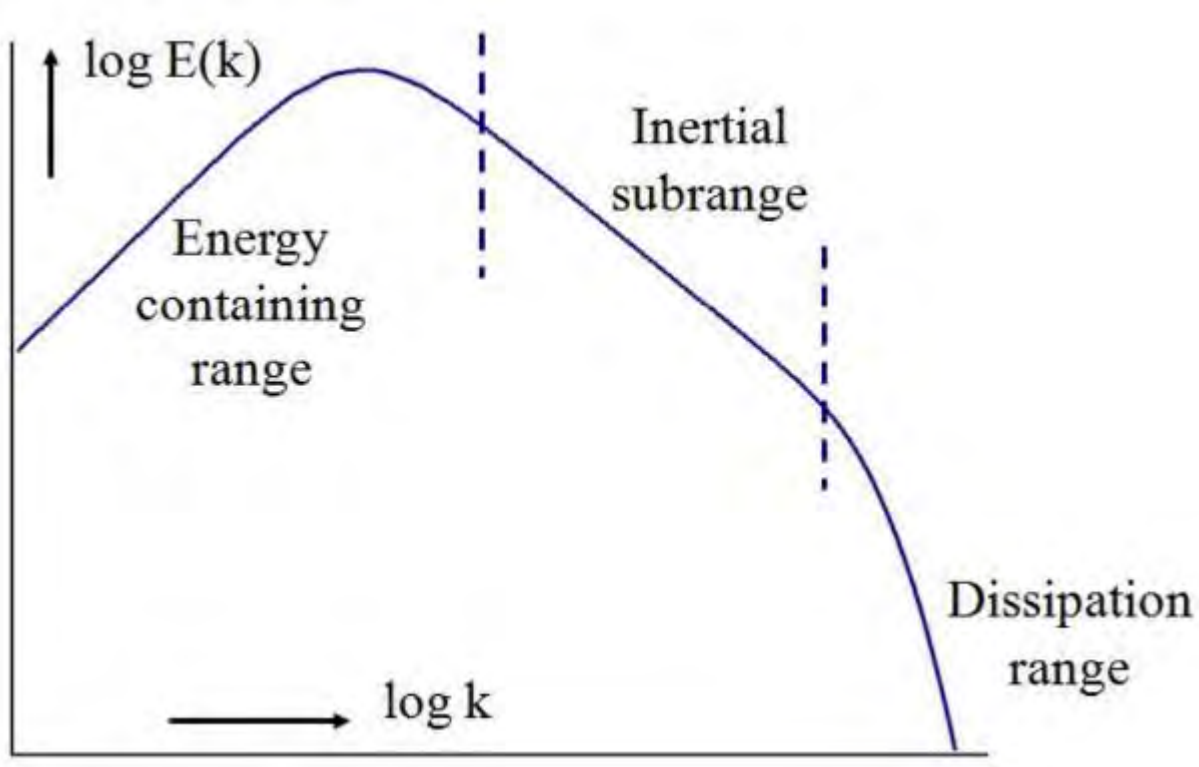

Figure 1.3: Theoretical Kolmogorov turbulent spectrum, with the wave-number k plotted versus the energy contained per wave-number. The picture originates from Noble et al. (2014). The y-axis has an energy unit, e.g., $m^2 s^{-2}$, with k wave-number being dimensionless unless converted to wavelength and in meters.

Isotropy means that a quantity is independent of direction. For calculations on turbulence to solve the patterns themselves, generally, turbulence is assumed isotropic. However, real turbulence is not isotropic and usually anisotropic along multiple spatial axes, meaning that turbulent properties change along the axes. The exact behavior of the anisotropy is a long-standing interest to close turbulent model equations. A multitude of theories exists to explain anisotropy and look for its cause. The first successful theory dates back to the K41 theory of Kolmogorov. In the last few decades, more research focused on anisotropy. The original anisotropy state tends to stay in local scales and not transport away, depending on the local situation (Liu & Pletcher, 2008). Stiperski et al., 2019 recently made progress in relating surface parameters to the type of anisotropy present.

1.1.4 Surface energy exchanges

The earth receives and reflects solar radiation (mainly shortwave), emits longwave radiation from the surface and receives longwave radiation from the atmosphere. The net energy from radiation is the energy source for turbulent and conductive fluxes in the boundary layer, generally causing instability during the day and stability at night. The soil cover and vegetation influence all these processes.

1.1.4.1 Radiation balance

At the earth's surface, most energy comes from the sun in as shortwave radiation. Here albedo reflects part of the radiation to space. Another way of energy loss is the surface-emission of longwave radiation. Wien's displacement law (eq. 1.9) determines the predominant wavelength, peak wavelength, at which a body emits radiation according to its surface temperature. According to the Stephan-Boltzmann relationship (eq. 1.10), all things with a temperature above zero Kelvin emit radiation. Applying it gives small or short wavelengths for the sun (effective emitting surface at ~6000 K) and long wavelengths for the earth (around 288 K) and eq. 1.10 gives the total amount of radiated energy.

$$\lambda_m T = c \qquad \textit{eq. 1.9}$$

$$F = \sigma \epsilon T^4 \qquad \textit{eq. 1.10}$$

In both eq. 1.9 and eq. 1.10, temperatures are in Kelvin. Where *c* is a constant of $2897\ \mathrm{K}\ \mu\mathrm{m}$, F is the flux density, σ is the Stephan-Boltzmann constant of $5.67 \times 10^{-8}\ \mathrm{Wm^{-2}K^{-4}}$ and ϵ is the emissivity of the surface (ϵ =1 signifies a perfect black body). For the net energy available to the earth's surface, we use the radiation balance (eq. 1.11), where ↑ indicates outgoing and ↓ incoming fluxes for shortwave (SW) and longwave (LW).

$$Q^* = SW^{\downarrow} - SW^{\uparrow} + LW^{\downarrow} - LW^{\uparrow} \qquad \textit{eq. 1.11}$$

The net radiation, Q^*, determines energy availability for the surface heat fluxes. For clear-sky daytime conditions, solar radiation ($SW^{\downarrow}$) enters the atmosphere, and the surface albedo reflects a fraction ($SW^{\uparrow}$). Not all shortwave radiation arrives directly from the sun, the atmosphere scatters and reflects a part of the shortwaves and these indirect sources of shortwave radiation are called diffuse radiation and are largest during partially thinly clouded skies (Page, 2012). Surfaces emit $LW^{\uparrow}$ towards space, while the in-between air and clouds emit both down $LW^{\downarrow}$ and upwards.

Clouds and air moisture play a significant role in determining the magnitude of the radiation fluxes. Clouds have a high albedo and reflect a substantial fraction of $SW^{\downarrow}$ to space. Where liquid water clouds reflect most radiation, ice clouds are more transparent (Ebert & Curry, 1992). However, the situation is more complicated due to mixed-phase clouds (Sun & Shine, 1994). Additionally, clouds replace the earth's surface as active black body emitters because of their opacity. Regarding LW radiation, greenhouse gases, such as water vapor, absorb it better than most gases and increase atmospheric temperatures, creating a larger $LW^{\downarrow}$ flux and increasing the surface net radiation and the earth's surface temperature.

1.1.4.2 Non-radiative surface energy fluxes

Surface fluxes are non-radiative fluxes of energy with their origin at the surface. In the surface energy balance, we consider two vertical turbulent fluxes, latent heat (LvE) and sensible heat (H), suplemented with a conductivity-based soil heat flux (G). LvE describes the evaporation at the surface, which consists of the moisture mass flux (E) and the energy required for evaporation (Lv = 2501 $*10^3$ J kg^{-1} at 0 °C), where L_v has a dependency on the actual air temperature, defining L_v as $L_v = [2501 - 2.37 * T(°C)] * 10^3\ J\ kg^{-1}$.

$$(Q^* + G) = L_v E + H \qquad \textit{eq. 1.12}$$

eq. 1.12 describes the surface energy balance, its left-hand side contains the net radiative energy and soil heat flux, and the right-hand side terms are the turbulent fluxes. Generally, non-radiative fluxes are negative when they transport energy away from the surface. However, in this thesis, I use the following sign convention: upwards equals positive. During the day, the balance typically has positive values, while they are usually negative at night. Effectively, Q^* supplies energy to the surface and is adjusted by the soil heat flux and storage, leaving the remaining energy for turbulent fluxes. Sometimes eq. 1.12 is supplemented with a storage or intake term, which considers the energy storage of vegetation and energy uptake by photosynthesis.

Easy calculation of soil heat flux requires Fourier's law approximation:

$$G = \lambda \frac{\partial \overline{T}}{\partial z} \qquad \textit{eq. 1.13}$$

Where λ is the thermal conductivity in $\mathrm{W\,m^{-1}\,K^{-1}}$, the exact conductivity depends on the soil moisture content and the type of soil. The usual evolution of G is opposite to the Q^* evolution, with a slight delay due to heat capacity, as the top layer of the soil heats before it starts heating up the atmosphere and lower soil layers. This temperature difference proceeds slowly increasing the time shift at deeper layers.

Description of averaged turbulent fluxes generally happens with use of covariances of u_i' and appropriate physical quantity X', density, and possible conversion constants such as Lv or Cp. We can approximate the transported amount (of energy) as described by the covariances by using the vertical gradients of the mean quantity (scalars like heat, momentum, moisture or CO_2). The gradients of heat and moisture are used for H and LvE respectively. Approximations of these turbulent fluxes, according to K-theory (Moene and Dam, 2014), look like:

$$H = \rho C_p \overline{w'T'} \approx -\rho C_p K_h \frac{\partial \overline{\theta}}{\partial z} \qquad \textit{eq. 1.14}$$

$$L_v E = \rho L_v \overline{w'q'} \approx -\rho L_v K_e \frac{\partial \overline{q}}{\partial z} \qquad \textit{eq. 1.15}$$

$$\tau = -\rho \left(\overline{u'w'}^2 + \overline{v'w'}^2 \right)^{\frac{1}{2}} \approx -\rho K_m \frac{\partial \overline{U}}{\partial z} \qquad \textit{eq. 1.16}$$

In eq. 1.14, eq. 1.15 and eq. 1.16 K_x is the turbulent exchange coefficient in $\mathrm{m^2\,s^{-1}}$, where the subscript h stands for heat, subscript e for water, and subscript m for momentum. C_p is the heat capacity of dry air at constant pressure in $\mathrm{J\,K^{-1}kg^{-1}}$. H is called sensible heat flux as it changes atmospheric temperature, whereas $L_v E$ indicates moisture transport caused by surface evaporation and potentially phase changes at higher altitudes. It represents energy for water phase changes but does not directly change the temperature, which changes available energy at the surface. Nonetheless, condensation in clouds does release energy at altitude. Eq. 1.16 is the transport mechanism of momentum, it is related to turbulence thus partly determines the magnitude of the other turbulent fluxes. In contrast with the two energy fluxes, the momentum flux is usually negative, transporting wind towards the surface where it is zero due to friction with the surface.

1.1.4.3 Bowen ratio

The ratio of H over $L_v E$ is called the Bowen-ratio, given in eq. 1.17. This ratio is indicative of the typical dryness of a surface area and is a component for soil evaporation calculations. Generally, the Bowen ratio is positive (at least during the daytime), and values above 1 indicate relatively dry areas from semi-arid landscapes at 2-6 to deserts with values above 10. While grasslands and temperate forests generally have ratios of 0.4 to 0.8, tropical oceans are below 0.1, indicating that, at these surfaces, more energy goes to evaporation than heating of air.

$$\beta = \frac{H}{L_v E} \qquad \textit{eq. 1.17}$$

1.1.4.4 Land cover and soil effects

As mentioned above, different surface covers have different Bowen ratios. Land cover and soil type contribute in several ways to the difference, and I will address some of them.

The soil cover is crucial because it directly influences the system's available energy. Vegetation, in turn, can enhance water infiltration and evaporation. Certain soil types have more water available for evaporation than others do. For example, clay can contain plenty of water, but it clings firmly to this water. On the other hand, sand contains less water but has no strong binding (Tuller & Or, 2005). At the surface evaporated water is replaced by groundwater through capillarity or with the next rain (or

flood). Thus, precise evaporation calculations require knowledge on soil cover, available water, and vegetation.

Evaporation is not the only process through which soils lose water. Plants need water just like any other living organism. They extract water from the ground through their roots and transpire with their leaves, whereas evaporation occurs in the skin layer, the net loss of water is referred to as evapotranspiration. To be more specific, different types of plants have different rooting depths and place the bulk of their root system at varying soil depths, drawing water from different depths. Generally, large plants have deeper rooting depths than small plants. The plants transport the absorbed moisture from their roots to their leaves to replenish the water evaporated through air exchange (transpiration) at the stomata. The combined amount of water released by the surface and plants is called evapotranspiration (Katul et al., 2012). In short, plants enlarge the latent heat flux over land at the expense of sensible heat flux.

Surface covers influence not only the surface exchange rates but also radiative parameters and hinder airflow. From the windless conditions at the surface, in idealized views wind increases with a quasi-logarithmic profile to geostrophic values at high levels, influencing the vertical transports. Besides surface friction, additional flow blocking comes from vegetation, enlarging the area with reduced wind speeds. Most vegetation density decreases with height, and wind can pick up. However, forests are an exception since they have their densest part several meters above ground (the canopy), creating a wind speed peak between the surface and the vegetation bulk. This peak makes low-level winds harder to represent (Kaimal & Finnigan, 1994). Further, vegetation density of forests can create flow sheltering, which leads to different temperatures at the soil surface in the forest than outside the forest due to reduced vertical mixing. Altogether, soil and cover thereof are vital parts of the land surface interaction. Most surfaces have vegetation and their flows are relatively close to the surface, making it essential to know how soil covers influence local flows.

1.1.5 Governing equations of atmospheric flows

To simplify the calculations of atmospheric variables, I describe the atmosphere as a fluid and assume that no mass is lost. Further, I apply several conservation principles in fluid mechanics and thermodynamics, resulting in the momentum, mass and enthalpy equations and a generalized equation applicable to most scalars. I write equations in the Eulerian form, describing them as observed from a fixed point. The conservation of mass, also known as the continuity equation (eq. 1.18), describes the mass at a location.

$$\frac{\partial \rho}{\partial t} + \rho \frac{\partial u_i}{\partial x_i} = 0 \qquad \textit{eq. 1.18}$$

Here and in the coming equations, a subscript “i” denotes Einstein’s summation notation, “j” covers a twin summation independent of “i”. eq. 1.18 is considered equal zero because of the assumption of constant mass in the atmosphere. Next to the mass equation, I have the momentum equation (Stull, 2009), eq. 1.19, and averaged it looks like:

$$\frac{\partial \overline{U_i}}{\partial t} + \overline{U}_j \frac{\partial \overline{U_i}}{\partial x_j} = -\delta_{i3} g + f_c \epsilon_{ij3} \overline{U_j} - \frac{1}{\bar{\rho}} \frac{\partial \bar{P}}{\partial x_i} + \frac{\nu \partial^2 \overline{U_i}}{\partial x_j^2} - \frac{\partial \left(\overline{u_i' u_j'} \right)}{\partial x_j} \qquad \textit{eq. 1.19}$$

With $\delta_{i3}$the Kronecker delta, set for the vertical and $f_c = 2\Omega \sin(\phi)$ the Coriolis parameter, where Ω is the rotation of the earth ($7.29 \times 10^{-5}\ rad\ s^{-1}$) and ϕ the latitude. ϵ_{ij3} is the Levi-Civita symbol, and ν is kinematic viscosity. Describing the momentum equation terms from left to right, the first term on the left-hand side represents momentum storage. The second term shows the advection of

momentum by wind. On the right-hand side, the first term describes gravity forces. The second term is the effect of apparent forces, the Coriolis force. The third term concerns the effect of pressure-gradient forces. The fourth term is the influence of molecular viscosity on motion. Lastly, the fifth term is the Reynolds' stress effect on motions. Altogether, eq. 1.19 has some simplification options for easier calculations of idealized cases. Other scalars such as moisture, heat, or gases concentrations follow a basic conservation equation depicted in eq. 1.20:

$$\frac{\partial \varphi}{\partial t} + \overline{U_j}\frac{\partial \varphi}{dx_j} = \frac{S_\varphi}{\rho} - \frac{\partial\left(\overline{u_j'\varphi'}\right)}{\partial x_j} \qquad \textit{eq. 1.20}$$

Note that S_φ can act both as source or sink and can be composed of several terms.

In the heat equation, potential temperature often proxies for heat and writes like:

$$\frac{\partial \overline{\theta_v}}{\partial t} + \overline{U_j}\frac{\partial \overline{\theta_v}}{\partial x_j} = -\frac{1}{\overline{\rho} C_p}\left[L_v W + \frac{\partial \overline{Q_j^*}}{\partial x_j}\right] - \frac{\partial\left(\overline{u_j'\theta_v'}\right)}{\partial x_j} \qquad \textit{eq. 1.21}$$

Where *W* signifies the mass of water vapor created from phase change per unit volume per unit time, thus negative for water vapor loss due to condensation. Q_j^* represents the net heat source related to radiation divergence, meaning the change in net radiation with height, mainly through either increasing LW upwelling by the atmosphere emission or reducing SW downwelling through scattering and absorption in the atmosphere.

1.2 Boundary layers

The planetary boundary layer (PBL) is part of the troposphere and directly interacts with the earth's surface. This section describes the different regimes and sections of boundary layers and a few typical flows relevant to valley winds, concluding with topography and complex terrain influence.

I will use the terminology for heights, as is common in aviation, meaning that the vertical distance of surface above mean sea level (amsl) is called elevation, a height means the distance above ground level, and altitude is the combination of the two, expressed in meters amsl. A small note is made on the word PBL height. In literature, it can be used for the altitude of the PBL top and the length of the PBL column. Duine & De Wekker (2020) propose to use PBL depth for the length of the PBL column and PBL height for the altitude of the PBL top.

1.2.1 Boundary-layer lifecycle

In contrast with the higher atmosphere layers, PBLs have a distinct daily cycle with highly varying depths, e.g., from a few 100 m (estimations) at night to more than 2 km at mid-latitudes during the day.

1.2.1.1 Daily cycle

The boundary layer is coupled with the solar cycle through surface heating. After sunrise, the sun starts to heat the surface and creates a convective boundary layer (CBL). Here, convection results from the instability due to a heated surface and colder air above, generally capped with a temperature inversion limiting growth. Growth of the CBL occurs at its top and arises through the entrainment and encroachment growth processes. Entrainment is the process of compensating air movements when an air parcel overshoots the equilibrium height at the CBL top and enters the layer above the CBL, mixing the layers and heightening the inversion. Encroachment is the process by which the CBL growth originates solely from surface heat flux, thus only causing growth in a CBL without an inversion. Entrainment is generally the faster process for CBL growth. At sunset, when the energy input for

convective mixing stops, under clear-sky conditions, a nocturnal or stable boundary layer (SBL) starts around sunset. Under cloudy or windy conditions, it remains more neutral. The layer between the top of the newly formed SBL and the top of the former CBL is called the residual layer and is initially neutral.

Regardless of the time, the bottom 10 % of a PBL is called the surface layer. Figure 1.4 shows a typical, mostly clear-sky day with all different components of a PBL.

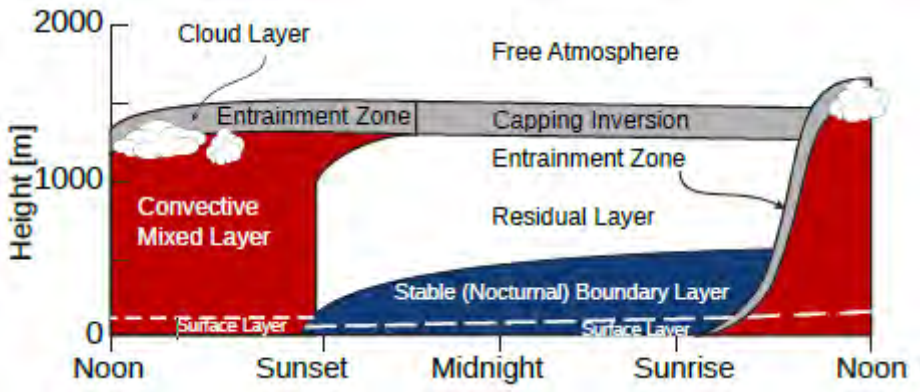

Figure 1.4: Diurnal cycle of a planetary boundary layer, with focus on one night. Graph originates from Stull (2009) and reprinted with permission from Springer.

1.2.1.2 Convective boundary layer

After sunrise, solar irradiation starts to heat the surface creating turbulent eddies due to instability and slowly increasing the CBL. At first, turbulence slowly integrates the SBL and then the residual layer by engulfing those layers with warm air parcels from the surface. Later, the fully formed CBL can nibble the free atmosphere (see Figure 1.4). In the free atmosphere, potential temperature increases, and the air is drier. Substantial gradients separate the free atmosphere and the CBL, suppressing fast CBL growth. During the overshoot period of entrainment, the thermals cause diffusion and mixing processes of the CBL with the air in the inversion layer, increasing the temperature and decreasing the moisture content. Altogether, in a CBL, surface fluxes bring both heat and moisture into the CBL through the surface heat flux and evaporation. At the same time, entrainment from the free atmosphere incorporates warm dry air, heating and drying the CBL. Leading to moistening of the CBL in the morning while the afternoon often dries, as more free-atmosphere entrainment occurs. Since in the morning the moist residual layer is entrained before, it reaches the free atmosphere in the afternoon.

1.2.1.3 Nocturnal boundary layer

The nocturnal boundary layer (NBL) starts when the solar radiation can no longer create convection and ends after sunrise when irradiation again creates convective turbulence. A nocturnal boundary layer cools from the ground and generally has less turbulence than a CBL since it lacks thermal convection created by solar irradiation. Because of cooling ground and reduced vertical mixing, the layer becomes stable. A different way of creating an SBL is by advection of warm air over a cold surface; however, I will not focus on this SBL type. Section 1.2.2 details the typical size and profiles, and 1.2.4 describes dominant processes in an SBL. Favorable conditions for SBL development are clear skies for radiative cooling and wind speeds low enough not to displace the cooled air but fast enough to create mechanical turbulence.

1.2.2 Vertical profile and depth

The previous sections already mentioned several profile structures because those are important for the SBL formation or CBL growth. I will describe the profiles and depths of mature stages in the PBL, starting with the CBL and then the SBL.

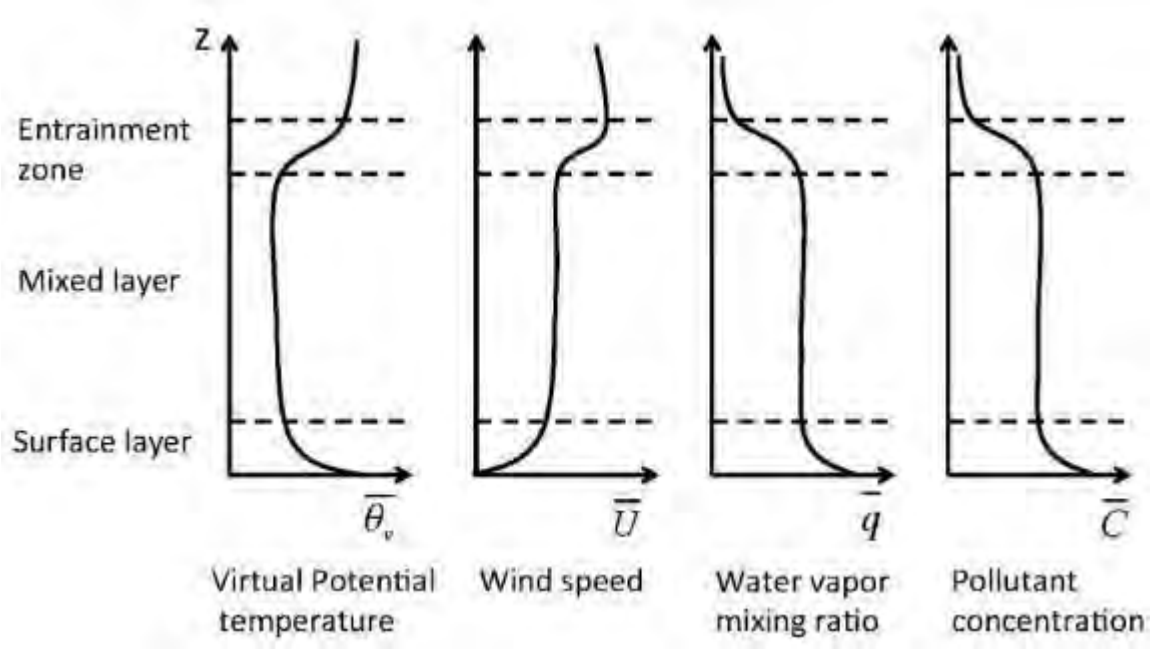

Figure 1.5: Typical vertical profiles of a mature convective boundary layer for temperature, wind, moisture, and other variables (or pollutants). Figure originates from Stull (2009) and reprinted with permission from Springer.

Figure 1.5 shows typical profiles of the CBL for different variables. PBL depths at mid-latitude reach 1-2 km maximum, peaking around noon or in the afternoon. In some desert areas, maximum CBL depths of 5 km can occur (Xu et al., 2018). Later in the day, turbulent eddies are still created but no longer reach the maximum height, leaving a neutral residual layer with less turbulence. In the residual layer, the air is well-mixed, similar to the recently decayed CBL, and values resemble the CBL since it was part of it.

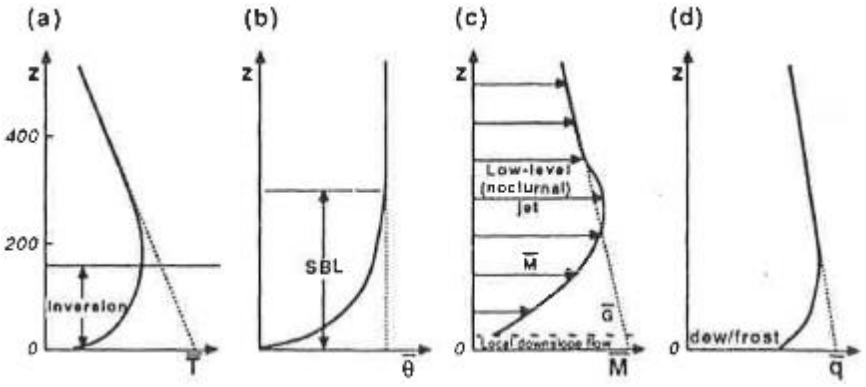

Figure 1.6: Typical profiles of the stable boundary layer of the mean (a) absolute temperature, (b) potential temperature, (c) wind speed, and (d) specific humidity. Figure originates from Stull (2009) and reprinted with permission from Springer.

In contrast to the CBL, Figure 1.6 shows the profiles of a mature SBL, which has its deepest stability at the surface and gradually becomes more neutral towards the neutral residual layer, having maximum depths around 200-400 m. It is classified as a temperature inversion when the stability is strong enough to increase T with height (Figure 1.6a). In that case, the SBL is synonymous with the nocturnal inversion.

Momentum has the same quasi-logarithmic profile near the surface as during the CBL, however, due to the reduced amount of vertical turbulent transport the wind speed near the surface is generally lower than during daytime. Sometimes, decoupling from the surface drag can lead to a small peak in the wind speed at the height where the wind would return to geostrophic values (Figure 1.6c). This peak is called a low-level jet.

Moisture in the SBL (Figure 1.6d) has a similar profile to θ (and θ_v) with a low near the surface in case of condensation, and a slow increase towards the residual layer, again decreasing towards the free atmosphere. However, the surface can continue to evaporate after precipitation or with dry air above. Note that when relative humidity is high enough, cooling can generate a fog layer close to the surface.

In contrast to the CBL, the SBL does not have an inversion cap, however for pollutant or dispersion calculations it is required to have an estimate of the PBL thickness h. The determination of h is therefore difficult. Several methods exist to estimate the layer depth. The most accessible options are to look for a particular condition with height, e.g., when stability becomes neutral or to consider the height of an LLJ. However, these methods are uncertain because the SBL often does not exactly meet these conditions but only approaches them, making them difficult to use. Stull, 2009 describes several other options and methods in detail.

Lastly, I point out the difference between the turbulence in the CBL and SBL. While buoyancy is the driving factor in the CBL, it is a sink of turbulence in the SBL. The SBL turbulence is produced through wind shear only (Stull, 2009). At night, turbulence is often patchy and intermittent, meaning that mixing happens locally and sporadically. Still, when averaging over long enough periods (hours) reliable values of fluxes, representative for larger areas can be obtained. In the SBL, turbulence is relatively independent of surface processes, and a surface forcing needs 7 – 30 h to influence the upper part, compared with 10 – 15 min across the CBL (Stull, 2009).

1.2.3 The surface layer

As mentioned before, the surface layer is either defined as the lowest 10 % of the PBL, or the layer where turbulent fluxes do not significantly vary with height, or the location where the log profile of wind is valid. It is here that, the vegetation influences the different fluxes. At the bottom of the surface layer, the exchange between the soil and atmosphere occurs in the microlayer, where molecular diffusion is a more effective transport mechanism than turbulence, with a depth of a few mm to centimeters.

Since relevant parameters evolve slowly in the surface layer, similarity theories with diagnostic descriptions can be used to represent the profiles. The most well-known is the Monin Obukhov similarity theory (MOST; Monin & Obukhov, 1954). The MOST relies on the friction velocity u_*, defined as $u_*^2 = \sqrt{(\overline{u'w'})^2 + (\overline{v'w'})^2}$. It is valid for both unstable and stable conditions, be it with less certainty for the latter as it has low friction velocity values. MOST applies in the surface layer and gives us an estimate of the profiles in this layer. Eq. 1.22 shows the application on the temperature gradient, but this form is adaptable for other variables, such as moisture or pollutants.

$$\frac{\partial \overline{\theta}}{\partial z} = \varphi_H\left(\frac{z}{L}\right) \frac{\theta_*^{SL}}{kz} \qquad \textit{eq. 1.22}$$

The superscript SL indicates the surface layer and the subscript '*' indicates the friction variant of the variable. *k* is the von Karman constant, the values of which range between 0.35 and 0.42. φ_H is the dimensionless potential temperature gradient in the surface layer, dependent on the measurement height (z) over the Obukhov length (L), defined in eq. 1.23. z/L is a stability indicator for the whole

layer up to height L. $z/L < 0$ indicates an unstable layer, $z/L = 0$ a neutral layer, and $z/L > 0$ a stable layer.

$$L = \frac{-\overline{\theta_v} u_*^3}{kg\left(\overline{w'\theta'_v}\right)} \qquad \textit{eq. 1.23}$$

Using the Buckingham Pi dimension analysis, it is shown that nearly all reduced variables are dependent on z/L, however L is not designed for calm wind conditions and other estimates are frequently proposed to replace it.

1.2.4 Processes and evolution of the nocturnal and stable boundary layer

In the energy balance of an NBL, processes such as subsidence and advection are relevant, while often irrelevant during the daytime because of the large influence of thermal mixing. Already introduced terms such as surface heat flux (see 1.1.4.2) and longwave radiation remain relevant even if their impact lessens. The near-surface $LW^{\uparrow}$ radiation value is lower than above, the radiation divergence becomes important at night. In NBLs, the net radiation can reach 100 W m^{-2} of outgoing energy under clear-sky and low greenhouse gas (mainly moisture) conditions. Cooling rates, resulting from this outgoing radiation, are in the order of 1-3 K h^{-1} at surface level, from where the cold air slowly propagates in the vertical through mechanical mixing. In comparison, radiative cooling of the air is typically around 0.2 K h^{-1} at 50 m above the surface. At the surface, heat passes through the microlayer, which is the only place where contributions from molecular heat conduction to thermal energy displacement are larger than the influence of turbulence. Above the microlayer, turbulence and radiation divergence cool the rest of the NBL.

Next, advection means possible temperature change because horizontally arriving air could have a different temperature, resulting in heating rates (Schaller and Wichmann, 1985). Carlson and Stull (1986) report values between -2 and 2 K h^{-1}, even though advection is potent, it is hard to quantify due to the interaction of abovementioned processes. Lastly, subsidence is the process of air moving down and bringing warmer air to lower levels as cooling causes the air volume to decrease. Vertical velocities at the top of an SBL can reach 0.1 to 0.5 m s^{-1} (Stull, 2009). All discussed heating rates can be in the same order of magnitude as radiation divergence. Because of the various possible contributions, it is thus ill-advised to ignore heat balance terms in the NBL, which are often not considered in the CBL, such as the discussed advection and subsidence.

Radiation, heat fluxes, advection, and subsidence are the driving forces behind all processes present in the SBL. Figure 1.7 shows prominent components and their interactions. A good understanding and description of these processes is necessary for high-quality models. Modeling in the SBL has more difficulty than in a CBL because of the smaller depth and smaller relevant scales. With more processes in a delicate balance, understanding all processes becomes crucial.

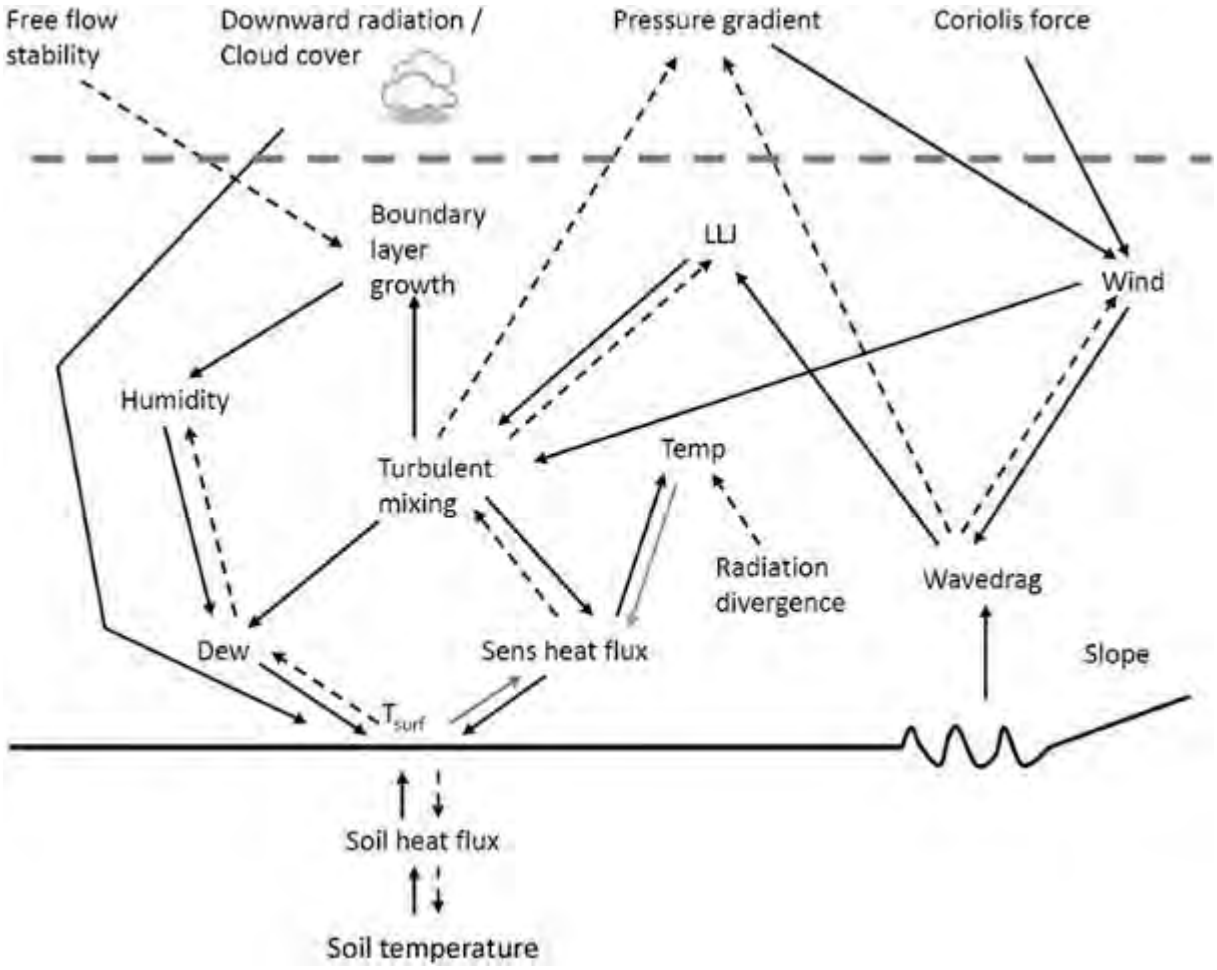

Figure 1.7: Schematic overview of physical components of a stable boundary layer, including their interactions. Positive feedbacks (—) are straight lines, and negative feedbacks (----) are dashed lines, grey lines could be either form of feedback depending on the state of the boundary layer —picture from (Steeneveld, 2014).

1.3 Effects of topography on air flow

This section discusses the topography effect, starting with slopes and valleys and ending with channeling and blocking. Concerning slope winds, 1.3.1 contains the explanation of thermally created slope winds on homogeneous surface. Under weakly stable conditions, the wind will follow the local gradients in the terrain (Haiden & Whiteman, 2005). Homogeneous slopes are rare, and airflows will interact over heterogeneous slopes. The most common example of confluent slopes is a valley, and its winds are called valley winds.

1.3.1 Thermally-induced slope flows

A simple interaction of topography with flows is the creation of slope flows. Facilitated by calm synoptic winds and clear-sky conditions, thermal wind exists in day and night conditions. At night an incline of 0.001 to 0.01 can generate wind speeds of 1 to 2 m s^{-1} (Wyngaard, 1978; Mahrt, 1981). These slope winds are subjected to a daily cycle under the influence of irradiation. They find their origin in horizontal temperature gradients, as shown in Figure 1.8, which displays an idealized slope wind on a homogeneous slope. During daytime (Figure 1.8a), solar radiation heats the surface, causing temperature and pressure to rise, creating less dense air relative to upslope air at the same height above the ground, resulting in an upslope wind. At night (Figure 1.8b), the opposite occurs, the surface cools, and the air becomes denser than a parcel of air at the same elevation further downslope.

Generally, nighttime downslope thermal winds are called katabatic winds. Since katabatic means downward, it is used for many other winds that do not necessarily have a temperature-related origin.

Other winds referred to as katabatic winds are foehn, bora, or winds forced over topography by large-scale pressure gradients.

Nocturnal slope flows are important because they need a very small inclination to appear and only large flat surfaces such as great lakes and seas do have slopes small enough to ignore their influence. They start forming as soon as sensible heat flux becomes negative, which happens depending on the slope angle, slope orientation, and local sunset (Nadeau et al., 2013). Nocturnal slope flows can remain in place as long as conditions remain calm and stable.

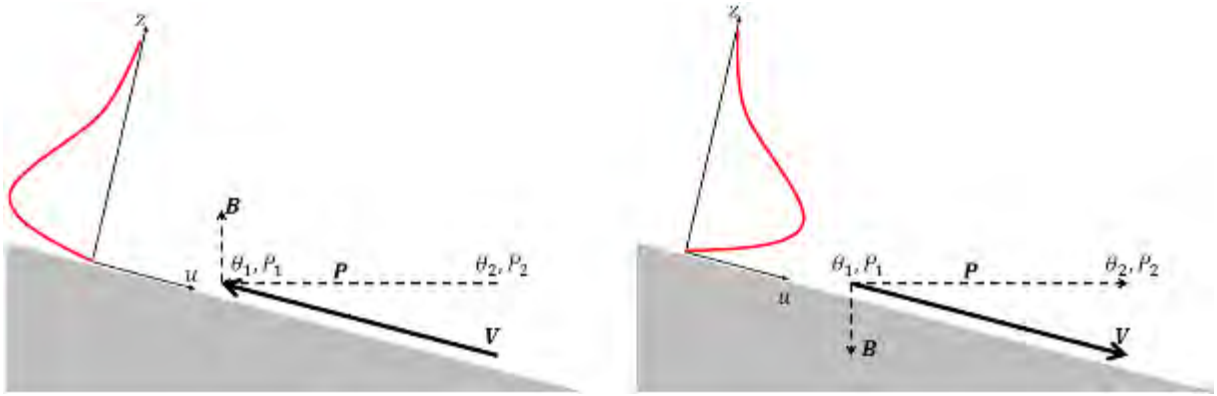

(a) Daytime: $\theta_1 > \theta_2$ and $P_1 < P_2$ (b) Night-time: $\theta_1 < \theta_2$ and $P_1 > P_2$

*Figure 1.8: Idealized schematic representation of slope effects on winds over a homogeneous slope in both clear day (left) and clear night (right) conditions. **V** is the wind speed, **B** is the resulting buoyancy force term, and **P** is the pressure force term. The red line indicates typical profiles of along-slope wind. Figure originates from Dupuy (2018)*

The following sections will talk about other flow impacts of mountains and valleys.

1.3.2 Valley flows

Valley winds are currents along the thalweg of a valley, including small valley-wall systems; generally, the name 'valley winds' is dedicated to thermal winds. However, other valley flows (see 1.3.5) can be referred to as valley winds as well. Without external disturbance, thermally created valley winds have two reversals of wind direction per day, around dusk and dawn. During nighttime, cold air drainage causes downslope winds. Typically, a thermal valley wind system consists of two sidewall flows to the center and a stronger along-valley flow. A small inverse flow around sidewalls height at the top of the along-valley flow may appear. An along valley flow can have wind speeds between 1 – 8 m s^{-1} (Neff & King, 1987). Typical wind speeds depend on valley size, stability, slopes, and its depth (Zardi & Whiteman, 2013). Section 2.1 describes our area of interest with the Durance valley and its tributary Cadarache valley. While peak speeds of 2 - 3 m s^{-1} are typical in the modest Cadarache valley, the Durance valley has peaks of 4 – 8 m s^{-1} (Duine, 2015). More detail of these valley winds is in section 2.3.2.

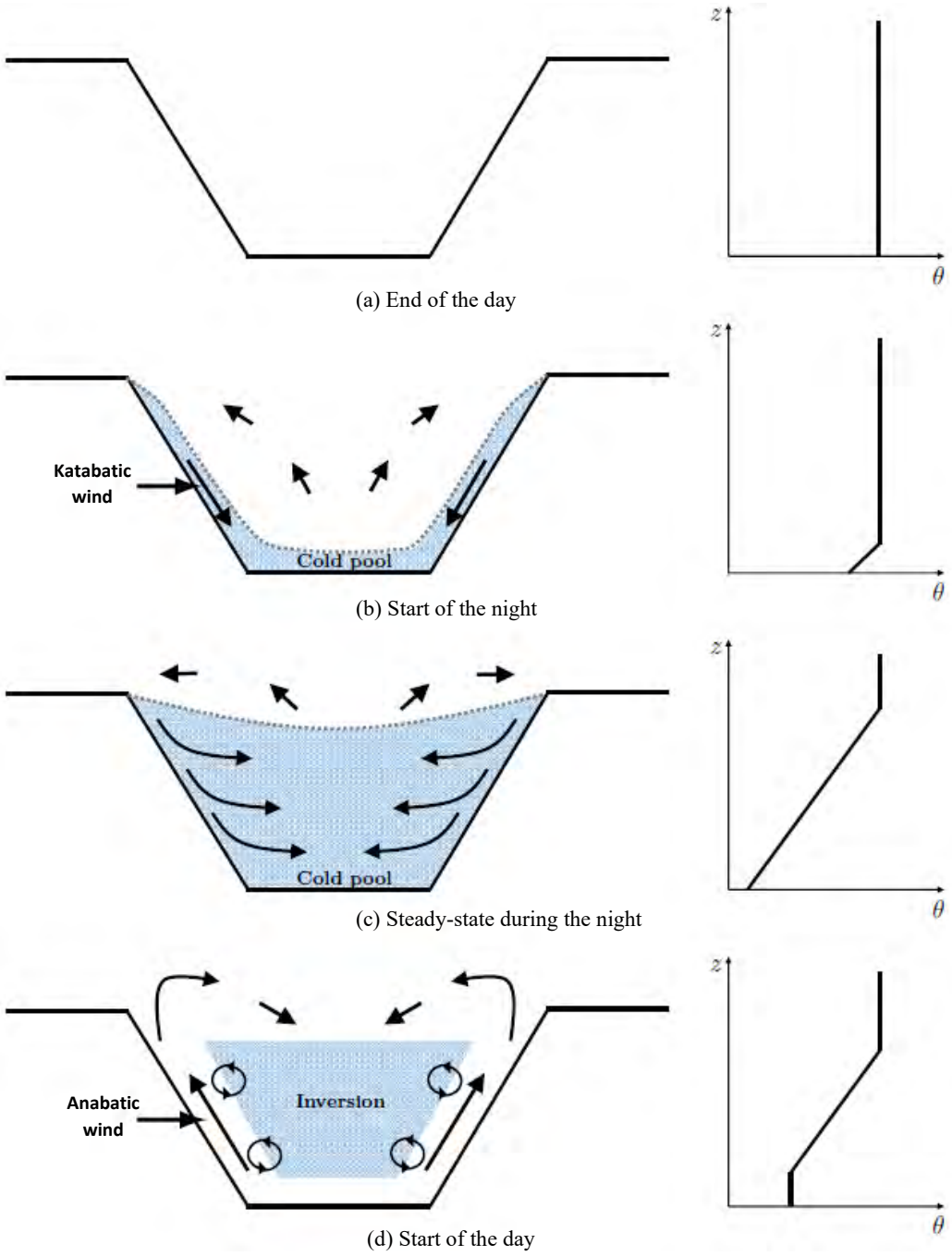

Figure 1.9: Cross-valley schematic overview of onset and dissipation of thermal valley winds and a cold pool. Based on (Stull, 2009)

Figure 1.9 shows the nocturnal part of the valley system's daily cycle, containing more complex processes than the day. When surface buoyancy flux becomes negative, the day-night transition starts, propagating along the thalweg from upslope to the lower sections (Duine, 2015; Giovannini et al., 2017). When the air begins to cool at night, it flows down and in case of stagnation, it creates cold air pools (CAP) at the valley bottom (Figure 1.9b and 1.9c), more details are in section 1.3.3. During the night, these pools keep growing until they reach the valley ridges. In a steady-state, subsidence should no longer play a significant role in the heat budget of the NBL system of the valley (Arduini et al., 2016). After sunrise, when irradiation becomes again strong enough to create a positive, sensible heat flux, the surface starts to heat and breaks down the CAP. Additionally, it is essential to see the valley system as a 3D system acting with the 2D processes from Figure 1.9 (Arduini et al., 2016).

Valleys have a broader heat range than flat areas with the same surface. A leading explanation is that less air needs to be heated in a valley than over a flat area due to geometric factors, sometimes called the Topographic amplification factor (TAF). (Steinacker, 1984; A. Wagner, 1932; Whiteman, 1990). Additionally, slopes lead to more surface in the valley, allowing for more radiation exchange, meaning more heat change for a smaller volume. Hahnenberger et al. (2009) show that the cooling rate ratios of a plain to a near-perfect meteor crater are within 10 % of the values expected based on TAF. However, the ratio does not hold under strong wind conditions. Even though the TAF assumption does not always apply, it remains an influential factor, especially around day-night transitions (Schmidli & Rotunno, 2010).

Thalweg or valley floor slopes are the principal factor in valley wind creation. However, numerical simulations of idealized valleys without a thalweg slope still create a valley wind daily cycle along the valley floor in fair weather conditions (Rampanelli et al., 2004; Schmidli & Rotunno, 2010; Wagner et al., 2015), showing that thalweg slopes are not the only factor creating valley flows. Rampanelli et al. (2004) explains that heat balance leads to a pressure difference causing valley flows even without a thalweg slope. In short, a u-shaped valley without a thalweg slope even can produce thermal-driven valley winds.

1.3.3 Classification of different types of valley flow systems

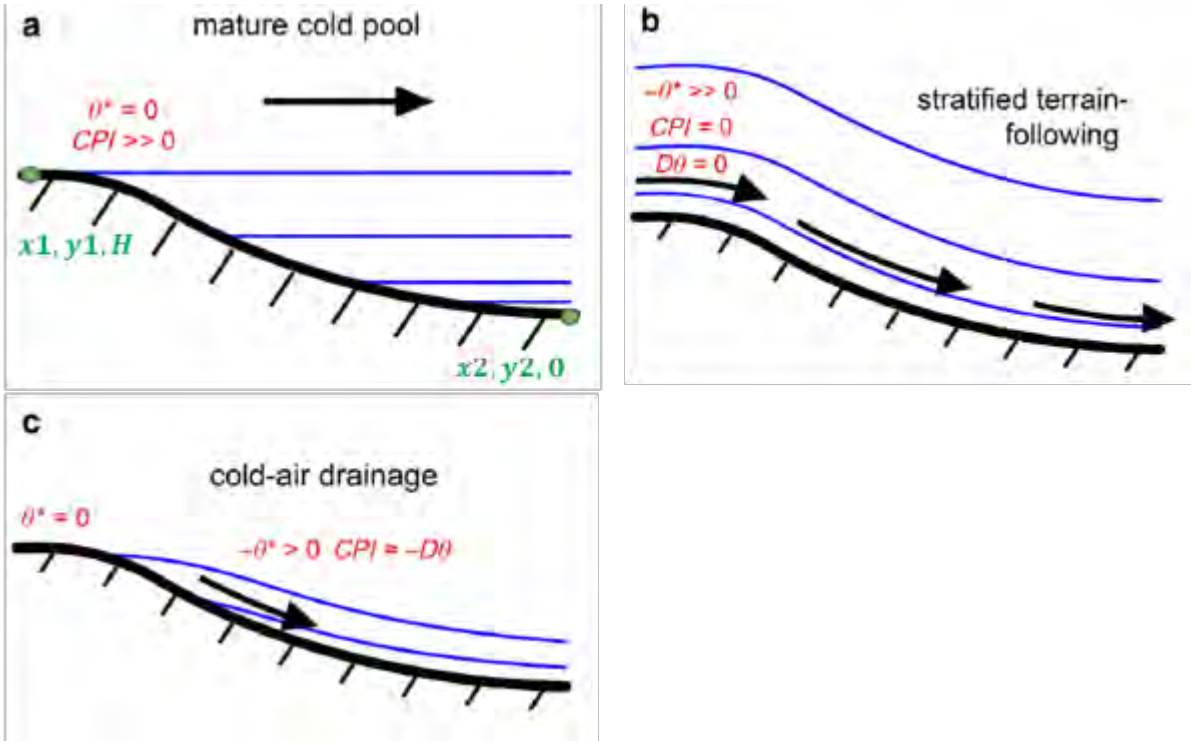

Figure 1.10: Possible forms of valley systems in stable night conditions; ***a)*** *Idealized cold pool where buoyancy effects theoretically vanish.* ***b)*** *Idealized terrain-following flow without CPI due to large-scale descending flows.* ***c)*** *Locally generated cold-air drainage with parcels cooling and crossing isentropic surfaces during their descent. These three systems are classified based on the cold pool intensity (CPI), a deficit of potential temperature at the top of the slope (-ϑ*) and parcel cooling along the slope (Dϑ). Black arrows indicate flow direction and the blue lines are isentropes. Figure originates from Mahrt, 2017.*

During nighttime, slopes and especially valleys may experience different types of flows, so can slope flows bring cold air to the bottom of a pool and cause stagnation in the valley. Following the work of Mahrt 2017 (Figure 1.10), I explain how to identify a mature cold pool, stratified terrain-following flows, and cold-air drainage with the use of three different quantities, the cold pool intensity (*CPI*),

potential temperature deficit (or stratification) at the slope top compared to the same elevation at the center of the valley (θ^*), and parcel cooling along the slope ($D\theta$), defined as:.

$$CPI \equiv \bar{\theta}(x1, y1, H) - \bar{\theta}(x2, y2, 0) \quad \textit{eq. 1.24}$$

$$\theta^* \equiv \bar{\theta} - \Theta \quad \textit{eq. 1.25}$$

$$D\theta = -L_s\left(\frac{\overline{w'\theta'}}{\partial z}\right)/U \quad \textit{eq. 1.26}$$

Where $\bar{\theta}$ is the average potential temperature at the top of a ridge $(x1, y1, H)$ and *H* the height above the valley floor located at $x2, y2, 0$, illustrated in Figure 1.10a. Θ is the potential temperature above the valley floor at the same altitude as a given station. L_s is the length of the path following the slope and U the representative downslope wind speed. Effectively, the absolute vertical difference in potential temperature can be expressed as $CPI - \theta^*$ (Mahrt et al., 2014).

The three main regimes are:

Mature cold pool

This regime is defined by horizontal isentropes, meaning that θ^* is near zero. Typical conditions that facilitate a mature cold pool are strong radiative cooling with little drainage flows along the valley; a mature cold pool does not necessarily span the whole depth of the valley.

Stratified terrain-following

This regime, as the name indicates, has isentropes parallel to the surface, meaning that the temperature remains constant at a constant height, resulting in a CPI close to zero and a considerable θ^*. In this situation, the above valley air flows into the valley and to maintain this system, the air should not cool along the descent, meaning that $D\theta$ is close to zero. Mahrt 2017 reports that shallow valleys are favorable for these types of flow systems.

Cold-air drainage

This regime describes flows that cool during descent, crossing isentropes. In its pure form, this cooling is the only process influencing the flows, causing the CPI to be roughly equal with the cooling ($-D\theta = CPI$), making it different from the terrain-following flows. This regime is generally found in the afternoon on slopes with shadows.

These are the three common systems; however, transitions and combinations of these three situations exist, for example, a marginal cold pool, which has a sizable *CPI* but $-\theta^*$ does not equal zero can become a mature cold pool later on.

1.3.4 Froude Number

Valleys are not the only way topography influences airflow. A tall mountain blocking a wind flow is a simple example of topography effects. A blockage can create several outcomes depending on three factors as described by Whiteman (2000):

- Stability of the approaching air mass
- Flow speed
- Typical geometry of the landmass

A neutral or unstable air mass will more easily flow over the obstruction. On the other hand, it is more complex to forecast the exact flow when the air is stable because vertical dodging is more difficult than horizontal. Nonetheless, the dimensionless Froude number (Fr, eq. 1.27) indicates what flow will be favored.

$$Fr = \frac{U}{NH} \qquad \textit{eq. 1.27}$$

Here U is windspeed, *N* is the Brunt-Väisälä angular frequency, and H is the blocking object's typical height length scale. Stull, 1988 and Whiteman, 2000 describe how flows behave with different Fr numbers. With $Fr < 1$, currents have difficulties passing over the mountain and stream around. Higher values indicate that air can proceed over the mountain more easily. If the obstacle is a mountain ridge and the flow layer is slightly higher than the ridge, the lee-side can exhibit a hydraulic jump when the flow layer is elevated enough, as a small area above the rise can have supercritical flow (Stull, 2009).

1.3.5 Various origins of valley flows

Additionally, where a ridge has a gap air can channel through, such as in a mountain pass (Figure 1.11a) or a valley (Figure 1.11b). Figure 1.11 displays these two situations with stable conditions (low Fr number). The wind has difficulties passing over the mountain and will flow around, leading to flow acceleration in the opening between mountain ranges. A well-known example of situations such as Figure 1.11a is the Mistral in southeastern France. In valleys, higher-up wind can move down and follow the valley orientation. In a situation similar to Figure 1.11b where the valley does not align with the above flow direction, the flows will make the slightest direction change possible. If these flows are powerful enough, a valley can have flow directions opposing the direction expected based on slope and thermal behavior as expected by the time of day.

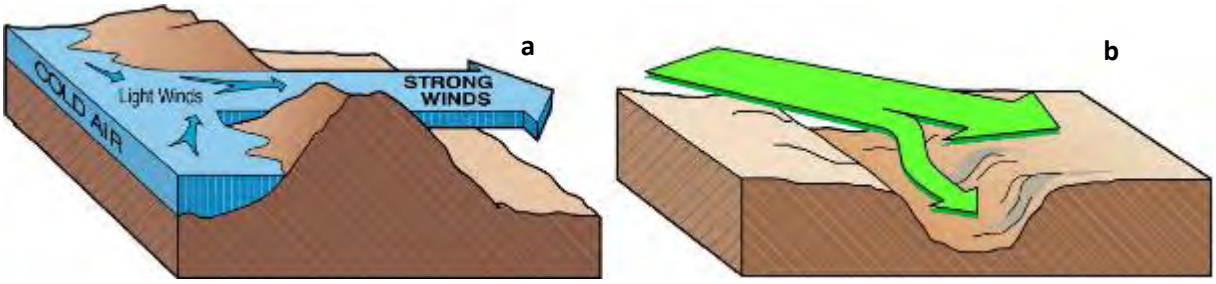

Figure 1.11: Schematic representation of flow canalization and acceleration through a mountain pass (left) and canalization of winds through a valley (right). (Whiteman, 2000).

Winds in a valley have more possible origins than just stratification and thermally induced flows, as discussed in section 1.3.1. Four principal driving mechanisms exist that cause winds in valleys (Whiteman & Doran, 1993). Figure 1.12 describes the four transport mechanisms in idealized form. Note that the above-valley wind is assumed to be geostrophic.

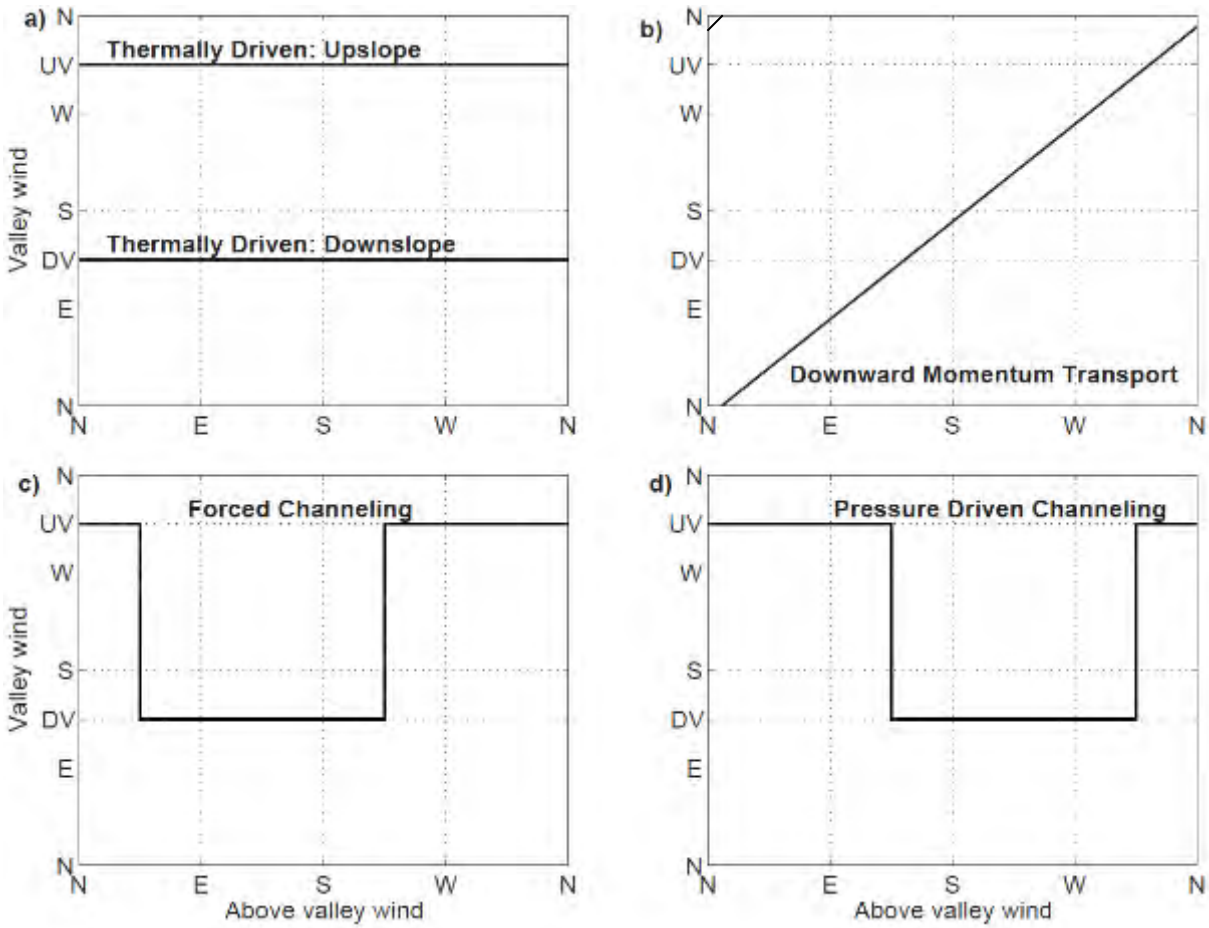

Figure 1.12: Different momentum transport options between above-valley flow and in-valley flows, based on a valley in northwest-southeast orientation, like the Cadarache valley, see section 2.2.2. Up-valley (UV) and down-valley (DV) on the y-axis indicate valley orientation. Graph adapted from (Whiteman & Doran, 1993).

Thermally driven wind (Figure 1.12a), was extensively discussed in previous sections. Winds in the valley follow the slope wind mechanisms. Forced by local gradients, the valley flow is completely decoupled from above-valley flows, flowing upslope in daytime and downslope during nighttime. For decoupling, clear-sky with low synoptic wind is beneficial. Similarly, the exact valley geometry plays a big part, as narrow valleys are more prone to decoupling. Figure 1.12a represents the relation between above-valley wind and in-valley wind. The valley is oriented similarly to the Cadarache valley (detailed description in 2.1.1).

Downward momentum transport (Figure 1.12b) is the second important mechanism that influences the wind direction between above-valley and in-valley winds. Momentum transport is driven mainly by vertical turbulence or gravity waves (Whiteman & Doran, 1993). After transport, the direction in-valley is close to the above direction, as depicted in Figure 1.12b by a diagonal line. Due to the friction at the surface, above and surface flows slightly change with the assumed geostrophic above-valley wind. A broad shallow flat valley is favorable for downward momentum transport, as low sidewalls do not block the transport and a thermal flow does not develop easily on a flat surface. In addition, convective situations enhance the vertical transport of momentum and thus direction.

Forced channeling (Figure 1.12c) mechanism describes wind forced into the valley with possible direction change because of topography. In the valley, the airflows follow the thalweg in either the upslope or downslope direction. Above winds force the current to flow with the closest resembling orientation, see Figure 1.12c. Narrow valleys under neutral or stable conditions favor flow channeling (Weber & Kaufmann, 1998).

Pressure-driven channeling (Figure 1.12d for northern hemisphere)**,** the fourth mechanism, describes how the geostrophic wind pressure components drive the valley wind. When the synoptic wind crosses the valley axis, the valley wind changes from up- to downslope (or vice versa), as shown in Figure 1.12d. It is possible to have counter-currents with pressure-driven flows, i.e., above-valley and in-valley flows have opposite directions (Weber & Kaufmann, 1998). Wide and shallow valleys with slight to moderate stability can have pressure-driven channeling as an essential component (Carrera et al., 2009).

1.3.6 Measurement campaigns on stable boundary layer flows

The BLLAST (Lothon et al., 2014), PASSY-15 (PACI et al., 2017; Staquet et al., 2015), NEWA-Perdigão (Wagner et al., 2019), MAP-Riviera (Rotach et al., 2004), COLPEX (Price et al., 2011), and ALPNAP (Heimann et al., 2007) campaigns focused on valley flows. Their data supplies observations for fine-resolution simulations of stable condition flows.

The BLLAST (Boundary Layer Late Afternoon and Sunset Turbulence) field experiment occurred from 14 June to 8 July 2011. Its main research goals were on daytime turbulence and its late afternoon and evening transitions. They focused on the "Plateau de Lannemezan", a few kilometers from the Pyrenean foothills in southwestern France.

Comparisons between LES (Large Eddy Simulation) and large-scale simulations do not show sizeable differences for the mesoscale winds during BLLAST (Udina et al., 2020). However, large-scale runs do not manage to reproduce realistic turbulent spectra. Even though LES produces too little TKE, it does produce realistic spectra and a correct TKE daily cycle. The LES with maximum horizontal resolutions at 111 m underestimated the daytime heat flux peaks and failed at night with the most negative fluxes. Part of the problem could be with many sub-grid processes and Udina et al. (2020) advise further research on both the vertical and horizontal resolution and the sub-grid scheme.

The PASSY-15 measurement campaign focuses on the deep Arve Valley in the French Alps and succeeded the GRENOPHOT campaign of 1999. PASSY-15 main goal was to understand return flows in prolonged cold air pools (CAPs) because these cold pools cause pollution to remain in the valley for several days. Zones prone to ventilation or stagnation were identified with methods described by Allwine & Whiteman, 1994. These analyses revealed that some tributary valleys become decoupled and no longer supply cleaner air to the central valley. In contrast, others still flow to the main valley but block the primary valley current, creating stagnation areas above the tributary valleys. Main findings show that more vertical grid points in models improve the representation of the boundary layer and thus the CAP.

To better understand the tributary valleys of the Arve valley, two simulations on idealized valley openings and the valley topography resembling the Arve valley were launched (Quimbayo-Duarte et al., 2019a, 2019b). These simulations showed that valleys with homogeneous slopes do not obstruct the flow of tracers from the valley; in contrast to valleys with a narrow section near the outlet, these valleys have stagnation of tracers in the valley upslope of the narrow section.

The NEWA-Perdigão campaign focuses on a complex terrain in southeastern Portugal and is part of the NEWA project. Their area of interest is the plain between "Serra da Estrela" and the Spanish "Serra de Gata" mountain ranges. In May-June 2017, they measured the valley winds and simulated 49 campaign days using LESs at 200 m horizontal resolution. The LES captures the day-night regime changes very well, but for unclear reasons, underestimates the wind speeds (Wagner et al., 2019). Future sensitivity runs will focus on land cover, forest parameterizations, and soil moisture. Van Veen (2018) applied the Cell Perturbation Method to reduce simulation times and found that it does not influence large-scale

wind structures. However, it improves the representation of the turbulent flows and small scales and allows smaller domain sizes, thus saving computing resources.

The Cold-Air Pooling Experiment (COLPEX) is a field campaign that was conducted from January 2009 to April 2010. Measurements were done in a hilly area close to the border of Wales and England. In this region, CAPs are common, and valley widths are typically 1-3 km, with differences between valley floors and tops ranging from 75 to 150 m. The primary study objective was to obtain information on the CAP formation and structure. Results commonly show CAPs with deepest values near the lowest valley point. Investigations show that each valley has a typical maximum stratification and temperature range. Simulating these nights with sufficiently fine-resolution well reproduces processes such as the nocturnal LLJ. On the other hand, SBL mixing (Jemmett-Smith et al., 2019) and wave activity remain very challenging for models (Jemmett-Smith et al., 2019; Vosper et al., 2014). Overall, the first 100 m resolution simulation shows plausible temperature distributions in the valley. However, the CAP formation and evolution remains a challenge due to the small-scale nature of the processes (Jemmett-Smith et al., 2019).

The RIVIERA field campaign focused on the Riviera valley in the southern Swiss province of Ticino in August 1999. Chow et al., 2006 simulated cases and performed several sensitivity tests on katabatic winds in the valley, starting with the effect of soil moisture. Comparisons of ECMWF soil moisture to water balance simulation (Water Flow and Balance Simulation Model; Jasper, 2001) concluded that more moisture in the soil decreases katabatic flow intensity because the humidity slows down cooling. All tests combined conclude that fine-resolution runs need more than fine topography and refined surface datasets for simulations to work well.

A measurement project of ALPNAP focused on the Adige Valley during the winter season of 2006, with a particular focus on near-surface temperatures. Fine-resolution runs with WRF perform poorly over snow, fail to create ground-based thermal inversions, and do not reproduce the thermal range between the sidewalls and valley floors (Tomasi, 2014). These errors are, in large part, attributable to the overestimation of the grid cell albedo. Tweaking the LSM parameterization scheme reduced these errors, leading to the decent influence of snow-related processes on the energy balance.

These measurement campaigns show processes similar to those encountered in our region of interest (Cadarache Valley; CV). However, their effects on the local meteorology are site-specific. A given site needs specific observations to understand the interactions between the synoptics, topography, and surface covers. Therefore, two measurement campaigns, called KASCADE, took place within the CV, described in 2.2.

1.4 Weather simulation strategies

Weather simulations can have several purposes: weather forecast for the public, aviation safety, or pollution dispersion, particularly in case of accidents.

Each of these purposes has dedicated model types. I address three techniques: the Lagrangian, Eulerian and statistical models. Most studies use an Eulerian model because they focus on a certain location, and only to a lesser extent to the destination of the flows, and I will use them in the rest of my thesis. Lagrangian models are flow following and are good for backtracking of pollution to its source. Artificial Neural Networks (ANNs) are an example of statistical models as explained in section 2.4.3, where I will address some work done with statistical modeling as done by previous PhDs.

1.4.1 The Weather Research Forecasting model

A well-known model in the weather research and forecast community is the WRF model. NCAR (National Centre for Atmospheric Research) maintains WRF and everybody is allowed to submit

additional codes to improve the model further. In 2008 V3 was released (Skamarock et al., 2008) with regular improvements and in 2019, a V4 (Skamarock et al., 2019) was released. Below is a summary of the important options and features of the Advanced Research WRF (ARW) model, starting with the domain set-up and continues with the different parameterization options, but see the technical note of Skamarock et al. (2019) for a full description

The part that solves the atmospheric flows is the dynamical ARW solver core. It uses a set of fully compressible non-hydrostatic Eulerian equations, including the Coriolis terms. At mid-latitudes, the default settings use horizontal discretization on a regular Cartesian grid with the Lambert Conic Conformal projection, with two options in vertical coordinate systems, namely, terrain-following or dry hydrostatic-pressure with optional vertical grid stretching. Several options exist in physics packages, allowing a large freedom of choice, making WRF an excellent model for research. Moreover, new additions are released a few times per year, bringing further improvements and new options.

WRF can only run with initial conditions created in the WRF preprocessing step (WPS). I will only discuss the 3D real case WPS steps, consisting of three steps. Its first step, “geogrid”, defines the 3D grid and interpolates static fields to these grids, such as land cover and elevation. A second independent step, “ungrib”, processes external weather analysis or forecast data from grib to WRF data format (NetCDF). Step three, “metgrid”, combines the domain of step one with the meteorological state files of step 2 and creates 3D snapshots at predefined intervals. Most variables are assigned to cell centers because they describe the cell state. However, the wind components are staggered in the grid, meaning that they are located on the cell boundaries, unlike other cell-centered variables. These velocities are defined normal to the grid cell boundaries to calculate the exchange between cells. These snapshot files continue to update the boundary conditions of the parent domain of a nested run.

Nested runs allow focus on areas within the grid by introducing a new finer grid within the original one. A subdomain or child domain is completely within the parent domain and can contain vertical refinement (new option). Child domains are aligned with grids of the parent domain and allow for any temporal refinement. For horizontal refinements any spatial integer ($\Delta x_{coarse}/\Delta x_{fine}$) is allowed. Initial variable states of child domains have four possible origins: interpolated from their parent domain, extracted from an external file, a combination of the two mentioned before, or in case of moving nests, the orography and land cover update as the domain moves. Regarding the boundary conditions and feedback of the child grid during the running, two main options exist, 1-way and 2-way nesting. In 1-way nesting, the parent domain functions as a lateral boundary forcing for the child domain but does not get feedback that would occur in the 2-way nesting. Two options exist for the feedback: it takes the averages of the child cells that covers a parent grid cell or it uses a single child cell as feedback.

The **physics packages** of WRF have a large diversity of choice. They include the processes of microphysics, cumulus parameterization, surface layer, land surface model, and planetary boundary layer and radiation, which describe additional processes or grid processes. The microphysics schemes cover the processes of water vapor, clouds, precipitations, and other mixed variables. Their calculation occurs at the end of the time-step as an adjustment process. It is advised to use mixed-phase schemes for resolution finer than 10 km as they can resolve updrafts, above all in convective or icing situations.

Cumulus parameterization describes the sub-grid interactions caused by convective and shallow clouds. These schemes work locally, meaning they only consider one column and do not interact on the horizontal plane. These columns represent the vertical fluxes of unresolved up- and downdrafts making moisture and heating profiles. Some schemes provide additional precipitation and cloud tendencies. In finer resolutions, the assumption of convection being a sub-grid interaction breaks

down. Generally, it should be turned off at resolutions smaller than 5 km. In comparison, the schemes can trigger convection at resolutions between 5 and 10 km. Note that some of the six options are scale aware and will turn off depending on the resolution or switch to shallow cumulus parameterization, where shallow-cumulus parameterization describes shallow clouds with scales smaller than the convective scales, meaning they can stay turned on at smaller resolutions.

Surface layer schemes are coupled to a specific PBL scheme. They calculate the friction velocities and exchange coefficients, enabling the calculations of surface heat and moisture fluxes by land surface models. All schemes work with the Monin-Obukhov similarity theory, with variations on the exact calculations of roughness length and coefficients. Diagnostic outputs of 2 m and 10 m quantities are consistently computed with the products of these schemes.

Land surface model (LSM) schemes use precipitation from microphysics and cumulus scheme, radiative forcing from the radiation scheme, atmospheric information of the surface layer scheme, and internal information of the soil to calculate the heat and moisture fluxes. These fluxes provide a lower boundary condition for the PBL schemes if operational. Otherwise, they provide their data to the vertical diffusion scheme in LES mode. In total, fifteen different options are available for LSM.

Planetary boundary layer (PBL) parameterization determines the sub-grid fluxes from eddy transport over the whole atmospheric column, not just the boundary layer and in any boundary-layer type. With horizontal resolution sizes below a few hundred meters, the assumption of sub-grid processes becomes less justifiable and the scheme can be replaced with a fully three-dimensional local sub-grid turbulence scheme (LES) such as the TKE diffusion scheme. In total, twelve different PBL schemes are available.

Lastly, **radiation** schemes provide atmospheric temperature tendencies caused by the radiative fluxes. The part for longwave and shortwave radiation schemes can be set separately. Here, the longwave part of the schemes considers infrared absorbed and emitted by clouds, surfaces, and gasses. In comparison, the shortwave schemes include the visible and surrounding wavelengths, including processes as surface and atmospheric scattering, reflection, and absorption. Possible additions of slope effects use the slope aspect angle. In the atmosphere, the radiation responds to modeled values of clouds, water vapor, CO_2, ozone, other prescribed trace gasses, and some allow for aerosol effects. All schemes are one-dimensional and thus only consider their vertical column for the radiation determination, which is a valid assumption at coarse grids where the vertical thickness is much smaller than the horizontal resolutions.

1.4.2 Known uncertainties with WRF

In recent years, the computing power has increased and therefore, allowed simulations with finer grids, giving rise to new challenges, such as the grey zones, also called “terra incognita”, indicating areas where a process is partially solved explicitly and remains partially sub-grid, thus needing parameterization. Similarly, as described above, the cumulus scheme has its grey zone at a resolution between 8 km and 500 m. Weisman et al., 1997 found that 4 km resolution grid sizes are fine enough for explicitly solving mesoscale weather. Jeworrek et al., 2019 summarized that explicitly solved convection provides a better land-atmosphere interaction (Mahoney, 2016), while for coarser grids, parameterizations have better precipitation estimates.

Another limitation of coarse resolution runs is that results are only one average value representing an area, which can contain a lot of spatial variability. Similarly, the simulation input is averaged to a coarse resolution representing all location variations. Topography and other surface characteristics become smooth and reduce the real gradients. However, steep slopes (>30°) cause numerical instability with

WRF default settings; thus, smoothening is required, which is only a problem in finer resolutions simulations.

Another problem that frequently occurs in simulations is the overestimation of LW↓ (Cerenzia, 2017; Kleczek et al., 2014; Steeneveld & de Bode, 2018; Sterk et al., 2013; Velde et al., 2010) likely related to emission errors due to too much moisture or too high temperatures in the upper atmosphere.

Surface variables are sensible to the soil parameters and especially soil moisture. However, fine-resolution maps of soil moisture content are not common, but they can be made with long-term simulations as they slowly refine the coarse water maps to local water balances.

1.4.3 Fine resolution runs

Fine-resolution, often called high resolution, describes simulations with the smallest mesh size at ranges below 1 km, often down to 100 m. Recently, a few WRF users started LES simulations down to 2 m mesh size (Wiersema et al., 2020). Still, these studies are exploratory as no clearly defined method exists to couple coarse domains of the model runs with the fine-scale domain.

These fine resolutions require equally fine input maps, primarily for topography and land cover, soil moisture, and soil types. Topography maps are relatively easy to find and even exist freely available with 1 arc second mesh for the world (Mukul et al., 2016). However, land cover maps are harder to find and change faster. Land covers are diverse and WRF has a specific way to aggregate these to its domain sizes. In Chapter 3, I will address this problem in more detail.

Several methods exist to overcome the turbulence grey zone. Some studies try to avoid the zone altogether; they use nesting ratios of 9 or large to directly go from 1 km resolutions to 111 m or smaller (Chow et al., 2019; Wiersema et al., 2020). At these resolutions, the vertical coordinate system is converted to an IBM (Immersed Boundary Method) approach preventing too steep terrain slopes and the accompanying numerical instability. Another option simulates the outer domains and only uses them as boundary conditions for the inner domains that no longer use parameterizations as demonstrated by Quimbayo-Duarte et al. (2021). In contrast, other options use schemes that are scale aware boundary-layer schemes, meaning a parameterization that adjusts for the size of horizontal resolution (Zhang et al., 2018). I test the integral and typical turbulent length scales before deciding what method I applied to the fine resolution runs.

Altogether, fine resolution runs pose new challenges and several methods exist to tackle them.

Chapter 2

Presentation and analysis of field campaigns in the Cadarache region

This chapter firstly details the site characteristics and its typical weather situations. Secondly, various measurement campaigns conducted in the region, especially the "KASCADE" campaigns of 2013 (KAS13) and 2017 (KAS17), are presented. The associated work of GJ. Duine (Duine, 2015) and F. Dupuy (Dupuy, 2018) carried out to characterize and nowcast the valley winds is also summarized. Finally, some new analyses of the KASCADE observations are presented, which were achieved in the frame of this thesis to complement the previous work and support the fine resolution WRF simulations.

2.1 Site description and typical winds

This paragraph describes the surroundings of the Cadarache and Durance valley to understand the local winds and other weather conditions typically present in the valleys.

2.1.1 Topography

The braided Durance River forms the Durance Valley (DV; Figure 2.1a). It flows from the Alps to the Rhône River and consists of three sections. The middle valley section is delimited by "Clue de Sisteron" ("Clue" means water gap in regional French) upstream in the north and "Clue de Mirabeau" downstream in the south. From the "Clue de Mirabeau", the up-valley direction is roughly NNE (30°), its thalweg has an average slope angle of 0.2° over a length of 67 km. The width of DV is roughly 5 km, widening to 8 km and narrowing to 200 m at Clue de Mirabeau. The elevation of the valley bottom is around 250 m above mean sea level (amsl) near Cadarache. In the middle valley section, the aspect ratio, defined as depth over width, is approximately 0.04; however, it varies along the valley up to 0.15 near the "Clues". About 7 km upvalley of the "Clue de Mirabeau", on its east bank, the DV receives the tributary Cadarache Valley (CV), as shown in Figure 2.1c.

The CV is oriented roughly SE upslope (127°), almost perpendicular to the DV. It has a width of about 2 km and is 5 km long, with an aspect ratio of 0.05. The slope along the thalweg is 1.2° and the sidewalls have around 6° steep slopes. Here, the valley is occupied by a mix of forest, grassland, and artificial surfaces, as shown in Figure 2.1b. The research facilities of CEA Cadarache occupy the CV and its confluent zone with the DV.

Other orographic features (Figure 2.1a) are noticeable in the region of the CV. The tallest features close by are the Southern Alps, with a height of 1500 m at 70 km to the NNW and 3000 m at 90 km to the NE, which is a distance that can influence local weather conditions under weak synoptic gradients (Jiménez & Cuxart, 2014). Closer in the region, two mountain ridges are present with an east-west orientation, the Luberon and Sainte-Victoire. With peak elevations between 900 and 1150 m, these ridges influence regional airflows. Closer by, the water gap "Clue de Mirabeau" is bordered by the

658 m high “La Vautubière” ridge SW of the CV. In particular, the “Clue de Mirabeau” enhances cold air pool forming. Lastly, on the northeast CV sidewall, the Maladroit hill (Figure 2.1c) has an elevation of 394 m. It is around 110 m above the valley floor level.

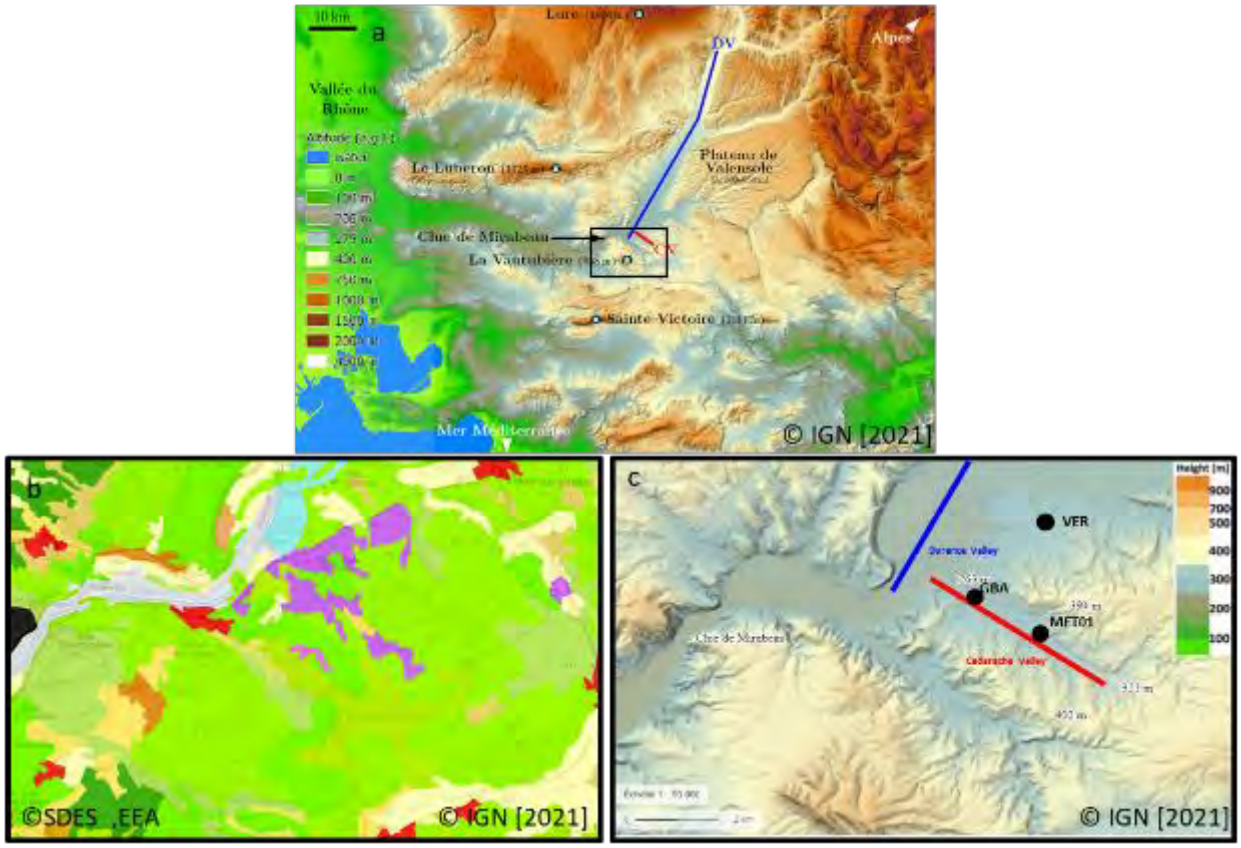

Figure 2.1: Topography around the area of interest (a), with additional zooms of the black rectangle focusing on the land cover, plotted over a map with major roads (b) and Cadarache valley topography (c). (see Appendix of the reproduced article in Chapter 4 for nomenclature of land cover categories). Based on https://www.geoportail.gouv.fr/ and https://land.copernicus.eu/pan-european/corine-land-cover/clc2018.

2.1.2 Typical weather conditions

From the 110 m agl anemometer of the GBA pylon (see Figure 2.1c), situated above the CV ridges, the wind rose in Figure 2.2 shows the wind direction and intensity from 17 February 2015 to 17 February 2016. Many of the winds have western origins; a second peak represents winds coming from the northeast. Lastly, there is a small spike of winds from the southeast. The origins of the three most frequent directions of the wind rose are commented below.

SW to NW winds

The general westerly circulation of mid-latitudes, channeled Mistral and summer sea-breeze, all contribute to the spikes of the wind rose with a westerly component. The Mistral is a well-known wind that is common in the Rhône Valley and the Provence region. It is a northern originating wind channeled between the Alps in the east and the Massif Central in the west. This channeling typically results in a cold and dry wind that can reach 100 km h^{-1}. In the CV, the Mistral comes from the northwest when it fans out as the Rhône valley widens while approaching the Mediterranean Sea and channeled through local valleys. Sea breezes from the Mediterranean Sea can enter the middle DV section in summertime, taking a western orientation.

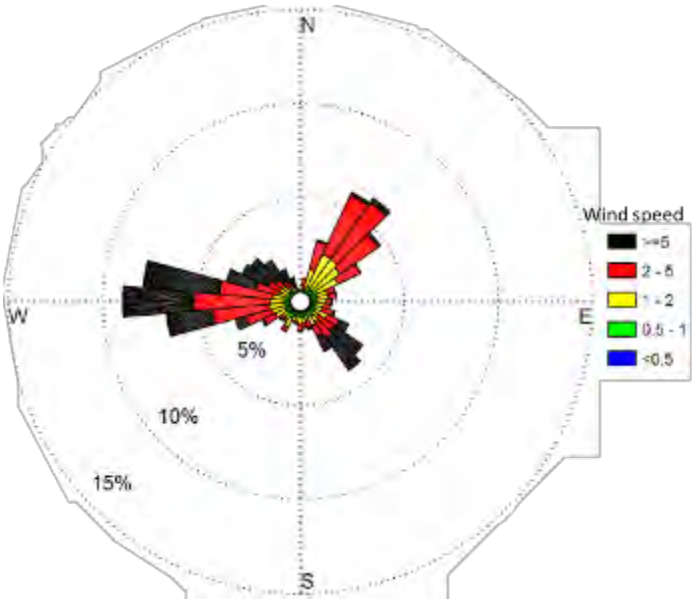

Figure 2.2: Wind rose at 110 m agl from the GBA in the Cadarache valley, from 17 February 2015 to 17 February 2016.

NE winds

For a large part, these winds are mesoscale or buoyancy-driven flows channeled by the orography, as explained in 1.3 matching the northeast DV orientation. The broad valley allows near-surface katabatic winds deep enough to reach the 110 m measurement height. In contrast, I will explain later that the valley winds emerging from the CV do not attain a comparable height.

SE winds

Winds from the southeast are often correlated to moist air and rain. Heavy rains are frequent in spring and early autumn when evaporation is large over the Mediterranean and convection/thunderstorms can be intense. However, rain events are not limited to these times.

2.1.3 Relevant field campaigns in Southern France

Before discussing the campaigns themselves in the valleys, I start with a few campaigns in the surroundings. ESCOMPTE (Cros et al., 2004) and HyMeX (Ducrocq et al., 2014) campaigns took place in southern France in areas overlapping with our study area.

The ESCOMPTE campaign had its primary interest in the chemical composition of the atmosphere around Marseilles and photo-oxidant pollution episodes in summer. The campaign focused mainly on land-sea breezes and their interactions with Mistral. There was limited interest in the very different local winds, for they are less essential in composition changes. However, it showed that Mistral and sea-breezes are common in the Cadarache region.

HyMeX investigated the moisture cycles at the Mediterranean coast of Spain, France, and Italy. Most heavy precipitation events are quasi mesoscale events, and 40 – 60 % of their moisture originates from evaporation over the Mediterranean Sea (Ducrocq et al., 2014). These events occur primarily in autumn, when the sea surface temperatures are still relatively warm.

2.2 KASCADE field campaigns and major findings

KASCADE is the acronym for “KAtabatic winds and Stability over CAdarache for Dispersion of Effluents”. Two measurement campaigns, KASCADE-2013 (KAS13, from 13 December 2012 to 18 March 2013) and

KASCADE-2017 (KAS17, from 17 December 2016 to 11 March 2017) were built to improve the knowledge of the local meteorology, especially in the CV and DV during stable conditions.

KAS13 focused on the existence of valley flows, their depth, the timing of their onset and disappearance, and their interaction during stable night conditions. Even though stable nights occur year-round, long winter nights are beneficial for SBL development. In complement, KAS17 focused on the spatial heterogeneity within the CV by instrumenting two cross-sections of the CV on its bottom (thalweg) and sidewalls (Figure 2.3), allowing research on the temperature distributions and surface wind of the valley and sidewall slopes. Their measurement stations and main findings are described hereunder. Having presented the general context and measurements carried out during KASCADE, the next paragraphs are dedicated to data analyses and the revealed flow characteristics.

2.2.1 Instrumentation layout of the KASCADEs

This section describes all stations that are available during both KASCADE campaigns. I discuss five main types of measurement stations, the Local Energy-budget Measurement Stations (LEMS), the Sonic Anemometers (AS), the Sodar (SOD), the balloons, and other types. A full description of the stations can be found in Annex 1: "Detailed description of the meteorological stations of KASCADE 2013 and KASCADE 2017", and here I present the data in a condensed form.

Table 2.1 summarizes all measurements of the KASCADEs, and Figure 2.3 displays their location during KAS17. One cross-section is along the valley thalweg and the second perpendicular to it, going from one sidewall to the other sidewall. Additionally, a few stations are placed outside the valley and on the top of the CV ridges. One measurement location, AS5, stands outside the CV to measure DV winds upslope in the confluent zone, close to the VER station.

The LEMS employed during KAS17 were developed and installed in collaboration with the University of Utah (Gunawardena et al., 2018). They were relatively simple to set up and measure many parameters; therefore, twelve LEMS were spread over the valley to investigate the spatial variation within the CV. Blue dots indicate their locations in Figure 2.3, and their names consist of a letter and a number. The letters indicate the valley slope type, namely bottom (B), north wall (N), or south wall (S), and all three have numbers 1-4 from the lowest to the highest elevation. They formed the largest share of measurement stations and S1, S2, B3, N1, N2, and N3 composed the perpendicular cross-section on the sidewalls. N1 also got a 2D sonic anemometer halfway through KAS17 to determine the threshold speed below which the cup anemometers no longer produce a reliable output.

The AS type stations represented the five Sonic Anemometers of KAS17 (red dots in Figure 2.3), four of them located along the CV axis. These stations measured the three wind components at roughly 2 m above the ground. AS3 was located where the cross-sections met (near B3), and it had additional sonic anemometers at 5 and 10 m agl on a mast called MET02. The AS5 station stood in the DV, just upstream of the CV confluent zone. At the AS1 site, close to B1 and the ANTEE station, a LICOR 7500 complemented the fast measurements with the moisture and CO_2 concentrations and a set of radiation balance measurements together with a soil heat-flux plate offered the possibility to do a complete energy balance at this spot. The additional rain gauge allows for the important part of the water balance.

Table 2.1: Summary of the available measurement stations, full detail of the measurement locations, heights and equipment is given in Annex 1: "Detailed description of the meteorological stations of KASCADE 2013 and KASCADE 2017".

Name	KAS13	KAS17	Permanent	Station type	Height; Measured quantities	Additional information
B1	-	Yes	-	LEMS	-0.25 m; T_{soil}, vwc -0.05 m; T_{soil}, vwc 1 m; P 1.5 m; RH, T 1.8; $SW^{\downarrow}$ 2 m; WS, WD 0; T_{skin}, $LW^{\uparrow}$	
B2	-	Yes	-	LEMS		
B3	-	Yes	-	LEMS		
B4	-	Yes	-	LEMS		
N1	-	Yes	-	LEMS		Got additional 2D sonic anemometer
N2	-	Yes	-	LEMS		
N3	-	Yes	-	LEMS		
N4	-	Yes	-	LEMS		
S1	-	Yes	-	LEMS		
S2	-	Yes	-	LEMS		
S3	-	Yes	-	LEMS		
S4	-	Yes	-	LEMS		
SOD1		Yes	-	SOD	75 – 500 m; WS, WD	Remtech PA2
SOD2	-	Yes	Yes	SOD	60 – 400 m; WS, WD	Metek PCS.2000-24
AS1	-	Yes	-	AS	2 m; U', V', W', T_{son}	Measures CO_2 and H_2O fluxes and radiation set (ANTEE)
AS2	-	Yes	-	AS		
AS3	-	Yes	-	AS		Three measurement heights (2, 5, 10 m), relocated at MET01 after KAS17
AS4	-	Yes	-	AS		
AS5	-	Yes	-	AS		In the DV
GBA	Yes	Yes	Yes	Other	2 m; RH, T, P 110 m; T, WS, WD	Near the confluent zone of CV and DV
ANTEE	-	Yes	-	Other	2 m; $SW^{\downarrow}$, $SW^{\uparrow}$, $LW^{\downarrow}$, $LW^{\uparrow}$	At the B1 site
VER	Yes	Yes	Yes	Other	2 m; P, RH, T 15 m; WS, WD	In the DV
M30	Yes	-	-	Other	See Table A1	Same location as MET01
MET01	-	Yes	Yes	Other	2 m; $SW^{\downarrow}$, P, T, RH, Rain 10 m; T, WS, WD	Started before KAS17
Radio-sondes	Yes	Yes	-	Balloon	P, RH, T, WS, WD	Released close to M30
Tethered balloon	Yes	-	-	Balloon	P, RH, T, WS, WD	0 – 300 m in KAS13, at M30 site

SOD indicates a Sodar installation. KAS13 had one Sodar station (Remtech PA2) measuring the vertical profile of the wind roughly from 75 m to 500 m agl. It stood outside the CV, in the DV near the permanent VER station. In KAS17, two Sodars measured the winds (green dots in Figure 2.3). One (measuring between 75 and 500 m) stood near GBA in the DV and CV confluent zone, another in the

CV center near MET01 (measuring between 60 and 400 m). After KAS17, SOD2 remained in place until it was taken down for maintenance in the summer of 2019. In the summer of 2021, it was relocated near GBA. Sodars are mostly used to investigate above valley winds, especially the Durance down valley flows.

Lastly, several meteorological sites deserve a little more attention, the VER, GBA, ANTEE, and MET (M30, MET01) sites. Starting with VER, the abbreviation of “La Verrerie”, it is a meteorological field outside the CV, on a left bank smooth slope of the DV. VER measures wind at 15 m agl and temperature at 2 m, supplemented with atmospheric pressure and relative humidity, resembling a typical weather station. The GBA indicates a site called “La Grande BAstide”, a meteorological site since the ‘60s, with a 112 m tower. The continuous observations are the temperature, atmospheric pressure and relative humidity at 2 m and temperature, wind speed and wind direction at 110 m. The top of the GBA is above the CV ridges and able to observe the above valley flows. During KAS17, the measurements of the site were enriched with a radiative energy balance measurement station (ANTEE). The MET01 site hosted two different stations, the M30 during KAS13 and MET01 since February 2015, described in more detail below. After KAS17, the MET02 mast was taken down and the sonic anemometers placed to MET01. Additionally, it was the site for the tethered balloon and radiosondes releases during both KASCADEs.

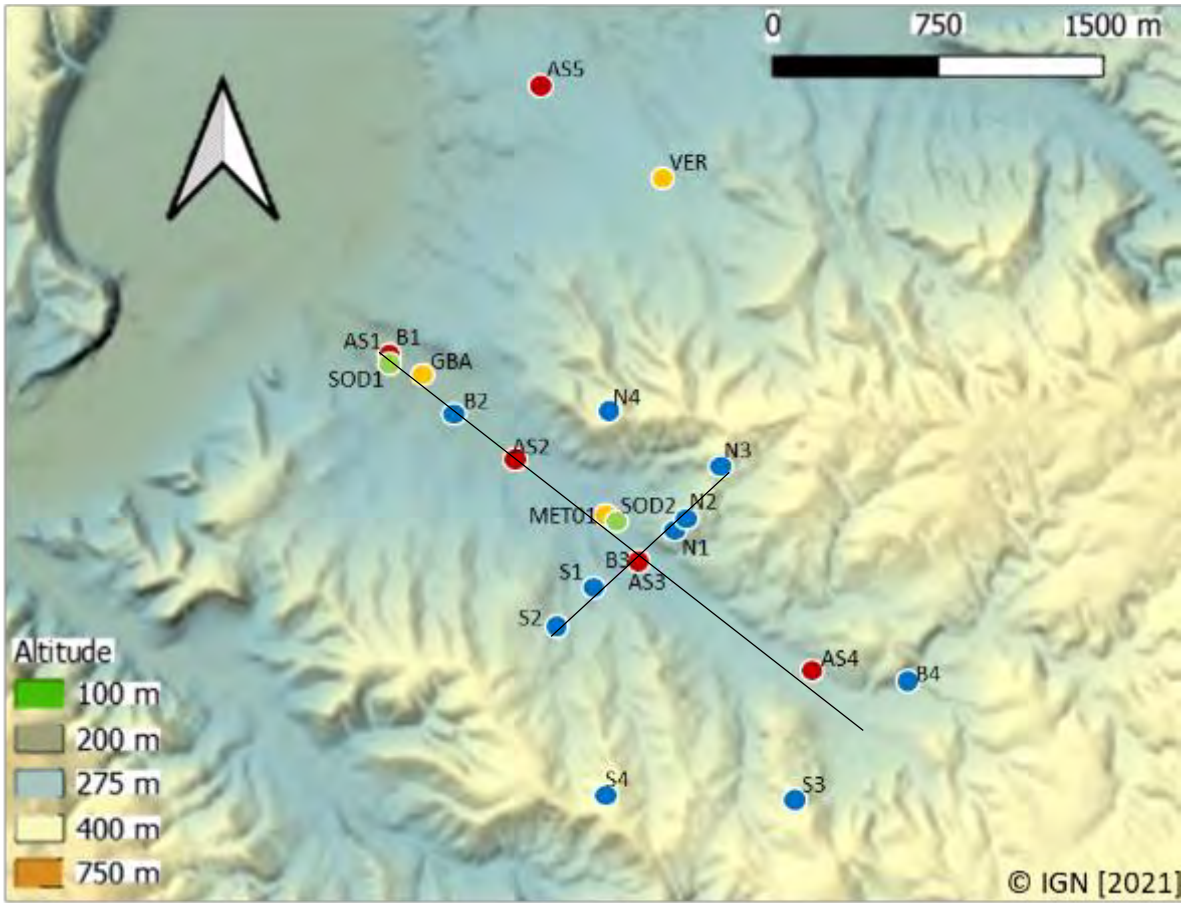

Figure 2.3: Heightmap with the location of KASCADE 2017 measurement equipment. Orange dots indicate permanent stations, red dots show Sonic anemometers, blue dots indicate LEMS, and green dots show the Sodar locations. Note that the site of MET01 is the location of M30 during KASCADE 2013. Two black lines indicate the cross-sections made with measurement stations in the CV.

During KAS13, the MET01 site hosted M30, a 30 m flux tower, which measured wind with sonic anemometers at 2, 10, and 30 m, the radiation balance at 2 and 20 m, and temperature and relative humidity at 2 and 30 m. A fast hygrometer was installed at 30 m. To avoid influence of the tower on the radiative measurements, the 2 m agl irradiation set was placed at a 25 m distance. Table A3 shows the MET01 site development up to the fall of 2021. It was built in February 2015 (about one and a half years before the start of KAS17) with measurements at 2 m of atmospheric pressure, temperature, relative humidity, incoming shortwave radiation, wind speed, and wind direction. In February 2016, the wind measurements were moved to 10 m agl.

The release of radiosondes (during KAS13 and KAS17) and tethered balloon (during KAS13) occurred in periods that are called Intensive Observation Periods (IOPs), and are described in detail in 2.2.4. These IOPs covered 24 h starting at noon and finishing at noon of the next day, for periods forecasted to have favorable stable conditions. An IOP had a radiosonde release every 3 hours when possible.

All details of the measurement equipment and exact height can be found in Table A1, Table A2, Table A3, and Table A4 in Annex 1: "Detailed description of the meteorological stations of KASCADE 2013 and KASCADE 2017".

2.2.2 KASCADE-2013: the vertical structure over Cadarache Valley

Having presented the general context and measurements carried out during KASCADE, this paragraph is dedicated to the treatment of the KAS13 dataset and the flow characteristics that it revealed. KAS13 focused on the existence of valley flows, their depth, timing of their onset and disappearance, and their interaction during stable night conditions.

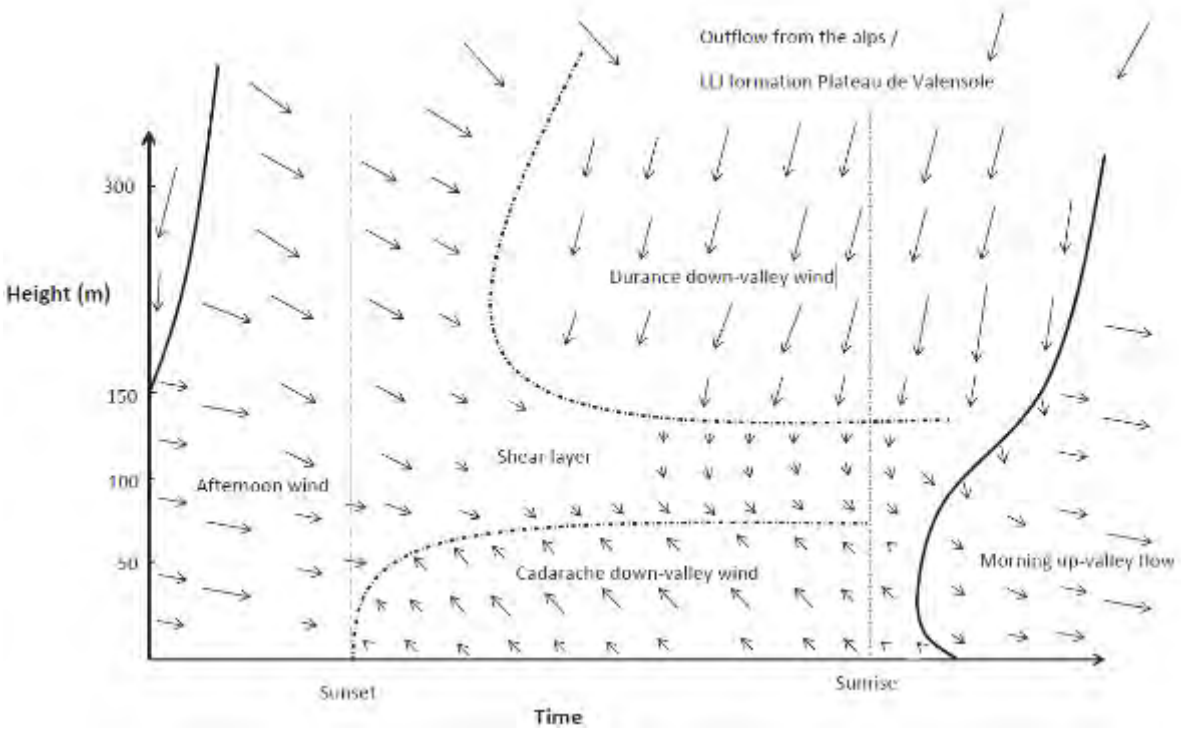

Figure 2.4: Conceptual drawing of typical flows above the Cadarache Valley during stable night conditions (Duine, 2015). Arrow orientations indicate the horizontal wind direction, and their length indicates wind speed.

As mentioned in section 2.2.1, Sodar, tethered balloons and radiosondes measured the wind profile above the M30 station during KAS13 IOPs, providing a dataset in and above the CV. The focus on typical stable night conditions (low wind, clear skies) led a previous Ph.D. to compose a conceptual drawing (Duine et al., 2017) of the winds during a typical diurnal cycle with stable night conditions, as shown in

Figure 2.4. The Cadarache down valley (CDV) wind starts around sunset and grows in a 50 to 80 m thick layer. It has a wind speed peak of 1 – 4 m s^{-1} at an altitude of 25 – 30 m above the ground. The CDV dissipates quickly after sunrise, and the daytime winds start up again.

Roughly 4 to 5 hours after sunset, the Durance down-valley (DDV) flow is observed passing above the CV. It is a stronger wind with a peak speed of 4 to 8 m s^{-1} at 175 – 225 m above the MET01 position. After Initialization, the DDV flow occupies heights between 100 m agl at the lowest point and extends above the maximum measurement height of the Sodar (~500 m agl). Radiosondes show DDV maxima up to 600 m agl, see Figure 2.7. The DDV flow has a NNE orientation and aligns well with the DV, indicating a flow of regional scale. In the morning, this system is strong enough to maintain DDV flows up to 3 hours after sunrise before daytime winds become strong enough to break it down.

With the DDV flow arrival, a shear layer forms between the CDV and DDV flows. This layer is associated with low wind speeds, and directions do not necessarily match terrain orientations. Its lower limit resembles a return flow for the CDV winds. Higher up, wind directions in the shear-layer seem to veer with height until matching the DV orientation and merging with the DDV flow. Above the DDV flow, drainage flows from the Alps are possible under weak synoptic conditions, similar to Pyrenean foothills flows observed by Jiménez & Cuxart, 2014.

2.2.3 KASCADE-2017: spatial investigation of the Cadarache Valley

This part describes the temperature in and above the CV, using the surface observations of the LEMS and the vertical profiles of the radiosondes. Its goal is to better understand the diverse nighttime temperature development in and along the CV during stable periods because temperature is sensitive to smaller-scale variation than during convective daytime situations.

The differences in virtual potential temperatures between 2 m and 110 m at GBA are estimated according to Dupuy (2018) (his Appendix A). Maximum stratifications of clear-sky night IOPs are commonly between 5 and 6 °C, with values up to 7 °C. However, due to the lack of measurements at intermediate heights, just a shallow layer could be stable, and the rest neutral or unstable. Nevertheless, measuring the temperature difference between the top and bottom of the GBA pylon is needed for nowcasting tools (see section 2.4) to indicate the presence and strength of valley winds in the CV.

The difference between the warmest moment of the day and the coldest at night is called the Daily Temperature Range (DTR). The DTR is maximum at the surface due to the surface losing and receiving most radiation. In weak wind, clear-sky days, the 2-m DTR typically ranges from 14 to 16 °C, the largest value seen during IOPs of KAS17 is 19 °C.

While the GBA station shows stratification at its location, the LEMSs distributed over the CV describe the ground-level spatial variability. Their temperatures differ due to two main processes, namely thermal stratification and surface heterogeneity. For example, Figure 2.5 (Dupuy, 2018) shows the relation between average night temperatures (averaged over five nights) and station altitude. Seemingly, there are two principal behaviors, a decreasing temperature system upslope along the valley thalweg (B1-B2-B3-B4) and an increasing temperature with altitude along the sidewalls (B3-S1-N1-S2-N2-N3-S3-N4-S4). Further investigations focus on the sidewall cross-section and ignore stations B1, B2, and B4. Temperatures on the cross-section show a clear increase with height, though not perfectly linear.

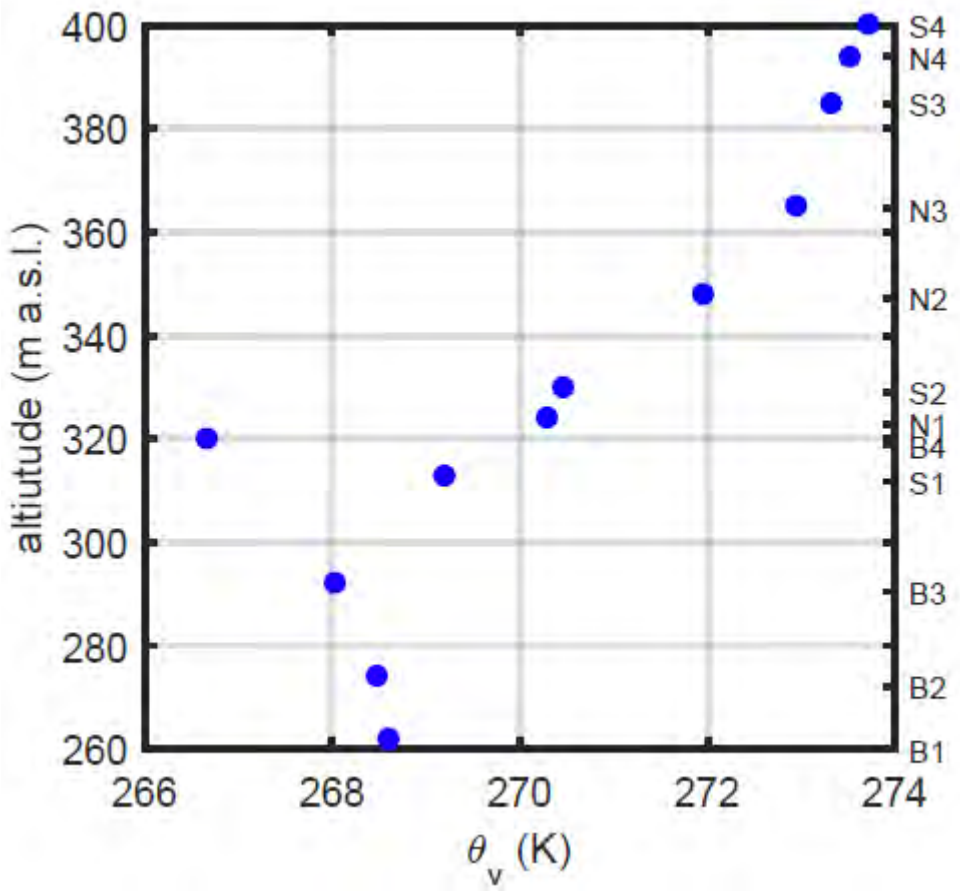

Figure 2.5: Virtual potential temperature of the LEMS stations averaged over the nights from 15 to 20 January 2017. The LEMS names are located on the secondary y-axis. Figure originates from (Dupuy, 2018).

LeMone et al. (2003) reported that under homogenous (surface) conditions, the temperature in stratified valleys should only depend on the height with a linear relationship. Thus, deviations from that straight line originate from surface heterogeneity. To differentiate between the effects of heterogeneity and those of the stratification, they introduced the variable θ_{ze} that represents the average vertical gradient (following the slope of the topography) of the potential temperature close to the surface. The deviations from this average gradient are attributed to the effects of spatial variability along the slope, which can be quantified by $\sigma_{\theta_{ze}}$, the standard deviation of θ_{ze}. Dupuy (2018) verified this method for the CV (his section 3.3.3a) and found good agreement. Analyses on $\sigma_{\theta_{ze}}$ showed variations of 1 K during the day to up to 8 K at night.

Figure 2.6 (Dupuy, 2018) shows the two valley system indicators: cold pool intensity (CPI) and horizontal stratification (θ*), while $D\theta$ requires measurements that are not available during the KASCADE campaigns as explained in section 1.3.3. Values are computed on five stable night KAS17 IOPs. They only use LEMS and radiosonde data since the vertical profile at GBA is in the confluent zone of CV and DV, thus less representative of the central CV situation. At night, all of them show large CPI values and θ* near zero. These IOPs indicate that typically the CV has a mature cold pool around B3. KAS17-IOP05 has a reduced CPI in the second half of the night, related to fog formation.

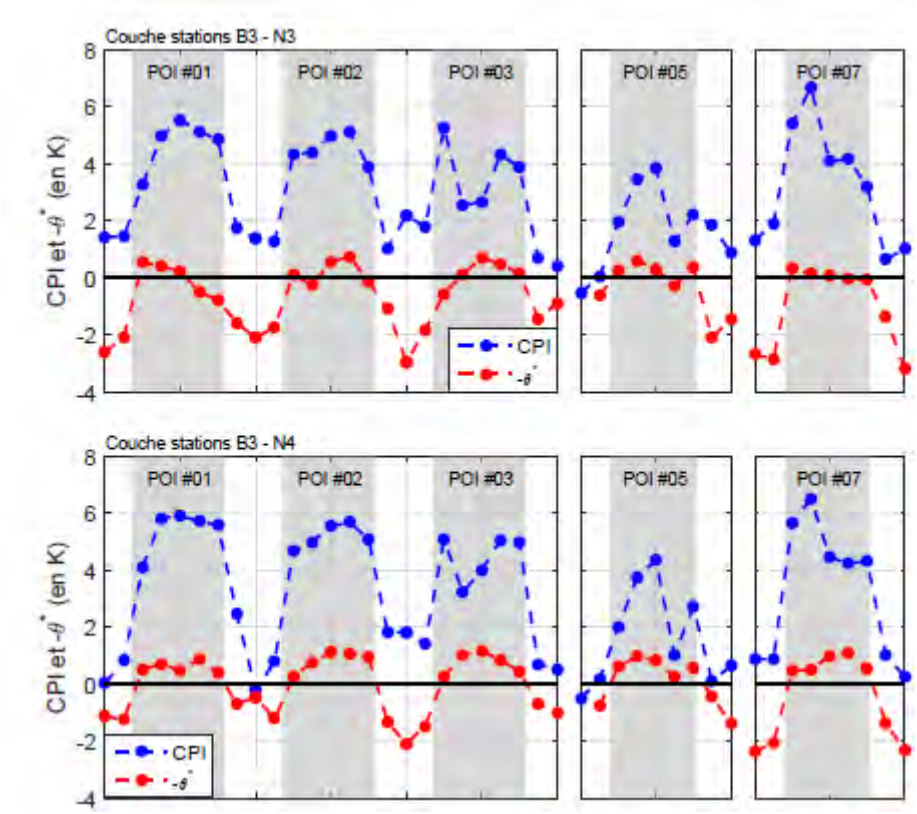

Figure 2.6: Cold pool intensity (CPI) and horizontal stratification (ϑ) of KAS17 IOP01-03, 05, and 07. Radiosondes released at MET01 provide data for the ϑ* calculations. The top row describes the layer between stations B3 and N3, while the bottom row is the layer between B3 and N4. Graphs are adapted from (Dupuy, 2018).*

Lastly, Dupuy (2018) noticed that the radiosonde profiles show that two zones are commonly near-neutral at night. Their depths stretch from 100 to 170 m and 260 to 330 m agl, respectively. In the 100 to 170 m layer, reduced stratification is likely due to the interaction between the DV and CV flows (see 2.2.2), where mixing is enhanced. The other layer from 260 to 330 m is just above the peak of the DV jet. It indicates the start of a near-neutral layer or weakly stratified layer up to the top of the DDV flow. A few cases show more near-neutral layers in the profiles, possibly indicating the drainage flows from the Alps reaching as far as the DV. Figure 2.7 shows six examples from KAS17.

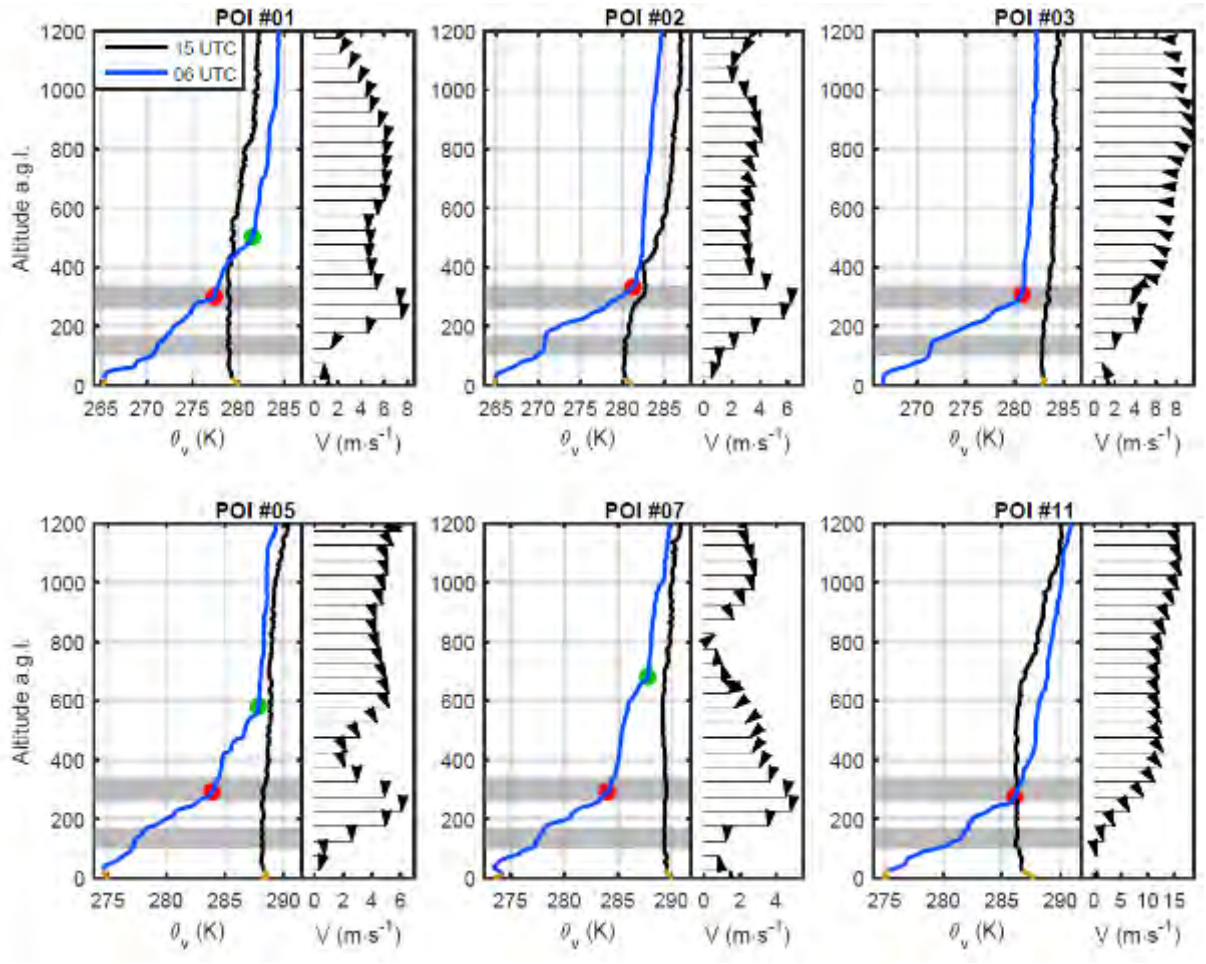

Figure 2.7: Temperature and wind profiles from radiosondes for the KAS17 IOPs 01, 02, 03, 05, 07, 11. Temperature profiles (left) are at 15 UTC (black line) and 06 UTC (blue line), while the wind profile (right) is from 06 UTC. Red dots in the temperature profile correspond to the visual estimate of the SBL top. In contrast, green dots indicate the height where 06 and 15 UTC radiosondes join, indicating the bottom of the residual layer. Grey zones indicate near neutral or weak stratification layers. The orange lines of the radiosondes correspond to the lowest 30 m, indicating questionable values. Graph originates from Dupuy (2018)

Like the along-valley and cross-valley temperature profiles, the near-surface wind at the valley bottom and on the slopes behave differently. Nevertheless, the whole valley consists of a buoyancy-forced system. Depending on the stability, the wind follows the local slope or the prevailing slope over a larger area (Haiden & Whiteman, 2005), making detailed topographic maps crucial. Weak stability allows the near-surface flows to follow the prevailing slopes. CV slopes have different steepness and have local orientations with up to 90° deviation from the prevailing slope. Figure 2.8 focuses on wind from the LEMS, when the valley flow is decoupled from the above valley winds, to visualize stable condition effects on surface wind direction. Timeslots with the dimensionless scale 1/Fr (see section 1.3.4) below 1 are included as decoupled winds.

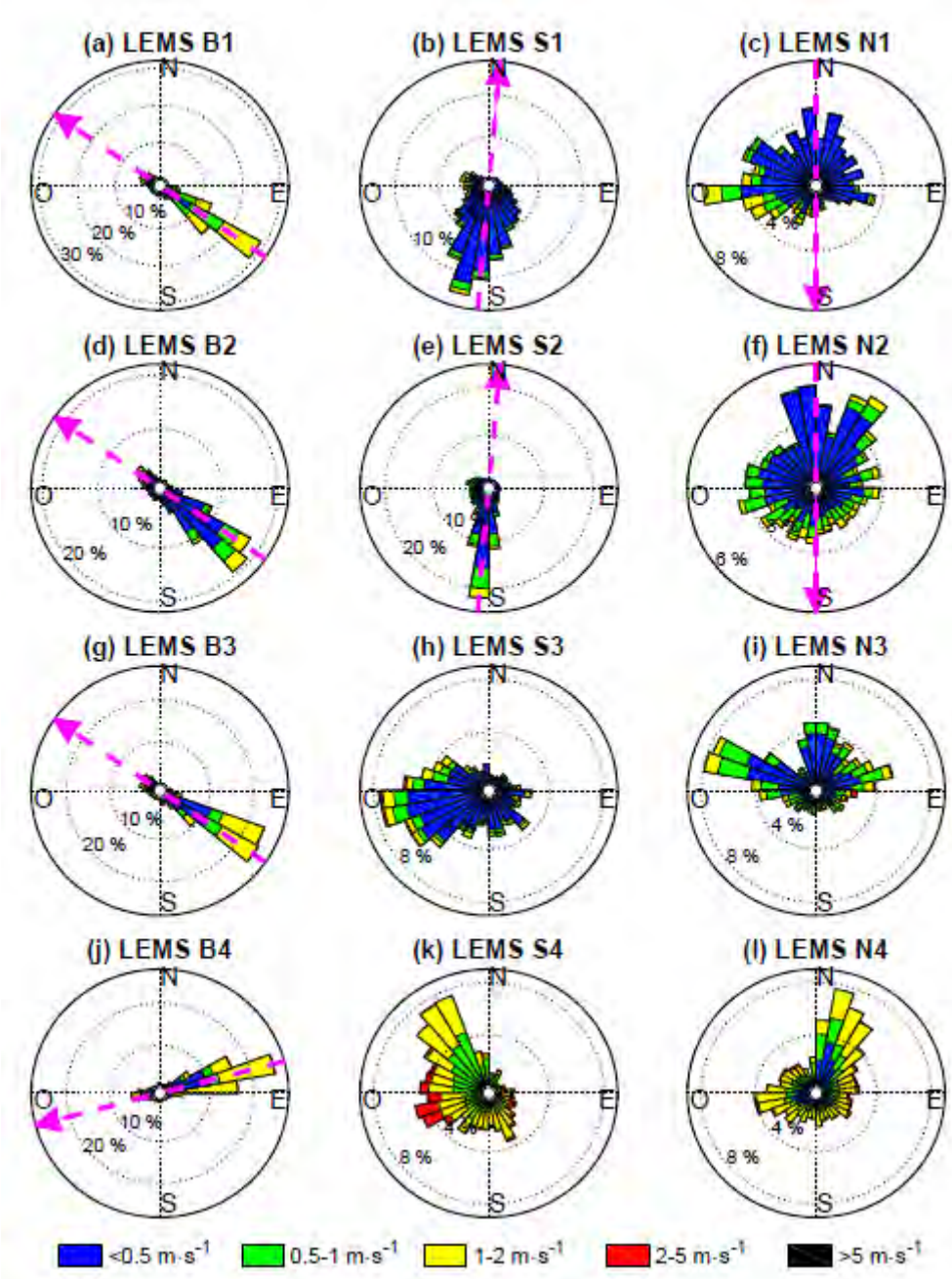

Figure 2.8: Wind roses of the twelve LEMS stations with 30 minutes averaged values of decoupled valley wind situations (1/Fr < 1). Magenta arrows indicate the orientation of the slope at that station, except where local topography does not allow for a precise determination. The original picture in Dupuy (2018)

Figure 2.8 (Dupuy, 2018) shows the wind roses of all twelve LEMSs. Especially stations on the valley bottom (B1 to B4) strongly correlate with their prevailing slope. Note that Figure 2.8 shows a large spread for winds below 0.5 m s^{-1}. This spread is largely because the wind vane gets stuck in the last position that had enough energy to move it (which corresponds to ~0.5 m s^{-1}). Regardless of the low wind speeds, the slope orientation determines the flow direction of the lower two stations at the south wall of the perpendicular cross-section (S1 and S2), while this seems not the case for the north wall (N1 and N2). A possible explanation is that S1 and S2 stations are sheltered in a local valley dimple, whereas N1-N3 are on top of a local ridge. N3 (Figure 2.8i) is roughly 100 m above the level of B3 (Figure 2.8g), and it shows a large percentage of winds matching the orientations of the shear layer between the DDV and CDV flows and resembling a return flow (see Figure 2.4). However, the LEMS are close to the ground, making above valley flows unlikely to be present. The influence of the surface is a

more likely contributor, but Figure 2.3 shows that the local surface slope does not match the flows of Figure 2.8i. Continuing with other LEMS, N4 (Figure 2.8l) is clearly above the CDV influence and receives DDV flows. The winds observed at S4 (Figure 2.8k) show a peak from the North West that mirrors the DDV winds peak seen at N4. Local topography may cause a direction change for the S4 winds, as Figure 2.3 shows that S4 is in a local dimple with NNW – SSE orientation. Another explanation is that a part of the DDV wind flows towards the Abéou Valley, the next tributary valley south of the CV, affecting the S4 because it is close to the ridge top.

2.2.4 KASCADE Intensive observation periods

In both campaigns, intensive measurements started in January and continued until March. When weather forecasts indicated clear-sky and low wind favorable for stable weather phenomena, an IOP started (although several IOPs include other non-stable phenomena). An IOP has additional measurements such as radiosondes and tethered balloon. Both are released near M30/MET01, see Figure 2.3. In KAS13, the tethered balloon carried three Vaisala probes staggered every 50 m. At a constant vertical low speed, it ascended and descended back to the ground in regular cycles to scan the vertical up to 300 m or higher if wind conditions permitted. Thus, IOPs have additional information on the vertical profile. Following sections include the IOPs of both Duine (2015) and Dupuy (2018), however creating a comprehensive overview of the cases, classifying and sorting the IOPs for case selection is part of the work I did, though it relies on the descriptions given by the previous works. The naming of IOPs happens in the format of KASyy-IOP##, where yy indicates the KASACADE campaign year, 13 for 2013 or 17 for 2017 and ## indicates the IOP number of that year in chronological order. When I have to name several IOPs, sometimes the campaign is only mentioned once.

Table 2.2 shows an overview of the IOPs available in the CV; for more detailed explanations, see the respective theses. Most IOPs have stable flows, which is the phenomenon of interest for these campaigns. However, several other weather conditions were captured as well. “Strong winds” indicate IOPs that observed strong winds at some part during the night. In most cases, this is a Mistral but also includes winds from other orientations, some of which cause DDV winds due to flow channeling. “Rain” indicates IOPs that had rain, which destroys stratification due to enhanced mixing. Snowfall has been mentioned for KAS13-IOP01. Other mentions of snow are a snow layer in KAS13-IOP18 and KAS13-IOP19, all classified as “Snow(fall)”. Clouds or fog are often inhibiting further development of stratification. In KAS13-IOP18, KAS17-IOP05, KAS17-IOP08, and KAS17-IOP09, the formation of radiative fog is reported.

Every IOP of KAS13 was also modeled with a WRF run at 1-km horizontal resolution by Duine (2015). IOPs that had a high percentage of correctly simulated DV winds were selected for sensitivity studies. A few exceptions were made for cases without observed DDV winds. Finally, KAS13-IOP16 was selected as a reference case to determine the best parameterization settings for DDV wind cases. This IOP has a relatively weak synoptic forcing and clear sky conditions, making it easy to select reference settings. Kalverla et al. (2016) explain this process in more detail. With the reference settings, a selection of 13 IOPs (see Table 2.2) permitted further sensitivity tests to see the effect of vertical levels and increased inner domain size. Duine (2015) gives a more detailed description of all KAS13 IOPs in Annex 2: Sodar data analysis.

KAS17 IOPs have not been simulated with a numerical weather prediction model (NWP) previously. However, IOP01, IOP02, IOP03, IOP05, and IOP07 have been marked as exceptionally favorable for generating CDV winds.

Table 2.2: Classification of the 37 IOPs of the two KASCADEs campaigns, complemented with the weather condition present. #RS indicates the number of radiosondes released that IOP, #TB is the number of tethered balloon profiles. A '-' indicates the absence in the IOP description, 'Y' indicates the presence, and an 'A' means it existed during the afternoon but not at night.

KAS	*IOP*	Start date	# RS	# TB	Stable	Strong Winds	Rain	Cloud/ fog	Snow (fall)	Sensitivity candidate
2013	*1*	14/01/2013	2	6	-	-	-	Y	Y	-
	2	21/01/2013	2	-	-	Y	-	-	-	-
	3	22/01/2013	2	6	-	-	Y	Y	-	-
	4	23/01/2013	2	42	Y	Y	-	Y	-	Y
	5	24/01/2013	2	50	Y	Y	-	-	-	-
	6	28/01/2013	2	20	Y	Y	-	-	-	Y
	7	29/01/2013	3	54	Y	-	-	A	-	Y
	8	30/01/2013	2	16	-	Y	-	-	-	-
	9	07/02/2013	2	30	Y	Y	-	-	-	-
	10	08/02/2013	1	10	-	Y	-	-	-	Y
	11	11/02/2013	2	20	Y	-	-	-	-	Y
	12	12/02/2013	3	36	Y	Y	-	-	-	-
	13	13/02/2013	3	34	Y	-	-	-	-	Y
	14	14/02/2013	3	42	-	-	-	-	-	Y
	15	18/02/2013	3	42	Y	-	-	Y	-	Y
	16	19/02/2013	3	38	Y	-	-	-	-	Y
	17	20/02/2013	2	48	Y	-	-	-	-	-
	18	21/02/2013	3	30	Y	-	-	Y	-	-
	19	25/02/2013	3	52	Y	-	-	-	Y	Y
	20	26/02/2013	4	46	Y	-	-	-	Y	Y
	21	27/02/2013	4	66	Y	-	-	-	-	Y
	22	28/02/2013	4	46	Y	-	Y	Y	-	-
	23	01/03/2013	3	26	Y	-	-	Y	-	Y
2017	*1*	17/01/2017	7	0 (3)	Y	-	-	-	-	-
	2	18/01/2017	9	4	Y	-	-	-	-	-
	3	19/01/2017	9	5	Y	-	-	-	-	-
	4	24/01/2017	7	-	-	-	Y	Y	-	-
	5	15/02/2017	7	4	Y	-	-	Y	-	-
	6	16/02/2017	9	4	-	-	-	Y	-	-
	7	20/02/2017	9	-	Y	-	-	-	-	-
	8	21/02/2017	9	4	-	Y	-	Y	-	-
	9	22/02/2017	9	3	-	-	-	Y	-	-
	10	23/02/2017	9	1	-	Y	-	-	-	-
	11	01/03/2017	9	-	Y	Y	-	-	-	-
	12	07/03/2017	8	-	Y	Y	-	-	-	-
	13	08/03/2017	9	-	Y	Y	-	-	-	-
	14	09/03/2017	9	-	Y	Y	-	-	-	-

2.3 Supplementary analyses of KASCADE data

The sections above contain work of previous PhDs of Duine (2015) and Dupuy (2018), although sometimes presented differently. In contrast, the next sections contain complementary analyses of the observations performed during this thesis. In particular, I will present a tool to select interesting stable conditions encountered outside of the IOPs, thus extending the data set available for statistical analysis of stable flow and its turbulence characteristics. A characteristic length scale of turbulence is

then computed on half-hour samples from sonic anemometer measurements as the base for orienting the sub-grid scale parameterization in fine-scale modeling toward the most appropriate scheme. I explored another path to characterize the turbulence structure during stable periods: based on the Lumley's triangle (Lumley, 1979) analysis and its barycentric conversion (Banerjee et al., 2007). Considering that the results were interesting but not directly usable in terms of relevant scales and subgrid-scale parameterization, I do not present them in the present chapter. Still, they can be consulted in Annex 3: "Anisotropy calculations". Eventually, I will present the illustrations of the principal Durance-valley wind regimes as they can be retrieved from a detailed analysis of the Sodar observations.

2.3.1 Determining typical stable situations in the CV

The majority of IOPs has many stable timeslots because those events were targeted. Even though the IOP dataset contains multiple days with stable conditions, the complete KASCADE contains more nights with stable conditions even if not selected as an IOP (e.g., weekends). Still, little attention has been given to these nights. To make these days more accessible, I developed on the KAS13 IOP data a filter method to extract timeslots outside of the IOPs where stable night CDV winds were present. I later applied a similar filter strategy to KAS17.

I focused on half-hour periods because this is a typical flux and spectra averaging time-length. In total, I applied four criteria called sunlight filter, description filter, directional filter, and lone slot filter. Additionally, two criteria verified the quality of the turbulent length-scale estimate.

The first filter discards daytime data. Observations in the CV show that the CDV flow can start forming just before sunset and remain up to one hour after sunrise. Admittedly, the sunlight filter might be a little too strict and should include the period with *local* sunrise (i.e., considering the topography). The second filter removes all slots whose description explicitly indicates non-stable night conditions. The third filter checks the wind directions retaining those between 90 and 180° (i.e., deviating from the 135° valley axis by less than 45°). The fourth filter removes all slots that do not have a slot of stability during the preceding or the following hour (i.e., one other stable slot in the two slots before or after) to avoid short-lived systems (occurring 8 times in KAS13 IOPs).

The integral length-scale is computed on 30-min time series of the turbulent vertical wind measured at 30 m by the sonic anemometer situated at M30. The methodology is described in the Appendix A of the article included in Chapter 4. However, I must mention that two supplementary criteria were introduced during this calculation: the first one checks if the fitting function used to compute the length-scale (see the article) has a determination coefficient (R^2) lower than 0.9. The second checks whether the fitting process did encounter any error or did not reach an acceptable result within the given number of iterations. Table 2.3 summarizes the selected sequences through KAS13 IOPs and colors show what filters led to the elimination of periods.

The filter result consists of 236 half-hour timeslots with observed CDV winds during IOPs. To find more slots within the rest of the 4 months of KAS13 data, I apply the sunlight, direction, lone slot filter, supplemented with a resemblance filter. This last filter replaces the description filter and uses the wind speeds at 30 m and stratification between 2 and 30 m of M30 of the 236 slots. To avoid extreme situations influencing the dataset, new slots must fall with the 5 – 95 % wind and stratification interval (1.0 – 2.5 m s^{-1} and 0.0 – 6.72 K) of the 236 IOP slots. Through these filters, 298 additional slots emerge over 36 nights, which could be useful for verifying relationships based on the data in the IOPs slots. Note that I only use the data at 2 and 30 m because the sonic 10 m observation shows lower wind speeds than those at 2 m or 30 m, as it had problems with frost. This reduced wind speed is also why I

did not attempt to compare two measurement heights as the 2 m shows similar errors, although to a lesser extent.

Table 2.3: Filtered half-hour slots of the 23 KASCADE 2013 IOPs. Numbers on the top row indicate the time in UTC. Yellow fields indicate moments with sunlight, and brown slots are non-stable night conditions. Measurement periods with no CDV winds are in blue, and measurements below 0.9 R^2 with the length scale calculations are red. Lone slots, only one in a 5-slot series is marked dark green. Black squares are slots where the spectrum is not easily calculated and exceeds a preset number of iterations. White squares are the slots that pass the filters.

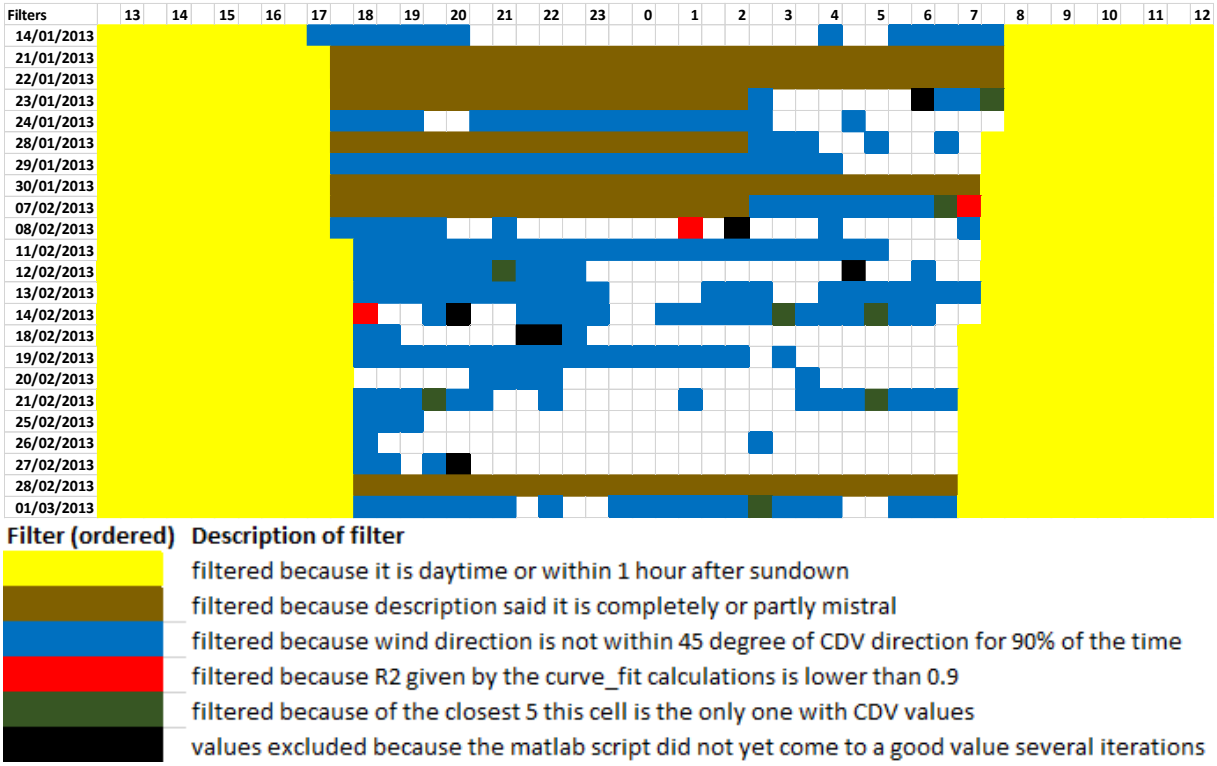

2.3.2 KAS13 filters applied on KAS17

I also applied the filter system developed above to the 14 IOPs of the KAS17. This filtering includes the filters of sunlight, direction, description, and lone slots. However, since the M30 is no longer in position and MET01 did not have sonic anemometers, I applied them to the 10 m AS3 data, classifying 235 stable night timeslots during the KAS17 IOPs.

Table 2.4 shows that days 18 and 24 January, 20 and 22 February 2017 (IOP 02, 04, 07, 09 of KAS17) are nights without many perturbations to the observations at 10 m agl at the AS3. Because AS3 was further upslope in the CV than was M30 during KAS13 (see Figure 2.3), influences from the DV are weaker. Furthermore, measurements at 10 m are lower than those at 30 m during KAS13, allowing less influence from above valley flows. Nonetheless, it seems that the stable nights of KAS17 were better selected than those of KAS13, since with fewer days, KAS17 has roughly the same number of stable night timeslots.

Table 2.4: Same as Table 2.3 but for the 14 IOP days of KAS17.

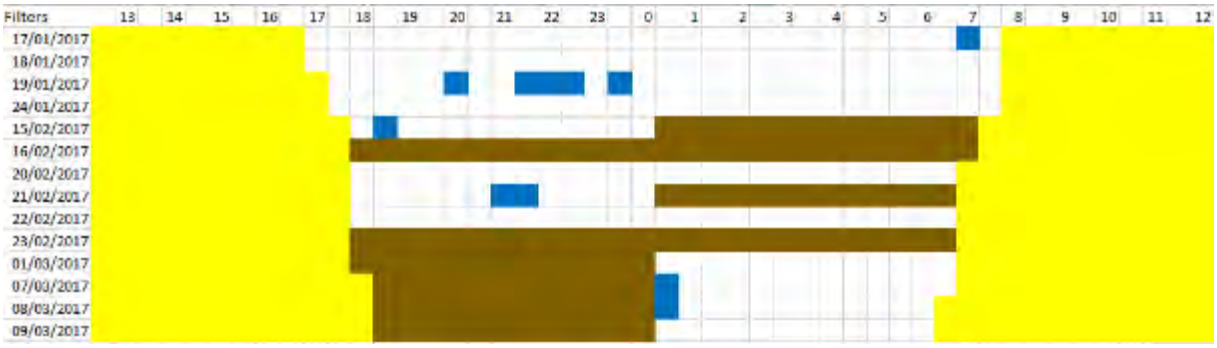

2.3.3 Length scale statistics of KAS17

The method to calculate the integral length scales and extrapolate them to the upper levels in the boundary layer is fully described in an appendix to the article included in Chapter 4. These extrapolations need knowledge of the boundary-layer depth, which can be estimated from radiosonde profiles. This section aims to provide statistics of the length-scale values computed over all the IOPs of KAS17 to determine which turbulence parameterization is most relevant for fine-scale simulations.

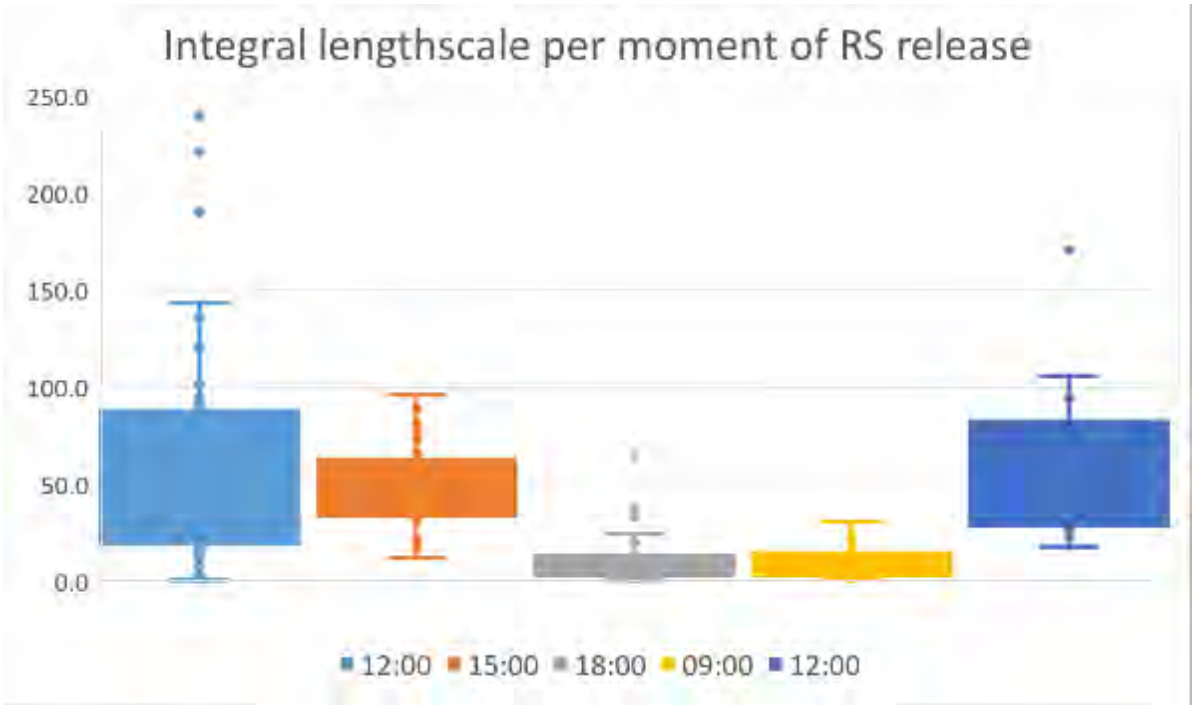

Figure 2.9: Boxplot of the turbulent integral length (in m) extrapolated from 10 m observations to the boundary-layer top for five different radiosonde release moments of IOPs in KAS17.

Figure 2.9 shows the integral scales for all KAS17 IOPs, computed at 10 m and extrapolated to the top of the boundary layer at the five different times when radio soundings were available. The noon release corresponds to the start of the IOP, 15:00 UTC, 18:00 UTC, 09:00 UTC the next morning and the noon last radiosonde of the IOP. Note that each radiosonde is included once and if a radiosonde falls into two IOPs, it is considered part of the second IOP. The graph shows that the mean value and the range of integral length scale is largest around noon. They can be near-zero when a stable layer is not yet removed. KAS17-IOP12 shows an exceptionally thick boundary layer with strong winds. It leads to the three points with scales larger than 190 m. The boundary-layer depth has become notably larger

three hours later, and no more near-zero values are reported. Early evening and early morning have most length scales smaller than 30 m, except with strong winds.

This work shows that at night the extrapolated length scale is always smaller than 100 m, with average values of the order of 10 m. Even during the day, the scale remains between 0 and 100, with a few exceptions when the winds are strong and the boundary layer is very thick. This analysis means that for modeling purposes with a horizontal resolution of 111 m, turbulence in the CV does not need explicitly resolved TKE in most cases, especially if the night period is concerned, although the exact conditions need to be examined.

2.3.4 SODAR wind profiles during IOPs and their typical patterns

Sodars provide useful data to visualize winds between 100 and 400 m agl (outside that range, their values become more uncertain). Because the Sodars have a blind window near the surface, they cannot observe the CDV flow as it reaches a maximum height of around 80 m agl (extracted from tethered balloon observations), while a large part of the DDV flow (100 – 500 m agl) can be observed with the Sodars. During my thesis, I have visualized all the IOPs to provide an easy way of estimating DDV wind strength, duration, and depth, see Annex 2: "Sodar data analysis". From these visualizations, I will highlight three worthwhile cases, namely KAS13-IOP02, KAS13-IOP17, and KAS17-IOP06. Note that during the whole KAS13, the Sodar stood near the VER station, while at KAS17, two Sodars stood in the CV, possibly leading to a slight mismatch in exact heights of the wind layers and wind speed peaks, but patterns should remain comparable. This mismatch comes from different elevation given different height above the valley floor. Similarly, the MET01 is at a distance from the DV, meaning that the flow shape can be different.

Figure 2.10 contains three types of situations commonly found in DDV winds, namely a strong and deep DDV wind case in Figure 2.10a and 2.10b, a West Wind case in Figure 2.10c and 2.10d, and a weak DDV wind case in Figure 2.10e and 2.10f. These are not the only types of events that occur and mixes of these events exist, but these three describe the most variety of IOPs. Below I describe the main type of cases with references to the specific situation as shown in Figure 2.10. They were selected because they have relatively little data missing and do not show mixing between types or less common phenomena.

A) A well-established DDV wind case often starts with daytime wind coming from the west that slow down at sunset (17:12 UTC). In Figure 2.10a, southern wind arrives, causing a short peak in wind speed after nightfall. This wind is common for well-established DDV cases but not required. This wind likely coincides with the advection of moist air from the Mediterranean, as a similar case is discussed in section 3.5 of the article in Chapter 4. After a moment of slow wind, the DDV winds arrive with their peak speed 200-300 m agl. Around 10:00 UTC, the daytime wind manages to overtake the DDV wind and the wind from the west start up.
B) A West Wind case shows fast wind throughout the day, from western directions. Figure 2.11 shows the synoptic conditions, with strong wind from the west over France, but not per se Mistral (see 2.1.2). Mistral is often associated with this wind direction (Duine (2015) mistakenly qualified this case as Mistral). Precise determination requires a synoptic map. In the case of Figure 2.10c, the wind speed peak falls at 02 UTC, but since it is pressure-driven, the timing of the peak varies with each event.
C) The weak DDV case shows wind stronger during daytime. In Figure 2.10f, it comes from the west. Again, the wind slows down after sunset until around midnight. A small amount of DDV flow manages to reach a height of 150-300 m agl. This wind is generally slower than during the well-established cases and can even show some intermittent pattern in its observations, such as KAS13-IOP16.

Most common are the three types described above, although other conditions occur as well, such as high wind speed around 400 m agl and above, which could come from any direction, whereas below this layer, it is possible to have DDV wind with a clear peak wind speed. So does the KAS13-IOP18 that has a DDV flow up to 300 m agl topped with stronger wind from the south; or KAS17-IOP01 that has DDV origin wind but mainly above 200 m agl with a peak between 300 – 400 m agl, which is 100 m higher than the common heights of the DDV peak.

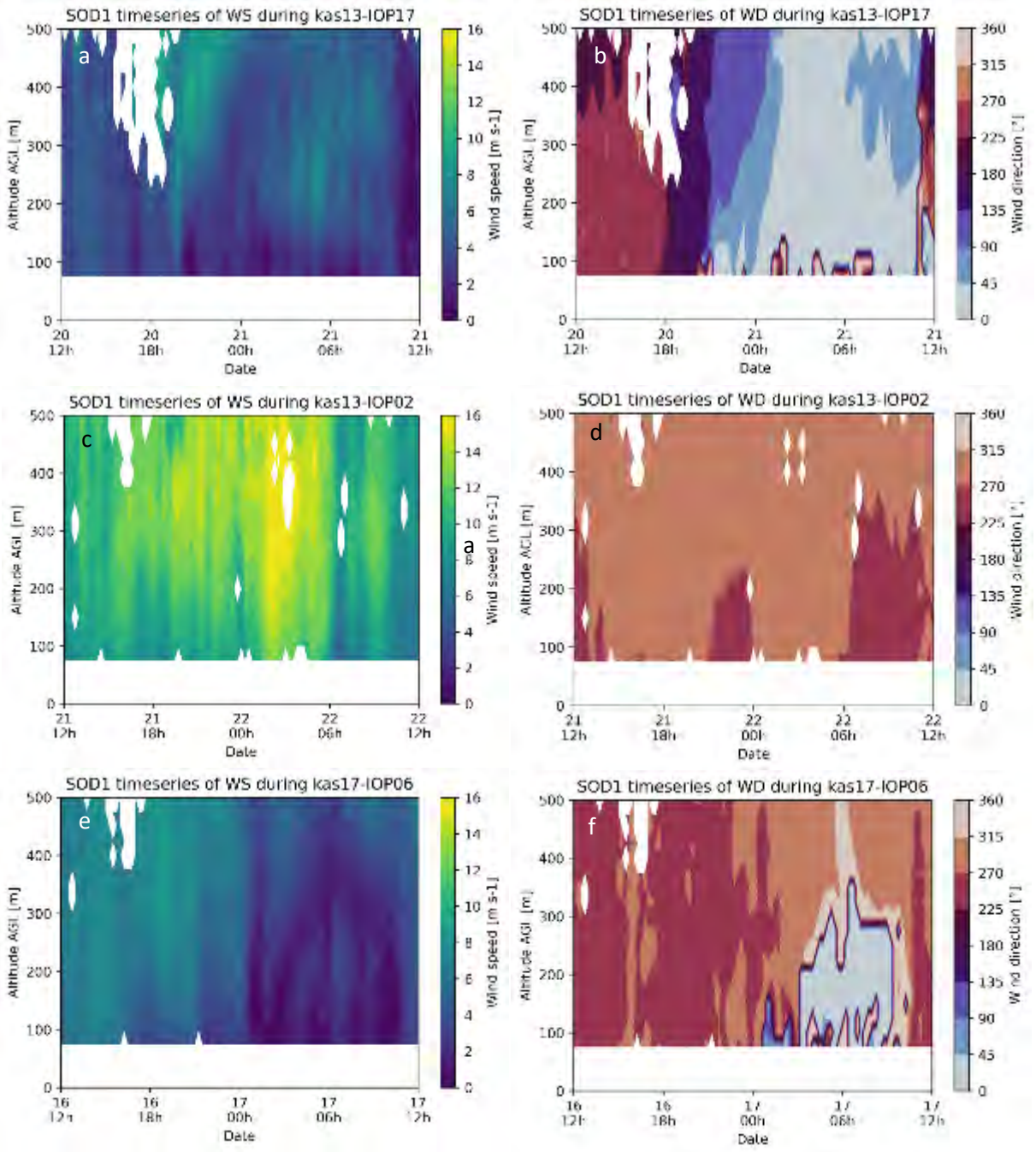

Figure 2.10: SODAR observations of KAS13-IOP17 (a-b), noon 20 February 2013 until noon 21 February 2013, KAS13-IOP02 (c-d), noon 21 January 2013 until noon 22 January 2013, and KAS17-IOP06 from noon 16 February 2017 until noon 17 February 2017. The Left column (a, c, and e) shows the wind speeds and the right column (b, d, and f) shows the corresponding wind directions.

Overall, the SODAR observations give a good picture of the winds. They help determine the differences between local or synoptic winds, as synoptic winds are relatively uniform in speed and direction in the observations.

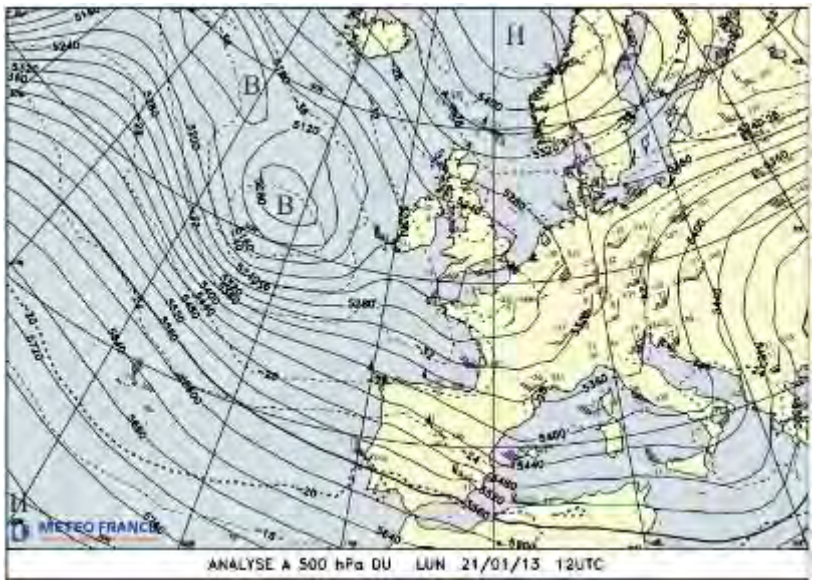

Figure 2.11: Geopotential height (in meters) at 500 hPa at the start of KAS13-IOP02, source: Météo-France

2.4 Existing calculation methods for the local valley winds

The valley winds of the CV cannot be reproduced explicitly by models at 1 km horizontal resolution (Kalverla et al., 2016) because the valley is too small. To nowcast or forecast the presence of the CDV winds, measurements from some specific location can be used and correlated to the CDV wind.

Duine et al. (2016) made the first attempt to nowcast CDV wind from observations done at a single location above the valley. Dupuy et al. (2019) used an Artificial Neural Network (ANN) to improve the results from Duine et al. (2016) further and apply them to forecasts. I will describe these methods and their results and discuss their limitations.

2.4.1 WRF simulations

Kalverla et al. (2016) investigated all KAS13 IOPs through WRF simulations and defined the reference setting for runs with 1-km horizontal resolution in the Cadarache region. They tested the following parameterizations for the PBL schemes, namely Yonsei University scheme (YSU; Hong et al. 2006), asymmetrical convective model, version 2 (ACM2; Pleim, 2007), Mellor-Yamada-Janjić (MYJ; (Janjić, 1994), quasi-normal scale elimination (QNSE; (Sukoriansky et al., 2005), and the Mellor-Yamada model proposed by Nakanishi and Niino (MYNN2.5; (Nakanishi & Niino, 2006). For the soil parameterizations, they tested the NOAH-LSM (Tewari et al., 2004) and the MM5 five-layer thermal diffusion (Dudhia, 1996).

In general, the Noah-LSM creates more realistic skin temperatures and mixing ratios and temperature profiles that resemble thermal diffusion. For the PBL scheme, the differences are less clear, but the QNSE performs better in surface temperatures and mixing ratios. Kalverla et al. (2016)'s work shows a good match with the DDV flows. However, the DTR is underpredicted and atmospheric moisture is generally over predicted. They tried to solve the problem with changes in soil moisture content, leading to improvements of the DTR and PBL depth, although it also increased the sensible heat flux bias.

Kalverla et al. (2016) pitched that these issues and the missing Cadarache down valley (CDV) winds would improve with refined horizontal resolutions, which was too costly at that time. Meanwhile, other nowcast methods are developed and tested, as described below.

2.4.2 Nowcasting with GBA threshold values

GBA is close to the CV center (MET01) and has measurements at 2 and 110 m agl. Since GBA is in the CV confluent zone, it shares vertical structures with the rest of the CV. Duine et al. (2016) tested several GBA variables to obtain the highest correlation with CDV winds. Possible GBA variables with a high correlation are the 110 m wind speeds (U_{110m}), the vertical stratification (ΔT; $T_{110m} - T_{2m}$), and the bulk Richardson number (Ri_B) because these variables are often similar over large areas as they are measured at height. So, a threshold value tested on each of these parameters as a diagnosis of the presence of a Cadarache down-valley wind. Ri_B was computed as:

$$Ri_B = \frac{g \cdot (\Delta T + \Gamma_d \Delta z) \cdot \Delta z}{T_{110m} \cdot (\Delta U)^2} \qquad \textit{eq. 2.1}$$

Where Γ_d is the dry adiabatic gradient, Δz is the difference between measurement heights, T_{110m} is the atmospheric temperature at the height of 110 m; ΔT and ΔU are the difference in temperature and wind between measurement heights, respectively. Eq. 2.1 represents the bulk Richardson formula adapted to the available GBA measurements of 2 and 110 m, created by Duine et al. (2016) because they cannot use the complete Ri_B formula (eq. 1.7). That equation uses virtual temperature, which requires pressure and humidity at 110 m, which are not available. Further problems come from the fact that GBA does not have wind measurements at 2 m; therefore, those winds are assumed zero, meaning that ΔU is reduced to U_{110m}. Measurements of the SODAR and two sonic measurement stations show that the roughness length (z_0) is 1.03 m and the displacement height is approximately 5 m (Duine et al., 2016). Consequently, the assumed zero-speed observations of the 2 m wind do not lead to a major error.

All variables highlight a connection between the GBA measurements and the low-level winds in the CV center. The U_{110m} values represent wind systems above the CV, while ΔT and Ri_B indicate stability, all possible indicators for the occurrence of CDV wind. Ri_B combines the wind speed and the temperature gradient, possibly achieving a better result than by only using U_{110m} or ΔT. Figure 2.12 shows the histogram of wind direction and the proposed criteria with threshold values. Winds for cases below the threshold are in blue and above the threshold in red. A too low threshold will classify too many cases as valley winds, while a too high threshold leaves many cases excluded, even though a valley wind was present. Selecting optimal threshold values requires an evaluation measure.

Table 2.5: Contingency table to verify the occurrence of CDV winds with criteria of U_{110m}, Ri_B, and ΔT.

		Valley wind observed	
		Yes	No
Criterion	Satisfied	a	b
ΔT, U_{110m}, Ri_B	Not satisfied	c	d

To test the skill of these parameters as an indicator of the valley wind presence, Duine, 2015 used the contingency table. It is a method to verify the bilateral events (Wilks, 2011) by counting the hits and misses. Table 2.5 shows the four combinations (a-d) of observed valley winds (yes or no) and a satisfied criterion (yes or no). The four classes are correct nowcast (a), false alarm (b), missed event (c), and correct rejection (d). a and d thus describe the instances where the criteria correctly relate with the

CDV winds. A measure of skill is the proportional correctness (PC) and is calculated as the ratio of correct nowcasts (a + d) overall nowcasted events (a + b + c + d).

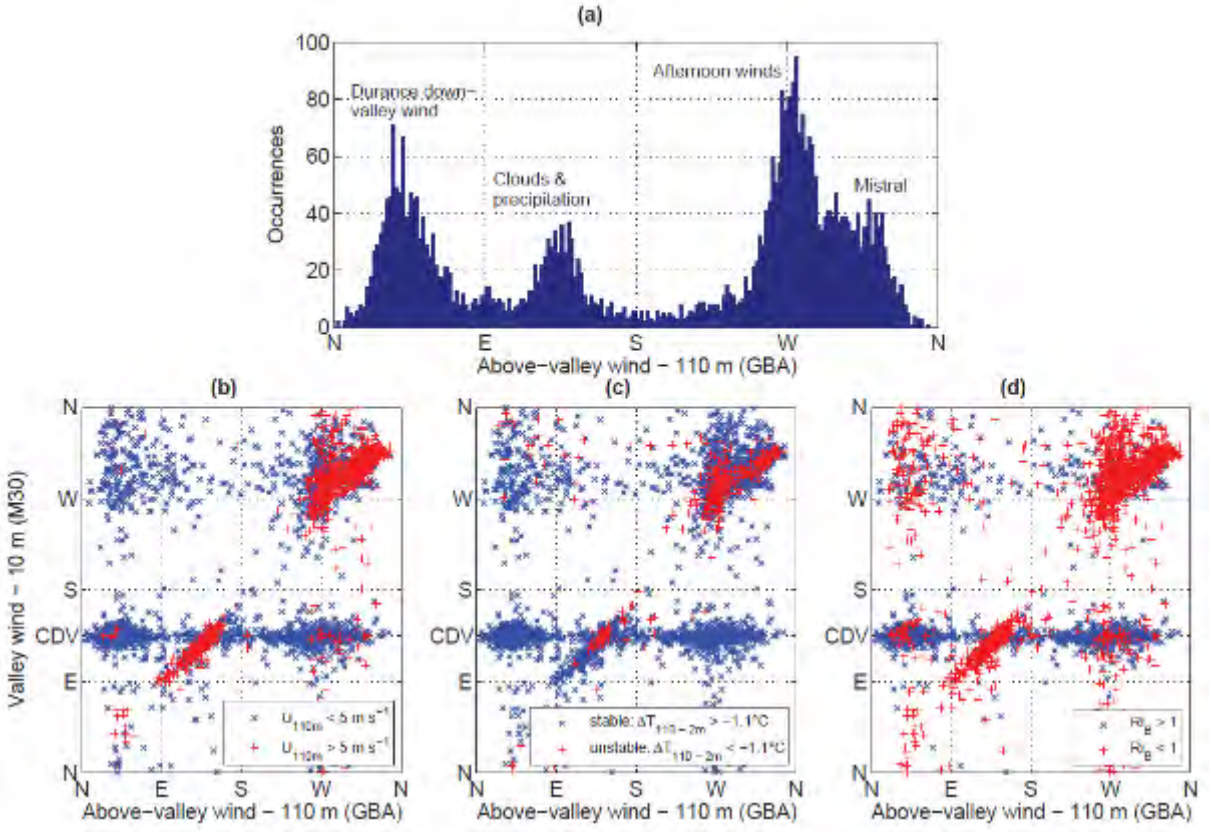

Figure 2.12: The analyses of the winds during KASCADE 2013, 13 December 2012 to 16 March 2013, general wind directions (a) and the relation between 110 m of GBA and the 10 m of M30 measurements (b-d). Graphs b-d differentiate between two types based on threshold values—original figure from Duine et al., 2016.

Determining the best threshold values requires plotting them against their PC scores. Tests show that the ΔT has an optimal value at 1.5 °C, resulting in a PC of 91 %. While the ΔT has the best scores, U_{110m} and Ri_B also show decent scores. The optimal wind threshold of 4.0 m s^{-1} has a PC of 72 %, and the optimal Ri_B of 0.8 obtains the best PC of 86 %. Altogether, an excellent result for ΔT confirms the thermally driven nature of the CDV winds.

2.4.3 Artificial Neural Network

Artificial neural networks (ANNs) are a statistical method to construct a relation between an input dataset and an output dataset. ANNs have three parts, the input variables, the hidden or calculation layer(s), and the output layer. An ANN uses a random function to calculate the best relation between the two datasets and optimize the function through machine learning. This function consists of weighted sub-functions (neurons) interconnected and arranged in one or more layers. In his thesis, Dupuy (2018) used a Multi-Layer Perceptron, which indicates that the neurons in the hidden layer are connected with all neurons of the other layers. Figure 2.13 shows a simple ANN with two input variables, one calculation layer, optional biases and one output layer.

Back to the input, Dreyfus et al. (2002) developed a two-step method to select the most relevant variables for the ANN input. The first step is to calculate the correlation between variables and keep only one variable among all highly correlated ones (correlation 0.9 or higher). The second step starts with the remaining input variables and creates a reference ANN with all of them. To determine which parameters are redundant, an ANN is built independently for each available variable. In iterations, new

variables are added to the ANNs. Each iteration adds another variable. Variables that do not significantly improve the performance metric are removed from the dataset.

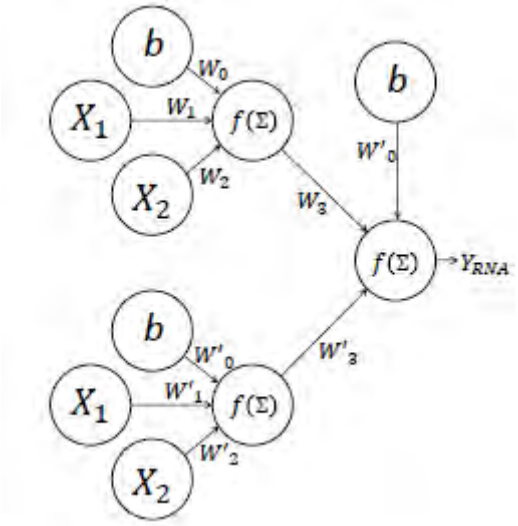

Figure 2.13: Schematic representation of a two-layer Artificial Neural Network structure (type "feedforward") with two hidden neurons and an output neuron producing Y_{RNA}. The network has two input variables (X_1 and X_2). W_i are the weights, b is the bias and f is the function to calculate an optimal output.

Dupuy et al. (2019) considered 9 variables (u_{110m}, v_{110m}, U_{110m}, P_{2m}, T_{110m}, T_{2m}, $\Delta\theta$, RH_{2m}, and q_{2m}) for the first step. They decided to work with u and v components of the wind as output variables since the cyclic nature of the wind direction could be difficult for ANN. Among those 9 variables, three sets of three variables were closely related and could be redundant. These sets were wind (u_{110m}, v_{110m}, and U_{110m}), temperature (T_{2m}, T_{110m}, and $\Delta\theta$), and humidity (RH_{2m}, q_{2m}, and T_{2m}). The first step led to removal of T_{2m} because it had a 0.92 correlation coefficient with T_{110m}. Their correlation with $\Delta\theta$ determined a final decision: since the correlations of T_{110m} and $\Delta\theta$ (-0,32) was closer to zero than T_{2m} and $\Delta\theta$ (-0,66), they retained T_{110m}. In the second step, they continued with the remaining 8 variables, and only inputs of $\Delta\theta$, u_{110m}, and v_{110m} were significant for the performance of the ANN.

After a series of tests with 5 to 50 neurons in the layer, 10 neurons showed the most promising results. They created two output variables, u and v, at 2-meter height within the CV. To train and test the ANN, they considered two datasets. One dataset matched the one used by Duine et al. (2016) and focused on stable night conditions. A second dataset covered a whole year, February 2015 to February 2016, to cover year-round meteorological phenomena and conditions. These datasets were divided into three groups, used for training (60 %), validation (30 %), and test (10 %). Only the test dataset was entirely independent and was therefore used to compare different ANNs.

To test the skill of the calculated winds, they deployed three different assessment methods. First, the directional accuracy (DACC; Santos-Alamillos et al., 2013) describes the percentage of calculated wind within an allowed directional difference from the observations, 45° in this research. Second, a PC2 criterion is the proportion of winds correctly falling into 2 sectors of the wind rose: one for down-valley flows and the other for all remaining winds. Third, a PC4 criterion considers four wind classes: down-valley flows, up-valley flows, cross-valley flows, and slow wind under 0.5 m s^{-1}, which means that the PC4 describes the fraction of the four correctly calculated winds from all data.

Results from the KAS13 period show a mean DACC of 84 %, mean PC2 of 89 %, and a mean PC4 of 84 %, a wind speed bias of 0.28 ms^{-1} and a mean absolute error (MAE) of 0.54 ms^{-1}. However, the ANN performs poorly on low wind speed (DACC of 53 %). Since training the ANN on a dataset without slow

winds introduces a bias, they excluded all periods with slow winds for performance calculations, then improving the mean DACC to 89 %, mean PC2 to 95 %, and mean PC4 to 86 %. Both wind speed bias and MAE improve by 0.02 m s^{-1}.

Dupuy et al. (2021) applied it on kilometric-resolution WRF forecasts instead of GBA observations to further test the ANN, extending the nowcast method into a forecasting method. Results show a 68 % DACC, a 76 % PC2, and a 71 % PC4, which are drastic improvements compared to raw WRF skill with a 50 % DACC, 68 % PC2, and 47 % PC4.

2.4.4 Limitations

Even though these methods provide good results, they are only valid at the teaching point. Both approaches of Duine et al. (2016) and Dupuy (2018) rely on statistical relations and do not include physics, thus are invalid when using their result for a large area. As a valley wind is likely to occupy the whole valley but is still influenced by variable local characteristics, every location would need a specific investigation by observation if one wants to apply these methods for nowcasting/forecasting the wind for a large area. In contrast, NWP models use physical relations that hold regardless of the site.

Besides, especially with ANNs, it is possible to overtrain the relationship, and all results will cluster, while the observations can show more spreading. Figure 9 of Dupuy et al., 2019 shows that the ANN remains less scattered than the observations. However, ANNs are good interpolators, but poor extrapolators (Gardner & Dorling, 1998) and therefore need large and heterogeneous datasets.

2.5 Chapter summary

This chapter shows the measurements and analyses already done on the Cadarache Valley and Durance Valley, with a few additional analyses, telling a story about two valleys under clear, stable night systems. The KAS13 campaign showed a very clear flow in both the CV and DV, with a thin intermediate shear layer with possible return flows between the two flows, around the height of the CV ridges. Investigations of the IOPs resulted in a conceptual understanding of the different flows in and above the CV.

To further the CV understanding, KAS17 aimed to measure the flows on the sidewalls and the variation along the flow path of the CV thalweg. Through a variety of stations spread over the CV, KAS17 collected much information about the spatial variation and stability systems of the CV. Among findings are the strength of the frequently occurring cold air pool, flow systems along the walls, and quantification of the effect of spatial heterogeneity on the stability within the CV.

After analysis of the observations, KAS13 had WRF simulations of all its IOPs leading to default settings for WRF simulations at a 1-km horizontal resolution. However, these simulations did not manage to produce the winds of the small CV. Therefore, statistical nowcasting methods to reproduce the CV winds (at MET01/M30 site) based on the measurements of the GBA have been developed. In KAS13, a threshold value on temperature stratification managed to create a 91 % certainty of the presence or absence of the Cadarache downvalley wind. In KAS17, an artificial neural network improved the nowcasting to include the values of wind speed components, thus providing the wind speed and direction. Further extension of the ANN makes it work to post-process WRF forecasts. This allows use of the WRF coarse resolution runs for the description of small-scale processes, with a 76 % correctness of the CDV presence, which is more than the 68 % of the unprocessed WRF results.

I complemented these previous works with further investigations into the stability of the KASCADE campaigns and investigation of the time series that the Sodars give during the IOPs. The stability conditions observed during the KAS13 IOPs show typical values for the parameters observed at the M30 tower, which leads to the finding, outside of the IOPs, of 298 slots presenting similar conditions,

making the total 534 timeslots. KAS17 seems to have a much larger efficiency when selecting stable moments. However, this could relate to a lower measurement tower 500 m up valley and thus sheltered from intrusion affecting stability and valley flow. On the other hand, the Sodar profiles show that recurring winds can be divided into three common and a leftover type.

Lastly, the extrapolation of the turbulent length scales from the CV KAS17 IOP observations to the boundary-layer top has led to maximum length scale determination during daytimes for use in the WRF model. The integral length scales generally remain smaller than 100, meaning that the 111 m horizontal resolution should still be coarse enough to include the dominant turbulent processes in most cases. Under strong wind conditions, length scales could reach lengths up to 240 m. Nevertheless, it remains important to verify the length scales before beginning a simulation or working with a system that can switch between explicit turbulence resolution and parameterized turbulence.

Chapter 3

Land cover in simulation: creation, evaluation, and illustration with two cases in the Durance Valley

This chapter aimed to prepare accurate land cover maps for the fine-resolution runs described in the next two chapters. It resulted in the submission of "A Method for Implementing Corine Land Cover data – in WRF – Simulation of a Nocturnal Valley Wind case" to AGU "Earth and Space Science", included below. The work and methods presented in this chapter are done either by me or in collaboration where I executed most of the work. I focused on the correct implementation of land cover datasets for the land-atmosphere interactions in the WRF model. These interactions are important for representing energy and mass fluxes at the surface, which are important factors of the boundary-layer processes, especially in stable conditions. WRF groups the land cover into several classes, each being characterized by their resemblance in parameters such as roughness length, albedo, emissivity, and surface heat exchange. One problem I try to fix is that while assigning land cover values to cells, WRF default settings select one class most common for the region regardless of the actual amount of classes represented on that cell. However, it may not be the most representative per se due to the coexistence of similar classes. E.g., let us consider a surface consisting of 40 % lake and 60 % forest, which would give the forest type as the most common class. A dataset with more detail shows that the forest consists of broad-leaved and coniferous forests, leading to three different classes. The new surface distribution is 40 % water, 36 % broad-leaved forest, and 24 % coniferous. Now the most common class is the water class, even though forest is more common. This way, models can introduce a bias at cells with at least three land cover types.

I discuss different land cover datasets available for WRF and show how to prepare them for WRF. A precise description of WRF is given by Skamarock et al. (2019) and I summarize it in section 1.4.1. I will focus on the Corine Land Cover (CLC) dataset and in the process of preparing this dataset for WRF, I will develop and test two new tools. First, I use a new aggregation method to tackle possible misclassification as described above. Second, I test a full integration of the CLC classes into the WRF model, similar to Golzio et al. (2021). I evaluate the different datasets with simulations over two periods: a one-day case and an eleven-day case. These additional analyses complement the work presented in the article by determining the skill of the different tools with more precision. A concern in the article was the lack of long-term validation, leading to this second longer simulation period as described in section 3.4. When I refer to a figure or table of the article, it is bold.

3.1 Summary of the article

The article below describes my work on Land Cover (LC). This work checks how representative the current LC selection is and its values assigned for simulations. LC influences many exchange processes between ground and atmosphere, making it crucial for correct weather forecasts. To save data and calculation time, resembling LC types are grouped into one class based on common physical characteristics. WRF has physical parameters tables (lookup tables; LUTs) connected to three LC datasets: USGS, MODIS, and NLCD. In this research, we tackle two problems connected to the LC datasets.

The first problem is that the CLC, a dataset made for Europe with high spatial accuracy, does not have a physical parameter table in WRF. To overcome this lack, Pineda et al. (2004) created a link between the USGS LUT and the classes of CLC, reducing the CLC diversity of 44 classes to 13 in the process. In a manner like that of Golzio et al. (2021), we create a 44-class LUT special for the CLC dataset and implement it in WRF.

A second problem exists in the aggregation of LC datasets to the simulation resolution grid. Selecting the most common (Single Level Mode; SLM) value to represent the cell can bias the selected classes. E.g., a surface consists of 40 % of water and the remaining 60 % is forest. However, the forest consists of two equal-sized forest classes, making SLM select the water instead of one of the forest types. Based on the CLC inherent hierarchical system, we introduce a new method, Multi-Level Mode (MLM), which checks superclasses before selecting its subclasses. Analyses of discrepancy over land between the two methods show 0.03 % mismatches at resolutions of 3 arcseconds (~111 m), increasing with coarsening resolution to a mismatch of 16.6 % at 5 arcminutes (~9 km).

Testing these aggregation methods and the two LUT options lead to four datasets based on the CLC dataset namely, CLC-MLM_{27}, CLC-MLM_{44}, CLC-SLM_{27}, and CLC-SLM_{44} where the numbers indicate the number of classes included in the LUT, 44 indicates the new physical parameter table and 27 indicates the conversion to USGS LUT. Adding them up to the already existing $USGS_{27}$ and $MODIS_{20}$ datasets allows the comparison between six datasets.

The simulations focus on the Durance Valley (DV) in the French pre-Alps, and the Cadarache Valley (CV), a tributary valley to the middle DV section that lies close to the 'clue de Mirabeau'. Previous research by Kalverla et al. (2016) has shown the importance of the orography during stable nights. Improvement of the LC dataset could enhance the simulation of the local flows.

The current simulation setup is based on Kalverla et al. (2016), using 4 nested domains with the parent domain at 27 km resolution and the three nested domains down to 1 km resolution decreasing at ratios of 3. The simulation runs from noon 19 to noon 20 February 2013. Its external forcing comes from the new ERA5 dataset at an hourly interval.

$USGS_{27}$ has the lowest roughness length and the highest albedo, whereas datasets of CLC_{44} classes have the largest roughness length and the lowest albedo. The domain average of 10 m wind speed reveals a correlation with the roughness length, whereas domain-averaged albedo seems to have little influence on the domain average 2-m temperatures. Further analyses with observations show that the $USGS_{27}$ has the worst performance of all tested simulations, while the CLC options outperform the $USGS_{27}$ and $MODIS_{20}$. Nevertheless, all CLC runs are relatively close, originating from the lack of discrepancy between SLM and MLM near the investigated locations and from the new LUT that is not yet complete. The best dataset is determined as the CLC-SLM_{27} for this 24-hour case.

3.2 Article

A Method for implementing Corine Land Cover Data in WRF illustrated with the Simulation of a Nocturnal Valley-Wind Case

M. de Bode[1,2], T. Hedde[1], P. Roubin[1], and P. Durand[2]

Submitted on Nov. 9, 2021 to *Earth and Space Science*, in the special section "Advances in scaling and modeling of land-atmosphere interactions"

[1] CEA, DES, IRESNE, DTN, Laboratory for Environmental Transfer Modeling, Cadarache F-13108 Saint-Paul-Lez-Durance, France
[2] Laboratoire d'Aérologie, Université de Toulouse, CNRS, UPS, Toulouse, France

Corresponding author: Michiel de Bode (Michiel.debode@cea.fr)

Abstract

For weather modeling purposes, incorporating land cover (LC) data highlights many problems. The straightforward Single Level Mode (SLM) aggregation is not adapted for high-resolution LC maps, with a high number of classes, because it could generate false classifications. We propose a Multi-Level-Mode (MLM) aggregation method that includes a hierarchical structure. This study focuses on the Corine Land Cover (CLC). Mismatch between MLM and SLM methods is weak at the finest horizontal resolution and increases to a value of around 16 % at 9 km horizontal resolution. To further integrate CLC data into WRF, we also built a dedicated table of physical parameters rather than using the classical conversion towards the USGS one. To evaluate the LC impact on the modeled boundary layer, we used WRF at 1 km to simulate a nocturnal valley-wind case in the heterogeneous western Alps area. We tested three LCs, USGS, MODIS, and CLC, with two physical parameter tables and two aggregation methods. CLC performs better than other tested LC. The CLC aggregation methods revealed limited differences between the simulated variables, although the MLM method gives slightly better results. Since these comparisons are restricted to 24 hours and to a single location with the same LC type, the differences between various simulations regarding atmospheric parameters probably result from horizontal advection from upwind areas where surface conditions differ. Extended time series with multiple locations need to be considered to assess the results presented here.

1. Introduction

It is crucial in meteorological simulations to accurately represent the exchange of momentum, energy, and matter between the surface and the atmosphere. These exchanges ("fluxes") are computed through parameterizations, relying on both a theoretical framework (i.e., a set of equations) and a set of physically measured coefficients required in the equations. For example, the friction velocity, which reflects the slowing down of the flow on the surface, is related to the wind in the surface layer and the value of the roughness length (z_0), which is a physical characteristic of the surface. Regarding the sensible heat flux, it is a component of the surface energy balance, in which surface albedo and emissivity are driving surface characteristics for the distribution between the radiative terms of this equation. Another critical component in this equation is the ground heat flux, dependent on the physical characteristics of the vegetation, soil, and soil water content. All these coefficients depend on the surface land cover (LC).

Consequently, the representation of LC in models through the appropriate parameters not only has a direct influence on the simulated processes close to the surface (Oke 2002), but it also affects mesoscale circulation (Hartmann 2015; Weaver and Avissar 2001; Yang 2004), and LC is crucial for correct simulations by numerical weather prediction (NWP) models (Jach et al., 2020). Most models, such as the Weather Research and Forecasting (WRF) model (Skamarock et al., 2019), often accommodate simulations of both small and large scales in a so-called grid-nesting mode for resource-saving and numerical error reduction purposes (Daniels et al., 2016; Wang and Gill 2012). This means that the fluxes are computed at different resolutions according to the different domains, and the question arises as to how to define an appropriate way to aggregate either the surface parameters or the fluxes to the considered cell size.

Two main approaches exist for using the LC information available in finer detail than the resolution of the grid (sub-grid variability). The first approach selects a unique representative LC from the available categories for each cell, often through the dominant approach (most common value a.k.a. SLM; Single Level Mode) or the nearest neighbor value. This LC type will represent the entire cell area, hence other LC types do not contribute to the surface parameters. This is the default option in WRF (Skamarock et al., 2019). The second approach includes all the fractions of LC and calculates fluxes based on the surface of each LC. For example, WRF has the Mosaic option to include sub-grid variation (Li, et al., 2013). All these methods highlight the need for good representative data sets.

Information on the LC type originates from data sets such as the commonly used USGS (Loveland et al., 2000) and MODIS (Broxton et al., 2014). Other data sets with more local coverage are Corine Land Cover (CLC; EEA 2020) for Europe and NLCD for the United States (Homer et al., 2020). A map like CLC offers a well-detailed description of LC, and therefore appears to be well adapted for meteorological models which resolve fine scales but since it is in a vector type, it requires a rasterization step (De Meij and Vinuesa 2014; Golzio et al. 2021; Prósper et al. 2019; Román-Cascón et al. 2021).

Meteorological models often offer an operational configuration in which a given number of classes represent the LC. For example, default WRF runs with surface parameters originating from 20 classes defined in the worldwide, 30'' resolution (~1 km) MODIS LC database. Each class corresponds to a specific value for each surface parameter through look-up tables (LUT) (with a seasonal variation of certain parameters like Leaf Area Index, albedo or roughness length). NWP models are generally equipped with one or more LC databases with their matching physical parameter LUT. For example, WRF may use native USGS or MODIS LC maps. If one wants to run the model with a new LC database containing its own class definitions, a new LUT has to either be defined or the new LC classes have to find an equivalent to an existing LUT. The creation of a new LUT minimizes the loss of information but is an intensive job as one has to determine the values for each physical parameter and each LC class index. Finding an equivalence with an existing LUT is easier but could lead to a loss of information if the existing LUT possesses fewer classes than the new one. Examples of both exist; the 44 classes of the European CLC data set were condensed to a 13-class subset of the 27 USGS LUT to run the MM5 model by Pineda et al. (2004). The use of a new LC is therefore easy, but at the expense of the initial richness of the LC description. Recently, a LUT has been built for the CLC data set so as not to lose the diversity of the 44 classes (Golzio et al., 2021).

In literature, one finds numerous studies which aim to evaluate the impact of LC representation on the simulation of atmospheric parameters: Schicker et al. (2016) analyzed WRF simulations based on MODIS or CLC instead of the default USGS LC data. Santos-Alamillos et al. (2015) compared simulations with USGS and CLC input maps. Li et al. (2018) investigated the Urban Heat Island with the USGS, CLC, and Urban Atlas (UA). Golzio et al. (2021) analyzed the effect of CLC with 44 classes, MODIS and USGS on heat fluxes. Most studies agree that over European areas, CLC represents the surface better than USGS, which improves weather simulation performance. Most studies convert CLC data to a USGS raster format however, preventing full benefit of the spatial and class detail that CLC offers. In this study, we will test the benefit of the CLC 44 classes LUT over the CLC converted to USGS, compared to MODIS and USGS.

One might assume that the higher the number of classes used to represent the LC, the better the description of the surface. Nevertheless, aggregation errors could be introduced by having a large number of classes as suggested by Román-Cascón et al. (2021). Figure 1 illustrates how the SLM aggregation option could generate a different output over an area according

to the initial number of classes available and could lead to a wrong class choice when the class number increases. For example, in Figure 1, the surface is composed of 44 % water, 37 % broad-leaved forest and 19 % mixed forest. Assuming the SLM approach, water prevails, even though the two forest types closely resemble each other and represent 56 % of the area. A convenient spatial aggregation method is therefore required to prevent misclassification when using a large class amount. To address the issue, this paper describes an approach for the performing of aggregation on a LC data set with many classes more correctly than with the SLM approach.

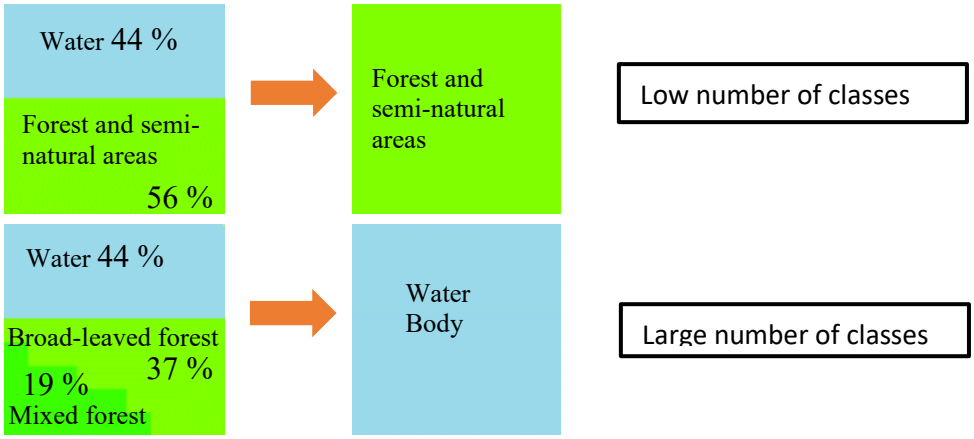

Figure 1: Example of SLM aggregation of an area and how the number of available classes affects the results.

Section 2 describes several LC data sets, presents the proposed aggregation method then finally analyses the aggregation results at various resolutions. This section will also explain how best to keep the detail of the original database through an appropriate LUT. Section 3 contains the description of the case study on which the WRF numerical simulations are run, in a well-instrumented valley of the French pre-Alps. The performance of the simulations, realized with different LC representations, is evaluated against the observations. Section 4 consists of the discussion of our results, and finally, section 5 concludes the paper.

2. Land cover data sets and aggregation

This section starts with the selection of an appropriate LC data set and its description. It continues by describing the newly proposed aggregation method and comparing the resulting maps with more traditional aggregation methods. Next, we discuss how to prepare CLC for WRF and add CLC specific parameters tables. Lastly, we describe all the data sets and options we have tested through the simulations.

a. Land cover data sets

To test the different means of aggregation, we start by selecting LC maps. Some of the available data sets have worldwide coverage, such as USGS, MODIS, Theia, and Globeland30, using resolutions with cell sizes ranging from 500 m down to 30 m (Table 1). Several other data sets are available or under development; for example, Open street map (© OpenStreetMap contributors 2021) is an initiative which tries to create a LC map based on local *in-situ* information. Although it is gaining in detail, it is not yet complete, as it relies on goodwill contributors. More generally, the choice of the data set and its associated resolution will depend on the intended purpose (Neumann et al., 2007). For instance, maps designed for meteorological purposes have a different focus from maps for agriculture or urban development, resulting in different nomenclatures.

Table 1 shows a selection of LC maps suited for meteorological use that are available for research without cost. For our WRF applications (de Bode et al., 2021), we require from a data set a spatial resolution of $O(100\ \text{m})$, many classes for a detailed surface representation, and regular updates. USGS nomenclature has a decent number of categories (based on the Anderson classification (Anderson et al., 1976), where USGS applies 24 (WRF extents it to 27 by adding the classes 'Playa', 'Lava', and 'White Sand'), with a 1 km resolution (a 500 m data set is available too) MODIS shares the same characteristics but with a yearly update and 20 classes. Alternatively, CLC has a large number of classes (44), a 3 level hierarchy organization and is updated every six years (2012 update described by Büttner 2014). CLC is a vector data set the surface polygons of which have a minimal area of 25 ha. CLC covers participating countries around Europe; the newest CLC map is based 10 m satellite images. Theia has two data sets, each of them with 22 classes, which differ in coverage and resolution (Inglada et al., 2017; Inglada et al., 2018). One data set covers the whole world at a 300 m horizontal resolution, and the other describes France at 10 m resolution. Lastly, Globeland30 (Gong et al., 2013) has a fine resolution map with 30 m horizontal resolution, covering the entire world, but it distinguishes only ten classes. Considering all these options, we will focus on CLC because it covers Europe, has a fine enough spatial resolution and distinguishes many classes.

Table 1: Details of several LC data sets covering Europe that are freely available for research purposes.

Name→ Property↓	USGS	MODIS	Corine Land Cover	Theia - France	Theia - World	Globelan d30
Coverage	World	World	Europe	France	World	World
Format	Raster	Raster	Vector	Raster	Raster	Raster
Most recent map	2001 - 2010	2019	2018	2019	2009	2020
Update period	Not specified	yearly	6 years	Mostly yearly	Not specified	3 years
Resolution	500 m	1 km (500 m)	Minimal width: 100 m Minimal surface: 25 ha polygons	10 m	300 m	30 m
Categories	24	20	44	22	22	10

b. The Corine Land Cover

CLC contains more detail than most other LC maps and even uses three levels of detail. The first and most basic level describes 5 level-1 classes, namely, "Artificial surfaces", "Agricultural lands", "Forest and semi-natural areas", "Wetlands", and "Water bodies". The second detail-level distinguishes 15 level-2 classes, which in turn can be further divided into a third and finest level of 44 classes, as described in https://land.copernicus.eu/Corinelandcoverclasses.eps.75dpi.png. For example, level-1 class "Forest and semi-natural areas" splits into three level-2 classes, namely "Forest", "Shrub and or herbaceous vegetation associations" and "Open spaces with little or no vegetation". Next, the level-2 "Shrub and or herbaceous vegetation associations" class splits into "Natural grasslands", "Moors and heathland", "Sclerophyllous vegetation" and "Transitional woodland-shrub" level-3 classes. Furthermore, a few attempts exist to create classifications at a more detailed level by adding another CLC classification level or taking into account e.g. the differences in local climate, as is done in the ECOCLIMAP database (Faroux et al., 2013; Gudowicz and Zwolinski 2016; Ikİel et al., 2012).

The CLC data set is a vector map consisting of polygon shapes, which entails spatial specifications different from those of a raster map. Their delineation is drawn from satellite observations, the latter having a horizontal resolution of 25 m in the older data set (2012) and 10 m in the newest one (Copernicus 2020). Every polygon spans an area of at least 25 hectares, has a minimum width of 100 m and is allocated to one of the 44 existing classes (Kosztra et al., 2019). Every six years, when an update of the LC occurs, an additional map highlights all surface changes larger than 5 ha. An overview of the latest coverage (2018) is displayed in Figure 2. Note that CLC only describes the 39 participating countries (since 2012) but it covers the whole of Western Europe. Sea surfaces are only included when they are less than 25 km off the nearest coast.

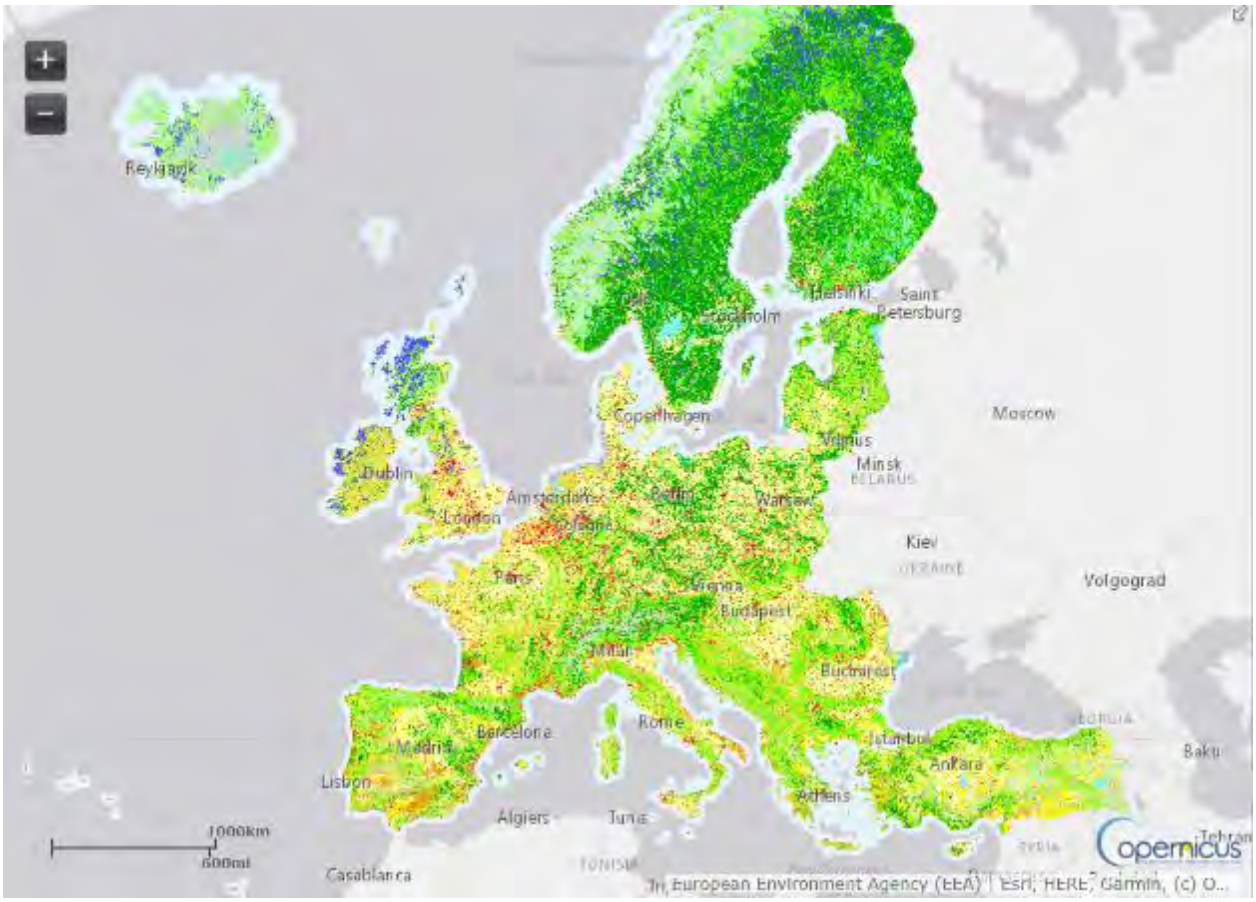

Figure 2: CLC Coverage 2018 at detail level 3. For nomenclature see https://land.copernicus.eu/Corinelandcoverclasses.eps.75dpi.png/view. Map from: https://land.copernicus.eu/pan-european/corine-land-cover/clc2018

c. New Multi-Level Mode Aggregation

i. Description of the method

As mentioned in the introduction, using the SLM aggregation technique can result in discrepancies between maps with many classes and maps with a limited amount of classes (Figure 1), with possible artifacts caused by a too high level of detail in the LC database. For this reason, we propose the use of a new multi-step aggregation to avoid such drawbacks whilst taking into account the richness of the initial data set. In order to do this, we use the three detail-levels provided by CLC through a method we call "Multi-Level Mode" (MLM) aggregation. This method is described below and illustrated in Figure 3 which shows the aggregation of the CLC data set on a real example restrained to a 6 x 6 arcminutes (11 x 11 km) domain containing 9 cells, each of them with a 2 x 2 arcminutes (~3 x 3 km). The figure details the complete process of MLM, starting with the vector map (Figure 3a) up until the creation of an aggregated grid (Figure 3i) at the end of the process. The aggregation consists of the following operations:

0. We preprocess the CLC vector data set by rasterizing it (Figure 3a) to a mesh size of roughly 10 m (⅓ arc second). With such a fine raster resolution, there is practically no information loss during this step as it is equal to or better than the satellite resolution from which CLC is computed (25 m for the 2012 data set, 10 m for CLC 2018 data set). The rasterization is made on a regular grid (⅓ arc second) in the longitude/latitude WGS84 geodesic system (EPSG:4326; Figure 3d).

I. Based on this raster map at ~10 m horizontal resolution, we create CLC level-1 (Figure 3b) and level-2 (Figure 3c) fine resolution maps by reducing all level-3 children classes to their corresponding parent class level, i.e., contracting 44 level-3 classes to 15 level-2 and 5 level-1 classes, respectively.

II. Here, we apply the SLM on the level-1 map (Figure 3b) in order to generate the first map with the targeted size of the mesh (Figure 3g; 3 km horizontal resolution in our example). Each cell matches the dominant level-1 class (e.g., the central cell belongs to level-1 class **2** "Agricultural areas"). The following steps will consist of selecting level-2 and 3 sub-classes from the dominant selected level-1 parent class surface.

III. Crossing this level-1 map (Figure 3g) with the fine-resolution (10 m) level-2 map (Figure 3c), we then build a fine-resolution map with only children classes of the selected dominant level-1 (Figure 3e). The level-2 data which are not children of a selected level-1 class are discarded and represented as white areas in Figure 3e (e.g. at the central cell, all level-1 areas with a value other than 2). The white areas are excluded from the aggregation process.

IV. We apply the SLM to the remaining level-2 classes (i.e. non-white areas from Figure 3e) so as to extract the level-2 dominant class at the final targeted resolution (here 2 arcminutes or roughly 3 x 3 km), represented in Figure 3h. To give an example, the central mesh now belongs to level-2 class **2.4** "Heterogeneous agricultural areas" which is a child class from level-1 class **2** "Agricultural areas".

V. Similarly to step **III**, we cross the previous level-2 map (Figure 3h) with the fine-resolution level-3 map (Figure 3d), and build a fine-resolution map where only children classes areas of dominant level-2 remain (Figure 3f). The level-3 areas which are not children classes of level-2 as selected in Figure 3d are thus discarded and represented as white areas in Figure 3f. This latter presents even more white areas than in Figure 3e, as for example on the central cell. All level-2 areas with value other than **2.4** were removed.

VI. Similarly to step IV, we apply the SLM on the remaining level-3 classes (built as explained in **V**, Figure 3f) for selecting level-3 classes at the final targeted resolution (2 arcminutes or roughly 3 x 3 km), represented in Figure 3i. To give an example, the central cell is now associated to level-3 class **2.4.2** "Complex cultivation patterns".

Figure 3i thus represents the final output of the MLM method. By comparison, Figure 3j shows the results of the traditional SLM applied directly to the Figure 3d map, which illustrates how the SLM output can differ from MLM. Figure 3j suggests more "Urban fabric" (red color with class index **1.1.2**) as a dominant type, which could be a consequence of "Urban fabric" being less spread in different level-3 types than the forested areas. On the other hand, in areas where land use is highly variable, the final outcome of the aggregation can be sensitive to the geographic division of the cells. If the 3 km grid borders had been slightly shifted to the north, the "Urban fabric" on the right side of Figure 3d would have occupied the mid-right cell rather than that of the top-right in Figure 3j, and would possibly also appear in Figure 3i.

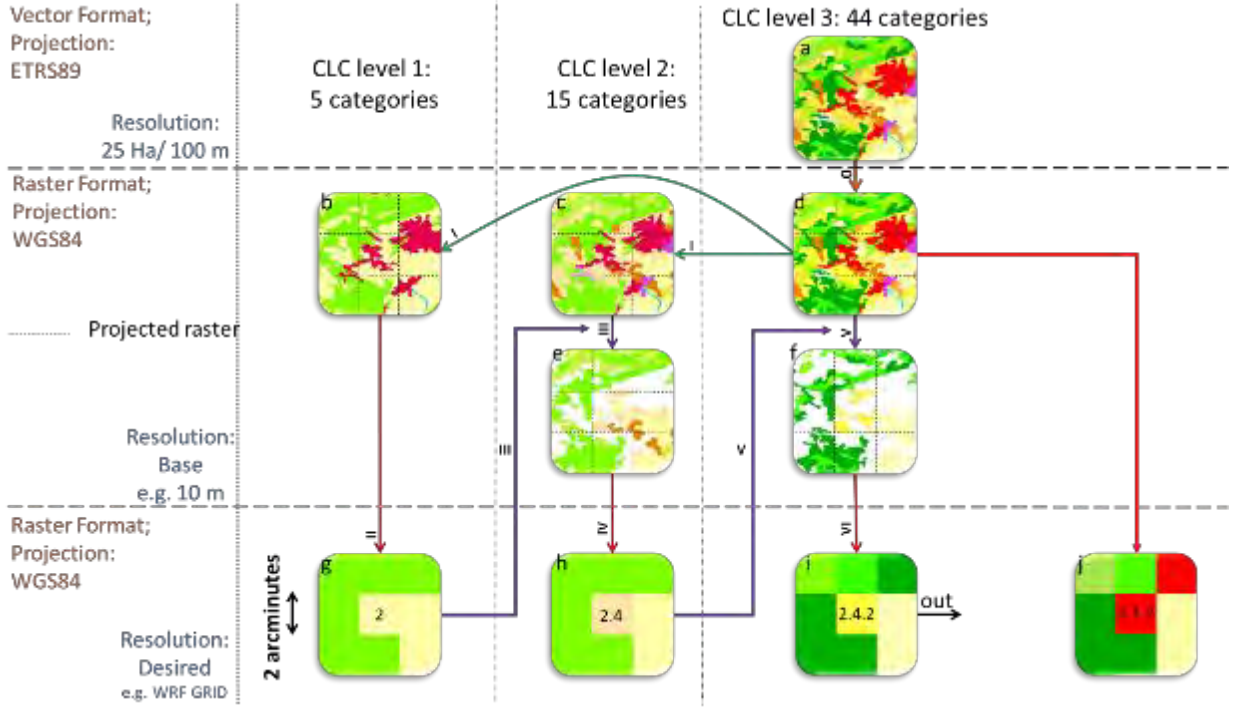

Figure 3: Flowchart for the new multi-level mode (MLM) aggregation for categorical data sets. The diagram depicts the steps performed in order to generate a map at a required horizontal resolution (here 2 arcminutes or ~3 km, represented by the dashed lines on finer resolution maps) from the CLC vector base map (a). Color-coding originates from the Copernicus color structure and is described in more detail at https://land.copernicus.eu/Corinelandcoverclasses.eps.75dpi.png/view. Each plot represents the same ~9 x 9 km area. The arrows indicate the process of each step described in the text. The brown arrow means rasterization and projection (step 0). Green arrows indicate reducing children classes to their parent class (step I). Red arrows denote SLM (steps II, IV & VI). Purple arrows indicate increasing detailed level of dominant classes (steps III & V). Plots b to f are ~10 m resolution maps, g to j are at target resolution (here 3 km). i is the final map obtained through MLM, j is the one obtained through SLM.

ii. Difference with a conventional aggregation method

We analyze the difference ("mismatch") between the two aggregation methods, as illustrated between the "i" and "j" plots of Figure 3, over an area covering the SE of France and NW of Italy. The land use of this area is represented in Figure 4a, according to the CLC classification. Two zones are highlighted, the first one (Z1) includes the Mediterranean shoreline, as well as the Marseilles conurbation at its eastern side, and the second one (Z2) is purely continental over the French-Italian border (encompassing a large homogeneous cultivated area in the Po valley). From the enlarged plots of Z1 and Z2, we can identify at a glance that the in-land part of Z1 presents a much higher diversity than Z2, either at the initial resolution (Figure 4b and 4c), or once reduced at a 3 km scale with the MLM method (Figure 4d and 4e). If we now examine the mismatch between the two aggregation methods (Figure 4f and 4g), we can see that locations with little LC spatial variability, such as sea, large lakes, and large homogeneous agricultural areas (as in Z2), are less affected by the aggregation method than highly variable areas (basically, the heterogeneous part of Z2 and the inland of Z1).

In order to establish a quantitative comparison between the two methods, we computed the mismatch (in % of the land surface) after aggregation for various horizontal resolutions; the results are presented in Table 2. All the domains cover the same area regardless of the mesh size. Additionally, the coarsest domain (9 km resolution) has a second entry, covering a larger area. The sea cells were excluded for mismatch computation, since aggregation is straightforward over sea. When comparing the different resolutions over the same domain, we move from a mismatch of 16.6 % at 9 km resolution to a mismatch of 0.03 % at 111 m. So, as we expected, for the finest resolution, the two aggregation methods behave quite similarly. Since a cell in a 111 m resolution grid covers around 1 ha, and the vector shapes have at least 25 ha surface, it leaves little chance for multiple classes to be present in a single cell. On the other hand, increasing the aggregation surface size leaves more classes to be present in a single cell, and the probability of mismatch between classification increases. In short, the coarser the resolution, the greater the difference between aggregation methods.

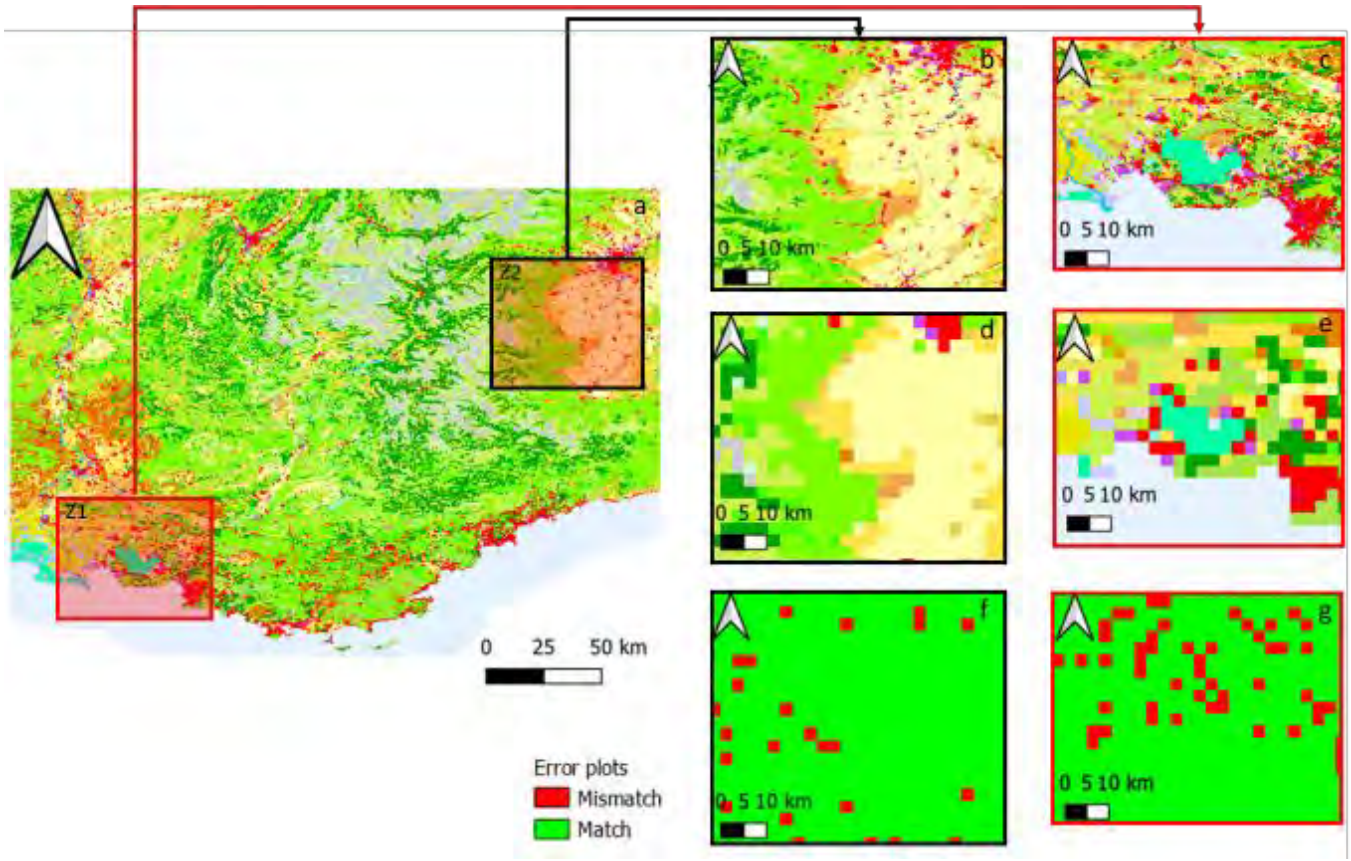

Figure 4: LCs in SE France and westernmost Italy at fine resolution. A zoom-in area Z1 encompasses the shoreline (c, e & g), and a second zoom-in area Z2 encompasses the French-Italian border (b, d &f). (b) & (c) show fine resolution LC map. (d) & (e) show the 3 km MLM-aggregated map for the same areas. (f) & (g) show the cells with a mismatch between the two aggregation methods in red. A legend for all 44 LC classes is in https://land.copernicus.eu/Corinelandcoverclasses.eps.75dpi.png/view.

Table 2: Mismatch statistics between SLM and MLM aggregation techniques for different grid resolutions. The mismatch metrics exclude all cells with sea from the data. The domain is D03 as shown in Figure 5 except for the last line which corresponds to D02 in Figure 5.

Final horizontal resolution (arc angle)	*Number of grid cells*	*Northwest corner*	*Southeast corner*	*Land fraction*	*Mismatch overland*
111 m (3'')	34560000			0.64	0.03 %
333 m (10'')	3110400			0.64	0.5 %
1 km (30'')	345600	3°E, 46°N	9°E, 42°N	0.63	8.3 %
3 km (2')	21600			0.63	12.0 %
9 km (5')	3456			0.63	16.6 %
9 km (5')	42336	4°W, 52°N	16°E, 38°N	0.80	11.6 %

d. How WRF uses LC

i. Physical parameter tables

The LC classes are associated to physical parameters through lookup tables (LUT) so they can be used by the land surface model parameterizations. The WRF model proposes such LUTs for USGS, MODIS and NCLD LC data sets: the

"LANDUSE.TBL" file contains summer and winter values of land use parameters, whereas, also depending on LC, the "VEGPARM.TBL" file allows maximum and minimum values of some vegetation parameters (other tables may be required for different land surface schemes). Before this work, CLC however did not have a dedicated LUT of its own: the use of CLC in a model such as WRF requires either the converting of CLC data to an already existing LUT or the creation of a new dedicated LUT.

A method developed by Pineda et al. (2004) converts each CLC class into the closest USGS class. This method matches the 44 CLC classes with 13 of the 27 USGS classes with a surjective but non injective function thus leading to a loss of LC information due to the aggregation of several CLC classes into the same USGS class. Alternatively, creating a new complete LUT with values for all 44 CLC classes requires the knowledge or the computation of the associated parameter values (obtained e.g. from satellite and *in-situ* measurements). Since the computation of these values is well beyond the scope of this study, we have endeavored to create a new CLC LUT with 44 classes, based however on existing parameter values.

Using methods similar to Golzio et al. (2021), we used albedo, roughness length, emissivity, thermal inertia, and moisture availability data provided by Pineda et al. (2004) in order to build a 44-class LUT. We consider Pineda et al. (2004)'s values valid for our study because they were estimated for northern Spain areas, which share, in terms of LC and climate, a great similarity with our study area: both are at similar latitudes, in Mediterranean climate, and include a part of a major mountain chain (the Pyrenees vs. the Alps). Afterwards, once we included the satellite-based data from Pineda et al. (2004), some parameters were still missing, such as leaf area index (LAI) and rooting depth. These gaps were filled with the values available from the USGS database. Since USGS has fewer classes than CLC, a USGS class can sometimes supply a value to several CLC classes. For example, LAI values of USGS class "Dryland Cropland and Pastures" will be attributed to the two CLC classes "Non-Irrigated arable land" and "Pastures". The final result is a 44-entry LUT, called CLC_{44}, which can now be used for WRF simulations. Since data from Pineda et al. (2004) is not as differentiated as are CLC classes however, some classes are clustered. To give an illustration, all the artificial surfaces classes share the same parameter values (11 3rd level classes in CLC). All these non-differentiated classes of the 44 CLC options lead to an effective number of 28 unique classes among the total of 44. This table is presented and freely available at https://github.com/MichieldeB/WRF_tables. In the future, this LUT might be easily enriched if more data would become available (e.g. parameter values reflecting the diversity of artificial surfaces). Having created this new CLC LUT, we encourage European WRF users to improve it.

ii. Assigning values to cells

The physical parameters associated with each of the WRF surface cells are determined during the WRF preprocessing. Since the WRF V3.8, the default method for representing LC class has been determined based on the largest LC fraction present in a cell from the given input LC map. It works similarly to a SLM approach, it is therefore important to give the model an input map with a resolution as close as possible to the actual WRF resolution, otherwise WRF would apply a SLM aggregation and we would lose the benefit of our MLM method. Over mid latitudes, WRF is usually run on a rectangular horizontal grid on a Lambert Conformal Conic (LCC) projection. This means that even with a similar resolution, a longitude/latitude square grid LC maps needs aggregation in order to implement the values in the Lambert grid.

As an alternative to the dominant approach, WRF provides the Mosaic option to account for the sub-grid LC variability that the input maps may contain in a cell (Li et al., 2013). It is a form of resolution dependency where physical parameters do not originate directly from one representative value from the LUT but are computed for each cell through a weighted average of the LUT parameters; the weights are computed from the N main LC classes area fractions (N is tunable). The computed value of each cell parameter reflects the main LC fractions within WRF domain cells. To assess the effect of this sub-grid option in the WRF model, we will also use this option among the various simulation tests described below.

e. Description of the simulations

i. Configuration of the series of experiments

We launched a series of simulations, in which WRF was run in a two-way nested mode with four domains of horizontal resolution from 27 to 1 km (details in section 3.2). We grouped these simulations into two experiments.

The first experiment was to test the influence of the chosen LC data set (USGS, MODIS and CLC), the influence of the aggregation method used to build up the CLC data sets and the influence of the CLC LUT. Six runs were performed: $USGS_{27}$, $MODIS_{20}$, CLC-SLM_{27}, CLC-MLM_{27}, CLC-SLM_{44}, and CLC-MLM_{44}. The subscript indicates the number of available classes in the LUT. USGS and MODIS are thus used in the WRF default configuration, with 27 and 20 classes, respectively. In the label of the CLC runs, "SLM" and "MLM" refer to the corresponding aggregation method. For the latter, two LUTs are used corresponding to 27 (USGS) or 44 classes (new CLC) as indicated by the subscript. Table 3 shows the settings in more detail: note that the only MODIS data set available is at 30 s (~1 km), so consequently it does not have adapted resolutions for coarser domains resolution from 3 to 27 km.

The second experiment tries to quantify the effects of the different LC input maps resolutions and how sub-grid availability influences the skill of the WRF model. We use the CLC-SLM$_{27}$ LC data set for this experiment, since it is a data set used in other comparison studies with CLC (Golzio et al., 2021; Li et al., 2018; Santos-Alamillos et al., 2015; Schicker et al., 2016) and has been shown to be similar or superior to MODIS and USGS. Since we focus here on input map resolution influence, the same aggregation method (SLM) is used for all the runs. The map resolutions tested were 111 m (named "res_111m") and 1 km ("res_1km") and the same map resolution is given whatever the WRF domain. One case ("res_dep") from experiment #1 is used as a reference; it is using a resolution map similar to the cell size. For these three runs, the SLM method and the dominant fraction option were adopted. A fourth simulation was run, identical to "res_111m" except that the Mosaic option was used instead of the dominant fraction. In total we compared three different dominant factor approaches complemented with one Mosaic approach simulation. Table 3 denotes the exact resolutions used for the different simulations.

Table 3: WRF runs of experiment #1 and #2. Bold indicates where simulations show differences compared to the USGS$_{27}$ simulation. SLM is the classic Single Level Mode aggregation. MLM is the new Multi-Level Mode aggregation. CLC$_{44}$ is the new LUT with 44 entries.

	Case name	Map provider	WRF domains (hor. res.)	Input map resolution	Map aggregation method	LUT	WRF cell representation
Land Cover, Experiment #1	USGS$_{27}$	USGS	D01 (27 km) D02 (9 km) D03 (3 km) D04 (1 km)	10 min 5 min 2 min 30 sec	-	USGS	dominant fraction
	MODIS$_{20}$	MODIS	D01 (27 km) D02 (9 km) D03 (3 km) D04 (1 km)	**30 sec**	-	**MODIS**	dominant fraction
	CLC-MLM$_{27}$	CLC	D01 (27 km) D02 (9 km) D03 (3 km) D04 (1 km)	10 min 5 min 2 min 30 sec	**MLM**	USGS	dominant fraction
	CLC-SLM$_{27}$	CLC	D01 (27 km) D02 (9 km) D03 (3 km) D04 (1 km)	10 min 5 min 2 min 30 sec	**SLM**	USGS	dominant fraction
	CLC-SLM$_{44}$	CLC	D01 (27 km) D02 (9 km) D03 (3 km) D04 (1 km)	10 min 5 min 2 min 30 sec	**SLM**	**CLC$_{44}$**	dominant fraction
	CLC-MLM$_{44}$	CLC	D01 (27 km) D02 (9 km) D03 (3 km) D04 (1 km)	10 min 5 min 2 min 30 sec	**MLM**	**CLC$_{44}$**	dominant fraction
Resolution, Experiment #2	res_dep same as CLC-SLM$_{27}$	CLC	D01 (27 km) D02 (9 km) D03 (3 km) D04 (1 km)	10 min 5 min 2 min 30 sec	**SLM**	USGS	dominant fraction
	res_1km	CLC	D01 (27 km) D02 (9 km) D03 (3 km) D04 (1 km)	**30 sec**	**SLM**	USGS	dominant fraction
	res_111m	CLC	D01 (27 km) D02 (9 km) D03 (3 km) D04 (1 km)	**3 sec**	**SLM**	USGS	dominant fraction
	res_mos	CLC	D01 (27 km) D02 (9 km) D03 (3 km) D04 (1 km)	**3 sec**	**SLM**	USGS	**Mosaic** **On 13 dominant classes**

ii. Domain-wide differences between the simulations

To evaluate the overall effect of using different LC data sets, aggregation methods, and LUT, we compare a few surface parameters averaged over the whole of the 1 km resolution domain ('D04' in Figure 5), an area of 100 x 121 km. The results are presented in Table 4, for albedo, emissivity and roughness length, which are crucial parameters for surface flux estimates. These three parameters have limited variations on short periods of time and thus can be compared independently of the atmospheric simulations. The average values correspond to the case study which will be detailed in section 3.

Differences in albedo are noticeable since CLC_{44} values are roughly 20 % lower than the others. Such differences can significantly impact the surface radiation budget during daytime, with direct consequences on surface temperature and heat fluxes, hence on the boundary-layer structure. As CLC_{27} values are close to those of USGS and MODIS, we may conclude that CLC_{44} values highlight the effect of more LC classes. Indeed, 20 or 27 classes lead to similar albedo values (~0.22) whatever the LC source (MODIS, USGS or CLC), whereas 44 classes result in significantly lower albedo (~0.17).

The same conclusion applies to the average emissivity, which does not deviate much from 0.93 except for CLC_{44}, for which it increases to ~0.96. However the impact on meteorological parameters is not expected to be great, since the increase in outgoing longwave radiation caused by a higher surface emissivity is in part compensated for by a higher absorption of incoming longwave radiation, and vice versa.

Looking at the roughness z_0, the $USGS_{27}$ gives a small value (17 cm), whereas all other LCs are around 30 cm. We may notice a light influence of using 44 classes, as the values increase from 27 cm for CLC_{27} and up to 32 cm for CLC_{44}. Such differences have a direct impact on the wind speed and friction velocity computed in the simulation. Since Table 4 presents values averaged over the domain, it may hide a local variability. Using MAE to measure domain variability for each variable and each case shows that variability is the smallest in the $USGS_{27}$ case (0.02, 0.006 and 11 cm for resp. albedo, emissivity and z0), whilst the other cases reveal a variability that increase to 0.05, 0.014 and 19 cm, respectively.

Table 4: 1-km resolution domain-wide (over a 100 x 121 km area) averaged values of albedo, emissivity and roughness length for all six different LCs corresponding to the case study described in section 3.1.

Parameter↓ Case →	*$USGS_{27}$*	*$MODIS_{20}$*	*$CLC\text{-}SLM_{27}$*	*$CLC\text{-}MLM_{27}$*	*$CLC\text{-}SLM_{44}$*	*$CLC\text{-}MLM_{44}$*
albedo [-]	0.221	0.217	0.211	0.212	0.171	0.171
emissivity [-]	0.925	0.924	0.928	0.929	0.964	0.964
z0 [cm]	17	29	27	27	32	32

3. WRF simulations

After creating LC maps with the new MLM method and a new LUT specifically associated with CLC, we have to test its performance with meteorological simulations and compare it with the performance of default LC and built-in LUT. This section starts with a description of our selected case: location, available measurements, and meteorological conditions. We then present the WRF configuration and eventually we discuss the results first in the form of domain-wide averages and then through a comparison with detailed observations at specific locations.

a. Case study

i. Location

Our case study takes place in the Alpine foothills of Southern France (Figure 5a), bordered by the Rhône valley on the west and the Alps to the north and east. In the south and west lie two mountain ridges, culminating around 1 km elevations (Luberon and Sainte-Victoire in Figure 5b). We focus on the middle segment of the Durance valley (DV), separated from its lower and upper parts by narrow paths ("clues" in French: The "Clue de Mirabeau" at the downstream end and the "Clue de Sisteron" at the upstream end). This section of the DV is a relatively straight and wide valley, with several small tributary valleys such as the Cadarache valley (CV) (Figure 5c), surrounded by high-raised reliefs preventing synoptic winds from easy access to the valley bottom. Typical winds in the area are the local "Mistral" (a NW wind which has been channeled down the Rhône valley and then up the Durance valley), SE winds which often come with precipitating perturbations, sea breezes and anabatic winds from the W, and katabatic valley winds. Most types of wind regimes have previously been realistically reproduced by simulations with a 1 km grid (Duine 2015; Kalverla et al., 2016).

ii. Observations

Observations come mainly from the "La Grande Bastide" (GBA) site, a permanent 110 m tower which stands within the confluent zone of the DV and the CV (Figure 5c), which means that funneled winds from the CV can influence low-level observations of the mast whereas the top of the mast is under the influence of DV winds. As a complement to these

installations a 30 m mast (M30) has been installed in the CV for the duration of the KASCADE-2013 campaign (Duine et al., 2017). M30 focused on observing nocturnal down-valley winds in CV, a recurring phenomenon in calm-wind, clear-sky periods. M30 measured sensible and latent heat fluxes at 30 m, and the four components of the net radiation (long- and shortwave, incoming and outgoing) at 2 m and 20 m. M30 was also the location for observations with radiosondes on both tethered and free ascending balloons. A Sodar was placed to the north and outside the CV to continuously measure the wind profile between 75 m and 500 m agl (above ground level).

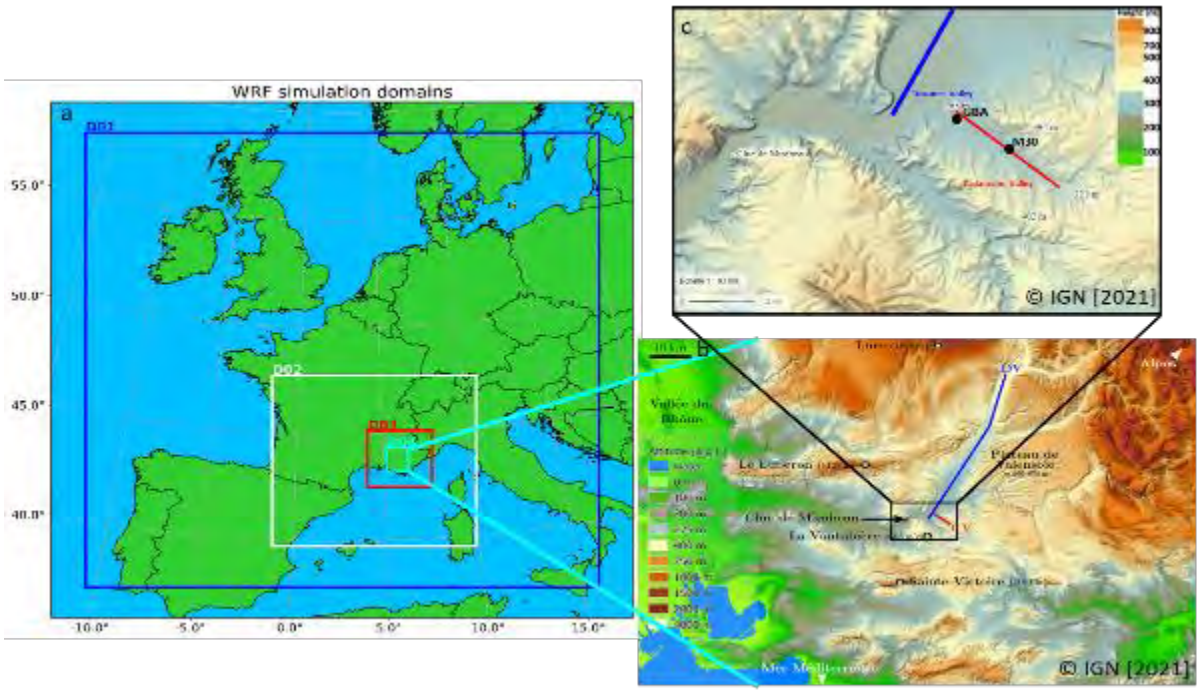

Figure 5: Map (a) shows the 4 nested domains (D01 to D04) used in WRF simulations. Map (b) shows D04 orography, around the pre-Alps, the middle Durance Valley (DV) (blue line) and Cadarache tributary Valley (CV) (red line). Map (c) is a zoom-in around the measurement site of KASCADE-2013 campaign inside CV. M30 30 m mast position is 43.6855°N, 5.7617°E and GBA 110 m 43.6944°N, 5.7461°E.

iii. Meteorological conditions of the selected case

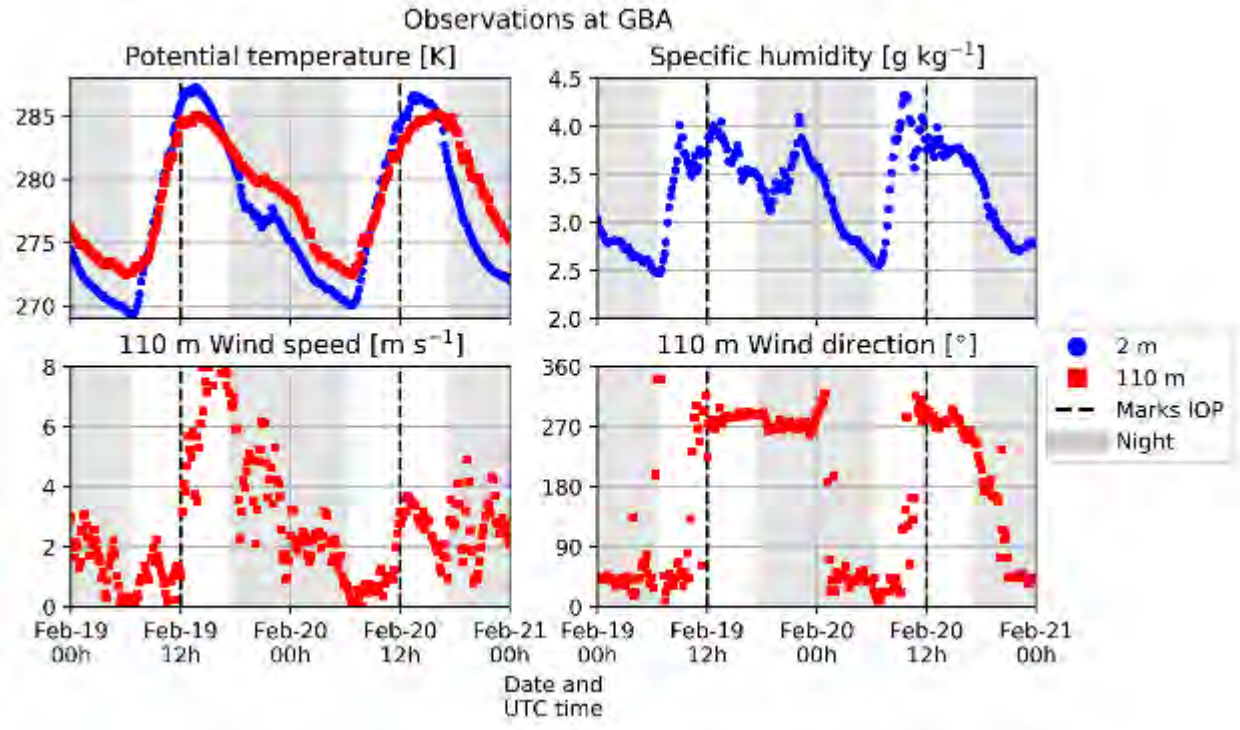

Figure 6: Quantities observed at GBA station from February 19 until February 20, 2013. (a) potential temperature at both 2 and 110 m heights. (b) specific humidity at 2 m. (c) wind speed and (d) direction at 110m. The night time periods are shaded. Considered IOP starts at 12:00 UTC 2021 February 19 and ends 24h later.

We selected an Intensive Observation Period (IOP) from KASCADE-2013 (Duine et al., 2017), which was used as a reference case to WRF settings by Kalverla et al. (2016). Our case study took place in February 2013 from noon on 19 February to noon on 20 February. The sky was clear, no fronts were present in the area surrounding the DV, and high-pressure conditions prevailed. At the geopotential height of 500 hPa, a weak pressure gradient existed, with pressures decreasing to the east (not shown). This pressure gradient, though adequately oriented, was too weak to ensure Mistral winds. Accordingly, weather briefings from Météo-France reported no Mistral wind something not detected in our observations either.

Figure 6 shows the 2-day period embracing the 24 hours of our case. The potential temperature exhibits a diurnal range of 18 K at 2 m and 12 K at 110 m, which are typical ranges for clear-sky, moderate wind events enabling stable stratification to develop at night. The specific humidity is quite constant during the daytime and diminishes at night, possibly caused by dew deposition since relative humidity at 2 m reaches 95 % and M30 measurements show that specific humidity at 2 m is lower than at 30 m (not shown). The wind speed at 110 m peaks in the afternoon, coming from the west (pre-alps anabatic wind favored by weak synoptic forcing), whilst at night the wind continuously slows down and orientates to the NE around midnight, following the DV downward. The wind direction shows dramatic changes between day- and night-time regimes. While the night-to-day change occurs 2 h after sunrise however, there is a 6-hour delay after sunset for the day-to-night change. This delayed setting results from the fact that DV down-valley wind starts in upslope parts of the DV (up to 80 km upstream) and progressively reaches lower regions (Duine et al., 2017). The arrival of the NE winds after 00 UTC on 20 February coincides with the more intense cooling observed on 110 m temperature observations.

Additionally, the radiative balance (analyzed in detail in section 3.5.1 and Figure 9) shows two near-perfect clear-sky days and nights, with net radiation maxima around 400 W m^{-2} just before 12 UTC. Furthermore, three radiosondes were released during the noon-to-noon IOP time-period so as to observe the tropospheric vertical structure (Figure 8). They show a neutral profile in the atmospheric boundary layer during the daytime (mixed layer), which persists after sunset as a residual layer, whereas after sunset a stable layer begins to grow from the surface upwards (more details will be given about these profiles in section 3.4.2). Sodar observations (not shown) show that, in the 75 to 500 m layer, the wind speed decreases during the night, similarly to the 110 m wind evolution in Figure 6c, though this slowing down is delayed at higher altitudes.

b. WRF settings, tables, and experiment plan

The KASCADE-2013 case was simulated with the WRF mesoscale model, maintained by UCAR and NCAR. WRF is a non-hydrostatic NWP model, the configuration of which can be adapted through a set of parameterizations available for the different modules, such as boundary layer, convection, microphysics, and radiation. Altogether, our settings follow the previous study's reference parameterization and domain settings as defined by Kalverla et al. (2016) for simulations of mesoscale valley winds. The WRF experiment common tunings are summarized in Table 5.

Table 5: Global WRF settings. The last column contains the relevant references.

Dates	2013-02-19 12:00:00 → 2013-02-20 12:00:00 UTC (KASCADE-2013, IOP16)				Duine, 2015
WRF model version	V4.0.2				Skamarock et al., 2019
Global data forcing (initial and boundary conditions)	ECMWF ERA 1 h time step, 0.25° horizontal resolution, 38 vertical levels				Hersbach et al., 2018b, 2018a
Simulation time	48 h (starting on 2013-02-18 at 12:00 UTC)				
Spinup time	The first 24 h				
Model top	50 hPa				
Two-way nested domain	D01	D02	D03	D04	
horizontal resolution	27 km	9 km	3 km	1 km	
Horizontal cell number (W-E x S-N)	89 x 89	106 x 100	100 x 100	100 x 121	
Time step	162 s	54 s	18 s	6 s	
Output interval	180 min	180 min	60 min	10 min	
Topography maps	10 min	5 min	2 min	30 s	
Vertical levels	46				
Microphysics	WRF Single–moment 6–class Scheme				Hong et al., 2006
Planetary Boundary Layer scheme	Quasi–normal Scale Elimination (QNSE) Scheme				Sukoriansky et al., 2005
Surface layer scheme	QNSE surface layer Unified				Sukoriansky 2008
Land surface option	NOAH land surface model				Tewari et al., 2004
Longwave radiation	RRTMG				Iacono et al., 2008
Shortwave radiation	RRTMG				
Radiation time step	10min				
Cumulus parameterization	Kain Fritsch		No parameterization		Kain 2004

The simulations are initialized and later constrained at a large scale every hour with ERA-5 reanalysis from ECMWF. In the simulations performed by Duine 2015 and Kalverla et al. (2016), the horizontal resolution of ECMWF available

reanalysis was 0.70° (~80 km). According to the WRF guidelines recommending a ratio of 3 between the horizontal resolution of a domain and its parent, the resolutions of the nested domains had thus been chosen by these authors as 27, 9, 3, and 1 km, keeping roughly the same ratio of 3 between reanalysis and coarsest domain resolutions. Since ERA-5 now offers a resolution as fine as 30 km, we wondered whether the outermost domain could be omitted in the simulations, starting with the coarsest resolution at 9 km. After some tests and comparisons between the model outputs (not shown here) with 3 and 4 nested domains and our measurements, we were able to conclude that 4 domains simulations starting with a 27 km parent domain were of higher quality. This conclusion was drawn from metrics computed on the differences between local observations and simulations in a style similar to the one used in the discussion section.
Regarding the finest resolution, we relied on Kalverla et al. (2016) stating that 1 km was fine enough to correctly simulate the flows and their diurnal cycle at the scale of the Durance Valley. Furthermore, our goal is to evaluate the impact of LC on the overall atmospheric structure, and not to resolve very local (tributary CV) circulations, as done by de Bode et al. (2021). Lastly, finer-scale (e.g. at 300 or 100 m) simulations require many more computational resources, not to mention the "grey zone" question with the possible need to adapt the turbulence scheme.

c. Domain-wide evaluation of the simulations

A domain-wide comparison was undertaken to evaluate the mean influence of the LC data sets on a large area. No comparison with observations is made at this stage. The studied domain is the innermost one (D04, the same as in section 2.5.2) with 1 km horizontal resolution (Figure 5b), a 100 x 121 km area encompassing the middle DV, the pre-Alps and a small part of the Mediterranean sea shore around Marseille's conurbation, i.e. comprising a wide variety of LC classes ($USGS_{27}$ uses 13 of 27 possible classes, $MODIS_{20}$ 15 of 20, $CLC\text{-}MLM_{44}$ 30 of 44, $CLC\text{-}SLM_{44}$ 31 of 44 and both CLC_{27} 10 of 27).

Two domain-wide and IOP-averaged quantities are compared in Table 6: the 2 m potential temperature (θ_{2m}) and 10 m wind speed (WS10) as these parameters give a first idea of how different LCs affect the meteorological variables near the ground. Further details are given by splitting out the spatial and temporal components of the average and looking for their minimum and maximum.

θ_{2m} presents little difference between simulations, which is striking because this result is in contrast with the different albedo and emissivity associated with CLC at least when 44 classes are considered (Table 4). Physical processes related to soil composition (in particular soil water evaporation) are probably of much larger importance in controlling the temperature close to the ground than the restricted modification of the radiation balance through an albedo variation of 0.05. The variability in time and space is comparable between the simulations, though slightly higher for the CLC runs.

Regarding wind speed, $USGS_{27}$ has the highest value, and $MODIS_{20}$ is ~0.3 m s^{-1} slower with a comparable decrease in value range. The CLC_{44} winds are slightly slower on average, but with a similar temporal variability to MODIS, which is valid for all CLC, irrespective of the aggregation method or the LUT used. As expected, the higher average winds are globally related to lower roughness lengths and vice versa (see Table 4): z_0 values of 17 cm correspond to WS10 value of 4.2 m s^{-1}, whereas z_0 value of 32 cm correspond to 3.8 m s^{-1}.

Table 6: Mean and range of values averaged over domain 04 for the 2 m temperature (θ_{2m}) and 10 m wind speed (WS10). In each table cell, the top value is the average over both the whole D04 domain (121 x 100 values) and the 24 h period; temporal min (max) is the 24 h period minimum (maximum) from the domain-averaged values; spatial min (max) is the domain minimum (maximum) determined among the 24 h-averaged cells values.

Quantity↓ Case →	*$USGS_{27}$*	*$MODIS_{20}$*	*$CLC\text{-}SLM_{27}$*	*$CLC\text{-}MLM_{27}$*	*$CLC\text{-}SLM_{44}$*	*$CLC\text{-}MLM_{44}$*
T2 [K]	277.0	277.1	277.1	277.0	277.0	277.0
temporal min, max	273.9, 282.5	273.9, 282.5	273.9, 282.7	273.8, 282.6	273.7, 282.7	273.7, 282.7
spatial min, max	271.9, 283.0	271.8, 283.2	271.8, 283.1	271.8 283.0	271.7, 283.0	271.6, 283.0
WS10 [m s^{-1}]	4.2	3.9	4.0	3.9	3.8	3.8
temporal min, max	2.4, 6.0	2.3, 5.5	2.4, 5.6	2.3, 5.5	2.3, 5.4	2.3, 5.4
spatial min, max	1.2, 10.8	1.1, 10.4	1.2, 10.6	1.1, 11.2	1.2, 10.1	1.1, 10.5

d. Local evaluation against observations

After checking differences due to the LC data sets over the whole domain, we will examine in the following sub-sections their effects on some variables at two localized points in the Cadarache valley, namely the GBA and M30 stations (see Figure 5 & Figure 7). We will evaluate the differences between the various simulations and compare them to observations: GBA tower observations for humidity and temperature at 2 m, and temperature and wind at 110 m agl; M30 mast for the radiation balance. We extracted from the simulation outputs the values at the cells which encompass the observation sites. Additionally, for the GBA measurements at 110 m agl, we interpolated the model output on the vertical to match the height of observations.

i. Local Land Cover maps

The LC around the case study site is quite rich, as seen from the full resolution CLC map, with 16 classes in the area (see Figure 7a): it is a mix of 7 forest or semi-natural covers (green areas), 4 agricultural (yellow to brown) and 4 urban (purple and red) with some water surfaces (blue). The USGS map (Figure 7b) is quite poor in spatial variability and far from terrain reality, as it mainly shows uniform dry land and crop pasture (brown) despite a theoretical resolution of 500 m. MODIS map (Figure 7c) is closer to terrain reality showing a mix of forest, agricultural and urban areas with two noticeable mistakes: the water surface does not appear though its surface is ~2 km^2 (i.e. 2 MODIS 1 km^2 pixels) and urban areas have a ~2 km shift to the North. The CLC maps (Figure 7d and e) even at 1 km resolution show a high variety of LC with both having 15 classes present among the 16 seen on the high resolution map (Figure 7a). When we compare the CLC maps obtained through SLM and MLM aggregation methods (Figure 7f) we count roughly 15% of cells with a different class. It is worth noticing that inside the observation site area (red line) there is no difference between the SLM and MLM maps at 1 km. We might highlight that the GBA and MET30 stations are located at the limit of an industrial area and a forest LC.

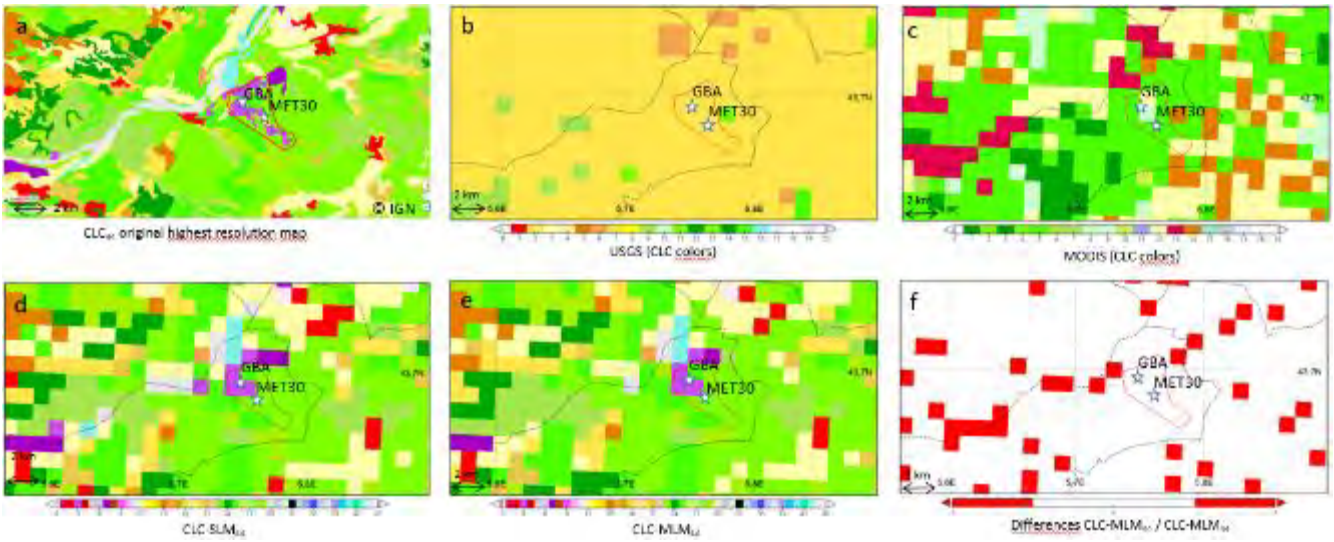

Figure 7 : LC maps around the observation site (the site is delimited with a red line); the map frame is as Figure 5c. GBA and M30 are the measurements stations used for the case study. (a) shows as a reference the original CLC_{44} highest resolution map. (b, c, d & e) are the 1 km resolution maps as used in the WRF domain D04; CLC standard colors (https://land.copernicus.eu/Corinelandcoverclasses.eps.75dpi.png/view) are used for all LCs. Map (b) is the LC from USGS data set. (c) is from MODIS data set. (d) is the map from CLC SLM aggregation with 44 classes. (e) is as (d) but from MLM aggregation. (f) shows the difference (in red) between the MLM and SLM aggregations.

ii. Radio soundings

The comparison of the radiosonde profiles with the different simulation cases (Figure 8) show that the influence of the LC maps on WRF simulations is weak and restricted to the boundary layer. The effect is more visible on the specific humidity plots. The observations show a boundary layer height of roughly 1500 m during the day time convective conditions (12 UTC plots). At 18 UTC, the cooling has clearly begun and has created a thin stable layer below the residual layer, whereas at 06:00 UTC, just before sunrise, the whole layer has become stable with a few sub-layers close to neutral. The simulations all show similar patterns and we will therefore describe only one. At noon, the model is roughly 1 K too cool within the PBL and ~3 K too cool above. At 18 UTC, the model and the observations nearly overlap, except for the fossil capping inversion, where the jump is smoothed in the simulations. The model is too cool at 12 UTC and matches well at 18 UTC, but the night cooling near the surface is under predicted as seen at 06 UTC.

The observed humidity shows a very clear mixed layer profile at 12 and 18 UTC, whereas the 06 UTC radio sounding shows a more mixed profile with a small peak around 250 m agl. This development is well simulated although the model seems to dry faster than the observations.

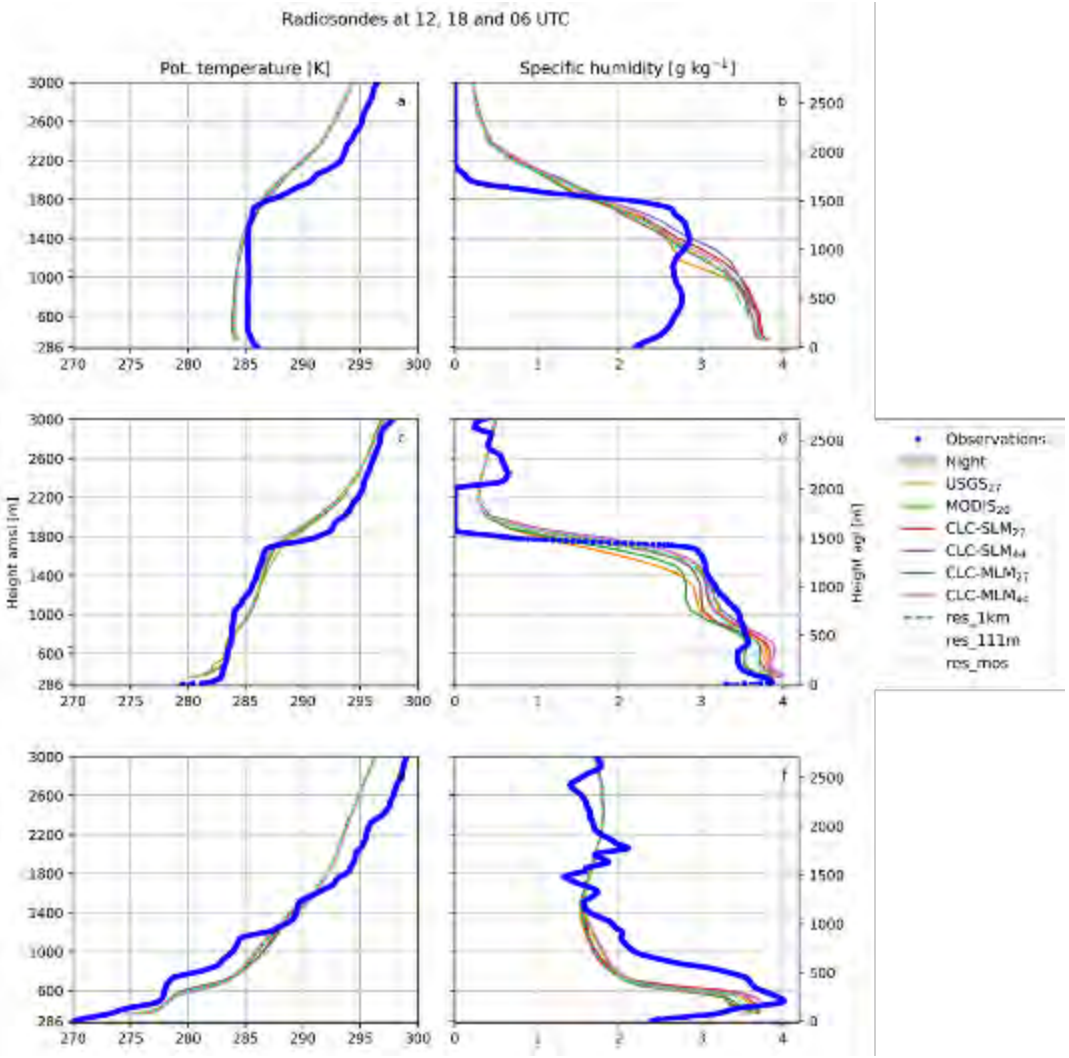

Figure 8 : Radio soundings and simulations results at M30 location during the case study at 12 UTC (top row) 18 UTC (middle row) and 06 UTC (bottom row) with potential temperature on the left and specific humidity on the right. Blue dots are observations, lines are the WRF simulations cases. 286 m is the actual terrain height above sea level, WRF ground level is slightly above due to discretization.

iii. Radiation

Figure 9 shows the radiation balance components observed at 20 m agl on M30 and the simulations with the six different LC maps and four different input settings (in total nine simulations).

For downward shortwave radiation (SWd Figure 9a), all simulations show a clear-sky day similar to the observation; the values are fairly identical for all the simulations and coincide well with the observations. Deviations are always below 25 W m^{-2}, and 24 h biases range from −1.3 to −0.3 W m^{-2}. In cloud-free conditions, this resemblance is not surprising because all the simulations use the same radiation transfer models and there is no direct influence of the LC on this quantity.

On the other hand, upward shortwave radiation (SWu; Figure 9b) is directly dependent on LC through albedo. The observed value during the IOP stands at 0.17 (close to the value of 0.16 computed from the whole KASCADE-2013 period), whereas the values at the corresponding cells are 0.23, 0.25, 0.17, and 0.16 for $USGS_{27}$, $MODIS_{20}$, CLC_{27}, and CLC_{44}, respectively. In $USGS_{27}$ and $MODIS_{20}$, SWu values are higher than observations, causing noon error overestimation maxima of +40 W m^{-2} and +52 W m^{-2}, respectively. This indicates an excessive reflection at this location. In contrast, CLC_{27} and CLC_{44} simulations are closer to the observed values, with an underestimation of 13 W m^{-2} of the noon maximum. 24 h biases range from −3.1 to −1.5 W m^{-2} in the CLC runs, whereas the bias reaches 9 W m^{-2} and 12 W m^{-2} for $USGS_{27}$ and $MODIS_{20}$. The differences resulting from the aggregation method (SLM vs. MLM) are not significant. This is due to the fact that the LC class of the cell at the M30 location was found to be the same CLC class ("Broad-leaved forest", index **3.1.1**, albedo=0.16) for either MLM or SLM as can be seen in Figure 7d & e. Since upward shortwave radiation depends only on local characteristics, the values are thus identical for the two methods.

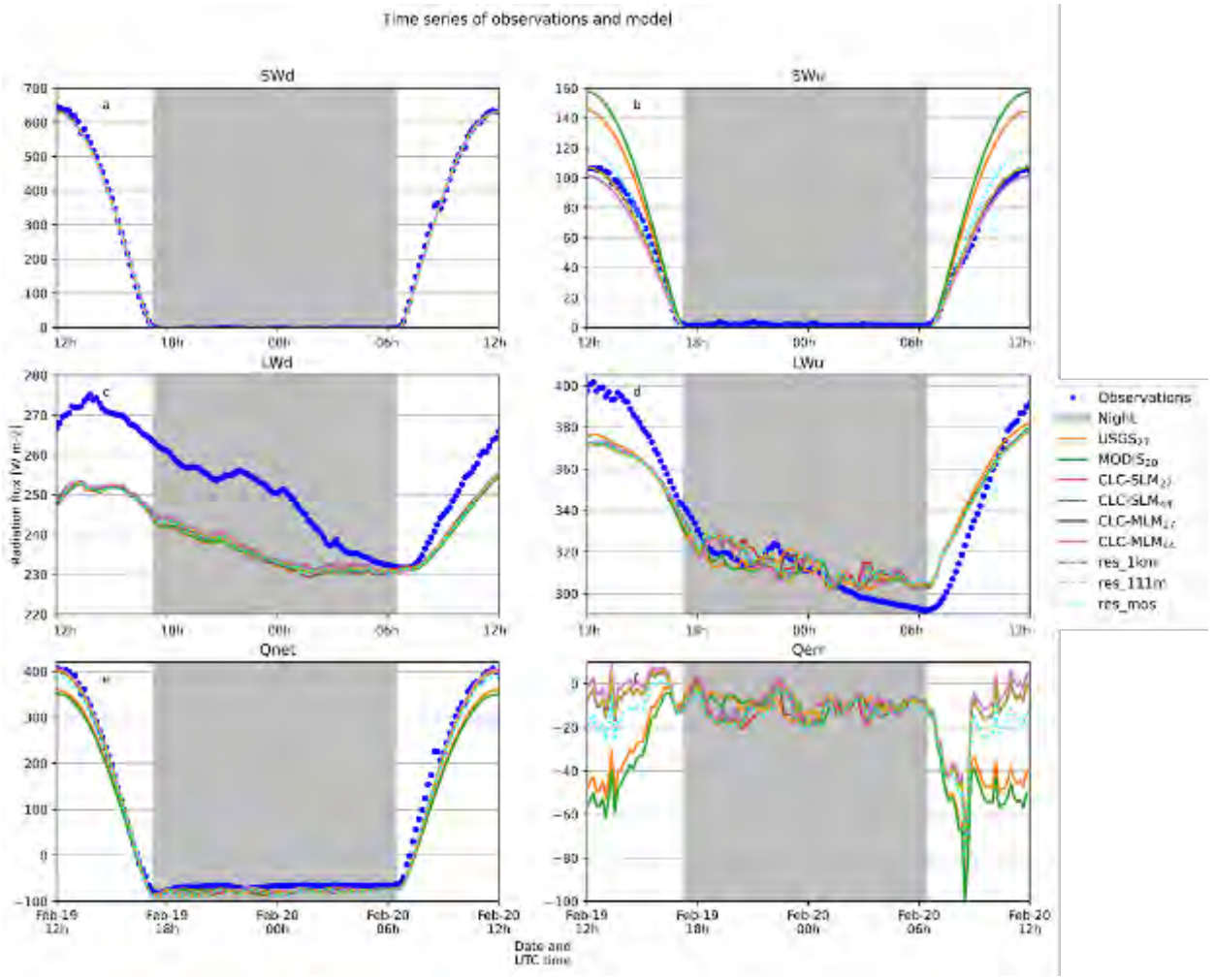

Figure 9: Modelled radiation components (lines) and 20 m observation at M30 (blue dots). SWd stands for shortwave downward, SWu shortwave upward, LWd longwave downward, LWu longwave upward, Qnet is the net radiation balance and Qerr the difference of Qnet between the simulations and the observations. All quantities are in W m^{-2}. Shaded areas are night-time periods.

Downward longwave radiation (LWd; Figure 9c) is underpredicted regardless of the simulation with maximum deficits of 22 to 25 W m^{-2} in the afternoon. This problem is not directly related to LC representation but could reflect a too dry and/or too cold overlying atmosphere, although radio soundings (Figure 8) at 12, 18 and 06 UTC do not indicate major differences between model and observation in the first three kilometers. This underestimation of LWd is a known issue with WRF (Cerenzia, 2017; Kleczek et al., 2014; Steeneveld & de Bode, 2018; Sterk et al., 2013; Velde et al., 2010). Nonetheless, the model seems to improve at dawn, and the minima of LWd coincide well with the observation, both in timing and magnitude, and the resulting IOP average biases range from −12 to −13 W m^{-2}, with CLC-SLM$_{27}$ performing slightly better. Even though this improvement at dawn is intriguing we shall not investigate it further, since it is not directly related to the LC representation.

Lastly, for upward longwave radiation (LWu; Figure 9d), directly related to the ground skin temperature (T_{SK}), all the models seem to be close to one another. The IOP average biases are quite low with values not exceeding −2.5 W m^{-2}. However this good bias performance results from a compensation of the nighttime overestimation (20 to 22 W m^{-2} at 6 TU) by the daytime underestimation (25 to 30 W m^{-2} at 12 TU). Thus, all the simulations clearly underestimate the daytime peak value, and overestimate the temperature of the cooling surface in the second half of the night. Such a diurnal course has direct feedback on air temperature, as we will see later on. Furthermore, the simulated time series show fluctuating behavior during the night, the origin of which is not yet determined but could lie in transient advection of air parcels with different thermodynamic characteristics.

Combining all four radiative fluxes (SWd - SWu + LWd - LWu; Figure 9e) gives us the net radiation (Qnet). In short, all the model simulations using the CLC maps are close to observations. MODIS$_{20}$ and USGS$_{27}$ runs have IOP biases of −24 and −21 W m^{-2} respectively, mainly since they use too high an albedo value. In comparison, the CLC runs have biases from −9 to −12 W m^{-2}. CLC-MLM$_{44}$ performs the best with a 24 h bias of -9 W m^{-2}, noon discrepancy of 1W m^{-2} and a midnight discrepancy of −17 W m^{-2}.

Evaluating the net radiation error over time (Qerr; Figure 9f), shows that the net radiation is generally underestimated, especially in early morning, whilst the afternoon provides the best results and errors are around zero. At night, the net radiation error is always under estimated. The $MODIS_{20}$ and $USGS_{27}$ have large underestimations during daytime, originating from overestimated albedo values, whilst at night they resemble the other runs. An error peak appears at ~9 TU: this is certainly due to an observation artifact. It may be a reflection on the mast.

For Experiment #2, no large differences exist between three of the four simulations. Their biases range within 1 W m^{-2} of each other. The last simulation of res_mos (Mosaic approach) has slightly larger differences seeing that it has its net radiation bias to −15 W m^{-2} compared to the −11 W m^{-2} of the other three simulations. This difference is a result of a 3 W m^{-2} bias increase in the shortwave outgoing radiation.

iv. Temperature

The radiative balance provides an excellent starting point for the temperature and nocturnal valley wind study. The finest resolution of our simulation is 1 km, which cannot adequately simulate the winds channeled by the small (1 – 2 km wide) tributary CV (see Figure 5). We therefore switch to observations at the GBA tower (110 m agl), which are better suited for comparisons with 1 km resolution simulations (Kalverla et al., 2016), as 100 m is the height of the surrounding ridges of CV with respect to its floor; thus, the tower top is above the flow channeled by this valley and is under the influence of the DV wind. Obviously, if GBA 110 m temperature is out of CV influence, the 2 m temperature remains under its influence.

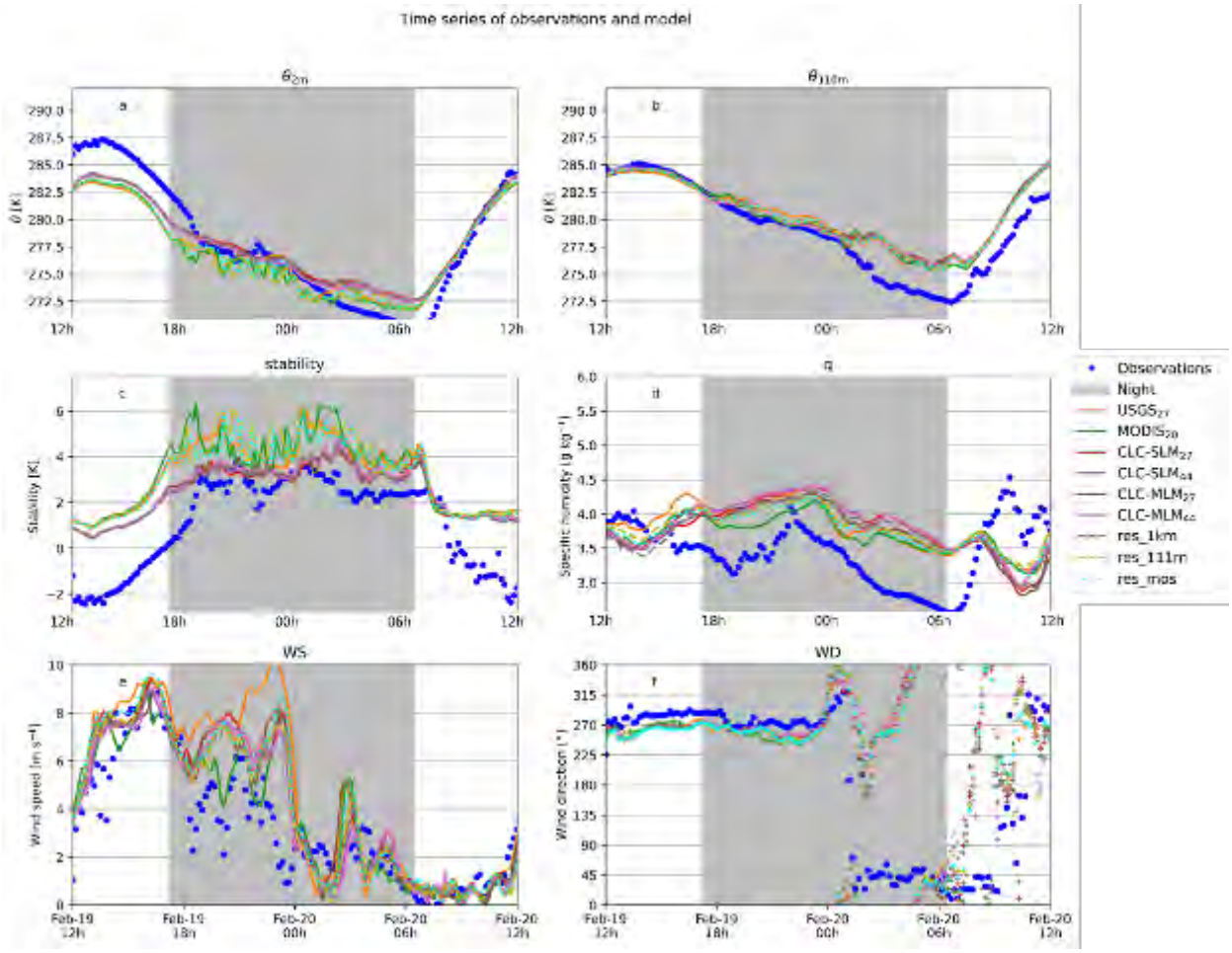

Figure 10: Potential temperature at 2 m (θ_{2m}, top left), 110 m (θ_{110m}, top right) and the difference between these two levels (θ_{110m}-θ_{2m}, mid left), specific humidity (q, mid right), wind speed (WS, bottom left), and wind direction (WD, bottom right) at 110 m agl from GBA location. The time series represents the simulations (lines and small dots for WD) and the observations (large blue dots), as in Figure 9. Shaded areas are night-time periods.

The time series of the observed and simulated temperatures and the corresponding statistics are presented in Figure 10 and Table 7, respectively. As expected, the daily course of the 2 m temperature (θ_{2m}) has a larger amplitude than that of the 110 m (θ_{110m}). In WRF simulations, the temperature at 2 m is a diagnostic variable (we call it θ_{2m_diag}), it is dependent on LC parameters through skin temperature, roughness length, and friction velocity (see WRF file module_surface_driver.F).

$$\theta_{2m\_diag} = T_{skin} - \frac{H}{\frac{P_{surf}}{R_d * T_{skin}} * C_p * CHS_2}$$

Where T_{skin} is the surface temperature in K, H is the upward heat flux at the surface in W m^{-2}, P_{surf} is the surface pressure in Pa, R_d is the gas constant for dry air in J kg^{-1} K^{-1}, C_p is the heat capacity of dry air at constant pressure in J kg^{-1} K^{-1}, and CHS_2 is the exchange coefficient for heat at 2 m in m s^{-1}, depending on both the roughness length and the friction velocity.

Overall 24 h (IOP) biases range from −0.9 to −0.1 K (Table 7), with CLC_{27} simulations performing better. During the daytime however, the simulated temperatures are generally cooler than the observations, whereas soon after midnight they become warmer. After sunrise, the simulations underpredict the observed temperature rise at 2 m. A daily temperature range (DTR) of 18 K is observed at 2 m whilst simulations range between only 11.5 and 12 K. An error of the same order was already mentioned by Kalverla et al. (2016). This DTR error consists of a 3-4 K underestimation of the daytime peak and an overestimation of 2-3 K of the night low. Errors in DTR are a general problem in many models and not only WRF (Lindvall and Svensson 2015; Wyszogrodzki et al., 2013). Kalverla et al. (2016) attribute the DTR to unresolved orography but in the fine-resolution simulation of de Bode et al., 2021 the expected DTR improvement did not occur in this location. More generally, in wintertime, temperature forecasting might have larger errors (Duan et al., 2018), because freezing processes add to the challenge of proper forecasts. In summary, improving LC representation is not the main lever for reducing DTR error.

Concerning θ_{110m}, Figure 10b shows that all simulations are close to the observations during the daytime of February 19. They miss however, the steep cooling around 1:00 UTC, the latter coinciding with a change of wind direction as visible in Figure 10f, the simulations thus miss at that time the influence of the DV winds. Consequently the simulations remain too warm thereafter. The metrics of the differences between simulations and observations (Table 7) show that $MODIS_{20}$ performs slightly better, with a bias of 1.3 K and an RMSE of 1.9 K, whereas the other runs have biases around 1.4 K and RMSE of 2.0 K. Considering the aggregation methods, they result in a minimal difference with a slight benefit (0.02 to 0.08 K) for the MLM runs. It is interesting to note that the CLC LUT tables perform better in MLM than in SLM runs.

Regarding stability, Figure 10c shows the potential temperature difference between 110 m and 2 m ($\Delta\theta$). All CLC runs have similar skills with biases ranging from 1.4 to 1.5 K and RMSE of 1.7 to 1.8 K, while $MODIS_{20}$ and $USGS_{27}$ have higher biases ranging from 2.1 to 2.2 K and RMSE from 2.3 to 2.5 K. In fact the biases of θ_{2m} and θ_{110m} combine to form the biases of stability, therefore, it is not unexpected that all CLC runs do relatively well in forecasting the stability, since they perform relatively well at the two levels.

Experiment #2 shows a variability in simulation skill comparable to Experiment #1 for the temperature and stability metrics, indicating that if the LC provider and its aggregation is crucial, the way in which it is presented to WRF is just as important. res_dep and res_1km are relatively close in skill, and in the way the res_111 m and res_mos resemble each other. We cannot therefore conclude on the best configuration for Experiment #2.

Table 7: Bias and RMSE for 2 m potential temperature (θ_{2m_diag}), 110 m potential temperature (θ_{110m}), stratification ($\Delta\theta$) and specific humidity (q) for simulations versus observations at the GBA tower site. Best performing cases are bold.

	Variable →	θ_{2m_diag}		θ_{110m}		$\Delta\theta$		q	
	Metric → Case↓	Bias [K]	RMSE [K]	Bias [K]	RMSE [K]	Bias [K]	RMSE [K]	Bias [g kg^{-1}]	RMSE [g kg^{-1}]
Experiment #1	*$USGS_{27}$*	−0.7	2.5	1.4	2.0	2.1	2.3	0.4	**0.6**
	$MODIS_{20}$	−0.9	**2.3**	1.3	1.9	2.2	2.5	**0.3**	**0.6**
	CLC-MLM_{27}	**−0.05**	2.6	1.4	2.0	**1.4**	**1.7**	**0.3**	0.7
	CLC-SLM_{27}	**0.09**	2.7	1.5	2.1	**1.4**	**1.7**	**0.3**	0.7
	CLC-MLM_{44}	**−0.1**	2.6	1.3	2.0	**1.5**	**1.8**	0.4	0.7
	CLC-SLM_{44}	**−0.07**	2.6	1.4	2.0	**1.5**	**1.8**	0.4	**0.6**
Experiment #2	*res_dep CLC-SLM_{27}*	**0.09**	2.7	1.5	2.1	**1.4**	**1.7**	0.4	0.7
	res_1km	**0.02**	2.7	1.4	2.0	**1.4**	**1.7**	**0.3**	0.7
	res_111m	−0.9	**2.4**	**1.3**	**1.9**	2.3	2.5	0.4	**0.6**
	res_mos	−0.7	**2.4**	**1.3**	**1.9**	2.1	2.3	**0.3**	**0.6**

v. Humidity

Figure 10d shows that all simulations resemble each other in humidity development, with generally an overestimation except in the early morning till noon. MODIS and USGS performs best, but there is no serious difference on specific humidity prediction as shown by Table 7 either through Experiment #1 or #2: the bias remains in the range 0.3 to 0.4 g kg^{-1} and the RMSE within 0.6 to 0.7 g kg^{-1} for all cases.

vi. Wind

Figure 10e and 8f show the wind speed and wind direction at 110 m agl: in general simulations manage to reproduce the moderate winds and have the typical daytime direction. The error in wind speed is characterized by the bias, whereas the method to determine the model wind direction skill is the directional accuracy ($DACC_X$) (Santos-Alamillos et al., 2013). $DACC_X$ is the percentage of forecasted wind within a specified angular deviation X (in degrees) from the observations:

$$DACC_X = \frac{\sum_N \begin{matrix} 1\ (if\ \Delta\emptyset\ \leq X) \\ 0\ (else) \end{matrix}}{N}\ x\ 100$$

$$\Delta\emptyset = \min[\ abs(WD_{obs} - WD_{mod}), abs(360 - (WD_{obs} - WD_{mod}))]$$

Where WD_{obs} is the observed direction and X is the threshold of the acceptable error (in degrees) in simulated wind direction (WD_{mod}). Figure 11 shows the plot of $DACC_{45}$ (i.e., x=45°) versus wind speed bias for all the runs. Simulations nearer to the top left corner perform the best in both wind speed and direction metrics whereas runs closer to the right bottom corner perform the worst in both metrics. There is no clear best compromise. The influence of LC data set on wind speed in WRF is more profound than that of resolution settings (Experiment #2). Variation due to LC ranges from 0.5 m s^{-1} bias for $MODIS_{20}$ to 1.4 m s^{-1} bias for $USGS_{27}$, with all CLC in between, CLC_{27} around 0.8 m s^{-1} and CLC_{44} around 0.6 m s^{-1}. Regarding the RMSE (not shown), the order of performance is similar with $MODIS_{20}$ performing best with 1.6 m s^{-1} and $USGS_{27}$ worst with 2.6 m s^{-1} and the CLC runs in between with values of 1.8 to 1.9 m s^{-1}. Looking at the $DACC_{45}$, Experiment #2 covers both extremes of the graph, res_dep (aka $CLC\text{-}SLM_{27}$) has a $DACC_{45}$ of ~72 % whilst the res_mos has 67 %. Generally, the MLM method seems to improve wind speed skill in simulations: it improves the $DACC_{45}$ in CLC_{44}. This is not the case for the CLC_{27} data set however.

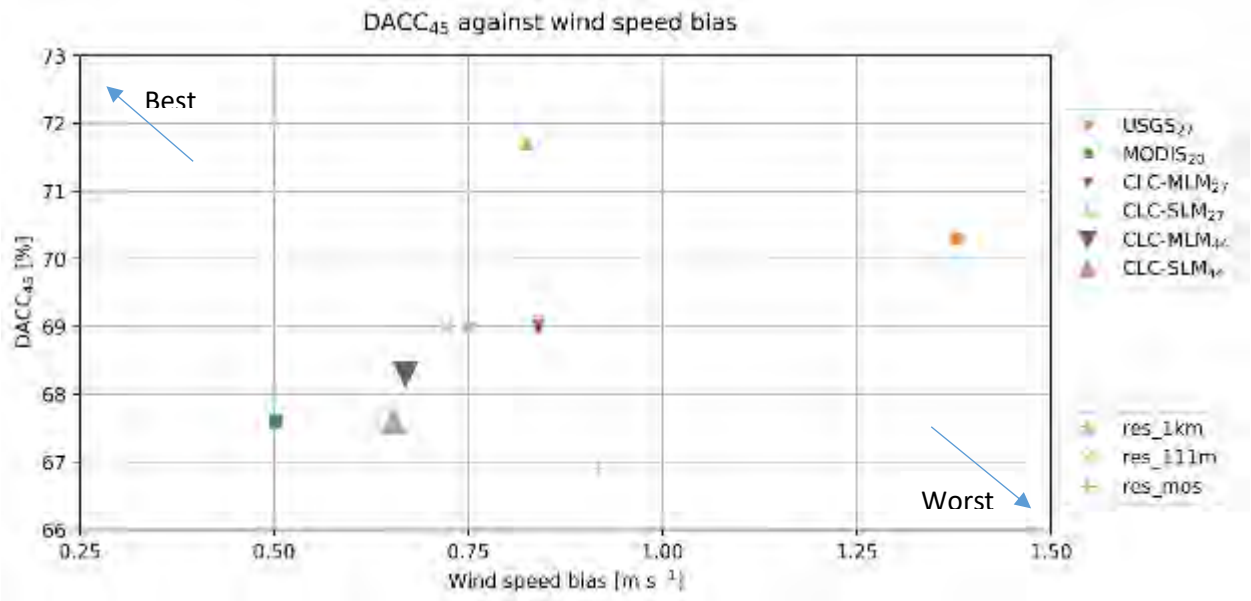

Figure 11: Directional accuracy ($DACC_{45}$) as a function of wind speed bias. The colors and shape indicate what type of LC data set is used, large symbols have 44 classes while smaller symbols use 20 or 27 classes. Experiment #2 runs are indicated with bronze color symbols.

4. Discussion

a. Performance evaluation

This section discusses the performance of the different simulation options. Here we try to determine the best overall simulation based on the bias and RMSE performances for the variables θ_{2m}, stability, humidity, wind speed, and wind direction at GBA. Determination of the skill of each simulation comes from the performance per variable. Each variable will get a score of between 0 and 1 (1 being the best). Regarding the bias, we consider for each variable the run with the worst bias B_w. Each run has a bias B_i, its score is defined as $1\text{-}|B_i|/|B_w|$. As an example, for θ_{2m}, a bias of 0.0 K will give a score of 1, and the worst score (−0.919 K) will get 0, the same is done for RMSE. The DACC can be used directly as a score since it represents a percentage of success. Furthermore it is attributed a weight of 2 seeing as all other variables contribute with two metrics to the global score. Altogether, our method results in 9 scores between 0 and 1. Based on their weighted average, we determine the ranking of simulations for this position. Note that weight attribution is subjective or could be linked to the finality of the forecasts (i.e. dispersion modeling could favor wind direction score with a higher weight); a change of weight could lead to a change of ranking.

Table 8 shows the normalized performance of all the previously discussed variables. The best runs are in bold. The best performing Experiment #1 simulation at the GBA location is the CLC-MLM$_{27}$. More generally CLC is the best LC data set to represent the surface with ranks in [0.38, 0.40] whereas MODIS and USGS LC remain below, ranking respectively 0.30 and 0.20. Furthermore, from Experiment #1, the results may not clearly settle the best aggregation method as they all rank closely to one another. This could be due to absence of mismatch close to the observation site (Figure 7f). Regarding the new LUT, it does not clearly outperform a conversion to USGS values. A possible explanation could be that the values from Pineda et al. (2004) are not the most appropriate, since we are in a different location, even though there are considerable similarities in the two locations. Nonetheless, our parent domain stretches as far as the UK, and the LC LUT can differ at large scale. Another possible factor is that our new 44-class LUT is not yet complete and requires work to specify all parameters for all 44 classes.

Experiment #2 has the best performing simulation of this study. res_1km outperforms the other simulations by ranking 0.42, although the weighted metric average is close to the best Experiment #1 simulations. As expected, res_111m remains below as using the LC high resolution map (111 x 111 m) may not lead to the most represented LC in the 1 x 1 km WRF cell. More astonishingly, Mosaic method "res_mos" does not lead to a better ranking: this should prompt further investigation.

Table 8: Normalized biases and RMSE of humidity, temperature, stability ($\Delta\theta$), wind speed and wind direction to determine the best performing run at the GBA location. 1 is the best, 0 the worst result for the weighted rank. The best options from either Experiment #1 or #2 are in bold.

	Variable → / Metric →	q bias	q RMSE	θ_{2m} bias	θ_{2m} RMSE	$\Delta\theta$ bias	$\Delta\theta$ RMSE	WS bias	WS RMSE	$DACC_{45}$	Weighted average
	Weight → / LC data set ↓	1	1	1	1	1	1	1	1	2	
		Ranking in [0, 1], 0 the worst, 1 the best, no units									
Experiment #1	*$USGS_{27}$*	0.06	0.14	0.27	0.02	0.07	0.07	0.00	0.00	0.70	0.20
	$MODIS_{20}$	0.34	0.24	0.01	0.01	0.02	0.00	0.64	0.37	0.68	0.30
	CLC-SLM27	0.09	0.01	0.90	0.11	0.39	0.31	0.40	0.27	0.72	0.39
	CLC-MLM_{27}	**0.23**	**0.06**	**0.95**	**0.13**	**0.36**	**0.30**	**0.39**	**0.25**	**0.69**	**0.40**
	CLC-SLM_{44}	0.00	0.00	0.92	0.16	0.36	0.29	0.53	0.32	0.68	0.39
	CLC-MLM_{44}	0.00	0.01	0.86	0.15	0.34	0.29	0.52	0.32	0.68	0.38
Exp. #2	*res_dep*	0.09	0.01	0.90	0.11	0.39	0.31	0.40	0.27	0.72	0.39
	res_1km	**0.21**	**0.04**	**0.98**	**0.12**	**0.38**	**0.31**	**0.46**	**0.30**	**0.69**	**0.42**
	res_111m	0.11	0.17	0.00	0.00	0.00	0.01	0.48	0.32	0.69	0.25
	res_mos	0.21	0.18	0.21	0.04	0.07	0.07	0.34	0.23	0.67	0.27

The two options we have introduced, the MLM method and the CLC 44-class LUT, do not substantially influence the metrics of the simulation much. Even if the MLM method produces comparable results to the SLM for fine resolution at a given location, we expect more differences with simulations that use coarser resolutions: as described in Table 2, the coarser the resolution the higher the mismatch between aggregation methods. Indeed, we may expect a higher discrepancy between simulations where the location of interest presents more mismatch between the methods; this was the case neither at M30 nor at GBA. The MLM produces the best simulation of the Experiment #1, regardless of the aggregation method applied and the LUT used.

Generally, the MLM method seems to perform well, although in a few cases the clustering of classes in the CLC groups might not be always the most appropriate from a meteorological point of view. For example, do orchards and olive groves fit best in agricultural land, or do they correspond more closely to forest types? The Pineda et al. (2004)'s conversion places both of them in an agricultural USGS class. Other class clustering structures exist. For example, Varga et al. (2020) tried two additional class clustering methods next to the conventional CLC class clustering, one method was based on physical behavior (Aldwaik et al., 2015) and the other method used thresholds of LC changes with the last edition of the CLC data set. Furthermore, MLM could be extended to other 1-level LC data sets by using hierarchical class system developed through meteorological parameters clustering.

Note that this research is too limited for a definite answer on the performance of the different LC data sets and aggregation methods since our case only covers 24 h of observations and specific weather conditions (clear sky, calm wind and stable night). Nonetheless, most of our results match well with findings of other researchers. In Schicker et al. (2016)'s study, using $MODIS_{20}$ or CLC_{27} instead of the default $USGS_{27}$ improves the temperature representation in simulations. Note that they did not specify whether they aggregate the 100 and 250 m resolution CLC data sets to match domain resolutions, nor whether they used the Mosaic option. Their study is related to two areas in Austria and the simulations are evaluated

against satellite data, surface observations and radio soundings. We agree with their conclusion that $MODIS_{20}$ and all CLC generally outperform $USGS_{27}$. Their prospect that a complete LUT would improve the forecasts of WRF does not seem to come into being for our LUT. Let us keep in mind however that this is not yet a finalized LUT (not all 44 classes lead to different parameters values) and that it needs further improvement before a final decision can be made.

Santos-Alamillos et al. (2015) compare the wind from simulations based on $USGS_{27}$ and CLC_{27} LC maps. No Mosaic option is mentioned for the 100 m CLC_{27} data set. They find that while CLC is more representative of the area, using USGS creates better wind fields. They suggest that the nearest neighbor approach could introduce this paradox. Their CLC input data set has a 100 m horizontal resolution for 1 km WRF resolution with the use of the nearest neighbor interpolation to aggregate. They mention that more studies are needed with different spatial interpolation procedures. In our study we did not apply the nearest neighbor approach as we expected it to be worse than SLM or MLM.

Li et al. (2018) simulate the Urban Heat Island of Berlin with the $USGS_{27}$, CLC_{27}, and Urban Atlas (UA) LC data sets, the latter being a product from Copernicus as is CLC. They applied the Mosaic approach on all three data sets. They found that the UA or CLC maps represent surface and air temperature better than the USGS does. In our study, CLC similarly improves the representation of 2 m temperatures. In Li et al. (2018), the change is mainly attributed to a better representation of the urban fraction as the USGS map is outdated (survey from 1994) compared to CLC (data from2012) and UA (from 2012, linked to CLC). We assume that the better surface representation of CLC is also the reason for the improvement in our study. Golzio et al. (2021) test $MODIS_{20}$, $MODIS_{21}$ ($MODIS_{20}$ with additional lake class), $USGS_{27}$, and CLC_{44}, where the CLC_{44} performs better than the other LC data sets. This matches with our results. Nonetheless, they have not checked CLC_{27} to verify if the CLC_{44} is indeed the best LC available at this location. Similarly to our results, their CLC_{44} LUT is not yet complete and needs further improvement.

b. Further improvements

This work shows that the way in which the LC maps are presented to WRF has a significant influence, which can be just as great as the influence of changing LC initial data set (range between experiment #1 and #2). More research is needed to determine optimal ways to present surface data sets to WRF. The inclusion of the MLM aggregation method as a basic option of WRF (or another NWP) is needed to fully evaluate its impact.

The comparison study only covered a period of 24 h which is enough to get a first estimate of the performances with different LC data sets but not enough to confirm them unambiguously. Obviously, as we computed the metric on a 24 h period (i.e. with 145 points from 10 minutes outputs), the confidence interval might be quite large. A longer time period (from 1 month to one year hourly time series) will enable us to estimate these confidence intervals (e.g. through a bootstrap method). Similarly, we checked the results of the simulations against two observation points which were not subjected to changes caused by the aggregation method. The evaluation against a higher number of locations would show in a broader sense how well the simulations perform. Weather stations installed at locations where the model shows a difference between SLM and MLM would help to compare the performance of the two methods. In this study, the only differences observed at the location are advected from other places where the MLM and SLM method do make a difference.

The 44-class LUT does not shows a great improvement with respect to the 27-class USGS LUT. A large number of parameters however are taken from the USGS tables. For more accurate comparisons between the two look-up tables the 44-class CLC table needs to have 44 unique classes. Therefore, more fieldwork and satellite data analyses are needed.

5. Conclusion

In this study, we introduced a new method with which to carry out aggregation on land cover data sets from fine resolution maps to ones of coarser resolution. This method, called Multi-Level Mode (MLM) aggregation, was developed to overcome the difficulty that occurs with conventional aggregation techniques that can result in discrepancies between maps with many classes and maps with a limited amount of classes, with possible artifacts caused by a too high level of detail in the initial database. The MLM avoids such drawbacks while taking into account the richness of the initial data set. We applied this technique to the European Corine land cover database which is well suited as it combines a high-resolution dataset and a high number of classes with a hierarchical classification of the land cover categories in three distinct levels. We took advantage of this hierarchy which allowed us to choose in an aggregated cell a category always in agreement with its upper hierarchical classes. There has not yet been a spatial aggregation method that considers such a categorical interdependency to the authors' knowledge. Furthermore, to enhance the benefit from the high number of classes in the CLC dataset, we created a freely available physical parameter table (LUT) with 44 classes which can be used in WRF simulations. For the time being, our method was applied to the CLC land cover data set, but it could be extended to other datasets, with the only condition being that one or two parent levels of grouped categories were defined beforehand

The impact of the aggregation method was evaluated through a mismatch count, i.e. a count of the cell number for which the retained category differs between the MLM and the conventional aggregation, both starting with the same original data set (CLC). These metrics were computed for different resolutions, over an area of 6° x 4° in southeastern France.

For the smallest resolution (111 m) we observed a difference of only 0.03 %, while the mismatch became 0.8 % at 333 m resolution and reached 16.6 % at 9 km resolution. These values, which are averages over the whole domain, can vary locally when a smaller area is considered, depending on the local LC variability.

A comparative study between various configurations combining different original land-cover datasets (CLC, MODIS and USGS), different classification and different aggregation methods was carried out through a series of WRF simulations. The WRF model was run over the 6° x 4° domain, with nested domain resolutions ranging from 27 to 1 km, the latter for the finest domain centered on an area well documented through a field campaign conducted in winter 2013. Over the finest domain, we noted considerable differences between some configurations regarding average roughness length and albedo, which directly impact momentum flux (and therefore wind in the atmospheric boundary layer) and surface energy budget (and therefore development of the atmospheric boundary layer).

To test the impact on the atmospheric flow of the various land cover configurations, we analyzed a 24 h case with clear sky, calm wind, diurnal convective boundary layer and nocturnal valley wind development along the French Durance Valley. In the finest domain, the simulations were evaluated against observations collected during the 2013 field campaign. Regarding the simulated net radiation, CLC outperform USGS and MODIS. More generally, all data sets improve the skill of the model compared to the default USGS dataset with 27 classes. Though for temperature, CLC does not show clearly better results than MODIS and USGS, for stability, CLC runs clearly show a lower bias and RMSE. Concerning wind speed and direction, CLC and MODIS clearly outperform the USGS simulation.

When we turned to more quantitative comparisons, the different CLC aggregation methods showed limited differences in bias and RMSE of the predicted variables, although the MLM method generally showed slightly better results. The new 44 classes WRF LUT did not improve the results, but this was not surprising as this LUT is not yet well differentiating parameters associated with different land cover classes. We must keep in mind that comparisons between observations and simulation were restricted to a single location, which has the same land cover type regardless of the aggregation method. The differences between various simulations regarding atmospheric parameters therefore do not have a local origin, but are the result of the horizontal advection from upwind areas where surface conditions could differ.

An experiment on WRF input resolution land cover maps showed that the best results were obtained with a unique map having the same resolution as the finest WRF domain (here 1 km). Surprisingly, the promising Mosaic option underperformed.

These simulations only span 24 h with 10 min outputs; this is a relatively short period which cannot represent many different meteorological conditions. An extended time series would cope with this restriction and would enable us to compute confidence intervals on the metrics used for comparing with observations. Additionally, multiple locations need to be considered, to verify whether results hold in different locations. To coarsen simulations (9 km horizontal resolution) over a greater area such as the whole of France should be undertaken to better quantify the effect of aggregation mismatch. Such simulations are proper tools with which to further the knowledge of the impacts of other land cover data sets.

Additionally, the WRF LUT might be improved in the future, thanks to appropriate observations which would help to improve the physical parameters such as albedo, roughness length, and other soil or vegetation quantities. From now on however, we are able to run coarse as well as high-resolution simulations which benefit from an improved land-use (de Bode et al., 2021).

Acknowledgments, Samples, and Data

Data available at: https://kascade-data.sedoo.fr/

References

© OpenStreetMap contributors. 2021. 'OpenStreetMap'. *OpenStreetMap*. Retrieved 9 July 2021 (https://www.openstreetmap.org/copyright).

Aldwaik, Safaa Z., Jeffrey A. Onsted, and Robert G. Pontius Jr. 2015. 'Behavior-Based Aggregation of Land Categories for Temporal Change Analysis'. *International Journal of Applied Earth Observation and Geoinformation* 35:229–38. doi: 10.1016/j.jag.2014.09.007.

Anderson, James R., Ernest E. Hardy, John T. Roach, and Richard E. Witmer. 1976. *A Land Use and Land Cover Classification System for Use with Remote Sensor Data*. U.S. Government Printing Office.

de Bode, Michiel, Thierry Hedde, Pierre Roubin, and Pierre Durand. 2021. 'Fine-Resolution WRF Simulation of Stably Stratified Flows in Shallow Pre-Alpine Valleys: A Case Study of the KASCADE-2017 Campaign'. *Atmosphere* 12(8):1063. doi: 10.3390/atmos12081063.

Broxton, Patrick D., Xubin Zeng, Damien Sulla-Menashe, and Peter A. Troch. 2014. 'A Global Land Cover Climatology Using MODIS Data'. *Journal of Applied Meteorology and Climatology* 53(6):1593–1605. doi: 10.1175/JAMC-D-13-0270.1.

Büttner, György. 2014. 'CORINE Land Cover and Land Cover Change Products'. Pp. 55–74 in *Land Use and Land Cover Mapping in Europe: Practices & Trends*, *Remote Sensing and Digital Image Processing*, edited by I. Manakos and M. Braun. Dordrecht: Springer Netherlands.

Cerenzia, Ines. 2017. 'Challenges and Critical Aspects in Stable Boundary Layer Representation in Numerical Weather Prediction Modeling: Diagnostic Analyses and Proposals for Improvement'. Tesi di dottorato, alma.

Copernicus. 2020. 'CORINE Land Cover — Copernicus Land Monitoring Service'. Retrieved 5 January 2021 (https://land.copernicus.eu/pan-european/corine-land-cover).

Daniels, Megan H., Katherine A. Lundquist, Jeffrey D. Mirocha, David J. Wiersema, and Fotini K. Chow. 2016. 'A New Vertical Grid Nesting Capability in the Weather Research and Forecasting (WRF) Model'. *Monthly Weather Review* 144(10):3725–47. doi: 10.1175/MWR-D-16-0049.1.

De Meij, Alexander, and Jean-François Vinuesa. 2014. 'Impact of SRTM and Corine Land Cover Data on Meteorological Parameters Using WRF'. *Atmospheric Research* 143:351–70. doi: 10.1016/j.atmosres.2014.03.004.

Duan, Haixia, Yaohui Li, Tiejun Zhang, Zhaoxia Pu, Cailing Zhao, and Yuanpu Liu. 2018. 'Evaluation of the Forecast Accuracy of Near-Surface Temperature and Wind in Northwest China Based on the WRF Model'. *Journal of Meteorological Research* 32(3):469–90. doi: 10.1007/s13351-018-7115-9.

Duine, Gert-Jan. 2015. 'Characterization of Down-Valley Winds in Stable Stratification from the KASCADE Field Campaign and WRF Mesoscale Simulations'. phd, Université de Toulouse, Université Toulouse III - Paul Sabatier.

Duine, Gert-Jan, Thierry Hedde, Pierre Roubin, Pierre Durand, Marie Lothon, Fabienne Lohou, Patrick Augustin, and Marc Fourmentin. 2017. 'Characterization of Valley Flows within Two Confluent Valleys under Stable Conditions: Observations from the KASCADE Field Experiment'. *Quarterly Journal of the Royal Meteorological Society* 143(705):1886–1902. doi: 10.1002/qj.3049.

EEA. 2020. 'CLC 2012 — Copernicus Land Monitoring Service'. *CLC 2012*. Retrieved 4 January 2021 (https://land.copernicus.eu/pan-european/corine-land-cover/clc-2012).

Faroux, Stéphanie, Armel T. Kaptué Tchuenté, Jean-Louis Roujean, Valéry Masson, Eric Martin, and Patrick Le Moigne. 2013. 'ECOCLIMAP-II/Europe: A Twofold Database of Ecosystems and Surface Parameters at 1 Km Resolution Based on Satellite Information for Use in Land Surface, Meteorological and Climate Models'. *Geoscientific Model Development* 6(2):563–82. doi: https://doi.org/10.5194/gmd-6-563-2013.

Golzio, Alessio, Silvia Ferrarese, Claudio Cassardo, Gugliemina A. Diolaiuti, and Manuela Pelfini. 2021. 'Land-Use Improvements in the Weather Research and Forecasting Model over Complex Mountainous Terrain and Comparison of Different Grid Sizes'. *Boundary-Layer Meteorology* 180(2):319–51. doi: 10.1007/s10546-021-00617-1.

Gong, Peng, Jie Wang, Le Yu, Yongchao Zhao, Yuanyuan Zhao, Lu Liang, Zhenguo Niu, Xiaomeng Huang, Haohuan Fu, Shuang Liu, Congcong Li, Xueyan Li, Wei Fu, Caixia Liu, Yue Xu, Xiaoyi Wang, Qu Cheng, Luanyun Hu, Wenbo Yao, Han Zhang, Peng Zhu, Ziying Zhao, Haiying Zhang, Yaomin Zheng, Luyan Ji, Yawen Zhang, Han Chen, An Yan, Jianhong Guo, Liang Yu, Lei Wang, Xiaojun Liu, Tingting Shi, Menghua Zhu, Yanlei Chen, Guangwen Yang, Ping Tang, Bing Xu, Chandra Giri, Nicholas Clinton, Zhiliang Zhu, Jin Chen, and Jun Chen. 2013. 'Finer Resolution Observation and Monitoring of Global Land Cover: First Mapping Results with Landsat TM and ETM+ Data'. *International Journal of Remote Sensing* 34(7):2607–54. doi: 10.1080/01431161.2012.748992.

Gudowicz, Joanna, and zbigniew Zwolinski. 2016.'The Fourth Level of the LULC Cassification in the Integrated Environmental Monitoring in Poland'. Presented at the 2nd EARSeL SIG LU/LC and NASA LCLUC joint Workshop, May 6, Prague, Czech Republic.

Hartmann, Dennis L. 2015. *Global Physical Climatology*. Newnes.

Hersbach, Hans, Bill Bell, Paul Berrisford, Gionata Biavati, András Horányi, Joaquín Muñoz Sabater, Julien Nicolas, Carole Peubey, Raluca Radu, Iryna Rozum, Dinand Schepers, Adrian Simmons, Cornel Soci, Dick P. Dee, and Jean-Noël Thépaut. 2018a. 'ERA5 Hourly Data on Model Level from 1978 to Present'. *Copernicus Climate Change Service (C3S) Climate Data Store (CDS)*. doi: 10.24381/cds.adbb2d47.

Hersbach, Hans, Bill Bell, Paul Berrisford, Gionata Biavati, András Horányi, Joaquín Muñoz Sabater, Julien Nicolas, Carole Peubey, Raluca Radu, Iryna Rozum, Dinand Schepers, Adrian Simmons, Cornel Soci, Dick P. Dee, and Jean-Noël Thépaut. 2018b. 'ERA5 Hourly Data on Pressure Levels from 1978 to Present'. *Copernicus Climate Change Service (C3S) Climate Data Store (CDS)*. doi: 10.24381/cds.bd0915c6.

Homer, Collin, Jon Dewitz, Suming Jin, George Xian, Catherine Costello, Patrick Danielson, Leila Gass, Michelle Funk, James Wickham, Stephen Stehman, Roger Auch, and Kurt Riitters. 2020. 'Conterminous United States Land Cover Change Patterns 2001–2016 from the 2016 National Land Cover Database'. *ISPRS Journal of Photogrammetry and Remote Sensing* 162:184–99. doi: 10.1016/j.isprsjprs.2020.02.019.

Hong, Song-You, Ju-Hye Kim, Jeong-ock Lim, and Jimy Dudhia. 2006. 'The WRF Single Moment Microphysics Scheme (WSM)'. *Journal of the Korean Meteorological Society* 42:129–51.

Iacono, Michael J., Jennifer S. Delamere, Eli J. Mlawer, Mark W. Shephard, Shepard A. Clough, and William D. Collins. 2008. 'Radiative Forcing by Long-Lived Greenhouse Gases: Calculations with the AER Radiative Transfer Models'. *Journal of Geophysical Research: Atmospheres* 113(D13). doi: https://doi.org/10.1029/2008JD009944.

Ikİel, Cercis, Ayse A. Dutucu, Beyza Ustaoglu, and Derya KİlİIc E. 2012. 'Land Use and Land Cover (LULC) Classification Using SPOT-5 Image in the Adapazari Plain and Its Surroundings, Turkey.' *The Online Journal of Science and Technology (TOJSAT)* 2(2):37–42.

Inglada, Jordi, Arthur Vincent, & Vincent Thierion. (2017). Theia OSO Land Cover Map 2106 [Data set]. Zenodo. https://doi.org/10.5281/zenodo.1048161.

Inglada, Jordi, Vincent, Arthur, & Thierion, Vincent. (2018). 2017 Metropolitan France Land Cover Map - CESBIO - OSO [Data set]. Zenodo. https://doi.org/10.5281/zenodo.1993596.

Jach, Lisa, Kirsten Warrach-Sagi, Joachim Ingwersen, Eigil Kaas, and Volker Wulfmeyer. 2020. 'Land Cover Impacts on Land-Atmosphere Coupling Strength in Climate Simulations With WRF Over Europe'. *Journal of Geophysical Research: Atmospheres* 125(18):e2019JD031989. doi: https://doi.org/10.1029/2019JD031989.

Kain, John S. 2004. 'The Kain–Fritsch Convective Parameterization: An Update'. *Journal of Applied Meteorology and Climatology* 43(1):170–81. doi: 10.1175/1520-0450(2004)043<0170:TKCPAU>2.0.CO;2.

Kalverla, Peter C., Gert-Jan Duine, Gert-Jan Steeneveld, and Thierry Hedde. 2016. 'Evaluation of the Weather Research and Forecasting Model in the Durance Valley Complex Terrain during the KASCADE Field Campaign'. *Journal of Applied Meteorology and Climatology* 55(4):861–82. doi: 10.1175/JAMC-D-15-0258.1.

Kleczek, Michal A., Gert-Jan Steeneveld, and Albert A. M. Holtslag. 2014. 'Evaluation of the Weather Research and Forecasting Mesoscale Model for GABLS3: Impact of Boundary-Layer Schemes, Boundary Conditions and Spin-Up'. *Boundary-Layer Meteorology* 152(2):213–43. doi: 10.1007/s10546-014-9925-3.

Kosztra, Barbara, György Büttner, Gerard Hazeu, and Stephan Arnold. 2019. 'Updated CLC Illustrated Nomenclature Guidelines'. *European Environment Agency: Wien, Austria* 1–124.

Li, Dan, Elie Bou-Zeid, Mary L. Baeck, Stephen Jessup, and James A. Smith. 2013. 'Modeling Land Surface Processes and Heavy Rainfall in Urban Environments: Sensitivity to Urban Surface Representations'. *Journal of Hydrometeorology* 14(4):1098–1118. doi: 10.1175/JHM-D-12-0154.1.

Li, Dan, Elie Bou-Zeid, Michael Barlage, Fei Chen, and James A. Smith. 2013. 'Development and Evaluation of a Mosaic Approach in the WRF-Noah Framework'. *Journal of Geophysical Research: Atmospheres* 118(21):11,918-11,935. doi: https://doi.org/10.1002/2013JD020657.

Li, Huidong, Michael Wolter, Xun Wang, and Sahar Sodoudi. 2018. 'Impact of Land Cover Data on the Simulation of Urban Heat Island for Berlin Using WRF Coupled with Bulk Approach of Noah-LSM'. *Theoretical and Applied Climatology* 134(1):67–81. doi: 10.1007/s00704-017-2253-z.

Lindvall, Jenny, and Gunilla Svensson. 2015. 'The Diurnal Temperature Range in the CMIP5 Models'. *Climate Dynamics* 44(1/2):405–21. doi: 10.1007/s00382-014-2144-2.

Loveland, Thomas R., Bradley C. Reed, Jesslyn F. Brown, DonaldO. Ohlen, Zhiliang. Zhu, Limin Yang, and James W. Merchant. 2000. 'Development of a Global Land Cover Characteristics Database and IGBP DISCover from 1 Km AVHRR Data'. *International Journal of Remote Sensing* 21(6–7):1303–30. doi: 10.1080/014311600210191.

Neumann, Kathleen, Martin Herold, Andrew Hartley, and Christiane Schmullius. 2007. 'Comparative Assessment of CORINE2000 and GLC2000: Spatial Analysis of Land Cover Data for Europe'. *International Journal of Applied Earth Observation and Geoinformation* 9(4):425–37. doi: 10.1016/j.jag.2007.02.004.

Oke, Tim R. 2002. *Boundary Layer Climates*. Routledge.

Pineda, Nicolau, Oriol Jorba, Juan Jorge, and José M. Baldasano. 2004. 'Using NOAA AVHRR and SPOT VGT Data to Estimate Surface Parameters: Application to a Mesoscale Meteorological Model'. *International Journal of Remote Sensing* 25(1):129–43. doi: 10.1080/0143116031000115201.

Prósper, Miguel A., Carlos Otero-Casal, Felipe C. Fernández, and Gonzalo Miguez-Macho. 2019. 'Wind Power Forecasting for a Real Onshore Wind Farm on Complex Terrain Using WRF High Resolution Simulations'. *Renewable Energy* 135:674–86. doi: 10.1016/j.renene.2018.12.047.

Román-Cascón, Carlos, Marie Lothon, Fabienne Lohou, Oscar Hartogensis, Jordi Vila-Guerau de Arellano, David Pino, Carlos Yagüe, and Eric R. Pardyjak. 2021. 'Surface Representation Impacts on Turbulent Heat Fluxes in the Weather Research and Forecasting (WRF) Model (v.4.1.3)'. *Geoscientific Model Development* 14(6):3939–67. doi: 10.5194/gmd-14-3939-2021.

Santos-Alamillos, Fransisco J., David Pozo-Vázquez, José A. Ruiz-Arias, Vicente Lara-Fanego, and Joaquín Tovar-Pescador. 2013. 'Analysis of WRF Model Wind Estimate Sensitivity to Physics Parameterization Choice and Terrain Representation in Andalusia (Southern Spain)'. *Journal of Applied Meteorology and Climatology* 52(7):1592–1609. doi: 10.1175/JAMC-D-12-0204.1.

Santos-Alamillos, Fransisco J., David Pozo-Vázquez, José A. Ruiz-Arias, and Joaquín Tovar-Pescador. 2015. 'Influence of Land-Use Misrepresentation on the Accuracy of WRF Wind Estimates: Evaluation of GLCC and CORINE Land-Use Maps in Southern Spain'. *Atmospheric Research* 157:17–28. doi: 10.1016/j.atmosres.2015.01.006.

Schicker, Irene, Dèlia Arnold Arias, and Petra Seibert. 2016. 'Influences of Updated Land-Use Datasets on WRF Simulations for Two Austrian Regions'. *Meteorology and Atmospheric Physics* 128(3):279–301. doi: 10.1007/s00703-015-0416-y.

Skamarock, William C., Josesph B. Klemp, Jimy Dudhia, David O. Gill, Zhiquan Liu, Judith Berner, Wei Wang, Jordan G. Powers, MichaelG. Duda, Dale M. Barker, and Xiang-yu Huang. 2019. 'A Description of the Advanced Research WRF Model Version 4'. doi: 10.5065/1dfh-6p97.

Steeneveld, Gert-Jan, and Michiel de Bode. 2018. 'Unravelling the Relative Roles of Physical Processes in Modelling the Life Cycle of a Warm Radiation Fog'. *Quarterly Journal of the Royal Meteorological Society* 144(714):1539–54. doi: https://doi.org/10.1002/qj.3300.

Sterk, H. A. Marina, Gert-Jan Steeneveld, and Albert A. M. Holtslag. 2013. 'The Role of Snow-Surface Coupling, Radiation, and Turbulent Mixing in Modeling a Stable Boundary Layer over Arctic Sea Ice'. *Journal of Geophysical Research: Atmospheres* 118(3):1199–1217. doi: https://doi.org/10.1002/jgrd.50158.

Sukoriansky, Semion. 2008. 'Implementation of the Quasi-Normal Scale Elimination (QNSE) Model of Stably Stratified Turbulence in WRF'. Beer-Sheva, Israel.

Sukoriansky, Semion, Boris Galperin, and Veniamin Perov. 2005. '"Application of a New Spectral Theory of Stably Stratified Turbulence to the Atmospheric Boundary Layer over Sea Ice"'. *Boundary-Layer Meteorology* 117(2):231–57. doi: 10.1007/s10546-004-6848-4.

Tewari, Mukul, Fei Chen, Wei Wang, Jimy Dudhia, Margaret A. LeMone, Kenneth E. Mitchell, Michael Ek, George A. Gayno, Jerry W. Wegiel, and Richard Cuenca. 2004. 'Implementation and Verification of the Unified NOAH Land Surface Model in the WRF Model (Formerly Paper Number 17.5)'. Pp. 11–15 in *20th Conference on Weather Analysis and Forecasting/16th Conference on Numerical Weather Prediction*. Seattle, WA, USA.

Varga, Orsolya G., Robert G. Pontius Jr, Zsuzsanna Szabó, and Szilárd Szabó. 2020. 'Effects of Category Aggregation on Land Change Simulation Based on Corine Land Cover Data'. *Remote Sensing* 12(8):1314. doi: 10.3390/rs12081314.

Velde, Ivar. R. van der, Gert-Jan Steeneveld, Ben G. J. Wichers Schreur, and Albert A. M. Holtslag. 2010. 'Modeling and Forecasting the Onset and Duration of Severe Radiation Fog under Frost Conditions'. *Monthly Weather Review* 138(11):4237–53. doi: 10.1175/2010MWR3427.1.

Wang, Wei, and David Gill. 2012.'WRF Nesting'. Presented at the WRF tutorial 2012 Brazil, October 18, Sao Paulo, Brazil.

Weaver, Christopher P., and Roni Avissar. 2001. 'Atmospheric Disturbances Caused by Human Modification of the Landscape'. *Bulletin of the American Meteorological Society* 82(2):269–82. doi: 10.1175/1520-0477(2001)082<0269:ADCBHM>2.3.CO;2.

Wyszogrodzki, Andrzej A., Yubao Liu, Neil Jacobs, Peter Childs, Yongxin Zhang, Gregory Roux, and Thomas T. Warner. 2013. 'Analysis of the Surface Temperature and Wind Forecast Errors of the NCAR-AirDat Operational CONUS 4-Km WRF Forecasting System'. *Meteorology and Atmospheric Physics* 122(3):125–43. doi: 10.1007/s00703-013-0281-5.

Yang, Zong-Liang. 2004. 'Modeling Land Surface Processes in Short-Term Weather and Climate Studies'. Pp. 288–313 in *Observation, Theory and Modeling of Atmospheric Variability*. Vol. Volume 3, *World Scientific Series on Asia-Pacific Weather and Climate*. WORLD SCIENTIFIC.

3.3 Additional analyses of KAS13-IOP16

In the article above, I discussed KAS13-IOP16 as a whole without making a difference between the nighttime and daytime. In the θ_{2m} temperature, and in humidity to a lesser extent, the bias is inversed between day and night. Resulting θ_{2m} daytime biases are near zero, while the RMSE indicates much larger errors. I will therefore split the error assessment between daytime and nighttime to evaluate the effects of the different conditions. These two periods are from 18:00 to 06:00 UTC for the nighttime metrics, and daytime metrics match the moments before 16:00 UTC and after 08:00 UTC, leaving two-hour gaps for the evening and morning transitions.

3.3.1 Daytime metrics

I will compare the daytime metrics of Table 3.1 hereunder to those displayed in **Table 7**, **Table 8**, and **Figure 11** of the paper above, with Table 3.1 similar in format to **Table 8**. Table 3.1 shows negative daytime biases for the specific humidity, while the whole 24 hours shows a positive bias. In contrast, the RMSE is smaller but remains close to the 24h metrics. Regarding the θ_{2m}, Table 3.1 shows a more negative bias and larger RMSE, meaning that the daytime forecasts are more difficult than the night. Similarly, the stratification ($\Delta\theta$) bias and RMSE become larger compared to the metrics of **Table 7**, indicating that vertical structures are prone to more errors during daytime. Lastly, Table 3.1 shows improvement of the wind speed metrics in daytime. At the same time, the $DACC_{45}$ gets only a slight increase compared to the whole IOP.

Table 3.1: The metrics and scores of the simulated variables before 16:00 UTC and after 08:00 UTC. q is the specific humidity at 2 m and ϑ2 is the potential temperature at 2 m. Stratification Δθ is the difference in potential temperature between 110 and 2 m, WS is the wind speed, and DACC is the directional correctness of the wind, with a 45° allowable error range. The scores of each run are given as the fraction between the best and worst metric, with 1 indicating the best score and 0, the worst.

Variable →	***q* [g kg^{-1}] (score)**		***θ_{2m}* [K] (score)**		***$\Delta\theta$* [K] (score)**		***WS* [m s^{-1}] (score)**		***$DACC_{45}$* [%]**	**Final score**
Metric →	bias	RMSE	bias	RMSE	bias	RMSE	bias	RMSE		
Weight → Case↓	1	1	1	1	1	1	1	1	2	
$USGS_{27}$	**-0.2 (0.54)**	0.5 (0.20)	-1.6 (0.04)	2.6 (0.00)	2.7 (0.03)	2.8 (0.03)	0.7 (0.00)	1.4 (0.00)	70	0.22
$MODIS_{20}$	-0.3 (0.35)	0.5 (0.23)	-1.7 (0.02)	2.5 (0.06)	2.8 (0.00)	2.9 (0.00)	0.2 (0.69)	1.2 (0.14)	68	0.28
CLC-SLM_{27}	-0.4 (0.10)	0.6 (0.07)	**-1.2 (0.31)**	2.1 (0.20)	2.4 (0.14)	2.5 (0.14)	0.3 (0.51)	1.3 (0.07)	70	0.29
CLC-SLM_{44}	-0.4 (0.18)	0.6 (0.14)	-1.3 (0.25)	**2.0 (0.22)**	2.4 (0.12)	2.5 (0.12)	0.2 (0.73)	1.1 (0.18)	66	**0.33**
CLC-MLM_{27}	-0.4 (0.04)	0.7 (0.00)	-1.3 (0.27)	2.1 (0.18)	2.4 (0.14)	2.5 (0.14)	0.2 (0.63)	1.2 (0.11)	**72**	0.30
CLC-MLM_{44}	-0.4 (0.22)	0.6 (0.16)	-1.3 (0.24)	2.1 (0.21)	2.5 (0.12)	2.5 (0.12)	**0.2 (0.77)**	**1.1 (0.19)**	66	**0.33**
res_dep (CLC-SLM_{27})	-0.4 (0.10)	0.6 (0.07)	**-1.2 (0.31)**	2.1 (0.20)	2.4 (0.14)	2.5 (0.14)	0.3 (0.51)	1.3 (0.07)	70	0.29
res_1km	-0.5 (0.00)	0.6 (0.04)	-1.3 (0.26)	2.1 (0.20)	**2.4 (0.14)**	**2.5 (0.14)**	0.3 (0.54)	1.2 (0.11)	64	0.27
res_111m	-0.2 (0.49)	**0.5 (0.29)**	-1.7 (0.00)	2.5 (0.04)	2.8 (0.00)	2.9 (0.00)	0.3 (0.54)	1.3 (0.10)	70	0.29
res_mos	-0.3 (0.34)	0.5 (0.23)	-1.6 (0.05)	2.5 (0.06)	2.7 (0.04)	2.8 (0.04)	0.5 (0.28)	1.3 (0.03)	62	0.23

Table 3.1 shows how the model scores (values between brackets). All scores show improvement relative to the worst scoring simulation, except for $DACC_{45}$ that does not need relative representation. Most noticeable is that the $USGS_{27}$ has terrible scores in wind speed, stratification and θ_{2m} metrics, while it excels in the humidity bias. Although the $MODIS_{20}$ is more comparable to the CLC simulations, it has several zero scores. Most differences during the daytime trace back to the difference in humidity performances since the other metrics are comparable among the runs, thus giving lower final scores in general. Altogether, the scores have a smaller spread, but they remain comparable to the whole IOP metrics, as given by **Table 8** in the article above.

Considering Experiment 2, the res_dep shares the best performance with the res_111m, while the res_mos is the worst performing case. It no longer ties with res_111m, as res_111m has better humidity scores, while other metrics are relatively similar to the whole IOP metrics.

3.3.2 Nighttime metrics

In this section, Table 3.2 shows nighttime metrics and corresponding scores, which I shall compare to the daytime metrics of Table 3.1 and the metrics of the whole case study as displayed in the article by **Table 7**, **Table 8**, and **Figure 11.**

Table 3.2: Same as Table 3.1, but for the 18:00 – 06:00 UTC period.

Variable →	***q*** **[g kg^{-1}] (score)**		**θ_{2m} [K] (score)**		**$\Delta\theta$ [K] (score)**		***WS*** **[m s^{-1}] (score)**		***DACC$_{45}$*** **[%]**	**Final score**
Metric →	bias	RMSE	bias	RMSE	bias	RMSE	bias	RMSE		
Weight → Case ↓	1	1	1	1	1	1	1	1	2	
$USGS_{27}$	0.7 (0.21)	0.7 (0.23)	**0.0 (0.99)**	**1.2 (0.17)**	1.7 (0.14)	1.8 (0.14)	2.1 (0.00)	3.4 (0.00)	66	0.32
$MODIS_{20}$	**0.5 (0.37)**	**0.6 (0.38)**	-0.4 (0.56)	1.5 (0.02)	1.9 (0.04)	2.1 (0.00)	**0.9 (0.59)**	**2.1 (0.40)**	63	0.36
CLC-SLM_{27}	0.8 (0.03)	0.8 (0.05)	0.9 (0.00)	1.5 (0.00)	**0.7 (0.65)**	**0.9 (0.58)**	1.3 (0.38)	2.4 (0.30)	70	0.34
CLC-SLM_{44}	0.8 (0.00)	0.8 (0.02)	0.7 (0.24)	1.3 (0.11)	0.8 (0.60)	1.0 (0.54)	1.2 (0.44)	2.3 (0.34)	69	0.37
CLC-MLM_{27}	0.7 (0.15)	0.7 (0.17)	0.8 (0.21)	1.4 (0.09)	0.8 (0.60)	1.0 (0.55)	1.4 (0.32)	2.5 (0.27)	63	0.36
CLC-MLM_{44}	0.8 (0.01)	0.8 (0.04)	0.6 (0.33)	1.3 (0.11)	0.8 (0.58)	1.0 (0.53)	1.2 (0.45)	2.3 (0.34)	**73**	**0.38**
res_dep (CLC-SLM_{27})	0.8 (0.03)	0.8 (0.05)	0.9 (0.00)	1.5 (0.00)	**0.7 (0.65)**	**0.9 (0.58)**	1.3 (0.38)	2.4 (0.30)	70	0.34
res_1km	0.7 (0.11)	0.8 (0.13)	0.9 (0.09)	1.5 (0.03)	0.8 (0.62)	0.9 (0.57)	1.2 (0.43)	2.3 (0.33)	69	0.37
res_111m	0.6 (0.22)	0.7 (0.24)	-0.4 (0.54)	1.5 (0.02)	2.0 (0.00)	2.1 (0.00)	1.1 (0.46)	2.3 (0.35)	67	0.32
res_mos	0.6 (0.25)	0.6 (27)	-0.2 (0.78)	1.3 (0.13)	1.7 (0.11)	1.9 (0.11)	1.3 (0.36)	2.5 (0.26)	66	0.36

The humidity metrics of Table 3.2 have overestimations, similar to the whole IOP metrics. In contrast, the daytime underestimates, showing the switch of sign between day and night with a tendency for overestimations. It is the opposite for θ_{2m}, showing underestimations during the day and over the

whole period, but not at night, except for $MODIS_{20}$ that always shows underestimations, causing a 1.5 K spread in bias among LC datasets. In comparison, the RMSE only differs by 0.3 K, indicating that the error remains relatively constant. For the stratification, Table 3.2 indicates better results during the night than during the day, with RMSE values of CLC below 1.0 K, but relatively constant errors among the CLC options. While $USGS_{27}$ and $MODIS_{20}$ were good with θ_{2m}, they perform worse in vertical temperature difference. Lastly, the wind speed is overestimated more at night than during daytime and the $DACC_{45}$ is slightly lower at night.

The bracket values of Table 3.2 show how this translates into scores. During daytime, the $USGS_{27}$ and $MODIS_{20}$ had several scores of zero. In comparison, this amount is smaller at night and contains a near-perfect score for temperature bias. Table 3.2 confirms the poor humidity forecasting skills of the CLC runs, while the $USGS_{27}$ and $MODIS_{20}$ perform better. Similarly, $USGS_{27}$ and $MODIS_{20}$ score high with θ_{2m} bias. On the other hand, in stratification the $MODIS_{20}$ is the worst simulation, closely followed by the $USGS_{27}$, while all CLC runs have less than half the error of $MODIS_{20}$ in both bias and RMSE. Regarding wind, the $USGS_{27}$ performs worst, while CLC runs perform with reduced errors of 30 to 40 % in the bias and 27 to 34 % in the RMSE, outperformed by $MODIS_{20}$, which has a 60 % smaller bias error and a 40 % reduced RMSE.

Regarding Experiment #2, res_111m has the worst metrics for stability and results in the worst settings for the nighttime metrics, comparable to $USGS_{27}$. While the res_1km shows the best results among four input methods, as $MODIS_{20}$ uses res_1km settings, not following the res_dep settings of the rest of experiment #1, see **Table 3** of the article. This res_1km benefit indicates that the $MODIS_{20}$ is likely to have a small advantage over the other simulations of Experiment 1.

In short, the day and night distinction of the KAS13-IOP16 metrics show that all metrics are composed of a good part and a bad part. Humidity and wind are better forecasted during the day, while the temperature and stratification predictions perform better at night. Nonetheless, the spread between the different simulations is smaller during daytime than at night, resulting in lower scores. $CLC\text{-}MLM_{44}$ has the best overall scores for day and night considered separately. The $CLC\text{-}MLM_{27}$ is better on the complete case, originating from the excluded four hours for morning and evening transitions. For the experiment settings, the res_111m simulation performs unexpectedly well during the day, while it remains one of the worse options for the whole IOP metrics. Overall, the best simulation remains situation-dependent, but a CLC dataset provides the best metrics except for humidity.

3.4 Eleven-day simulation analyses

As mentioned in the article, a case of 24 hours is too short for a reliable determination of the best performing simulation. Therefore, I ran an additional experiment with the Experiment #1 dataset on the same location (**Figure 5**) and the same WRF settings (**Table 5**) for eleven days, including 12 hours spin-up. This section starts with a brief description of the eleven days and the IOPs of KAS13 it includes. This description is followed by the analysis of the metrics given by the simulation and trends revealed by separating the metrics into day and night periods.

I made one small difference in the WRF settings, as I activated spectral nudging allowing the WRF simulation to simulate long periods without reinitialization at regular intervals. I describe the use and methods in more detail in the Annex 4: WRF technical explanations.

3.4.1 Period description

My period of interest starts at 00:00 18 February 2013 and it runs until 00:00 1 March 2013, completing eleven days, and includes IOP15 to IOP21 and half of IOP22. The first twelve hours are spin-up and will not be discussed as part of the long-term simulation period (LTP).

Figure 3.1 shows the radiation balance and temperature of the simulated period. Radiation in Figure 3.1a shows mostly clear-sky conditions, except for a few days in the middle of the period, thus creating three different periods in the LTP. The first starts at 12:00 18 February and continues until 12:00 22 February, having clear-sky conditions and containing four IOPs. The second does not have IOPs and has cloudy conditions, spanning the period of 12:00 22 February to 12:00 25 February. The third period, which resembles the first period in radiative conditions, starts 25 February at 12:00 and continues up to the end of the LTP, including three and a half IOP.

Figure 3.1b contains the potential temperatures of the GBA data at 2 m and 110 m and has their temperature difference on the second y-axis. The three periods in the LTP also exist in the temperature curves of Figure 3.1b showing DTRs of at least 15 K during both clear-skied periods, while the cloudy periods show amplitudes ranging from 7 to 15 K. The main reason for a large DTR in the second period comes from a spare clear sky moment at night causing rapid cooling at 02:00 25 February. Another reason is the arrival of warm air, rising temperatures in the night of 22 February (KAS13-IOP18).

Figure 3.2a describes the specific humidity trends and consists of three different regimes matching the three earlier described periods. During the first period, humidity shows daily cycles around roughly the same value of 3.2 g kg^{-1} with a 0.8 g kg^{-1} amplitude, where moisture decreases throughout the night with a minimum at dawn and increases fast in the morning until it stabilizes between 3.5 and 4.0 g kg^{-1}. The second period starts with moisture advection, occurring simultaneously as the temperature advection shown in Figure 3.1b but loses moisture afterward with adecrease to 2.0 g kg^{-1}. In period three, humidity increases by roughly 0.4 g kg^{-1} per daily cycle, resembling the daily cycle patterns of the first period.

Figure 3.2b shows the wind speeds and directions of the LTP; here, the three previously described periods are less discernable. Nonetheless, the wind direction seems to have clear nighttime flow patterns during the clear-sky periods, with a DDV flow in the second half of the night and early morning. The rest of the day has a less stable wind direction, the wind comes from the south or west but is often not a steady or long-lived flow. During the cloudy period, the winds are clearly from the west and do not show much deviation from this direction, with commonly high wind speeds. In contrast, wind speeds of the clear-sky periods show a daily pattern with wind speed falling after sunset, becoming slow at night. These slow winds linger in the morning, then slowly increase without a typical daytime wind speed maximum.

In conclusion, the LTP largely consists of clear sky conditions but has a period with cloudy sky conditions and winds from the west. Other variety of weather conditions more diverse situations in the LTP allows for more thorough testing the new tools.

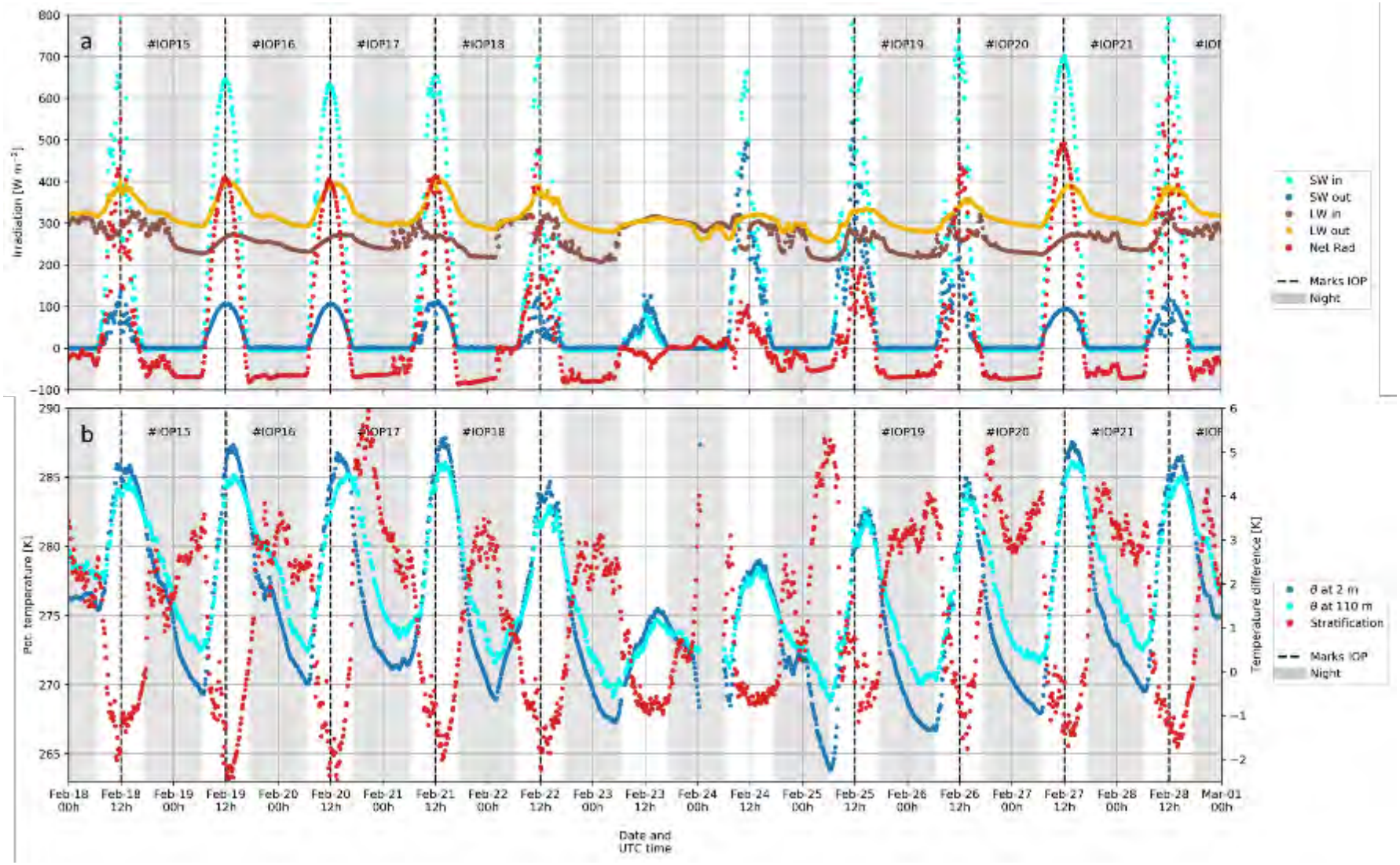

Figure 3.1: Situation during the eleven-day simulation period, containing 7.5 IOPs of the KASCADE-2013 campaign. Plot (a) contains observed radiation series at M30. Plot (b) contains observed potential temperature series at GBA, both at 2 and 110 m. The secondary y-axis shows the difference between the two.

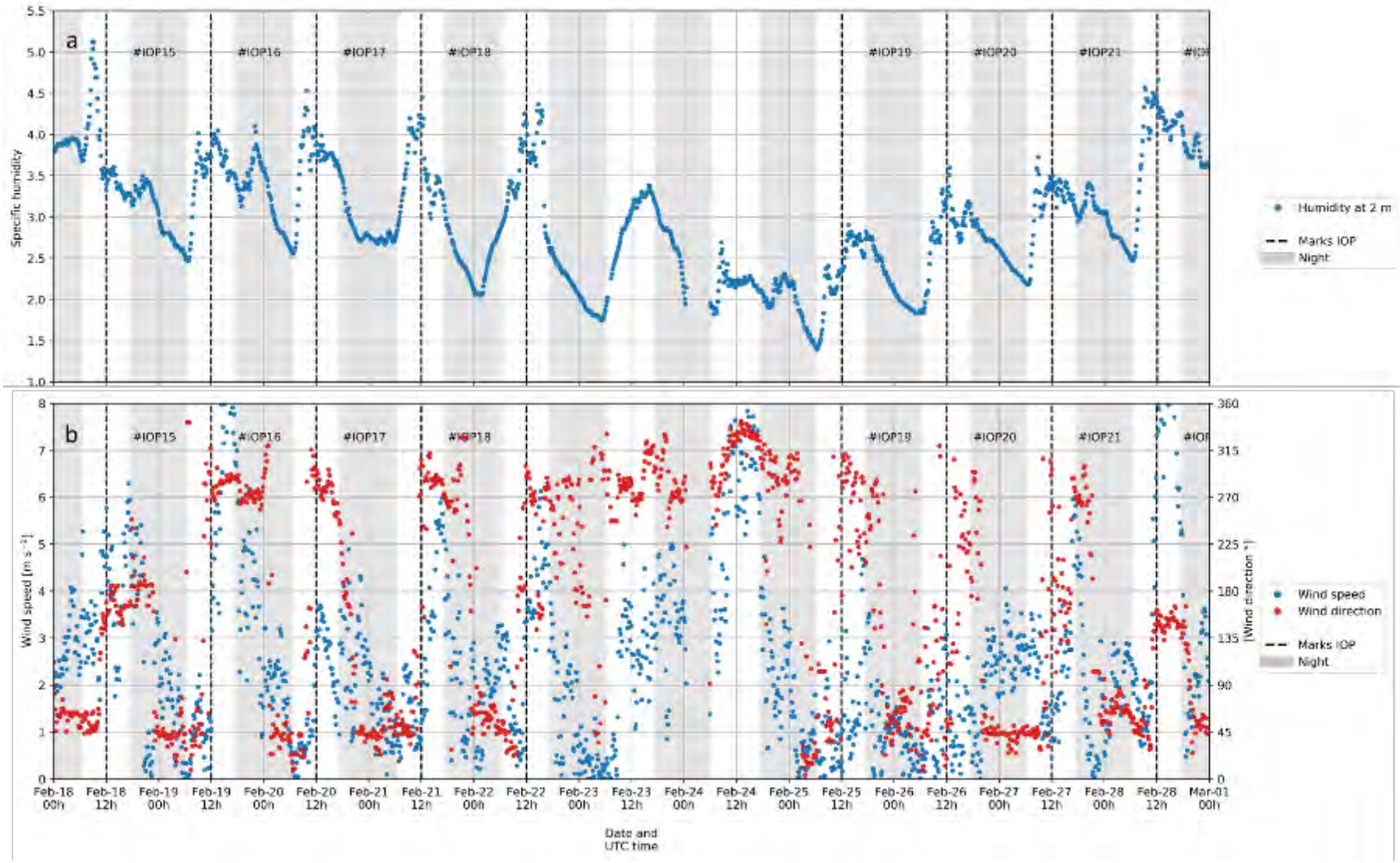

Figure 3.2: The observed humidity (a) and wind (b) series at GBA during the eleven days of the long-term simulation, containing 7.5 IOPs of the KASCADE-2013 campaign. Plot (b) has wind direction on the secondary y-axis.

3.4.2 Complete simulation analysis

I have simulated the six configurations of Experiment 1, as described in **Table 3** of the article, to determine with more confidence which one is the best performing since the LTP includes more phenomena. I will start with the whole dataset and compare the metrics and scores with those presented in **Table 7, Table 8**, and **Figure 11** of the article. Comments on trends of the day and nighttime metrics follow.

Table 3.3 displays the metrics for the complete LTP. In contrast to the findings for the 24h-case, the LTP does not contain underestimations and is always overestimated. Notably, the humidity overestimation has increased compared to the 24h-case, but the difference between the LC datasets remains minimal in both the bias and RSME. Regarding the temperature metrics, all θ_{2m} metrics improve their bias but deteriorate in RMSE. Here, the $USGS_{27}$ has a near-zero bias while it has the worst RMSE. The spread in RMSE is limited, resembling that of humidity, while stratification shows a degradation in bias and RMSE for $USGS_{27}$ and $MODIS_{20}$. The CLC runs improve bias compared to the 24h-case, but with a slight degradation of the RMSE. Lastly, the wind speed is overpredicted, increasing its bias and RMSE, and the $DACC_{45}$ decreases by roughly 20 % compared to the 24h-case.

Metrics show similar patterns in the 24h-case and the LPT, as the LPT has many clear sky days alike IOP16. Another possibility is the location has a preference for a certain LC dataset, more research to location is already advised in the article. A general degradation of the model skill matches with the findings of Duine (2015), who mentioned KAS13-IOP16 as an IOP with exceptional WRF metrics.

Table 3.3: Metrics of the different variables used to evaluate the performance of the long-term simulation, evaluation starts at 12:00 UTC on 18 February and continues until 00:00 of 1 March. Here q is specific humidity at 2 m and ϑ2 is the potential temperature at 2 m. Stratification is the difference in potential temperature between 110 and 2 m, WS is the wind speed, and DACC is the directional correctness of the wind, with a 45° allowable error range.

Variable →	***q* [g kg^{-1}] (score)**		**θ_{2m}[K] (score)**		***Δθ* [K] (score)**		***WS* [m s^{-1}] (score)**		***DACC$_{45}$* [%]**	**Final score**
Metric →	bias	RMSE	bias	RMSE	Bias	RMSE	bias	RMSE		
Weight → LC dataset ↓	1	1	1	1	1	1	1	1	2	
$USGS_{27}$	**0.8 (0.07)**	**1.2 (0.06)**	**-0.1 (0.89)**	3.3 (0.00)	2.2 (0.12)	2.7 (0.09)	1.7 (0.00)	3.4 (0.00)	49	0.22
$MODIS_{20}$	0.9 (0.04)	1.1 (0.05)	-0.4 (0.59)	3.2 (0.03)	2.4 (0.00)	3.0 (0.00)	1.5 (0.16)	3.0 (0.11)	48	0.19
CLC-SLM_{27}	0.9 (0.06)	1.1 (0.02)	0.9 (0.00)	3.2 (0.02)	**1.4 (0.44)**	**2.1 (0.31)**	1.2 (0.31)	2.7 (0.22)	49	0.24
CLC-SLM_{44}	0.9 (0.02)	1.1 (0.01)	0.7 (0.23)	3.2 (0.03)	1.4 (0.43)	2.1 (0.30)	1.1 (0.35)	2.5 (0.25)	49	0.26
CLC-MLM_{27}	0.9 (0.01)	1.1 (0.00)	0.6 (0.32)	3.2 (0.03)	1.4 (0.42)	2.2 (0.28)	1.3 (0.26)	2.8 (0.18)	49	0.25
CLC-MLM_{44}	0.9 (0.00)	1.1 (0.00)	0.7 (0.22)	**3.1 (0.04)**	1.4 (0.42)	**2.3 (0.29)**	**1.0 (0.40)**	**2.5 (0.25)**	**50**	**0.26**

Table 3.3 details the scores of these metrics between brackets, showing lower scores than the 24h-case, meaning relatively smaller differences among the input datasets. $MODIS_{20}$ has the lowest scores, while the CLC-MLM_{44} has the best. $USGS_{27}$ is roughly in between thanks to the 0.89 score in the θ_{2m} bias, in spite of having in three cases the worst metric. As mentioned above, the spread within RMSE is relatively small, although the experiments cluster in two groups, the $USGS_{27}$ and $MODIS_{20}$ generally having comparable scores and the four CLC runs being often close to each other. The largest influences on the final score originate from the θ_{2m} bias, RMSE and bias of stratification, as well as the wind speed RMSE and bias, while other metrics show differences of less than 10 %. Possible explanations of the

uniformness of the metrics might result from processes less influenced by the LC, such as soil moisture evaporation, keeping the runs relatively close. Another option causing more resemblance in the LTP scores than in the 24h-case is that the nudging pulls all simulations towards the same trends and thus reduces the differences that the LC datasets can make.

In contrast with the 24h-case presented in the article, the CLC-MLM$_{44}$ shows the best results. Remember that the score reflects relative ability compared to the worst option, except for the DACC$_{45}$ score that has a defined best and worst option.

3.4.3 Day- and Nighttime metrics

Similar to Table 3.1 and Table 3.2, I will discuss the separate metrics of the day- and nighttime trends. Nighttime values are calculated after 18:00 UTC and before 06:00 UTC. The daytime counterpart originates from 08:00 UTC up to 16:00 UTC. Since it is winter the sun sets at 17:10 on 18 February and 17:24 UTC on 28 February. On the other hand, the sunrise is at 06:31 UTC on 18 February. I do not consider the morning and evening transitions, thus the two-hour gaps between the averages. This split between the day and night is performed to see if it matters for the performance of the model as it does for the 24h-case.

Table 3.4: Same as Table 3.3 but for night conditions, including values between 18:00 and 06:00 UTC.

Variable →	q [g kg^{-1}] (score)		θ_{2m}[K] (score)		$\Delta\theta$ [K] (score)		WS [m s^{-1}] (score)		$DACC_{45}$ [%]	**Final score**
Metric →	bias	RMSE	bias	RMSE	bias	RMSE	bias	RMSE		
weight → LC dataset ↓	1	1	1	1	1	1	1	1	2	
USGS$_{27}$	0.9 (0.14)	1.0 (0.01)	0.6 (0.68)	**2.5 (0.10)**	1.9 (0.19)	2.5 (0.13)	1.7 (0.00)	3.3 (0.00)	49	0.23
MODIS$_{20}$	**0.9 (0.14)**	**1.0 (0.12)**	**0.3 (0.83)**	2.5 (0.09)	2.3 (0.00)	2.9 (0.00)	1.5 (0.09)	3.0 (0.09)	51	0.24
CLC-SLM$_{27}$	1.0 (0.03)	1.1 (0.01)	1.8 (0.00)	2.8 (0.00)	0.9 (0.62)	1.8 (0.40)	0.9 (0.43)	2.2 (0.33)	50	0.28
CLC-SLM$_{44}$	1.0 (0.01)	1.2 (0.00)	1.6 (0.10)	2.7 (0.02)	**0.8 (0.63)**	**1.7 (0.41)**	1.1 (0.33)	2.4 (0.29)	51	0.28
CLC-MLM$_{27}$	1.0 (0.03)	1.1 (0.02)	1.6 (0.10)	2.8 (0.02)	0.9 (0.62)	1.8 (0.38)	1.1 (0.33)	2.4 (0.28)	51	0.28
CLC-MLM$_{44}$	1.0 (0.00)	1.2 (0.00)	1.6 (0.12)	2.7 (0.03)	0.9 (0.62)	1.8 (0.39)	**0.9 (0.48)**	**2.2 (0.36)**	**53**	**0.30**

Humidity metrics of the LTP have a larger error at night than during the day (0.1 – 0.5 g kg^{-1} in bias) with the complete LTP in between, with MODIS$_{20}$, the smallest difference and CLC-SLM$_{27}$ the largest. Although the differences result in relatively uniform errors over the six LC datasets, the USGS$_{27}$ and the MODIS$_{27}$ are distinguishably better at night in their bias and RMSE. Note that the CLC RMSE is better at both night and day compared to the complete LTP metrics. Altogether, the whole LTP has a smaller variation than either day or night, confirming the partial dampening effect of the diurnal cycle.

For θ_{2m}, the night bias becomes positive (0.3 – 1.6 K) and RMSE improves (0.4 – 0.8 K improvement). At the same time, the day bias deviates strongly toward the negative side (-0.4 – -1.2 K with comparable RMSE (0.0 – 0.1 K improvement). The pattern in the bias still follows that set by the 24h-case, overestimations at night and underestimations during the day with smallest errors at night. The best scoring LC datasets remain MODIS$_{20}$ and USGS$_{27}$, with worst scores during the day. Notably, the MODIS$_{20}$ scores best at night while USGS$_{27}$ has the best complete LTP scores, which is inverse of what

the 24h-case shows. In contrast, the RMSE scores match well with the 24h-case, as little spread in scores exists between the different RMSE values (<10 %).

Regarding the stratification, the metrics are better at night (0.8 – 1.9 K bias and 1.7 – 2.5 K RMSE) than during the day (2.1 -2.5 K bias and 2.4 – 2.7 K RMSE), showing very good values for the CLC runs, with biases below 0.9 K and RMSE below 2 K. Improvement of stratification forecasts at night matches the trend shown in the 24h-case metrics, with comparable differences in bias. RMSE is better in the 24h-case (0.9 – 2.1 K). In contrast, daytime stratification is overestimated, which matches the results of the 24h-case when the model showed near-neutral conditions while the observation had unstable conditions during daytime. Daytime skill spread shows a small difference between the runs (<17 %), with CLC-SLM_{27} performing best.

Lastly concerning the winds, CLC has modestly improved wind speed biases and RMSE for the nighttime metrics (0.9 – 1.7 m s^{-1} bias and 2.2 – 3.3 m s^{-1} RMSE) compared to the daytime ones (1.1 – 2.0 m s^{-1} bias and 2.7 – 3.0 m s^{-1} RMSE). In contrast, the $USGS_{27}$ and $MODIS_{20}$ remain with similar errors regardless of the time of day (1.5 – 2.0 m s^{-1} bias and 3.0 – 3.4 m s^{-1} RMSE), $USGS_{27}$ has this trend comparable to the 24h-case. It is here that the largest difference exists between the different CLC runs. The CLC-SLM_{27} and CLC-MLM_{27} perform less good (1.6 – 1.8 m s^{-1} bias and RMSE at night 2.2 m s^{-1} and 3.1 m s^{-1} during the day) than the CLC-SLM_{44} and CLC-MLM_{44} (0.9 – 1.2 m s^{-1} bias and 2.2 – 2.8 RMSE), a trend already visible in the 24h-case. In contrast, the improvement of $DACC_{45}$ at night does not match the 24h-case trend. The lower $DACC_{45}$ was expected as Duine (2015) explained that KAS13-IOP16 is relatively well forecasted among the IOPs.

The final scores clearly show that the daytime conditions have lower improvements in the LC datasets (0.13 to 0.26) than the nighttime conditions (0.23 to 0.30) have. As reflected in their low final scores, the $USGS_{27}$ and $MODIS_{20}$ perform worse than the other datasets during the day (both score 0.13). The CLC datasets have comparable performances and remain close to each other in final scores.

Table 3.5: Same as Table 3.3 but for day conditions, including values between 08:00 and 16:00 UTC.

Variable →	***q* [g kg^{-1}] (score)**		**θ_{2m} [K] (score)**		**$\Delta\theta$ [K] (score)**		***WS* [m s^{-1}] (score)**		***DACC*$_{45}$ [%]**	**Final score**
Metric →	bias	RMSE	bias	RMSE	bias	RMSE	bias	RMSE		
Weight → **LC dataset ↓**	1	1	1	1	1	1	1	1	2	
$USGS_{27}$	0.7 (0.12)	1.0 (0.06)	-1.0 (0.19)	3.4 (0.00)	2.5 (0.02)	2.7 (0.01)	2.0 (0.00)	3.4 (0.00)	**48**	0.13
$MODIS_{20}$	0.8 (0.00)	1.0 (0.00)	-1.2 (0.00)	3.2 (0.06)	2.5 (0.00)	2.7 (0.00)	1.6 (0.22)	3.1 (0.09)	46	0.13
CLC-SLM_{27}	**0.5 (0.31)**	1.0 (0.06)	**-0.4 (0.64)**	3.2 (0.08)	**2.1 (0.16)**	**2.4 (0.14)**	1.6 (0.19)	3.1 (0.09)	46	0.26
CLC-SLM_{44}	0.6 (0.24)	**1.0 (0.07)**	-0.7 (0.44)	3.1 (0.10)	2.2 (0.12)	2.4 (0.11)	**1.1 (0.43)**	**2.7 (0.22)**	45	**0.26**
CLC-MLM_{27}	0.7 (0.15)	1.0 (0.01)	-0.9 (0.28)	3.1 (0.10)	2.1 (0.14)	2.4 (0.12)	1.6 (0.20)	3.1 (0.08)	45	0.20
CLC-MLM_{44}	0.6 (0.19)	1.0 (0.06)	-0.6 (0.51)	**3.1 (0.12)**	2.2 (0.12)	2.5 (0.11)	1.2 (0.38)	2.8 (0.17)	45	0.25

In short, the humidity error reduces during the daytime, while other parameters are better forecasted at night. The LPT metrics trends generally resemble the 24h-case, except for the wind as reflected by the scores in Table 3.3, **Table 7**, and **Figure 11**. The day- and nighttime do not exactly match the 24h-case, but deviations are not large. The trend established in the 24h-case where CLC performs best

except for humidity holds, for the most part, however the θ_{2m} is now better in the $USGS_{27}$ and $MODIS_{20}$ simulations.

As discussed above, although more spread exists in the bias, the RMSE values of humidity and θ_{2m} show less than 15 % difference between the six simulations, which raises the questions whether the main errors are elsewhere in the model. In contrast, $\Delta\theta$ and wind speed show up to 41 % differences between the six runs, with most variation during the nighttime metrics. In the daytime metrics, it is clear that the $USGS_{27}$ and $MODIS_{20}$ have many (near) zero scores, reflecting the worst-performing simulations in this comparison. They only produce better $DACC_{45}$ than the other simulations. The $CLC\text{-}SLM_{44}$ performs best together with the $CLC\text{-}SLM_{27}$ (0.26) during the daytime, while $CLC\text{-}MLM_{44}$ performs best at night and the complete LTP (0.26 and 0.30). The wind speed metrics show the largest differences between the CLC runs, leading them to determine the best LC dataset.

However, humidity errors resemble among the datasets, and their origin is presumably not in the LC but other parts of the model, such as the soil moisture or exchange processes. The tests done by Kalverla et al. (2016) showed great sensitivity to the initial soil moisture conditions at this location. Other options for the reduced variability among the dataset could relate to the active nudging applied during these simulations. As described in the Annex 4: WRF technical explanations, nudging influences the grid cell values throughout the whole simulation, pushing them in the direction of the nudge dataset. These external forcings are the same for all simulations, thus reducing the amount of freedom the model has. A second part that reduces the amount of variation in the LTP simulations is the number of runs. Here, the reduced number of simulations reduces the possible variation among those runs.

3.5 Conclusions

This chapter shows and tests two new tools to optimize CLC for WRF simulations. The first tool I introduce is the Multi-Level Mode (MLM) aggregation, allowing a cluster of resembling classes to trump over a larger single class surface when the combined surface of the resembling classes is larger. Tests on the CLC datasets show increasing effectiveness of the new method with coarsening horizontal resolution, since the method shows a 0.03% difference from the standard aggregation at 111 m, increasing to 16.6% at 9 km. The second tool is a physical parameter table created for the 44 classes of CLC, allowing CLC to use the full diversity of its classes.

Case studies with the two new tools show that CLC performs better than the two classical land cover datasets of USGS and MODIS. Further research of the MLM and the 44-class table show that CLC with MLM but without the 44 classes performs best on a 24h-case, while over eleven days, the CLC with MLM and 44 classes performs best. Further analysis of the daytime and nighttime sections of the simulations shows that daytime metrics resemble RMSEs, while the bias can differ more. Nighttime is when the influences of LC datasets are more profound, with RMSE differences being larger. Lastly, biases of humidity and 2-m temperatures flip between day and night in accordance with the pattern seen in the reduced amplitudes of the simulation.

A second experiment on the 24h-case investigated methods of presenting the input LC dataset to the WRF model. This second experiment showed that a too fine input resolution is the worst option for the WRF simulation. In comparison, matching the input datasets with the WRF simulation resolution is inferior to giving all WRF domains 1-km resolution as input data. As this setting is the default for the MODIS simulations, it has slight benefits compared to the other datasets. Lastly, the mosaic option did not seem to perform well. However, this could relate differences between reality and WRF as to how a land fraction contributes to the average of the total surface.

Concerning the aggregation methods, the simulations show promising results. However, the observations do not include locations where the two aggregation methods differ since forecasts skill improves, the advected values are better with the new method. For a better determination, more case studies at different locations are needed. The 44-class physical parameter table is not yet fully completed and needs further improvements. Filling the remaining values of the 44-class table requires additional satellite data or in-situ measurements, depending on the parameter. Nevertheless, it produces better results than the default options, indicating that further development would improve simulation skills even further.

Chapter 4

Evaluation of a fine-resolution simulations over the Cadarache and neighboring valleys

After the work on land cover representation and verification with WRF simulations, I resume the research I conducted on fine-resolution runs in this chapter. A significant part of the results is published in de Bode et al. (2021), adjoined below. However, I was keen to extent the article further with additional investigations on stability and flows in the Cadarache Valley (CV) and finest simulation domain. Thus, the chapter is structured as follows, and it starts with the article, followed by the extra analyses on the GBA, stability on the south sidewall, in-depth analyses of the nocturnal temperature development, and visualizations of flows.

4.1 Introduction

As mentioned in 2.4.3, local winds of the CV are problematic to simulate. In particular, the Cadarache Down Valley (CDV) wind was not simulated before this study because of non-resolved topography, as noted by Kalverla et al. (2016). Other methods to assess the CV wind were devised, but those approaches did not address the local variability since they were only valid at one point. Consequently, working with finer resolutions appears a promising way to improve the CV wind simulation.

As mentioned in section 2.4, the statistical methods of threshold and ANNs give good wind indicators in a location but only give wind components because they were not trained for other variables such as temperature and humidity. In comparison, numerical weather models have topographic and land cover maps that inherently incorporate spatial variability. Statistical methods would need training for every location that differs from the original location. For example, the bottom of the valley and one of the sidewalls can have different flows throughout the day. Their local slope and orientation are different, receiving more or less irradiation and forcing winds in different directions.

Numerical simulations with operational NWP models are generally used to represent large areas. Thus, large cells have average values of the surface and lose their spatial details, making small valleys or small lakes disappear in the average of the cell. Finer-scale resolutions ensure that these local variations are preserved in the model, and consequently, weather patterns can form at scales resulting from these small variations. Sekiyama et al. (2015) argue that fine resolution runs are best to represent weather phenomena, but coarser simulations are preferable at times due to computational limitations.

4.2 Summary of the article

The region around the CV is part of the complex terrain in the pre-Alps of southern France, where the CV is a small valley with a width of 1 km that opens into the larger Durance Valley (DV). The previous modeling study of Kalverla et al. (2016) could not succeed in forecasting the stable night flows of the CV with 1 km horizontal resolution simulations. The current study tries to realize WRF simulations of the stable night CV flows with a horizontal resolution as fine as 111 m.

The model runs with five domains: a parent domain with 9 km horizontal resolution, and four nested domains, each decreasing resolution with a 3 ratio step to the innermost domain at 111 m. The new ERA5 data at 27 km resolution imposes boundary-layer conditions hourly. An analysis of turbulent length scales demonstrates that they remain smaller than the finest horizontal resolution, which allows the simulation to remain in a fully-parameterized turbulence mode instead of switching to LES.

The model simulated the IOP07 of the KASCADE-2017 campaign. The 24-hour IOP is noon to noon. Its observed diurnal cycle of temperature reflects a fair-weather, cloudless situation, with a diurnal temperature range (DTR) reaching 19 K. The wind speed always remains weak in the CV lower layer, but a spectacular day-night reversal was observed, with a westerly orientation during the daytime, and an SE, CV-channeled down-valley wind during the stable stratification period. Above the CV, a DV-channeled wind started about 3 hours after sunset.

Refining the horizontal resolution from 1 km to 111 m improves the percentage of correctly forecasted 10 m wind from 46% to 60%, showing a good visual agreement with the nighttime observations. As an illustration, the time series of the Sodar wind profile shows a good resemblance with the model results. However, the simulated 12 K DTR underestimates the observed 19 K. Consequently, stability within the CV does not have good simulated values at night, although it is relatively well forecasted early in the night. The model thus allows transport of the above valley conditions, such as humidity, into the CV, whereas the observations rather resemble a mature cold pool. Vertical cross-sections extracted from the model output show that the confluent zone between CV and DV generally has low surface wind speeds, whereas the DDV peak is around 200 m agl.

In conclusion, the simulation realistically depicts the different flows in the CV and the DV. The vertical structure of temperature and wind match well. However, the spatial distribution of temperature and humidity does not match well within the CV due to the small simulated DTR. Hence, the cold pool simulated in the CV is not the right type because of too much vertical transport along the sidewalls. This discrepancy was possibly reinforced by the early arrival (at 17:30 UTC) in the model of a moist air mass with strong southeasterly winds arriving, roughly 1.5 hours before the observations.

4.3 Article

atmosphere

Fine-Resolution WRF Simulation of Stably Stratified Flows in Shallow Pre-Alpine Valleys: A Case Study of the KASCADE-2017 Campaign

Michiel de Bode [1,2,*], Thierry Hedde [1], Pierre Roubin [1] and Pierre Durand [2]

[1] CEA, DES, IRESNE, DTN, Laboratory for Environmental Transfer Modeling, Cadarache, F-13108 Saint-Paul-Lez-Durance, France; Thierry.Hedde@cea.fr (T.H.); Pierre.Roubin@cea.fr (P.R.)
[2] Laboratoire d'Aérologie, Université de Toulouse, CNRS, UPS, 31400 Toulouse, France; pierre.durand@aero.obs-mip.fr (P.D.)
* Correspondence: michiel.debode@cea.fr

Abstract: In an overall approach aiming at the development and qualification of various tools designed to diagnose and/or forecast the flows at the local scale in complex terrain, we qualified a numerical model based on the WRF platform and operated in a two-way nested domain mode, down to a horizontal resolution of 111 m for the smallest domain. The area in question is the Cadarache valley (CV), in southeast France, which is surrounded by hills and valleys of various sizes. The CV dimensions (1 km wide and 100 m deep) favor the development of local flows greatly influenced by the diurnal cycle and are prone to thermal stratification, especially during stable conditions. This cycle was well documented due to permanent observations and dedicated field campaigns. These observations were used to evaluate the performance of the model on a specific day among the intensive observation periods carried out during the KASCADE-2017 campaign. The model reproduced the wind flow and its diurnal cycle well, notably at the local CV scale, which constitutes considerable progress with respect to the performances of previous WRF simulations conducted in this area with kilometric resolution, be it operational weather forecasts or dedicated studies conducted on specific days. The diurnal temperature range is underestimated however, together with the stratification intensity of the cold pool observed at night. Consequently, the slope drainage flows along the CV sidewalls are higher in the simulation than in the observations, and the resulting scalar fields (such as specific humidity) are less heterogeneous in the model than in the observations.

Keywords: WRF simulation; fine-resolution; stratified flow; cold pool; KASCADE-2017; valley wind

1. Introduction

The flows over complex terrain represent a challenge for both their observation and numerical simulation. At a large scale, the major mountain chains constrain the flows in the entire troposphere, and their effect has to be adequately taken into account for an accurate weather forecast. To date, one may consider this question as having been satisfactorily addressed, although some improvements are still required [1]. At the local scale, the topography has a direct impact on the lower layers of the atmosphere (the atmospheric boundary layer; ABL), with a marked diurnal cycle. While at a large scale, the mechanical effects of the topography are dominant, at the local scale, the flow is driven by a combination of both mechanical and buoyancy effects. Furthermore, what we call "local" in fact covers quite a large range of scales, ranging from the smaller hill–valley systems (of O(10 m) in height and O(100 m) in length) to systems of one or two orders of magnitude higher. All these systems interact with each other, but on different time scales.

Such complexity results in great difficulty in monitoring the local transport, and stagnation/blocking effects can generate air quality concerns with polluted air masses trapped in valleys even in rural areas. In cold pool systems, the stagnation can be extreme with the consequence of very low temperatures sometimes observed on the ground (Lehner et al. [2] mentioned a recorded minimum temperature of −52. 6 °C observed in the Grünloch basin in 1932). In the French Alps, the Arve valley has recently received a great deal of attention due to dedicated observations and high-resolution numerical simulations [3–5]. For a localized potential pollution source, a question arises regarding the behavior of the particle plume, that is, how it is transported and dispersed in a complex terrain, especially during stable stratification conditions with suppressed turbulent vertical mixing. In complex terrain, simple dispersion models fail in the prediction of plume behavior, and the interaction between orographic systems of different forms and sizes may produce unexpected stagnation effects [6,7].

According to the academic interest in local process knowledge, and to the societal importance of the possible impacts of complex topography, many studies have been launched over recent decades, often based on observation field campaigns. We cannot report an exhaustive list of these programs here. We will therefore only mention a few relevant campaigns. Density-driven valley and slope flows and/or cold air pooling were studied during VTMX [8], COLPEX [9], METCRAX [10], MATERHORN [11], ASCOT [12], and the Passy project [13,14]. Rotach et al. [15] published a description of the i-Box setup in the Inn valley. Recently, the Perigão 2017 campaign [16] observed and quite successfully simulated the local valley flows and their reversal during the diurnal cycle. Other studies focused on the effect of slope orientation on surface fluxes and local flows [17–19]. All these campaigns saw the deployment of meteorological observation means at the surface and aloft, including remote sensing platforms (sodars, radars, and lidars), among which the scanning Doppler lidar offers a high potential for the fine study of flows in stable layers in which oscillations are often observed (e.g., [20]).

The Cadarache CEA site (CEA stands for "Commissariat à l'Énergie Atomique et aux Énergies Alternatives", the French nuclear research agency) is located in southeastern France, on the border of the Alps mountain chain and the Rhône river. The area has a complex system of hills and valleys of different sizes (a description is provided in Section 2). The chronic or accidental release of contaminants requires the ability to monitor the transport and dispersion of effluents in this area, especially during stable stratification periods when local, thermally driven valley winds and/or cold pool systems may be established. For a decade, therefore, an effort has been made to better understand the meteorology at a very local scale, and to develop various simulation tools. In particular, the KASCADE-2013 campaign [21] observed the diurnal cycle of valley winds and their stacking in the area, whereas the KASCADE-2017 campaign [22], the observations of which are the base of the present study, focused on the spatial variability of the flow and the stratification inside the valley. Various ways were thus explored to nowcast or forecast the local scale flows. Duine et al. [23] developed a simple but robust method with which to diagnose the presence of a down valley wind in stable conditions based on the observation of a stratification index. Dupuy et al. [24] used artificial neural networks (ANNs) in order to estimate the wind speed and direction in a small valley from routine observations representative of a larger scale. Finally, [25] extended this ANN technique to forecast the valley wind from operational weather simulations performed with a resolution which was too coarse to represent the fine-scale flows.

In this paper, we present an attempt to simulate the flows by running a weather model with a fine (~ 100 m) horizontal resolution. Recent studies have demonstrated the potential of such simulations in complex areas (e.g., [4,5] for the Arve valley with the Meso-NH model; [26] for the large Inn valley in Alpine Austria with the COSMO model), though stable conditions often remain more difficult to simulate than convective boundary layers [27,28]. Our study is based on the Weather Research and Forecasting (WRF) model [29,30]. Starting from the version of previous research by [31] with a 1 km horizontal resolution, we developed a grid-nested mode version with the finest domain

centered on the Cadarache site with a 111 m horizontal resolution. The model was run on a specific day corresponding to a well-documented case of the KASCADE-2017 campaign. The paper is organized as follows: The next section presents the site of the study and its geographical characteristics, the observations made during KASCADE-2017, the case study, and the numerical platform used for the simulation. The results of the simulation are then analyzed in line with the corresponding observations. The following section is a discussion about the performances of the simulation and the perspectives with which to improve it in the future. Our conclusions are presented in the final section.

2. Location, Observation, Case Study, and Numerical Platform

2.1. Location

The study area is located in the Alpine foothills of southeastern France. Figure 1 presents the five domains of the numerical simulation, which will be detailed in Sections 2.4 and 2.5. This map allows these domains in western continental Europe to be situated. We will focus our study on the central part of the domain (enlarged in Figure 1b and 1c together with a representation of its topography). The main features are the mountainous areas of the Alps to the north and the east, the Mediterranean to the south, and the Rhône river valley to the west. We will focus especially on the Durance river (indicated as DV in Figure 1b), which flows to the SSW whilst separating plateaus of the pre-Alps. The main weather characteristics of this area are described in [24]. To summarize, the most frequent wind regimes are as follows: the "Mistral" wind, a cold and dry flow blowing from the north in the Rhône valley and then deviated according to the local topography. Southeastern flows, often moist and warm, bringing precipitation over the area. We then have spring-to-summer sea breezes, with an overall orientation from the south. These can be deviated along the valleys and deeply penetrate the Rhône valley as well as its tributary valleys [32]. The Mediterranean climate is characterized by frequent sunny and cloudless periods, with rainfall mainly occurring in the fall during short but sometimes heavy precipitation events.

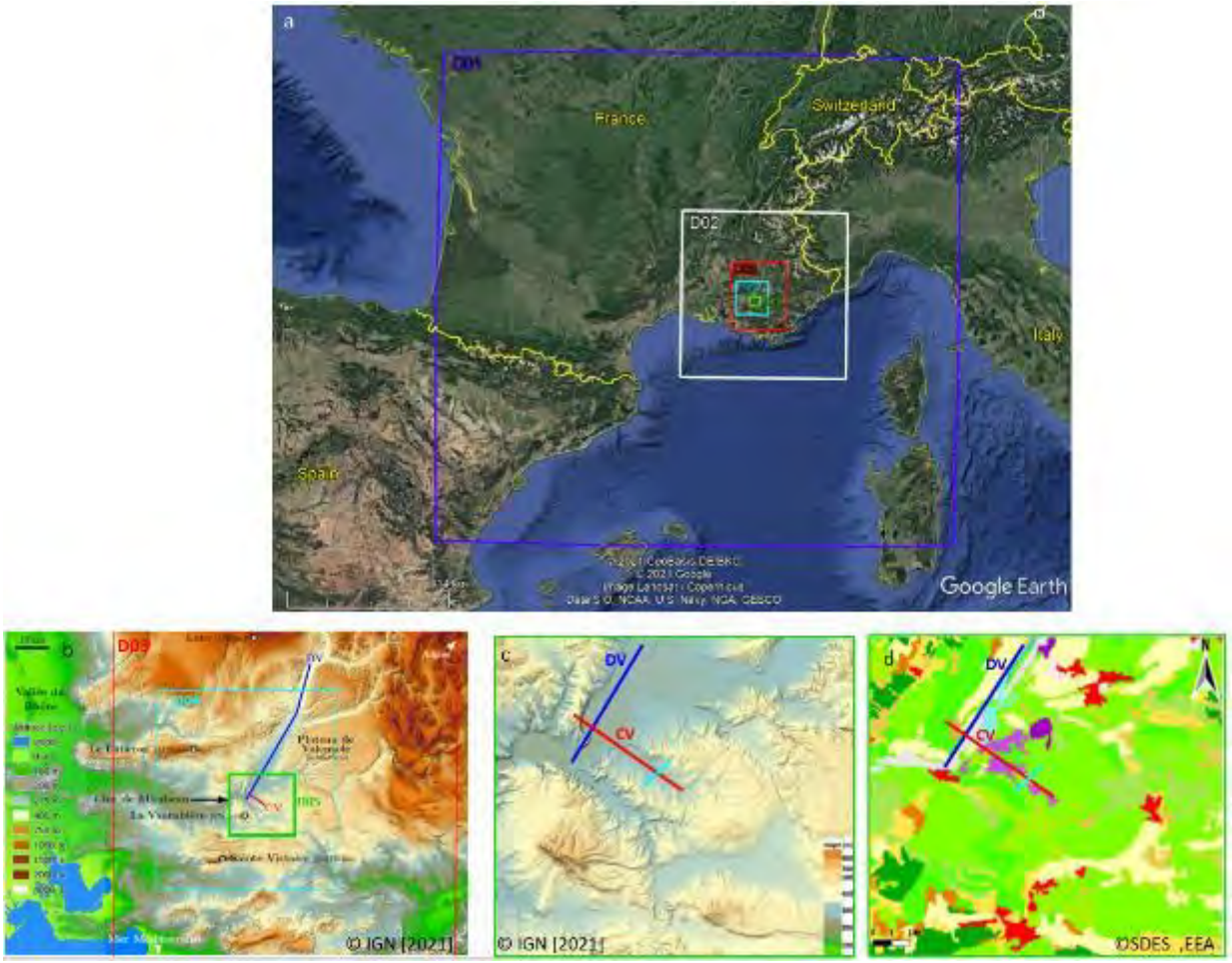

Figure 1. The locations of the different WRF nested domains used in this study (**a**), zooming in on the topography around the three inner domains (**b**) and the zoomed innermost domain with its topography (**c**) (steep slopes are shaded) and land cover (**d**) (see Appendix B for the color definition). CV, DV, and the corresponding red and blue lines in (**b**) represent the axes of the Cadarache and Durance valleys, respectively. The blue, red, and cyan lines in (**c**,**d**) mark the location of the cross-sections presented and discussed in Section 3.6.

At the local scale, which interests us (Figure 1c) the DV transitions from a ~6 km-wide, quite straight, and NNE–SSW-oriented valley (blue line in Figure 1b) to an E–W-oriented valley flowing towards the Rhône river, through an S-curve and a water gap (called the "Clue de Mirabeau"). Just upstream of this lies the smaller tributary, the Cadarache valley (CV), the primary focus of our simulation. It is SE–NW oriented (red line in Figure 1c), approximately 6 km long, 100 m deep, and 1–2 km wide, and its thalweg has a mean slope of 1.2°. The land use of the area is represented in Figure 1d, according to the Corine Landcover classification (https://sdi.eea.europa.eu/catalogue/srv9008075/api/records/5a5f43ca-1447-4ed0-b0a6-4bd2e17e4f4d, accessed on 17 August 2021). The CV floor and surroundings are mostly meadows with sparse trees (light green areas), non-residential buildings (purple), urbanized areas (red), and bodies of water (blue), whereas the hillsides and ridges are covered by denser vegetation from shrubs to sclerophyllous forests (medium and dark green).

2.2. Observations

The location of the various sites of observation is indicated in Figure 2. The first set of observations are continuous measurements routinely made at the low end of the Cadarache valley. The GBA station is a 110 m tower measuring pressure, relative humidity, and temperature at 2 m, as well as wind speed, wind direction, and temperature at 110 m, a level situated just above the adjacent ridgelines. In the central part

of the CV, a Doppler sodar (Metek PCS.2000-24) is installed. This sodar measures the profile of the horizontal wind. The lowest height of observation is 60 m, and the highest is around 400 m, with a possible variation according to the propagation conditions of sound waves. At the same location, hereafter called "MET01" (see Figure 2), there is a weather station with observations at 2 m of atmospheric pressure, temperature, relative humidity, and incoming shortwave radiation, as well as wind speed and direction at 10 m.

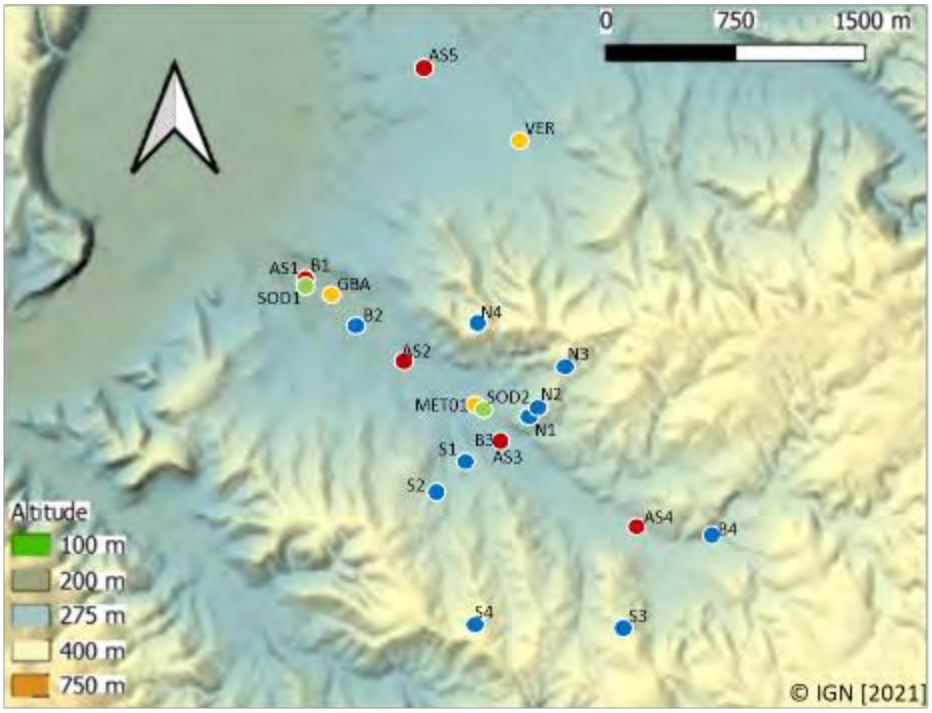

Figure 2. Location of the observation sites: the permanent platforms are the 110 m GBA tower, the Metek sodar (SOD2), and the MET01 weather station. The other platforms were installed during the KASCADE 2017-campaign: SOD1 is the Remtech sodar, AS1 to AS5 are sonic anemometers, and B1 to B4, S1 to S4, and N1 to N4 are the LEMS stations installed at the bottom and on the southern and northern sidewalls of the CV, respectively. The color scale represents the topography of the terrain.

From these continuous observations, it was possible to describe the overall cycle of the flows inside and just above the CV. Dupuy et al. [24] presented the wind roses at 10 m and 110 m, which revealed a frequent decoupling of the flows between the two levels: during stable conditions, SE winds follow the bottom of the CV; constrained between the valley sides in the first tens of meters in height, they are topped by NNE winds channeled by the larger Durance valley.

This superposition of flows on the vertical was observed in more detail during two field campaigns. The first one (KASCADE-2013) was conducted during the winter of 2012–2013. Thanks to regular profiling of the low atmosphere with radiosondes carried below either a tethered balloon or a free ascending balloon, it has been possible to build a consistent scheme of the complete cycle of these valley winds [21]. The second campaign (KASCADE-2017), on which we will focus in this paper, was conducted in the winter and spring of 2016–2017. The objective was to go beyond the first campaign and target horizontal variations in near-surface flows at the scale of the CV. For that purpose, a set of 12 weather stations was deployed during the entire campaign on both the bottom of the valley along its main axis, and on the flanks at various heights. To complement this, radiosondes were launched every three hours during the intense observation periods (IOPs) to document the evolution of the atmospheric profile. These local energy-budget measurement stations (LEMSs), developed at the University of Utah [33], measure wind speed and direction, incoming shortwave radiation, air temperature, and relative humidity at 2 m as well as atmospheric pressure at 1 m above the ground. In addition, surface temperature is measured with an infrared radiometer, and soil temperature and

moisture content are measured at 5 and 25 cm depths. Furthermore, sonic anemometers were installed at four locations along the bottom of the valley and one in the DV, to document the turbulent structure of the flow close to the surface (2 m), through the record of the three wind components at a rate of 10 or 20 s^{-1}. Eventually, one site (AS1, close to GBA) was equipped with a four-component (short- and longwave, incoming and outgoing) radiation sensor. The location of these instruments is indicated in Figure 2. Eventually, a 2nd sodar (Remtech PA2) was installed close to the GBA tower, with the characteristics of 15 min, 25 m, 75 m, and 500 m regarding the time resolution, vertical resolution, and lowest and highest heights of observation, respectively. The KASCADE-2017 field campaign data are archived at: https://kascade.sedoo.fr, accessed 17 August 2021.

2.3. Selection and Characteristics of the Case Study

Among the 14 IOPs which benefited from radiosonde profiles during KASCADE-2017, we selected IOP07, which lasted from 12:00 UTC February 20 to 12:00 UTC February 21. This choice was dictated by the availability of a complete set of observations during this period and suitable meteorological conditions for valley wind development during a stable stratification period (calm wind at the synoptic scale and cloud-free conditions). At a large scale, a high-pressure area was present over the Atlantic Ocean, and a low-pressure area over Central Europe, with a slight pressure difference between the two systems and therefore a very low pressure gradient over southern France (Figure 3). This W–E pressure gradient is favorable for the triggering of the Mistral wind in the Rhône valley, but with a moderate strength (average wind speeds of the order of 6–8 m s^{-1} were observed, with gusts of up to 20 m s^{-1}), allowing the flow to enter tributary valleys of the Rhône river. During the daytime, the Mistral reaches locations as distant as our study area, where it arrived, in this case, abated and rotated to the west by the lowermost section of the Durance valley.

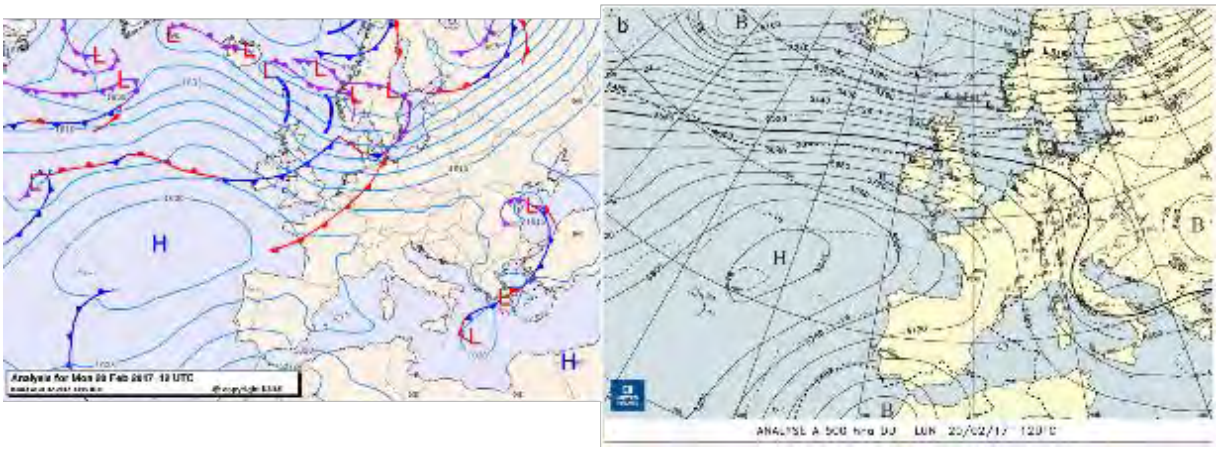

Figure 3. Synoptic situation at the beginning of the IOP: sea level pressure chart (**a**) and geopotential height (in meters) at 500 hPa (**b**). Plots originate from the KNMI (**a**) and MeteoFrance (**b**).

Figure 4 presents the time series of potential temperature, specific humidity, and wind, observed at a low level in the central part of the CV (MET01) and at the confluent zone of the DV and the CV (GBA). The diurnal cycle of temperature reflects a fair-weather situation, with a fast increase from dawn and a decrease initiated in mid-afternoon, accelerating just one hour before dusk. The diurnal temperature range (DTR) reaches around 18 K, which is only possible in cloudless, weak wind conditions. The wind and temperature observations allowed us to characterize the stability through estimates of a simplified bulk Richardson number, according to the formulation expressed in [23] (their equation (1)). Such estimates return different results, according to the depth of the layer considered. The values computed at the GBA site, characteristic of the entire depth of the valley (110 m), reveal a very stable flow, with Ri values generally between 1 and 10

throughout the night, i.e., well above the critical threshold. On the contrary, the estimates at the MET01 site, computed in the layer below 10 m above ground, were below the critical threshold of 0.25, except at nightfall and during the period between 19 h and 23 h UTC. This means that the flow at the global scale of the valley is very stable throughout the night, while locally and near the surface, the stratification is closer to neutrality, and turbulent episodes can occur. We will discuss more about stability in Section 3.4. The wind speed always remains below 2.5 m s^{-1} during IOP07. The day–night wind reversal is spectacular, with a westerly orientation during the daytime, behaving like a Mistral tail, as explained above, and an SE, CV-channeled katabatic wind during the stable stratification period [21], topped with a DV-channeled katabatic wind starting ~3 h after sunset. The specific humidity presents a complex evolution, with a rapid increase after sunrise. This could be related to the wind reversal occurring at this time, starting with vertical mixing, and/or to the start of evaporation with the availability of radiative energy. Other variations occur during periods of a stable wind direction and would require a more in-depth analysis in relation to the complexity of the wind field to be explained.

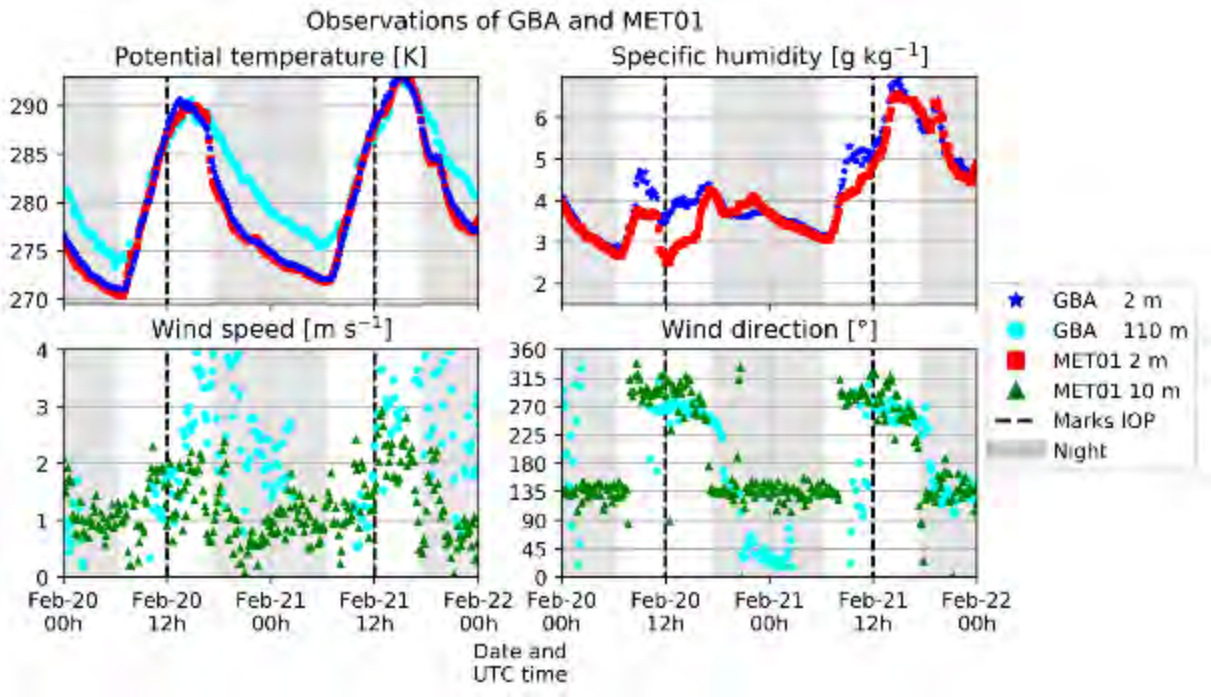

Figure 4. Observations of 20 and 21 February 2017 at the GBA and MET01 stations. The beginning and end of the IOP are indicated by dashed lines. The nighttime periods are shaded.

2.4. Configuration of the Numerical Simulation

2.4.1. Domain Settings

The WRF model [29] was run in order to simulate the IOP in a grid-nested mode. This mode allows simulations of both local and large scales of the flow while sparing computational resources and reducing numerical errors [34,35]. In this mode, the cell number of a given domain has the same order of magnitude whatever the domain. The cell size of the domain with the finest resolution is defined according to the scale of the local processes one wants to simulate, whereas that of the coarsest resolution is generally defined according to the resolution of large-scale forcing (operational analysis or reanalysis). The intermediate domains are staggered with a constant factor between the cell size of a domain and that of its parent and child domains. For WRF nested simulations, an odd factor has a better overlap with the parent domain, though this is not mandatory, as the two domains will have a common cell center [29], and lower factors require less interpolation.

WRF is routinely run in an operational forecast mode in southeast France by CEA with a horizontal resolution of 3 km. This resolution is too coarse to solve the thermally driven flows in the local valleys such as those observed during IOP07 [25]. Focusing on specific situations of KASCADE-2013, [31,36] have shown that WRF simulations with a kilometric horizontal resolution, though unable to resolve CV flows during stable conditions, are quite successful for the representation of the Durance down valley flow which develops in the lowest hundreds of meters above the ground some hours after sunset.

Since the CV, in which we are interested, has a width of 1–2 km, the horizontal resolution required to properly simulate the topographic forcing on the flows is *O*(100 m). For external boundary forcing, ECMWF reanalysis are available with a horizontal resolution of 27 km. We thus deployed five nested domains, named D1 to D5, with resolutions of 9000, 3000, 1000, 333, and 111 m, respectively. A constant factor of 3 is therefore kept between the resolution of two consecutive WRF domains, as well as between the coarsest WRF domain and the reanalysis. The 5 domains are displayed in Figure 1, the largest domain covering western continental Europe, and the finest one being an area of 18.5 x 17 km centered on the CV observations of KASCADE-2017.

For numerical constraints related to the two-way nesting mode, it is more practical to have identical vertical dimensions of the cells whatever the domain. The number and staggering of vertical levels are therefore defined to be consistent with the horizontal resolution of the finest domain, as well as with the physical processes we are planning to simulate. We defined 46 vertical levels, with stretching as one moves away from the surface. The lowest level center is at 6 m agl (above ground level), 9 levels are within the first 100 m agl, and 28 levels are within the first kilometer.

Table 1 summarizes the model settings, where the time step varies according to the domain and is defined so as to satisfy CFL conditions. It ranges from 45 s for domain D1 to 0.125 s for domain D5. The model output is stored every 3 h for the D1 and D2 domains, and every 10 min for the D3 to D5 domains.

Table 1. Summary of the WRF domain and parameterization settings used for the simulations.

Date	**2017-02-20 12:00:00 to 2017-02-21 12:00:00**				
WRF version	*V 4.2*				
Global data forcing	ECMWF ERA5 1 h time step, 0.25° horizontal resolution, 38 vertical levels [37,38]				
Nesting	*Two-way*				
Vertical levels	*46*				
Simulation time (h)	*36*				
Spin-up (h)	*12*				
Top of model (hPa)	*50*				
Domain	*D1*	*D2*	*D3*	*D4*	*D5*
Horizontal resolution (m)	*9000*	*3000*	*1000*	*333.333*	*111.111*
Number of cells	*106,100*	*100,100*	*100,121*	*175,178*	*169,154*
Topography map resolution	*5′*	*2′*	*30″*	*15″*	*3″*
Time step (s)	*45*	*15*	*5*	*0.5*	*0.125*
Output interval (min)	*180*	*180*	*10*	*10*	*10*
	Parameterizations				
Microphysics	*WRF single-moment 6-class scheme* [39]				
Planetary boundary layer	*Quasi-normal scale elimination (QNSE) scheme* [40]				
Cumulus parametrization	*Kain Fritsch* [41]				
Surface layer	*QNSE surface layer unified* [42]				
Longwave radiation	*RRTMG* [43]				
Shortwave radiation	*RRTMG* [43]				
Land surface option	*NOAH land surface model* [44]				

2.4.2. Representation of the Ground

We used maps with resolutions close to the resolutions of WRF and not too resource-intensive. From SRTM topographic maps [45,46], we extracted a 90 m resolution map for domain D5, whereas coarser resolutions were used for the other domains, up to 5 arcminutes for the 9 km domain.

The representation of the land cover in the model has received particular attention, the methodology of which will be detailed in a forthcoming paper. Here, in order to go beyond the usual USGS land use dataset and its associated lookup tables, we took advantage of the Corine Land Cover (CLC) land use well suited for our European area, and we developed an aggregation method preventing misclassification when different land use categories are present in a single cell, at any given resolution. Although we developed new lookup tables (described in a forthcoming paper) assigning physical parameters (albedo, roughness length, etc.) appropriately suited to all CLC land use categories, in the present study, we used those derived for the USGS categories as devised by [47] so as not to burden the interpretations and to remain closer to existing studies using CLC.

Figure 5 illustrates how land use and topography are represented in the real situation, and in the 1 km and 111 m resolution domains. Starting from the greatest possible resolution on the left plots (the "ground truth" from the most detailed CLC map), we can see on the central plots that the 1 km resolution is unable to reproduce the real spatial heterogeneity both for land use and for orography. Furthermore, several weather stations deployed during the field campaign lie in the same cell; thus, the variability observed between these stations cannot be simulated. In contrast, at the finest resolution (right plots), the CV is clearly represented, and all stations are in different cells of the model.

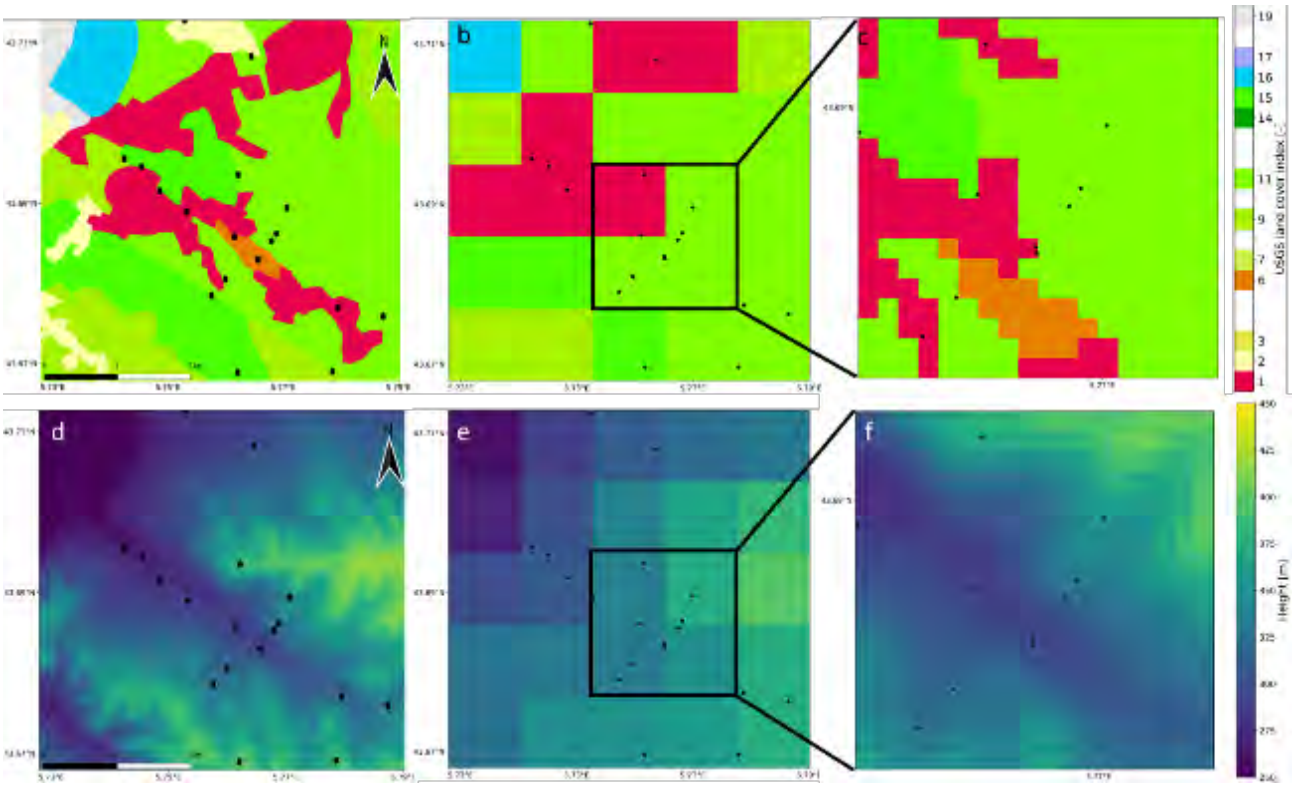

Figure 5. Representation of the surface characteristics (land use on the top and topography on the bottom) according to the horizontal resolution. In (**a**,**d**), the finest available resolution is presented on an area of 5 x 5 km encompassing the Cadarache valley. In (**b**,**e**), the description is degraded to a single value for each 1 x 1 km cell, whereas in (**c**,**f**), a sub-area is zoomed in on with the corresponding values for the 111 m horizontal resolution. The locations of the stations (black dots) sometimes fall in a single cell for the 1 km resolution (their names are provided in Figure 2), whereas at the finest resolution, all the stations lie in different cells. Appendix B contains a table with the color coding of the land use classes.

2.5. Parameterizations

The choice of the schemes among the various possibilities offered by WRF mainly resulted from the sensitivity tests conducted by [31] in the simulation of a KASCADE-2013 case with a 1 km horizontal resolution. In substance, Table 1 mentions the settings that were adopted, and we provide a brief summary of our used parameterizations.

For land surface parameterization, we used the NOAH parameterization, which uses 4 soil layers and includes the freezing process, surface runoff, and a possible snow layer and calculates the soil moisture prognostically. We used the WRF single moment 6 for the microphysics; it prognostically calculates the mass of its six water species (rain, snow, water vapor, cloud water, cloud ice, and graupel). For both longwave and shortwave parameterization, we used the RRTMG model, which calculates the transmissivity of the atmosphere based on greenhouse gases and uses 14 wavelength bands. Lastly, for the PBL parameterization, we used the QNSE schemes, which include prognostic equations for the turbulent kinetic energy (TKE) and allow for TKE advection. They use a self-consistent, quasi-normal scale elimination algorithm and spectral space representation. We considered QNSE as a reference because previous studies have proven its good behavior at 1 km resolution [31], as well as at finer resolutions such as in the complex terrain of Sofia, Bulgaria, where QNSE has proven to be one of the most suitable parameterization schemes [48,49]. The boundary-layer parameterization merits further discussion, since it relates to the parameterization of subgrid-scale (SGS) turbulence. For kilometric (and coarser) resolutions, it is generally assumed that 3D turbulence occurs at scales which are lower than the horizontal dimension of the cell. The corresponding eddies are not solved by the model: the turbulence is entirely an SGS process and therefore is fully parameterized. At sub-kilometer resolutions, the largest eddies become of the same order as, or even greater than, the size of the cell, and a fraction of the TKE is thus explicitly solved by the simulation. The SGS turbulence scheme therefore has to be adapted, and when the major part of TKE is explicitly resolved, the model is run in the so-called large eddy simulation (LES) mode. Between fully parameterized and LES modes, there exists a range of scales belonging to the "gray zone", where the dominant scales (i.e., the size of the most energetic eddies) are of the same order as the horizontal size of the cell, and the SGS parameterization is hard to define (Wyngaard [50] appropriately called this regime the "terra-incognita").

We therefore attempted to estimate the size of the turbulent eddies in our case study. We know from the observations performed in the boundary layer during recent decades that the size of the energetic eddies increases with height, is larger in convective (i.e., daily) than in stable (i.e., nocturnal) conditions, and is commensurate with the boundary layer thickness [51]. Furthermore, flat and homogeneous areas are favorable for the development of coherent structures, which are of a size larger than that of structures over complex terrain such as our area.

We characterized the size of turbulence eddies through the estimate of the integral scale of the vertical wind computed from the signal recorded with a sonic anemometer installed at 10 m above the ground in the bottom of the CV (MET01 site in Figure 2). This value was then extrapolated up through the boundary layer thanks to the parameterization proposed by [52]. This parameterization requires the knowledge of the boundary layer depth (BLD), which was estimated from the radiosonde profiles. The method is explained, in detail, in Appendix A. In substance, during the daytime convective period, the BLD was of the order of 600– 800 m, and the integral scales, computed from observations at 10 m, were in the range of 3–8 m and remained below 100 m when extrapolated through the boundary layer. Such results warranted the use of the fully parameterized SGS turbulence mode, even during the daytime part of the simulation. This choice was even more justified by the focus we have on stable stratification periods, where the characteristic scales are reduced with respect to daytime periods.

In order to bolster this choice, we also tested the SMS-3DTKE [53] scheme, released in WRF v4.2, which is a scale-adaptive TKE subgrid mixing scheme, extending the original

TKE model [54] to the mesoscale and the gray zone resolutions. It functions, therefore, either as an LES or as a parameterized PBL scheme, depending on the domain resolution. In this test, the SMS-3DTKE scheme did not improve the wind at the lower levels of the CV or the global stability within the CV. Therefore, we will only discuss the results of the QNSE in the following sections. Similarly, the cumulus schemes (also known as convection schemes) have a gray zone from 8 km to 500 m. Weisman et al. [55] found that 4 km resolution grid sizes are fine enough for explicitly solving mesoscale weather. Jeworrek et al. [56] summarized that explicitly solved convection provides a better land–atmosphere interaction [57], while for coarser grids, parameterizations have better precipitation estimates. As we selected a case with neither rain nor clouds, we switched off the convection parameterization schemes at resolutions of 3 km and finer.

3. Results: Simulation vs. Observations

3.1. Improvement in the Refined Simulation

As mentioned in Section 2.3 and illustrated in Figure 4, IOP07 is characterized by a striking wind reversal, with a Cadarache down valley flow starting at dusk and persisting during the entire night. In spite of the light wind velocities (always below 2.5 m s^{-1}), the observed wind direction is quite steady. In order to evaluate the benefit brought by grid refinement, we performed three different runs of the model, in which the resolution of the innermost domain was either 1 km, 333 m, or 111 m. The results are illustrated in Figure 6 with the time series of the 10 m wind speed and direction at the MET01 location, both observed and simulated with various horizontal resolutions. All the results presented here are outputs of the finest domain of the run, preventing a two-way nested feedback to the parent domain. In the simulation with the coarse resolution (1 km), the model clearly fails to reproduce the wind direction during the night. This is not surprising and confirms the results obtained by [25,31,36]. Even with a 333 m resolution, the valley topography is too smooth, and thus the wind is not correctly simulated. In contrast, at the finest resolution (111 m), the characteristic dimensions of the valley, such as its depth, length, and width, are adequately represented, and the wind direction is correctly simulated, though the variability is higher than in the observations. During the daytime, the NW wind is well simulated in the afternoon of 20 February., but a discrepancy of 30 degrees–40 degrees is seen in the morning of 21 February. The performances of the simulations are characterized through the wind speed bias (with respect to the observations) and the direction accuracy (DACC45), the latter being the percentage of simulated directions which remain within ±45 degrees from the observation. These two metrics are computed over the 24 h period of the IOP. For the 111 m resolution, the DACC increases up to 60%, while the bias remains similar to the other resolutions around −0.32 m s^{-1}.

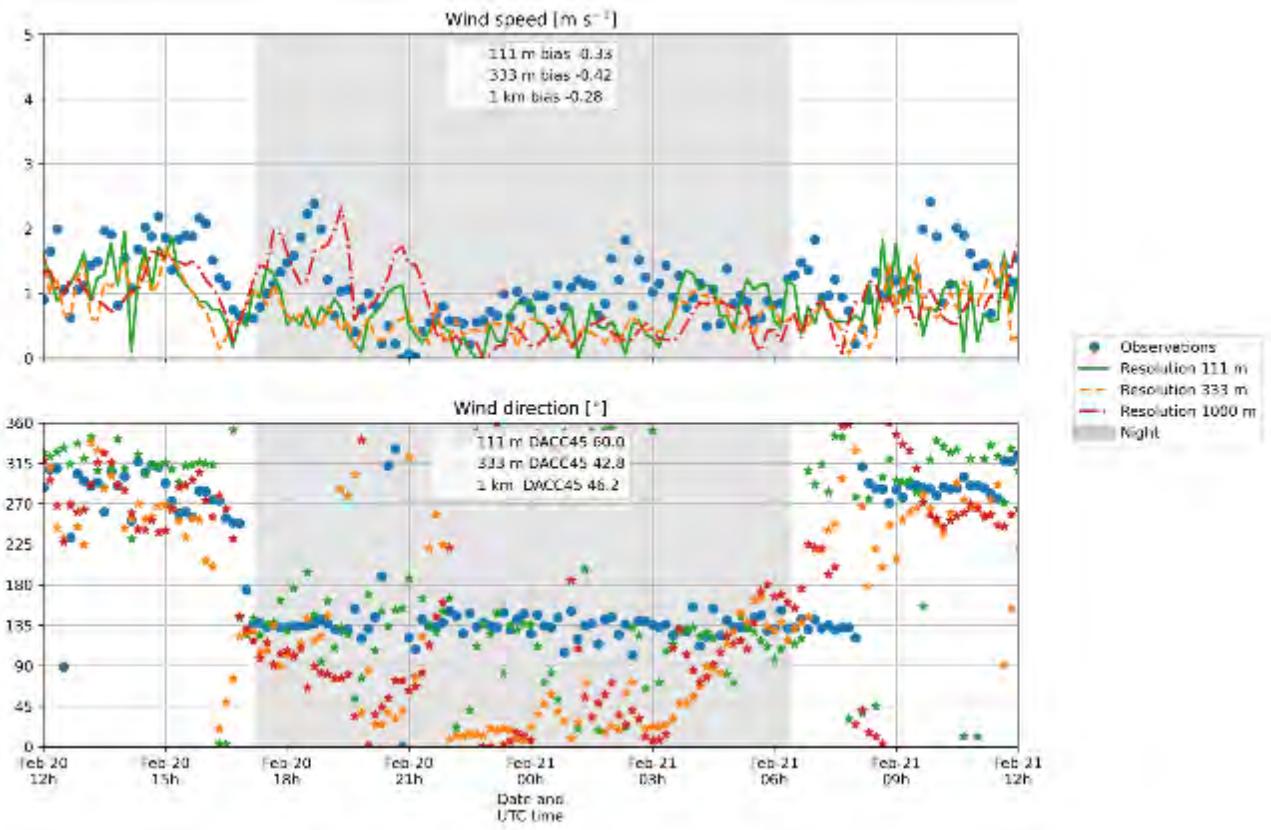

Figure 6. Performance of the model in simulating wind speed (top) and direction (bottom) at MET01 for different resolutions of the finest domain. The blue dots are observations, whereas the red, orange, and green lines (dots) represent the simulated wind speed (direction) for the 1000, 333, and 111 m resolutions, respectively. The shaded area represents nighttime. The average bias on the wind speed (in m s^{-1}) and the direction accuracy (DACC45, in %) are indicated on the plots for the three resolutions.

Another benefit from using a fine resolution is that the topography is close to reality, and a cell which contains a measurement station is in the model at an altitude (height above mean sea level; amsl) that does not differ from the true altitude of the station by more than 10 m, whereas at kilometric resolution, the topography is smoothed, and this difference can be as high as 50 m. Such altitude differences can have a considerable impact on the conditions of intense stratification, as observed during IOP07. For all these reasons, we will concentrate on the results of the finest (111 m) simulation in the following sections.

3.2. Overall Vertical Structure

Figure 7 presents the profiles of the potential temperature, specific humidity, and wind, both observed and simulated, at 18:00, 00:00 and 06:00 UTC during the IOP, roughly coinciding with sunset (17:13 UTC), the middle of the night, and sunrise (06:26 UTC). The radiosondes were launched from the MET01 location, and the simulated profiles were extracted from the finest domain simulation along the vertical in the cell that contains MET01. The profiles are represented below 1000 m amsl (i.e., 714 m agl at the site) only, since we are interested in the details of the low-level flows. Considering an ascending velocity of 5 m s^{-1} for the balloon, and an average wind speed of 2 to 3 m s^{-1} (as it was observed), the radiosonde observations presented in the figure are not strictly over the plumb line of MET01 but remain within a horizontal distance of 300– 400 m, i.e., within the central part of the CV. It was found (not shown) that extracting the simulated values at the cells corresponding to the exact location of the balloon led to indistinguishable modifications on the profile.

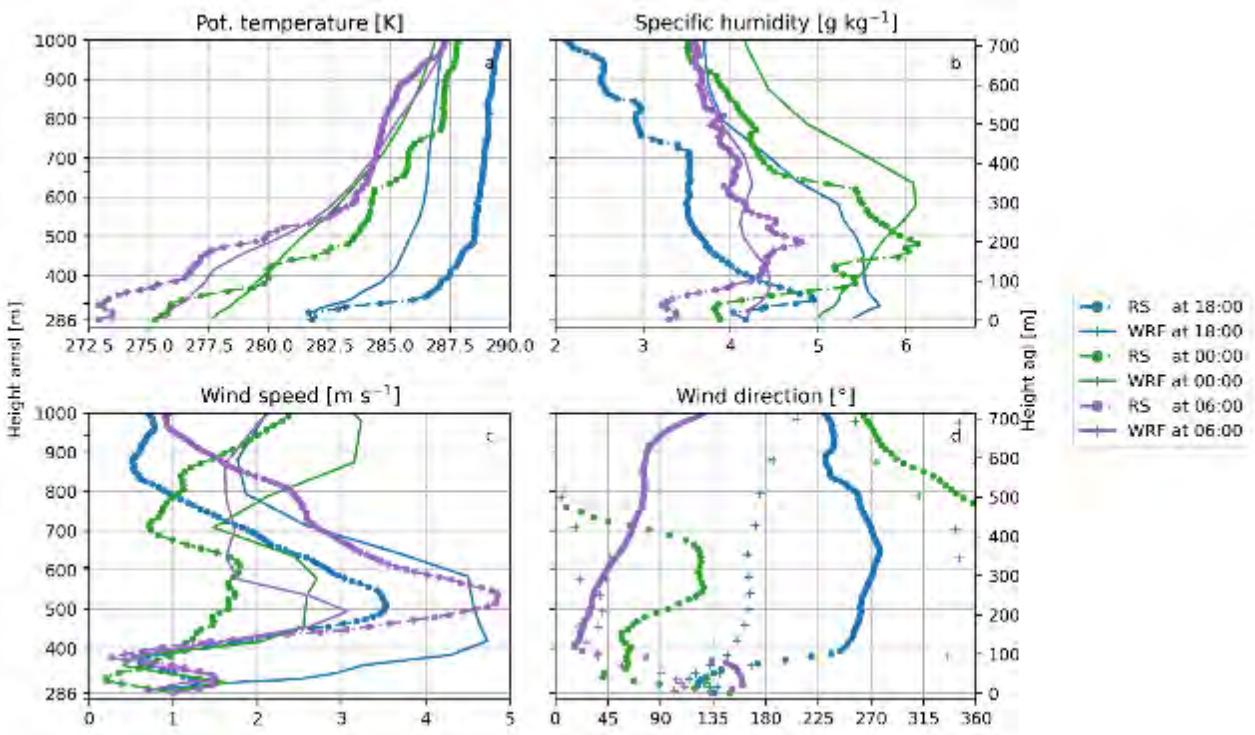

Figure 7. Radiosonde profiles and corresponding simulated profiles of potential temperature (upper left), specific humidity (upper right), and wind speed (lower left) and direction (lower right), at 18:00 UTC (blue), 00:00 UTC (green), and 06:00 UTC (violet). Dots mark observations, and continuous lines mark simulations, except for wind direction where lines were replaced with pluses at the levels of the model. The scales on y-axes are the absolute altitude (on the left) and the corresponding height above the ground (on the right).

The three profiles represent the early, middle, or late nighttime periods. Huge changes are observed from one profile to the next one, whatever the parameter. The 18:00 UTC potential temperature profile reveals that the surface layer is already strongly stratified, with an increase of about 6 K in the first hundred meters (observations), in spite of the short elapsed time since dusk. The surface continuously cools during the night, with a temperature 7 K cooler before dawn than after dusk, together with the boundary layer stratification, reaching 11 K between the surface and 300 m. At the top of the displayed profiles, we observe a cooling of the residual mixed layer, restricted to around 2 K during the night. Such cooling is not simulated by the model, which presents very close values at the top for the three profiles. With this restriction, the overall shape of the profiles is rather well reproduced. As in the observations, the model simulates a continuous cooling in the lower layers, together with an increasing stratification throughout the night. However, this cooling and the related intensity of the stratification are underpredicted, whatever the time. We will discuss low-level temperature simulation more in due course.

The moisture profiles are satisfactorily simulated at 00:00 and 06:00 UTC, with a surface layer which is, however, too moist (in excess by around 1 g kg^{-1} with respect to the observations). In contrast, the 18:00 UTC profile is significantly too moist throughout the layer, exceeding the observations by 1–2 g kg^{-1}. This matter will be discussed in due course (Section 3.5).

The observed wind profiles reflect the development and evolution of the valley winds during stable conditions, as it was already described by [21]. At 18:00 UTC, the Cadarache down valley wind (direction in the range 115 degrees–155 degrees) has already started and persists throughout the night. It is restricted to a few tens of meters in depth, and its speed is below 2 m s^{-1}, as previously shown in Figure 4. NNE winds (Durance valley winds) reach the site around midnight, restricted below 200 m agl with weak velocities. The observations of the SOD1 (Figure 8), performed close to the GBA location, reveal that this flow strengthens and develops in height rapidly from this time, and during the 01–09 UTC period, the profile resembles that of 06:00 UTC, with a low-level jet (LLJ)

of 4–5 m s^{-1} in the 200– 300 m agl layer. The development of valley winds is quite well simulated by the model, at least regarding the timing, wind direction, and vertical extensions (Figures 7 and 8), even though the observations are at slightly higher altitudes than the model. The speed of the Durance LLJ is, however, underestimated on the 06:00 UTC profile (3 m s^{-1} simulated instead of 5 m s^{-1} observed), but examination of the sodar and model time–height cross-sections reveals that the agreement is rather good in the whole 00–06 UTC period. The major difference occurs at 18 UTC, with southerly winds simulated in the bulk of the 200– 600 m agl layer (Figure 7), whereas westerly winds are observed there. In fact, the wind rotation from west to south does exist, as revealed by sodar observations. It is quite sudden and concerns the whole layer observed by the sodar (up to 500 m agl) but occurs around 19 UTC. The model simulates this rotation too early, which also explains the differences between observations and simulations in the temperature and moisture profiles of Figure 7. Another difference between observations and simulations is related to the deep layer of NNE wind (the Durance down valley wind, light blue color on the plot) occurring from around 20 UTC to the early morning of 21 February: it extends in the model down to heights lower than in the observations.

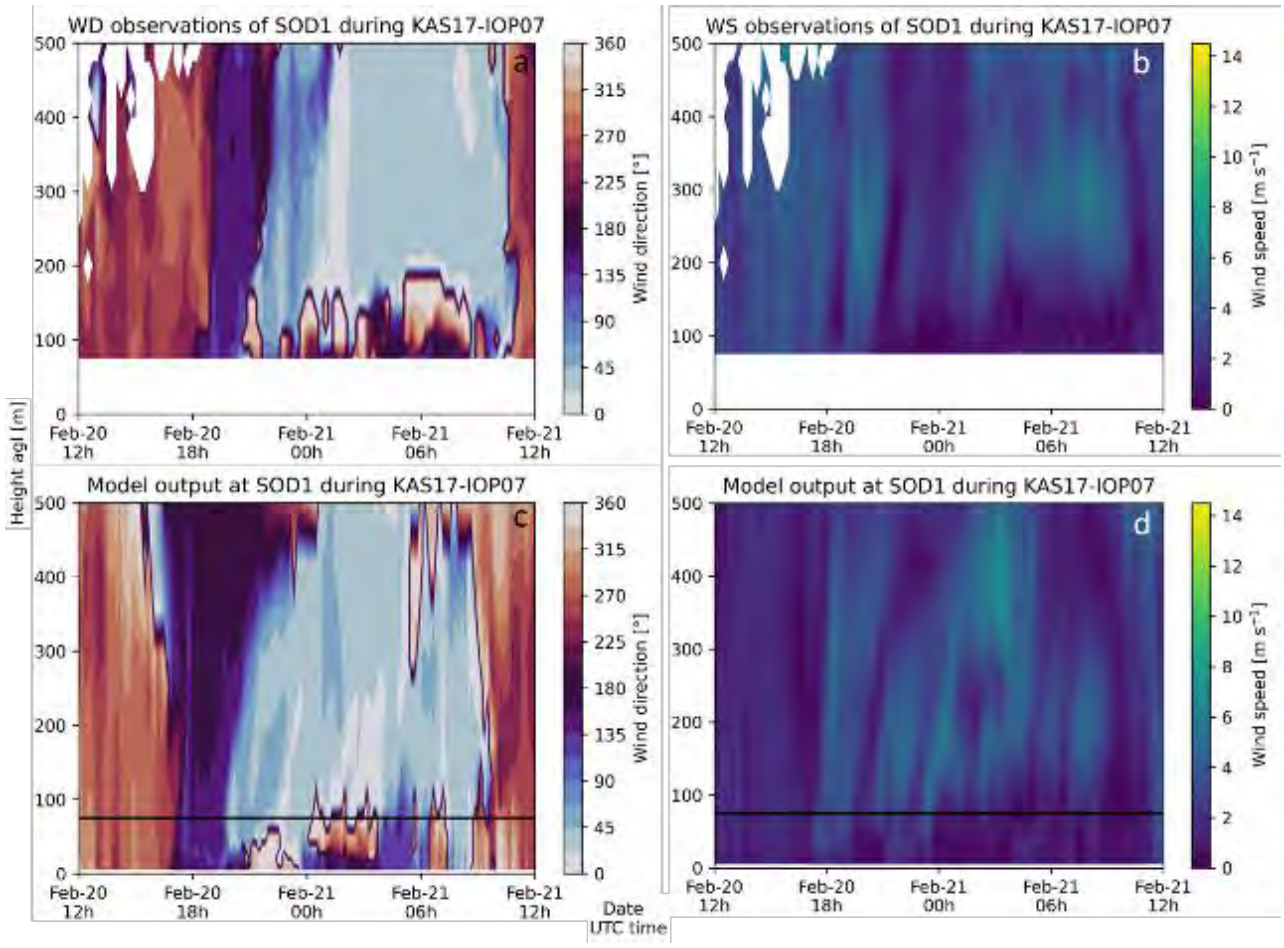

Figure 8. Time–height diagram of wind direction (left) and speed (right) above the MET01 site (center of the CV), observed by the sodar (top) and simulated (bottom). Black lines in simulated plots indicate the lowest height of sodar observations.

3.3. Diurnal Cycle

The diurnal cycle of the potential temperature and specific humidity at 2 m, as well as the wind speed and direction at 10 m, observed at the bottom of the CV (MET01 station—see Figure 2), is presented in Figure 9. While the wind evolution is rather well simulated, with an adequate wind speed and the reversal in the direction between the diurnal and nocturnal periods, we observe a large underestimation by the model of the daily temperature, whilst at night, it was overestimated. As a consequence, though the mean bias computed over the complete diurnal cycle is weak, the observed diurnal

temperature range (DTR) is around 18 K, whereas only 12 K is simulated with a mean absolute error of 2.4 K. The main discrepancy occurs at the beginning of cooling: during the 3 h period starting 1 h before sunset, the observed temperature drops by around 12 K, whereas in the simulation, the corresponding cooling does not exceed 6–7 K. In contrast, during the rest of the night, the simulated temperature regularly cools down in a way fairly similar to the observations (−0.35 K h^{-1}). From sunrise on 21 February the simulated temperature increases less rapidly than observed and is therefore caught rapidly by the observed temperature, although heating rates remain similar from 10 UTC. DTR underestimation by WRF is a common problem and was already underlined in the same area by [25,31]. Lindvall and Svensson [58] even mentioned that DTR underestimation is a general problem in weather models. In our case, the origin of the cooling problem could lie in an incorrect representation of the soil properties, and/or a simulation of an air mass advection that differs from reality. We will speak more of stratification in a following section.

Concomitantly with the too weak cooling simulated in the early night, the model does not reproduce the evolution of the specific humidity. In the late afternoon, we observe a moistening of 2 h, followed by two hours of drying out, whereas the model continues to bring moisture to this location. The observed humidity always remains well below saturation, meaning dew deposition cannot be invoked to explain this decrease in the specific humidity. A possible explanation comes from an evening transition where turbulent vertical transport stops but evaporation continues, thus explaining the humidity peak. At first, humidity increases, since it is no longer transported away from the surface, whilst later, the humidity decreases when evaporation ceases or the nighttime regime starts, restarting some vertical transports [59,60]. A dip in the wind speed (Figure 9) and the reduced TKE (not shown) underpin a transport breakdown. For the remainder of the night, the observed and simulated moistures evolve similarly but maintain the difference created during the early night. From sunset on 21 February, as it is already observed in the temperature, the simulated moisture content increases less rapidly than in the observations, but after 10 UTC, the simulation and observations resemble each other more.

In the afternoon, wind directions match relatively well, although the observations are more spread out. The wind reversal of the evening transition occurs around the same time, after which the observations are constant around 135°, while the simulation shows more spreading, as previously mentioned. The timing of the morning transition does not match the observations precisely, as they maintain the valley orientation longer than the model. An earlier study showed that the wind direction change typically coincides with sunrise [21], resembling the current model behavior.

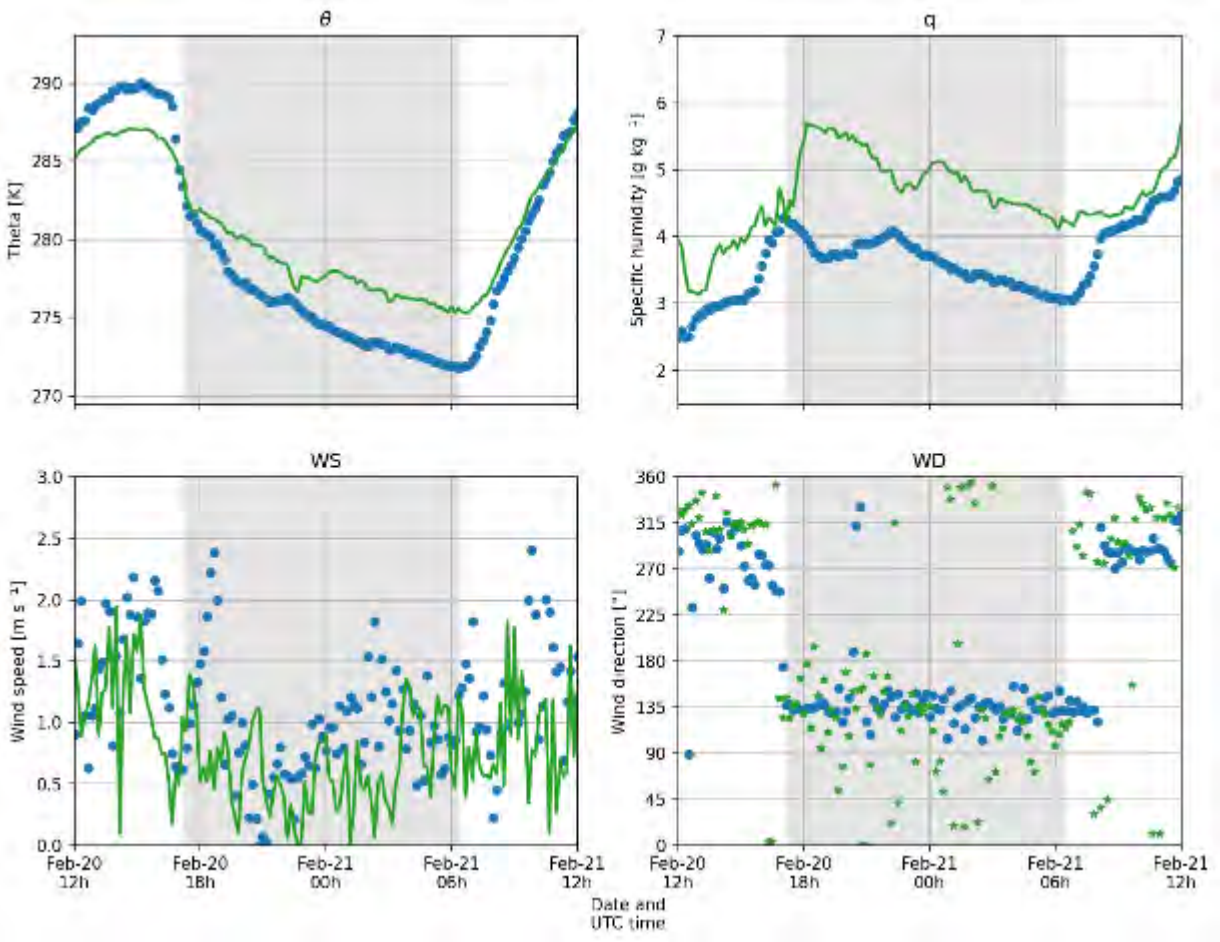

Figure 9. Time series of potential temperature (θ), specific humidity (q), wind speed (WS), and wind direction (WD) at the MET 01 site, observed (blue) and simulated (green).

3.4. Simulation of the Stratification

For calm synoptic wind conditions, stratification is the leading mechanism for local wind development. In a vertical section crossing a valley, we could observe either horizontal isentropes, reflecting what is called a "mature cold pool", or terrain-following isentropes, for "stratified terrain-following" situations, or an intermediate situation called "cold-air drainage" [61]. In the first situation, there are no slope flows; in the second, there are katabatic flows descending along the slopes whilst keeping the same potential temperature; and in the third situation, the downslope winds cross the isentropes and cool progressively. Mahrt [61] primarily characterized these different regimes through two parameters:

The cold pool intensity (CPI), which is the potential temperature difference between the top of the flank and the bottom of the valley;

The potential temperature difference on a horizontal plane between the top of the flank and the center of the valley (θ*).

For mature cold pools, $\theta^* = 0$, whereas CPI >> 0; for stratified terrain following, CPI = 0 and $\theta^* << 0$; and for cold-air drainage, $\theta^* < 0$ and CPI > 0.

In order to evaluate the performance of the model to simulate the stratification in the valley, we thus computed the θ* and CPI parameters from the observations and from the model. The CPI was estimated with the observations of two LEMS. One is situated at the bottom of the valley (B3, see Figure 2), while the other is situated on the northern flank, being either N3, which is situated at the top of the cross-valley instrumented axis, or N4, which is on the highest crest of this flank, but on an isolated hill and shifted to the north with respect to the instrumented axis. Meanwhile, θ* was estimated from the temperature difference between either N3 or N4 and the radiosonde values taken at the same altitude

as the considered station. The observed θ* was therefore available every three hours, whereas CPI was observed every 5 min, since all LEMS have 5 min output intervals. CPI and θ* from the simulation were calculated at the same locations as for the observations and were available every 10 min.

The time series of the two parameters are presented in Figure 10, computed with either the N3 or N4 LEMS. The two estimates (with N3 or N4) are quite consistent. The observations reveal that the situation is close to that of a mature cold pool, with very high CPI values, reaching 7 K in the early night. The observed θ* values are close to zero or slightly positive, indicating a situation close to a "pure" mature cold pool (note that −θ* is represented instead of θ*, following the convention adopted by [61]). High values of the observed CPI prevent great cold-air drainage along the slopes of the valley flanks. On the contrary, the simulated CPIs increase around nightfall but remain much lower during the night, and θ* is weak or slightly negative during the night, but when combined, they reveal a possible drainage of the flow along the slopes of the valley flanks. We will discuss this question in due course.

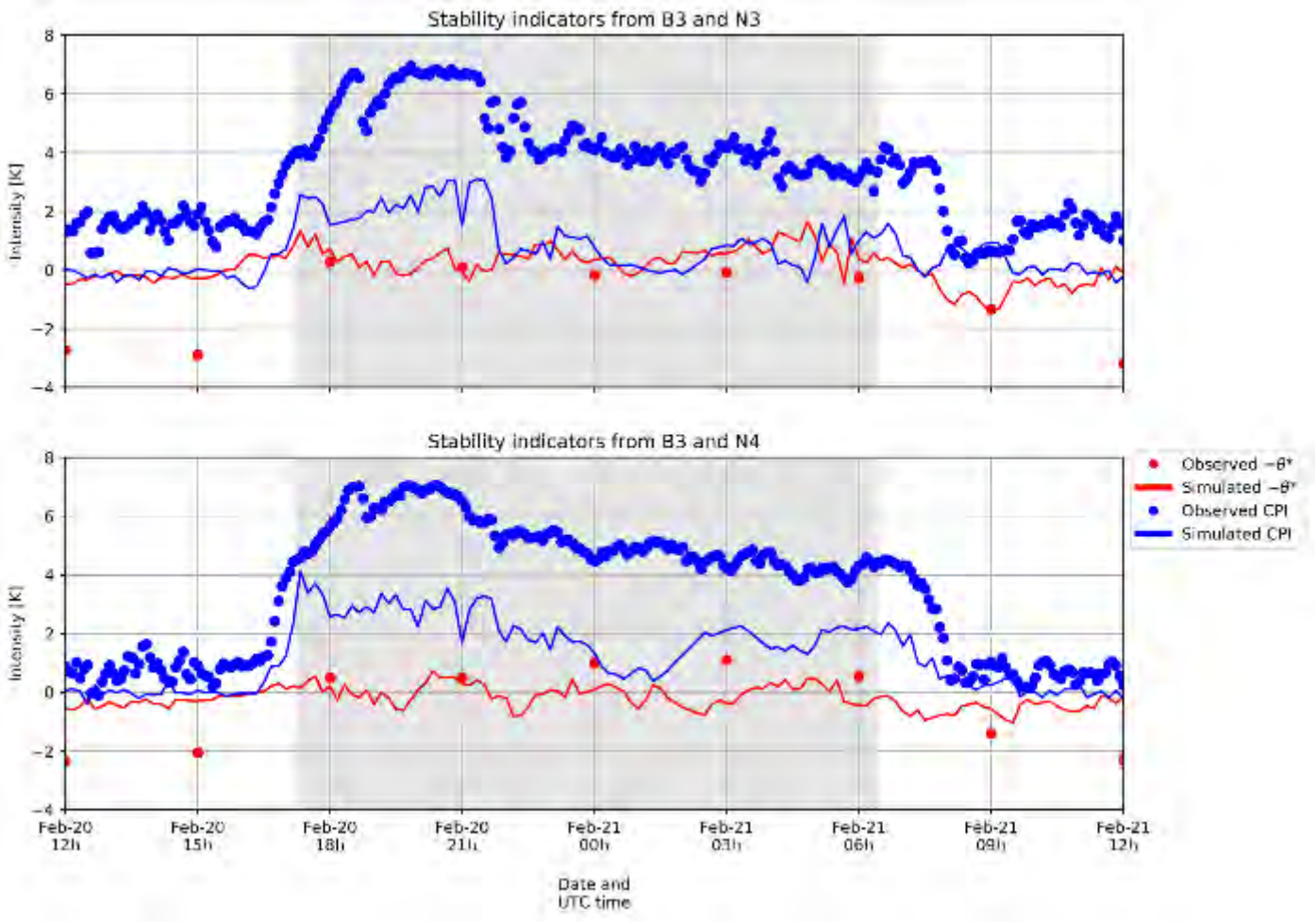

Figure 10. Time series of CPI and θ* parameters, observed (dots) and simulated (lines). The LEMS used to represent the top of the CV flank is either N4 (bottom), which is the highest station but located on an isolated hill, or N3 (top), which is at the top of the cross-valley instrumented axis (see Figure 2 for the location).

3.5. Moisture Fields

In light of the model performance to simulate the winds and the stratification, we can now interpret the moisture fields. Figure 11 presents the horizontal fields of the simulated specific humidity close to the surface, on a horizontal domain of around 29 (lon.) x 25 km (lat.) surrounding the Cadarache valley, at 15:30 and 18:00 UTC, i.e., at the end of the diurnal convective period and at the beginning of the stable stratification period. The fields of the simulated wind direction at 10 m are also drawn at the same times. In the late

afternoon, the E to SE winds establish along the valleys/ridges in the central part of the represented domain (see the purple and violet bands on the wind direction 18:00 plot). As a consequence, the area with higher specific humidity observed in the SE corner at 15:30 is advected throughout the domain to the NW and reaches the Cadarache valley. We do not discern any variation related to the local topography at the 15:30 fields; in other words, the values are about the same at the bottom of the local valleys or at the neighboring crests.

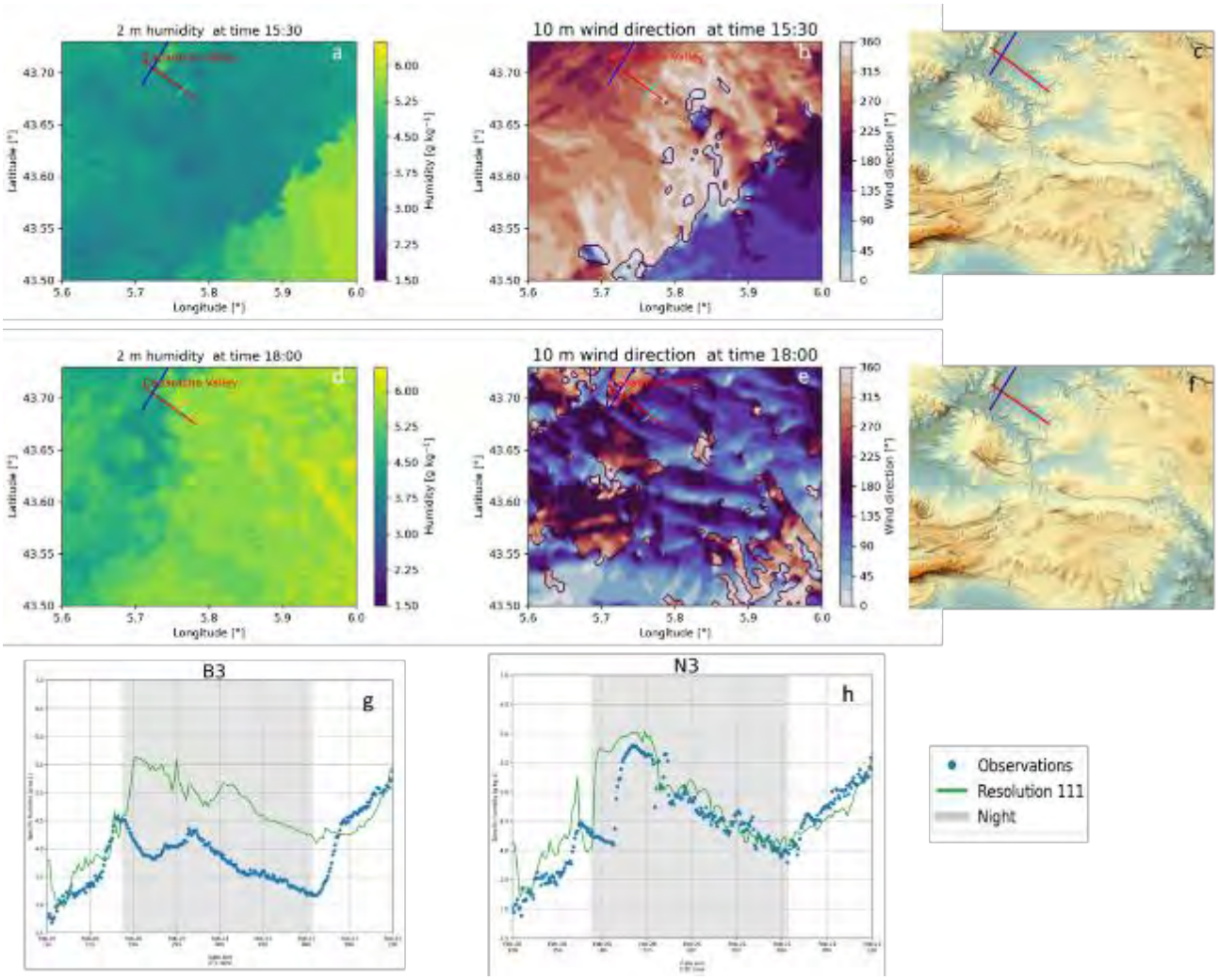

Figure 11. Horizontal field of simulated specific humidity at 2 m (left; a, d) and wind direction at 10 m (central; b, e), at 15:30 UTC (top; a, b) and 18:00 UTC (middle; d, e). The topography of the surface is recalled on the right (c, f). Bottom (g, h): time series of specific humidity observed (blue dots) and simulated (green lines) at the bottom of the valley (site B3, left), and at the northern top of the cross-valley axis (right). The blue, red, and cyan lines mark the location of the cross-sections presented in Figure 12. Note that the cross-section represented by the blue line extends beyond the border of the plot.

This is also illustrated in the time series simulated throughout the IOP, which is very comparable at the bottom of the valley or at the top of its flank (Figure 11g, h). In contrast, the observed values at the same locations reveal a considerable difference: while the plot at N3 resembles the simulation output, the B3 values at the valley bottom are significantly lower during the night. One hour before sunset, the observed moisture decreases at the bottom of the CV, which is not simulated by the model. Meanwhile, on the crest, we also observe a decrease starting at the same time as that at the bottom of the valley, but this is rapidly compensated for by a sudden increase occurring one hour after sunset. At this location, the model matches the observed time series quite well but anticipates the sudden increase by around 1.5 h.

The differences between the observed and simulated time series at the bottom of the valley can be related to the differences between the observed and simulated stratification

in the valley. As mentioned above (Section 4.4), the observations reveal quite a mature cold pool situation, which implies that there are almost no downslope flows along the flanks of the CV. The air mass observed at MET01 during the night, therefore, was constrained close to the bottom of the valley where it circulated following the valley's orientation. In contrast, the model simulates a mix of such a flow with downslope currents along the valley flanks, which tends to homogenize the air physical properties at the various levels.

The timing of the humid air arrival seems to affect the cold pool development. Comparing Figure 10 with Figure 11h shows that the CPI increases until the arrival of the moist air mass. In the simulation, the CPI growth stops earlier, coinciding with the early humidity arrival (at 17 UTC), and the simulated CPI remains constant thereafter. The observations in Figure 10, however, show that the observed CPI continues to increase, up to the observed arrival of the humid air mass. At that moment (a little before 19 UTC), the CPI shows a dip but restores relatively quickly and does not increase further. In both the simulation and observation, the humidity arrival matches the moment with the largest CPI values and occurs earlier in the simulation.

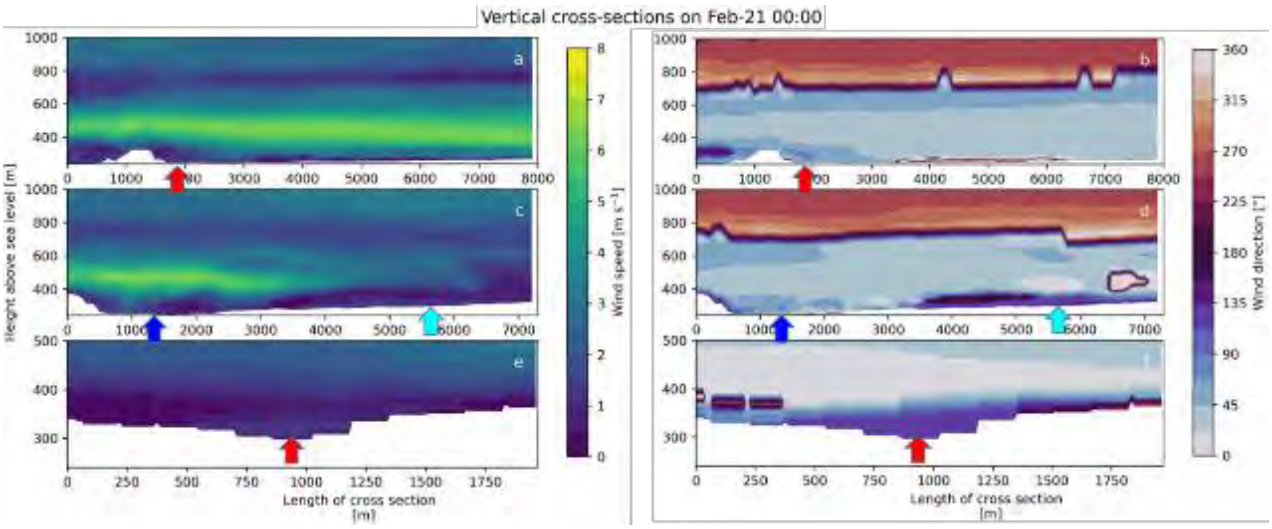

Figure 12. Vertical cross-sections of wind speed (left) and wind direction (right) along the Durance valley, moving down the valley from the right to the left (a, b; blue line in Figure 1c), along the Cadarache valley, moving down the valley from the right to the left (c, d; red line in Figures 1c and 11), and perpendicular to the Cadarache Valley, from the SW to the NE (e, f; cyan line in Figures 1c and 11). Red arrows indicate crossing points with the Cadarache valley cross-section, dark blue arrows indicate the crossing points with the Durance valley cross-section, and cyan shows where the cross-section perpendicular to the CV axis passes.

3.6. Vertical Cross-Sections

Three vertical cross-sections of the wind speed and direction at 00 UTC are presented in Figure 12, along the tracks indicated in Figures 1 and 11. The top one, 8 km long along the Durance valley, shows a down valley flow, 300– 400 m thick, with a well-marked LLJ of around 7 m s^{-1} at 150– 200 m above the ground. The shear layer, between the down valley wind and the regional-scale westerly flow lying above, is quite thin and slightly rises in the up-valley direction. The apparently south-originating flow layer at 700 m amsl in Figure 12b, and d is an artifact originating from the interpolation, which cannot handle cyclic color scales and will linearly rotate from NNE to NNW (0° to 359°) flows. For this reason, the simulated wind at 5000 to 7000 m along the CV cross-section (Figure 12d) shows the slow transition from NNE to NNW, with a sharp artifact change at the 0° to 359° transition. The terrain elevation, close to the lower end of the DV section, corresponds to a protrusion of the S-shaped right bank of the valley, with a cliff-like sidewall about 100 m high (Figure 1). This wall guides the DV katabatic flow and forces it to follow the river bend. Similarly, on the downstream side of this obstacle, the patch of low-altitude SE flow reflects the direction of the S-shaped valley, where it turns to the northwest (close

to the Clue de Mirabeau), possibly reinforced by another down valley flow from the small valley parallel to the CV. At higher levels (i.e., above 400 m asl), the flow is hardly disturbed by this obstacle, as shown by the continuation of the LLJ which is only ascending marginally. It is interesting to note that the CV flow is not visible here (the CV axis crosses the section at an abscissa of about 2 km, indicated by the red arrow), meaning that this flow does not penetrate the Durance valley at that point. Upstream in the DV (at abscissas between 4 and 6 km) and very close to the surface, we can observe weak winds from the west, probably resulting from down valley flows in the many small tributary valleys discharging on the right bank of the DV.

The section along the CV confirms that the down valley flow is weak, confined to a shallow layer (a few tens of meters), and does not reach the DV at this time. The Durance down valley flow is present all along the CV, just above it, but the LLJ is restricted to a zone of around 3 km wide, centered above the Durance river. In the section perpendicular to the CV axis (Figure 12e andf), we see that the Cadarache down valley flow is mainly present in the central part of the valley, where its depth reaches around 100 m. The figure also reveals the asymmetrical behavior of the flow on the two sidewalls, with a thicker (~ 100 m) layer of very weak winds on the southern flank than on the northern flank. With such an orientation, these winds in the model descend the grade and contribute to supplying the thalweg of the CV with air masses from above, as we suggested earlier.

4. Discussion

4.1. Wind Modeling—Vertical Profiles

With respect to the previous WRF simulations conducted in this area with a kilometric resolution, be it operational simulations as analyzed by [25], or case studies such as in [31,36], we demonstrated that a simulation with a hectometric resolution is clearly able to reproduce, with some accuracy, the observed winds and their diurnal cycle in the small-scale valley, which was unreachable with coarser resolutions. The main driving mechanism of the local flow, i.e., topographic forcing, is adequately simulated by the model. As a consequence, the diurnal cycle of the wind profile, as observed by a sodar, and the shear layer, during nocturnal stable periods, between the Cadarache down valley SE flow, close to the surface, and the Durance down valley NNE flow above, are well simulated. We can now consider that a reliable tool is available for the simulation of the vertical structure of the flow as it has been described by [21] thanks to the observations of the KASCADE-2013 field campaign. This WRF platform extends the predictive capability of already available tools, be it the simple diagnosis of the Cadarache down valley wind of [23], the nowcasting based on downscaling from routine observations of [24], or the forecasting based on operational coarse simulations and ANNs by [25].

Vertical cross-sections show a well-developed Durance down valley flow, stretching over the CV, which matches the observations of [21], even though the simulated Cadarache flow is shallower than the observations. Regarding the Cadarache down valley flow, the simulations show a smaller layer on the south flank than on the north flank, which could not have been observed with observations on a single vertical.

The Durance LLJ has limited influence on the winds close to the surface, in contrast to what was reported by [62] in relatively uncomplicated terrain (a valley leading to a plateau in the Pyrenean foothills). Nevertheless, further up the valley, the jet in [62] appears to break away from the surface near the confluent zones of wider valleys, which resembles the situation around the confluent zone of the CV and DV. Such jet streams are sometimes associated with internal waves, as reported by [63] through Doppler lidar observations, but such events were beyond the capabilities of our observations.

4.2. Stratification and Slope Flow

The sensor network deployed at the surface during the KASCADE-2017 campaign, together with the profiles obtained from radiosondes, allowed us to characterize the stratification inside the valley. We must admit that the model does not reproduce the temperature field structure accurately enough. In line with the underestimation of the

DTR, already highlighted by [31], the cold pool predicted during the night is far from being as mature as that revealed by the observations, agreeing with the findings of [28] on the difficulties of creating a cold pool in fine-scale simulations and demonstrated with the values of the CPI and θ* parameters. An effort had been undertaken to improve the representation of the land use in the model, but the consequences on the DTR remained modest. As a consequence, the simulated temperature differences between the bottom of the valley and the top of the sidewalls (CPI) were underestimated, with the model generating downslope flows which are probably not realistic given the observed CPI values. We have to note, however, that the observations on the sidewalls were insufficient for a full diagnosis of downslope flows, since (1) only horizontal wind components were measured, whereas a complete diagnosis would require 3D anemometers at the locations of the LEMS stations; and (2) the wind velocities observed during the nighttime periods were often very weak, i.e., below the threshold for which the cup and vane anemometer measurements can be considered as reliable. For future improvements, we are planning to incorporate into the model a better representation of the soil characteristics. In particular, the soil water content is known to play a crucial role in the surface energy partitioning (evaporative fraction), and previous studies have shown that ECMWF analyses overestimate soil moisture, especially for dry areas [63]. The consequence is a too low surface sensible heat flux and surface temperature during the daytime.

4.3. Moisture Field and Transport

To summarize, the horizontal advection is quite well simulated, whereas the vertical transport (along the slopes) is not. As a consequence, the specific humidity is vertically more homogenized in the simulations than in reality. The air mass observed at a given station at the bottom of the valley comes from an upstream area close to the ground, whereas the model mixes this air with downslope currents. The observed humidity is therefore much more dependent on the local terrain over which the down valley flow has passed.

4.4. Perspective

The perspectives of this work are therefore to improve the model performance in the representation of the DTR and the stratification. In particular, we will explore the effect of the moisture in the soil, which could be overestimated in the simulation, leading to a reduced DTR. Once we are confident enough in the performance of the model, the goal will be to generate a high enough number of fine-scale simulations to train ANNs on as many locations as necessary to downscale the 1 km operational weather simulations and generate a reliable representation of the flow in a complex area whilst avoiding a computationally expensive operational, fine-scale simulation.

Kalverla et al. [31] found that the QNSE is a good PBL parameterization for this location at 1 km resolution grids. Sensitivity tests with different PBL schemes at sub-kilometer resolution under stable conditions benefited only from limited research because most studies focused on the daytime simulations, where the turbulent scales are larger and LESs are required. PBL parameterization at these resolutions in stable conditions remains a very open question.

5. Conclusions

The study presented in this paper is a contribution to an overall approach aiming at the development and qualification of various tools intended to diagnose and/or forecast the flows at the very local scale in complex terrain areas. It focuses on stable stratification conditions because they are often more penalizing regarding the consequences of chronic or accidental release of pollutants or contaminants, due to the fact that vertical dilution by turbulence is reduced. Furthermore, combined channeling and stratification effects in complex terrain challenge the monitoring of plume behavior and render conventional transport and dispersion models based on crude assumptions regarding, e.g., horizontal homogeneity and wind field structure ineffective.

We thus developed, over recent years, various tools, ranging from very simple diagnostics of valley flows based on routine observations [23], or statistical methods based on the ANN technique applied either to routine observations [24] or operational forecasts [25]. The ANN technique is certainly very efficient in nowcasting/forecasting the wind at a given spot; however, it remains difficult to extend to a large number of locations because the learning process would have to be based on a long series of observations at each targeted location ("long" meaning here that all possible weather conditions have been encompassed during observation periods).

For these reasons, we engaged in the qualification of a high-resolution weather model able to solve the flows at the very local scale. This model is based on the WRF platform used worldwide, which is already run in an operational mode at a kilometric scale resolution in southeastern France. The version developed during this work has five nested domains, the horizontal resolutions of which range from 9 km for the coarsest to 111 m for the finest. The latter is centered on the area we are interested in, the central part of which has been widely documented during the two field campaigns of KASCADE-2013 and KASCADE-2017. These observations revealed that, during stable stratification periods with calm to moderate winds, the low-level flow has a well-marked diurnal cycle, with, in particular, a shallow down valley wind layer starting at sunset in the small Cadarache valley.

The model was run on the IOP07 of the KASCADE-2017 campaign. The 24 h simulation encompassed the afternoon, the entire night, and the following morning. When confronted with the observations, the model revealed its capacity to simulate the diurnal cycle of the flow. In particular, the nocturnal down valley flow in the 1 km-wide CV is well reproduced, regarding its strength, orientation, thickness, and diurnal cycle. This constitutes considerable progress with regard to the performances of previous WRF simulations performed in this area, be it operational weather forecasts or dedicated studies conducted on specific days with kilometric resolution. The good comparison with sodar profiles shows that the flow is also well simulated above the CV, thus indicating that the simulation is also relevant at scales greater than those of the CV.

As it stands, the model, however, suffers from some weaknesses. The diurnal temperature range is underestimated, and as a consequence, the stable stratification does not have the appropriate intensity. Rather than a mature cold pool in the CV, as suggested by the observations, the model simulates a mixed cold pool, with significant drainage along the sidewalls, whereas the observed winds do not show slope flows, at least in the moments with wind speeds high enough to activate the cup anemometers. As a consequence, the model overestimates the transport of scalars, such as the specific humidity, from the sidewalls toward the bottom of the valley, which is not observed.

Author Contributions: Conceptualization, all; methodology, M.B.; software, M.B.; formal analysis, M.B.; investigation, M.B.; resources, T.H., P.R.; writing—original draft preparation, all; writing—review and editing, all; visualization, all. All authors have read and agreed to the published version of the manuscrip**t.**

Funding: This work was funded by the MRISQ project at the CEA

Institutional Review Board Statement:

Informed Consent Statement:

Data Availability Statement: Observations are available at https://kascade.sedoo.fr. Simulation results and scripts are available upon request.

Conflicts of Interest: The authors declare no conflict of interest

Appendix A

In this section, we present an attempt to estimate the characteristic size of the turbulent eddies in the boundary layer during the 24 h IOP. The goal is to determine how this size compares to the horizontal dimension of the cell for the various nested domains of the simulation. In other words, is the assumption of fully subgrid-scale turbulence valid

or not? The criterion is based on estimations of the integral scale, which is a relevant parameter for the characterization of the size of the energy-transporting eddies in the boundary layer. It is defined as the integral of the autocorrelation function R, computed on the time series of a velocity component u_i. We chose to compute this parameter on the vertical component w because the signals of horizontal fluctuations often mix turbulent fluctuations and larger-scale variations; as a consequence, there is no clear spectral gap between the turbulence and the "mean" velocities, and the value of the integral scale is not clearly defined (it inexorably grows when the duration of the record increases, as shown by [64]).

Various estimations of this parameter can be found in the literature. Lenschow and Stankov [52] recommended integrating the autocorrelation function up to its first zero, in order to avoid spurious values of R due to erratic behavior for very large intervals. Based on aircraft observations in the convective boundary layer, they proposed the following relation:

$$\frac{\lambda_w(z)}{z_i} = \frac{\lambda_{w^2}(z)}{0.67 z_i} = \frac{0.16}{0.67}\left(\frac{z}{z_i}\right)^{1/2} = 0.24\left(\frac{z}{z_i}\right)^{1/2} \quad \text{(A1)}$$

where $\lambda_w(z)$ is the integral scale of the vertical wind w, λ_{w^2} is the integral scale of the instantaneous w^2, and z_i is the thickness of the ABL. This expression was established for convective boundary layers; therefore, it might be not completely valid for stable conditions. Since the characteristic scales are larger in convective conditions than in stable conditions however, it allows us to establish an upper limit of the integral scales over the diurnal cycle. The estimation of z_i, as it can be conducted from the radiosonde profiles, therefore allows us to obtain a first estimate of λ_w. Since we have a continuous increase in λ_w from the surface to the top of the boundary layer, the value of 0.24 z_i constitutes the upper limit for this parameter. Given the maximum ABL thickness observed during the IOP (855 m from the 15:00 UTC radiosonde profile, see Table A1), this gives us a value of 205 m, which is about twice the horizontal dimension of the cell in the finest domain.

We went further in the determination of the integral scales by using the observations performed with a sonic anemometer installed at 10 m above the ground in the central part of the valley. From the time series of w, recorded at a 10 s^{-1} rate, we computed λ_w according to the method proposed by [65,66]. It consists of fitting the w spectrum with the analytical model of [67]. This model provides a mathematical relation between the spectrum energy at a given wavenumber, κ, the integral scale λ_w, and a so-called "sharpness" parameter μ which controls the curvature of the spectrum in the transition between the energy production region (at a low wavenumber) and the inertial sub-range. The values of λ_w and μ are adjusted in order to minimize the distance (in the least square sense) between the observed spectrum and the analytical spectrum. The spectra were estimated on overlapping 30 min time series starting every 15 min. An example of daytime turbulence is provided in Figure A1, where a spectrum is represented as a function of the wavenumber $\kappa = 2\pi n/U$, where n is the frequency of the recorded w time series, and U is the mean wind on the sequence. The value of the wavenumber corresponding to the size of the cell in the simulation (111 m) is indicated in the figure. In the example presented here, most of the TKE is at wavenumbers higher (i.e., wavelengths smaller) than this size. Nighttime turbulence has smaller length scales, and the energy is reduced. Figure 2 of [68] shows how the nighttime turbulent spectra have varying shapes.

Since λ_w is computed at 10 m above the ground, we extrapolate the computed value at larger heights z in the ABL, according to Lenschow and Stankov's relation, as

$$\lambda_w(z) = \lambda_w(10)\left(\frac{z}{10}\right)^{1/2} \quad \text{(A2)}$$

The results are presented in Table A1, at the top of the ABL (i.e., for the maximum values of λ_w), for the values either computed from the relation (A1) or estimated from the spectra at a height of 10 m and then extrapolated to the z_i level using (A2). The values computed from the w observations are much lower than those deduced from (A1) and remain well below 100 m, i.e., smaller than the size of the cells in the finest domain of the

model. At this time, we do not have an explanation of the discrepancy between the two estimates of $\lambda_w(z_i)$. We are inclined to trust in the estimates involving our observations rather than in those deduced from a parameterization only. For these reasons, we remain in fully parameterized subgrid-scale turbulence mode, even for the daytime convective conditions.

Table A1. From left to right: time of the radiosonde profiles; starting time of the 30 min w time series; ABL thickness estimated from the radiosonde profiles; integral scales computed from w time series at 10 m and extrapolated at z_i level; integral scales computed at z_i from (A1).

Time of Radio-Sounding (UTC)	Start of 30 min w Time Series at 10 m (UTC)	Boundary Layer Height z_i (m agl)	Integral Scale at 10 m from Spectra (m)	Integral Scale Extrapolated at z_i with (A2) (m)	Integral Scale Computed at z_i with (A1) (m)
12:00	11:30	592	3.6	28	142
	11:45		3.6	28	
	12:00		3.5	27	
15:00	14:30	855	3.9	36	205
	14:45		8.3	77	
	15:00		4.0	37	
18:00	17:30	29	2.0	3	7
	17:45		2.1	4	
	18:00		4.0	7	
12:00	11:30	716	5.8	49	172
	11:45		6.9	58	
	12:00		3.9	33	

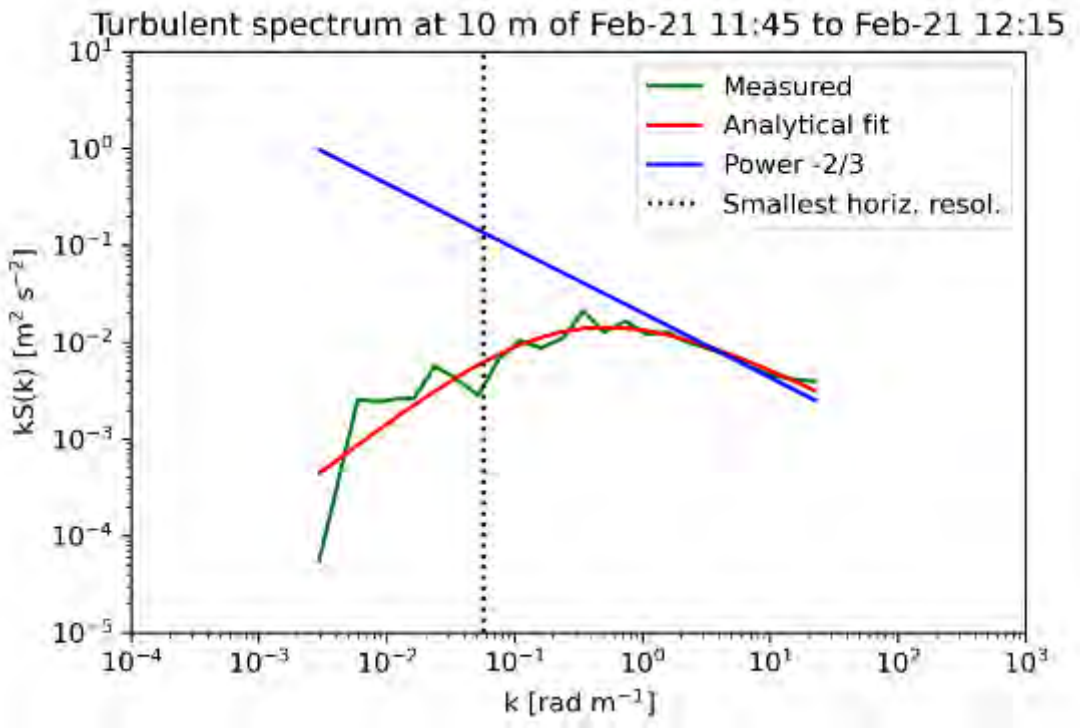

Figure A1. Example of an observed spectrum at 10 m agl and the fit with the model from [67] (matching to the last entry of Table A1). The abscissa is the wavenumber (in rad m^{-1}), and the spectrum energy is in m^2 s^{-2}. The green line represents the observed spectrum (values averaged on wavenumber bins), and the red line is the fit from [67]. The blue line is the −2/3 power law. The dotted line indicates the wavenumber value corresponding to the size of the horizontal cell in the finest simulation domain.

Appendix B

Corine Land Cover consists of 44 classes, as shown in Figure B1, matching Figure 1. USGS has 27 different ones in the default settings of WRF, which are not all used for CLC maps; therefore, we do not name the missing classes. Table B1 shows all classes available for CLC after conversion to USGS classes, matching Figure 5.

Table B1. USGS classes that are used by the CLC after the conversion of [47].

Class Number	Full Name	Color
1	"Urban and Build-Up land"	
2	"Dryland Cropland and Pasture"	
3	"Irrigated Cropland and pastures"	
6	"Crops/Wood mosaic"	
7	"Grassland"	
9	"Mix Shrubland/Grassland"	
11	"Deciduous Broadleaf Forest"	
14	"Evergreen Needleleaf"	
15	"Mixed Forest"	
16	"Water Bodies"	
17	"Herbaceous Wetland"	
19	"Barren or Sparsely Vegetated"	
24	"Snow or Ice"	

Figure B1. Classifications of all 44 Corine Land Cover classes with three hierarchical levels.

References

1. Sandu, I.; van Niekerk, A.; Shepherd, T.G.; Vosper, S.B.; Zadra, A.; Bacmeister, J.; Beljaars, A.; Brown, A.R.; Dörnbrack, A.; McFarlane, N.; et al. Impacts of Orography on Large-Scale Atmospheric Circulation. *npj Clim. Atmos. Sci.* **2019**, *2*, 1–8, doi:10.1038/s41612-019-0065-9.
2. Lehner, M.; Whiteman, C.D.; Dorninger, M. Inversion Build-Up and Cold-Air Outflow in a Small Alpine Sinkhole. *Bound. -Layer Meteorol.* **2017**, *163*, 497–522, doi:10.1007/s10546-017-0232-7.
3. Chemel, C.; Arduini, G.; Staquet, C.; Largeron, Y.; Legain, D.; Tzanos, D.; Paci, A. Valley Heat Deficit as a Bulk Measure of Wintertime Particulate Air Pollution in the Arve River Valley. *Atmos. Environ.* **2016**, *128*, 208–215, doi:10.1016/j.atmosenv.2015.12.058.
4. Sabatier, T.; Paci, A.; Lac, C.; Canut, G.; Largeron, Y.; Masson, V. Semi-Idealized Simulations of Wintertime Flows and Pollutant Transport in an Alpine Valley: Origins of Local Circulations (Part I). *Q. J. R. Meteorol. Soc.* **2020**, *146*, 807–826, doi:10.1002/qj.3727.
5. Sabatier, T.; Largeron, Y.; Paci, A.; Lac, C.; Rodier, Q.; Canut, G.; Masson, V. Semi-Idealized Simulations of Wintertime Flows and Pollutant Transport in an Alpine Valley. Part II: Passive Tracer Tracking. *Q. J. R. Meteorol. Soc.* **2020**, *146*, 827–845, doi:10.1002/qj.3710.
6. Quimbayo-Duarte, J.; Staquet, C.; Chemel, C.; Arduini, G. Dispersion of Tracers in the Stable Atmosphere of a Valley Opening onto a Plain. *Bound. -Layer Meteorol.* **2019**, *172*, 291–315, doi:10.1007/s10546-019-00439-2.
7. Quimbayo-Duarte, J.; Staquet, C.; Chemel, C.; Arduini, G. Impact of along-Valley Orographic Variations on the Dispersion of Passive Tracers in a Stable Atmosphere. *Atmosphere* **2019**, *10*, 225, doi:10.3390/atmos10040225.
8. Doran, J.C.; Fast, J.D.; Horel, J. The Vtmx 2000 Campaign. *Bull. Am. Meteorol. Soc.* **2002**, *83*, 537–554, doi:10.1175/1520-0477(2002)083<0537:TVC>2.3.CO;2.
9. Price, J.D.; Vosper, S.; Brown, A.; Ross, A.; Clark, P.; Davies, F.; Horlacher, V.; Claxton, B.; McGregor, J.R.; Hoare, J.S.; et al. COLPEX: Field and Numerical Studies over a Region of Small Hills. *Bull. Am. Meteorol. Soc.* **2011**, *92*, 1636–1650, doi:10.1175/2011BAMS3032.1.
10. Whiteman, C.D.; Muschinski, A.; Zhong, S.; Fritts, D.; Hoch, S.W.; Hahnenberger, M.; Yao, W.; Hohreiter, V.; Behn, M.; Cheon, Y.; et al. Metcrax 2006: Meteorological Experiments in Arizona's Meteor Crater. *Bull. Am. Meteorol. Soc.* **2008**, *89*, 1665–1680, doi:10.1175/2008BAMS2574.1.
11. Fernando, H.J.S.; Pardyjak, E.R.; Sabatino, S.D.; Chow, F.K.; Wekker, S.F.J.D.; Hoch, S.W.; Hacker, J.; Pace, J.C.; Pratt, T.; Pu, Z.; et al. The MATERHORN: Unraveling the Intricacies of Mountain Weather. *Bull. Am. Meteorol. Soc.* **2015**, *96*, 1945–1967, doi:10.1175/BAMS-D-13-00131.1.
12. Clements, W.E.; Archuleta, J.A.; Gudiksen, P.H. Experimental Design of the 1984 ASCOT Field Study. *J. Appl. Meteorol. Climatol.* **1989**, *28*, 405–413, doi:10.1175/1520-0450(1989)028<0405:EDOTAF>2.0.CO;2.
13. Sabatier, T.; Paci, A.; Canut, G.; Largeron, Y.; Dabas, A.; Donier, J.-M.; Douffet, T. Wintertime Local Wind Dynamics from Scanning Doppler Lidar and Air Quality in the Arve River Valley. *Atmosphere* **2018**, *9*, 118, doi:10.3390/atmos9040118.
14. Quimbayo-Duarte, J.; Chemel, C.; Staquet, C.; Troude, F.; Arduini, G. Drivers of Severe Air Pollution Events in a Deep Valley during Wintertime: A Case Study from the Arve River Valley, France. *Atmos. Environ.* **2021**, *247*, 118030, doi:10.1016/j.atmosenv.2020.118030.
15. Rotach, M.W.; Stiperski, I.; Fuhrer, O.; Goger, B.; Gohm, A.; Obleitner, F.; Rau, G.; Sfyri, E.; Vergeiner, J. Investigating Exchange Processes over Complex Topography: The Innsbruck Box (i-Box). *Bull. Am. Meteorol. Soc.* **2017**, *98*, 787–805, doi:10.1175/BAMS-D-15-00246.1.
16. Wagner, J.; Gerz, T.; Wildmann, N.; Gramitzky, K. Long-Term Simulation of the Boundary Layer Flow over the Double-Ridge Site during the Perdigão 2017 Field Campaign. *Atmos. Chem. Phys.* **2019**, *19*, 1129–1146, doi:10.5194/acp-19-1129-2019.
17. Rotach, M.W.; Andretta, M.; Calanca, P.; Weigel, A.P.; Weiss, A. Boundary Layer Characteristics and Turbulent Exchange Mechanisms in Highly Complex Terrain. *Acta Geophys.* **2008**, *56*, 194–219, doi:10.2478/s11600-007-0043-1.
18. Whiteman, C.D.; Allwine, K.J.; Fritschen, L.J.; Orgill, M.M.; Simpson, J.R. Deep Valley Radiation and Surface Energy Budget Microclimates. Part II: Energy Budget. *J. Appl. Meteorol. Climatol.* **1989**, *28*, 427–437, doi:10.1175/1520-0450(1989)028<0427:DVRASE>2.0.CO;2.
19. Lehner, M.; Rotach, M.W.; Sfyri, E.; Obleitner, F. Spatial and Temporal Variations in Near-Surface Energy Fluxes in an Alpine Valley under Synoptically Undisturbed and Clear-Sky Conditions. *Q. J. R. Meteorol. Soc.* **2021**, *147*, 2173–2196, https://doi.org/10.1002/qj.4016.
20. Banakh, V.A.; Smalikho, I.N. Lidar Observations of Atmospheric Internal Waves in the Boundary Layer of the Atmosphere on the Coast of Lake Baikal. *Atmos. Meas. Tech.* **2016**, *9*, 5239–5248, doi:10.5194/amt-9-5239-2016.
21. Duine, G.-J.; Hedde, T.; Roubin, P.; Durand, P.; Lothon, M.; Lohou, F.; Augustin, P.; Fourmentin, M. Characterization of Valley Flows within Two Confluent Valleys under Stable Conditions: Observations from the KASCADE Field Experiment. *Q. J. R. Meteorol. Soc.* **2017**, *143*, 1886–1902, doi:10.1002/qj.3049.
22. Dupuy, F. Amélioration de la Connaissance et de la Prévision des Vents de Vallée en Conditions Stables: Expérimentation et Modélisation Statistique Avec Réseau de Neurones Artificiels. Ph.D. Thesis, Université de Toulouse, Université Toulouse III-Paul Sabatier, Toulouse, France, 2019.
23. Duine, G.-J.; Hedde, T.; Roubin, P.; Durand, P. A Simple Method Based on Routine Observations to Nowcast Down-Valley Flows in Shallow, Narrow Valleys. *J. Appl. Meteor. Climatol.* **2016**, *55*, 1497–1511, doi:10.1175/JAMC-D-15-0274.1.

24. Dupuy, F.; Duine, G.-J.; Durand, P.; Hedde, T.; Roubin, P.; Pardyjak, E. Local-Scale Valley Wind Retrieval Using an Artificial Neural Network Applied to Routine Weather Observations. *J. Appl. Meteorol. Climatol.* **2019**, *58*, 1007–1022, doi:10.1175/JAMC-D-18-0175.1.
25. Dupuy, F.; Duine, G.-J.; Durand, P.; Hedde, T.; Pardyjak, E.; Roubin, P. Valley Winds at the Local Scale: Correcting Routine Weather Forecast Using Artificial Neural Networks. *Atmosphere* **2021**, *12*, 128, doi:10.3390/atmos12020128.
26. Goger, B.; Rotach, M.W.; Gohm, A.; Fuhrer, O.; Stiperski, I.; Holtslag, A.A.M. The Impact of Three-Dimensional Effects on the Simulation of Turbulence Kinetic Energy in a Major Alpine Valley. *Bound. -Layer Meteorol.* **2018**, *168*, 1–27, doi:10.1007/s10546-018-0341-y.
27. Udina, M.; Sun, J.; Kosović, B.; Soler, M.R. Exploring Vertical Turbulence Structure in Neutrally and Stably Stratified Flows Using the Weather Research and Forecasting–Large-Eddy Simulation (WRF–LES) Model. *Bound. -Layer Meteorol.* **2016**, *161*, 355–374, doi:10.1007/s10546-016-0171-8.
28. Jemmett-Smith, B.C.; Ross, A.N.; Sheridan, P.F.; Hughes, J.K.; Vosper, S.B. A Case-Study of Cold-Air Pool Evolution in Hilly Terrain Using Field Measurements from COLPEX. *Q. J. R. Meteorol. Soc.* **2019**, *145*, 1290–1306, https://doi.org/10.1002/qj.3499.
29. Skamarock, C.; Klemp, B.; Dudhia, J.; Gill, O.; Liu, Z.; Berner, J.; Wang, W.; Powers, G.; Duda, G.; Barker, D.; et al. A Description of the Advanced Research WRF Model Version 4. *Natl. Cent. Atmos. Res.* **2019**, 145, doi:10.5065/1dfh-6p97.
30. Skamarock, W.C.; Klemp, J.B.; Dudhia, J.; Gill, D.O.; Barker, D.M.; Duda, M.G.; Huang, X.-Y.; Wang, W.; Powers, J.G. A Description of the Advanced Research WRF Version 3, NCAR/TN-475+STR; National Center for Atmospheric Research (NCAR), Boulder, CO, USA, 2008; **113p**.
31. Kalverla, P.C.; Duine, G.-J.; Steeneveld, G.-J.; Hedde, T. Evaluation of the Weather Research and Forecasting Model in the Durance Valley Complex Terrain during the KASCADE Field Campaign. *J. Appl. Meteor. Climatol.* **2016**, *55*, 861–882, doi:10.1175/JAMC-D-15-0258.1.
32. Bastin, S.; Drobinski, P.; Dabas, A.; Delville, P.; Reitebuch, O.; Werner, C. Impact of the Rhône and Durance Valleys on Sea-Breeze Circulation in the Marseille Area. *Atmos. Res.* **2005**, *74*, 303–328, doi:10.1016/j.atmosres.2004.04.014.
33. Gunawardena, N.; Pardyjak, E.R.; Stoll, R.; Khadka, A. Development and Evaluation of an Open-Source, Low-Cost Distributed Sensor Network for Environmental Monitoring Applications. *Meas. Sci. Technol.* **2018**, *29*, 024008, doi:10.1088/1361-6501/aa97fb.
34. Wang, W.; Gill, D. WRF Nesting. WRF tutorial 2012 Brazil. Sao Paulo. Brazil. 2012,
35. Daniels, M.H.; Lundquist, K.A.; Mirocha, J.D.; Wiersema, D.J.; Chow, F.K. A New Vertical Grid Nesting Capability in the Weather Research and Forecasting (WRF) Model. *Mon. Weather. Rev.* **2016**, *144*, 3725–3747, doi:10.1175/MWR-D-16-0049.1.
36. Duine, G.-J. Caractérisation Des Vents de Vallée En Conditions Stables à Partir de La Campagne de Mesures KASCADE et de Simulations WRF à Méso-Échelle. Ph.D. Thesis, Université de Toulouse, Université Toulouse III-Paul Sabatier, Toulouse, France, 2015.
37. Hersbach, H.; Bell, B.; Berrisford, P.; Biavati, G.; Horányi, A.; Muñoz Sabater, J.; Nicolas, J.; Peubey, C.; Radu, R.; Rozum, I.; et al. ERA5 Hourly Data on Pressure Levels from 1978 to Present, Copernicus Climate Change Service (C3S) Climate Data Store (CDS). **2018**, doi:10.24381/cds.bd0915c6.
38. Hersbach, H.; Bell, B.; Berrisford, P.; Biavati, G.; Horányi, A.; Muñoz Sabater, J.; Nicolas, J.; Peubey, C.; Radu, R.; Rozum, I.; et al. ERA5 Hourly Data on Model Level from 1978 to Present, Copernicus Climate Change Service (C3S) Climate Data Store (CDS). **2018**, doi:10.24381/cds.adbb2d47.
39. Hong, S.-Y.; Kim, J.-H.; Lim, J.; Dudhia, J. The WRF Single Moment Microphysics Scheme (WSM). *J. Korean Meteorol. Soc.* **2006**, *42*, 129–151.
40. Sukoriansky, S.; Galperin, B.; Perov, V. Application of a New Spectral Theory of Stably Stratified Turbulence to the Atmospheric Boundary Layer over Sea Ice. *Bound. -Layer Meteorol.* **2005**, *117*, 231–257, doi:10.1007/s10546-004-6848-4.
41. Kain, J.S. The Kain–Fritsch Convective Parameterization: An Update. *J. Appl. Meteorol. Climatol.* **2004**, *43*, 170–181, doi:10.1175/1520-0450(2004)043<0170:TKCPAU>2.0.CO;2.
42. Sukoriansky, S. Implementation of the Quasi-Normal Scale Elimination (QNSE) Model of Stably Stratified Turbulence in WRF, Report on WRF-DTC Visit of Semion Sukoriansky, Beer-Sheva, Israel, 2008; 8p.
43. Iacono, M.J.; Delamere, J.S.; Mlawer, E.J.; Shephard, M.W.; Clough, S.A.; Collins, W.D. Radiative Forcing by Long-Lived Greenhouse Gases: Calculations with the AER Radiative Transfer Models. *J. Geophys. Res. Atmos.* **2008**, *113*, https://doi.org/10.1029/2008JD009944.
44. Tewari, M.; Chen, F.; Wang, W.; Dudhia, J.; LeMone, M.; Mitchell, K.; Ek, M.; Gayno, G.; Wegiel, J. Implementation and Verification of the Unified NOAH Land Surface Model in the WRF Model (Formerly Paper Number 17.5). In Proceedings of the Proceedings of the 20th Conference on Weather Analysis and Forecasting/16th Conference on Numerical Weather Prediction, Seattle, WA, USA, January 14 2004; pp. 11–15.
45. Farr, T.G.; Kobrick, M. Shuttle Radar Topography Mission Produces a Wealth of Data. *Eos Trans. Am. Geophys. Union* **2000**, *81*, 583–585, doi:10.1029/EO081i048p00583.
46. Mukul, M.; Srivastava, V.; Mukul, M. Accuracy Analysis of the 2014–2015 Global Shuttle Radar Topography Mission (SRTM) 1 Arc-Sec C-Band Height Model Using International Global Navigation Satellite System Service (IGS) Network. *J. Earth Syst. Sci.* **2016**, *125*, 909–917, doi:10.1007/s12040-016-0716-8.
47. Pineda, N.; Jorba, O.; Jorge, J.; Baldasano, J.M. Using NOAA AVHRR and SPOT VGT Data to Estimate Surface Parameters: Application to a Mesoscale Meteorological Model. *Int. J. Remote. Sens.* **2004**, *25*, 129–143, doi:10.1080/0143116031000115201.
48. Vladimirov, E.; Dimitrova, R.; Danchovski, V. Sensitivity of WRF Model Results to Topography and Land Cover: Study for the Sofia Region. *Annu. Univ. Sofia St. Kliment Ohridski* **2018**, *111*, 87–101.

49. Egova, E.; Dimitrova, R.; Danchovski, V. Numerical Study of Meso-Scale Circulation Specifics in the Sofia. *Bul. J. Meteorol. Hydrol.* **2017**, *22*, 54–72.50.
50. Wyngaard, J.C. Toward Numerical Modeling in the "Terra Incognita". *J. Atmos. Sci.* **2004**, *61*, 1816–1826, doi:10.1175/1520-0469(2004)061<1816:TNMITT>2.0.CO;2.
51. Kaimal, J.C.; Finnigan, J.J. *Atmospheric Boundary Layer Flows: Their Structure and Measurement*; Oxford University Press: Oxford, UK, 1994; ISBN 978-0-19-536277-0.
52. Lenschow, D.H.; Stankov, B.B. Length Scales in the Convective Boundary Layer. *J. Atmos. Sci.* **1986**, *43*, 1198–1209, doi:10.1175/1520-0469(1986)043<1198:LSITCB>2.0.CO;2.
53. Zhang, X.; Bao, J.-W.; Chen, B.; Grell, E.D. A Three-Dimensional Scale-Adaptive Turbulent Kinetic Energy Scheme in the WRF-ARW Model. *Mon. Weather. Rev.* **2018**, *146*, 2023–2045, doi:10.1175/MWR-D-17-0356.1.
54. Deardorff, J.W. Stratocumulus-Capped Mixed Layers Derived from a Three-Dimensional Model. *Bound. -Layer Meteorol.* **1980**, *18*, 495–527, doi:10.1007/BF00119502.
55. Weisman, M.L.; Skamarock, W.C.; Klemp, J.B. The Resolution Dependence of Explicitly Modeled Convective Systems. *Mon. Weather. Rev.* **1997**, *125*, 527–548, https://doi.org/10.1175/1520-0493(1997)125<0527:TRDOEM>2.0.CO;2.
56. Jeworrek, J.; West, G.; Stull, R. Evaluation of Cumulus and Microphysics Parameterizations in WRF across the Convective Gray Zone. *Weather. Forecast.* **2019**, *34*, 1097–1115, doi:10.1175/WAF-D-18-0178.1.
57. Mahoney, K.M. The Representation of Cumulus Convection in High-Resolution Simulations of the 2013 Colorado Front Range Flood. *Mon. Weather. Rev.* **2016**, *144*, 4265–4278, doi:10.1175/MWR-D-16-0211.1.
58. Lindvall, J.; Svensson, G. The Diurnal Temperature Range in the CMIP5 Models. *Clim. Dyn.* **2015**, *44*, 405–421, doi:10.1007/s00382-014-2144-2.
59. Acevedo, O.C.; Fitzjarrald, D.R. The Early Evening Surface-Layer Transition: Temporal and Spatial Variability. *J. Atmos. Sci.* **2001**, *58*, 2650–2667, https://doi.org/10.1175/1520-0469(2001)058<2650:TEESLT>2.0.CO;2.
60. Blumberg, W.G.; Turner, D.D.; Cavallo, S.M.; Gao, J.; Basara, J.; Shapiro, A. An Analysis of the Processes Affecting Rapid Near-Surface Water Vapor Increases during the Afternoon to Evening Transition in Oklahoma. *J. Appl. Meteorol. Climatol.* **2019**, *58*, 2217–2234, doi:10.1175/JAMC-D-19-0062.1.
61. Mahrt, L. Stably Stratified Flow in a Shallow Valley. *Bound. -Layer Meteorol.* **2017**, *162*, 1–20, doi:10.1007/s10546-016-0191-4.
62. Jiménez, M.A.; Cuxart, J.; Martínez-Villagrasa, D. Influence of a Valley Exit Jet on the Nocturnal Atmospheric Boundary Layer at the Foothills of the Pyrenees. *Q. J. R. Meteorol. Soc.* **2019**, *145*, 356–375, doi:10.1002/qj.3437.
63. Albergel, C.; de Rosnay, P.; Gruhier, C.; Muñoz-Sabater, J.; Hasenauer, S.; Isaksen, L.; Kerr, Y.; Wagner, W. Evaluation of Remotely Sensed and Modelled Soil Moisture Products Using Global Ground-Based in Situ Observations. *Remote. Sens. Environ.* **2012**, *118*, 215–226, doi:10.1016/j.rse.2011.11.017.
64. Durand, P.; Thoumieux, F.; Lambert, D. Turbulent Length-Scales in the Marine Atmospheric Mixed Layer. *Q. J. R. Meteorol. Soc.* **2000**, *126*, 1889–1912, doi:10.1002/qj.49712656616.
65. Darbieu, C.; Lohou, F.; Lothon, M.; Vilà-Guerau de Arellano, J.; Couvreux, F.; Durand, P.; Pino, D.; Patton, E.G.; Nilsson, E.; Blay-Carreras, E.; et al. Turbulence Vertical Structure of the Boundary Layer during the Afternoon Transition. *Atmos. Chem. Phys.* **2015**, *15*, 10071–10086, doi:10.5194/acp-15-10071-2015.
66. Brilouet, P.-E.; Durand, P.; Canut, G. The Marine Atmospheric Boundary Layer under Strong Wind Conditions: Organized Turbulence Structure and Flux Estimates by Airborne Measurements. *J. Geophys. Res. Atmos.* **2017**, *122*, 2115–2130, doi:10.1002/2016JD025960.
67. Kristensen, L.; Lenschow, D.H.; Kirkegaard, P.; Courtney, M. The Spectral Velocity Tensor for Homogeneous Boundary-Layer Turbulence. *Bound. -Layer Meteorol.* **1989**, *47*, 149–193, doi:10.1007/BF00122327.
68. Kovadlo, P.G.; Shihovtsev, A.Y. The Study of Turbulence and Optical Instability in Stably Stratified Earth's Atmosphere. In Proceedings of the 21st International Symposium Atmospheric and Ocean Optics: Atmospheric Physics; International Society for Optics and Photonics, Tomsk, Russian Federation, 19 November 2015; Volume 9680, p. 968074.

4.4 Additional analyses

The rest of this chapter aims to complement the results presented in the article by focusing on additional flow and thermal analyses. The data illustrating the analyses comes from the 111 m resolution output. I will describe the flow in the CV through the variables at GBA, the stability at the CV south sidewall, and particular jumps in CV stability. I will also discuss the region in a broader sense with some vertical cross-sections of other valleys and surface wind patterns in a broader view. All cross-sections presented here correspond to one specific simulation moment, but hourly plots are given in Annex 5: "Hourly plots of the fine-resolution simulation" and 10 min updates are available at google drive[1]. References to sections or figures of the article reproduced in this chapter are bold in the following sections.

4.4.1 Structures and flows within the CV

This section details a few additional analyses of flows and structures in the CV before discussing other flows in the simulation domain. I start with a discussion of the model performance against the GBA observations and the stability structure on the southern sidewall of the CV. After that, I continue with more in-depth analyses of the vertical temperature structure in the valley to understand the stability development in the evening and night. Finally, I have additional wind vector analyses on the comparability of wind measured by the stations and simulated by the model.

4.4.1.1 Time series at GBA

Figure 4.1 shows the GBA observations and the corresponding simulation values interpolated to the observation altitude. The observed temperature shows a DTR of 19 K at 2 m height and 15 K at 110 m, matching the clear-sky conditions. Similarly, to what happens at the MET01 site (see the article), the 2-m temperature drops rapidly around nightfall. In the simulation, the trend matches the observations but is too low. At 2 m, the daytime maximum is underestimated by 3.8 K whilst at night, the overestimation of the minimum is 2.8 K. However, at 110 m, the night values match better. In contrast, the daytime maximum underestimation remains comparable to that at 2 m.

If I look at the resulting stratification between 2 m and 110 m, the observations are generally unstable before 16:00, with a strength of about 2 K before 14:00, and become near-neutral thereafter. From 16:30 UTC, the stability intensifies until reaching a maximum of 6.3 K at 21:30 UTC, followed by a decrease to 4 K at midnight, closely resembling the pattern shown in **Figure 10 (p. 17)** of the article above. In contrast, the simulation is neutral throughout the early afternoon. Stability starts to grow at around 14:00 UTC and reaches a maximum of 4 K at dusk around 17:00 UTC, after which it decreases and remains within the 1.5 – 3.5 K range for the rest of the night.

Simulated and observed humidity follow a pattern similar to MET01 (see the article). The observed humidity remains between 3 – 4.5 g kg^{-1} until the morning when it increases from 3 g kg^{-1} to 5 g kg^{-1}. It is noticeable that the strong increase of moisture after sunset seems present in the simulation though delayed by several hours and reduced in amplitude. During the IOP, the simulation follows a trend resembling observations at MET01, characterized by an increase during the day and early night, followed by a continuous decrease until sunrise, after which it starts to increase again.

[1] https://drive.google.com/drive/folders/11Kh1ZoWTaiX6hJyS2GSQ3FGWnp9mfhKl?usp=sharing

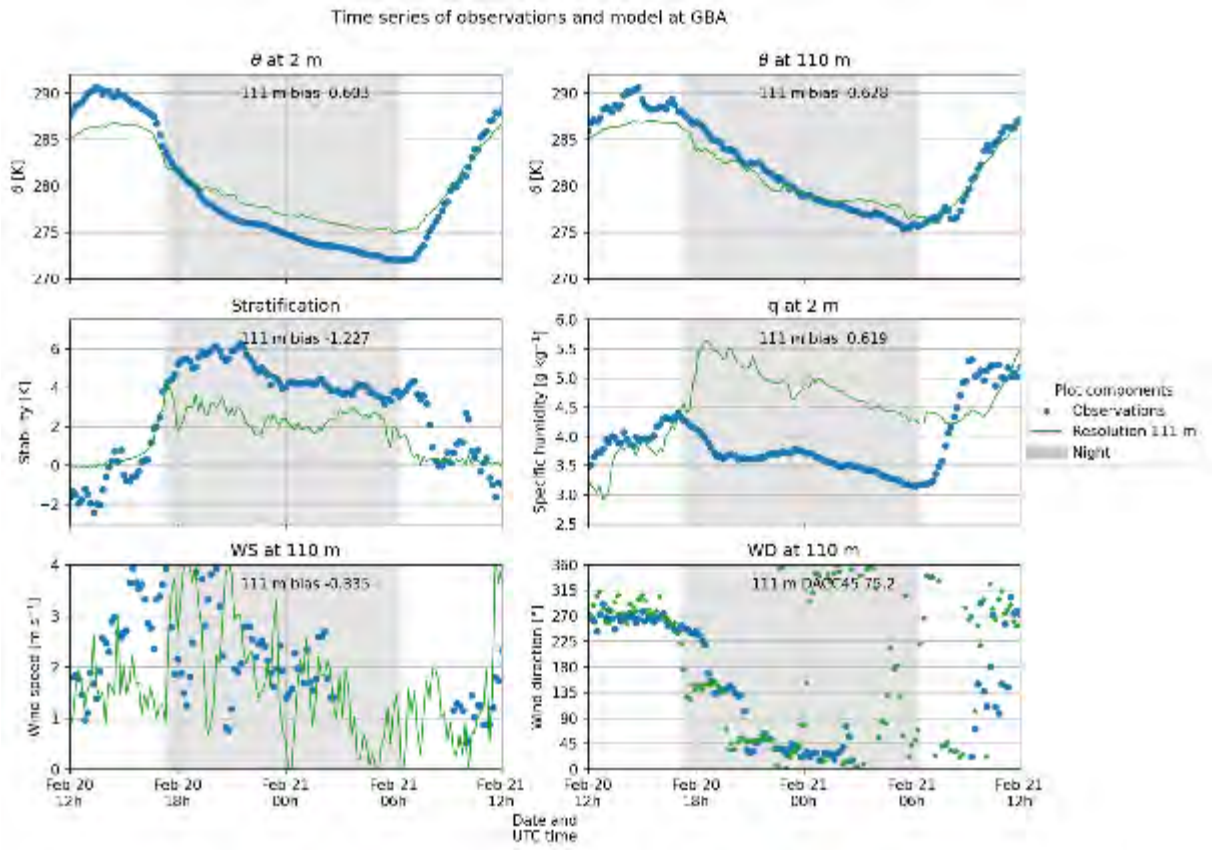

Figure 4.1: Time series of the observations and the 111 m simulation at the GBA tower site. Potential temperature at 2 and 110 m agl, their difference (stratification), humidity at 2 m, and wind speed and direction at 110 m. The mean difference between simulation and observation (bias) is indicated, except for wind direction, where it is replaced with the direction accuracy at 45° (DACC45). The nighttime period is shaded.

For the wind, the observations show an increase at the start of the IOP from 1 m s^{-1} to 4 m s^{-1}, with a direction coming from the west until nightfall, when the wind direction changes from west to south, coinciding with a dip in speed with an amplitude of 3 m s^{-1} that restores quickly. At 21 UTC, a second wind direction change occurs with another drop in speed. After that drop, the wind restores briefly and continuously decrease to 1.5 m s^{-1} at 03 UTC. Wind observations are missing between 03 and 09 UTC because either the data were discarded when the wind speed dropped below a certain limit or an error occurred in the acquiring equipment. However, because the other variables are still measured, the data filter seems the more logical option. After 09 UTC, they restored with weak winds and varying wind directions. Just before noon, the winds from the west start again and wind speed increases.

For the model, the wind speed is underestimated in the late afternoon, and then increases to 4 m s^{-1} after dusk and decreases until the IOP end. Similar to the observations, the simulation also displays dips and peaks of the wind speed at night but does not place them at the right time. The afternoon wind directions simulated by the model tend to be slightly veered from the observed directions, whereas after 21:00 UTC simulations are backed. At GBA, the model produces between 16:00 and 07:00 UTC a layer with southern winds near the surface. Though a Sodar (SOD2) was installed closely, it had no observations in this layer corresponding to its blind zone. Near the GBA tower top height, the model has regular NNW and NNE winds, whereas the SOD2 predominantly observed NNE winds. Here, the model seems to produce a shear layer, as Duine et al. (2017) mentioned, which means the DDV flow occurs too high in the simulation. In the morning, the simulated wind pattern resembles that of the observations, except for a timing offset.

Figure 6 (p. 12) of the article in Chapter 3 shows that during KAS13-IOP16, at GBA, the cooling reinforces when the DDV flow arrives. Here, in KAS17-IOP07, we do not have such an effect. A small halt in cooling is even discernable around the DDV arrival, but the cooling continues at similar rates afterward. This halt is less discernable in simulations due to timing errors of the wind regime changes and cooling rates more diverse than those observed.

In short, the additional verifications show that the fine resolution model manages its forecast skill not only at MET01 but also at GBA. Figure 4.1 shows that the model has comparable temperature curves at GBA and MET01 and shows that the temperature at higher altitude is better than close to the surface. The resulting stratification shows patterns comparable to that already seen in the article above. This resemblance indicates that model and observations have a similar system in the whole valley. One of the sparse DDV winds observations is available at GBA, even though it has a gap in the data due to acquisition errors. In the end, the modeled winds show good behavior match with the observations however a slight shift in timing of the wind regime changes. A noteworthy aspect in the modeled data at GBA is a slight shift in the wind direction, coming from an intermediate layer that has flows more from the north(west) than the observations do, similar to the shear layer identified by Duine et al. (2017). Finally, both the model and the observations do not show a clear relation between the DDV arrival and cooling rates of temperature.

4.4.1.2 Stability development at the south sidewall

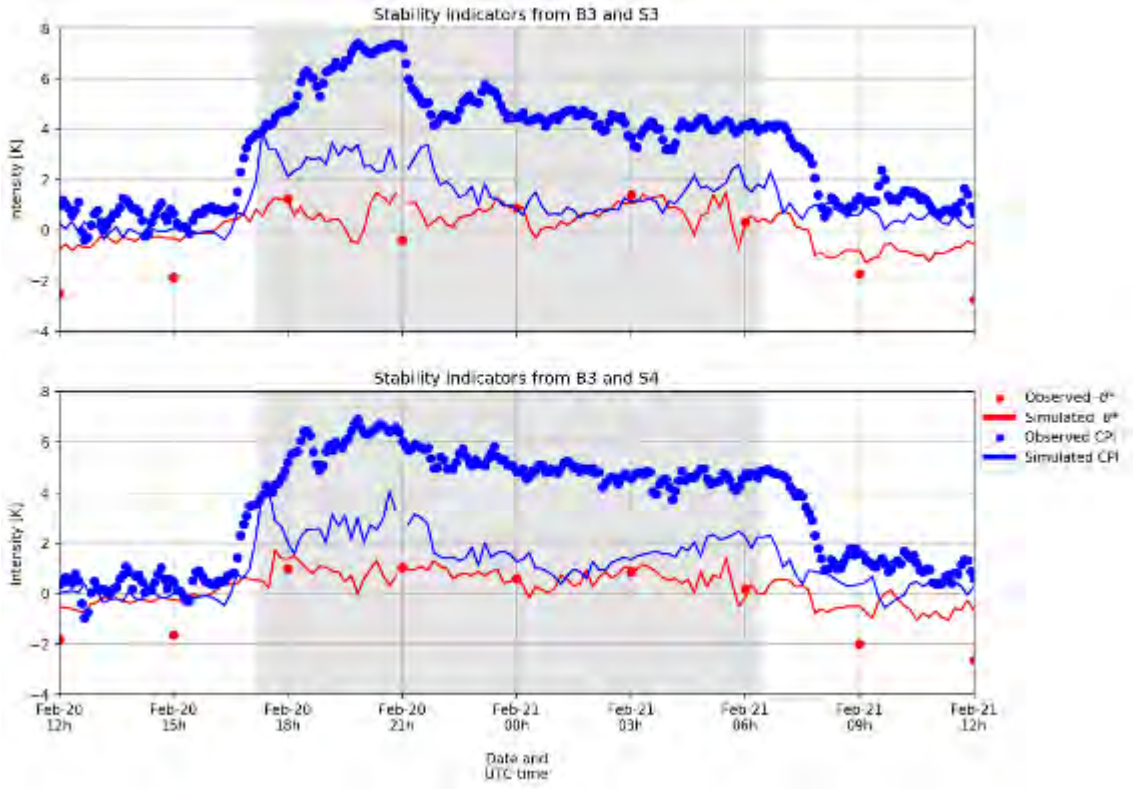

Figure 4.2: Time series of CPI and ϑ parameters, observed (dots) and simulated (lines). The LEMS used to represent the top of the CV south flank is either S4 (bottom plot), which is the highest station near the top of the south flank near the top of or S3 (top), which is located on a local high near the high end of the CV (see **Figure 2** of the paper for the location).*

In **Figure 10 (p. 17)** of the article above, I described the stability on the CV northern sidewall by looking at CPI and θ*. It is interesting to examine these parameters on the southern sidewall to check similarities and differences. Figure 4.2 shows the stability parameters of the southern sidewall. It resembles the northern sidewall. During the day, CPI is near 0 K for both simulation and observation. Before nightfall, the CPI starts to increase and observations reach their maximum between 19 and

21 UTC, followed by a steady decrease (with an initial pronounced drop at S3) to 4 K throughout the night. In the simulation, the values increase around nightfall but remain between 2 and 4 K until 22 UTC, and then remain between 1 and 2 K for the rest of the night. For -θ*, the observations show values of -2 K during daytime and 1 – 2 K at night. The simulations agree quite well with the observations during the night but are weaker during the day.

The noticeable difference with the northern sidewall is that the observed increase of the CPI values does not stop around 19 UTC but continues until 21 UTC, especially with the S3 station. Nonetheless, around 19 UTC, the CPI shows a disturbance, matching the arrival of the humid air mass mentioned in the article. Additionally, between 20 and 21 UTC, the stability with S3 is stronger than it is with S4, even though S4 is at a more elevated location than S3. After the drop at 21 UTC, S3 again become less stable then S4.

Looking back at 110 m wind speed in Figure 4.1, we can see that the observed 18:30 UTC disturbance and the 21:00 UTC drop seem to correlate with the wind speed peaks of 4 m s^{-1}. Thus, a hypothesis can be made that mechanical turbulence introduced by even moderate winds increases the cooling at the valley crest while the valley floor remains undisturbed. A more in-depth analysis follows in the next paragraph.

4.4.1.3 Vertical temperature and wind structures in the CV

In this section, I will try to understand the origin of sudden changes in the nocturnal vertical structure of the whole CV. Hopefully, this will give us some understanding of how the stability and hence the CPI change. I will select a few moments to highlight the vertical profiles of temperature and wind speed in the CV. All the hourly plots are represented in Annex 5: Hourly plots of the fine-resolution simulation, whereas corresponding plots every 10 minutes can be viewed online[2]. I now focus on two changes in the observed CPI development: the evening increase until 21 UTC and the following decrease. I will illustrate the evening change with three different moments. First, there is a regular CPI development represented with the 16:30 UTC and 17:30 UTC vertical profiles in Figure 4.3. Second, the 17:30 and 18:00 UTC plots in Figure 4.4 illustrate how the observations and model start to divert. Lastly, to understand the 21 UTC drop, I will compare profiles at 21:00 UTC and 21:30 UTC in Figure 4.5. Based on the stability plot of Figure 4.2 and **Figure 10 (p. 17)** of the article, the trends in Figure 4.3, Figure 4.4, and Figure 4.5 should reveal the origin of the S3 stability drop. The LEMS locations are shown in **Figure 2 (p. 5)** and Figure 2.3.

These figures deserve an introduction because they are dense in data. Each figure contains four profiles with the altitude amsl of the variable temperature or wind speed. In total, each plot contains three or four profiles, which are from LEMS and GBA observed data, simulated data at LEMS and GBA locations, the simulated profile at the MET01 location, and when available, the radiosonde profile (released at MET01). The LEMS are surface observations, so the corresponding profile does not refer to a single location. Remember that the model and radiosonde are instantaneous data while the LEMS observation is averaged over 5 minutes and the GBA one over 10 minutes. The corresponding observed and simulated values of the LEMS and GBA are connected on the plots with a thin dotted line to highlight they do not exactly match the altitude. This unequal height results from elevation representing a 111 x 111 = 12 346 m^2 area in the model with one value, the error ranging from a few meters to over twenty for S3. In some temperature plots, I add additional lines to connect the three different valley slopes: the thalweg, the northern and the southern sidewall. These slope lines help

[2] https://drive.google.com/drive/folders/11Kh1ZoWTaiX6hJyS2GSQ3FGWnp9mfhKl?usp=sharing

determine if these slopes have their own system or if they are connected. Note that wind observations below 0.5 m s^{-1} are filtered and thus have no symbol in the plot.

Figure 4.3 shows the vertical profiles of wind speed and temperature around sunset. Figure 4.3a shows that both the model and the observations had a near-neutral straight profile. Most simulated stations remained between 287 and 287.5 K, whereas the observations were roughly 2 K warmer and most fell within the 289.5-290 K range. Two stations on the northern sidewall were warmer than the rest, which were the stations that remained in the sunshine for the longest.

One hour later, Figure 4.3b shows the new profile; the observed valley bottom cooled down by 6 K or more (with cooling-rate peaks approaching 12 K h^{-1}). In comparison, the sidewall stations cooled down by 4 K or less, except S1 that cooled as a valley bottom station. The rest of the two sidewalls had a comparable stratification of roughly 0.02 K m^{-1}. The sidewall cooling can be attributed to radiative divergence, typically around the 1 – 3 K h^{-1} (Stull, 2009). The cooling at the valley bottom needed more contributions than radiative, such as cold air advection. Additional measurements would be needed to determine the processes at S1, whether it is an extension of the valley floor cold layer, or advection along the south sidewall. Considering the two other slopes, the northern sidewall showed a roughly straight line of almost 0.02 K m^{-1}, matching the south sidewall slope for S2 – S4 with stronger stability between S1 and S2.

Below I aim to understand this enhanced cooling better. I resume with the simulated temperature description before I continue with analyses of the effects of wind speed since the wind direction for all stations is roughly around 270° at 16:30 UTC and around 135° at 17:30 UTC (see Annex 5: Hourly plots of the fine-resolution simulation).

In comparison, Figure 4.3a showed that the model at 16:30 UTC is cooler than the observations. An hour later, the stations at the valley bottom cooled down more than the model (Figure 4.3b) as the model cooling was 4 K in B3 and B4. In contrast, S4 cooled down only by 0.5 K. At the other stations, the underestimation became smaller, except for the B4 station. The model resembled the observations fairly well at this moment. The vertical profile above MET01 showed roughly the same profile as the LEMS in both simulation and observation and matched the simulated LEMS temperatures. This coherence between the stations at the valley top leads to a resemblance between all four stability plots of Figure 4.2 and **Figure 10 (p. 17)** of the article. The simulations showed lower temperatures from S1 to S2 than at N1, translating as the simulated valley flow did not have horizontal isotherms since the altitude of N1 is lower than that of S1 (Figure 4.3b).

If we look at the winds matching these moments, Figure 4.3c showed the wind speed of the LEMS and GBA at 16:30 UTC. Wind speeds were relatively low, remaining below 1.9 m s^{-1}, except for GBA, which reached 2.8 m s^{-1} at 110 m above the ground. The model produced slightly lower values, but generally had comparable wind speeds between 0.5 and 1.3 m s^{-1}. An hour later, Figure 4.3d showed three groups in the observed wind speeds: the bottom of the valley, with 1.2 m s^{-1} to 1.6 m s^{-1}; a middle section with filtered wind speeds below 0.5 m s^{-1}, from S1 up to N3; and at the top of the valley, the stations show a layer with speeds comparable to the valley bottom. At the top of GBA tower, the wind speed in the model increased from 1.6 m s^{-1} to 2.6 m $s^{-1,}$ while the observations increased even harder from 2.8 m s^{-1} to 4.2 m s^{-1}. In the simulation, the north sidewall had a pattern of raised wind speeds. Further, the simulated vertical profile at MET01 indicates an LLJ in the downvalley flow (110°) between 40-50 m agl, matching the LEMS measurements on the northern transect.

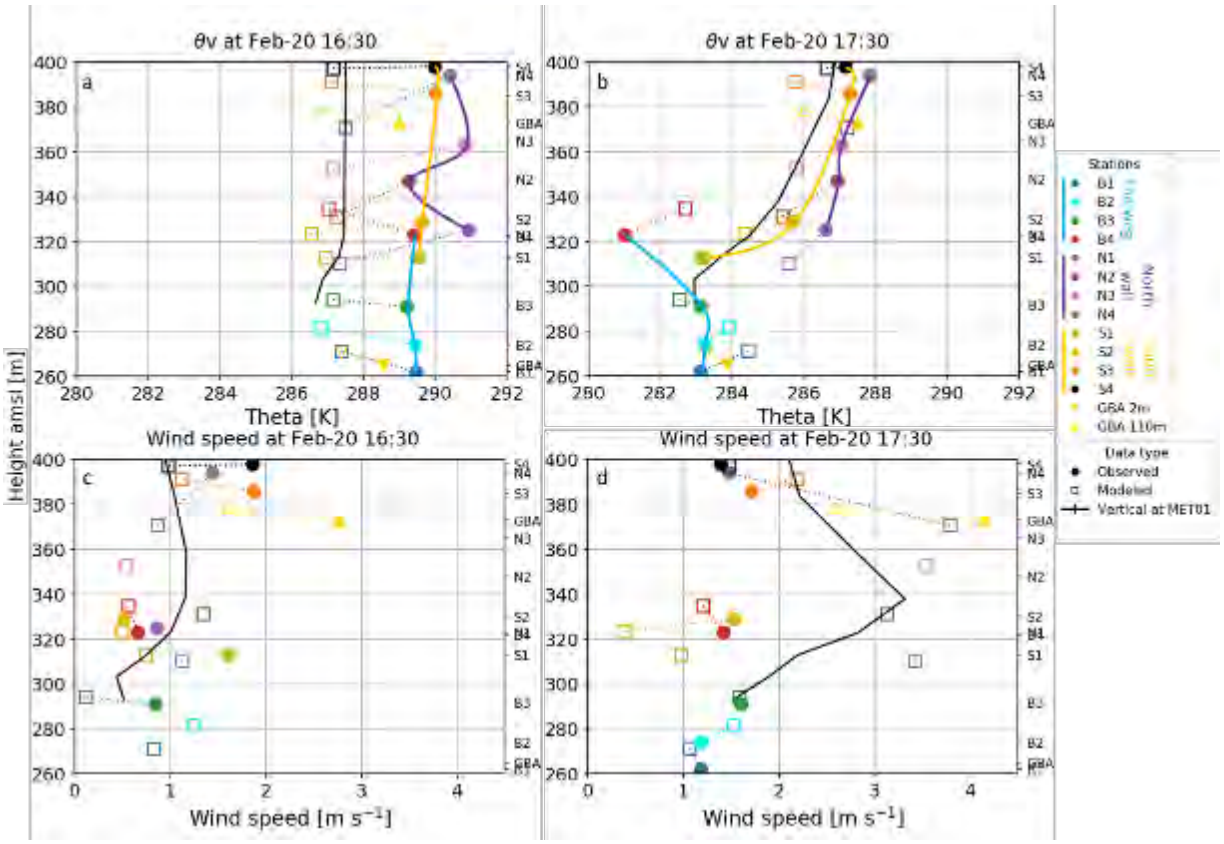

Figure 4.3: Observations (filled symbols) and simulations (open symbols) of the potential temperature (top – a, b) and wind speed (bottom – c, d) at the LEMS (circles and squares) and GBA (triangles) locations, at 16:30 UTC (left - a, c) and 17:30 UTC (right - b, d). The solid black lines represent the simulated profiles along the vertical above MET01. The dotted lines connect the observed and simulated values for a given location. The secondary y-axis shows the names of the different stations at their observational altitude. The temperature plots have additional colored solid lines connecting the various stations of the thalweg, north, or south slope. Wind speed observations below 0.5 m s^{-1} at the LEMS stations are considered uncertain and unreliable for their direction. Therefore, they are not represented here. The values are represented at the true altitude for the observations and the altitude of the corresponding cell in the model for the 111 m simulation.

Figure 4.3 showed that the sidewalls cooled down slower than the valley bottom, except S1. These exceptional cooling of 6 K during an hour meant that a mechanism such as wind advection of cold air must play a role. Investigation of the wind showed the directions aligned in the same direction. In contrast, the wind speed differed in the valley profile. The valley floor showed wind speeds between 1 and 2 m s^{-1}, with a layer of wind observations discarded because they are below 0.5 m s^{-1}. Winds in higher locations on the sidewalls of the valley had wind speeds comparable to that of the valley floor. Based on the cooling rates and the observed wind speeds in the valley, I conclude that the sidewalls show typical radiative cooling rates without large amounts of advection. In contrast, the valley bottom received additional cooling through air advection, from upvalley with the valley segment containing B4 as likely origin of a cold foot entering the valley. The S1 station deserves more attention because it had cooling rates comparable to that of the valley floor while not having winds faster than the detection limit at 17:30 UTC, in contrast to the hour before. These reduced wind speeds might relate to the forest at roughly 50 m upslope. Altogether, I assume that the cold valley floor winds extended far enough up the sidewalls to affect the lower regions of the sidewalls. Although unlikely, it may be an effect of the sidewall system itself.

At the same time, in the simulation, the cooling was less distinct than in the observations. B3 and B4 cooled down by 4 K, exceeding the 2 K cooling of most other locations (Figure 4.3a and 4.3b). Simulated wind showed higher values than observed, especially on the north sidewall stations. These faster winds did not seem to affect the simulated temperatures more on any slopes.

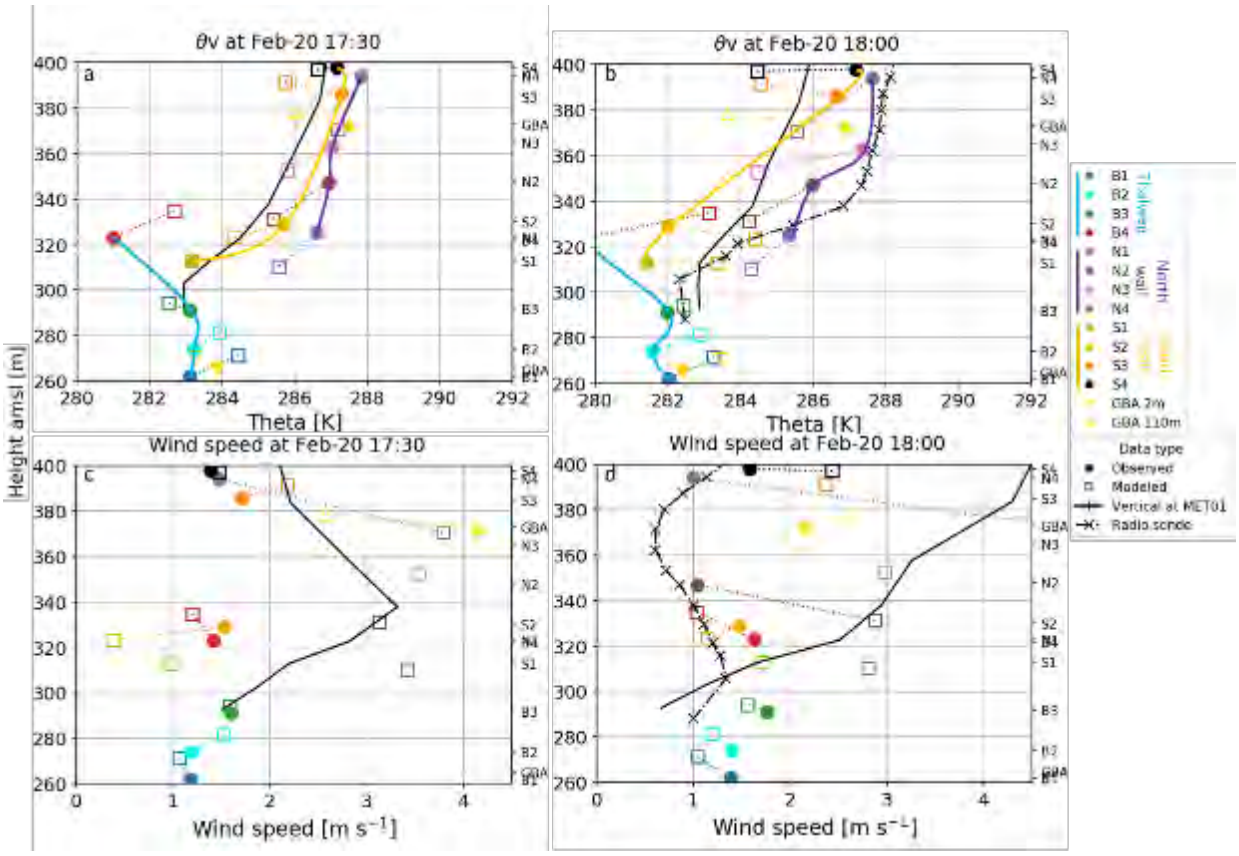

Figure 4.4: Similar to Figure 4.3, but for the times 17:30 and 18:00 UTC.

Figure 4.4 continues with the next half hour when model and observation started to deviate because of a stability weakening in the simulations. Figure 4.4a and 4.4c were already discussed above as they were the same as Figure 4.3b and 4.3d. Figure 4.4b shows the temperature half an hour later at 18:00 UTC. The valley floor cooled down by 1 K and B4 by 1.6 K. The north sidewall cooled down at N1 and N2 by roughly 1.3 K. N3 warmed up by 0.3 K. In total, the north slope became more stable. On the south slope, S1 and S2 cooled down by 1.8 K and 3.7 K, exceeding the typical radiative cooling rate. However, the S3 and S4 stations showed lower cooling, 0.6 K at S3 and 0.0 K at S4. It is possible that the cold layer from the valley floor has grown to encompass S2 or that another cooling system on the sidewall between S2 and S3 supplied cold air. The radiosonde at 18:00 showed a 20 m thick cold layer above the valley floor, indicating that either another system cooled S2 and S1 down, or the isotherms are not horizontal and extent to higher altitudes on the sidewalls.

Figure 4.2 and **Figure 10 (p. 17)** suggest that the simulation diverted from the observed trends and stability decreased during this interval. Figure 4.4a and b showed that the simulated valley floor does not cool. Both the north and south sidewalls cooled down by -0.2 – 2.2 K, reducing the stability in the simulated valley.

In this paragraph, I discuss the wind development to see if there is a clear relation with cooling. The wind direction showed most observed and all simulated winds lie within 45° of the CV downslope orientation (see Annex 5: Hourly plots of the fine-resolution simulation). Observed GBA wind was at 240° whereas at S4 and N4 the wind direction is 200°, intermediate between the CV orientation and GBA. Within the valley, observed N1 is at 45° and B4 at 90°. The simulated wind speed at the valley floor remained similar to the observed values (see B1 to B4 in Figure 4.4c and 4.4d). Likewise, the rest of the LEMS remained below the 0.5 m s^{-1} limit or between 1 and 2 m s^{-1}, whereas N2 exceeded the limit and S3 became too slow. At GBA, measurements showed a reduction in wind speed to 2.2 m s^{-1}.

This pattern was roughly matched with the radiosonde, showing an increasing wind up to 305 m amsl and reducing above until 370 m amsl. The altitude where the radiosonde showed wind speeds equal or superior to the surface winds matched with the altitude of S2 and the colder area. In the simulation, wind patterns remained similar to those of half an hour before, with wind speeds increased further near N4 and in the vertical profile above MET01.

Analysis of Figure 4.4 showed continued cooling in the observations with a system similar to that already described above. Only the cold layer extended to S2, which was more elevated than the not cooled N1. Possible explanations are a south sidewall preferring valley bottom system or a secondary cooling flow on the south sidewall. It would require additional measurements to determine the exact cause. A secondary advection system is less likely because of the wind speeds at S1 and S2.

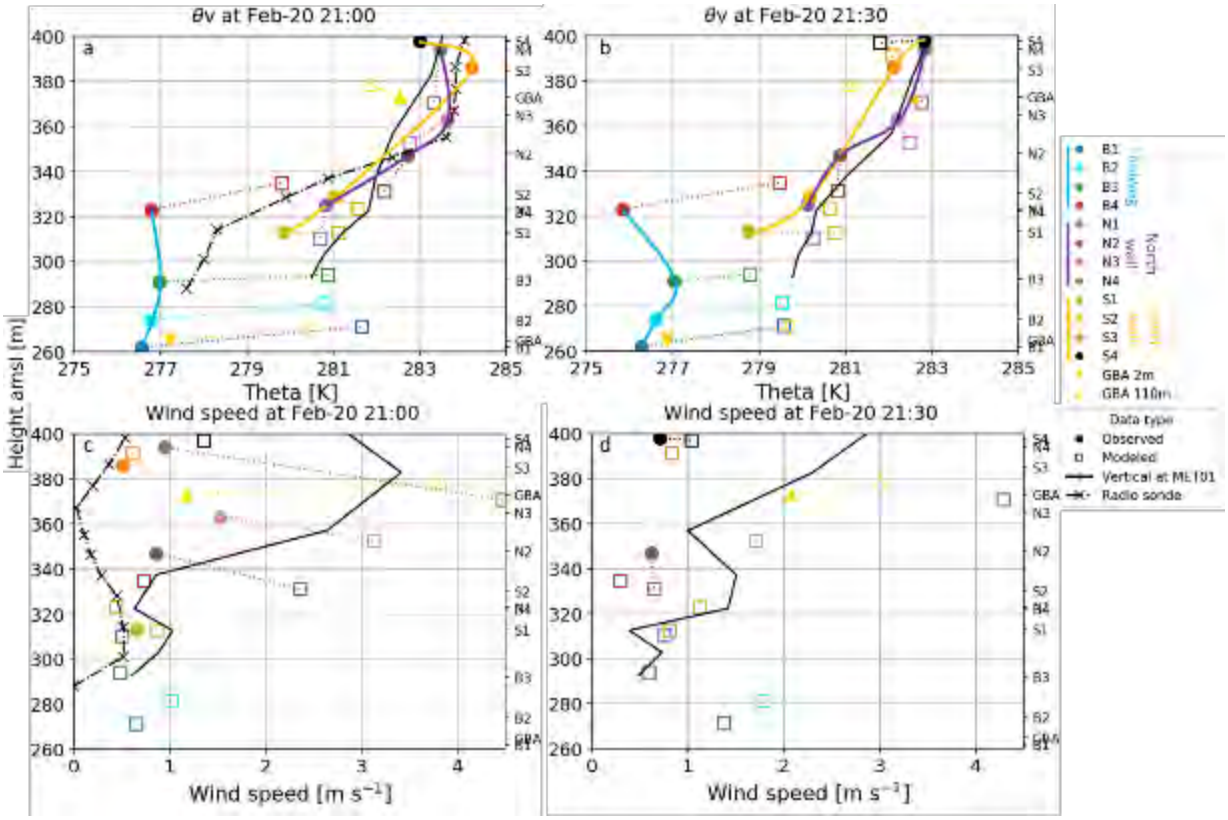

Figure 4.5: Similar to Figure 4.3, but for 21:00 UTC and 21:30 UTC.

To investigate the observed stability decrease, I focus on the observations shown in Figure 4.5. In contrast to Figure 4.3, Figure 4.5 showed faster cooling at the higher part of the valley sidewalls than at the bottom, except S4 that remained at a constant temperature. B1 – B3 cooled down by less than 0.5 K, while the LEMS on the sidewalls (S1 – S3 and N1 – N4) cooled down by 0.9 – 1.8 K, and B4 cooled down by 1 K showing it remained a place with relatively strong cooling. The both sidewall slopes in Figure 4.5a and 4.5b showed great overlap. The observations revealed that the valley is likely stratified over its whole width with near-horizontal isotherms. Observations at both moments showed vertical profiles that resemble those in Figure 4.3b, but only S1 showed valley floor temperatures in Figure 4.3b and 4.4b. Here, the profiles from the LEMSs showed a straight line, especially Figure 4.5b showed a connected line from B1 to S4. Noteworthy is the decreasing temperature trend on the south slope between S3 and S4 in Figure 4.5a, being in sharp contrast with the stable trend of the sidewall station (S1 to S3 and N1 to N3). Extrapolating these two trends would imply a regime change between 365 m and 385 m amsl. However, Figure 4.5b no longer shows any stable sections.

In the model, the stability increased during this time interval, the 21:00 UTC had a small dip in the stability, which was caused by warming of the B3 station, afterward all LEMS cooled down at a pace of roughly 0.3 K h^{-1}. From 22:00, cold air seemed to propagate to the elevated LEMS, first the lower sidewall LEMSs (S1, N1, and S2) cooled to temperatures similar to the valley bottom, later followed by N2, N3. Sometimes the S3 and S4 have moments of neutral conditions within the simulated valley. Observed winds at the valley bottom dropped below the measurable limit (0.5 m s^{-1}), except for sporadic moments. Most moments with winds exceeding the limit occurred on the top of the sidewalls, especially starting at 21:00 UTC, see Figure 4.6a and 4.6b, coinciding with the decrease in stability illustrated in Figure 4.5. A remarkable observation in Figure 4.6b is that between 19:00 and 21:00 UTC the winds at N3 are stronger than at N4. These lowered wind speeds originate from N4 being sheltered from winds coming from the south, as shown in **Figure 2 (p.5)**, which are present during that time interval, as described in **Figure 11 (p.18)**.

Simulated winds at 21:00 UTC remained below 1.5 m s^{-1}, except for the N2, N3, and N4 stations with winds of 2.4 to 4.5 m s^{-1}. While the N2 and N3 winds dropped to lower wind speeds at 21:30 UTC, the N4 wind remained around 4.5 m s^{-1}. Simulated winds at N4 remained elevated until 23:30 UTC, when they resembled the rest of the valley, with another strong wind episode between 02:00 and 04:00 UTC, as depicted in Figure 4.6.

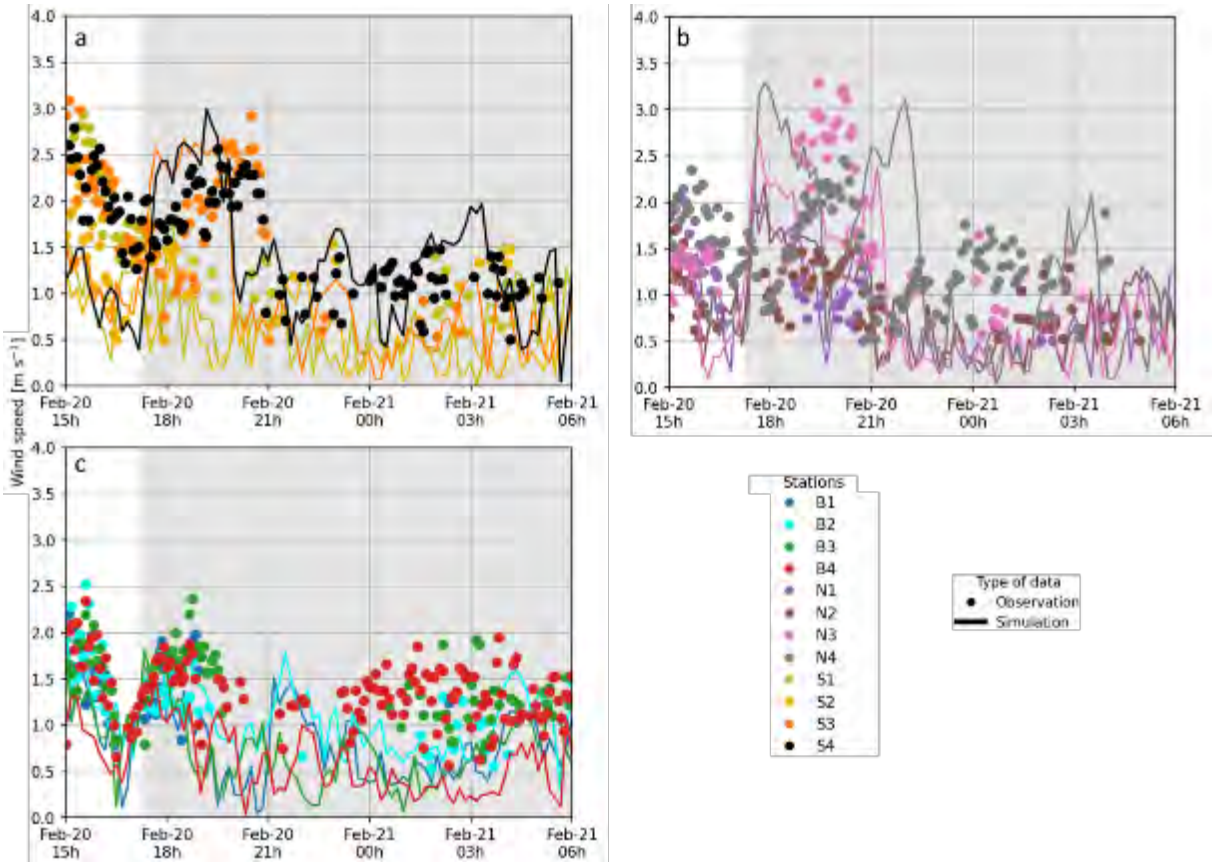

Figure 4.6: Time series of wind speed observations (dots) and simulations (lines) at the 12 LEMSs. Plot (a) contains the LEMSs on the south sidewall, (b) contains the LEMSs of the north sidewall, and (c) contains the LEMSs of the thalweg.

Overall, the in-depth observations analyses showed that the valley bottom cools very fast around nightfall, leading to stability within the valley. Later at night, cooling of the ridges coincided with winds higher in the valley, starting the slow stability reduction. Wind speed seemed to affect cooling rates on the sidewalls, with low wind speeds connected to locations with colder temperatures. In comparison, the temperature in the simulation had a similar trend of stronger cooling at the valley

bottom than on the sidewalls. The cooling happened less organized than in observations. This unorganized cooling could relate to simulated peak speed at too high levels in the valley compared to the observations, as shown by the radiosondes and vertical profile of MET01 in Figure 4.4c.

These analyses improved my understanding of how stability develops within the valley. During the evening transition, the valley bottom starts cooling at higher rates than the sidewalls, rapidly increasing stability. These cooling rates exceed those typical for radiative cooling, meaning another source provides cooling, most likely cold air arriving from upvalley near B4. Early in the night, the cooling continues at the valley floor, increasing the stability. However, the simulations no longer show cooling at the surface but only at the sidewalls, reducing the stability of the valley, while this cooling happens later in the night on the observations. After 21:00 UTC, the observations show stronger cooling at the valley ridges than at the valley floor, coinciding with the arrival of the DDV winds and increased winds on the CV ridges. Actually, the cooling regime changes with wind regimes in both the simulation and observations. In the simulation, the too early arriving moist air is the strongest influence. In the observations, it is the DDV arrival.

4.4.1.4 Analysis of arrow plots at stations in the Cadarache valley

However, not all moments during the night produced winds fast enough to exceed the measurable limit of the LEMS equipment (0.5 m s^{-1}), giving uncertain wind speeds and invalid directions. Keeping in the simulation only the moments when the observations are valid leads average vectors of Figure 4.7b, 4.7d, and 4.7f. This filter aims to identify how well the model forecasts the moments with low wind speeds, which do not occur simultaneously throughout the CV. If the model pattern matches the observations, applying this filter should improve the direction forecasts and increase the wind speed because it filters moments with slow winds. I begin with a description of the observations and continue with the model without the filter in the next paragraph.

The observations along the CV floor (Figure 4.7a and 4.7b) align relatively well with the valley orientation, with a slight deviation towards the north, as the cross-section is not exactly at the lowest point of the valley floor. LEMS wind speeds are around 1 m s^{-1}, while the sonic anemometers show lower speeds, the highest being AS3 (Figure 4.7c and 4.7d) and AS4 (Figure 4.7e and 4.7f). The flows on the slopes (Figure 4.7c and 4.7d) show orientations towards the valley bottom at roughly 45° of the valley axis with wind speeds above 1 m s^{-1}. N3, S3, and S4 (Figure 4.7c to Figure 4.7f) have winds approaching 2 m s^{-1} but holds the same orientation. Winds outside the CV (AS5 and VER) are too weak to have a clear direction. Above the valley floor, the 110 m agl winds at GBA slightly veer from the DV orientation with average speeds of 2.5 m s^{-1} (Figure 4.7a and 4.7b).

The model agrees with the observations along the valley floor and has flows aligned with the CV orientation. On the northern sidewall, flows increase their speed as they come closer to the top of the ridge and exceed observed speeds. Their direction backs towards a cross- CV orientation. On the southern sidewall, winds at S1 and S2 are slower than the observations, at S1 the flows are along the valley direction whereas at S2 they are perpendicular. S3 also presents a perpendicular flow (Figure 4.7e) that filtering corrects (Figure 4.7f) but with a simulated speed larger than observed. Lastly, the S4 flow is in the direction opposite to the observations and with much larger speeds. Outside the valley, in the DV, the model shows directions towards the west with average speed superior to 1 m s^{-1}. At the GBA height, the direction aligns better with the DV than observed, but at too slow speeds, it aligns slightly better with the filter (Figure 4.7f).

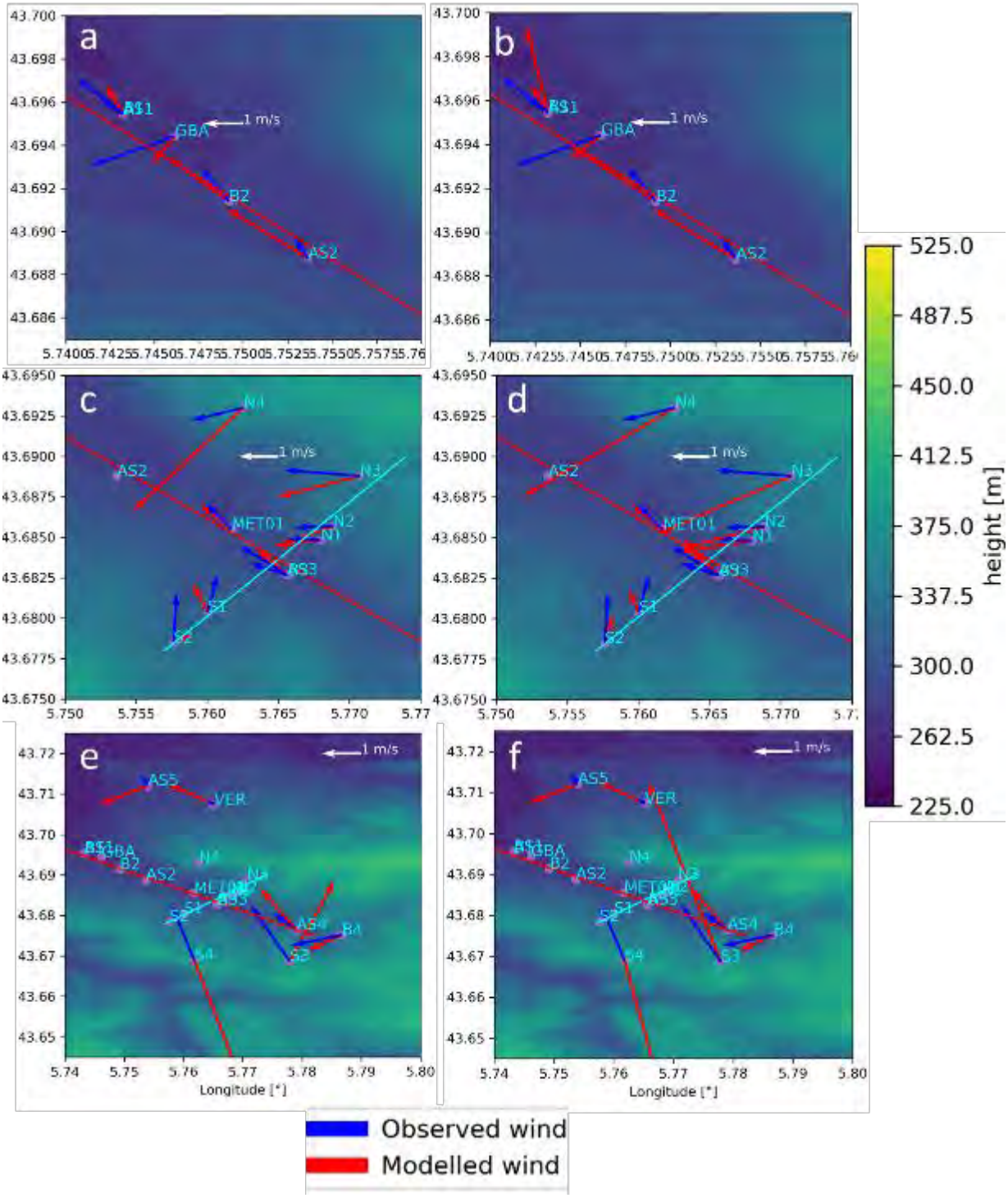

Figure 4.7: Arrow plots of winds in the Cadarache valley averaged from 18:00 to 06:00. (a), (c), and (e) show the wind vectors of simulation (in red) and observation (in blue) as averaged over the whole night. (b), (d), and (f) show the same as the other half, but the model is averaged only when the observations are deemed correct. Plot (a) and (b) show the stations at the lower end of the CV. (c) and (d) show the stations around the perpendicular cross-section in the CV. Lastly, (e) and (f) show the remaining stations. All the arrows represent winds close to the surface, except at GBA where they are at 110 m above the ground. Note that the frames do not maintain a correct ration between latitude and longitude.

This type of filter does not have a clear benefit to represent the model data. For a rigorous comparison, it seems fair to only use simulation data at instances that can be validated with valid observations. However, this filter punishes incorrectly timed regime changes harder than might be desirable, as the filter will include the wrong moment of the simulation.

4.4.2 Analyses of wind outside of the CV

Here, I expand the view of analyses to include a larger part of the domain and inspect the flows with possible influence on the CV

4.4.2.1 Vertical cross-sections of the Verdon, Durance, and Abéou valleys

Two other valleys around the CV had not been resolved in simulations before, so looking at them could be interesting. These are the Verdon and Abéou river valleys. They are displayed in Figure 4.8, with the tracks of the vertical cross-sections presented below.

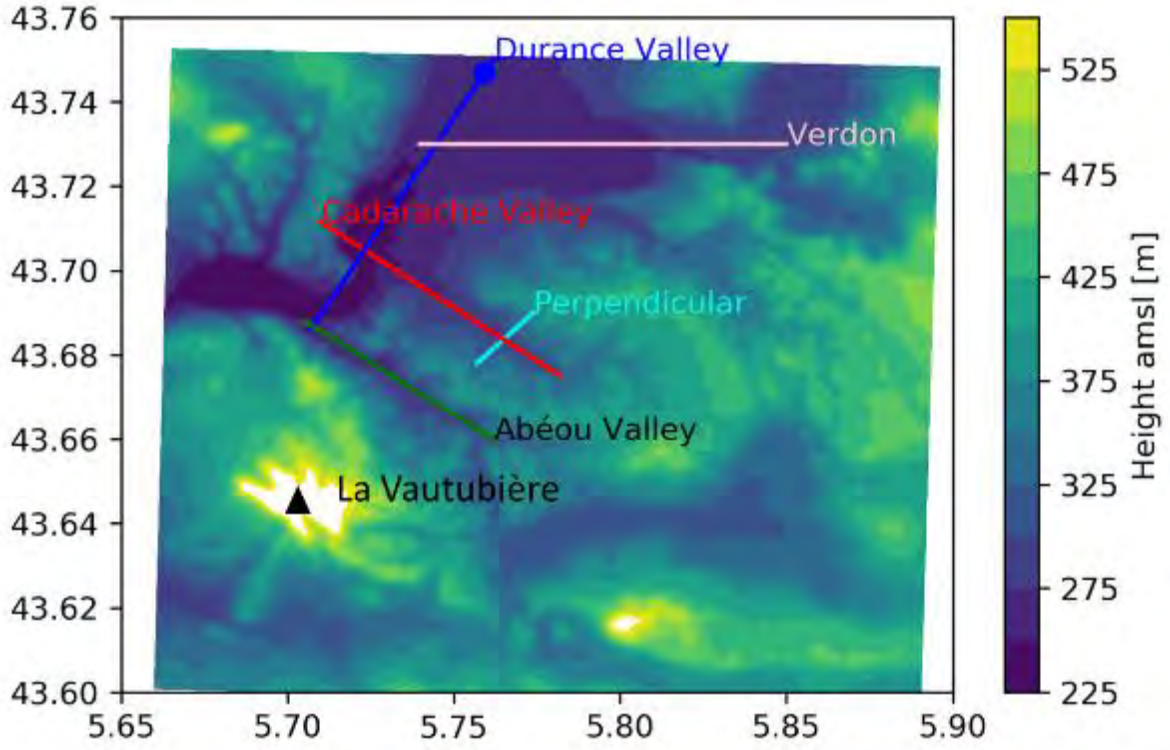

Figure 4.8: Height map of the smallest domain as resolved in WRF, with all the cross-sections discussed in this chapter. The blue line is the Durance Valley, the pink line is the Verdon Valley, the green line is the Abéou Valley and the red line indicates the Cadarache Valley, where the cyan line shows a section crossing the Cadarache Valley

In addition to the vertical cross-section in **Figure 12 (p. 19)** of the article, Figure 4.9 presents the vertical cross-sections along the Abéou, Durance, and Verdon valleys at 00 UTC. The top plots are a 6000 m long cross-section of the Abéou Valley (AV), located roughly 2 km southwest of and parallel to the CV. It shows a 200 – 300 m thick layer of DV orientated winds with an LLJ around 6 m s^{-1} between 400 and 500 m amsl, its maximum lying near the crossing of the DV. Near the ground is a limited region of winds from the south, covering roughly the confluence zone with the DV, at 0 – 1000 m distance of the cross-section. These flows originate from downslope flows along “La Vautubière” (Figure 4.8) which blocks the flow as shown in Figure 4.10. This flow is also present in the northwest corner of Figure 4.11b. Upslope of the confluent zone, an upslope wind occupies a layer of 50 – 200 m depth. However, the flow turns with height and aligns itself with the DV wind, see Figure 4.10 for more detail. Figure 4.9c and 4.9d show the already presented flow above the DV, which is here for reference purposes to the other valleys, see **section 3.6** of the article for a more detailed description of this flow.

Figure 4.9e and 4.9f show a near 10 km cross-section encompassing the end of the Verdon valley (VV) before its confluence with the DV. This cross-section shows a 300 – 400 m thick layer with DV orientated winds, with an LLJ of roughly 7 m s^{-1} between 300 – 500 m amsl. In the western part of the

VV cross-section (0 – 3000 m), the DDV flows seem to strongly influence local winds since the VV fades out entirely here. Going up the valley eastward, from 4000 to 7500 m, elevated sidewalls prevent the wind from flowing in DDV orientation at low heights there, and local flows (without a consistent orientation) reach a height of roughly 100 m, see Figure 4.6 (43.74°N; 5.82°E). Going further up the valley (around 8000 m), a turn and widening in the valley allows DDV orientated winds to become more influential again. Figure 4.7e shows that the wind speeds also become higher near the surface. There are two possible origins of these flows, either the DDV flows that manage to pass the hill mentioned above and reduce in speeds this way, or a flow coming from the "Plateau de Valensole" and reaching the VV, shown in Figure 2.1. A drainage flow from Valensole would explain the weaker winds, but its origin lie outside of this simulation domain. Checks of the larger 333 m resolution domain have confirmed that the flow indeed originates from Valensole area (not shown).

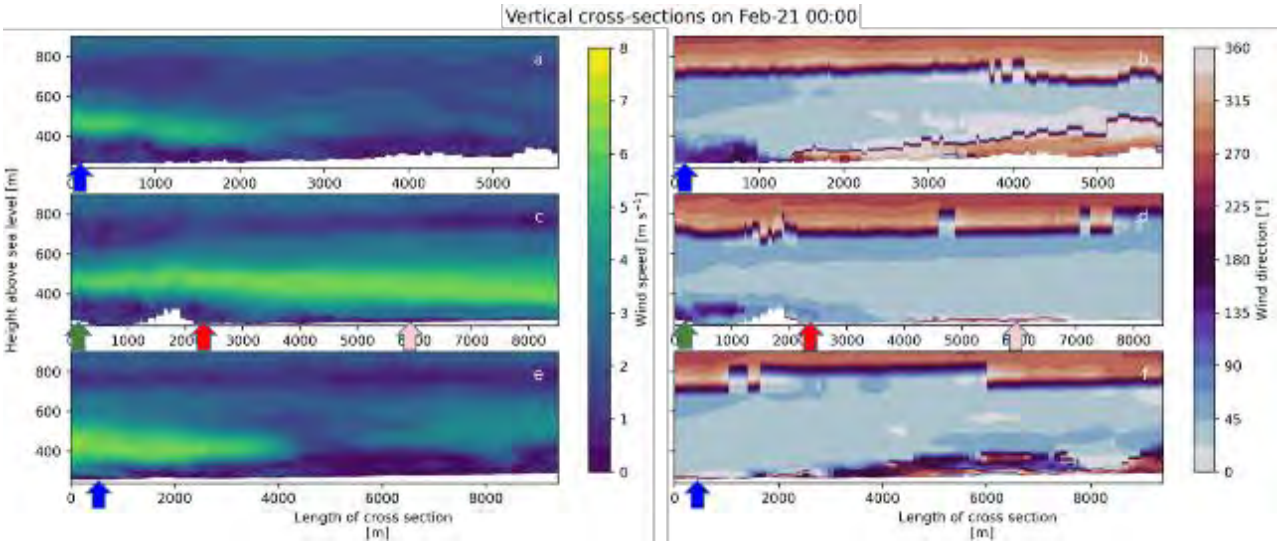

*Figure 4.9: Similar to the **Figure 12** of the article, but concerning valleys of Abéou (a and b), Durance (c and d) and Verdon (e and f). The blue, green, red and pink arrows indicate the crossing points with the Durance valley, the Abéou valley, the Cadarache valley and the Verdon valley, respectively. The ground tracks of the cross-sections are shown in Figure 4.8, with the left extremity of the graphs matching the western most point of the cross-sections.*

These cross-sections show that the DDV is dominant on the flows of the tributary valleys, especially if there is no surrounding topography that shelters smaller valley winds from its influence. The DDV flow has then reached the lower end of the DV middle section and enters the lower DV section. However, the DDV flow does not have the same thickness over the AV as it does over the VV, which could originate from topography, although the time series of the DV cross-section suggests that it is still growing in strength. Between 3000 and 7500 in distance, the VV shows flows that have a direction opposite to the DDV orientation, which could be inversed flows caused by the overlying DDV flow. Another option is that they originating from DDV winds pushed along the south sidewall of the VV since a slight flow with a western direction matching the valley orientation is simulated below this flow opposite to the DDV flows.

After additional investigations on the vertical cross-sections of several valleys, I switch to a few horizontal cross-sections to show the importance of multiple analyses in complex terrain and the essentialness for both types of cross-sections to complement information on the flow or temperature system.

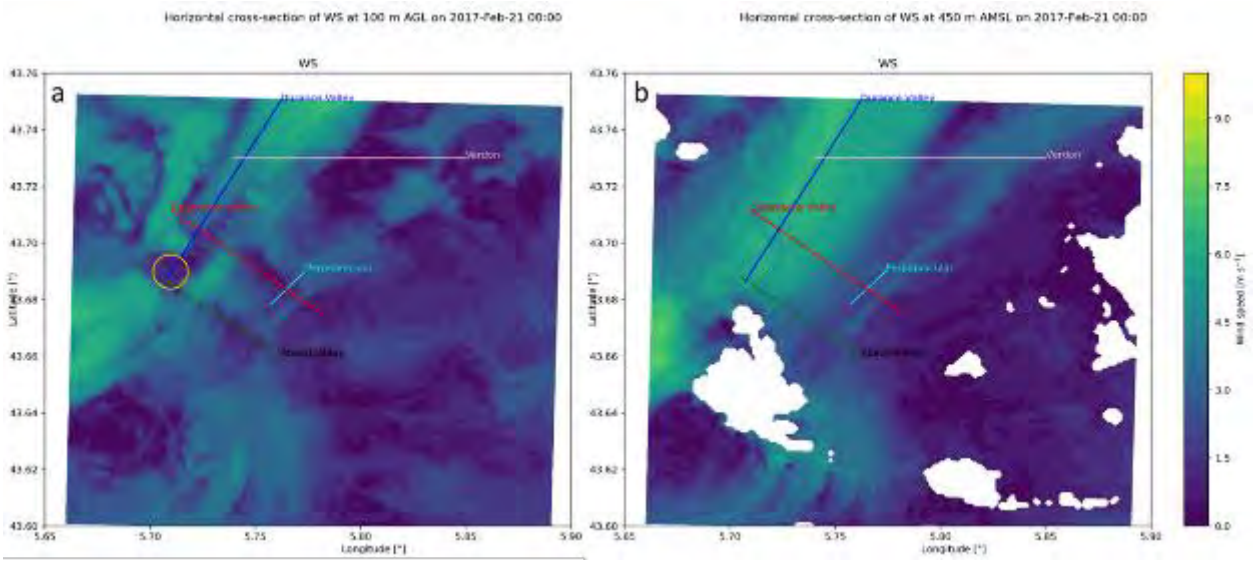

Figure 4.10: Two horizontal cross-sections of wind speed for the 111 m resolution domain. Plot (a) is a terrain-following cross-section at 100 m agl. (b) is a horizontal cross-section at 450 m amsl. The white areas in (b) are those with elevation higher than 450 m. The colored lines are defined in Figure 4.5. The gold circle highlights an area with downslope flows resulting from the blocking effect.

Figure 4.10a shows the wind speed fields in the innermost domain at the height of 100 m agl. In the Durance valley (blue line), there seem to be two parallel flows, one above the valley bottom (somewhere on the right of the blue line) and the other on its north-western sidewall, both having wind speeds around 4-6 m s^{-1}, and being separated by a section of low wind speeds around 1 m s^{-1}. To understand this separation of flows, I did a closer inspection on the cross-sections along the CV (**Figure 12c and 12d; p. 19**) and several horizontal cross-sections at different fixed altitudes. These cross-sections show that the flow is not separated, but all are part of the DDV flows. The illusion of separated flows is created because of the valley sidewalls (Figure 4.8) and that the DDV jet does not have a terrain-following shape. More precisely, the west valley sidewall makes a sharp drop while the jet gradually decreases. This difference leaves an area of low wind speeds near the sidewall, shown around 750 m along the CV cross-section of **Figure 12c (p. 19)**. Similarly, the fixed altitude plots do not show a split in the DDV plume. This terrain-following way of creating the cross-section explains the origin of the odd-shaped flows on the western sidewall, as it shapes like the terrain elevation as depicted in Figure 4.8. To verify the DDV being one flow, Figure 4.8b shows the altitude close to that of the western parallel flow of Figure 4.10a (elevation + height; 350 m amsl + 100 m agl). In conclusion, the DDV flow is more a fixed altitude flow than a terrain-following flow, confirmed by Figure 4.9, showing the importance of verifying different forms of representation and not create false ideas of separated flows or systems.

A few other noteworthy behaviors are the flow blocking effects of the Vautubière ridge, as it is located at the lower end of the DV middle section and just in its axis. This is indicated by the yellow circle in Figure 4.10a, based on the information collected in Figure 4.9 and Figure 4.10, confirmed by Figure 4.11.

Furthermore, in Figure 4.10b the VV flow extends from the NE corner of the plot, with a slightly different orientation than the DV, indicating that it likely has different origins as suggested above. This flow passes over the CV and AV, and joins the side flow on the SE border of “La Vautubière”. However, whether this is a connected flow or just elevated winds needs to be investigated with tracers, which the next chapter will focus on one source located at the northern end of the VV.

4.4.2.2 Spatial variation of surface winds in the simulation domain

The wind at the surface originates from many different driving mechanisms. Near the top of a ridge, it might catch the above valley flow. At the same time, within valleys, it might be buoyancy-forced. I will describe in more detail the situation at midnight in the AV and the VV, plus a small valley (43.70°N; 5.83°E) between the VV and the CV, where the 'Ruisseau de Boutre' flows. Figure 4.11a is the height map of Figure 4.8, without featuring the valley cross-section imprints, but with two areas highlighted, the AV in Figure 4.11b and the VV including some minor valleys to the south in Figure 4.11c.

Figure 4.11b shows that in the AV, the winds near the surface flow in the upvalley direction, especially on the southwest slope of the valley, which agrees with the findings of Figure 4.9b and Figure 4.10, as a branch of the DDV flow channeled after being blocked by topography. The ridge between the CV and the AV has higher wind speeds than the surroundings, as it is under the influence of the above valley flows. Similarly, the ridges on the southeast end of the AV show higher wind speeds, matching the orientation of the AV, which shows the strength of the DV flows channeled through the AV, as more wind is channeled over these obstacles. In contrast, the CV, as shown in Figure 4.11b, has downvalley flows along the thalweg. The flow on slopes differs per location, around 43.68°N; 5.75°E a small section of the southwest sidewall has slope-following flows, but on other parts of the southwest sidewall (43.675°N; 5.76°E), the winds are mostly from the north, an orientation not far from the above DDV direction. Investigation of the time series shows that these flows are not stationary and can inverse their directions, see Annex 5: "Hourly plots of the fine-resolution simulation". On the slopes on the northeast sidewall the flow is toward the south (not shown), but it is difficult to distinguish between slope flows, the effects of above valley flows, or possibly a combination of the two flows.

Figure 4.11c shows the VV and surroundings. The time series show a down flow direction before 22:00 UTC, but no strong winds are visible afterwards. In the narrow section of the valley (43.73°N; 5.83°E), the flow direction is upvalley, while in the wider upvalley section, both up- and downvalley flows are distinguishable. However, a few locations seem to indicate the presence of slope flows, especially at 43.71°N; 5.85°E and 43.71°N; 5.81°E. The latter is near a small water gap, which indicates a possible flow acceleration.

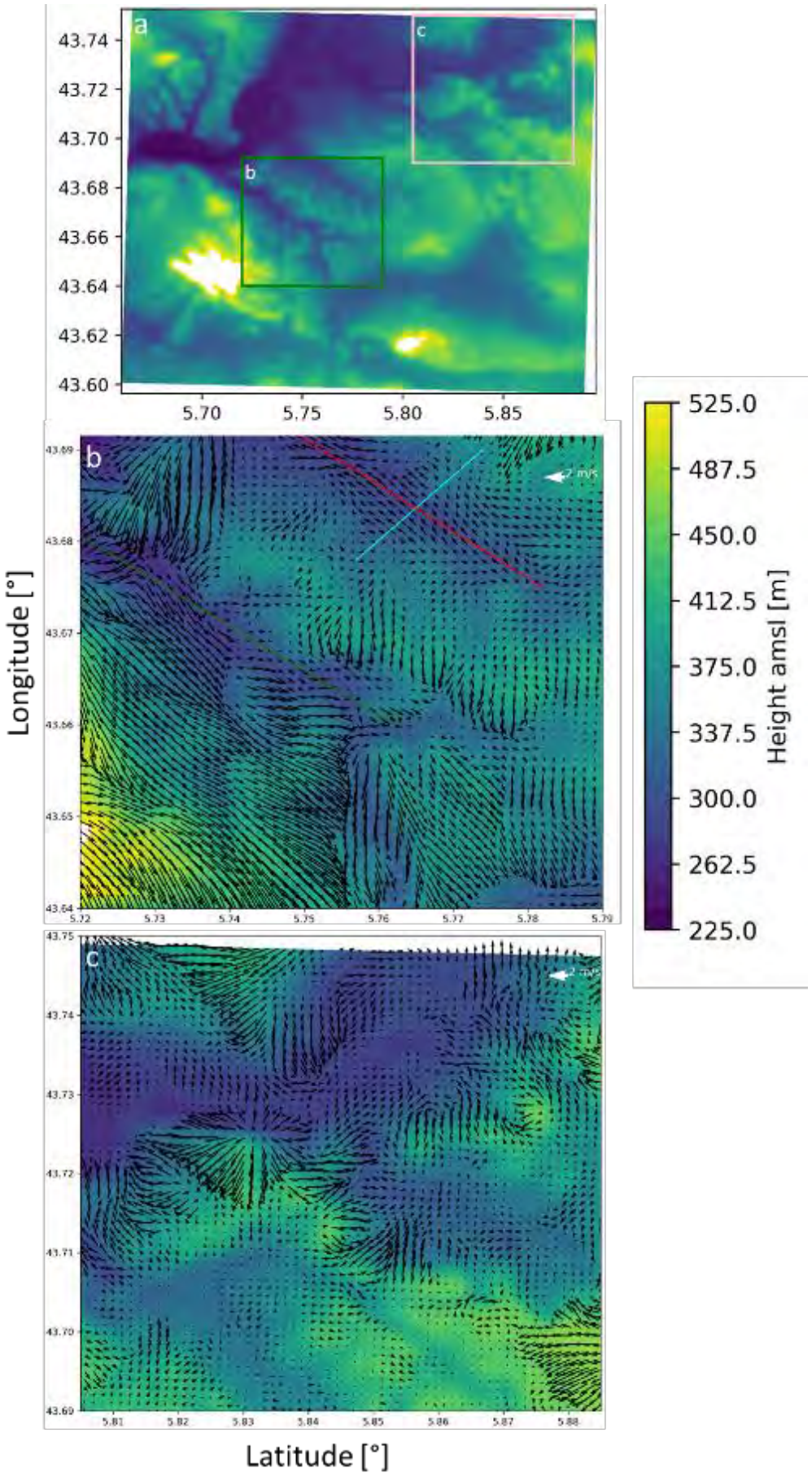

Figure 4.11: Height map and two arrow plots of the Cadarache region at midnight, focusing on the Abéou valley (b) and the Verdon valley (c).

4.5 Summary of Chapter 4

Altogether, the article shows that flows in sub-kilometric scale valleys can be resolved during stable night conditions with WRF in a parameterized setting. It improves the detail and the skill for the wind direction and shows good wind patterns. However, the finer-scale simulation brought no improvements on the daily temperature range, or they were inhibited by a too early arrival of advected moisture. However, the vertical structure above the valleys matches relatively well with radiosondes and Sodar observations.

The fine-scale simulated flow allows additional analyses in and around the Cadarache Valley. They revealed many different processes affecting the local flows, emphasizing the importance of a correct representation of complex terrain and its related circulations. Even when the CV has a downvalley flow, other valleys may show upvalley flows or little flow altogether.

The stability in the CV originates from faster cooling of the valley floor than cooling at the sidewalls. Changes and disturbances of this cooling system coincide with wind regime changes. At first, the arrival of the moist air flips the simulation to a system where the sidewalls cool at similar rates as the valley floor or faster, while it only causes a disturbance in the observations. The wind change to a DDV regime has little effect on the simulations but causes the observation to change to a system with stronger cooling on the sidewalls.

Model simulations at these scales give a lot of interesting data and many more analyses can be done based on the one presented here. Especially these fine-scale simulations show how processes interact and highlight the huge impact of topography more clearly.

Chapter 5

Transport and dispersion of passive tracers in the fine resolution simulation over the Cadarache Valley and neighboring valleys

In this chapter, I discuss the flows within the region of the Cadarache Valley, using tracers to understand the flow paths and possible stagnations through buildup of tracers. I completed this research near the end of my thesis thus the analyses are not extensive everywhere. This chapter will describe passive tracers, their use, release points, and release rates. I continue with a section describing flow development within the region during KAS17-IOP07, already studied in chapter 4. Lastly, I conclude the chapter with my major findings and prospects of the use of tracers.

5.1 Background on tracers

In the Annex 4: WRF technical explanations, I explain the numerical methods for implementing tracers in the WRF model and describe a problem with numerical models and tracers. This section focuses on the types of tracers, their uses, and some examples in meteorological models.

5.1.1 What are tracers

Simply put, tracers are substances (aerosols or trace gases) transported by the wind and dispersed by turbulence. Over time, their distribution in space makes it possible to understand the air motions responsible for their displacement.

From a model development point of view, tracer plumes give ideas of how otherwise hard to observe quantities or processes take place. Tracers explain how the model works and its flows move, allowing the evaluation of parameterization of uncertain features. From a more observational point of view, they can help make easier the analyses of the major contributions of releases or sinks of pollutants, radionuclides, or greenhouse gases.

For each purpose, different types of tracers exist; the two main types are passive and active tracers that can have a certain lifetime or decay, making them more suited for long-term simulation as the removal keeps newly emitted high-concentration plumes visible. Another option to remove tracers is gravitational settling, which moves any tracer towards the soil until it deposits.

Passive tracers are chemically inactive and only move as the model displaces air parcels. These are often used in model development, flow investigation, or tracing components with little interaction. In contrast, active tracers interact with other species, radiation or the surface. E.g., WRF-CHEM extends the default WRF simulation with active tracers in the form of chemical species, allowing the study of methane or NO_x emissions, their transformation and sinks.

5.1.2 Numerical tracer release in weather models

Numerical tracers have no limit to where or how they should be released. A common way of introducing the tracers is by releases at a certain point, over a line, or a surface. In models, these release locations are not limited to a certain height. i.e., they can be at the surface or at the height of a chimney. An example of a surface emission would be methane from a swamp. In contrast, a chimney has a point emission. For the timing of tracer releases, common options are continuous releases, sporadic releases, and periodic releases. Sporadic releases happen at one moment and continuous releases add more tracer to the simulation at every time-step. The periodic releases can combine the two, allowing releases to happen only during certain times or a sporadic release at an interval. Examples of periodic releases are volatile organic compounds released by plants under the influence of sunlight or temperature (Peñuelas & Llusià, 2001), while a leaking tank has a continuous release, and an explosion has a sporadic release.

As mentioned above, tracers are a common tool in evaluating and developing models. Bhimireddy and Bhaganagar (2018) show parcel trajectories of tracers released at several heights in different types of convective atmosphere to determine the effects of boundary-layer schemes on particle spread. Otherwise, the development and verification of convective and thermal schemes from comparisons of LES and mesoscale modeling is based on tracer thresholds by Couvreux et al. (2010) and Rio et al. (2010). Ngan and Stein (2017) have four tracer cases simulated with several models and settings, comparing the results for dispersion applications, revealing that WRF has slightly better statistics than the NARR (North American Regional Reanalysis). Yver et al. (2013) verify the improvements of WRF settings through the improvements of tracer fields. Similarly, Angevine et al. (2014) assess the uncertainty of WRF simulations with tracers spread. While some studies look to understand flows in real places, Quimbayo-Duarte et al. (2019a, 2019b) investigate flows of idealized valleys with help of tracers, showing valley interaction and internal flows. Other research uses them for pollution dispersion as Blaylock et al. (2017), where tracers indicate the effects of lake winds on ozone produced in Salt Lake Valley (containing Salt Lake City).

In short, tracers help visualize possible trajectories of gases or particles transported by the wind or help understand how a model handles a situation such as a valley wind or processes like turbulence. These applications show that tracers are a useful tool, but tracer simulations are hard to verify without measurements datasets of particles or gases.

Next to limited verification options, tracers in Eulerian models suffer from numerical diffusion reducing the reliability of the simulated tracer fields, because it reduces the sharpness of concentration transitions. Since Eulerian models work with well-mixed cells finer resolution reduces the diffusion error and a point release concerns a whole cell. Even though the expected diffusion is small, the tracer plumes should not be examined per cell but according to their wider patterns.

The benefit of Eulerian models over Lagrangian model is that the Eulerian have their own wind fields at every calculation step and include much more temporal variation. In comparison, Lagrangian models have a temporal resolution as fine as the wind fields supplied to them.

I implement the tracers by adding extra variables to the WRF code using the same calculation steps as other scalar variables such as water vapor. My implementation follows the work of Blaylock et al. (2017) described in Annex 4: "WRF technical explanations”.

5.2 Tracer set-up

Above I have introduced passive tracers, their implementation into WRF, and a main problem of tracers in Eulerian models. The tracers are released in a simulation of the already investigated KAS17-IOP07 to complement and extend the analyses done in Chapter 4. This section will detail the release locations, times, and fluxes.

5.2.1 Locations

In total, I have implemented eight different cells with tracer releases, which are divided into two groups of four, the CV release points and the regional release points. Half of the release points are in the CV because that is the area with my main interest, while the other four serve to better understand surrounding flows that possibly influence the CV flows. Figure 5.1 shows the different locations and Table 5.1 has extra details on the exact locations and quantities of tracer released.

In the CV, I selected four locations, consisting of two places with both a near-surface and an above-surface release. The low valley release points (CV1 and CV2) are near the confluent zone of the CV and DV, slightly on the southern sidewall. The others (CV3 and CV4) are up-valley, near the end of the SE-NW orientated section, again on the southern sidewall. Both locations have near surface releases (CV1 and CV3, level at 0 – 10 m agl), while CV2 is in the fourth model level (30 – 40 m agl) and CV4 in the third (21 – 30 m agl). The strategy of these four release points (even though I refer to it as a point, it is actually one cell) is to differentiate releases at the ground and at altitude while also investigating the difference between low- and up-valley releases. To show if the wind interactions near the confluent zone differ from those in the upper valley and if the height of the release is important in the simulations. Figure 5.1 describes the region around Cadarache: the DV is north and west of the CV; to the south, parallel to the CV, is the Abéou Valley (AV) and the mountain ridge “La vautubière” (LV); in the southeast, there is a plane called “plan de Valavès”; in the northeast corner is the Verdon Valley (VV).

I also selected four locations in the region that will show how the flows work around the CV. I placed the release point at locations that should show the typical flows in the region. These release points are in the previously mentioned valleys of the Durance, Abéou, and Verdon. In the DV, the tracer release is within the area with peaks of the valley wind jet (113 – 153 m), showing where the DDV flows have their strongest influences. In the AV, the tracer location is at the valley floor, where it is well protected from the direct influence of the DV, and just down-valley of the junction of two upslope valleys, ensuring information on the flows of the AV. In the VV, I placed two tracer release spots, VV1 on the east side of the large basin, at heights similar to those of CV1 and CV3 (0 – 10 m), to investigate the flows in and around the basin. A second tracer release point near the west wall of the basin in the fifth model level (40 – 60 m) accompanies VV1 to understand higher VV flows that possibly pass over or penetrate the CV. I placed two tracer sources in this valley because in Chapter 4 I showed the possibility of flows from the VV entering the CV, which merits further investigation.

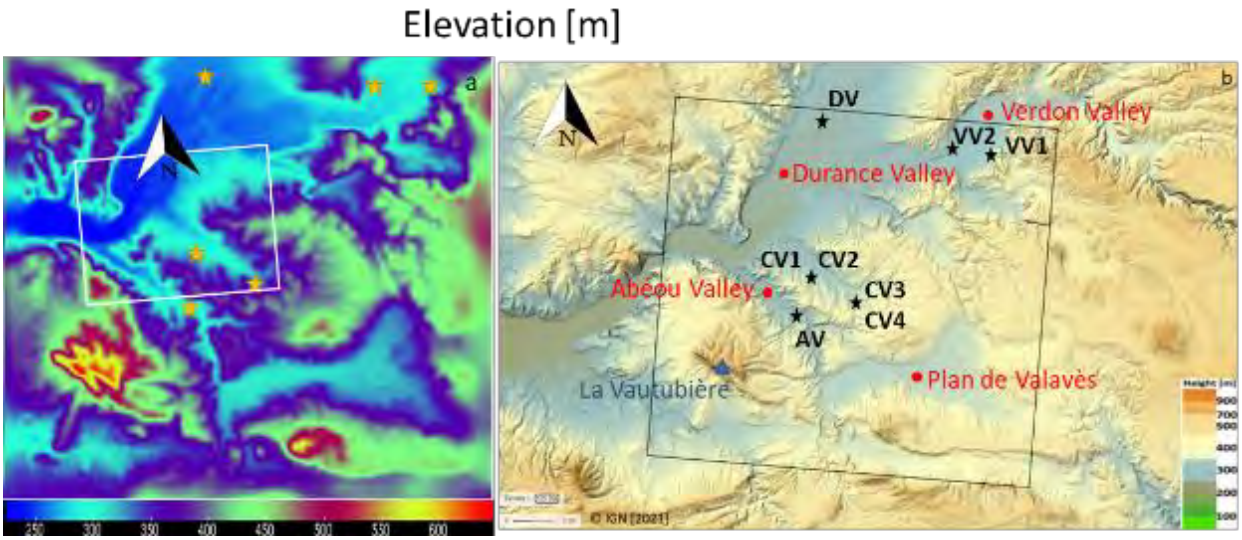

Figure 5.1: Topographic map indicating the locations of tracer release points in the 111 m resolution domain of the WRF simulations, (a) shows the heights as used by WRF with a white rectangle pointing to the zoom-in area over the CV for section 5.3.1.1, while (b) shows the real heights, with a black rectangle indicating the WRF domain. Stars indicate tracer release points, gold in (a) and black in (b). Red dots indicate valleys and basins in (b) and a blue triangle indicates the "La Vautubière" peak.

5.2.2 Magnitude of tracer releases

Table 5.1 gives additional information on the locations, release timing, and release flux. I release all tracers simultaneously, with the same amount released per second, but without a burst at their first-time step. However, the amount that resides within the domain can vary due to advection out of the domain, meaning it is lost. Nonetheless, this allows comparing the different tracers because each point adds similar quantities to the domain. Thus, concentrations are adequately comparable, allowing the determination of places with stagnation and comparing those locations with other tracer release points.

Table 5.1: Details about the tracer release locations, release duration, and the amount of released tracer.

TRACER RELEASE LOCATION	LOCATION [°N; °E]	RELEASE HEIGHT [M AGL]	START TIME	END TIME	CONTINUOUS RELEASE [S^{-1}]	TOTAL RELEASE [-]
CV1	43.686; 5.754	5				144
CV2	43.686; 5.754	35				144
CV3	43.672; 5.784	5	18:00	06:00		144
CV4	43.672; 5.784	25	UTC 20	UTC 21	$3.33*10^{-3}$	144
DV	43.747, 5.759	133	February	February		144
VV1	43.737, 5.872	5	2017	2017		144
VV2	43.737, 5.851	50				144
AV	43.667; 5.749	5				144

5.2.3 Timing

I set the starting time for tracer release at 18:00 UTC, roughly one and a half hours after sunset, allowing the formation of small valley nighttime flows and after most of the southern advecting winds (see Chapter 4) faded. In contrast, the larger scale DDV flow did not yet reach this section of the DV at this time. I stop the analysis after 12 hours at 06:00 UTC, roughly one hour before sunrise, to ensure that I remain in nighttime conditions and avoid convective conditions since those are not my main interest for this study.

5.3 Results

After describing the tracer types, exact quantities and timing of the releases into the domain, I will continue with the analysis and the comparison among the different plumes. I start with the horizontal maps of the four CV tracers, followed by an additional analysis of vertical cross-sections in the CV, and then analyses of the other valleys. Note that all horizontal cross-sections show a column sum including the lower 16 model cells unless explicitly said otherwise. This column sum does not allow for in-depth analysis of vertical distributions but allows me to see trajectories and horizontal behavior changes because vertical movements is limited in stable conditions. When needed, additional knowledge on the vertical distribution is obtainable with vertical cross-sections.

The simulation uses the same model settings as given in the article of Chapter 4. It has 46 vertical levels, with a spread that gives the lowest seven model layers with their cell center below 100 m agl and fourteen cell centers in the lowest 500 m agl.

5.3.1 Cadarache valley tracers

This section starts with a zoom on the CV, outlined by the white rectangle in Figure 5.1a and discusses CV3 and how the other three CV plumes vary from the CV3 plume; vertical cross-sections of the CV and its perpendicular are displayed. Afterward, I continue with an analysis of the CV1 and CV3 tracer because the others resemble them a lot. The section finishes with the other 4 tracers over the full domain.

5.3.1.1 Flow within the CV

Figure 5.2 only shows CV3 but since within the valley the four CV plumes resemble, I only show the CV3 and make a few comments where other CV plume differ. A common trend between the higher release points (CV2 and CV4) and their near-surface equivalent (CV1 and CV3) is that the high releases are more spread out than the near-surface ones and are slightly further displaced from their source, indicating stronger mixing and slightly faster wind speeds higher aloft.

Early in the night, Figure 5.2a shows the CV3 plume moving to the NW. However, it does not match the exact CV orientation as it shifts toward the north compared to the CV axis (red line), capturing the last moments of the moisture advecting winds (see **Figure 11; p. 18)** of the article in Chapter 4 for more information on these winds). This pattern is the same for all plumes but note that the CV1 and CV2 release progress further to the west and penetrate the DV deeper. I do not consider these early night winds yet representative for stable night flows as they originate from large-scale advection. However, they could be confused with Cadarache down-valley (CDV) flows because they are close in orientations (see the wind direction at GBA in Figure 4.1). The moisture advecting wind dies down and the plume resumes the CV orientation at 19:00 as shown in Figure 5.2b.

Later at night, flows cause the CV plume to move in up CV direction, as I will discuss with Figure 5.3, especially on the southern sidewall as highlighted with the CV1 and CV2 tracers. At the same time, the northern sidewall and valley floor shows more tracers towards the DV, as shown by Figure 5.2c and the vertical cross-sections of Figure 5.3 and Figure 5.4. These northern sidewall plumes do not pass a certain location in the valley (43.70°N; 5.74°E). Until sunrise, the situation remains roughly constant with the same amount of tracer leaving the CV as added by their release point. Before sunrise, Figure 5.2d shows that the flows cause plumes within the CV, with up and down-valley components. The flow still does move beyond 43.70°N; 5.74°E and a built-up of tracer starts here.

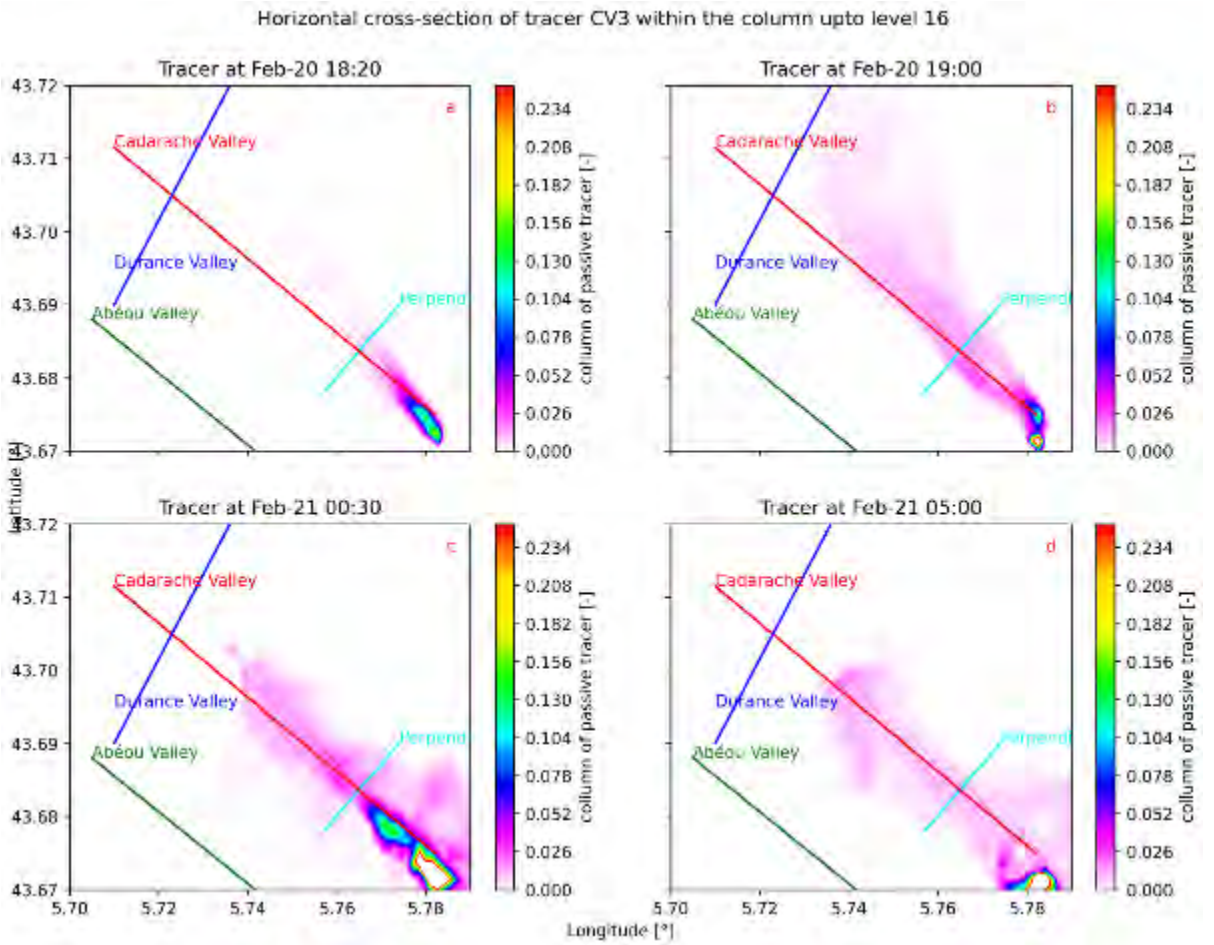

Figure 5.2: Column amounts of the CV3 (0 – 10 m agl) tracer at four different times. Plot (a) at 18:20 UTC, 20 minutes after the start of the continuous release, (b) at 19:00, (c) at 00:50, and (d) at 05:00

The up-valley winds are surprising because studies of Duine (2015) showed they started above the valley ridges and LEMS in Dupuy (2018) observed up-valley flows near the top of the ridges but hardly over the valley thalweg. Regarding flows on the sidewalls, Dupuy (2018) finds that the sidewalls and ridges of the valley have more directions than only the CDV flow, indicating the presence of other flows. Nevertheless, the model exaggerates these influences and subjects the whole valley to them. Clear conclusions are hard to achieve because I have limited observations in the CV-DV confluent zone. The main candidate for the source of these up-valley flows is the DDV flow, which arrives around the same time as the flow reversal occurs. I will discuss this flow after presenting the broad view of the domain.

Figure 5.3 and Figure 5.4 show vertical cross-sections within the CV at 00:30 UTC, when all CV plumes reveal upvalley winds but tracer concentrations remain considerable in the valley. Figure 5.3 shows the perpendicular cross-section and Figure 5.4 the along valley cross-section, as indicated on the previous figures by the cyan and red lines, respectively. All vertical cross-sections show a plume at around 800 m amsl, which forms around 20:30 when the DDV arrival pushes back the CV plumes that entered the DV (Figure 5.2b) and elevates these plumes. This plume moves up-valley slowly, visible in Figure 5.4 (or disappears in the west before disappearing in the east). Further analyses of the cross-sections of Figure 5.3 and Figure 5.4 show that the plume is removed first above the southwest sidewall (Figure 5.3) and the northwest lower sections of the CV (Figure 5.4), meaning that a western wind pushes away the plumes from that part of the CV.

Now below 500 m amsl, Figure 5.3 shows how they distribute themselves over the valley sidewalls, showing two layers with tracers. The first layer is at the valley floor highlighted by CV3 (Figure 5.3c) and CV4 (Figure 5.3d), with its concentration close to the surface and deeper near the north sidewall than the south sidewall. The second layer is roughly 100 m above the valley floor and is almost at equal altitude along the perpendicular cross-section. It shows its highest concentrations close to the sidewalls and not above the thalweg. Note that the CV1 and CV2 tracers are released downvalley of this cross-section. Lastly, between these two layers is a small layer with less tracer.

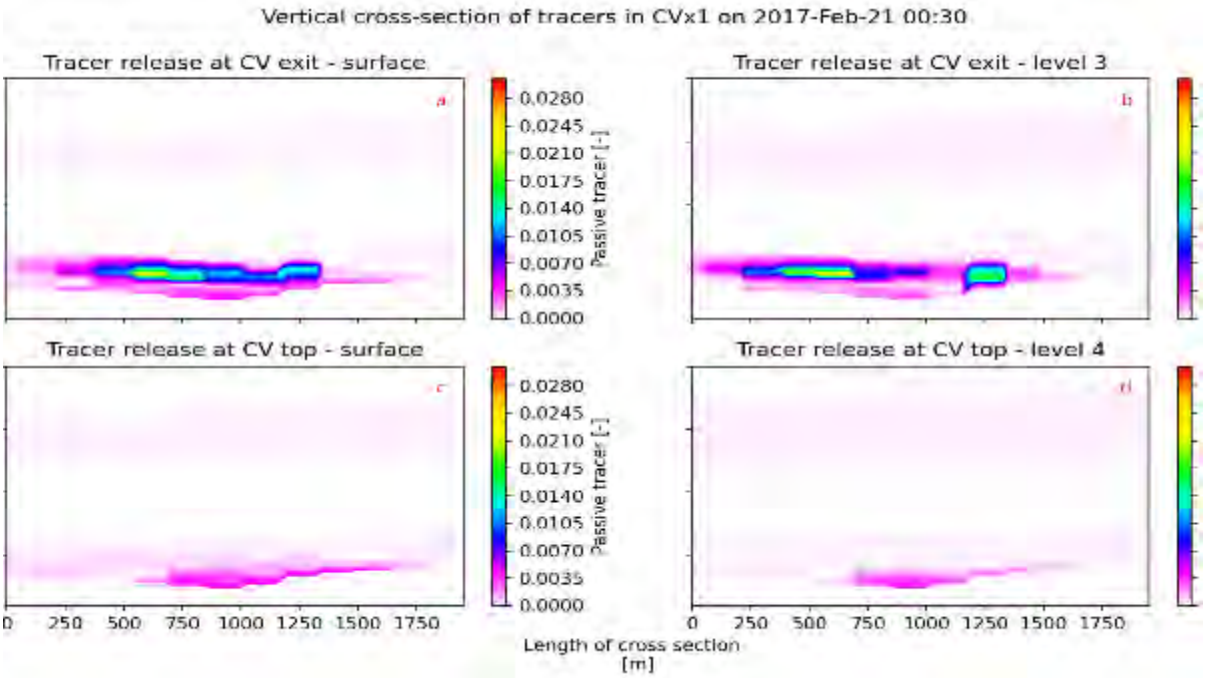

Figure 5.3: Vertical cross-section of the CV perpendicular to its axis, with tracer amounts present at 00:30 UTC. Plot (a) is CV1, (b) is CV2, (c) is CV3 of Figure 5.2, and (d) is CV4. The left side of the cross-section corresponds to the southwest end of the cyan line of Figure 5.2.

Figure 5.4 shows the along-valley situation of tracer flows at 00:30. Considering the cross-sections of plumes of CV1 and CV2 between 5000 and 7000 m along the thalweg, they show the two layers, confirming the observations made on Figure 5.3a and 5.3b, both seem terrain following in the along valley direction.

Additional investigation of the time series of the two vertical cross-sections reveals that the higher of these two flows transport plumes up-valley, whereas the near surface flow has a CDV direction. The order of these layers matches with the CDV, shear layer with opposite direction as displayed in Duine et al. (2017) except for their heights. However, surface flows are less thick than observations of Duine et al. (2017) and the shear layer much thicker. The layers seem to split from a small bump in the thalweg around 5000 m and further upvalley. In the model, the bump causes a low point that can cause stagnation of air, where during down-valley flow moments, part of the flow sticks to the surface while another part remains at roughly the same altitude. Around this bump, all release points show the thickest layer. Inspection of the time series shows that the separation between the two layers is not present in the simulations downvalley of the aforementioned bump. Further inspection of the vertical cross-section around 05:00 shows a vertical column of tracers building in CV3 and CV4 near the halting point visible in Figure 5.2c and 5.2d.

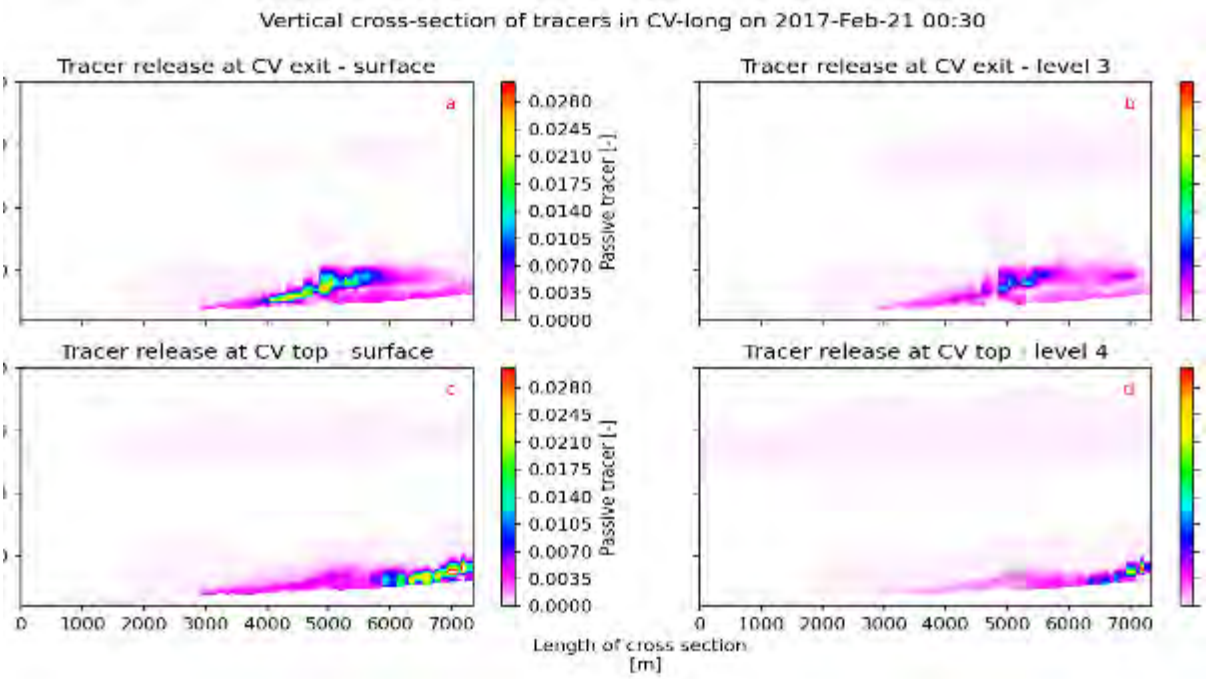

Figure 5.4: Along the CV thalweg cross-section showing the four tracers released in the CV at 00:30 UTC, (a) is CV1, (b) is CV2, (c) is CV3 of Figure 5.2, and (d) is CV4. The left part of the plot coincides with the northwest end of the red CV line in Figure 5.2.

Altogether, the tracer fields show that the model produces both up- and downslope winds. Within the CV, two flow layers exist, the valley floor flows, and equal altitude flows with opposing directions. Flows along the CV slope contribute to the flows at the valley floor, especially releases at the surface show a larger contribution to the floor flows, but the above surface releases contribute too.

5.3.1.2 Flows exiting the CV

I discuss the CV1 and CV2 together, because they show the same pattern. Figure 5.5 shows the CV1 plume over the complete domain. After plumes leave the CV early in the night, they move in up-valley direction on the DV (Figure 5.2a), then DDV flow arrives and pushes them back down, as shown in Figure 5.5a. The plumes move towards the western border and some penetrate the Abéou Valley, CV2 also flows towards the AV, but remains more compact. In the next few hours, the upvalley winds continue in the CV and Figure 5.5b shows that the plume leaves the CV on its southeast end, then flows south through a gap in the mountain ridge (see Figure 5.1). The plume that passes through the gap continues west towards the DV lower section. During a period with less up-valley flows, as seen in Figure 5.5c, the CV has built-up tracer, but a large part continues to the south and passes through the “plan de Valavès” basin on the east, to leave the domain on the southeast corner. Before sunrise, large outflows from the CV cease and its local flows become more important, as the plume remains within the CV. Figure 5.5d shows that the plume splits. One part starts a descent along the AV and eventually reaches the DV again through either the CV or the AV. Another section of the plume begins to stagnate in the “plan de Valavès”.

The CV2 tracer shows nearly identical patters as the CV1 but has lower concentrations.

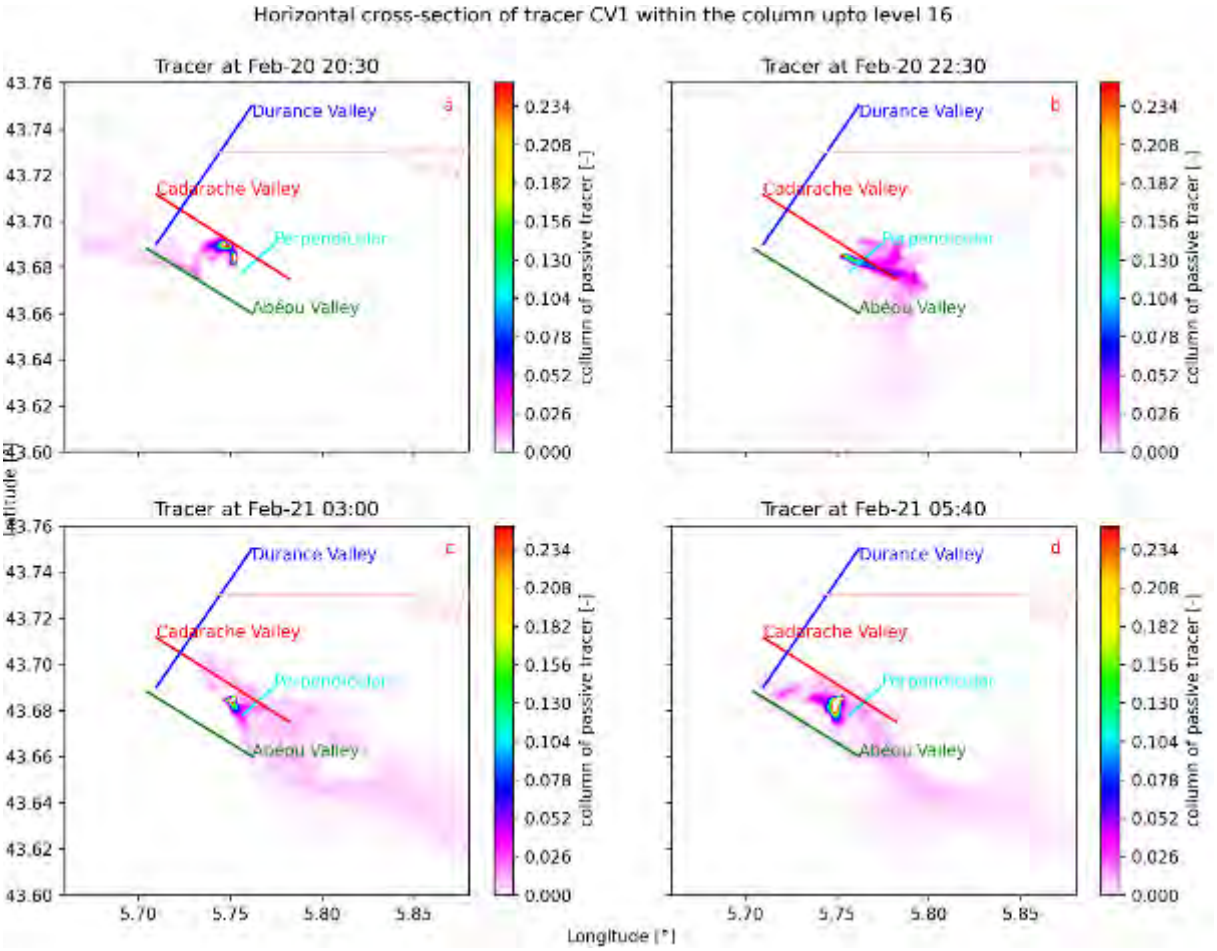

Figure 5.5: Column amounts of the tracer released near the surface of the Cadarache Valley center are shown over the whole domain at four different times. The blue line indicates the Durance Valley, the red line indicates the Cadarache Valley, and the cyan line indicates the perpendicular cross-section, Green is the Abéou Valley, and pink indicates the Verdon Valley. Plot (a) shows plumes at 20:30, (b) at 22:30, (c) at 03:00 and (d) at 05:40.

CV3 in Figure 5.6 shows similar patterns to those of the already discussed tracers of CV1. A noteworthy difference in the early night is that this tracer of CV3 does not enter the AV, as shown by Figure 5.6a. Further development in the night shows the starting influences of up-valley wind in Figure 5.6b, causing the tracer to concentrate near the CV high-end and flow toward the south but not as far as CV1 and turns to the “plan de Valavès”. These winds strongly influence this release, leading to Figure 5.6c, where the plume goes to the southeast corner of the domain. This pattern persists for the rest of the night, although it diminishes in strength. In Figure 5.6d, the slowing down of the flows is noticeable through the return of CDV flows, the stagnation in the plan de Valavès, and with closer inspection flows down the AV, with a large plume near the entry of either AV branch valleys.

In short, the CV plumes that exit the CV on the southeast end generally flow into the basin “plan de Valavès”, continue towards the southeast and exit the basin and simulation domain in that direction. Near the end of the night, stagnation starts in the basin, but still, a part of the tracer leaves the basin and exits the simulation domain. Simultaneously, the tracer exiting the CV have down-valley flows penetrating at both AV ends.

These findings shed a new light on the previous valley studies since earlier the CV downvalley flow was considered the only important flow for transport at low heights in the CV. However, the plumes show that on the sidewalls and near the high-end of the valley have influences of the shear layer observed by Duine et al. (2017) above valley. And that flows from the CV can leave the valley in its southeast corner.

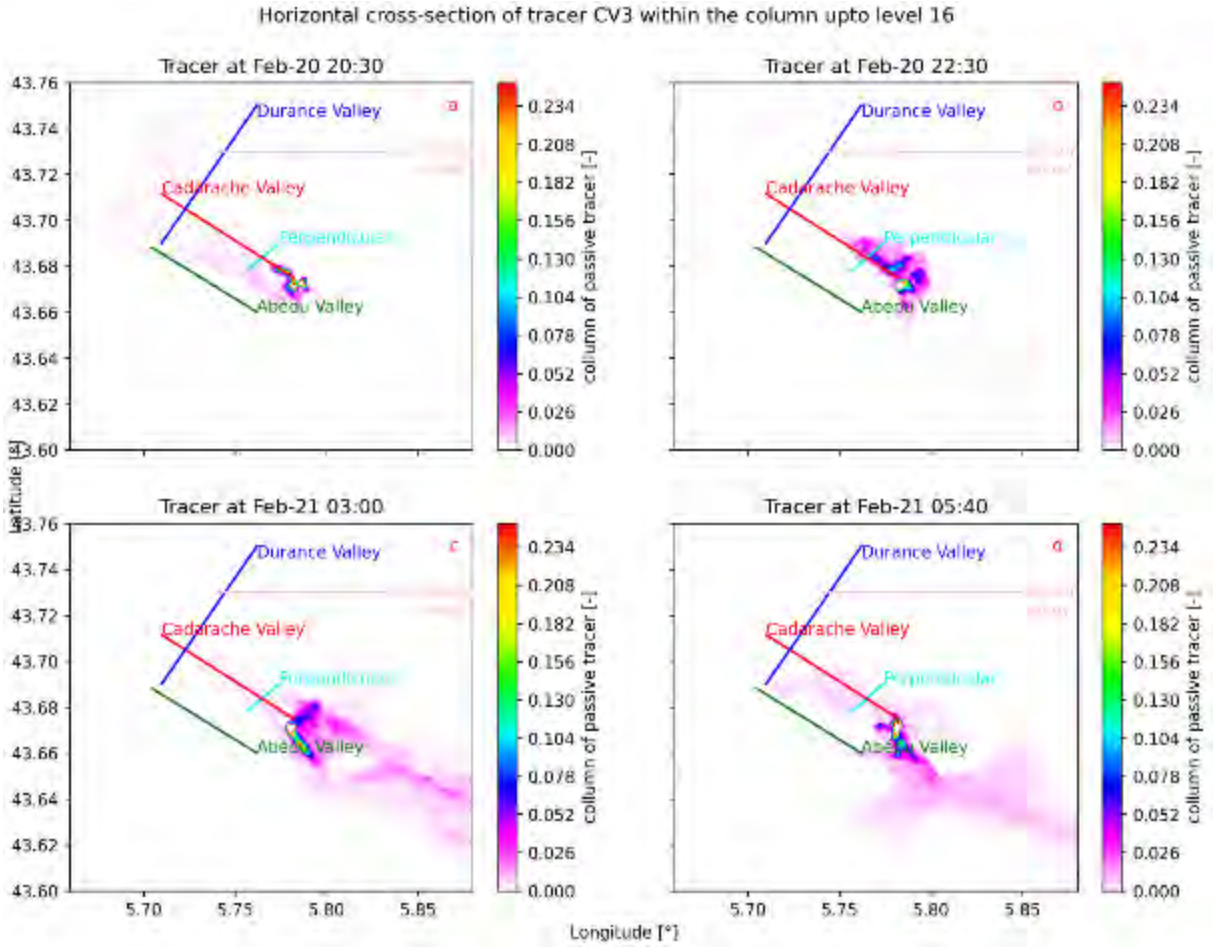

Figure 5.6: Same as Figure 5.8 but for the CV3 tracer released near the surface at the high-end of the Cadarache Valley.

5.3.2 Durance Valley

After focusing on the Cadarache Valley, I will describe the other valleys that received a tracer release point. Starting with the Durance, the tracer is released at a height within the DDV flow jet.

5.3.2.1 Flow remaining in the DV

The flow in the DV arrives later near the CV because it needs roughly 6 hours moving from up-valley to down-valley (Duine, 2015). Figure 5.7a shows the situation before the DDV wind arrival when the tracers still leave the domain toward the north and are therefore not visible, as the release is very close to the border. Half an hour later, the DDV flow starts and needs two hours to settle, like in Figure 5.7b. Starting after four hours, which is two hours before the typical 6 hours described in Duine et al. (2017) and one hour before the observations, see Figure 4.1. The DDV flow inhibits the CV and other tributary valleys (Figure 5.8, Figure 5.9, and Figure 5.10) from further draining into the DV during its settling and removes all tracers deposited in the DV by other valleys, shown above for the CV tracers. Figure 5.7b shows the plume in the settled DDV flow as a narrow line that veers when approaching the mountain ridge of LV.

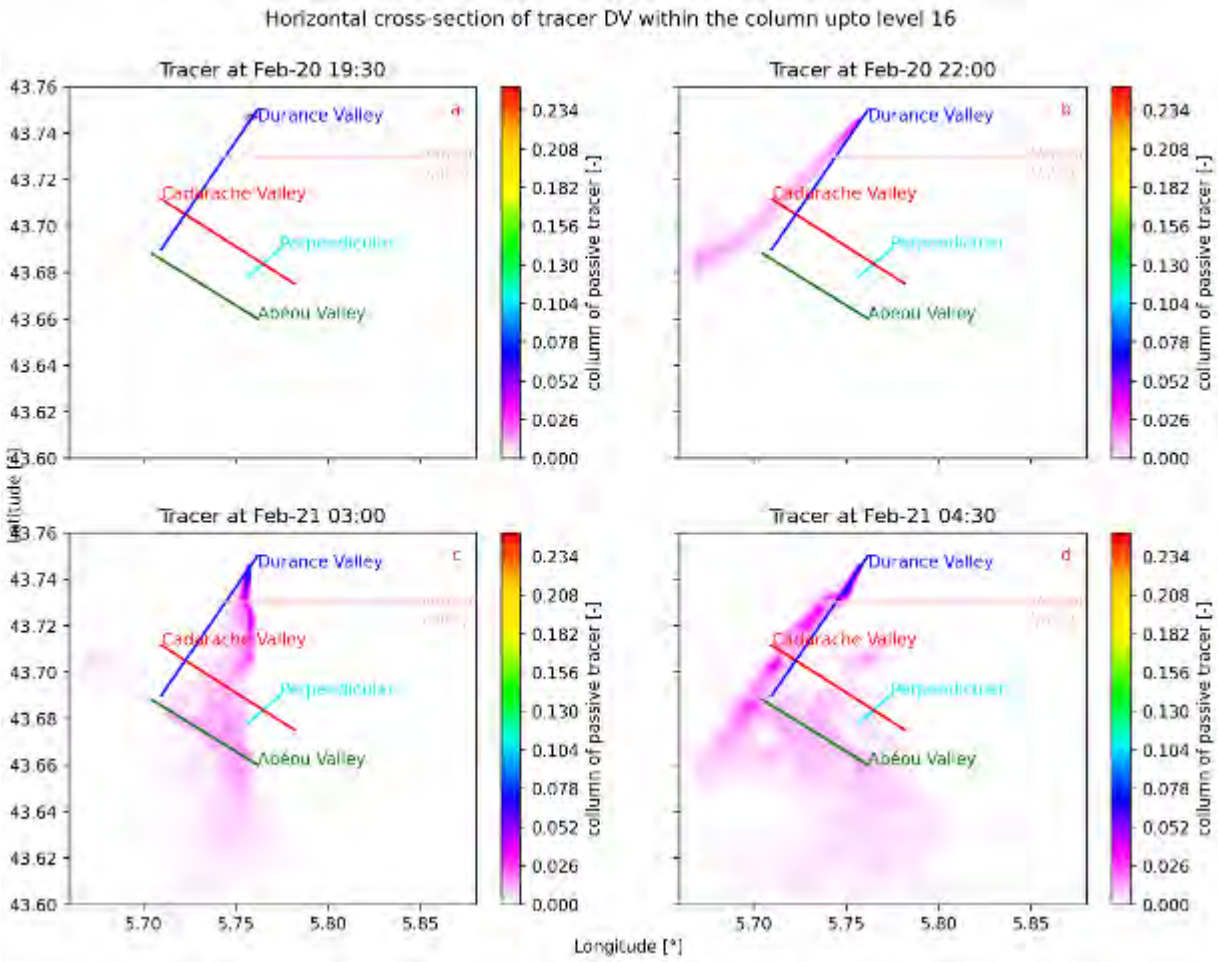

Figure 5.7: Column amounts of the Durance Valley tracer released at 113 – 153 m agl at four different times. Plot (a) 19:30, (b) 22:00, (c) 03:00, and (d) 04:30. The blue line shows the Durance Valley. The red and cyan lines are the Cadarache Valley and its perpendicular, respectively. The green line shows the location of the Abéou Valley and the pink line shows the last section of the Verdon Valley.

After 22:00, the plume slowly turns to the south until 03:00 UTC, when it flows directly south and starts to meander as shown in Figure 5.7c, losing strength in the flow demonstrated by increasing tracer amounts. This reduced DDV flow strength allows other valley flows to return to behaviors from before the DDV arrival. Figure 5.7c shows that the plume hardly leaves the DV in the DDV direction as earlier. They now fill up the AV and flow to the south near the gap on the east side of the Vautubière ridge.

At 04:30 UTC, Figure 5.7d shows that the DDV flow restored its previous direction. However, the plume spread is still visible over the area between the CV and LV. Now, the DV plume is present in the AV as well as around LV, is channeled through the AV and then to the south, whereas the CV contributes to filling the basin of plan de Valavès. Only a small tracer amount enters the basin (a small bulge at 43.63°N; 5.81°E in Figure 5.7d is going to the basin), which eventually flows to the SE corner as the CV tracers do. In the DDV flow itself, a few locations have higher tracer concentrations than others, which relates to lower wind speeds and less continuous flows, allowing parcels to gain more tracer before moving along the DV. After restoring the DDV flow system, the flow around LV fans out wider than before.

5.3.2.2 Flow blocking by La Vautubière ridge

As mentioned above, the DDV flow veers where it meets the ridge that includes LV (43.70°N; 5.70°E). In the early night, when the DDV flow reaches the south end of the middle DV, it veers and continues into the Durance lower valley, having only a small change in direction, as illustrated in Figure 5.7b. The

plume remains in comparable situations until the flow turns to the south and the plume comes closer to the surface, entering the AV and circumventing the LV ridge on its eastern side through another gap. These flows go in the Abéou up-valley direction, after exiting the AV, they move south and through the gap to join the DV in its lower section. Generally, the LV has limited influence on the western part of the DDV flow, as shown by tracer fields in Figure 5.7. However, investigations of the AV (section 5.3.3) show that the influence of the DDV wind starts earlier.

To investigate the parts of the DDV flow that influences the AV, I assume that the perturbation of the DDV flow results in situations representable for the normal situation of the AV when the DDV flow influences it. Based on those flows, I can say that the DDV flow enters the AV through downslope flows along the sidewall and causes up-valley flows in the AV, influencing low elevation areas. Most of the flows circumventing LV on the east will flow south and fan out south of the ridge, although a fraction will enter the basin north of the ridge. Showing that the DDV flow causes up-valley flows in the AV, investigation of the AV tracer should hold for DDV flows entering the AV.

The DDV wind exerts a strong influence on the valleys in the region, as it has the strongest wind and moves on the largest scale, especially the AV experiences large influences from the DDV wind. When the DDV flows weaken, other flow regimes start in smaller valleys that react faster to the change than the large DV system. The steadiness of the DDV flow determines to a large extent the effects it has on the DV tributary valleys.

5.3.3 Abéou Valley

After discussing the DV, I will now continue with smaller valleys such as the Abéou Valley, which experiences influences of the DDV flow as discussed above, but here I investigate the whole night flow instead of a few highlights. Figure 5.8 shows the flow development as visualized by the release of tracer in the upper end of the valley, just down-valley of the junction of two small valleys. See Figure 5.1 for a recap of the topographic situation.

Early night development shows that the AV has a down-valley flow system in place, as seen in Figure 5.8a, resembling the CDV flow (Figure 5.2b) in the early night. The AV flow does match the valley orientation already in the early releases, indicating the absence of influence from the larger-scale SW winds that do not match the valley orientation. I assume that the better match of the plume with the valley orientation in the AV than in the CV likely results from the valley geometries: the AV is deeper and less wide than the CV, as seen in Figure 5.1, which shelters the AV better from above valley influences. When the Abéou down-valley (ADV) flow reaches the DV, it fills the lower part of the DV and fans out north to a minor tributary valley west to the DV, as the “Clue de Mirabeau” causes a blockage for low-level flows. The blockage is enhanced by reduced topography, as the simulation smoothens the topography near the domain borders to prevent errors with the coarser domain. After the DDV flow arrival, the AV flow reverses and starts to flow up-valley, likely caused by channeling of the DDV flow that reaches the LV and is forced around, as seen in Figure 4.9b. At 22:00 UTC, Figure 5.8b shows all tracer transported further upslope from the release point, causing the AV plume to flow eastward and split into multiple streams. Part of them flows to the south and another part turns towards the plan de Valavès, similarly to the CV flows. Later the plume exits the basin through its south border or southeast corner and leaves the simulation domain in that direction, as displayed in Figure 5.8c. This plume does not match the DV flows through the AV of Figure 5.7, indicating that flow layers are at different heights and have different directions.

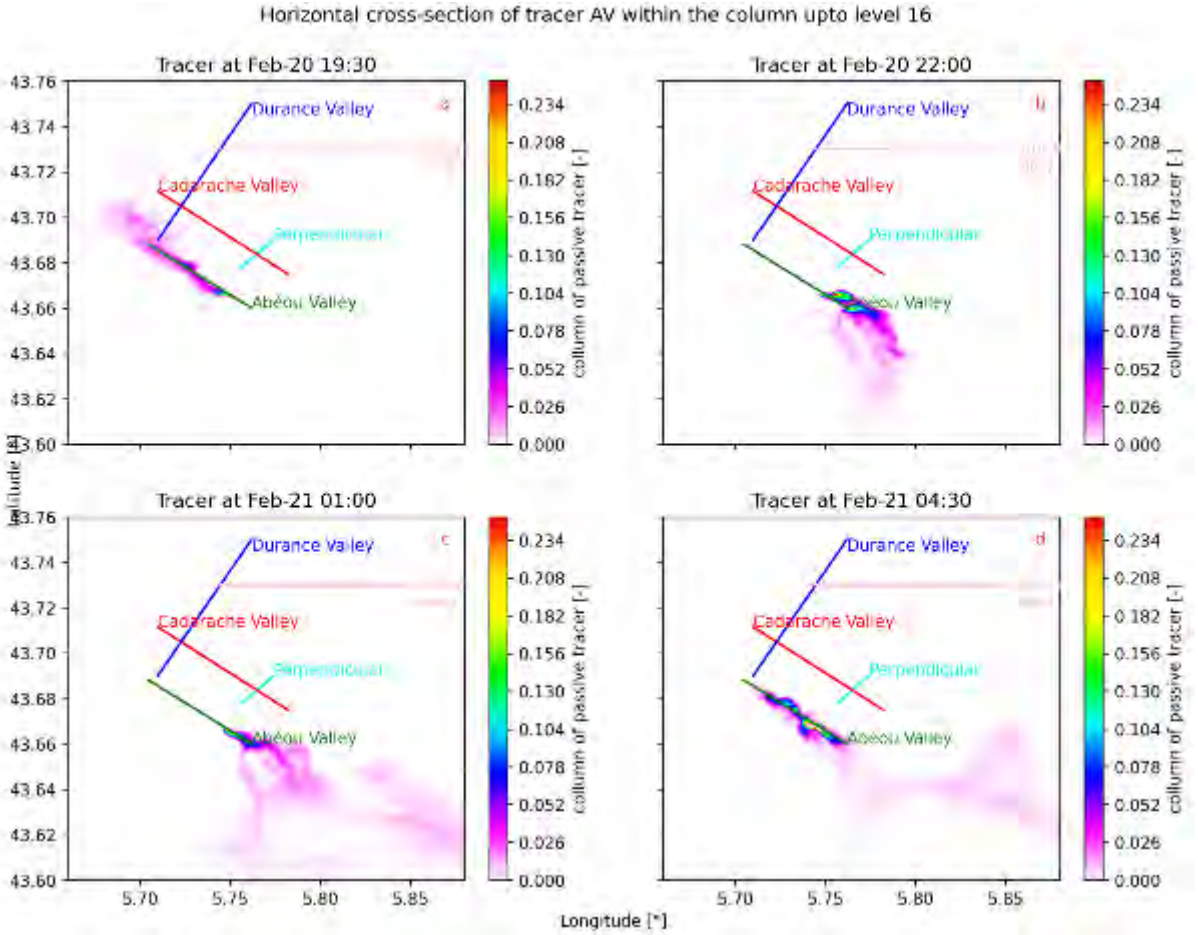

Figure 5.8: Column amounts of the Abéou Valley tracer released near the surface at (a) 19:30, (b) 22:00, (c) 01:00, and (d) 04:30. The blue line shows the Durance Valley, the red and cyan lines are the Cadarache valley and its perpendicular cross-section, respectively. The green line shows the location of the Abéou valley and the pink line shows the lower section of the Verdon Valley.

During the weakening and meandering of the DDV flow between 02:00 and 04:30 UTC, the AV flows return to down-valley flows but proceed more slowly towards the DV than earlier in the night since the DV provides flows that fill up the valley, preventing other valleys unobstructed flow towards the DV. Figure 5.8d shows that the plume past the ridge between the AV and the basin continues to flow towards the southeast, where a part exits the simulation domain. At the same time, most of the plume stays within the valley and flows in downslope AV direction.

Altogether, the AV flow is marginally influenced by above valley winds, as shown by its good match with the valley orientation. An exception is DDV flows forced into the AV through flow blocking, but the AV channels the orientation of the flows, leading to discharges into the basin to the east and to the south in the gaps in the Vautubière ridge. Vertical cross-section analyses of the AV tracer (not shown) show that the AV flow layer has depths comparable to the valley ridges. Extending these findings to the CV studies teaches that the AV flows have a depth comparable to that of the CDV flow observed during the KAS13 and KAS17, showing that the model can simulate valley deep flow layers as seen in the CV. However, the model does not create these layers in the CV, which is likely a result of small topographic mismatches, indicating that the CV topography is delicate for simulations.

5.3.4 Verdon Valley

Lastly, I will discuss the two tracers in the Verdon Valley (VV1 and VV2). These are VV1, east tracer, in Figure 5.9 and VV2, west tracer in Figure 5.10. These two release points are close to the sidewalls of a basin in the VV. Several valleys join just northeast of the domain, as depicted in Figure 2.1a.

5.3.4.1 Development in the valley

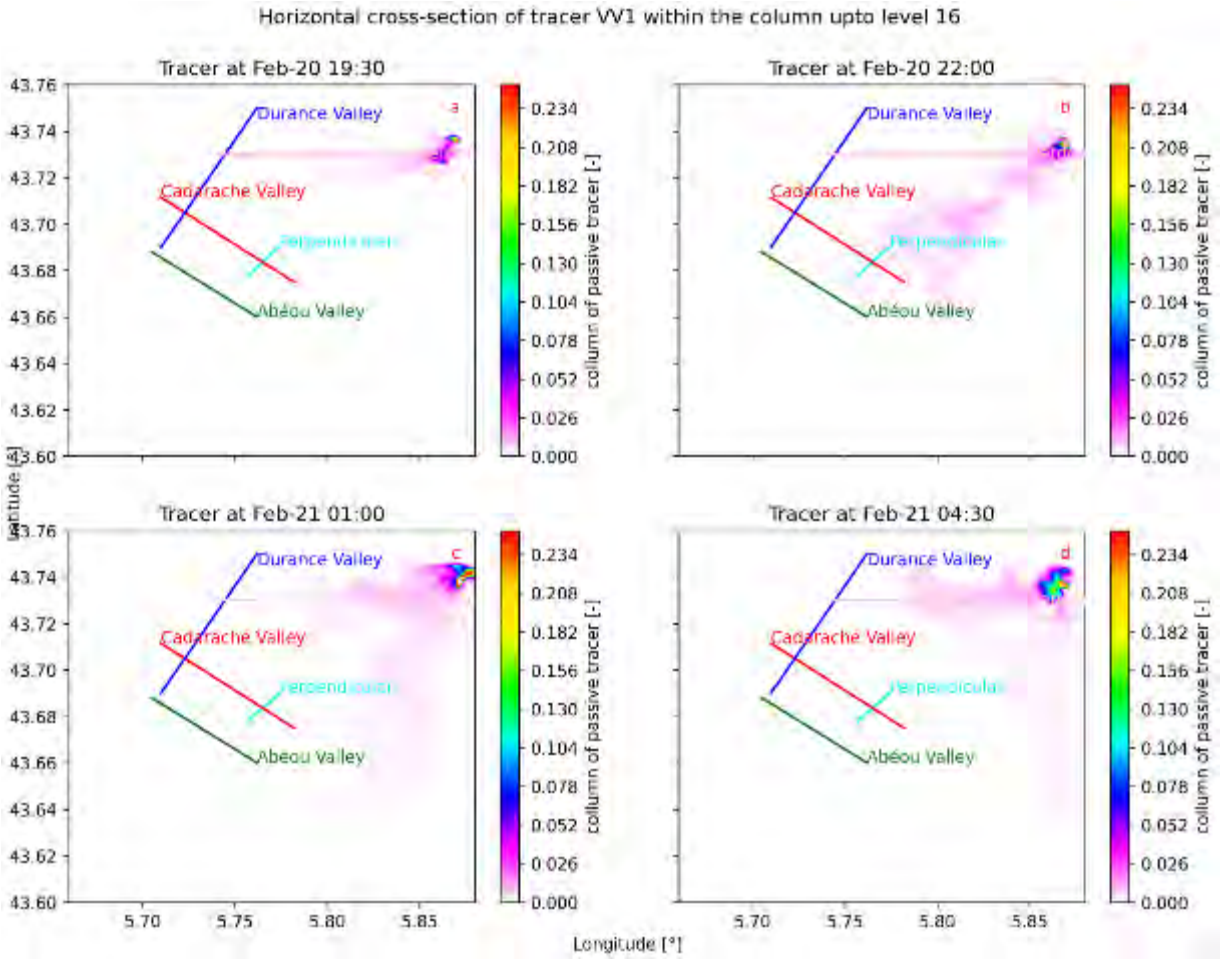

Figure 5.9: Same as Figure 5.8 but for tracer release in the Verdon valley (VV1) released near the surface.

Early in the night, both VV tracers have a direction that roughly aligns with the valley orientation, similar to the AV flow. Figure 5.9a and Figure 5.10a show that the VV flows fan out over a large area, in this case over the area between the DV and the VV mouth (Figure 5.1), especially VV2 contributes a lot of tracer to this area. At the arrival of the DDV flows, the tracer supply from the VV to the DV stops and tracer already present moves along with the DDV flows, while some additional plumes leave the VV, see Figure 5.9b and Figure 5.10b plumes. Figure 5.9b with VV1 has smaller tracer amounts in the simulation domain than VV2 (Figure 5.10b), indicating more Verdon down-valley flow along the west side. In contrast, the east side is subjected to more up-valley flows, which cause tracer to leave the simulation domain. This difference between the two valley sides could result from circulation or different heights of the release positions, where surface releases are generally more diverse in their flow directions.

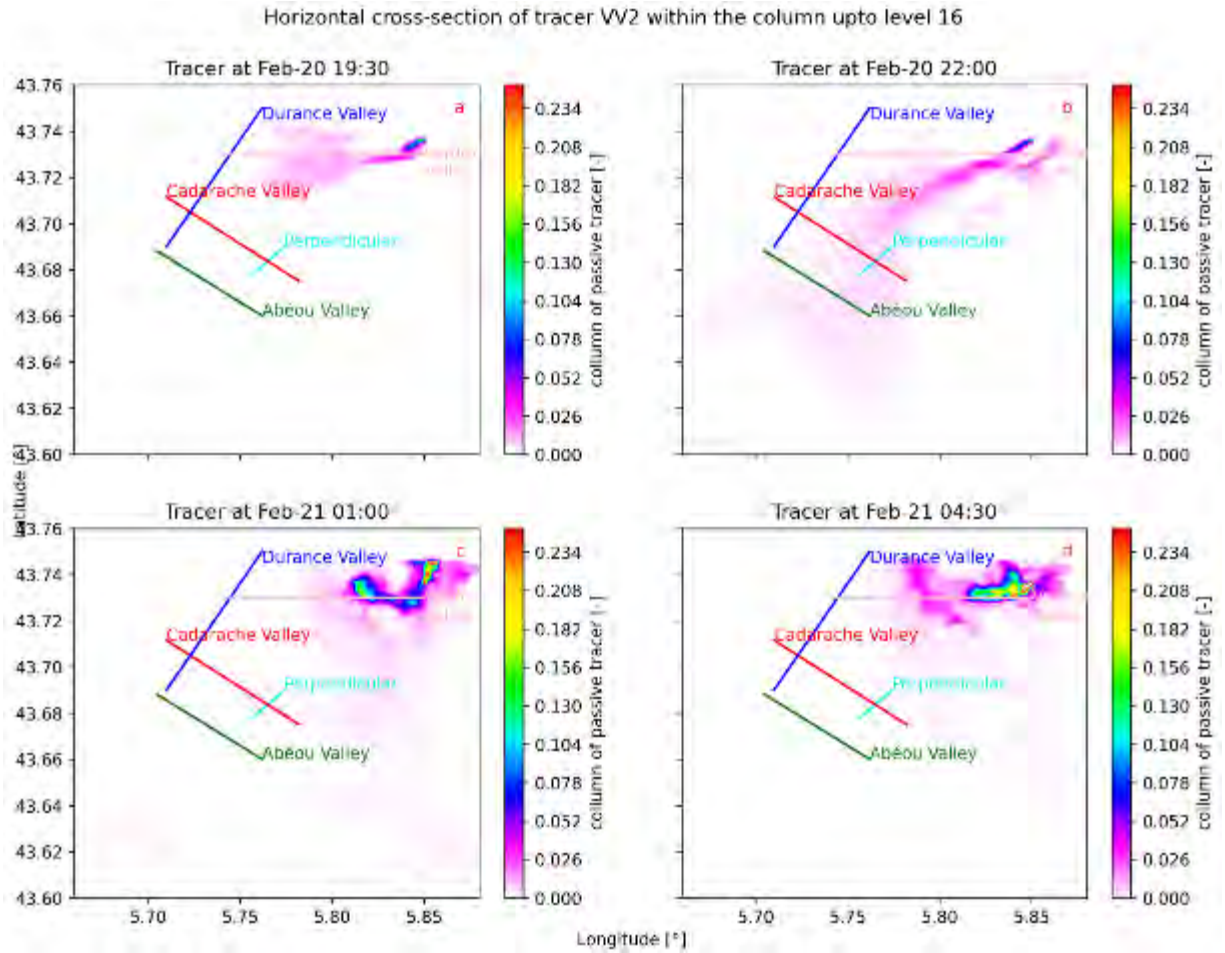

Figure 5.10: Same as Figure 5.8 but for tracer release in the Verdon valley (VV2) released at 40 – 60 m agl.

Later in the night, Figure 5.9c and Figure 5.10c show that the VV tracer stagnates with only limited amounts leaving the VV. Note that up-valley flowing tracer leaves the simulation domain and could return with a southern direction but such tracer is lost for the simulation. Most of the plume remains within the valley or stagnates near the confluent zone with the DV, as is clear in Figure 5.10c. The built-up of tracer starts with the arrival of the DDV flow, making it likely that this flow prevents further outflow. Lastly, some Verdon flows reach the "plan de Valavès" as visible in Figure 5.10c, while this is not the case for the flows originating from the surface, as Figure 5.9c shows. To resume, when the DDV flows start to weaken, the flows leaving the VV reach again the DV and flow up-valley in the DV, out of the simulation domain, as seen in Figure 5.9d but more clearly in Figure 5.10d

In summary, the VV flows into the DV early in the night, and becomes trapped in the VV basin at the arrival of the DDV winds. Then tracers start to built-up in this basin, of which a small amount can escape at height, from where they flow parallel to the DDV wind and leave in the southeast corner. When the DDV flow weakens, the VV plumes can again go into the DV, but instead of fanning out over the larger open area, they follow a DV upslope direction. VV1 discharges at higher altitudes than VV2 does, but this matters little for the stagnation that forms in the domain, although the VV1 tracer seems to have more tracer leaving the VV. Regardless, the surface flows of VV1 seem to have more up-valley flows than the higher VV2 releases.

5.3.4.2 Possible flow introduction into the CV

As shown above and by Figure 4.7, there is a possibility that flows from the VV penetrate the CV, highlighted by VV2 in Figure 5.10b. Since Figure 5.10 is a column sum, it does not show at what height the plumes move, meaning they could be either above or inside the CV.

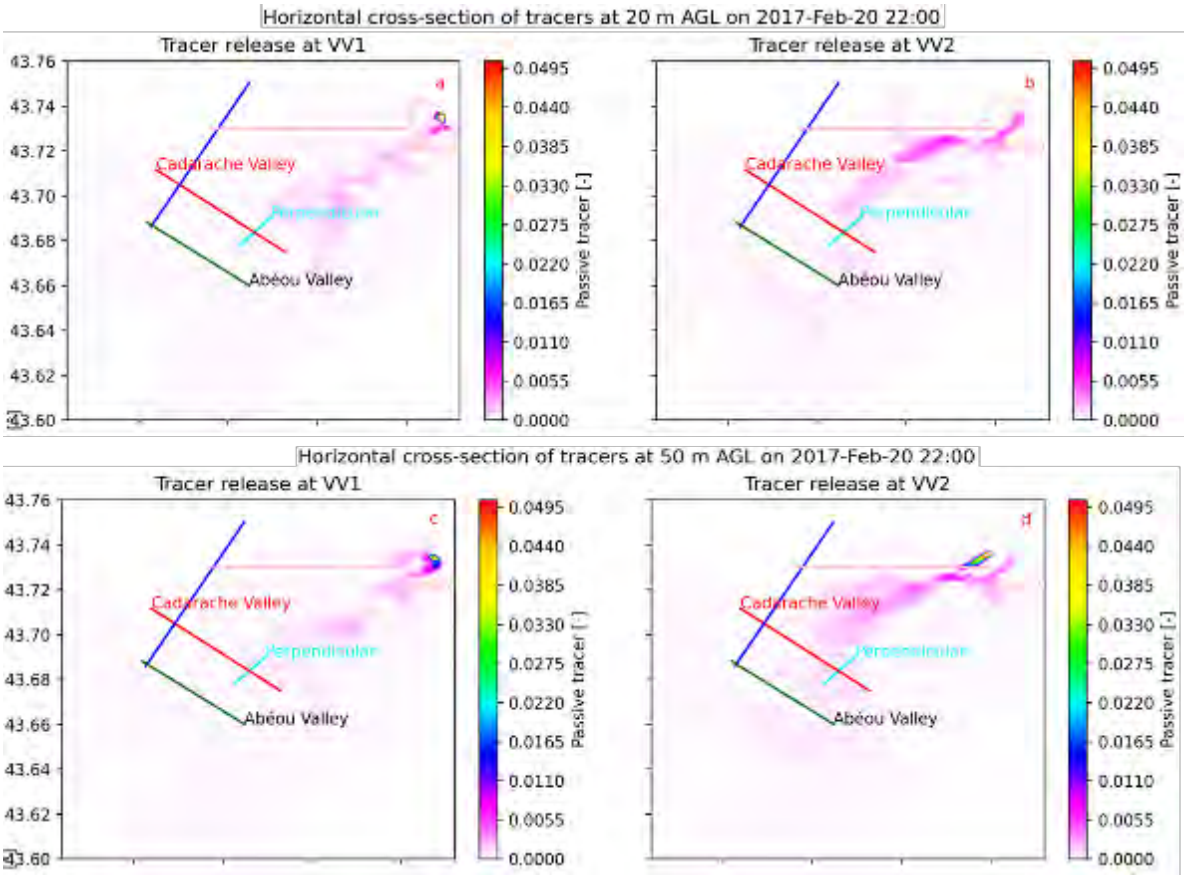

Figure 5.11: Horizontal cross-sections at fixed height of tracers from the Verdon Valley at 20 m agl at 22:00 UTC in (a) and (b) and at 50 m agl in (c) and (d). the VV1 tracer in (a) and (c) and the VV2 in (b) and (d).

Figure 5.11a and 5.11b show the VV1 and VV2 plume at 20 m agl, with a large amount on the northern ridge of the CV, but only low amounts at the CV floor. VV2 plume seems to penetrate the CV curve near B4 but does not propagate in a CDV direction because the CV has upslope winds at 22:00 UTC. If I look higher at 50 m agl, Figure 5.11c and 5.11d show that the VV1 plume mostly concentrates over the CV northern ridge and does not manage to flow close to the CV floor. On the other hand, the VV2 release generates a denser plume passing over the valley. Looking closely at the lowest parts of the CV (indicated by the red line), the amounts are lower close to the center than on either of the two sidewalls, indicating that the plumes over the CV have a roughly fixed altitude rather than a terrain-following flow or slope flow behaviors. This is supported by a wave-like behavior in the plume, with high amounts over ridges and low amounts along the thalweg. In conclusion, VV plumes flow aloft, passing the CV and not into the CV but do influence sections around B4, as demonstrated by Figure 5.11.

The VV flow structure is completely different from the CV, AV, and DV. After the DDV arrival, the VV has a stagnation of tracers not seen in any of the other valleys, although a small amount escapes at the top end and flows parallel to the DDV flow but does not enter any of the valleys. A better understanding of these flows could follow from an enlargement of the simulation domain to include a larger part of the Verdon basin and reduce the tracer lost that way.

5.4 Discussion

The tracers permit to visualize the flows in the CV and the other surrounding valleys well. Regardless of the results, release location is very important since every location can have different winds. For this

simulation, the CV only had release locations on its south sidewall; however, the north wall and valley floor might be more sheltered from the influences of the DDV flow, as suggested by Figure 5.2b and other CV releases. A useful way to determine better locations would be a Lagrangian model, searching interesting locations. However, it would need verification with WRF simulation because of the temporal resolution difference. To improve the understanding of the whole valley, more release points along the two transects of the CV would allow for a better understanding of the CDV flows in the simulations, showing further detail on how well the model can create different wind regimes.

The CV tracer of Figure 5.2 show that up-valley winds occur when the DDV flow reaches the CV. However, the observations of Duine (2015) show a shallow layer with upvalley flows, comparisons with a real case should give a better idea of the actual situation. Dupuy (2018) documented the second measurement campaign, which does not show the DDV flows near the CV floor. However, the LEMS do show a wide variety of flow directions on the sidewalls of the CV, Figure 2.8 show many western originating winds indicating the possible occurrence of up-valley flows on the sidewalls.

Figure 5.8 shows the AV, parallel to the CV, with clear up-valley and down-valley flows, extending on scales roughly equal to the CV, with a slight exception in the size of the valley opening and the deepness of the valley. Possible adjustments to the topographic map in the model to reduce elevation mismatches, would result in a deeper and more closed CV, thus reducing the strength of winds penetrating the CV. The flow depth of the AV is close to the valley depth, which matches the observations in the CV. However, the CV does not have a similar depth but experiences large influences of up-valley flows. In simulations, a height increase of the northern CV ridge might shelter the CV enough to move to comparable situations as found in the AV and observations. However, exanimating Figure 5.6d shows that a two-sided system is possible in the CV, where the high-end of the valley experiences up-valley flow direction.

All flows in tributary valleys show a strong influence of the DDV flow presence, whereas the VV only undergoes a flow blockage; the CV and the AV have their flows reversed in the model. Future measurements should show if these influences do indeed exist. In Chapter 4, I discussed the arrival of humidity and its penetration of the CV, which does not match the observations. While this is a problem of the simulation, it does not occur everywhere in the model, which can simulate the lack of influence of the advective winds on the AV, with flow layer depths similar to what is expected for the CV, based on the KASCADE observations. Regardless of the model skill, these simulations show a possibility for flows going to until now ignored directions. Future measurement campaigns need an even broader view to understand the complex interactions in and around the CV.

5.5 Conclusion and prospects

These investigations lead to interesting findings that fuel the interest in understanding the exact flow in and around the complex area of Cadarache.

5.5.1 Conclusion

Regardless of the model skill, these simulations show a possibility for visualizing flows going to until now ignored directions. Future measurement campaigns need an even broader view to understand the complex interactions in and around the CV.

The tracer release points are useful for understanding the flow and dispersion. Even though they can be hard to verify experimentally, they show trajectories. After successfully implementing tracers into the WRF model, I investigated the Cadarache Valley region flows during the night of KAS17-IOP07, as was already studied in Chapter 4, to gain even more insight into the flows and their development. The tracers are released at eight points, four are located in the CV, at two different locations with two

different heights. The other four distributed among other valleys, one in the Durance Valley, one in the Abéou Valley and the last two in the Verdon Valley.

The plumes show that the CV flows penetrate the DV at the beginning of the night, beginning in the direction of the moist advecting winds from the south (see article of Chapter 4), which does not match the CV orientation. After this wind dies, the CV has a short period of winds that flow down-valley and into the DV. Reversal flows start after the arrival of the DDV flow in most of the valley, while only shortly near the valley floor. These flows exit the CV on the southeast end and enter the basin behind, called “plan de Valavès”, continuing and leaving the simulation domain.

The DDV flow starts to build-up after 20:00 UTC and influence the other valleys by blocking their flow or even causing flow reversal of the AV (and sometimes the CV) flow. A blocking mountain ridge with its highest point almost directly in the DDV flow axis causes this reversal of AV flows. Later at night, the DDV wind weakens, allowing the other valleys to return to a situation as before the DDV flow arrival. Especially the VV had a large buildup of tracer since the DDV flow cannot penetrate the valley during the flow blocking. A small part of the VV tracers can leave the VV and flow parallel to the DV to the south at roughly constant altitudes.

5.5.2 Prospects

Since I started the tracer runs near the end of my PhD, the analyses have not yet reached their full depth. Therefore, I advise further investigation of the Cadarache valley flows in the form of a sensitivity study, where the tracer implementation serves to evaluate improvements of the WRF model. Since tracers are relatively easy to implement in the model and show the movement of air parcels, it is a good tool to compare the (turbulent) transport originating from different parameterization schemes.

A major drawback of the tracers is that there are very limited datasets available for comparisons, the ones available are mostly from accidents. In a future campaign, release points of soot aerosols can be a good addition for tracer comparisons since particular matter measurements have become more affordable and of decent quality (Vogt et al., 2021), leading to an easier analysis of pollutant concentration or evaluation of flow origins.

General Conclusion and prospects

Airflows in the atmosphere are the reason for the circulation of pollutants. The boundary layer mixes pollutants faster and in a larger volume in daytime conditions than during the night. The topography can also affect and reduce air mixing. Altogether, night flows in complex terrain remain one of the more difficult situations for NWP models because scales involved are small and more processes contribute to the development of these stable night flows.

My research aimed to refine the flow description further and improve an NWP model. Today, this model can simulate flows in a small valley (the Cadarache valley) with more detail than coarse operational simulations and downscaling through statistical approaches. For this result, I addressed the following research questions: 1) “How does an improved land cover representation affect the WRF model outputs in the Cadarache area and over a larger domain?” And 2) “How does the WRF model with a 100 m horizontal resolution grid represent nocturnal Cadarache valley winds?”. To support the second research question, I had to answer two sub-questions: “What are typical turbulent length scales of the Cadarache valley wind, and are parameterization schemes appropriate for these lengths?” and “How well are the interactions between the flows in the Durance and its tributary valleys simulated?”.

Previous studies

For health and safety reasons, forecasting the flow of pollutants is necessary. This demand warranted this research and two previous PhD studies focused on describing the flows in the Cadarache and Durance valleys. These previous studies were based on the observations collected during the two KASCADE field campaigns performed in 2013 and 2017, described in Chapter 2. KASCADE-2013 provided a detailed view of the nighttime flows at one vertical above the CV, and of interactions between the CV and the DV wind above. Even though this campaign primarily focused on stable night conditions, it captured several other common weather phenomena such as strong winds, precipitation events, and cloudy conditions. Altogether, the campaign depicted the two local flows of the DV and the CV, with their typical daily cycle and a description of their velocity profiles (Duine et al., 2017). The CV jet maximum is roughly 30 m above the surface with speeds around 2 – 3 m s^{-1} and the DV jet peaks around 175 – 225 above the CV surface with speeds between 4 and 8 m s^{-1}.

Four years later, the KASCADE-2017 measurement campaign again studied the stable night conditions in the CV. This campaign focused on the spatial variability close to the surface. In total, sixteen measurement stations observed the CV flows, of which eight were on the sidewalls or ridges and eight along the CV thalweg. Two measurement locations were added in the DV. They revealed several interesting findings; the most relevant were the wind patterns on the sidewalls and their typical thermal profiles during stable night conditions. It was shown that the valley often has a strong stability over its depth and would match with a mature cold pool in the classifications of Mahrt (2017). However, the wind direction clearly correlated with valley orientation only in stations on or near the thalweg, whereas stations on the sidewalls had uncertain correlations.

During these field campaigns, 37 IOPs of 24-hour had been conducted from noon to noon to focus on the night flow and temperature development. In these periods, additional data of the vertical structure was obtained through the release of radiosondes at a 3-hour interval. I classified the IOPs based on the wind profiles and other phenomena descriptions. This classification helped with the determination of case studies for further research. I selected IOP16 of KASCADE-2013 (19 to 20 February 2013) as it had stable night conditions and the previous modeling has shown relatively high forecasting skills. I used this case to evaluate the land cover interactions. I also selected IOP07 from KASCADE-2017 (20 to 21 February 2017) as the second case to perform a fine-resolution simulation because this IOP had the

clearest stable conditions throughout the night and the LEMS captured the spatial variability present in the CV, thus allowing simulation evaluation on multiple locations.

In the previous studies, the KASCADE observations have helped NWP model developments based on the WRF numerical model. After set-up, WRF managed to simulate the flows of the larger DV, but its computing grid was not fine enough to produce the flows of the CV adequately. The studies conducted by Dupuy et al. (2021) trained statistical models based on NWP simulations to determine the speed and direction of the flow at one central point in the CV, compensating for the lack of CV wind information. Altogether, they gave a good idea of the large-scale flows of the region with additional information at a single point.

Land cover representation in WRF simulations

As described in Chapter 3, I prepared land cover maps appropriate for fine and coarse grid scales. These maps are important inputs, as they determine for a large part the soil-atmosphere interactions. I focused on the CLC dataset because it has many classes, great spatial detail, and has shown good results in previous studies. However, two problems existed with CLC in WRF. Firstly, it had no parameter table in the WRF model and a conversion to use the table of another dataset was needed. Therefore, I created a simple physical parameter table specially for the CLC classes and incorporated it into the WRF model. Secondly, since spatial aggregation of a dataset with many classes can cause misrepresentation errors when selecting the most common instead of the most representative class, I created a new aggregation method that avoids these misrepresentations by clustering classes of the CLC dataset. This method, called Multi-Level Mode aggregation, was developed to overcome the difficulty that occurs with conventional aggregation techniques while considering the richness of the initial data set.

The modifications resulting from the new aggregation method showed a strong relationship with the target resolution. For example, at resolutions of 111 m, the new method has a discrepancy with a conventional aggregation of 0.03 %, growing to 16.6 % for a 9 km resolution. Especially heterogeneous areas are impacted by the aggregation method since it requires at least three classes before it can produce results different from the default aggregation.

WRF simulations at 1 km resolution of KASCADE-2013 IOP16 showed the effects of both the LC datasets and the aggregation method through a series of simulations combining various options with these two parameters. Over the whole domain, the average roughness length increased with CLC, while albedo and emissivity decreased. These shifts led to decreased winds in the CLC simulations while having limited effects on the surface temperatures. Further analyses, in particular comparison with the observations, determined the effects of the new land cover compared to the more common land cover maps already present in WRF. CLC outperformed the other datasets in predicting variables except for humidity. Among the different options applied on the CLC dataset, combining the new aggregation with default CLC conversion for classes gave the best results. However, all treatment options for the CLC showed comparable results. These comparable results came from the absence of discrepancy between land cover options near the spots with observations.

A second simulation experiment on IOP16 investigated the best practices for input resolution sizes of LC for the WRF model in its preprocessing step. It showed that the input resolution caused an effect with a comparable amplitude in results as the difference caused by the LC datasets. A constant size of 1 km resolution proved better than the finest resolution or a resolution that matches the WRF domain resolution.

Eventually, a long-term simulation lasting 11 days (18 February to 01 March 2013) showed an overall behavior similar to that produced by the 24h case study. However, the relative difference between the LC datasets decreased. CLC remained the best performing LC dataset in forecasting variables except for humidity. Among the CLC runs, the simulation with both the new aggregation method and parameter table performed better than the other options. Altogether, the improvement in land cover representation increased the simulation skills for temperature, stability, and wind but did not improve the quality of humidity forecasts.

Fine-resolution simulations

As preparation for fine resolution runs, I determined the correctness of using turbulence parameterization schemes instead of explicitly solved LES methods. High-frequency measurements performed throughout the KASCADE-2017 campaign allowed the determination of the integral length scale of the turbulence. However, the largest turbulent structures – and thus the largest integral length scales – are generally in the core of the upper part of the boundary layer. I extrapolated the surface-layer length scales to the top of the boundary layer with a relationship determined by Lenschow & Stankov (1986). This relation includes the boundary layer depth, determined from the radiosondes. These extrapolated length scales remained below 100 m, except around 15:00 UTC. With this information, I determined that the runs with the WRF model at 111 m resolution can be done with fully parameterized turbulence since integral lengths remain below the horizontal resolution.

The fine resolution simulation, described in Chapter 4, managed to resolve the flows in the CV, which was not attainable with the 1 km model. The improvement was quantified by, e.g., the percentage of simulated wind direction differing by less than 45° from observations, which passed from 46 % to 60 %. Further investigation of the spatial situation in the CV revealed that the simulated nighttime stability is too weak compared to the observations. A humid air mass arrived over the CV 1.5 hour earlier than observed and managed to reach the valley floor. At the same time, in the observations, it remained on the ridges and sidewalls, not reaching the floor until thermal mixing started in the morning. Nevertheless, the simulation showed promising skill of stability development before it was disturbed by the early arrival of moist winds.

Previous simulations forecasted a reduced diurnal temperature range (12 K) compared to the observations (19 K) and attributed these temperature errors to unresolved topography. After increasing the topography in the fine-resolution simulations (Chapter 4), the error remained of comparable size, showing no improvement as was the case with the LC test performed in Chapter 3.

Additional analyses of the CV flow revealed that stability occurred by rapid cooling of the valley floor, at rates of 6 K h^{-1} (with a 12 K h^{-1} peak), at least double of common radiative cooling rates over flat terrain (1 – 3 K h^{-1}). At the same time, the top of the ridge stayed warmer, leading to stratification intensities of almost 8 K over a vertical distance of 108 m. Later in the night, the valley floor cooling slowed, the ridge tops had stronger cooling and the stratification in the valley weakened.

Investigation of simulated flow directions showed surface winds with both up- and downslope directions on the southern sidewall of the CV. In contrast, the valley bottom had mostly downvalley flows. Similarly, the effects of wind speed are different depending on the location within the valley; cooling rates were higher at the valley floor with fast wind speeds. In contrast, cooling rates were lower with fast winds on the valley sidewalls. Because winds at the valley bottom brought cold air and fast winds at the valley top caused mixing.

Looking broader than the CV to the surrounding valleys and ridges gave an idea of the spatial variation of flows throughout the complex terrain. Horizontal cross-sections showed more flow diversity than

originally expected. In the AV, south of the CV, upvalley directions were simulated throughout the valley, except near its opening. In the VV, to the northeast of the CV, the flows did not display a consistent direction. Further investigations with vertical cross-sections revealed that these flows behaved similarly over the valley depth.

As the AV flow showed an unexpected turn near the valley opening, further investigations in the simulated domain showed the DDV flow meeting a local ridge, which lay in the flow. This blockage pushed air down into the AV. Most of the flow moved further to the west, aligning with the lower section of the DV. At the same time, the rest turned to the east through the AV. A second noteworthy stream of relatively high wind speeds is depicted in these horizontal cross-sections: a flow coming from the VV and passing the CV at its high end, indicating possible penetrations of the CV by flows from other valleys.

Tracers in fine-resolution simulations

To investigate the local flows and determine, for example, if some could enter the CV, I added passive tracers in the fine-resolution simulation, as described in Chapter 5. These tracers are released at a constant rate from 18:00 to 06:00 UTC, i.e., during the whole night, at single point locations, either in the DV at the height of the well-established DV flow or in the surface layer in the tributary valleys (CV, AV, and VV).

This study showed that the VV tracer plumes flowed above the CV flow system and did not enter the valley in large amounts. At the same time, further investigation of the plumes showed that the DDV wind arrived around 22:00 UTC and changed the flows of every other valley. Around 02:00, the DV flow weakened, allowing the other valleys to return to flows resembling their early night flows. Under the influence of the DDV flow, I observed in the CV and AV a transport toward the southeast corner while in the VV flows appeared stagnation.

A closer inspection of the plumes within the CV showed two flow streams, one near the valley floor and the other above, roughly centered halfway of the valley depth. There was always a downvalley flow at the valley floor, bringing tracer down the valley but stagnating near the confluent zone.

The implementation of tracers in the fine-scale simulation showed how complex the interaction of the shallow regional valleys could be. Comparing the simulations to the observations of the KASCADE campaigns revealed a more complex and changing organization than inferred previously. Those structures are not always understandable from measurements with a limited number of locations, confirming the usefulness of fine-scale simulations even though their correctness, in reality, remains to be validated with actual tracers, for instance.

Prospects

The work presented above shows many details on the local flows in the CV and the region. It offers illustrations of how the different flows interact. Nevertheless, extra verifications are needed to understand the flows throughout the region fully. Below, I will describe a few ideas and projects that could improve the understanding of stable flows and their modeling.

A new measurement campaign should check the reality of several flows suggested by the fine-resolution simulations. Several locations should have more attention than they have received before. Most importantly are the flows on the southeast corner of the CV. Do CV flows exist that leave the valley and enter surrounding valleys, as was visualized with tracers? Other interesting places are the confluent zone of the CV and DV because it does not have any measurements yet. At the same time, the visual perception of fog and smoke on site indicates a stronger influence of the CV not matched by

the model. Further, additional observations in the surrounding valleys would help understand and confirm regional flows, thus further validating our fine resolution WRF model.

It would be very useful for these new locations to have a fine vertical wind profile because surface flow layers are possibly very shallow. Another method to understand the transport in the CV and region is measurements of soot aerosol released at some strategic points. Advised measurement locations are the CV confluent zone, CV high end, “plan de Valavès”, one in the AV and one near the “clue de Mirabeau”, if possible, all locations with measurements at 2 and 10 m agl. Nowadays, it is obtainable with relatively good quality because good particular matter sensor equipment is affordable (Vogt et al., 2021). Future modeling developments will benefit from these additional observation points.

More generally, the current comparisons already show that the model needs other improvements not associated with the horizontal resolution. Future wind forecasting skills will benefit from extra vertical levels, allowing the model to differentiate better between thin flow layers and have sharper gradients, allowing more realistic layers. Similarly, improving the temperature forecast skill in stable conditions leads to better predict stability in the model, allowing more forcing terms for the stable night winds. For example, the 1 km resolution and 111 m resolution simulations show comparable errors for the daily temperature range, and given that LC representation methods have limited impacts, working on parameterizations of ground-atmosphere exchanges appears as a logical option for future improvements.

I think that temperature forecasts could be improved by extensions in parameterization schemes, as they will need to consider horizontal variation. As mentioned in Chapter 1, the radiation schemes consider only the vertical column and processes for each cell, while in complex terrain horizontal effects such as shading and slopes are important. Other options are the interaction of the soil and atmosphere. Too much energy exchange dampens the atmosphere temperature amplitudes. Note that this justifies research to both the formulation in the model as well as the soil type and soil moisture fields used for calculations.

Regarding the representation of land cover in the simulations, this thesis introduced two new tools: the 44-class physical parameter table for CLC and the new Multi-Level Mode aggregation method. While they have promising results, they have received limited testing. The new CLC table is not yet finished and needs verified parameters, requiring extensive data of both satellite and *in-situ* observations. The MLM shows better results than the default aggregation method, even at locations with a small mismatch between the two methods. Additional simulations are needed to indicate the effectiveness of MLM in other places. Since the MLM method helps select the most representative class for a categorical dataset where classes share similarities, its applications are not restricted to land cover but could serve in many fields, as it is a data treatment tool.

The fine grid WRF model elaborated in this thesis takes too much calculation time to serve as a forecast set-up but can create a dataset of 3D detailed flow fields during a given period or serve in case studies. Until calculation power improves sufficiently, a different approach could connect the systems depicted in the fine-resolution model to the system available in the coarse operational model through statistical interpolation such as neural networks. The intention is to create a tool that gives information on non-resolved flows based on coarse-scale information. This work would first require building a long-term dataset containing fine- and coarse resolution simulations.

Conclusion générale et perspectives

Les écoulements dans l'atmosphère sont à l'origine de la circulation des polluants. Dans les conditions diurnes, la couche limite mélange les polluants plus rapidement et dans un plus grand volume que pendant la nuit. La topographie peut également modifier voire réduire le mélange de l'air. D'une façon générale, les écoulements nocturnes en terrain complexe restent l'une des situations les plus difficiles à prédire pour les modèles météorologiques, car les échelles concernées sont petites et davantage de processus contribuent au développement de ces écoulements.

Mes recherches ont visé à affiner la description de ces écoulements et à améliorer un modèle de simulation météorologique. Aujourd'hui, ce modèle peut simuler les écoulements dans une petite vallée (la vallée de Cadarache, VC) avec plus de détails que ceux fournis par les simulations opérationnelles à faible résolution et/ou la descente d'échelle par des approches statistiques. Pour ce faire, j'ai tenté de répondre aux questions suivantes : 1) "Comment une représentation améliorée de l'occupation des sols affecte-t-elle les sorties du modèle WRF dans la région de Cadarache et sur un domaine plus large ?" ; 2) "Comment le modèle WRF avec une grille de résolution horizontale de 100 m représente-t-il les vents nocturnes de la vallée de Cadarache ?". Cette deuxième question à son tour a engendré deux sous-questions : "Quelles sont les échelles de longueur turbulentes typiques du vent de la vallée de Cadarache, et quels sont les schémas de paramétrisation adaptés à ces longueurs ?" et "Dans quelle mesure les interactions entre les écoulements de la vallée de la Durance (VD) et de ses vallées affluentes sont-elles bien simulées ?".

Etudes précédentes

Pour préserver la santé et la sécurité, la prévision des écoulements de polluants est nécessaire. Cette motivation a sous-tendu cette recherche ainsi que deux précédentes thèses axées sur la description des écoulements dans les vallées de Cadarache et de la Durance. Ces études antérieures étaient basées sur les observations collectées lors des deux campagnes de terrain KASCADE réalisées en 2013 et 2017, décrites dans le chapitre 2. KASCADE-2013 a permis d'obtenir une vue détaillée des écoulements nocturnes sur une verticale au-dessus de la VC, et des interactions entre le vent de la VC et le vent de la VD. Même si cette campagne s'est principalement concentrée sur les conditions nocturnes stables, elle a permis d'observer plusieurs autres phénomènes météorologiques courants tels que les vents forts, les événements de précipitation et les conditions nuageuses. Au total, la campagne a permis de représenter les deux écoulements dans la VC et la VD, avec leur cycle diurne typique et leurs profils de vitesse (Duine et al., 2017). Le maximum du jet dans la VC se situe à environ 30 m au-dessus de la surface avec des vitesses autour de 2 - 3 m s^{-1} et le jet dans la VD culmine autour de 175 - 225 au-dessus du fond de la VC avec des vitesses entre 4 et 8 m s^{-1}.

Quatre ans plus tard, la campagne de mesure KASCADE-2017 a eu pour but d'étudier les conditions nocturnes stables dans la VC. Cette campagne s'est focalisée sur l'étude de la variabilité spatiale près de la surface. Au total, seize stations de mesure ont été déployées dans la vallée, dont huit sur les flancs ou les crêtes et huit le long du thalweg. Deux sites de mesure ont été ajoutés dans la VD. Ces observations ont révélé plusieurs résultats intéressants, en particulier les configurations de vent sur les flancs de la vallée et les profils thermiques typiques. Il a été montré que la vallée est souvent le siège d'une forte stabilité dans toute sa profondeur, ce qui correspondrait à une « mature cold pool » dans la classification de Mahrt (2017). Cependant, si le vent est clairement parallèle à l'axe de la vallée quand on reste à proximité du thalweg, il s'avère que les stations situées sur les parois latérales ont observé des directions beaucoup plus variables.

Au cours de ces campagnes de terrain, 37 périodes d'observation intensive (POI) ont été réalisées. Chacune durait 24 heures, de midi à midi, pour se focaliser sur l'écoulement nocturne et le

développement de la stratification. Au cours de ces POI, des données supplémentaires sur la structure verticale ont été obtenues par le lâcher de radiosondes à un intervalle de 3 heures. J'ai effectué un classement de ces POI sur la base des profils de vent et d'autres paramètres. Cette opération a aidé à déterminer des cas adaptés à des recherches plus approfondies. J'ai choisi la POI 16 de KASCADE-2013 (19 au 20 février 2013) car les conditions nocturnes étaient stables et des simulations antérieures avaient montré des performances relativement bonnes. J'ai utilisé ce cas pour mes études sur la question de l'occupation des sols. J'ai également sélectionné la POI 7 de KASCADE-2017 (20 au 21 février 2017) comme deuxième cas pour effectuer une simulation à résolution fine car ce cas présentait les conditions stables les plus claires tout au long de la nuit et les stations de mesures avaient bien observé la variabilité spatiale dans la VC, permettant ainsi d'évaluer la performance de la simulation en plusieurs points sur plusieurs sites.

Dans les études précédentes, les observations de KASCADE avaient aidé au développement de modèles météorologiques basés sur le code numérique WRF. Une fois mis au point, WRF avait alors réussi à simuler les écoulements dans la grande VD, mais la maille n'était pas assez fine pour représenter les vents dans la VC de manière satisfaisante. A la suite de quoi l'étude menée par Dupuy et al. (2021) a consisté à entraîner des modèles statistiques à partir de ces simulations pour déterminer la vitesse et la direction de l'écoulement en un point central de la VC, compensant ainsi le manque d'informations sur le vent local. Dans l'ensemble, ces simulations ont donc donné une bonne idée des écoulements à grande échelle de la région avec des informations locales complémentaires, mais en un seul point.

Représentation de l'occupation des sols dans les simulations WRF

Comme cela est décrit dans le chapitre 3, j'ai constitué des cartes d'occupation du sol appropriées à la fois pour les échelles de grille fine et grossière. Ces cartes sont des entrées importantes du modèle, car elles déterminent en grande partie les interactions sol-atmosphère. Je me suis concentré sur le jeu de données Corine Land Cover (CLC) car il comporte de nombreuses classes, une grande précision spatiale et a donné de bons résultats dans des études antérieures. Cependant, il y avait jusqu'à présent deux problèmes avec CLC dans WRF. Premièrement, il n'y avait pas de table de paramètres correspondante dans le modèle, et une conversion pour utiliser la table d'un autre jeu de données était donc nécessaire. J'ai donc créé une table de paramètres physiques spéciale pour les classes CLC et je l'ai intégrée au modèle. Deuxièmement, étant donné que l'agrégation spatiale d'un ensemble de données comportant de nombreuses classes peut entraîner des erreurs de représentation lorsqu'on sélectionne la classe la plus commune au lieu de la classe la plus représentative, j'ai créé une nouvelle méthode d'agrégation qui évite ces erreurs de représentation en regroupant les classes de l'ensemble de données CLC. Cette méthode, appelée « multi-level mode (MLM) aggrégation », a été développée pour surmonter la difficulté qui survient avec les techniques d'agrégation conventionnelles tout en conservant la richesse de l'ensemble de données initial.

Les modifications résultant de la nouvelle méthode d'agrégation ont montré une forte dépendance à la résolution ciblée. Par exemple, pour une résolution de 111 m, la nouvelle méthode présente un écart de 0,03 % par rapport à une agrégation conventionnelle, alors que ce score passe à 16,6 % pour une résolution de 9 km. Les zones hétérogènes sont particulièrement touchées par la méthode d'agrégation puisqu'à partir de trois classes différentes on peut produire des résultats qui diffèrent de la méthode d'agrégation par défaut.

Les impacts du choix de données d'occupation des sols et de la méthode d'agrégation ont été étudiés à partir de la simulation de la POI 16 de KASCADE-2013 avec une résolution de 1 km Une série de simulations combinant diverses options de ces deux paramètres a été faite. Sur l'ensemble du domaine, la moyenne de la longueur de rugosité a augmenté avec CLC, tandis que l'albédo et l'émissivité ont diminué. Ces changements ont entraîné une diminution des vents dans les simulations

utilisant CLC tout en ayant des effets limités sur les températures près de la surface. D'autres analyses, en particulier la comparaison avec les observations, ont déterminé les effets de la nouvelle occupation des sols par rapport aux cartes plus courantes déjà présentes dans WRF. CLC a obtenu de meilleurs résultats que les autres jeux de données, à l'exception de l'humidité. Parmi les différentes options appliquées sur le jeu de données CLC, la combinaison de la nouvelle agrégation avec la conversion de CLC vers les classes pré-existantes dans WRF a donné les meilleurs résultats. Ceci dit, toutes les options de traitement de la CLC ont donné des résultats voisins, ce qui est dû au fait que tous les jeux de données d'occupation des sols avaient les mêmes classes aux endroits où les observations ont été réalisées.

Une deuxième expérience de simulation sur la POI16 a permis de montrer que les différences sur la résolution d'entrée des données d'occupation des sols provoquait un effet aussi important que la différence entre les différents jeux de données. Une résolution de 1 km s'est avérée meilleure que la résolution la plus fine ou qu'une résolution calquée sur la résolution du domaine WRF.

Finalement, une simulation sur une durée de 11 jours (du 18 février au 1er mars 2013) a montré un comportement globalement similaire à celui du cas de 24 heures. Néanmoins, la différence relative résultant des différents jeux de données d'occupation des sols a diminué. CLC est resté le jeu de données le plus performant pour les variables de la simulation, à l'exception de l'humidité. Parmi les différentes mises en œuvre de CLC, la simulation avec la nouvelle méthode d'agrégation (MLM) et la nouvelle table de paramètres a donné de meilleurs résultats que les autres options. Dans l'ensemble, l'amélioration de la représentation de l'occupation des sols a augmenté les performances de simulation pour la température, la stratification et le vent, mais ne les a pas augmentées pour l'humidité.

Simulations à haute résolution

En prélude aux simulations à résolution fine, j'ai étudié la pertinence des schémas de paramétrisation complète de la turbulence en lieu et place des méthodes LES où elle est en partie résolue explicitement. Les mesures à haute fréquence effectuées tout au long de la campagne KASCADE-2017 ont permis de déterminer l'échelle de longueur intégrale de la turbulence près de la surface. Cependant, les plus grandes structures turbulentes - et donc les plus grandes échelles de longueur intégrale - se trouvent généralement au cœur ou dans la partie supérieure de la couche limite. J'ai donc extrapolé les échelles de longueur de la couche de surface jusqu'au sommet de la couche limite grâce à une relation déterminée par Lenschow & Stankov (1986). Cette relation fait intervenir la hauteur de la couche limite, qui a été déterminée à partir des radiosondages. Ces échelles de longueur extrapolées se sont avérées être inférieures à 100 m, sauf pour la situation de 15:00 UTC. Avec cette information, j'ai pu conclure que les simulations avec le modèle WRF à une résolution de 111 m pouvaient être faites avec une turbulence entièrement paramétrée puisque les longueurs intégrales restaient en deçà de la résolution horizontale.

La simulation à résolution fine, décrite au chapitre 4, a permis de représenter les écoulements dans la VC, ce qui n'était pas réalisable avec le modèle à 1 km. L'amélioration a été quantifiée, par exemple par le pourcentage des vent simulés différant de moins de 45° des observations, qui est passé de 46 % à 60 %. Une étude plus approfondie de la répartition spatiale dans la VC a révélé que la stratification nocturne simulée est plus faible que les observations. Dans la simulation, cela est dû à l'arrivée sur la VC, une heure et demie plus tôt qu'observé, d'une masse d'air humide qui réussit à atteindre le fond de la vallée. Dans les observations, cette masse d'air est restée sur les crêtes et les parois latérales, et n'a pas atteint le fond de la vallée. Au final, la simulation a montré sa capacité à reproduire le développement de la stratification avant qu'elle ne soit perturbée par l'arrivée précoce d'un écoulement humide.

Les simulations antérieures à ce travail avaient produit une amplitude diurne de température plus réduite (12 K) que dans les observations (19 K). Cette erreur avait été attribuée à l'effet de la topographie non résolue dans le modèle. Cependant, avoir affiné la topographie dans les simulations à haute résolution (chapitre 4) n'a produit aucune amélioration significative sur la simulation de l'amplitude thermique, de la même façon que les essais effectués sur l'occupation des sols (chapitre 3) n'avaient eu aucun impact sur ce paramètre.

Des analyses complémentaires de l'écoulement dans la VC ont révélé que la stabilité est apparue à la suite d'un refroidissement rapide du fond de la vallée, à des taux de 6 K h^{-1} (avec un pic de 12 K h^{-1}), soit au moins le double des taux de refroidissement radiatif courants sur un terrain plat (1 - 3 K h^{-1}). Dans le même temps, le sommet de la crête reste plus chaud, ce qui entraîne des intensités de stratification de près de 8 K sur une couche d'une centaine de mètres. Plus tard dans la nuit, le refroidissement du fond de la vallée ralentit, le sommet de la crête se refroidit davantage et la stratification globale dans la vallée s'affaiblit.

L'examen des vents simulés a montré que les vents de surface pouvaient remonter ou descendre long du flanc sud de la VC. En revanche, au fond de la vallée, les vents suivaient principalement l'axe du thalweg. De même, les effets thermiques de l'écoulement étaient différents selon l'endroit dans la vallée ; les taux de refroidissement étaient plus élevés au fond de la vallée avec des vitesses de vent plus rapides. En revanche, sur les flancs de la vallée, les taux de refroidissement étaient plus faibles avec des vents plus rapides. En fait, les vents au fond de la vallée apportent de l'air froid alors que les vents rapides au sommet de la vallée accentuent le mélange.

En élargissant l'analyse vers les vallées et les crêtes voisines on a pu donner une idée de la variation spatiale des écoulements sur l'ensemble du terrain complexe. Les coupes horizontales ont montré une diversité d'écoulement plus grande que prévu. Dans la vallée de l'Abéou (VA), au sud de la VC, les vents simulés remontent dans toute la vallée, sauf près de son embouchure. Dans la vallée du Verdon, au nord-est de la VC, les écoulements étaient très variables. Des investigations plus poussées avec des coupes verticales ont révélé que ces écoulements se comportaient de manière similaire sur toute la profondeur de la vallée.

Il est apparu que l'écoulement dans la VA prend un virage inattendu près de l'embouchure de la vallée. Des analyses plus poussées dans le domaine simulé ont montré que l'écoulement dans la VD but contre une crête locale qui divise le flux dont La plus grande partie se déplace vers l'ouest, s'alignant avec la section inférieure de la VD, alors que dans le même temps, le reste tourne vers l'est et pénètre dans la VA. Un deuxième courant avec des vitesses relativement élevées est apparu dans ces coupes horizontales : il s'agit d'un écoulement venant de la VV et entrant dans la VC par sa partie amont, ce qui reflète de possibles pénétrations de la VC par des flux provenant d'autres vallées.

Lâcher de traceurs dans les simulations à haute résolution

Pour étudier les écoulements locaux et déterminer si, par exemple, certains peuvent entrer dans la VC, j'ai ajouté des lâchers de traceurs passifs dans la simulation à haute résolution, comme cela a été décrit au chapitre 5. Ces traceurs sont relâchés à un taux constant de 18h00 à 06h00 UTC, c'est-à-dire pendant toute la nuit, à des emplacements ponctuels, soit dans la VD à la hauteur où le vent de Durance est bien établi, soit dans la couche de surface dans les vallées affluentes (VC, VA et VV).

L'étude a montré que les panaches de traceurs de la VV se propageaient au-dessus du vent descendant la VC et n'y pénétraient pas en quantités importantes. L'étude plus détaillée des panaches a montré que le vent de Durance arrive vers 22:00 UTC et modifie les écoulements de toutes les autres vallées. Vers 02:00 UTC, le vent de Durance s'affaiblit, permettant aux autres vallées de retrouver des

écoulements ressemblant à ceux du début de la nuit. Sous l'influence du vent de Durance, on observe dans la VC et la VA un transport vers l'extrémité sud-est tandis que dans la VV apparaît une stagnation.

Une inspection plus approfondie des panaches dans la CV a montré deux d'écoulements superposés, l'un près du fond de la vallée et l'autre au-dessus, celui-ci à mi-profondeur de la vallée. Au fond de la vallée, il y avait toujours des courants descendants, transportant le panache vers l'embouchure de la vallée mais stagnant près de la zone de confluence.

La mise en œuvre de traceurs dans la simulation à échelle fine a montré à quel point l'interaction des vallées peu profondes pouvait être complexe. La comparaison des simulations avec les observations des campagnes KASCADE a révélé une organisation plus variée et changeante que celle déduite des études précédentes. Ces structures ne sont pas toujours compréhensibles à partir de mesures avec un nombre limité d'emplacements, confirmant l'utilité des simulations à échelle fine même si leur exactitude, dans la réalité, reste à valider avec des traceurs réels, par exemple.

Perspectives

Le travail présenté ci-dessus décrit de nombreux détails sur les écoulements locaux dans la VC et aux alentours. Il offre des illustrations sur la manière dont les différents écoulements interagissent. Néanmoins, des vérifications supplémentaires sont nécessaires pour comprendre pleinement les écoulements dans toute la région. Je vais décrire ci-dessous quelques idées et projets qui pourraient améliorer la compréhension des conditions stables et leur modélisation.

Une nouvelle campagne de mesure devrait vérifier la réalité de plusieurs écoulements suggérés par les simulations à résolution fine. Plusieurs endroits devraient recevoir plus d'attention qu'ils n'en ont reçu auparavant. Les plus importants sont les écoulements dans l'extrémité sud-est de la VC. Existe-t-il des écoulements de la VC qui quittent la vallée et entrent dans les vallées environnantes, comme cela a été visualisé par simulation avec des traceurs ? D'autres endroits intéressants sont la zone de confluence de la VC et de la VD parce qu'elle n'a pas encore fait l'objet de mesures, tandis que la perception visuelle du brouillard et des fumées sur le site indique une forte influence de la VC qui ne correspond pas aux simulations. De plus, des observations supplémentaires dans les vallées environnantes aideraient à comprendre et à confirmer les écoulements régionaux, validant ainsi davantage notre modèle WRF à résolution fine.

Pour ces nouveaux emplacements, il serait très utile de disposer d'un profil de vent finement résolu, car les couches des écoulements près de la surface sont probablement très minces. Une autre méthode pour comprendre le transport dans la VC et les alentours consisterait à mesurer des aérosol de suie relâchés à certains points stratégiques. Les sites de mesure à recommander sont la zone de confluence de la VC, l'amont de la VC, le "plan de Valavès", un site dans la VA et un près de la "clue de Mirabeau", avec si possible à tous ces sites des mesures à 2 et 10 m agl. De nos jours, il serait possible de réaliser ces observations avec une qualité satisfaisante car les capteurs de matière particulaire de bonne qualité sont devenus abordables (Vogt et al., 2021). Les futurs développements de modélisation bénéficieraient largement de ces points d'observation supplémentaires.

Plus généralement, les comparaisons actuelles montrent déjà que le modèle a besoin d'autres améliorations indépendamment de la résolution horizontale. Les améliorations en matière de prévision du vent devront s'appuyer sur des niveaux verticaux supplémentaires, permettant au modèle de mieux différencier les fines couches d'écoulement et d'avoir des gradients plus nets, permettant de représenter des couches plus réalistes. De même, l'amélioration de la prévision de la température dans des conditions stables entraînera une meilleure représentation de la stabilité dans le modèle, ce qui permettra d'obtenir de meilleurs termes de forçage pour les vents nocturnes stables. En effet, les

simulations à résolution de 1 km ou de 111 m montrent des erreurs comparables pour l'amplitude diurne de température, et étant donné que les méthodes de représentation de l'occupation des sols ont des impacts limités, travailler sur les paramétrisations des échanges sol-atmosphère apparaît comme une option logique pour les améliorations futures.

Je pense que l'amélioration des prévisions de température pourrait être obtenue par des affinements dans les schémas de paramétrage, qui devront prendre en compte la variation horizontale. Comme mentionné dans le chapitre 1, les schémas de rayonnement ne considèrent que la colonne verticale et les processus sont décrits globalement pour chaque cellule, alors que dans les terrains complexes, les effets horizontaux tels que l'ombrage et les pentes sont importants. D'autres options sont d'améliorer l'interaction du sol et de l'atmosphère. Un échange d'énergie trop important atténue les amplitudes de température de l'atmosphère. A noter que cela justifie une recherche à la fois sur la formulation dans le modèle et sur le type de sol et les champs d'humidité du sol utilisés pour les calculs.

En ce qui concerne la représentation de l'occupation du sol dans les simulations, cette thèse a introduit deux nouveaux outils : la table de paramètres physiques à 44 classes pour CLC et la nouvelle méthode d'agrégation « Multi-Level Mode ». Bien que leurs résultats soient prometteurs, ils ont été peu testés. La nouvelle table CLC n'est pas encore terminée et nécessite des paramètres vérifiés, ce qui requiert de nombreuses données d'observations satellitaires et/ou in-situ. La MLM donne de meilleurs résultats que la méthode d'agrégation par défaut, même aux endroits où il n'y a qu'un écart léger entre les deux méthodes. Des simulations supplémentaires sont nécessaires pour évaluer l'efficacité de la MLM à d'autres endroits. Dans la mesure où la méthode MLM permet de sélectionner la classe la plus représentative dans un ensemble de données où les classes partagent des similitudes, ses applications ne se limitent pas à la couverture du sol mais pourraient servir dans de nombreux domaines, puisqu'il s'agit d'un outil de traitement des données.

Le modèle WRF à grille fine élaboré dans cette thèse nécessite trop de temps de calcul pour être actuellement utilisé en prévision opérationnelle, mais il peut créer un ensemble de données de champs d'écoulement détaillés en 3D pendant une période donnée ou servir pour des études de cas. En attendant que la puissance de calcul s'améliore suffisamment, une approche différente pourrait connecter les champs décrits dans le modèle à résolution fine à ceux disponibles dans le modèle opérationnel, par le biais d'une interpolation statistique telle que les réseaux neuronaux. L'objectif est de créer un outil qui donne des informations sur les écoulements non résolus sur la base d'informations obtenu à une échelle plus grossière. Ce travail nécessiterait d'abord de construire un ensemble de données sur une longue période contenant à la fois des simulations à résolution fine et grossière.

Bibliography

Acevedo, O. C., & Fitzjarrald, D. R. (2001). The Early Evening Surface-Layer Transition: Temporal and Spatial Variability. *Journal of the Atmospheric Sciences*, *58*(17), 2650–2667. https://doi.org/10.1175/1520-0469(2001)058<2650:TEESLT>2.0.CO;2

Allwine, K. J., & Whiteman, C. D. (1994). Single-station integral measures of atmospheric stagnation, recirculation and ventilation. *Atmospheric Environment*, *28*(4), 713–721. https://doi.org/10.1016/1352-2310(94)90048-5

Angevine, W. M., Brioude, J., McKeen, S., & Holloway, J. S. (2014). Uncertainty in Lagrangian pollutant transport simulations due to meteorological uncertainty from a mesoscale WRF ensemble. *Geoscientific Model Development*, *7*(6), 2817–2829. https://doi.org/10.5194/gmd-7-2817-2014

Arduini, G., Staquet, C., & Chemel, C. (2016). Interactions Between the Nighttime Valley-Wind System and a Developing Cold-Air Pool. *Boundary-Layer Meteorology*, *161*(1), 49–72. https://doi.org/10.1007/s10546-016-0155-8

Banerjee, S., Krahl, R., Durst, F., & Zenger, C. (2007). Presentation of anisotropy properties of turbulence, invariants versus eigenvalue approaches. *Journal of Turbulence*, *8*, N32. https://doi.org/10.1080/14685240701506896

Bhimireddy, S. R., & Bhaganagar, K. (2018). Short-term passive tracer plume dispersion in convective boundary layer using a high-resolution WRF-ARW model. *Atmospheric Pollution Research*, *9*(5), 901–911. https://doi.org/10.1016/j.apr.2018.02.010

Blaylock, B. K., Horel, J. D., & Crosman, E. T. (2017). Impact of Lake Breezes on Summer Ozone Concentrations in the Salt Lake Valley. *Journal of Applied Meteorology and Climatology*, *56*(2), 353–370. https://doi.org/10.1175/JAMC-D-16-0216.1

Carrera, M. L., Gyakum, J. R., & Lin, C. A. (2009). Observational Study of Wind Channeling within the St. Lawrence River Valley. *Journal of Applied Meteorology and Climatology*, *48*(11), 2341–2361. https://doi.org/10.1175/2009JAMC2061.1

Cerenzia, I. (2017). *Challenges and Critical Aspects in Stable Boundary Layer Representation in Numerical Weather Prediction Modeling: Diagnostic Analyses and Proposals for Improvement* [Tesi di dottorato, alma]. https://doi.org/10.6092/unibo/amsdottorato/8067

Chemel, C., Arduini, G., Staquet, C., Largeron, Y., Legain, D., Tzanos, D., & Paci, A. (2016). Valley heat deficit as a bulk measure of wintertime particulate air pollution in the Arve River Valley. *Atmospheric Environment*, *128*, 208–215. https://doi.org/10.1016/j.atmosenv.2015.12.058

Chow, F. K., Schär, C., Ban, N., Lundquist, K. A., Schlemmer, L., & Shi, X. (2019). Crossing Multiple Gray Zones in the Transition from Mesoscale to Microscale Simulation over Complex Terrain. *Atmosphere*, *10*(5), 274. https://doi.org/10.3390/atmos10050274

Chow, F. K., Weigel, A. P., Street, R. L., Rotach, M. W., & Xue, M. (2006). High-Resolution Large-Eddy Simulations of Flow in a Steep Alpine Valley. Part I: Methodology, Verification, and Sensitivity Experiments. *Journal of Applied Meteorology and Climatology*, *45*(1), 63–86. https://doi.org/10.1175/JAM2322.1

Couvreux, F., Hourdin, F., & Rio, C. (2010). Resolved Versus Parametrized Boundary-Layer Plumes. Part I: A Parametrization-Oriented Conditional Sampling in Large-Eddy Simulations. *Boundary-Layer Meteorology*, *134*(3), 441–458. https://doi.org/10.1007/s10546-009-9456-5

Cros, B., Durand, P., Cachier, H., Drobinski, Ph., Fréjafon, E., Kottmeier, C., Perros, P. E., Peuch, V.-H., Ponche, J.-L., Robin, D., Saïd, F., Toupance, G., & Wortham, H. (2004). The ESCOMPTE program: An overview. *Atmospheric Research*, *69*(3), 241–279. https://doi.org/10.1016/j.atmosres.2003.05.001

de Bode, M., Hedde, T., Roubin, P., & Durand, P. (2021). Fine-Resolution WRF Simulation of Stably Stratified Flows in Shallow Pre-Alpine Valleys: A Case Study of the KASCADE-2017 Campaign. *Atmosphere*, *12*(8), 1063. https://doi.org/10.3390/atmos12081063

Dreyfus, G., Martinez, J. M., Samuelides, M., Gordon, M. B., Badran, F., Thiria, S., & Herault, L. (2002). Réseaux de neurones-Méthodologie et applications.

Ducrocq, V., Braud, I., Davolio, S., Ferretti, R., Flamant, C., Jansa, A., Kalthoff, N., Richard, E., Taupier-Letage, I., Ayral, P.-A., Belamari, S., Berne, A., Borga, M., Boudevillain, B., Bock, O., Boichard, J.-L., Bouin, M.-N., Bousquet, O., Bouvier, C., … Tamayo, J. (2014). HyMeX-SOP1: The Field Campaign Dedicated to Heavy Precipitation and Flash Flooding in the Northwestern Mediterranean. *Bulletin of the American Meteorological Society*, *95*(7), 1083–1100. https://doi.org/10.1175/BAMS-D-12-00244.1

Dudhia, J. (1996). A multi-layer soil temperature model for MM5. *Preprints, The Sixth PSU/NCAR Mesoscale Model Users' Workshop*, 22–24.

Duine, G.-J. (2015). *Characterization of down-valley winds in stable stratification from the KASCADE field campaign and WRF mesoscale simulations* [Phd, Université de Toulouse, Université Toulouse III - Paul Sabatier]. http://thesesups.ups-tlse.fr/2980/

Duine, G.-J., Hedde, T., Roubin, P., & Durand, P. (2016). A Simple Method Based on Routine Observations to Nowcast Down-Valley Flows in Shallow, Narrow Valleys. *Journal of Applied Meteorology and Climatology*, *55*(7), 1497–1511. https://doi.org/10.1175/JAMC-D-15-0274.1

Duine, G.-J., Hedde, T., Roubin, P., Durand, P., Lothon, M., Lohou, F., Augustin, P., & Fourmentin, M. (2017). Characterization of valley flows within two confluent valleys under stable conditions: Observations from the KASCADE field experiment. *Quarterly Journal of the Royal Meteorological Society*, *143*(705), 1886–1902. https://doi.org/10.1002/qj.3049

Dupuy, F. (2018). *Amélioration de la connaissance et de la prévision des vents de vallée en conditions stables: Expérimentation et modélisation statistique avec réseau de neurones artificiels* [Phd]. Université de Toulouse, Université Toulouse III - Paul Sabatier.

Dupuy, F., Duine, G.-J., Durand, P., Hedde, T., Pardyjak, E., & Roubin, P. (2021). Valley Winds at the Local Scale: Correcting Routine Weather Forecast Using Artificial Neural Networks. *Atmosphere*, *12*(2), 128. https://doi.org/10.3390/atmos12020128

Dupuy, F., Duine, G.-J., Durand, P., Hedde, T., Roubin, P., & Pardyjak, E. (2019). Local-Scale Valley Wind Retrieval Using an Artificial Neural Network Applied to Routine Weather Observations. *Journal of Applied Meteorology and Climatology*, *58*(5), 1007–1022. https://doi.org/10.1175/JAMC-D-18-0175.1

Ebert, E. E., & Curry, J. A. (1992). A parameterization of ice cloud optical properties for climate models. *Journal of Geophysical Research: Atmospheres*, *97*(D4), 3831–3836. https://doi.org/10.1029/91JD02472

Fernando, H. J. S., Pardyjak, E. R., Sabatino, S. D., Chow, F. K., Wekker, S. F. J. D., Hoch, S. W., Hacker, J., Pace, J. C., Pratt, T., Pu, Z., Steenburgh, W. J., Whiteman, C. D., Wang, Y., Zajic, D., Balsley, B., Dimitrova, R., Emmitt, G. D., Higgins, C. W., Hunt, J. C. R., … Zsedrovits, T. (2015). The MATERHORN: Unraveling the Intricacies of Mountain Weather. *Bulletin of the American Meteorological Society*, *96*(11), 1945–1967. https://doi.org/10.1175/BAMS-D-13-00131.1

Gardner, M. W., & Dorling, S. R. (1998). Artificial neural networks (the multilayer perceptron)—A review of applications in the atmospheric sciences. *Atmospheric Environment*, *32*(14), 2627–2636. https://doi.org/10.1016/S1352-2310(97)00447-0

Giovannini, L., Laiti, L., Serafin, S., & Zardi, D. (2017). The thermally driven diurnal wind system of the Adige Valley in the Italian Alps. *Quarterly Journal of the Royal Meteorological Society*, *143*(707), 2389–2402. https://doi.org/10.1002/qj.3092

Golzio, A., Ferrarese, S., Cassardo, C., Diolaiuti, G. A., & Pelfini, M. (2021). Land-Use Improvements in the Weather Research and Forecasting Model over Complex Mountainous Terrain and Comparison of Different Grid Sizes. *Boundary-Layer Meteorology*, *180*(2), 319–351. https://doi.org/10.1007/s10546-021-00617-1

Hahnenberger, M., Whiteman, C., & Hoch, S. (2009). Topographic Amplification Factor in a Closed Basin. *Spring Runoff Conference*. https://digitalcommons.usu.edu/runoff/2009/AllAbstracts/26

Haiden, T., & Whiteman, C. D. (2005). Katabatic Flow Mechanisms on a Low-Angle Slope. *Journal of Applied Meteorology*, *44*(1), 113–126. https://doi.org/10.1175/JAM-2182.1

Heimann, D., Clemente, M., Olny, X., Defrance, J., Suppan, P., Castelli, T., Lercher, P., Uhrner, U., Öttl, D., Rexeis, M., Franceschi, M. de, Antonacci, G., Seibert, P., Obleitner, F., Botteldooren, D., Elampe, E., Miege, B., Baulac, M., Schäfer, K., … Renterghem, T. V. (2007). *ALPNAP Air Pollution, Traffic Noise and Related Health Effects in the Alpine Space*. Università degli Studi di Trento, Dipartimento di Ingegneria Civile e Ambientale. https://graz.pure.elsevier.com/de/publications/alpnap-air-pollution-traffic-noise-and-related-health-effects-in-

Hobbs, P. V. (2000). *Introduction to Atmospheric Chemistry*. Cambridge University Press.

Holtslag, A. A. M. (2003). Atmospheric Turbulence. In R. A. Meyers (Ed.), *Encyclopedia of Physical Science and Technology (Third Edition)* (pp. 707–719). Academic Press. https://doi.org/10.1016/B0-12-227410-5/00039-9

Hong, S.-Y., Noh, Y., & Dudhia, J. (2006). A New Vertical Diffusion Package with an Explicit Treatment of Entrainment Processes. *Monthly Weather Review*, *134*(9), 2318–2341. https://doi.org/10.1175/MWR3199.1

Janjić, Z. I. (1994). The Step-Mountain Eta Coordinate Model: Further Developments of the Convection, Viscous Sublayer, and Turbulence Closure Schemes. *Monthly Weather Review*, *122*(5), 927–945. https://doi.org/10.1175/1520-0493(1994)122<0927:TSMECM>2.0.CO;2

Jasper, K. (2001). *Hydrological modelling of alpine river catchments using output variables from atmospheric models* (p. 162 S.) [ETH Zurich; Application/pdf]. https://doi.org/10.3929/ETHZ-A-004329041

Jemmett-Smith, B. C., Ross, A. N., Sheridan, P. F., Hughes, J. K., & Vosper, S. B. (2019). A case-study of cold-air pool evolution in hilly terrain using field measurements from COLPEX. *Quarterly Journal of the Royal Meteorological Society*, *145*(720), 1290–1306. https://doi.org/10.1002/qj.3499

Jeworrek, J., West, G., & Stull, R. (2019). Evaluation of Cumulus and Microphysics Parameterizations in WRF across the Convective Gray Zone. *Weather and Forecasting*, *34*(4), 1097–1115. https://doi.org/10.1175/WAF-D-18-0178.1

Jiménez, M. A., & Cuxart, J. (2014). A study of the nocturnal flows generated in the north side of the Pyrenees. *Atmospheric Research*, *145–146*, 244–254. https://doi.org/10.1016/j.atmosres.2014.04.010

Kaimal, J. C., & Finnigan, J. J. (1994). *Atmospheric Boundary Layer Flows: Their Structure and Measurement*. Oxford University Press.

Kalverla, P. C., Duine, G.-J., Steeneveld, G.-J., & Hedde, T. (2016). Evaluation of the Weather Research and Forecasting Model in the Durance Valley Complex Terrain during the KASCADE Field Campaign. *Journal of Applied Meteorology and Climatology*, *55*(4), 861–882. https://doi.org/10.1175/JAMC-D-15-0258.1

Katul, G. G., Oren, R., Manzoni, S., Higgins, C., & Parlange, M. B. (2012). Evapotranspiration: A process driving mass transport and energy exchange in the soil-plant-atmosphere-climate system. *Reviews of Geophysics*, *50*(3). https://doi.org/10.1029/2011RG000366

Kleczek, M. A., Steeneveld, G.-J., & Holtslag, A. A. M. (2014). Evaluation of the Weather Research and Forecasting Mesoscale Model for GABLS3: Impact of Boundary-Layer Schemes, Boundary Conditions and Spin-Up. *Boundary-Layer Meteorology*, *152*(2), 213–243. https://doi.org/10.1007/s10546-014-9925-3

Kovadlo, P. G., & Shihovtsev, A. Y. (2015). The study of turbulence and optical instability in stably stratified Earth's atmosphere. *21st International Symposium Atmospheric and Ocean Optics: Atmospheric Physics*, *9680*, 968074. https://doi.org/10.1117/12.2205997

Kristensen, L., Lenschow, D. H., Kirkegaard, P., & Courtney, M. (1989). The spectral velocity tensor for homogeneous boundary-layer turbulence. *Boundary-Layer Meteorology*, *47*(1), 149–193. https://doi.org/10.1007/BF00122327

LeMone, M. A., Ikeda, K., Grossman, R. L., & Rotach, M. W. (2003). Horizontal Variability of 2-m Temperature at Night during CASES-97. *Journal of the Atmospheric Sciences*, *60*(20), 2431–2449. https://doi.org/10.1175/1520-0469(2003)060<2431:HVOMTA>2.0.CO;2

Lenschow, D. H., & Stankov, B. B. (1986). Length Scales in the Convective Boundary Layer. *Journal of the Atmospheric Sciences*, *43*(12), 1198–1209. https://doi.org/10.1175/1520-0469(1986)043<1198:LSITCB>2.0.CO;2

Liu, K., & Pletcher, R. H. (2008). Anisotropy of a turbulent boundary layer. *Journal of Turbulence*, *9*, N18. https://doi.org/10.1080/14685240802191986

Lothon, M., Lohou, F., Pino, D., Couvreux, F., Pardyjak, E. R., Reuder, J., Vilà-Guerau de Arellano, J., Durand, P., Hartogensis, O., Legain, D., Augustin, P., Gioli, B., Lenschow, D. H., Faloona, I., Yagüe, C., Alexander, D. C., Angevine, W. M., Bargain, E., Barrié, J., … Zaldei, A. (2014). The BLLAST field experiment: Boundary-Layer Late Afternoon and Sunset Turbulence. *Atmospheric Chemistry and Physics*, *14*(20), 10931–10960. https://doi.org/10.5194/acp-14-10931-2014

Lumley, J. L. (1979). Computational Modeling of Turbulent Flows (Ed.), *Advances in Applied Mechanics* (Vol. 18, pp. 123–176). Elsevier. https://doi.org/10.1016/S0065-2156(08)70266-7

Mahoney, K. M. (2016). The Representation of Cumulus Convection in High-Resolution Simulations of the 2013 Colorado Front Range Flood. *Monthly Weather Review*, *144*(11), 4265–4278. https://doi.org/10.1175/MWR-D-16-0211.1

Mahrt, L. (2017). Stably Stratified Flow in a Shallow Valley. *Boundary-Layer Meteorology*, *162*(1), 1–20. https://doi.org/10.1007/s10546-016-0191-4

Mahrt, L., Sun, J., Oncley, S. P., & Horst, T. W. (2014). Transient Cold Air Drainage down a Shallow Valley. *Journal of the Atmospheric Sciences*, *71*(7), 2534–2544. https://doi.org/10.1175/JAS-D-14-0010.1

McTaggart-Cowan, R., & Zadra, A. (2015). Representing Richardson Number Hysteresis in the NWP Boundary Layer. *Monthly Weather Review*, *143*(4), 1232–1258. https://doi.org/10.1175/MWR-D-14-00179.1

Miguez-Macho, G., Stenchikov, G. L., & Robock, A. (2004). Spectral nudging to eliminate the effects of domain position and geometry in regional climate model simulations. *Journal of Geophysical Research: Atmospheres*, *109*(D13). https://doi.org/10.1029/2003JD004495

Moene, A. F., & Dam, J. C. van. (2014). *Transport in the atmosphere-vegetation-soil continuum*. Cambridge University Press. https://library.wur.nl/WebQuery/wurpubs/452475

Monin, A. S., & Obukhov, A. M. (1954). Basic laws of turbulent mixing in the surface layer of the atmosphere. *Contrib. Geophys. Inst. Acad. Sci. USSR*, *151*(163), e187.

Mukul, M., Srivastava, V., & Mukul, M. (2016). Accuracy analysis of the 2014–2015 Global Shuttle Radar Topography Mission (SRTM) 1 arc-sec C-Band height model using International Global Navigation Satellite System Service (IGS) Network. *Journal of Earth System Science*, *125*(5), 909–917. https://doi.org/10.1007/s12040-016-0716-8

Nadeau, D. F., Pardyjak, E. R., Higgins, C. W., Huwald, H., & Parlange, M. B. (2013). Flow during the evening transition over steep Alpine slopes. *Quarterly Journal of the Royal Meteorological Society*, *139*(672), 607–624. https://doi.org/10.1002/qj.1985

Nakanishi, M., & Niino, H. (2006). An Improved Mellor–Yamada Level-3 Model: Its Numerical Stability and Application to a Regional Prediction of Advection Fog. *Boundary-Layer Meteorology*, *119*(2), 397–407. https://doi.org/10.1007/s10546-005-9030-8

Neff, W. D., & King, C. W. (1987). Observations of complex-terrain flows using acoustic sounders: Experiments, topography, and winds. *Boundary-Layer Meteorology*, *40*(4), 363–392. https://doi.org/10.1007/BF00116103

Ngan, F., & Stein, A. F. (2017). A Long-Term WRF Meteorological Archive for Dispersion Simulations: Application to Controlled Tracer Experiments. *Journal of Applied Meteorology and Climatology*, *56*(8), 2203–2220. https://doi.org/10.1175/JAMC-D-16-0345.1

Noble, J. M., Alberts, W. C. K., Raspet, R., Collier, S. L., & Coleman, M. A. (2014). Infrasound wind noise reduction via porous fabric domes. *The Journal of the Acoustical Society of America*, *135*(4), 2409–2409. https://doi.org/10.1121/1.4877982

PACI, A., STAQUET, C., ALLARD, J., BARRAL, H., CANUT, G., COHARD, J.-M., JAFFREZO, J.-L., MARTINET, P., SABATIER, T., TROUDE, F., ARDUINI, G., BURNET, F., BRUN, C., CHEMEL, C., DABAS, A.,

DONIER, J.-M., GARROUSTE, O., GUILLOT, R., LARGERON, Y., … ZIN, I. (2017, November 6). *La campagne Passy-2015: Dynamique atmosphérique et qualité de l'air dans la vallée de l'Arve* [Text]. http://irevues.inist.fr/pollution-atmospherique; Association pour la prévention de la pollution atmosphérique. https://doi.org/10.4267/pollution-atmospherique.5903

Page, J. (2012). Chapter IIA-1—The Role of Solar-Radiation Climatology in the Design of Photovoltaic Systems. In A. McEvoy, T. Markvart, & L. Castañer (Eds.), *Practical Handbook of Photovoltaics (Second Edition)* (pp. 573–643). Academic Press. https://doi.org/10.1016/B978-0-12-385934-1.00017-9

Peñuelas, J., & Llusià, J. (2001). The Complexity of Factors Driving Volatile Organic Compound Emissions by Plants. *Biologia Plantarum*, *44*(4), 481–487. https://doi.org/10.1023/A:1013797129428

Pineda, N., Jorba, O., Jorge, J., & Baldasano, J. M. (2004). Using NOAA AVHRR and SPOT VGT data to estimate surface parameters: Application to a mesoscale meteorological model. *International Journal of Remote Sensing*, *25*(1), 129–143. https://doi.org/10.1080/0143116031000115201

Pleim, J. E. (2007). A Combined Local and Nonlocal Closure Model for the Atmospheric Boundary Layer. Part I: Model Description and Testing. *Journal of Applied Meteorology and Climatology*, *46*(9), 1383–1395. https://doi.org/10.1175/JAM2539.1

Price, J. D., Vosper, S., Brown, A., Ross, A., Clark, P., Davies, F., Horlacher, V., Claxton, B., McGregor, J. R., Hoare, J. S., Jemmett-Smith, B., & Sheridan, P. (2011). COLPEX: Field and Numerical Studies over a Region of Small Hills. *Bulletin of the American Meteorological Society*, *92*(12), 1636–1650. https://doi.org/10.1175/2011BAMS3032.1

Quimbayo-Duarte, J., Chemel, C., Staquet, C., Troude, F., & Arduini, G. (2021). Drivers of severe air pollution events in a deep valley during wintertime: A case study from the Arve river valley, France. *Atmospheric Environment*, *247*, 118030. https://doi.org/10.1016/j.atmosenv.2020.118030

Quimbayo-Duarte, J., Staquet, C., Chemel, C., & Arduini, G. (2019a). Impact of Along-Valley Orographic Variations on the Dispersion of Passive Tracers in a Stable Atmosphere. *Atmosphere*, *10*(4), 225. https://doi.org/10.3390/atmos10040225

Quimbayo-Duarte, J., Staquet, C., Chemel, C., & Arduini, G. (2019b). Dispersion of Tracers in the Stable Atmosphere of a Valley Opening onto a Plain. *Boundary-Layer Meteorology*, *172*(2), 291–315. https://doi.org/10.1007/s10546-019-00439-2

Rampanelli, G., Zardi, D., & Rotunno, R. (2004). Mechanisms of Up-Valley Winds. *Journal of Atmospheric Sciences*, *61*(24), 3097–3111. https://doi.org/10.1175/JAS-3354.1

Rio, C., Hourdin, F., Couvreux, F., & Jam, A. (2010). Resolved Versus Parametrized Boundary-Layer Plumes. Part II: Continuous Formulations of Mixing Rates for Mass-Flux Schemes. *Boundary-Layer Meteorology*, *135*(3), 469–483. https://doi.org/10.1007/s10546-010-9478-z

Rotach, M. W., Calanca, P., Graziani, G., Gurtz, J., Steyn, D. G., Vogt, R., Andretta, M., Christen, A., Cieslik, S., Connolly, R., Wekker, S. F. J. D., Galmarini, S., Kadygrov, E. N., Kadygrov, V., Miller, E., Neininger, B., Rucker, M., Gorsel, E. V., Weber, H., … Zappa, M. (2004). Turbulence Structure and Exchange Processes in an Alpine Valley: The Riviera Project. *Bulletin of the American Meteorological Society*, *85*(9), 1367–1386. https://doi.org/10.1175/BAMS-85-9-1367

Santos-Alamillos, F. J., Pozo-Vázquez, D., Ruiz-Arias, J. A., Lara-Fanego, V., & Tovar-Pescador, J. (2013). Analysis of WRF Model Wind Estimate Sensitivity to Physics Parameterization Choice and Terrain Representation in Andalusia (Southern Spain). *Journal of Applied Meteorology and Climatology*, *52*(7), 1592–1609. https://doi.org/10.1175/JAMC-D-12-0204.1

Schmidli, J., & Rotunno, R. (2010). Mechanisms of Along-Valley Winds and Heat Exchange over Mountainous Terrain. *Journal of the Atmospheric Sciences*, *67*(9), 3033–3047. https://doi.org/10.1175/2010JAS3473.1

Sekiyama, T. T., Kunii, M., Kajino, M., & Shimbori, T. (2015). Horizontal Resolution Dependence of Atmospheric Simulations of the Fukushima Nuclear Accident Using 15-km, 3-km, and 500-m Grid Models. *Journal of the Meteorological Society of Japan*, *93*(1), 16.

Skamarock, W. C., Klemp, J. B., Dudhia, J., Gill, D. O., Barker, D. M., Duda, M. G., Huang, X.-Y., Wang, W., & Powers, J. G. (2008). *A Description of the Advanced Research WRF Version 3*.

Skamarock, W. C., Klemp, J. B., Dudhia, J., Gill, D. O., Liu, Z., Berner, J., Wang, W., Powers, J. G., Duda, MichaelG., Barker, D. M., & Huang, X. (2019). *A Description of the Advanced Research WRF Model Version 4*. https://doi.org/10.5065/1dfh-6p97

Staquet, C., Paci, A., Allard, J., Arduini, G., Barral, H., Barret, M., Blein, S., Brun, C., Burnet, F., Canut, G., Chapuis, D., Chemel, C., Chevrier, F., Cohard, J.-M., Dabas, A., Guyard, H., Jaffrezo, J.-L., Martinet, P., Mercier, S., … Zin, I. (2015, August 31). *The Passy project: Objectives, underlying scientific questions and preliminary numerical modelling of the Passy Alpine valley.* 33rd International Conference on Alpine Meteorology ICAM 2015. https://hal.archives-ouvertes.fr/hal-02330672

Steeneveld, G.-J. (2014). Current challenges in understanding and forecasting stable boundary layers over land and ice. *Frontiers in Environmental Science*, *2*. https://doi.org/10.3389/fenvs.2014.00041

Steeneveld, G.-J., & de Bode, M. (2018). Unravelling the relative roles of physical processes in modelling the life cycle of a warm radiation fog. *Quarterly Journal of the Royal Meteorological Society*, *144*(714), 1539–1554. https://doi.org/10.1002/qj.3300

Steinacker, R. (1984). *Area-height distribution of a valley and its relation to the valley wind*. 64–71.

Sterk, H. A. M., Steeneveld, G.-J., & Holtslag, A. A. M. (2013). The role of snow-surface coupling, radiation, and turbulent mixing in modeling a stable boundary layer over Arctic sea ice. *Journal of Geophysical Research: Atmospheres*, *118*(3), 1199–1217. https://doi.org/10.1002/jgrd.50158

Stiperski, I., Calaf, M., & Rotach, M. W. (2019). Scaling, Anisotropy, and Complexity in Near-Surface Atmospheric Turbulence. *Journal of Geophysical Research: Atmospheres*, *124*(3), 1428–1448. https://doi.org/10.1029/2018JD029383

Stull, R. B. (2000). *Meteorology for Scientists and Engineers* (2nd edition, Vol. 1). Brooks/Cole.

Stull, R. B. (2009). *An Introduction to Boundary Layer Meteorology* (Vol. 13). Springer Science+Business Media.

Sukoriansky, S., Galperin, B., & Perov, V. (2005). 'Application of a New Spectral Theory of Stably Stratified Turbulence to the Atmospheric Boundary Layer over Sea Ice'. *Boundary-Layer Meteorology*, *117*(2), 231–257. https://doi.org/10.1007/s10546-004-6848-4

Sun, Z., & Shine, K. P. (1994). Studies of the radiative properties of ice and mixed-phase clouds. *Quarterly Journal of the Royal Meteorological Society*, *120*(515), 111–137. https://doi.org/10.1002/qj.49712051508

Tewari, M., Chen, F., Wang, W., Dudhia, J., LeMone, M. A., Mitchell, K. E., Ek, M., Gayno, G. A., Wegiel, J. W., & Cuenca, R. (2004). Implementation and verification of the unified NOAH land surface model in the WRF model (Formerly Paper Number 17.5). *20th Conference on Weather Analysis and Forecasting/16th Conference on Numerical Weather Prediction*, 11–15. https://www2.mmm.ucar.edu/wrf/users/physics/phys_refs/LAND_SURFACE/noah.pdf

Tomasi, E. (2014, June 12). *High-resolution numerical simulations of wintertime atmospheric boundary layer processes in the Adige Valley during an ALPNAP project field campaign*. 21st Symposium on Boundary Layers and Turbulence. https://ams.confex.com/ams/21BLT/webprogram/Paper248123.html

Tuller, M., & Or, D. (2005). WATER RETENTION AND CHARACTERISTIC CURVE. In *Encyclopedia of Soils in the Environment* (pp. 278–289). Elsevier. https://doi.org/10.1016/B0-12-348530-4/00376-3

Udina, M., Montornès, À., Casso, P., Kosović, B., & Bech, J. (2020). WRF-LES Simulation of the Boundary Layer Turbulent Processes during the BLLAST Campaign. *Atmosphere*, *11*(11), 1149. https://doi.org/10.3390/atmos11111149

Velde, Ivar. R. van der, Steeneveld, G.-J., Wichers Schreur, B. G. J., & Holtslag, A. A. M. (2010). Modeling and Forecasting the Onset and Duration of Severe Radiation Fog under Frost

Conditions. *Monthly Weather Review*, *138*(11), 4237–4253. https://doi.org/10.1175/2010MWR3427.1

Vogt, M., Schneider, P., Castell, N., & Hamer, P. (2021). Assessment of Low-Cost Particulate Matter Sensor Systems against Optical and Gravimetric Methods in a Field Co-Location in Norway. *Atmosphere*, *12*(8), 961. https://doi.org/10.3390/atmos12080961

Vosper, S. B., Hughes, J. K., Lock, A. P., Sheridan, P. F., Ross, A. N., Jemmett-Smith, B., & Brown, A. R. (2014). Cold-pool formation in a narrow valley. *Quarterly Journal of the Royal Meteorological Society*, *140*(679), 699–714. https://doi.org/10.1002/qj.2160

Wagner, A. (1932). *Wagner: Der UI iche Luftdruck-und Temperaturgang... - Google Scholar*. https://scholar.google.com/scholar_lookup?hl=en&volume=37&publication_year=1932&pages=315-344&journal=Gerlands+Beitr.+Geophys.&author=A+Wagner&title=Der+t%C3%A4gliche+Luftdruck%E2%80%90+und+Temperaturgang+in+der+freien+Atmosph%C3%A4re+und+in+Gebirgst%C3%A4lern

Wagner, J., Gerz, T., Wildmann, N., & Gramitzky, K. (2019). Long-term simulation of the boundary layer flow over the double-ridge site during the Perdigão 2017 field campaign. *Atmospheric Chemistry and Physics*, *19*(2), 1129–1146. https://doi.org/10.5194/acp-19-1129-2019

Wagner, J. S., Gohm, A., & Rotach, M. W. (2015). The impact of valley geometry on daytime thermally driven flows and vertical transport processes. *Quarterly Journal of the Royal Meteorological Society*, *141*(690), 1780–1794. https://doi.org/10.1002/qj.2481

Wallace, J. M., & Hobbs, P. V. (2006). *Atmospheric Science* (second, Vol. 92). ELSEVIER. https://books.google.com/books/about/Atmospheric_Science.html?id=HZ2wNtDOU0oC

Weber, R. O., & Kaufmann, P. (1998). Relationship of Synoptic Winds and Complex Terrain Flows during the MISTRAL Field Experiment. *Journal of Applied Meteorology*, *37*(11), 1486–1496. https://doi.org/10.1175/1520-0450(1998)037<1486:ROSWAC>2.0.CO;2

Weisman, M. L., Skamarock, W. C., & Klemp, J. B. (1997). The Resolution Dependence of Explicitly Modeled Convective Systems. *Monthly Weather Review*, *125*(4), 527–548. https://doi.org/10.1175/1520-0493(1997)125<0527:TRDOEM>2.0.CO;2

Whiteman, C. D. (1990). Observations of Thermally Developed Wind Systems in Mountainous Terrain. In R. M. Banta, G. Berri, W. Blumen, D. J. Carruthers, G. A. Dalu, D. R. Durran, J. Egger, J. R. Garratt, S. R. Hanna, J. C. R. Hunt, R. N. Meroney, W. Miller, W. D. Neff, M. Nicolini, J. Paegle, R. A. Pielke, R. B. Smith, D. G. Strimaitis, T. Vukicevic, … W. Blumen (Eds.), *Atmospheric Processes over Complex Terrain* (pp. 5–42). American Meteorological Society. https://doi.org/10.1007/978-1-935704-25-6_2

Whiteman, C. D. (2000). *Mountain Meteorology: Fundamentals and Applications*. Oxford University Press.

Whiteman, C. D., & Doran, J. C. (1993). The Relationship between Overlying Synoptic-Scale Flows and Winds within a Valley. *Journal of Applied Meteorology*, *32*(11), 1669–1682. https://doi.org/10.1175/1520-0450(1993)032<1669:TRBOSS>2.0.CO;2

Wiersema, D. J., Lundquist, K. A., & Chow, F. K. (2020). Mesoscale to Microscale Simulations over Complex Terrain with the Immersed Boundary Method in the Weather Research and Forecasting Model. *Monthly Weather Review*, *148*(2), 577–595. https://doi.org/10.1175/MWR-D-19-0071.1

Wilks, D. S. (2011). *Statistical Methods in the Atmospheric Sciences*. Academic Press.

Xu, H., Wang, Y., & Wang, M. (2018). The Performance of a Scale-Aware Nonlocal PBL Scheme for the Subkilometer Simulation of a Deep CBL over the Taklimakan Desert. *Advances in Meteorology*. https://doi.org/10.1155/2018/8759594

Yver, C. E., Graven, H. D., Lucas, D. D., Cameron-Smith, P. J., Keeling, R. F., & Weiss, R. F. (2013). Evaluating transport in the WRF model along the California coast. *Atmospheric Chemistry and Physics*, *13*(4), 1837–1852. https://doi.org/10.5194/acp-13-1837-2013

Zardi, D., & Whiteman, C. D. (2013). Diurnal Mountain Wind Systems. In F. K. Chow, S. F. J. De Wekker, & B. J. Snyder (Eds.), *Mountain Weather Research and Forecasting: Recent Progress*

and Current Challenges (pp. 35–119). Springer Netherlands. https://doi.org/10.1007/978-94-007-4098-3_2

Zhang, X., Bao, J.-W., Chen, B., & Grell, E. D. (2018). A Three-Dimensional Scale-Adaptive Turbulent Kinetic Energy Scheme in the WRF-ARW Model. *Monthly Weather Review*, *146*(7), 2023–2045. https://doi.org/10.1175/MWR-D-17-0356.1

Annex 1: Detailed description of the meteorological stations of KASCADE 2013 and KASCADE 2017

Table A1.1: Summary of instruments used during the KASCADE-2013 campaign. acq.: acquiring, elev.: elevation, freq.: frequency, hgt.: height, meas.: measurement. The information in this table originates from the work of (Duine, 2015). GBA and VER are permanent stations, and M30 was only there for the duration of KASCADE-2013 (13 December, 2012 to 18 March, 2013)

Site	Station	Coordinates (°N, °E)	Elev. base (m asl)	Meas. hgt. (m agl)	Instrument	Variable(s)	Acq. freq. (Hz)	Output freq. (Hz)	Additional information
M30	id.	43.68550	286	30.36	Campbell Sci. HMP45 thermohygrometer	T, RH	0.1	0.1	
		5.76169		30.29	Campbell Sci. CSAT sonic anemometer	U', V', W', T'	10.0	10	
				30.29	LI-COR LI-7500A open path analyzer	H2O', CO2'	10.0	10	
				20.11	Kipp & Zonen CNR4 net radiometer	$SW^{\uparrow}$, $SW^{\downarrow}$, $LW^{\uparrow}$, $LW^{\downarrow}$	0.1	0.1	
				10.50	Young 81000 sonic anemometer	U', V', W', T'	10.0	10	
				1.90	Campbell Sci. HC2S3 thermohygrometer	T, RH	0.1	0.1	
				1.90	Young 81000 sonic anemometer	U', V', W', T'	10.0	10	
	CNR1	43.68564 5.76147	286	1.18	Kipp & Zonen CNR1 net radiometer	$SW^{\uparrow}$, $SW^{\downarrow}$, $LW^{\uparrow}$, $LW^{\downarrow}$	0.1	0.1	
	TB	43.68511 5.76233	287	2-300	Vaisala TTS111 Tethersondes (3)	T, RH, PP, FF, DD	0.25	Check	3 profiling sensors $v_z = 30\ cm\ s^{-1}$
				1.50	Vaisala TTS111 Tethersonde (1)	T, RH, PP, FF, DD	0.25		Height correction sensor
	RS	43.68550 5.76169	286	0-5000	MODEM M2K2-DC Radiosonde system	T, RH, PP, FF, DD	1.0	1.0	Ballon type cosmoprene KE 45 g
VER	id.	43.70744	295	15.0	Dégréane DEOLIA96 cup anemometer	FF, DD	0.1	0.0017	
		5.76233		2.0	Vaisala PT100 thermometer	T	0.1	0.0017	
				2.0	Vaisala hygrometer	RH	0.1	0.0017	
				2.0	Vaisala barometer	PP	0.1	0.0017	
				2.0	PréciMéca R30295 rain gauge	RR	0.1	0.0017	
	SODAR	43.70697 5.76531	297	75-400	Remtech PA2 Sodar	FF, DD $\sigma_u, \sigma_v, \sigma_w$	0.001	0.001	
GBA	id.	43.69442	265	110.0	PT100 thermometer	T	0.1	0.0017	

	5.74614	110.0	Metek sonic anemometer	FF, DD	0.1	0.0017
		2.0	PT100 thermometer	T	0.1	0.0017
		2.0	Rotronic hygrometer	RH	0.1	0.0017
		2.0	Vasala PTB1001C barometer	PP	0.1	0.0017

Table A1.2: All temporal meteorological stations for the Kascade 2017 campaign. FF is wind speed, DD is wind direction, LW is longwave, and SW is shortwave. Superscript arrows indicate up-going flux and downcoming flux by up- and downward arrows. T is temperature, where subscript "s" means surface temperature, "son" gives temperature based on sonic anemometer measurements. Vwc is volumetric water content. U, V, and W are the three wind components. Exact locations and operation times can be found in Table A4.

Station	Meas. Hgt. (m agl)	Instrument	Variable(s)	Remark
LEMS	2	Coupled Anemometer and vane Davis 7911	FF, DD	
	1.8	Pyranometer LI-COR LI-200R	$SW^{\downarrow}$	
	1.5	Thermo-hygrometer Sensirion SHT15	T, RH	
	1	Barometer Bosch BMP085	PP	
	0	Sensirion Zytemp TN9	T_s	
	-0.05	Decagon 5TM	T, vwc	
	-0.25	Decagon 5TM	T, vwc	
	?	?	WS_{son}, WD_{son}, T_{son}	Only at N1
AS1/	2	Campbell Sci. CSAT3 sonic anemometer	U', V', W', T_{son}	
	2	Licor 7500	H_2O, CO_2	
	1	EML ARG100 pluviometer	Precipitation	
	-0.05	Hukseflux HFP01 fluxmeter in the ground	PP	
ANTEE		Kipp & Zonen CNR4 net radiometer	$SW^{\uparrow}$, $SW^{\downarrow}$, $LW^{\uparrow}$, $LW^{\downarrow}$	Next to AS1
AS2	2	Campbell Sci. CSAT3 sonic anemometer	U', V', W', T_{son}	
AS3	10	Young 81000 Sonic anemometers	U', V', W', T_{son}	Mast is called MET02
	5	Young 81000 Sonic anemometers	U', V', W', T_{son}	Mast is called MET02
	2	Young 81000 Sonic anemometers	U', V', W', T_{son}	Mast is called MET02
	1	Campbell 52203 tip bucket pluviometer	Precipitation	
AS4	2	Campbell Sci. CSAT3 sonic anemometer	U', V', W', T_{son}	
AS5	2	Campbell Sci. CSAT3 sonic anemometer	U', V', W', T_{son}	
SODAR1	100 – 500	Remtech PA2	FF, DD	
SODAR2	60 – 400	Metek PCS.2000-24	FF, DD	

These graphs contain a detailed description of the measurement equipment available, Table A1 contains descriptions of the permanent and M30 measurement locations. Supplemented with Table A1.2 of the KASCADE-2017 measurement equipment and Sodars. In Table A1.3 I describe the development of the MET01 station since it was built in 2015. Table A1.4 contains the exact location of the stations available during the KASCADE-2017.

Currently the GBA instrumentation is being extended with additional measurements at 15, 27, 50, 75, and 100 m agl. These measurements will contain wind, temperature and humidity. Similarly, the MET01 station receives additional soil measurements. Measuring the soil temperature, moisture, and tension at 5 different depths, being 0.15, 0.30, 0.60, 1.00 and 1.50 m below ground. They were still calibrated in November 2021. Further information of the water ground level at different soil layers is available since September 2021 through the installation of two piezometers with their membrane at -8.20 and -30 m depth.

Table A1.3: List of the MET01 development up to now.

Station	Meas hgt (m agl)	Instrument	Variable(s)	Duration (dd/mm/yyyy)
MET01	10	Coupled anemometer and vane Campbell Sci. 05103	FF, DD	Between: 17/02/2016 - 31/05/2017
	10	Young 81000 Sonic anemometers	U', V', W', T_{son}	Starting: 01/07/2017
	5	Young 81000 Sonic anemometers	U', V', W', T_{son}	Starting: 01/07/2017
	2	Pyranometer Campbell Sci. LP02	$SW^{\downarrow}$	Starting: 17/02/2015
	2	Barometer Campbell SCi. CS100	P	Starting: 17/02/2015
	2	Sonde Campbell Sci. ARG100	T, RH	Starting: 17/02/2015
	2	Coupled anemometer and vane Campbell Sci. 05103	FF, DD	Between: 17/02/2015 - 17/02/2016

Table A1.4: Location, surface elevations and times of operation of the different temporal stations of KASCADE-2017.

Name	Coordinates		Elevation base	Start	End
	N°	E°	[m amsl]	(dd/mm/yyyy)	(dd/mm/yyyy)
ANTEE	43.69540	5.74320	262	15/12/2016	13/03/2017
AS1	43.69540	5.74320	262	15/12/2016	13/03/2017
AS2	43.68877	5.75364	278	13/12/2016	06/06/2017
AS3	43.68296	5.76518	291	13/12/2016	02/05/2017
AS4	43.67643	5.77903	312	14/12/2016	06/06/2017
AS5	43.71205	5.75394	283	15/12/2016	06/06/2017
B1	43.69548	5.74324	262	14/12/2016	03/07/2017
B2	43.69141	5.74919	274	15/12/2016	03/07/2017
B3	43.68264	5.76568	291	13/12/2016	03/07/2017
B4	43.67519	5.78672	323	14/12/2016	03/07/2017
N1 **N1 sonic**	43.68483	5.76804	325	14/12/2016 03/02/2017	03/07/2017
N2	43.68568	5.76885	347	14/12/2016	03/07/2017
N3	43.68879	5.77072	363	15/12/2016	03/07/2017
N4	43.69300	5.76254	394	15/12/2016	29/06/2017
S1	43.68039	5.76004	314	14/12/2016	03/07/2017
S2	43.67849	5.75764	329	15/12/2016	03/07/2017
S3	43.66871	5.77792	386	14/12/2016	23/06/2017

S4	43.66899	5.76180	398	12/01/2017	03/07/2017
SOD1	43.70744	5.76514	295	21/11/2017	06/01/2014
	43.68546	5.76171	287	06/01/2014	18/02/2015
	43.69526	5.74329	262	18/02/2015	31/03/2017
SOD2	43.6851	5.7625	287	15/12/2016	31/06/2019
	43.6944	5.7459	265	01/06/2021	Present

To illustrate the measurement locations, every location has a photo, if available, with a small description of its surroundings. The photos will show the LEMS, AS, Sodars, and other stations of both KAS13 and KAS17.

LEMS

These photos are created thanks to the KASCADE 2017 team, especially Thierry Hedde and Pierre Durand.

As mentioned in the main text, the twelve LEMS are divided into three groups of four each on a valley slope. I will present them in these groups, Figure A1.1 shows the Valley floor stations, Figure A1.2 shows the north sidewall LEMS and those on the south sidewall are in Figure A1.3. Most of these photos are taken during the installations of the displayed station. Otherwise, they are taken soon after their installation.

Figure A1.1: The LEMS station along the valley floor a) shows a view towards the west with AS1 on the left and B1 on the right. b) shows B2 under construction partially covered by a orange safety vest and in the background the GBA pylon shows. c) shows the nearly finished B3 and shows the north side slope of the CV. d) shows B4 with its nearest slope. e) shows B4 with in downvalley direction.

The GBA is visible in Figure A1.1b, and stands on the same terrain as shown in Figure A1.1a. Figure A1.4 shows the part of the valley with M30 and later MET01 will take its place. The photos of Figure A1.5 - A1.8 contain the sonic anemometers and the Sodars. However, the photos of AS2 and AS4 are currently not available.

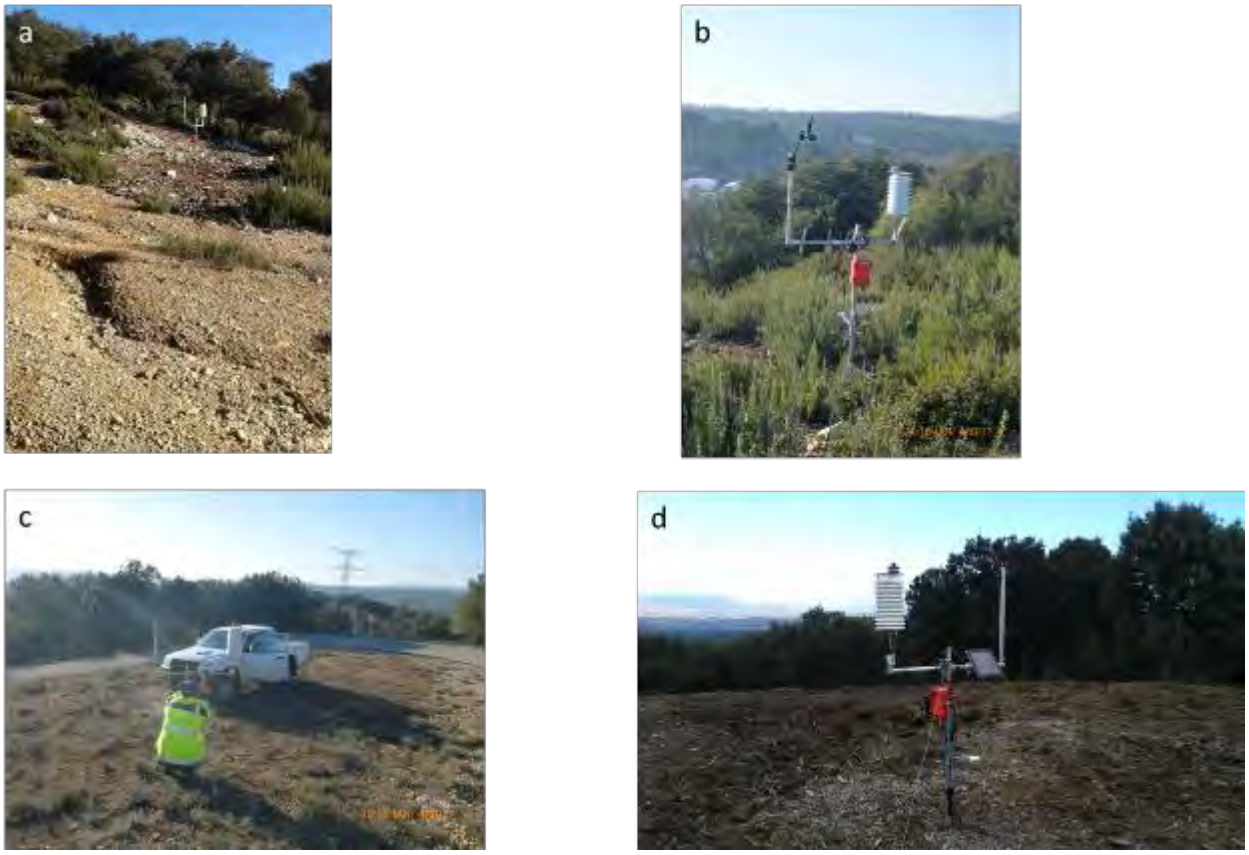

Figure A1.2: Stations on the northern sidewall of the CV, containing N1 to N4. a) shows N1, b) shows N2 with the CV in the background, c) shows N3, and d) shows N4 with part of the DV in the background.

Figure A1.3: Stations on the south slopewall of the CV, containing S1 to S4. a) shows S1 with the CV in the background, b) shows S2, c) shows S3, and d) shows S4.

Figure A1.4: Photo of the M30 station at roughly the same location where later will be the MET01 station. Photo taken from the north sidewall towards the south sidewall.

Figure A1.5: Two photos of AS1 showing its proximity to the pluviometer and B1.

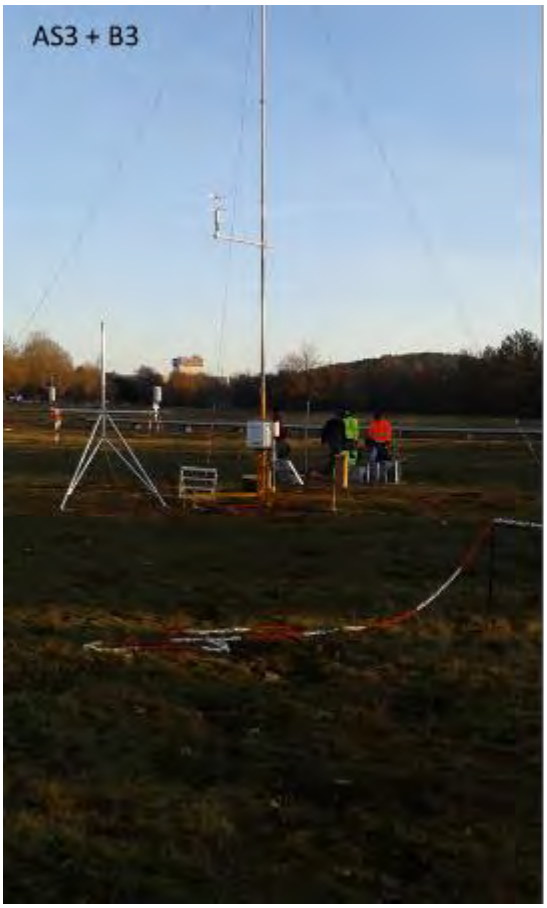

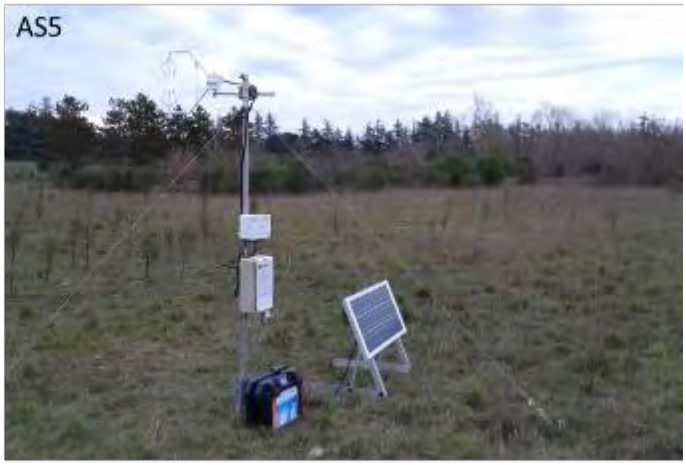

Figure A1.6: On the left photo station AS3 with B3 in the background and AS5 on the right photo.

Figure A1.7: Sodar2, photograph taken in upvalley direction.

Figure A1.8: Sodar1 installation close-up photo.

Annex 2: Sodar data analysis

All Sodar observations have been visualized to better understand the vertical wind profiles, as described in 2.3.4. Here I give an overview of all the IOPs, and plot for references. They can also be found digitally[3].

Table A2.1: Classification of the different types of winds based on the data collected by the Sodars of the KASCADE campaigns.

KAS-IOP	*Established DDV*	*Mistral*	*Weak DDV*	*Other*	*Lacking data*
KAS13-01	Y	Y	-	-	-
KAS13-02	-	Y	-	-	-
KAS13-03	-	-	-	Y	-
KAS13-04	Y	-	-	-	-
KAS13-05	-	-	-	Y	-
KAS13-06	Y	Y	-	-	Y
KAS13-07	-	-	Y	-	-
KAS13-08	-	Y	Y	Y	-
KAS13-09	-	-	-	-	Y
KAS13-10	-	-	Y	Y	Y
KAS13-11	-	Y	Y	-	-
KAS13-12	-	-	Y	-	-
KAS13-13	-	-	-	Y	Y
KAS13-14	-	-	Y	-	-
KAS13-15	Y	-	-	-	-
KAS13-16	-	-	Y	-	-
KAS13-17	Y	-	-	-	-
KAS13-18	-	-	Y	Y	-
KAS13-19	Y	-	-	-	-
KAS13-20	Y	-	-	-	-
KAS13-21	-	-	Y	Y	-
KAS13-22	-	-	-	-	Y
KAS13-23	-	-	-	-	Y
KAS17-01	-	-	Y	-	-
KAS17-02	Y	-	-	-	-
KAS17-03	Y	-	-	-	Y
KAS17-04	Y	-	-	-	Y
KAS17-05	-	-	Y	-	-
KAS17-06	-	-	Y	-	-
KAS17-07	Y	-	-	-	-
KAS17-08	-	-	Y	Y	-
KAS17-09	Y	-	-	-	-
KAS17-10	-	Y	-	Y	-

[3] https://drive.google.com/drive/folders/11Kh1ZoWTaiX6hJyS2GSQ3FGWnp9mfhKl?usp=sharing

KAS17-11	-	Y	Y	-	-
KAS17-12	-	Y	-	-	Y
KAS17-13	-	Y	Y	-	Y
KAS17-14	-	Y	Y	Y	Y

Annex 3 Anisotropy calculations

This section briefly describes invariant calculation for the anisotropy tensor and how to proceed to a Lumley triangle and a barycentric map. Additionally, it contains the plots for KAS17-IOP07 as an example. The other days can be found digitally[4] under Isotropy.

The anisotropy tensor is based on the turbulent stress tensor normalized by two times TKE, corrected with a third of the Kronecker delta to set the normalized first invariant to zero. Note that u is defined as the along wind direction.

$$a_{ij} = \frac{\overline{u'_i u'_j}}{2e} - \frac{\delta_{ij}}{3}$$

Where e is the TKE per unit mass, from a_{ij} I calculate the principal invariants (I, II, III). The first invariant is defined as $I = a_{ii}$, which is the trace of the matrix. The second invariant is defined as $II = \frac{1}{2}(\left(tr(a_{ij})\right)^2 - tr(a_{ij}^2))$. The last invariant is the determinant of a_{ij}, written as $III = \det(a_{ij})$.Of these three invariants, I is zero (resulting from the above equation) and II always has a negative value. The opposite of II plotted against III shows the (an)isotropy type. If all three invariants are zero, the turbulence state is 3-D (resembling a sphere). At the same time, the other triangle extremes indicate either a pure 1-D turbulence, resembling a line (-2/3 for II and 2/9 for III), or a pure 2-D isotropic turbulence, resembling a pancake (-1/6 for II and -1/36 for III).

However, this situation causes some problems with the transition between flows since the plot is not linear and the center (where all three types of turbulence contribute equally) is not in the center of the plot. To create plots that are easier to read, I create barycentric maps as described by Banerjee et al. (2007). Here I focus only on the diagonal section of a_{ij}, a_{ii}, from which I determine two independent anisotropy eigenvalues, λ_1 and λ_2, defined as the maximum value in a_{ii} and the second highest values. The third anisotropy eigenvalue, λ_3, can be either determined based on the first two ($-\lambda_1 - \lambda_2$) or defined as the lowest a_{ii} value, because the sum of the diagonal terms is zero.

To determine the amount of each type of (an)isotropy within a range of 0 – 1, these eigenvalues are converted to C_{1c}, C_{2c}, and C_{3c}. These are the fractions of types of isotropy, and they combine to 1 in a barycentric map, making the solutions unique.

$$C_{1c} = \lambda_1 - \lambda_2$$

$$C_{2c} = 2(\lambda_2 - \lambda_3)$$

$$C_{3c} = -3\lambda_3$$

Where C_{1c} is the linear turbulence, C_{2c} is the planar turbulence and C_{3c} is the spherical turbulence. In the equilateral triangle, each flank is the base for an axis, the base side (along the x-axes) is the zero line for 3-D turbulence, at the opposite side (in the top corner of the triangle), turbulence is completely 3-D. The left side indicates zero 1-D turbulence and the right side indicates zero 2-D turbulence. At the triangle center, they all contribute 33 % to the type of turbulence, making the determination of the turbulence composition much easier.

Figure A3.1 shows the Lumley triangles filled with the different types of anisotropy occurring during KAS17-IOP07. They have a part in the 1-D turbulence section and only AS3 at 10 m and AS1 seem to have strong 2-D isotropy and even have strong 3-D tendencies, especially during daytime. However,

[4] https://drive.google.com/drive/folders/11Kh1ZoWTaiX6hJyS2GSQ3FGWnp9mfhKl?usp=sharing

the plots do not have a clear center; thus, the exact amounts of different types of isotropy are hard to distinguish. Figure A3.2 shows the barycentric maps of the same instances as shown in Figure A3.1. It shows that the apparent tendency towards 3-D isotropy was in fact a distortion caused by the Lumley triangle shape. The barycentric maps show a tendency for high quantities of 2-D isotropy mixed with some 1-D anisotropy and only during daytime does the 3-D turbulence start to play a major role. Plots of other IOPs can be found digitally[5].

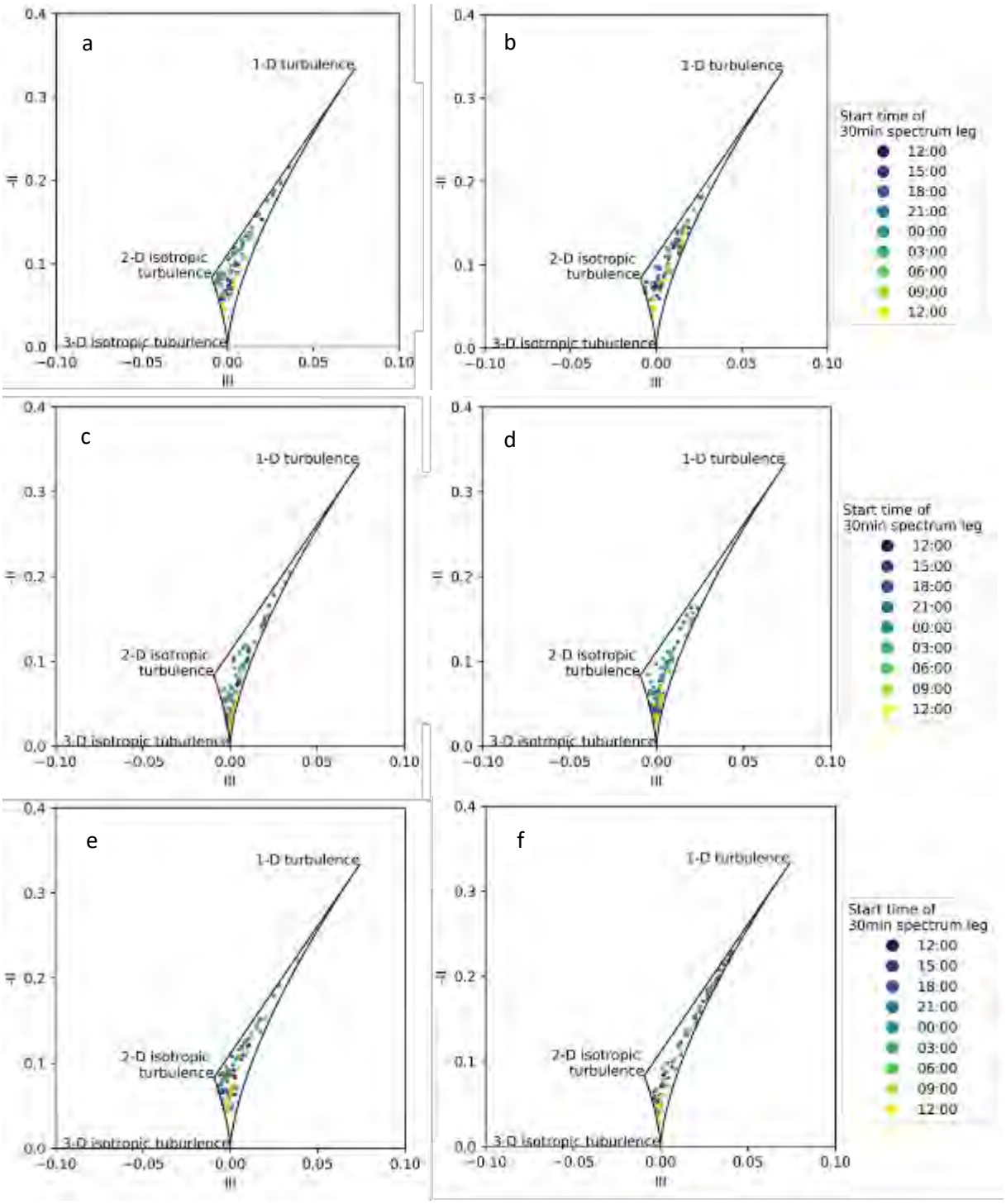

[5] https://drive.google.com/drive/folders/11Kh1ZoWTaiX6hJyS2GSQ3FGWnp9mfhKl?usp=sharing

Figure A3.1: Lumley triangles containing isotropic state of half-hour slots from noon 20 February 2017 until noon 21 February 2017. Showing AS1 and AS2 in the top row, AS3 2 m and AS3 5 m in the middle, and AS3 10 m and AS4 in the bottom row.

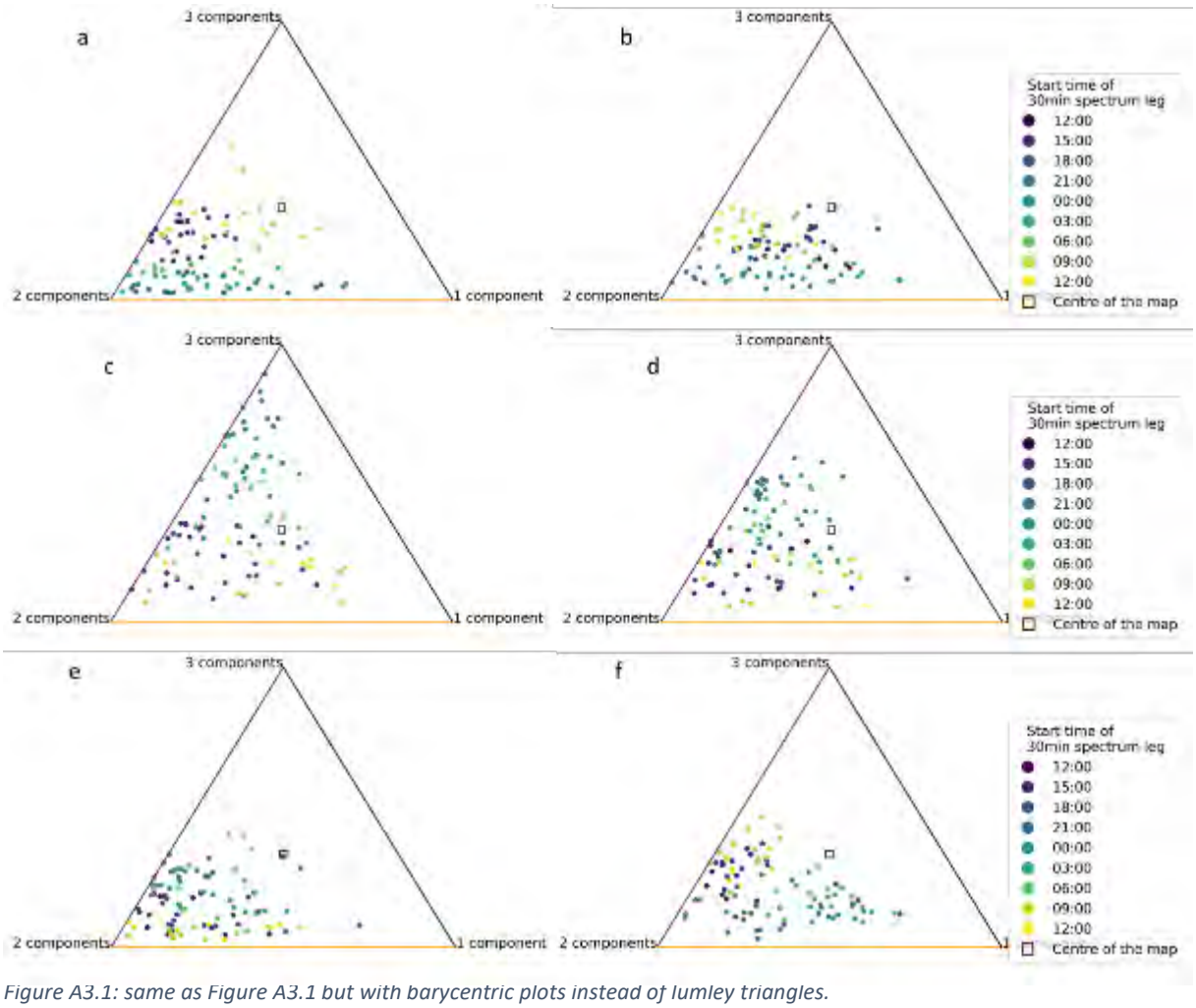

Figure A3.1: same as Figure A3.1 but with barycentric plots instead of lumley triangles.

Annex 4: WRF technical explanations

Here I describe additional information on WRF that has not been discussed in Chapter 1, including dataset nudging and implementing tracers into the WRF model.

WRF spectral nudging explanation

To avoid restarts and new spin-up time, WRF has the option to activate the nudging settings of WRF (Skamarock et al., 2019). Nudging will keep the simulations close to observations or analysis (such as ERA-5) by applying extra forcing terms during an integration. Three types of nudging are available in WRF: Grid- or analysis-nudging, observational- or station-nudging, and spectral nudging. Grid nudging forces the simulation cell by cell towards the analysis. Observational nudging pushes the simulations locally towards the observational data. Lastly, spectra nudging forces the model towards spectral waves that resemble the analysis. The variables that can be nudged are u and v wind components, potential temperature, and water vapor mixing ratios.

Spectral and grid nudging share how they nudge the simulation and works grid by grid. Nudging has direct corrections in a four-dimensional datasets grid, while spectral nudging does not directly influence the simulation. Spectral nudging decomposes the simulated parameter fields spectrally and nudges the simulation towards the waves that correspond to the input analyses. These pushes are added to the tendencies based on the selected waves transformed back to physical quantities. This method originates from (Miguez-Macho et al., 2004).

With temperature as an example, the influence of nudging in WRF looks like:

$$\frac{\partial \theta}{\partial t} = F(\theta) + G_\theta W_\theta (\hat{\theta}_0 - \theta)$$

Where the left-hand side is the tendency in the model that follows the trends of the regular terms described by $F(\theta)$ with the addition of the nudging term. In the latter, G_θ is a timescale controlling the nudging strength with an extra scale W_θ which can be set for periods or selected levels, excluding the boundary layer or certain model levels. Lastly, $\hat{\theta}_0$ is the analysis field towards which the solution is relaxed.

WRF tracer implementation

I implement these tracers into the WRF model following the methodology proposed by Brian Blaylock, which was used in Blaylock at al. (2017) and available at their site[6]. I summarize the exact methods and describe instances where I added diverted from his methodology. Note that line numbers vary among WRF versions and those given intexts are only valid for WRF 4.2. The functionality required for our passive tracers approach is available from WRF v3.7 onwards. I changed the code in five files to implement the tracers and their releases, the 'WRFV4/run/namelist.input', 'WRFV4/Registry/Registry.EM', WRFV4/Registry/Registry.EM_COMMON', 'WRFV4/dyn_em/_module_initialize_real.F', and 'WRFV4/dyn_em/solve_em.F'. Changes in any mentioned file, except namelist.input, require re-compiles of the WRF model.

To introduce eight different passive tracers, I have to make adjustments. In the 'namelist', I activate the 'tracer_opt' by setting it to '2' for all domains. I further added three variables 'tracer_dom = 5', to easily change the domain with tracers releases, 'tracer_init = false', indicating if the model is not initialized with tracers, and 'tracer_release = 648000', indicating at what model calculation step the

[6] https://home.chpc.utah.edu/~u0553130/Brian_Blaylock/tracer.html

tracers are released (18h into the simulation). Simple future expansions could be the amount of tracer released and the cell coordinates to release tracers (now hardcoded).

The last three variables I set do not exist yet and need to be defined in the 'Registry.EM_COMMON', their lines consist, in order, of 'rconfig', type (real, logical, integer, etc.), name, how set, Nentries, default, IO, dname, description, and units. Table 1 describes the values I use for every new namelist.input variable. Where 'name' is the variable name used within the WRF model and 'dname' is the name given in the output files (when included). 'How set' indicates the expected namelist.input section to declare the variable. 'Nentries' indicates the number of values expected and it is often set as a unique value or specific to every domain. 'Default' indicates the value the variable gets if not defined in the namelist.input. 'IO' indicates at what moment and how it is integrated with the calculations, 'i' indicates initial dataset, 'r' restart dataset, and 'h' is for history of the IO. 'Description' allows for extra detail of the variable, and 'units' gives the type of units associated with this variable, which is not set for tracers.

Table A4.1: A short description of the variables integrated into the WRF registry.EM_COMMON.

Rconfig	Type	Name	How set	Nentries	Default	IO	dname	description
Rconfig	Logical	Tracer_init	Namelist, dynamics	1	.true.	irh	Tracer_init	Are tracers integrated at the initial release
	Integer	Tracer_dom			1	rh	Tracer_dom	What domain contains tracers
	Integer	Tracer_release			0	irh	Tracer_release	At what model calculation step to start with the tracer release

Further, I again follow the work of Blaylock et al. (2017) to define the tracer variables for WRF simulations, which continues in 'Register.EM', defining variables used in WRF calculations. Adding the tracer variables requires a tr17_* line, where '*' indicates the name of the tracer. Concluded with a common line to include all new tracers into WRF as the tracer package.

Next, I can initialize the tracers in the 'module_initialize_real.F'; here, I made small adjustments because I want a release at a specific location and not over a larger area, and thus can discard the proposed loops and set everything at the specific coordinates. This small section on line 4243 starts with checking if the 'tracer_opt' is set to 2. Followed by two extra checks, I implemented the check for the correct domain with 'tracer_dom' instead of a hardcoded value and if an initial amount of tracer is required with 'tracer_init'. After this, I set every tracer location with its specific amount of tracer, written as 'tracer(i, k, j, P_tr17_*) = X'. Where 'i' is the grid cell in the x-axis (longitude), 'j' is the y-axis (latitude) direction, and 'k' is the vertical level, '*' indicates the name of the tracer and 'X' indicates the amount of tracer that is added to the simulation at the initialization step. All tracer names need a 'P_' before their name; otherwise, the tracer function does not work.

Similarly, to 'module_initialize_real.F' I set in the 'solve_em.F' the same checks for the correct 'tracer_opt', 'tracer_dom' settings, and ends with a check on the calculation step with 'tracer_release' instead of the initial release. If the calculation step is equal or greater than the number given to

‘tracer_release’ in the namelist.input it will start to release tracers. This is described as ‘tracer(i, k, j, P_tr17_*) = tracer(i, k, j, P_tr17_*) + Y’, where Y is the amount that is added at every calculation step. These values include themselves or replace the location with predefined values and do not allow tracer storage at the release location. Possible future adjustments to ‘solve_em.F’ could include a difference between the first moment of release (when the calculation step equals the release value) and after that moment, which relies on splitting out the equal to and greater than comparisons for the ‘tracer_release’ value.

A downside of this tracers approach is that they are domain-bound and once they have left a domain, they do not return when winds inverse their direction. This reversal leads to lower concentrations for some flows. Although this could miss some parcels that cross the borders several times. In this research, it is less important to know the exact concentration, but the occurrence of tracers is more important.

Annex 5: Hourly plots of the fine-resolution simulation

This annex contains the hourly plots of vertical cross-sections of the fine-resolution simulations as well as hourly horizontal cross-section with column sums of the tracers. For 10-minute data and more, please go to:
https://drive.google.com/drive/folders/11Kh1ZoWTaiX6hJyS2GSQ3FGWnp9mfhKl?usp=sharing.

Vertical profiles

This part shows the hourly development of the vertical profile in the CV according to the LEMS for three variables: virtual potential temperature, wind speed, and wind direction. These figures cover the interval from 16:00 UTC 20 February 2017 until 06:00 UTC 21 February.

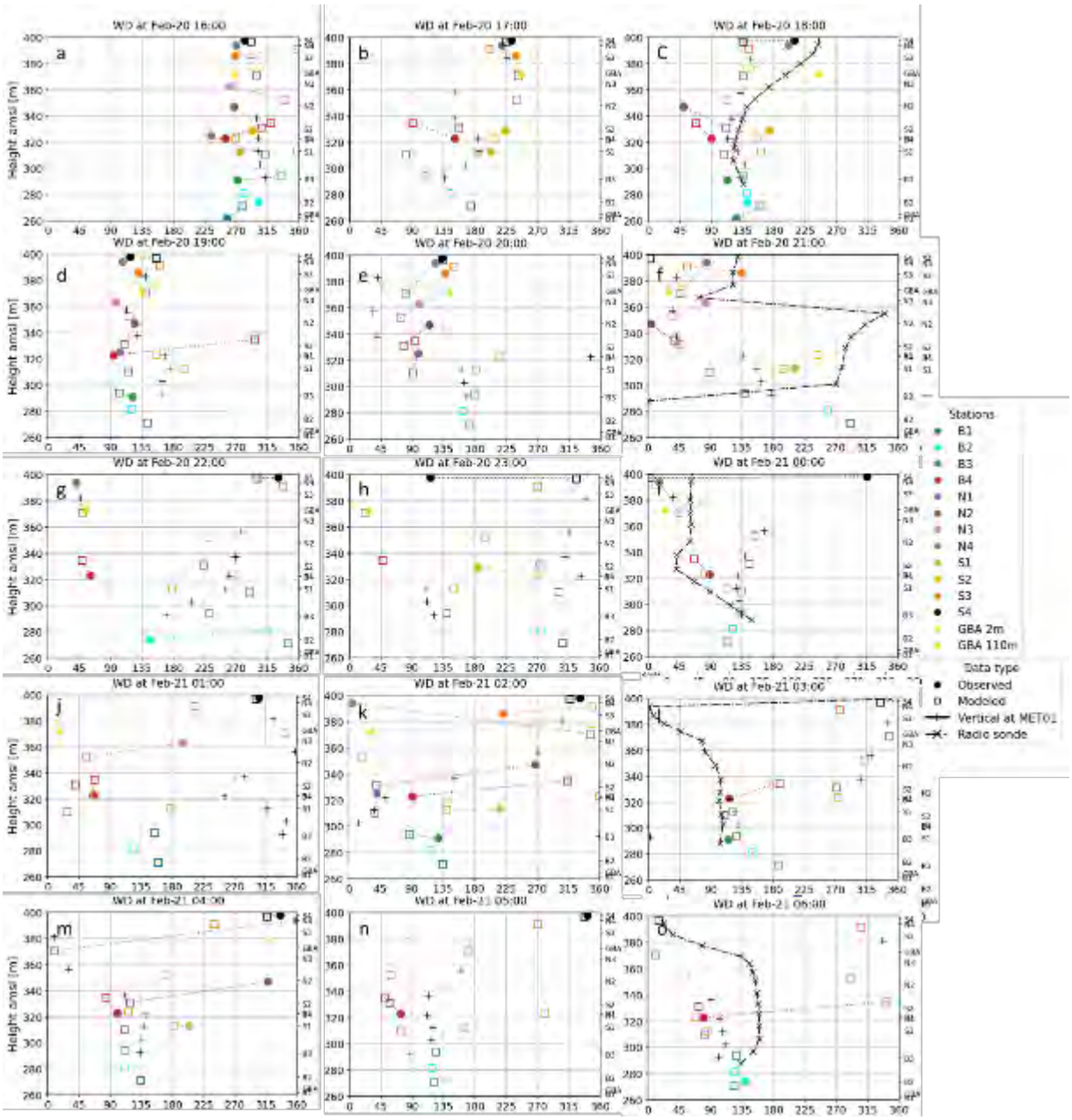

Figure A5.1: The hourly wind direction in the Cadarache Valley as observed by the LEMS (filled circles) and the GBA (filled triangles) and the matching simulations (open symbols). The vertical profile above the MET01 is a given by crosses for the model and crosses with a connected line when radiosonde observations are available.

Figure A5.1 shows the wind direction of the LEMS, manyu of the observations are not available later in the night because the wind speed over five minutes were not strong enough to push the wind vane. Although at the beginning of the night the wind makes the shift from west to align with the CDV orientation. Similarly, in Figure A5.2 the wind speeds are not observed during most of the night. At the same time, the model produces slow winds close to the sidewall orientation during the times that are not fast enough to determine properly the winds speeds and directions.

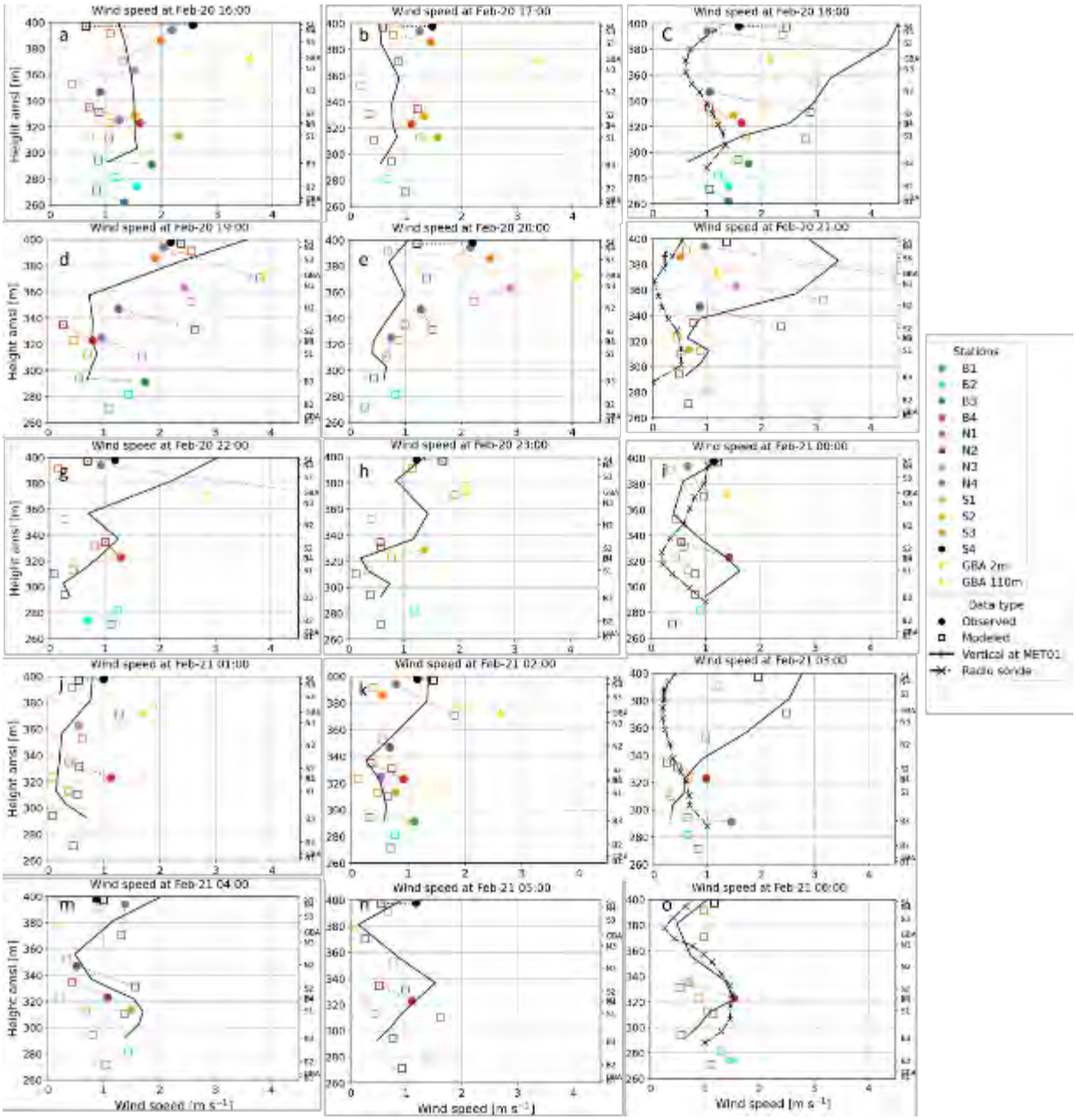

Figure A5.2: Similar to Figure A5.1 but the vertical profiles above MET01 have continuous vertical lines.

The temperature of Figure A5.3 starts warm and gradually cools over the night. The observations match relatively well with the radiosondes and the simulations with the vertical profiles above MET01.

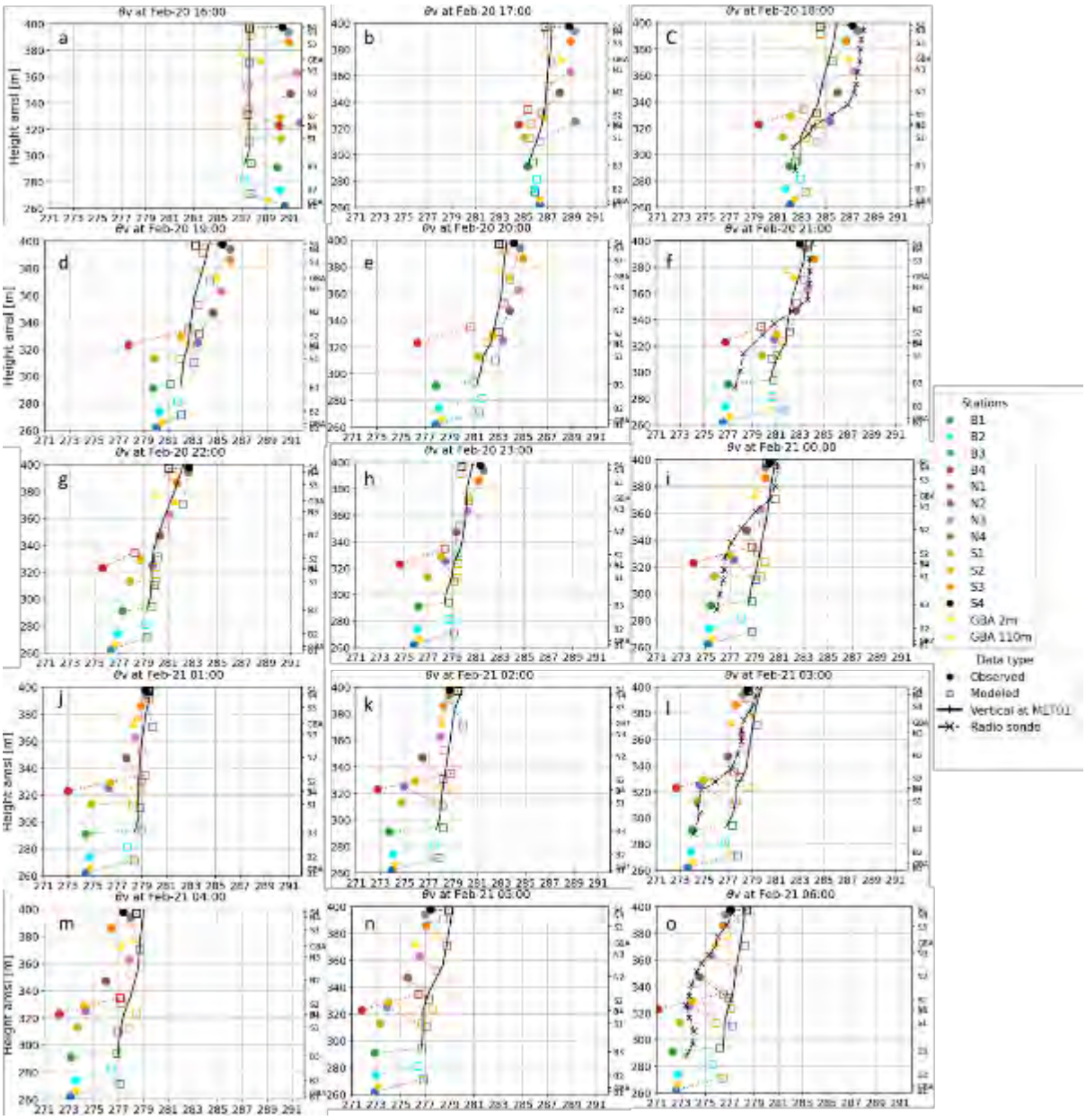

Figure A5.3: Similar to Figure A5.1 but the vertical profiles above MET01 have continuous lines.

Vertical cross-sections

Again, this section only contains hourly plots from 16:00 UTC February 20 until 06:00 UTC February 2017, for the 10-minute descriptions see the drive files[7].

Durance and Cadarache Valley

The vertical cross-sections in Figure A5.4 to Figure A5.17 supplement the cross-sections shown in the article of Chapter 4, with an extension from 16:00 UTC 20 February to 06:00 UTC February 2017. Note that the midnight pictures are already present in Chapter 4. They show a movement from western winds and an arrival of the Durance winds which is present above all the valleys.

[7] https://drive.google.com/drive/folders/11Kh1ZoWTaiX6hJyS2GSQ3FGWnp9mfhKl?usp=sharing

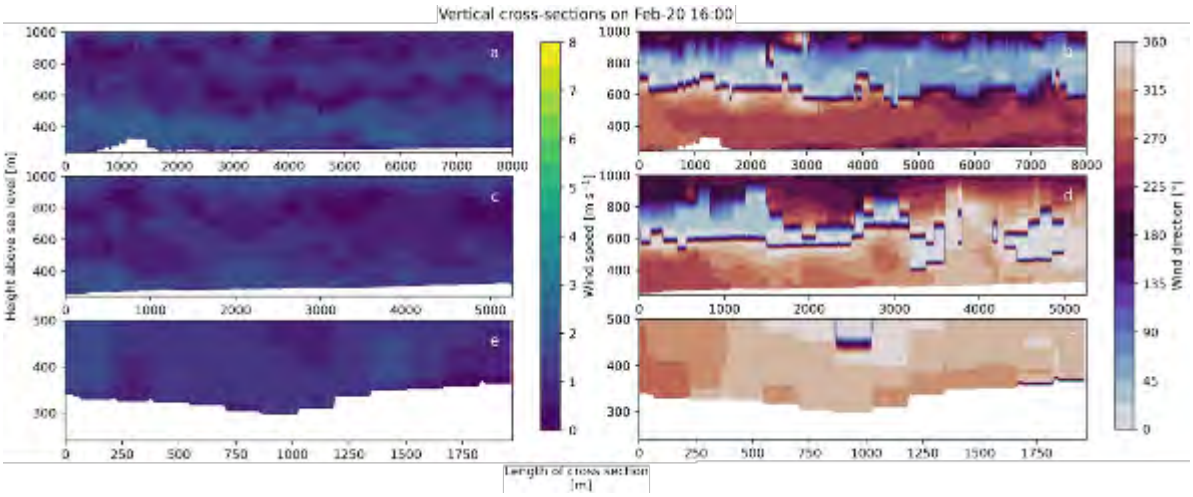

Figure A5.4: Vertical cross-sections at 16:00 UTC, of wind speed (left) and wind direction (right) along the Durance valley, moving down the valley from the right to the left (a, b), along the Cadarache valley, moving down the valley from the right to the left (c, d), and perpendicular to the Cadarache Valley, from the SW to the NE (e, f).

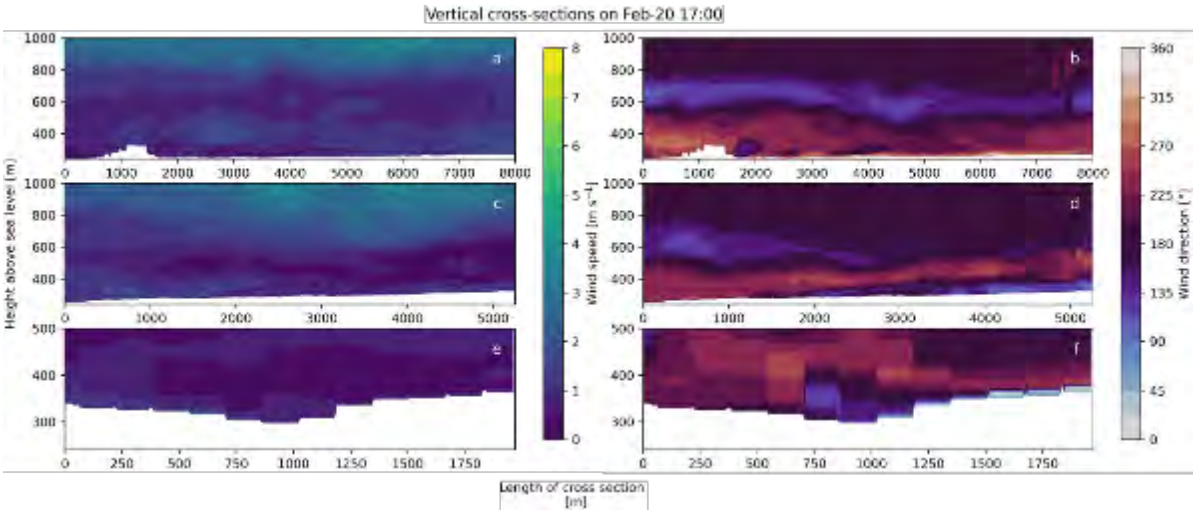

Figure A5.5: Same as Figure A5.4 but at 17:00 UTC.

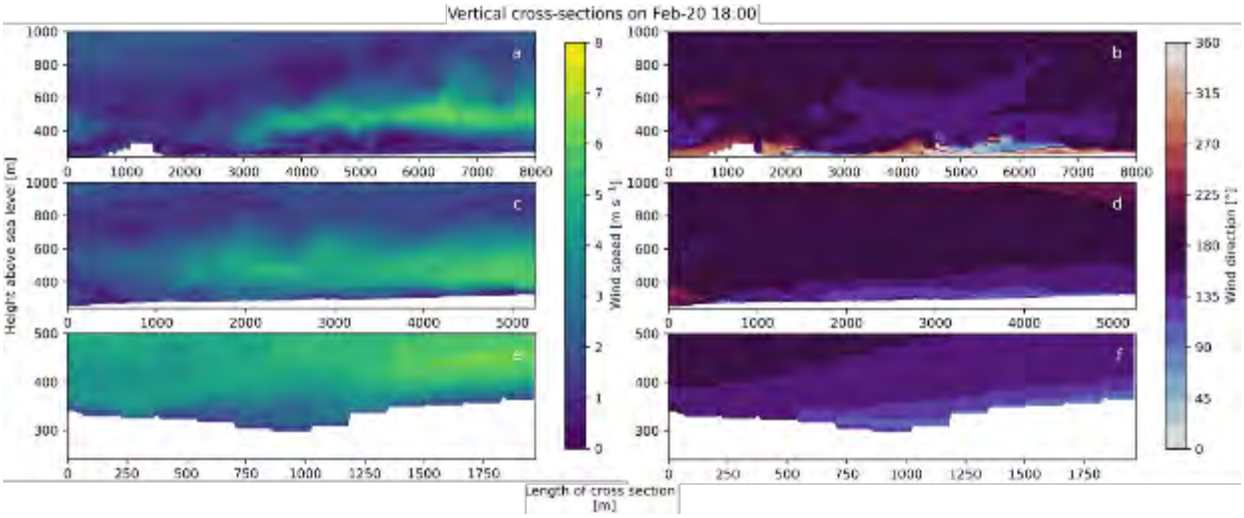

Figure A5.6: Same as Figure A5.4 but at 18:00 UTC.

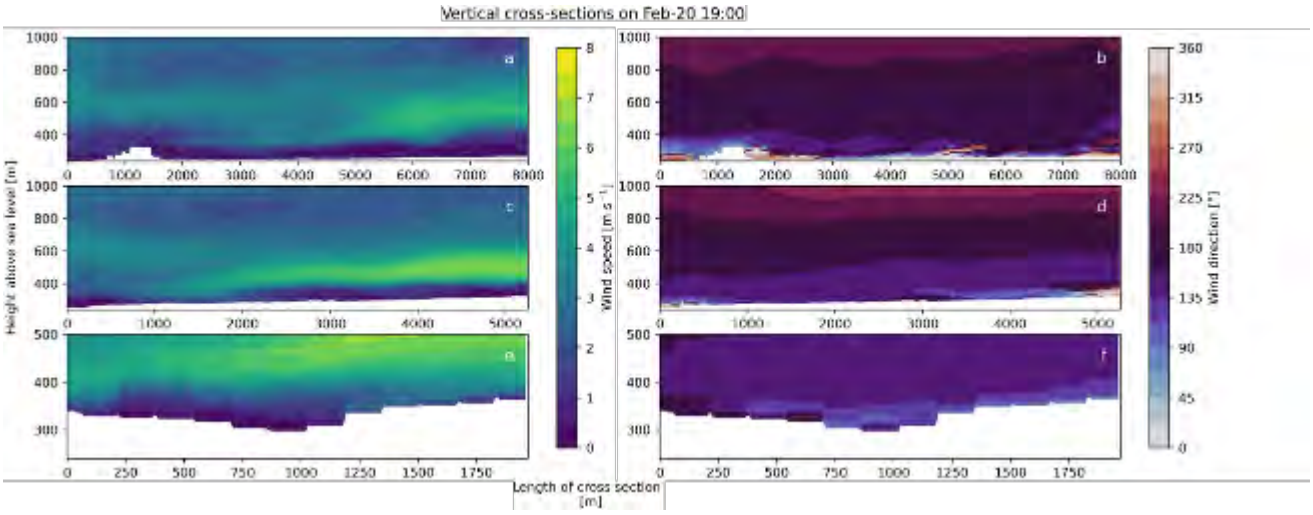

Figure A5.7: Same as Figure A5.4 but at 19:00 UTC.

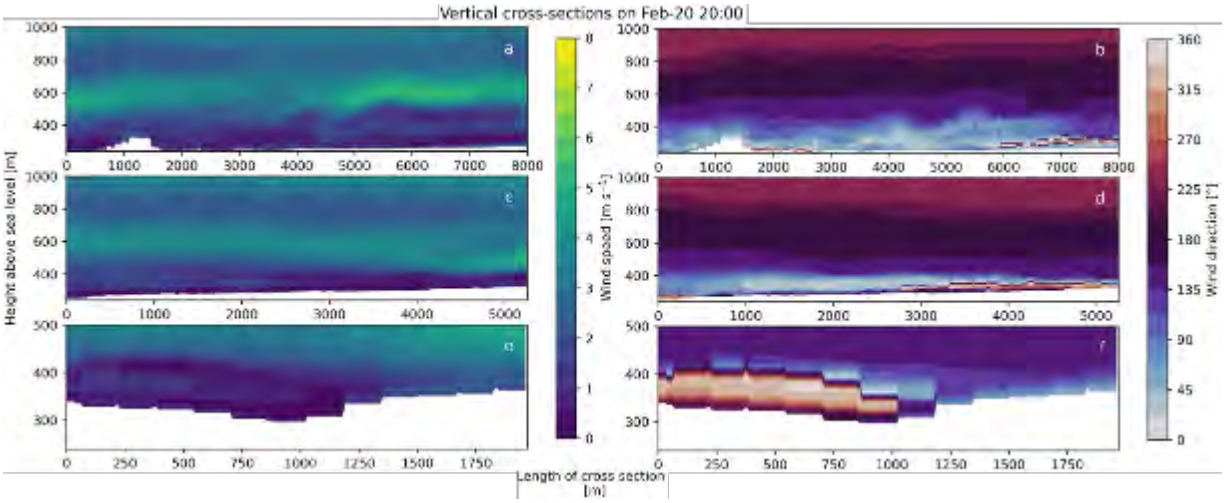

Figure A5.8: Same as Figure A5.4 but at 20:00 UTC.

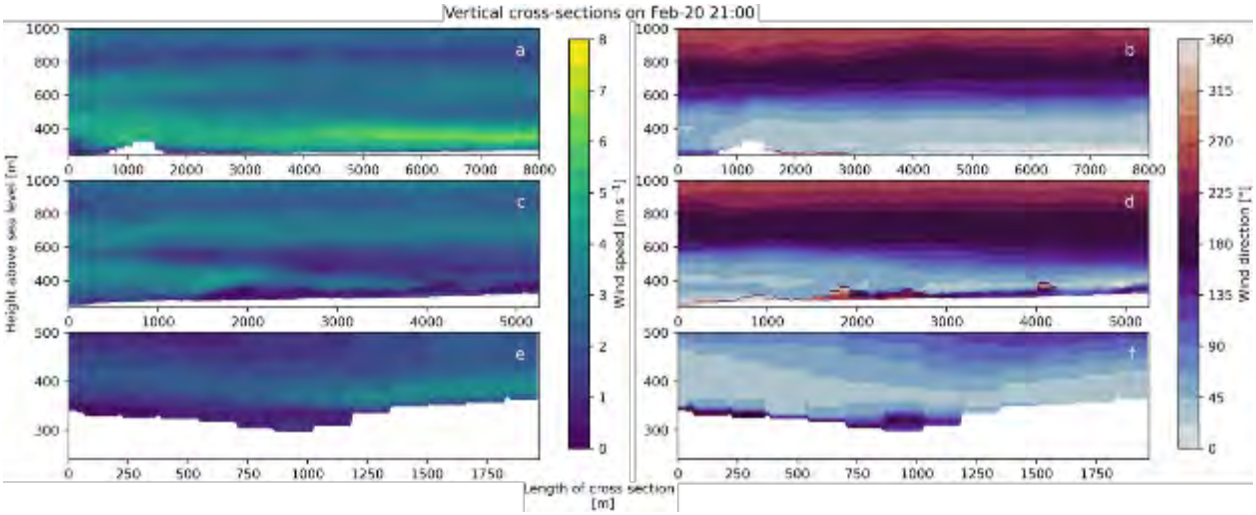

Figure A5.9: Same as Figure A5.4 but at 21:00 UTC.

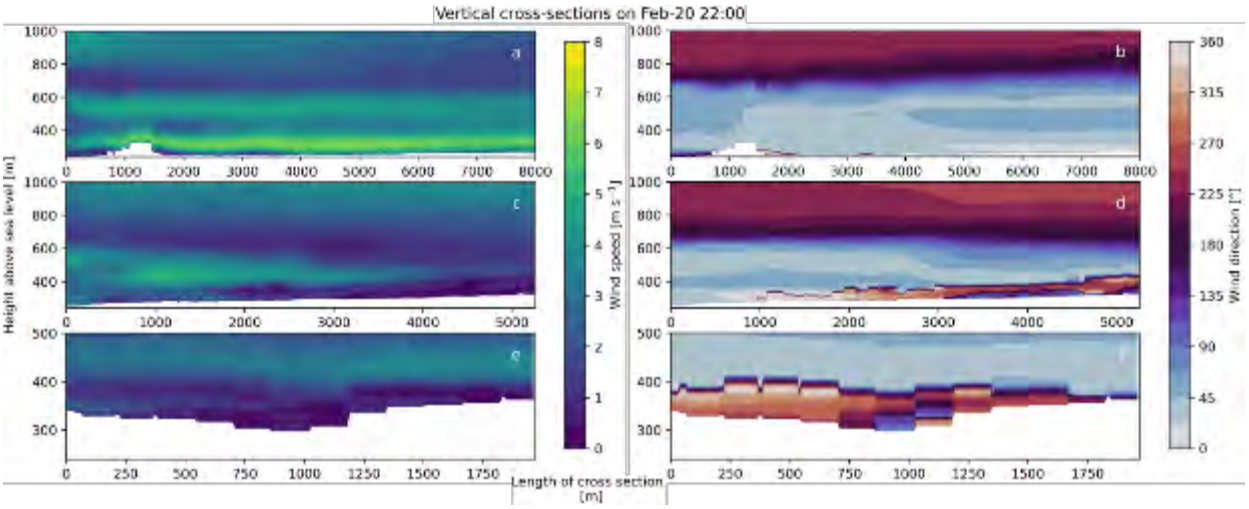

Figure A5.10: Same as Figure A5.4 but at 22:00 UTC.

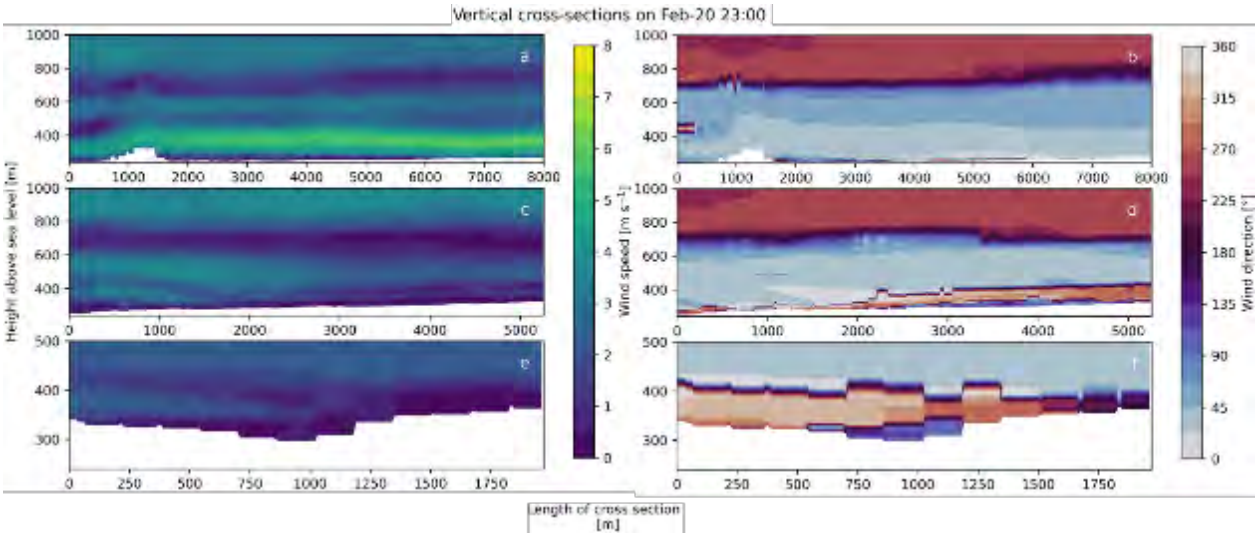

Figure A5.11: Same as Figure A5.4 but at 23:00 UTC.

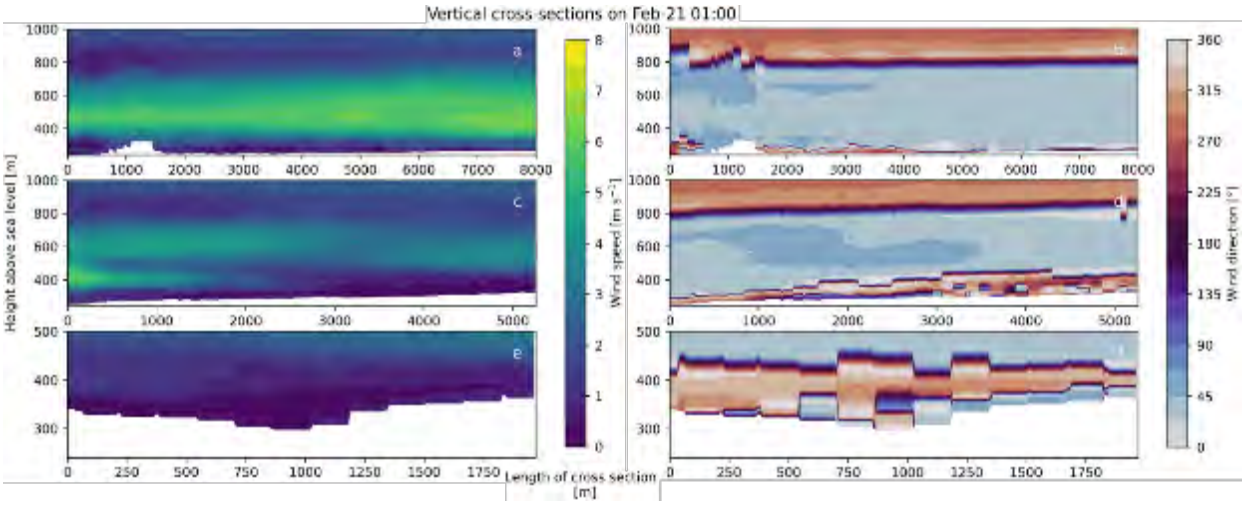

Figure A5.12: Same as Figure A5.4 but at 01:00 UTC the day after.

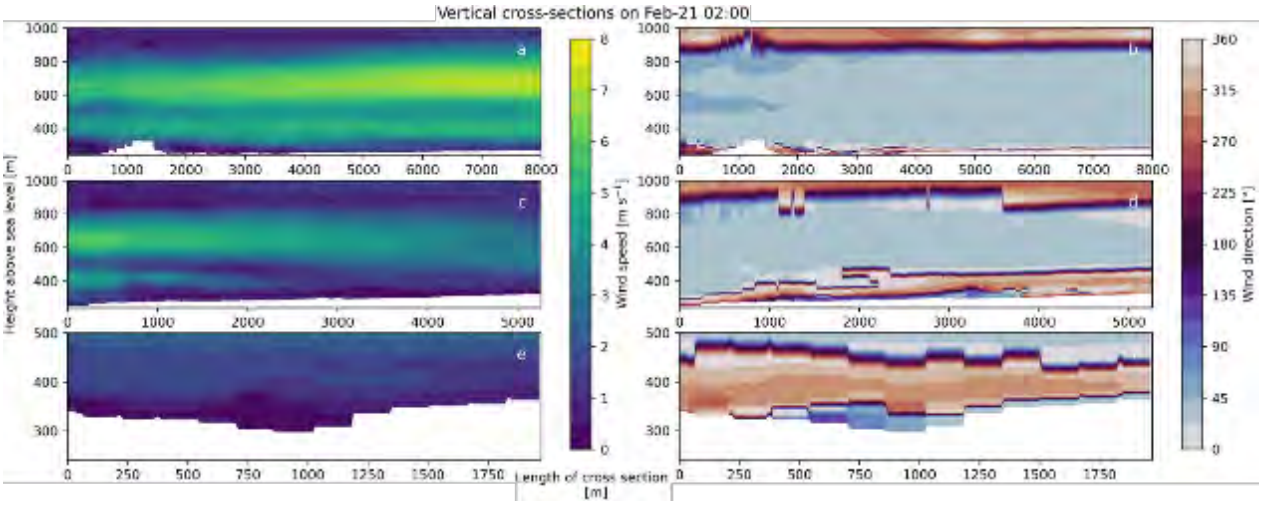

Figure A5.13: Same as Figure A5.4 but at 02:00 UTC the day after.

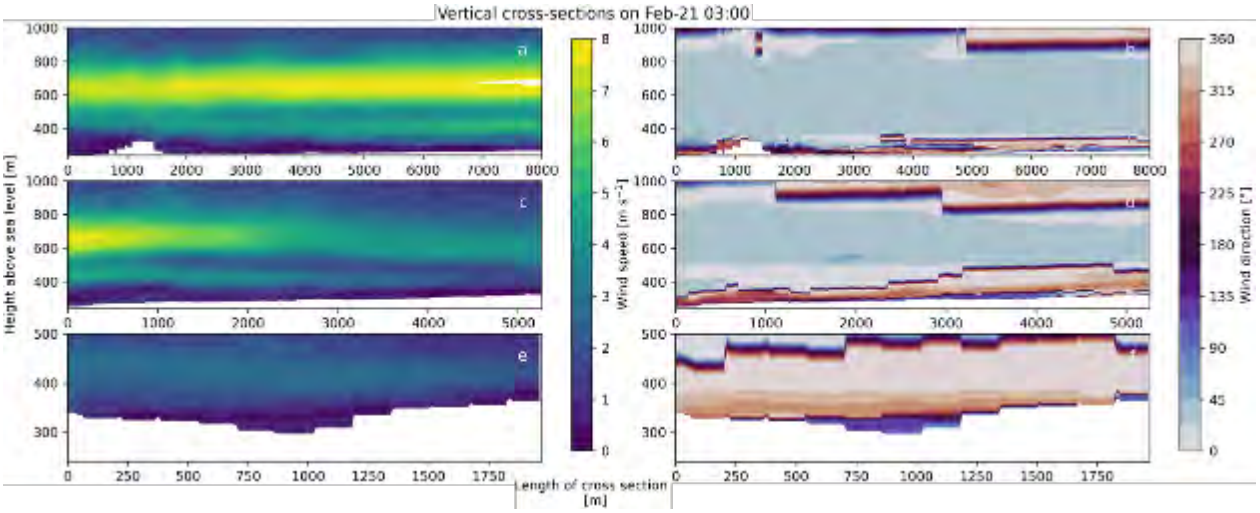

Figure A5.14: Same as Figure A5.4 but at 03:00 UTC the day after.

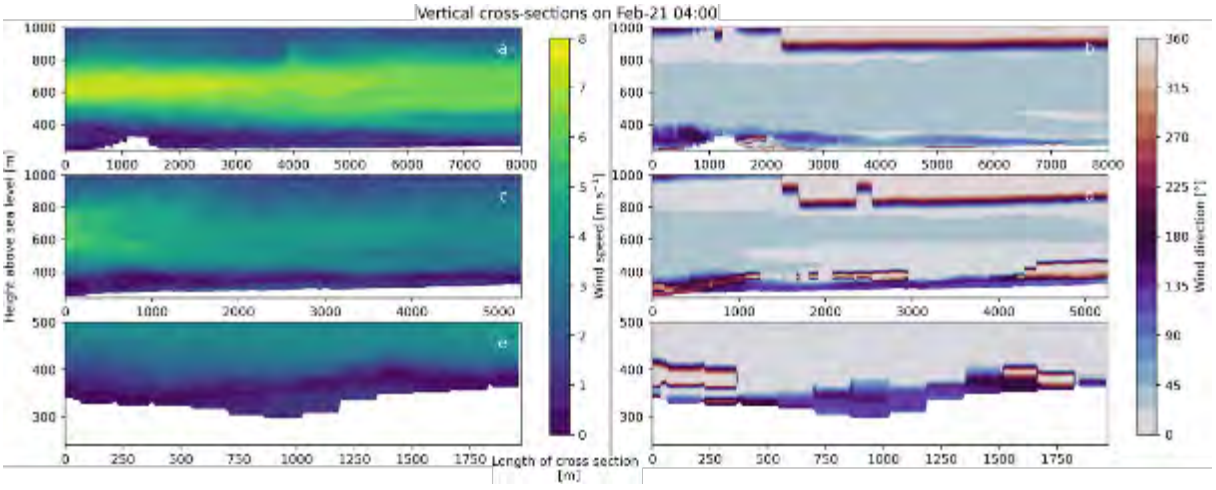

Figure A5.15: Same as Figure A5.4 but at 04:00 UTC the day after.

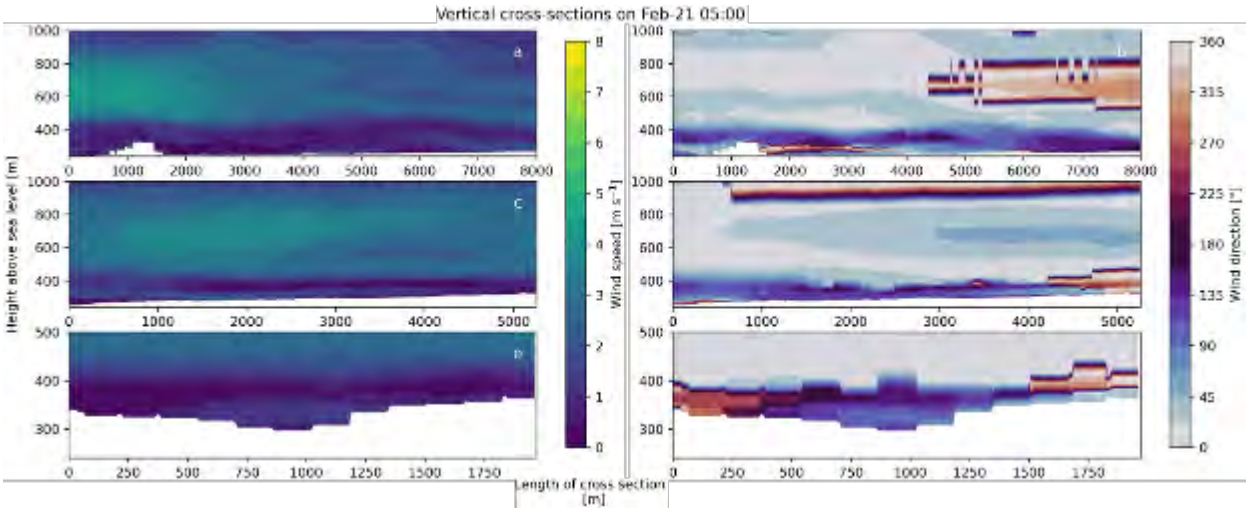

Figure A5.16: Same as Figure A5.4 but at 05:00 UTC the day after.

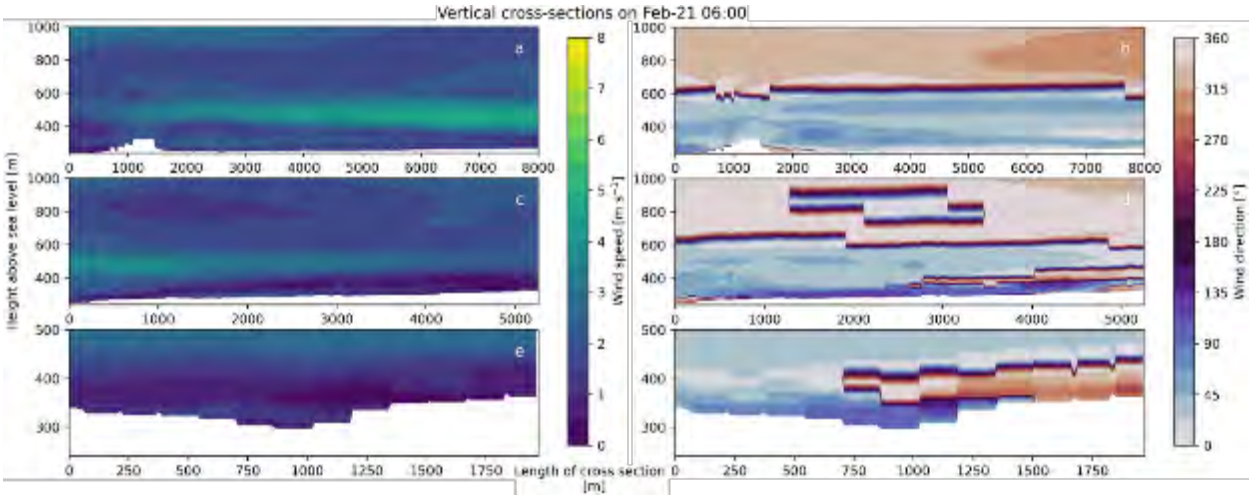

Figure A5.17: Same as Figure A5.4 but at 06:00 UTC the day after.

Abéou, Durance, and Verdon Valley

To complement these cross-sections, I also add the Abéou and Verdon Valley cross-sections in Figure A5.18 to Figure A5.31 and they follow the format of Figure 4.9. They show change to the western winds at the end of the day and later, they turn towards winds from the south followed with the Durance Valley influences.

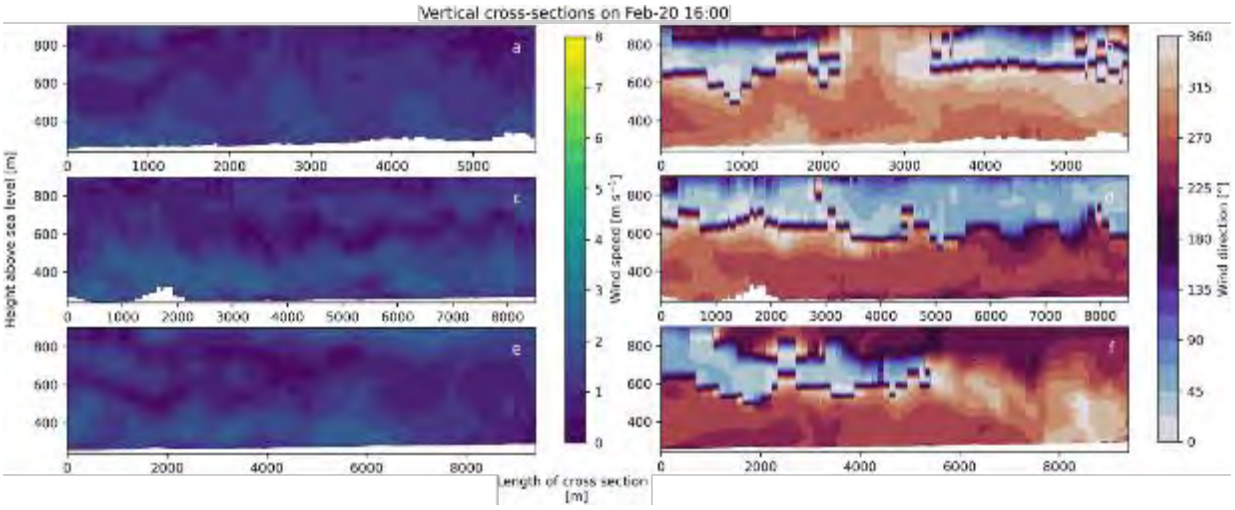

*Figure A5.18: Similar to the **Figure 12** of the article in Chapter 4 and Figure 4.9, but concerning the valleys of Abéou (a and b), Durance (c and d) and Verdon (e and f). The lines of the cross-sections are shown in Figure 4.8, with the left extremity of the graphs matching the westernmost point of the cross-sections.*

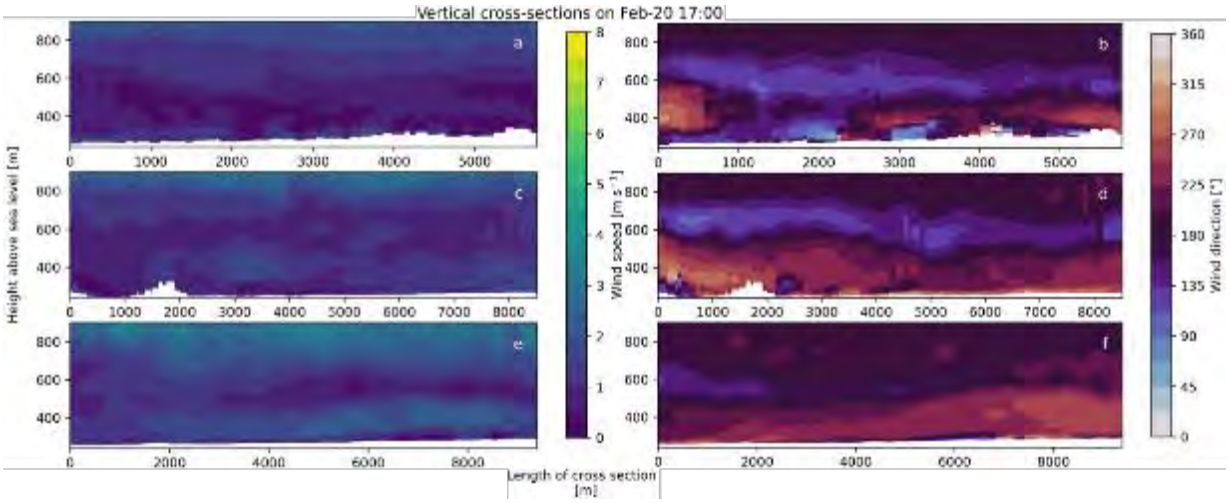

Figure A5.19: Similar to Figure A5.18 but at 17:00 UTC.

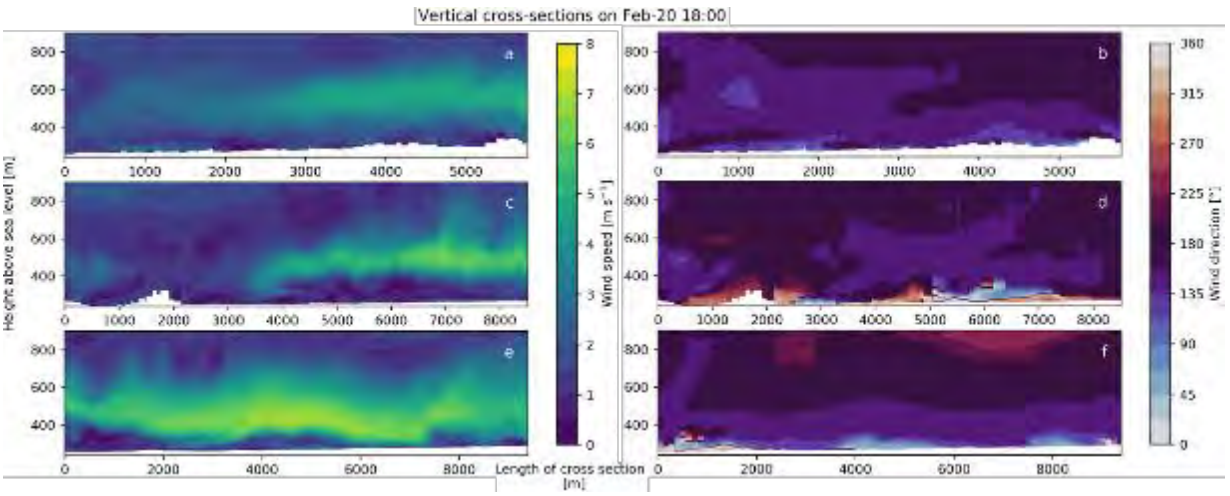

Figure A5.20: Similar to Figure A5.18 but at 18:00 UTC.

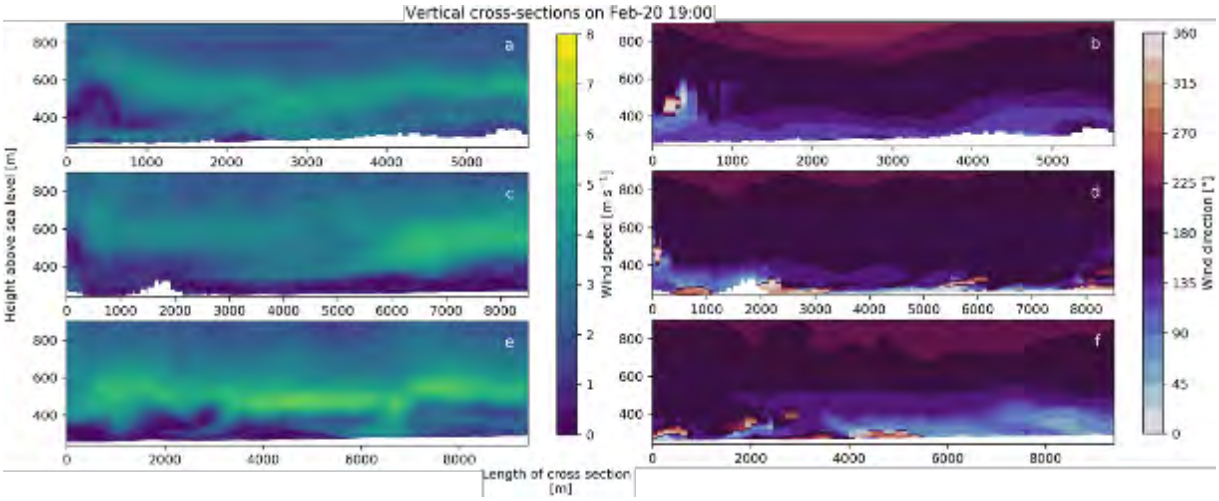

Figure A5.21: Similar to Figure A5.18 but at 19:00 UTC.

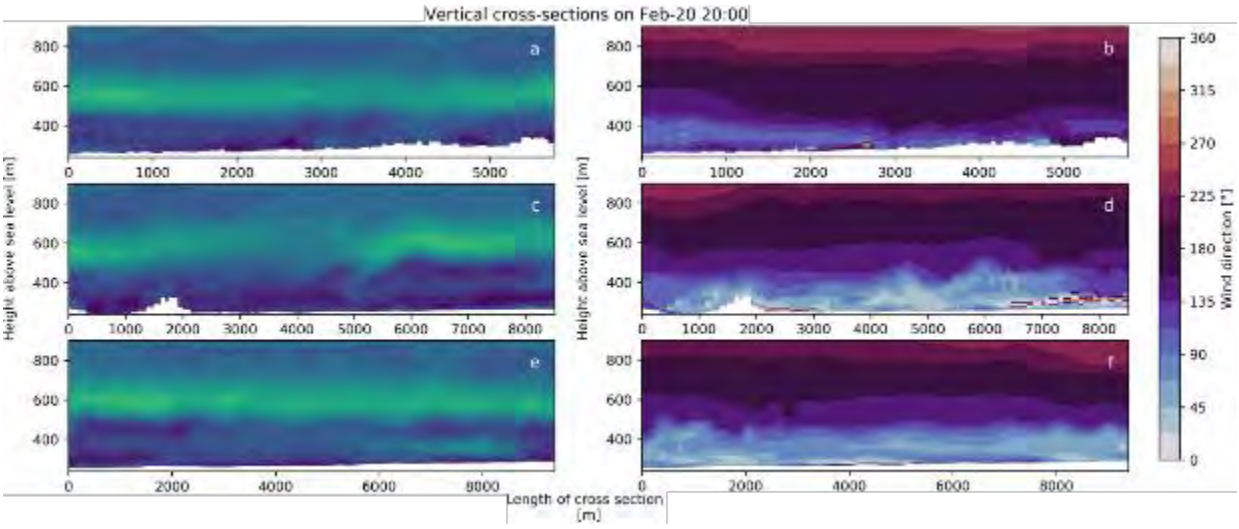

Figure A5.22: Similar to Figure A5.18 but at 20:00 UTC.

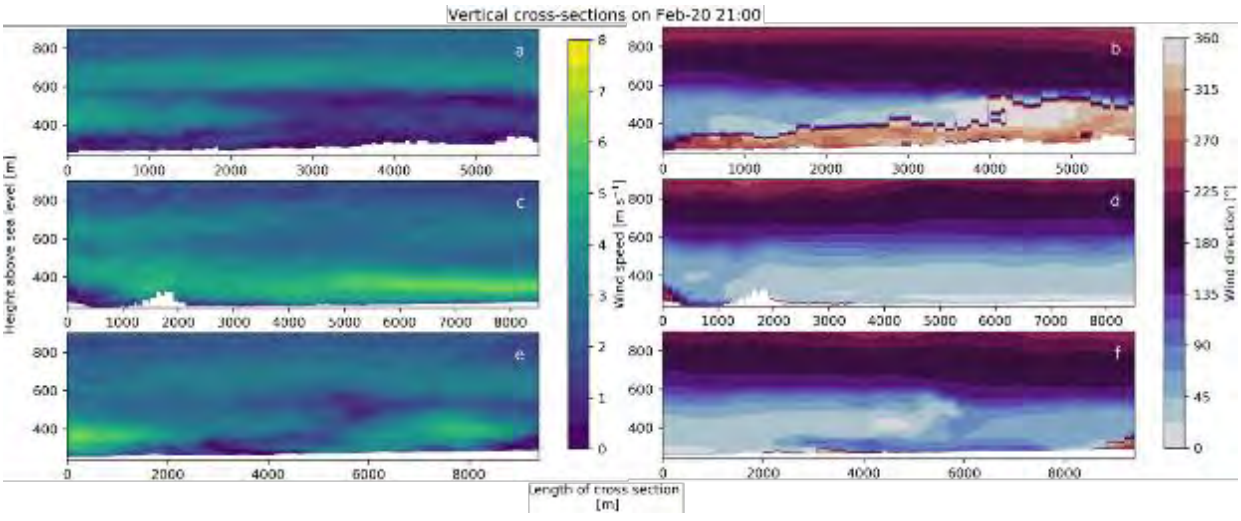

Figure A5.23: Similar to Figure A5.18 but at 21:00 UTC.

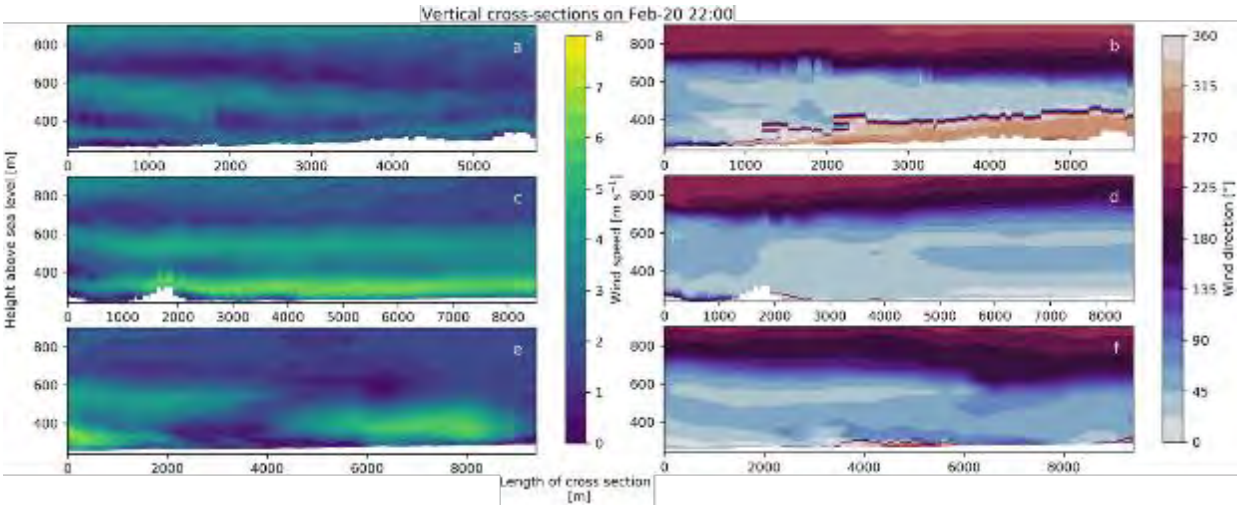

Figure A.24: Similar to Figure A5.18 but at 22:00 UTC.

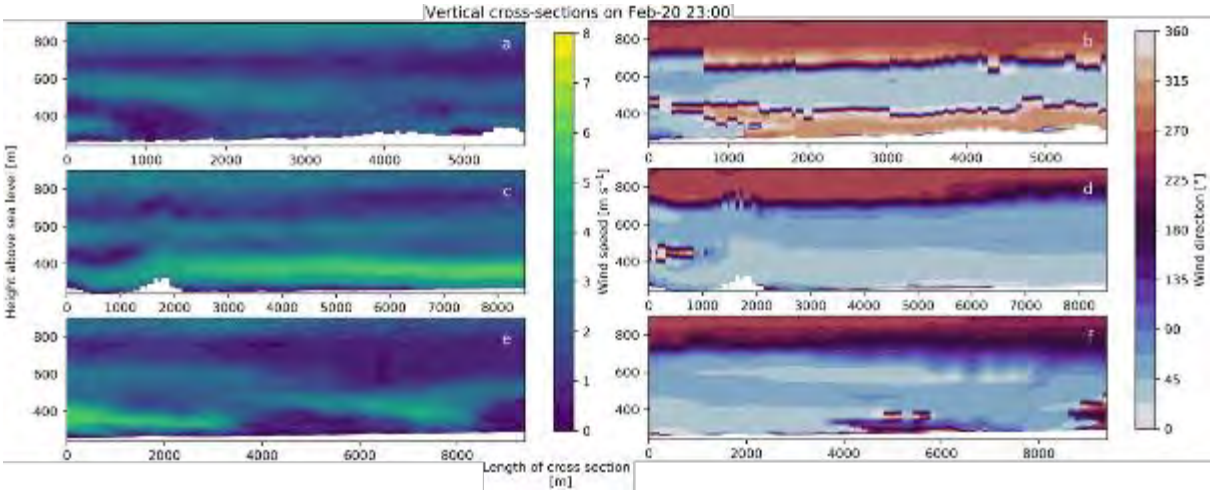

Figure A.25: Similar to Figure A5.18 but at 23:00 UTC.

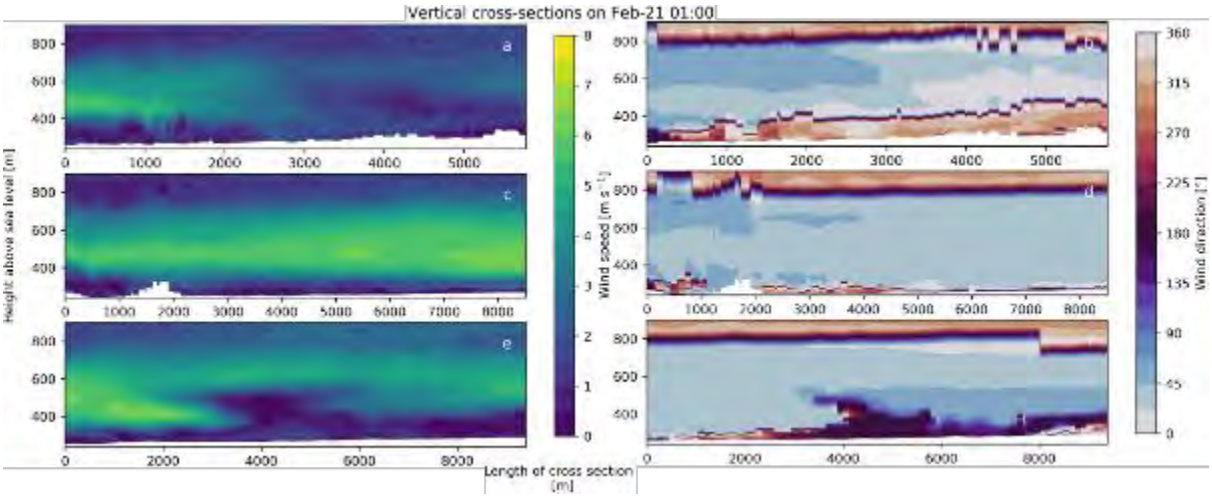

Figure A.26: Similar to Figure A5.18 but at 01:00 UTC the day after.

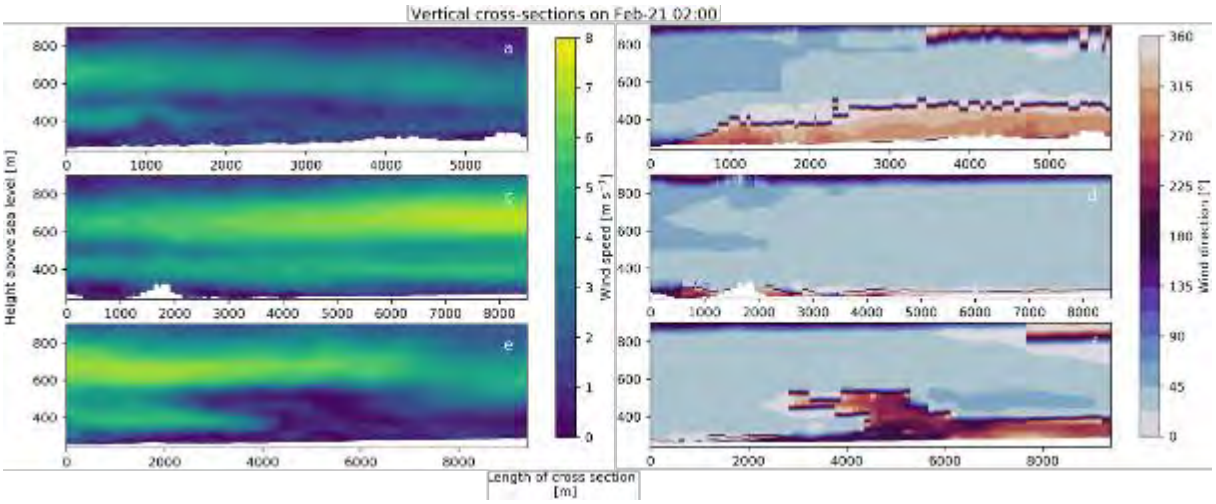

Figure A5.27: Similar to Figure A5.18 but at 02:00 UTC the day after.

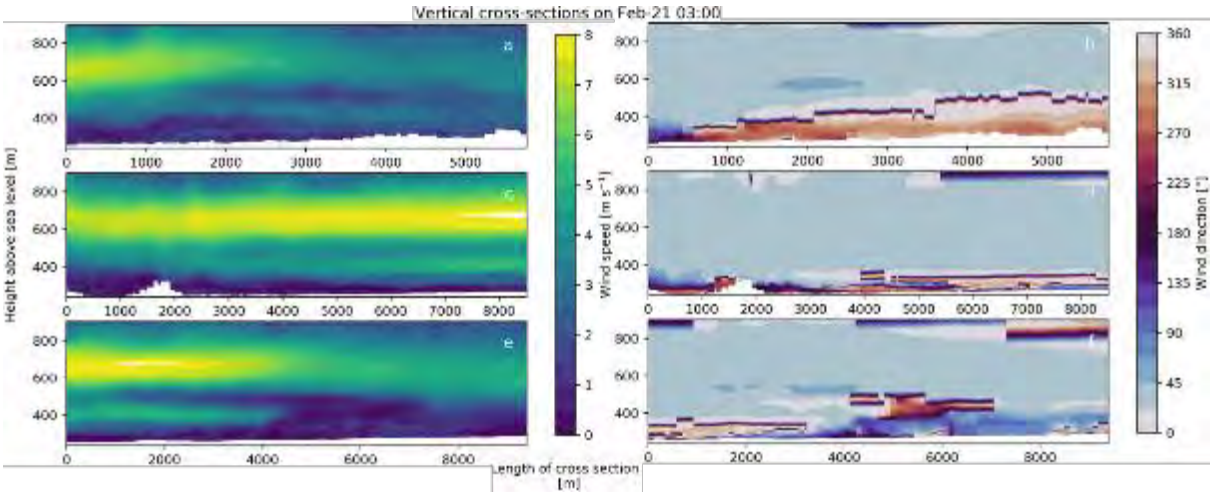

Figure A5.28: Similar to Figure A5.18 but at 03:00 UTC the day after.

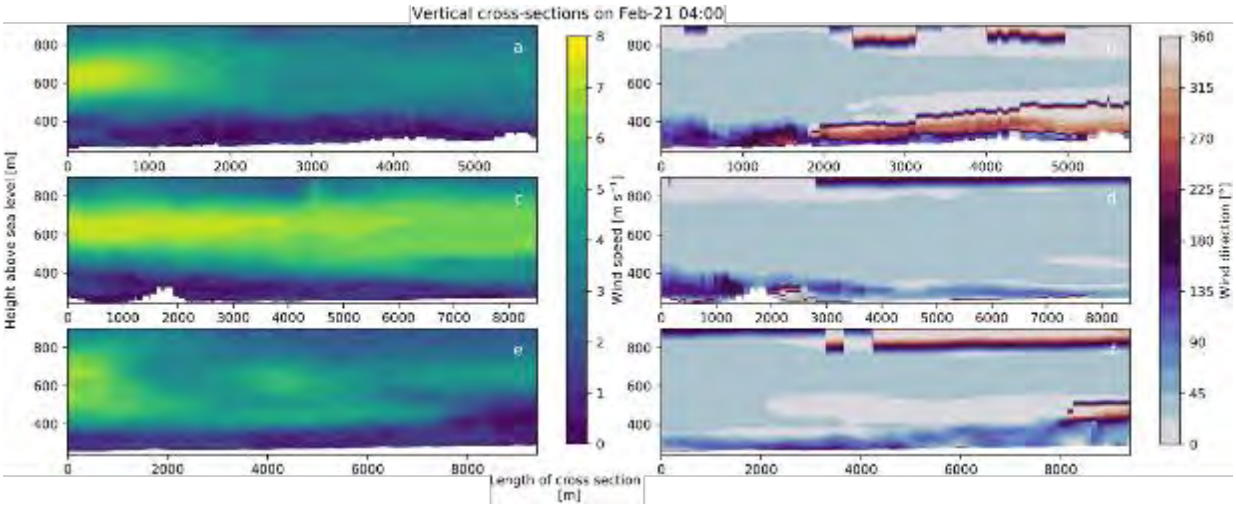

Figure A5.29: Similar to Figure A5.18 but at 04:00 UTC the day after.

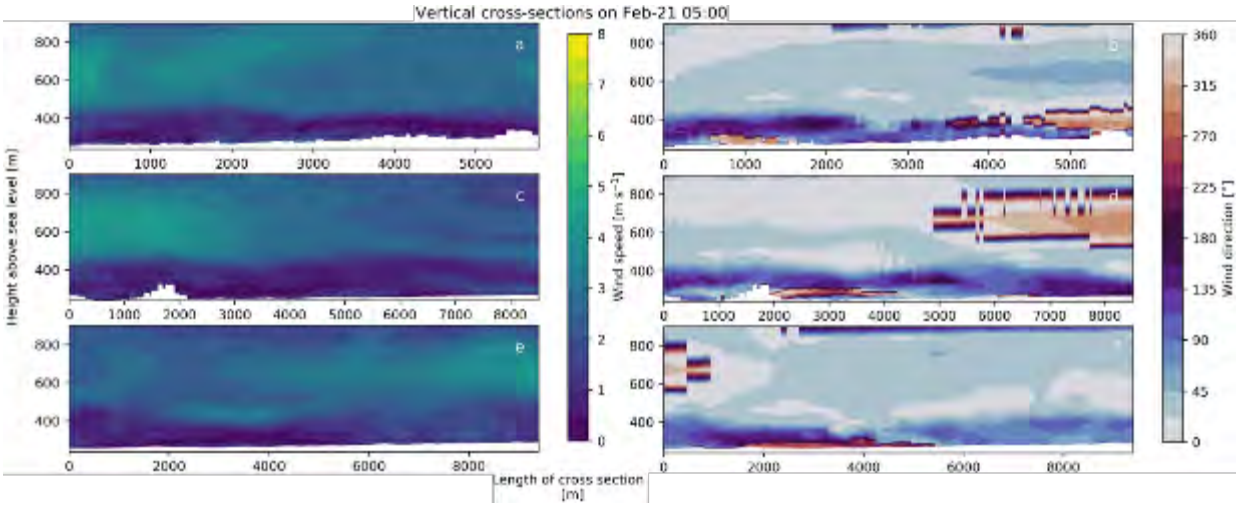

Figure A5.30: Similar to Figure A5.18 but at 05:00 UTC the day after.

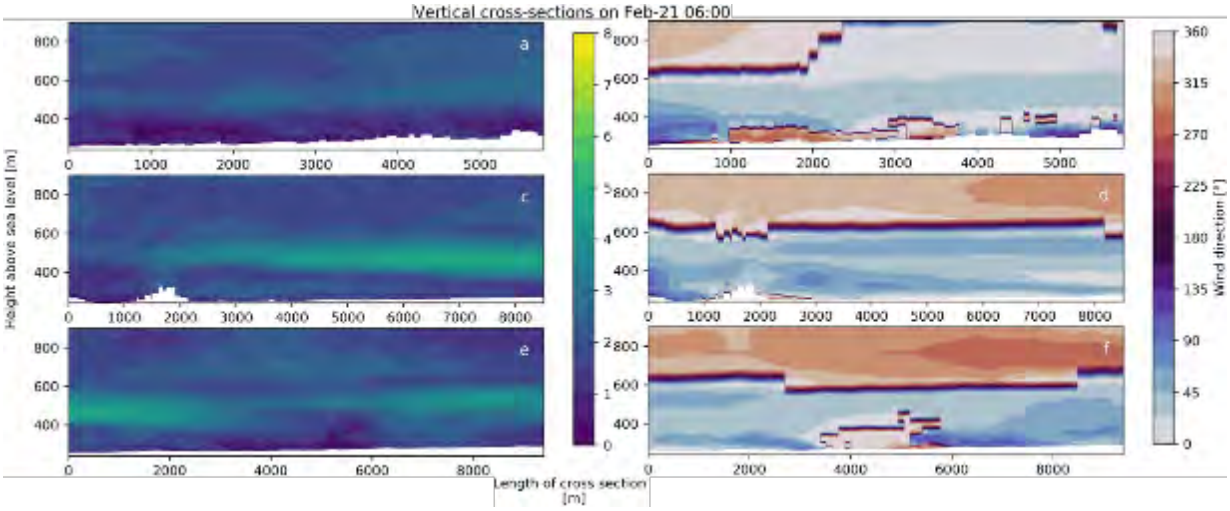

Figure A5.31: Similar to Figure A5.18 but at 06:00 UTC the day after.

Horizontal cross-section

Figure A5.32 shows the wind evolution at 100 m agl for the smallest simulation domain. This part contains the two different heights as contained in Figure 4.10. It shows the last moments of the daytime conditions and the arrival of the moist winds from the southeast. Afterward it shows the development of the local winds in the valley.

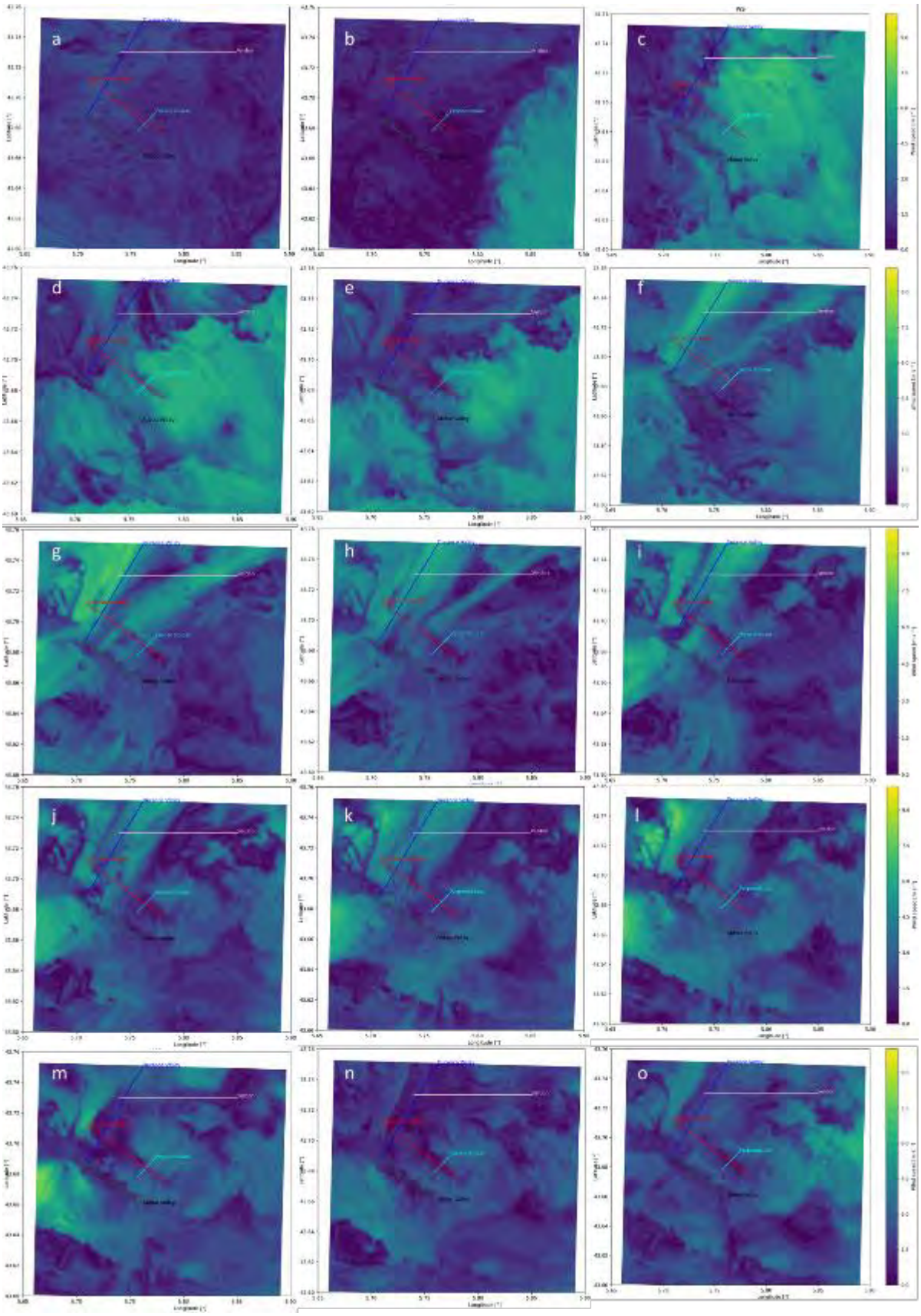

Figure A5.32: Horizontal cross-sections of the wind speed above the 111 m resolution domain at 100 m agl. Plot (a) is the situation at 16:00 UTC and every letter increases the time by one hour up to 06:00 UTC (o).

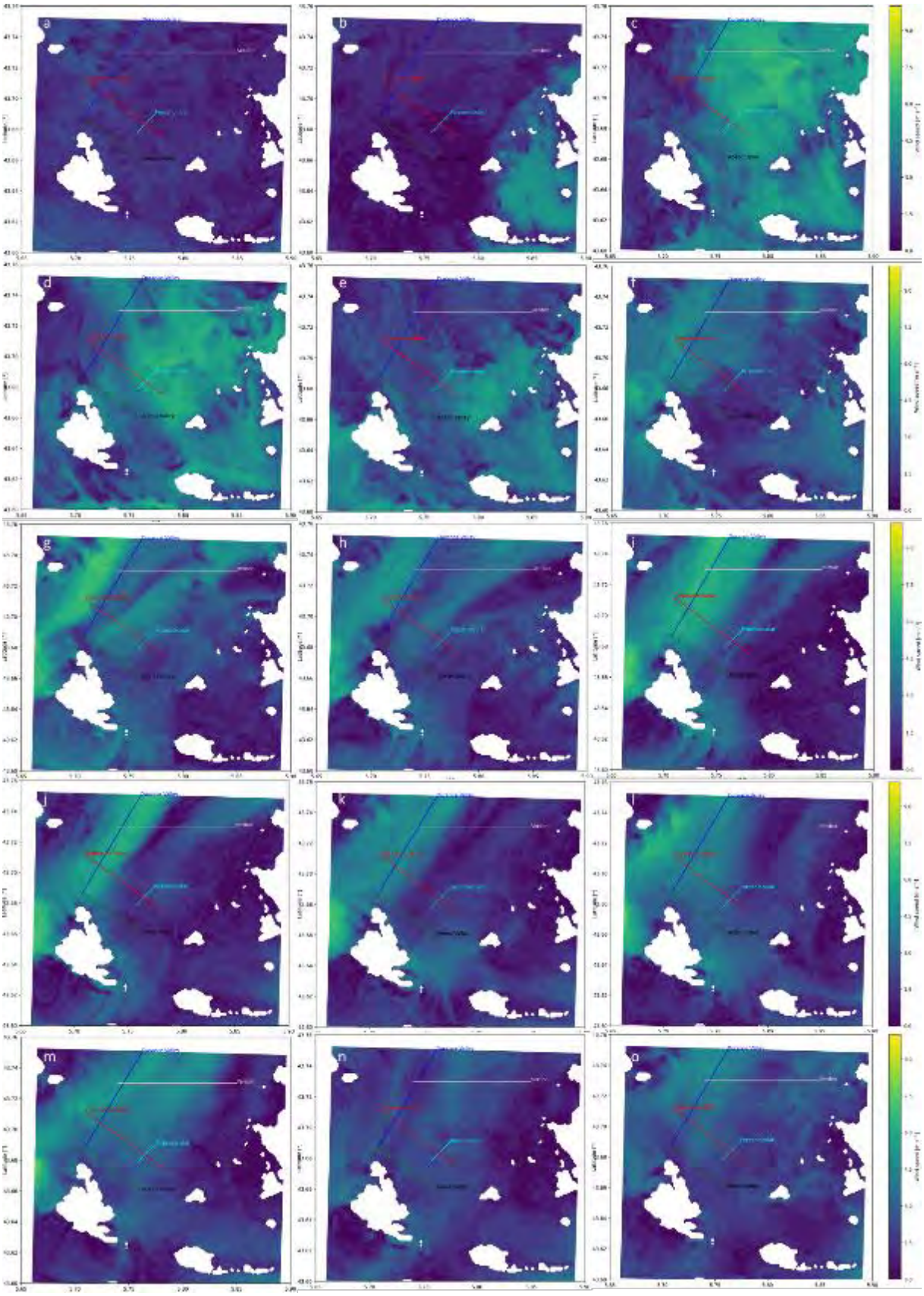

Figure A5.33: Horizontal cross-sections of the wind speed above the 111 m resolution domain at 450 m amsl. Plot (a) is the situation at 16:00 UTC and every letter increases the time by one hour up to 06:00 UTC (o).

Arrow plots of the 111 m domain

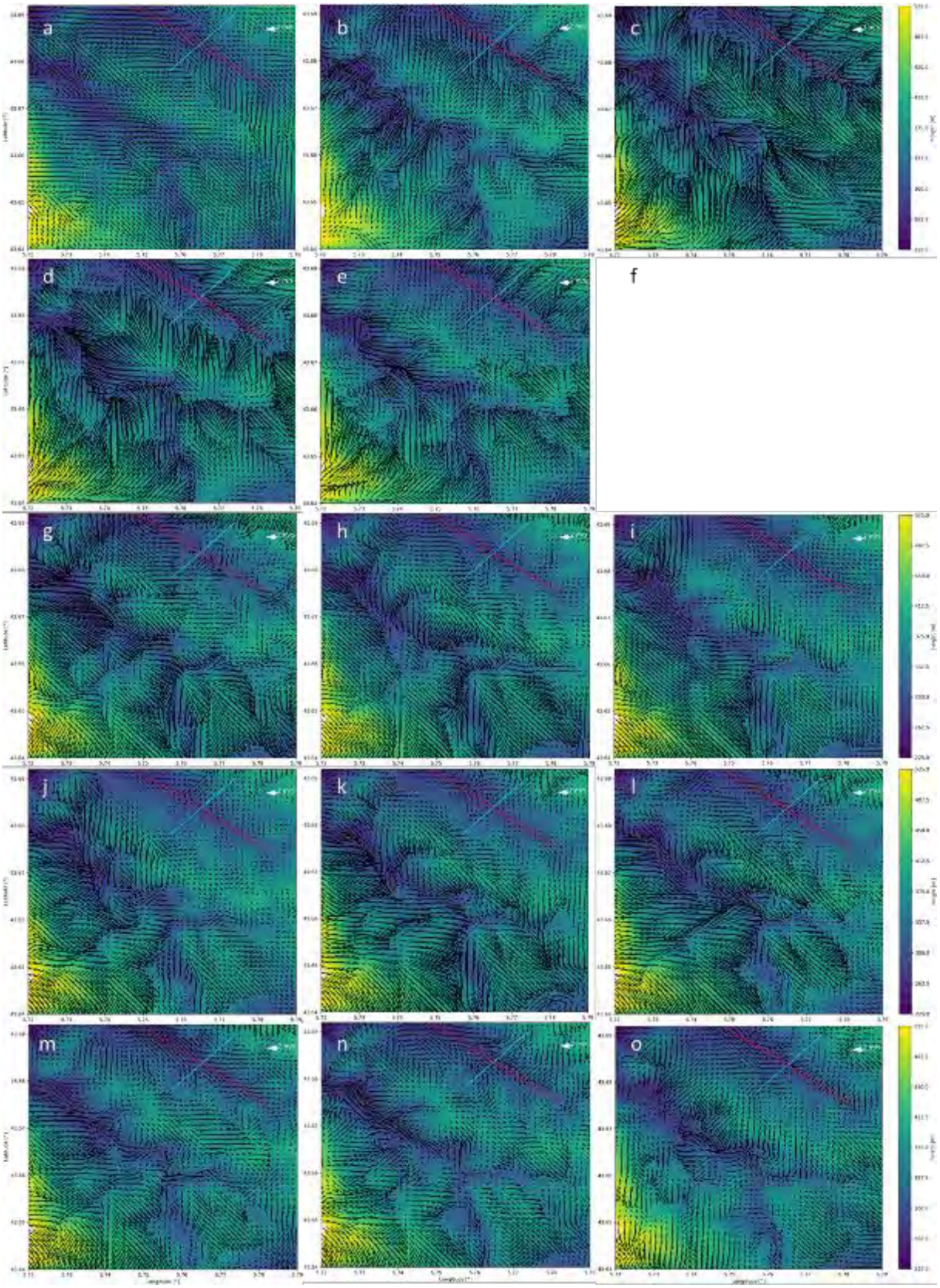

Figure A5.34: Wind vectors around the Abéou Valley and the south ridge of the CV from (a) 16:00 UTC 20 February to (o) 06:00 UTC 21 February 2017 with an hourly interval. Note that (f) is absent due to an error in the simulation data.

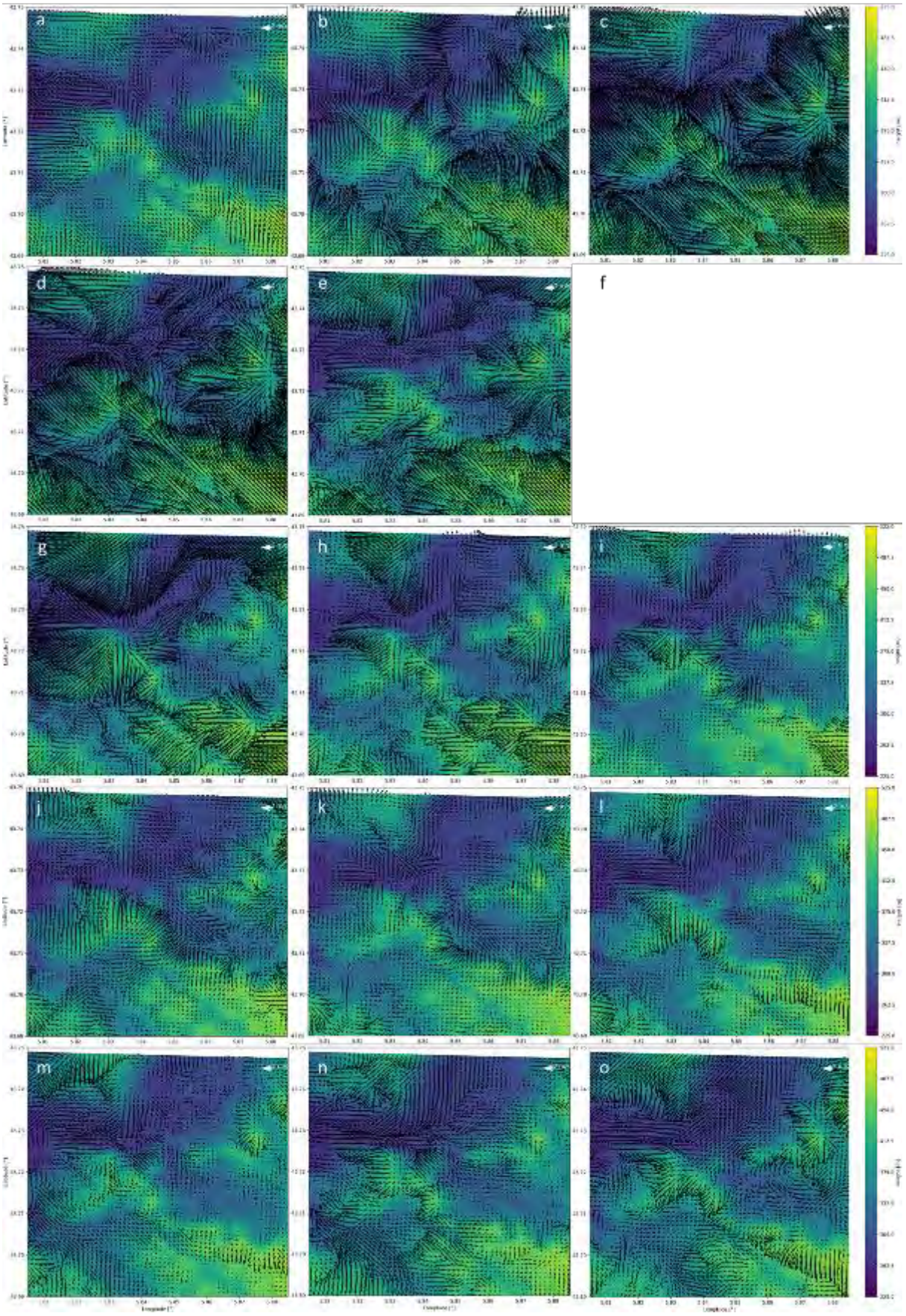

Figure A5.35: Wind vectors around the Verdon Valley and the valley between the VV and the CV from(a) 16:00 UTC 20 February to (o) 06:00 UTC 21 February 2017 with an hourly interval. Note that (f) is absent due to an error in the simulation data.

Figure A5.34 shows the simulated wind development at 10 m agl in the AV and the southern ridge of the CV. It starts with winds from the west and later the local winds take over, showing a strong influence of the topography. Most notable is the downslope flows in the southwest plot corner that turn to flows towards the southeast. Figure A5.35 shows the VV development, at the floor of the basin the flows remain diverse while the higher parts show faster wind speeds.

Tracer plots

This section contains plots that first show the four CV tracers over time, followed by the other four release points. Figure A5.36 to Figure A5.47 show the hourly development of the tracers released in the CV and move as described in Chapter 5. I did not include the 18:00 UTC release, as it is the starting moment and therefore empty. At the same time, Figure A5.48 to Figure A5.59 show the development of the other four tracers.

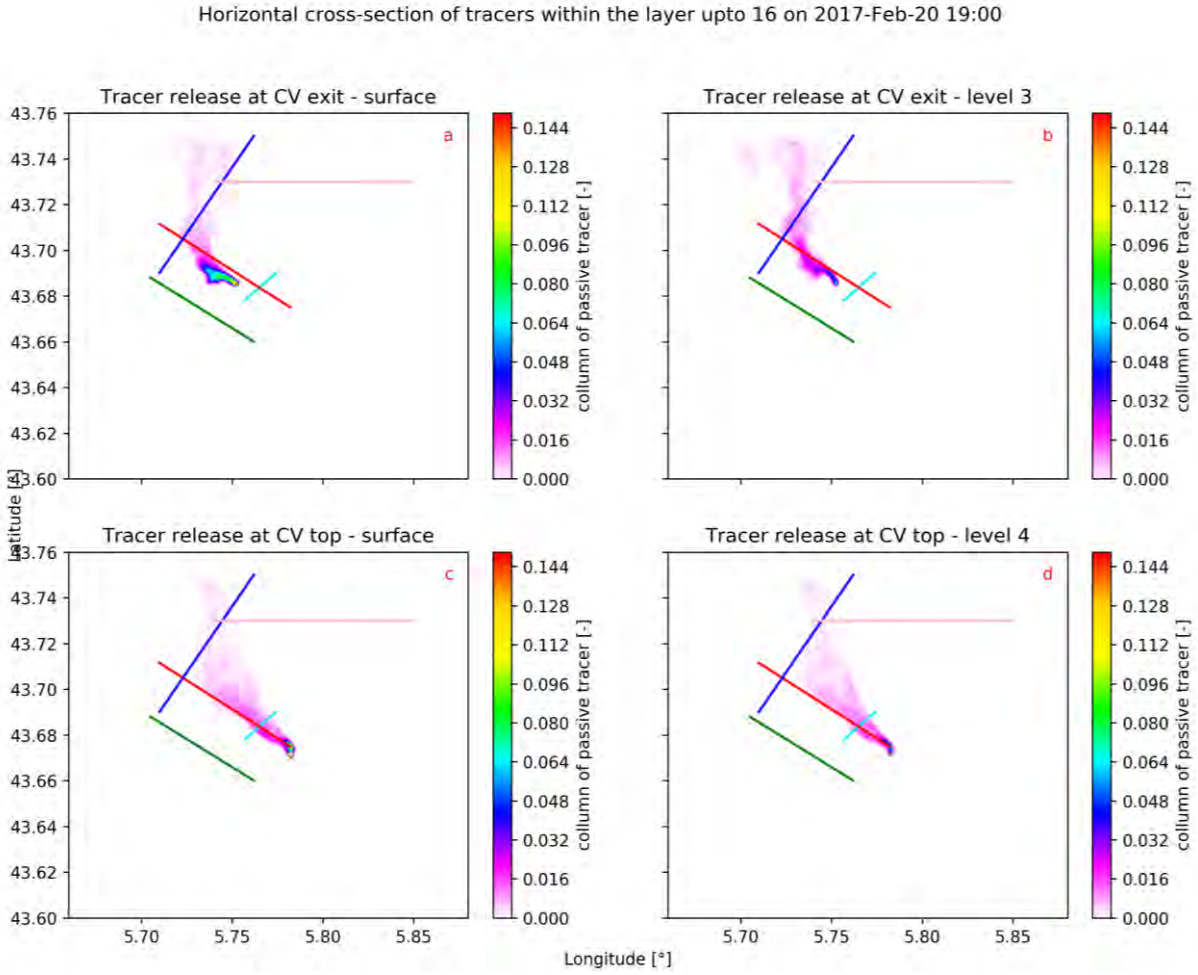

Figure A5.36: Tracer plumes at 19:00 UTC 20 February 2017. Plot (a) has CV1, (b) CV2, (c) CV3, and (d) CV4.

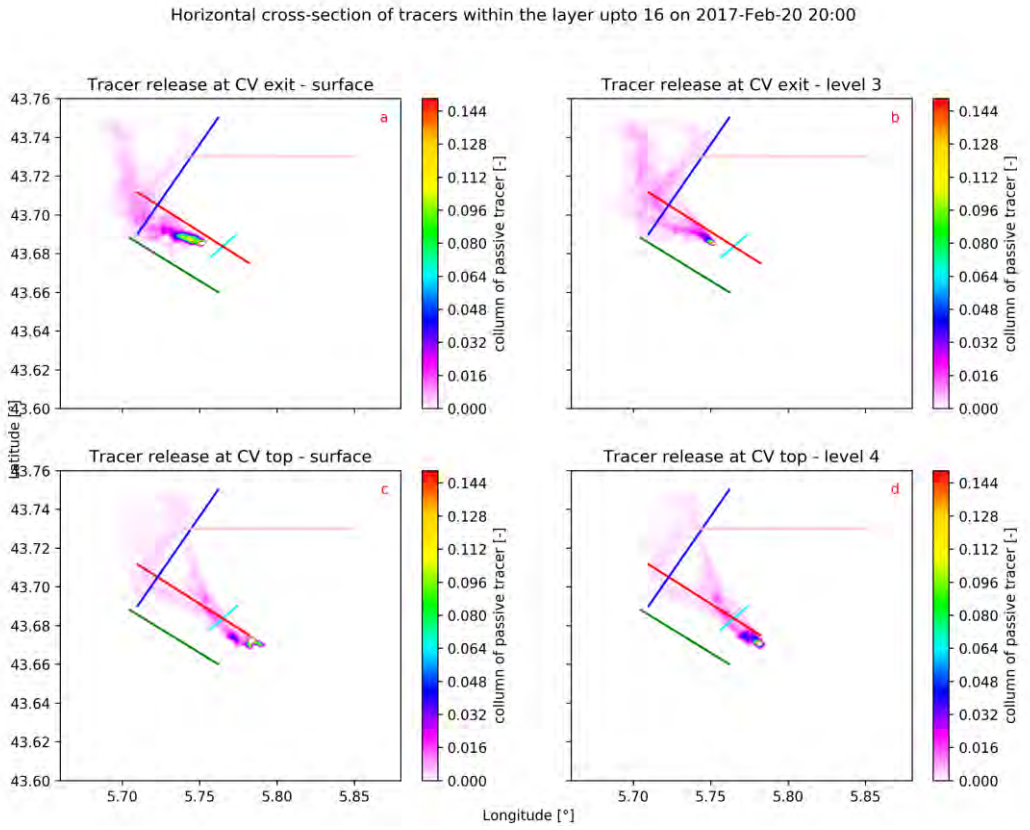

Figure A5.37: Similar to Figure A5.36 but at 20:00 UTC.

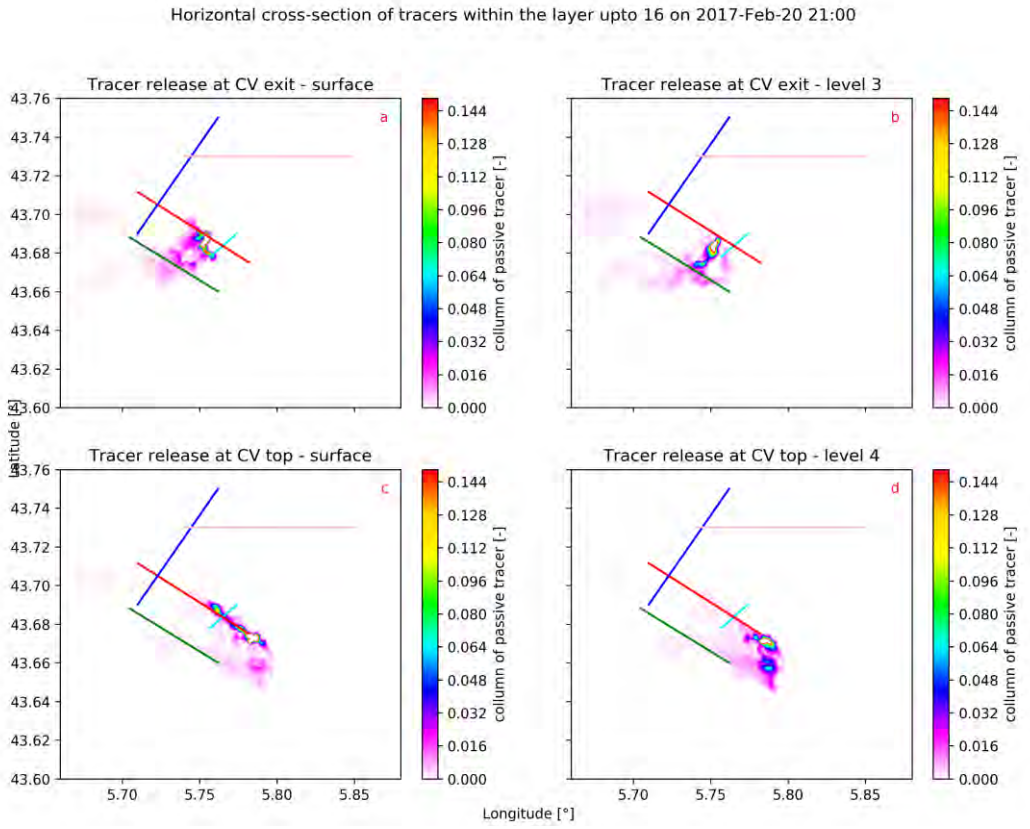

Figure A5.38: Similar to Figure A5.36 but at 21:00 UTC.

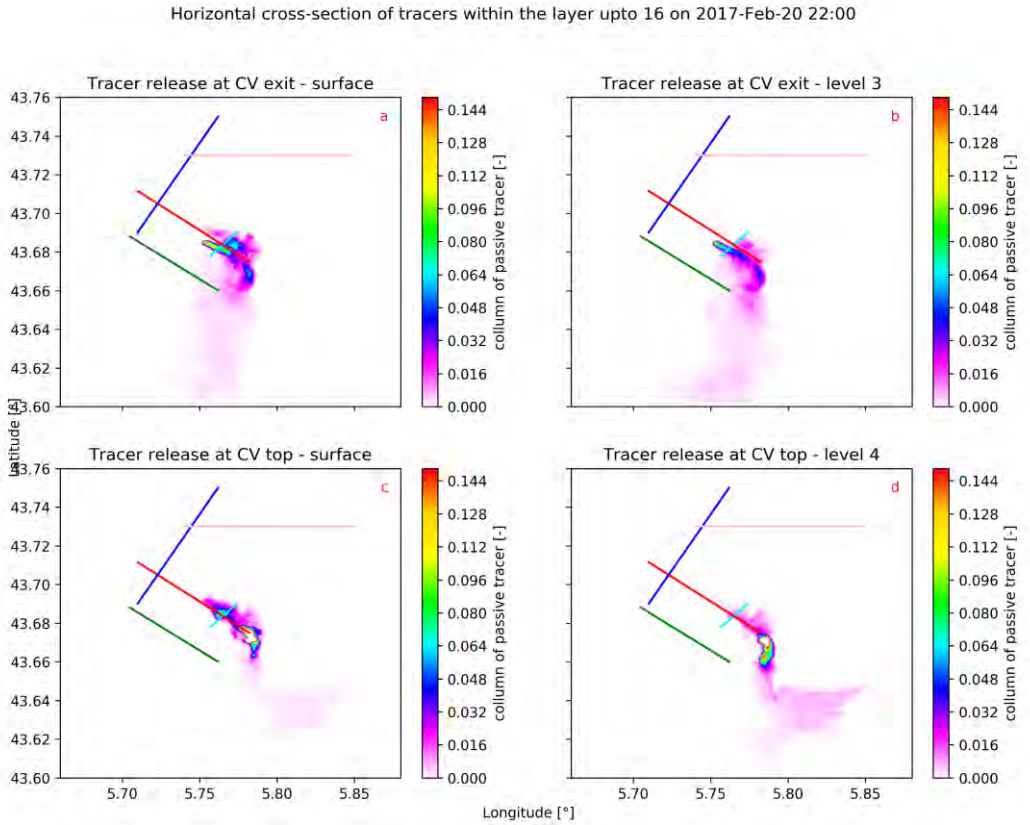

Figure A5.39: Similar to Figure A5.36 but at 22:00 UTC.

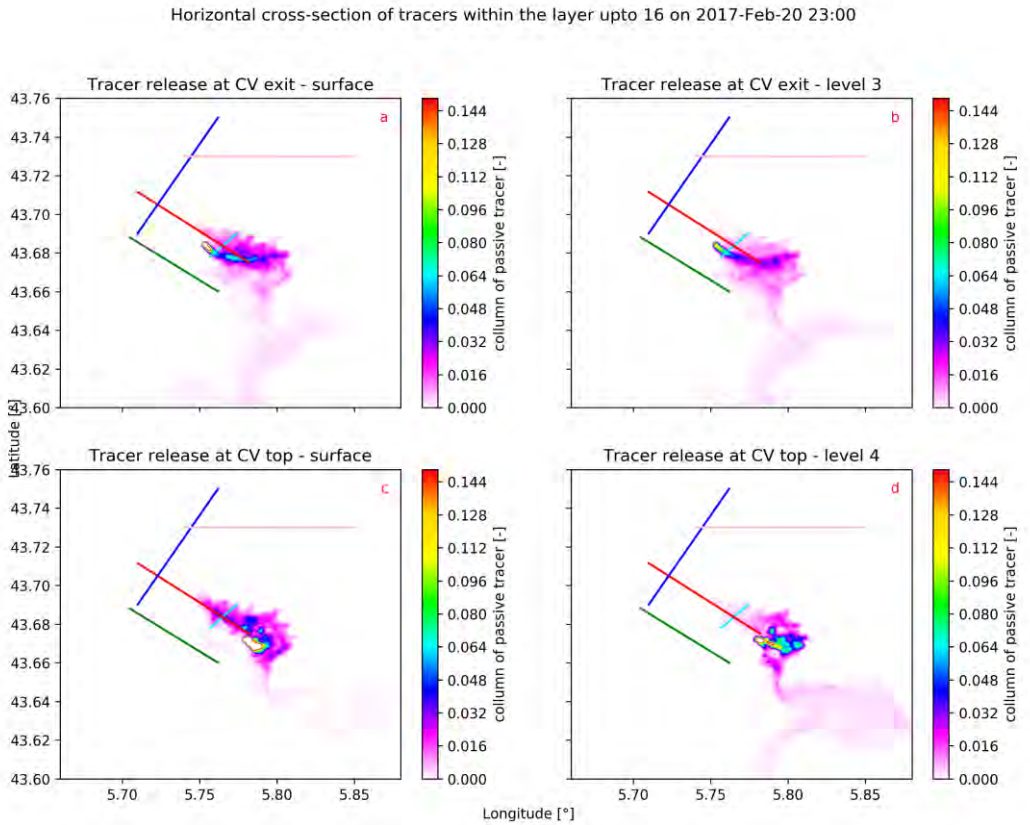

Figure A5.40: Similar to Figure A5.36 but at 23:00 UTC.

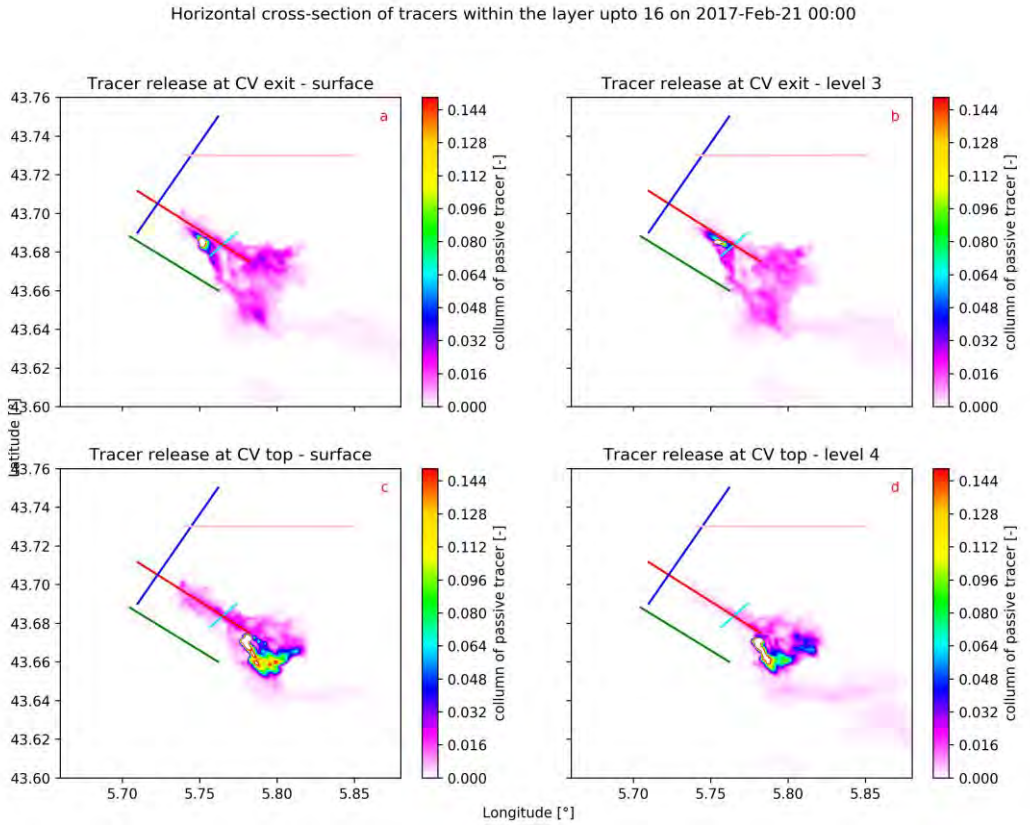

Figure A5.41: Similar to Figure A5.36 but at 00:00 UTC.

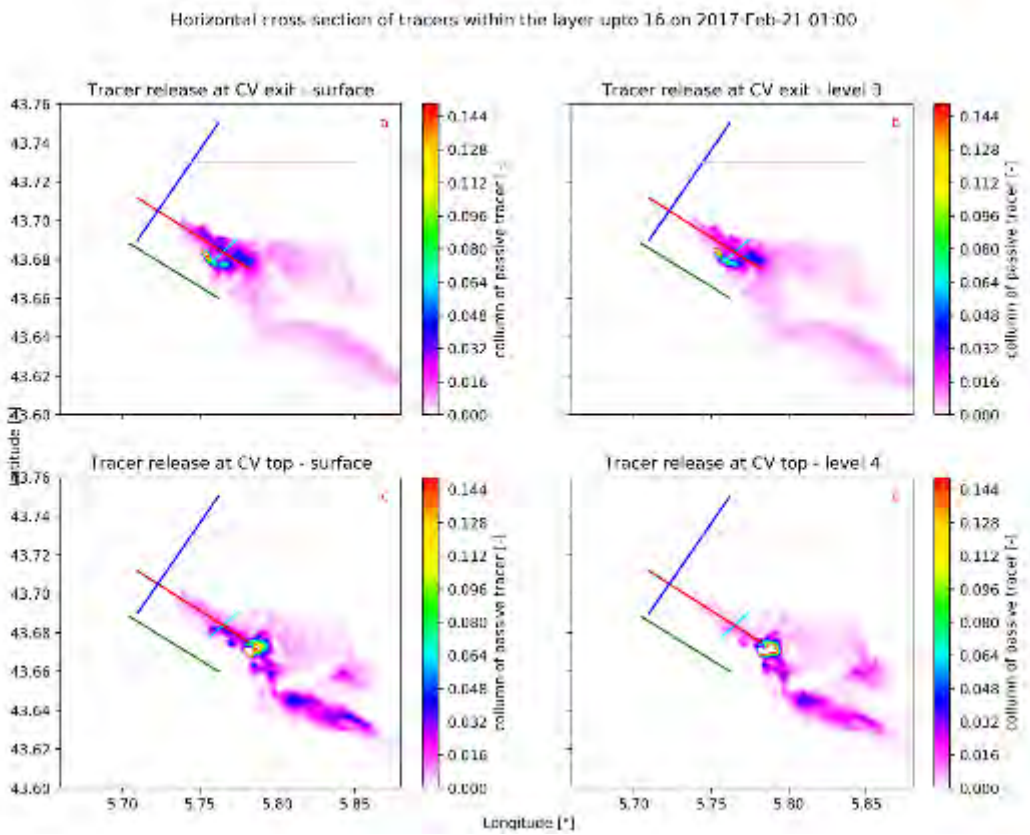

Figure A5.42: Similar to Figure A5.36 but at 01:00 UTC the day after.

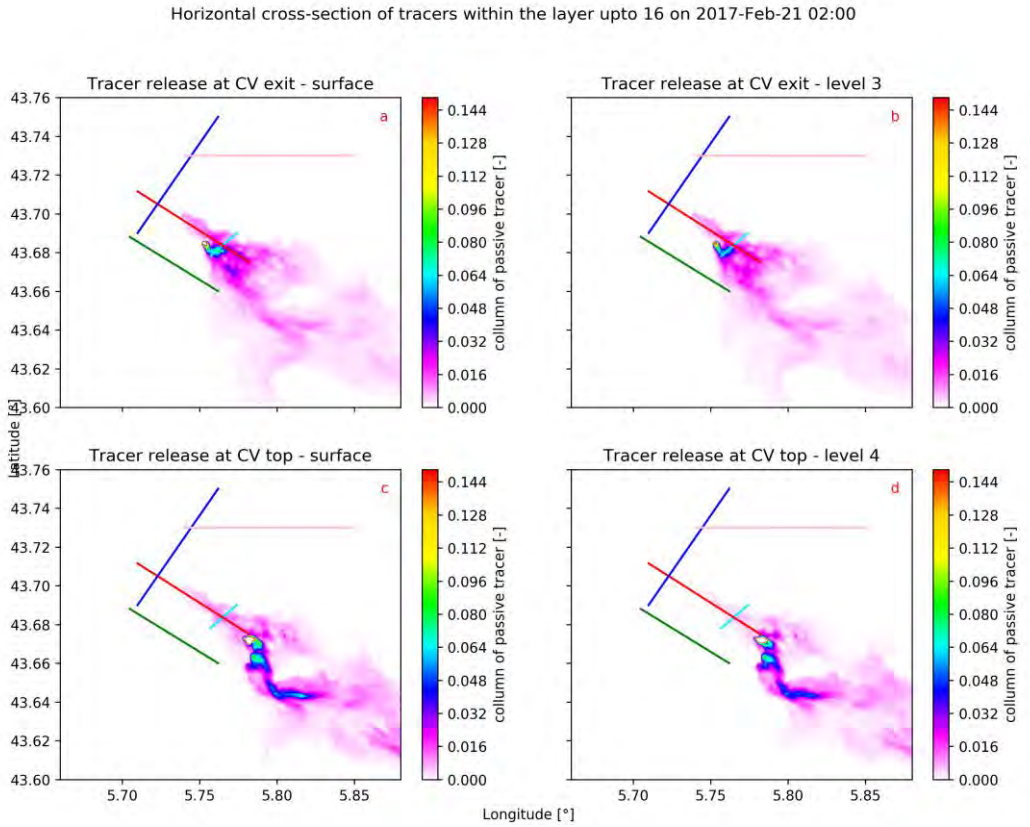

Figure A5.43: Similar to Figure A5.36 but at 02:00 UTC the day after.

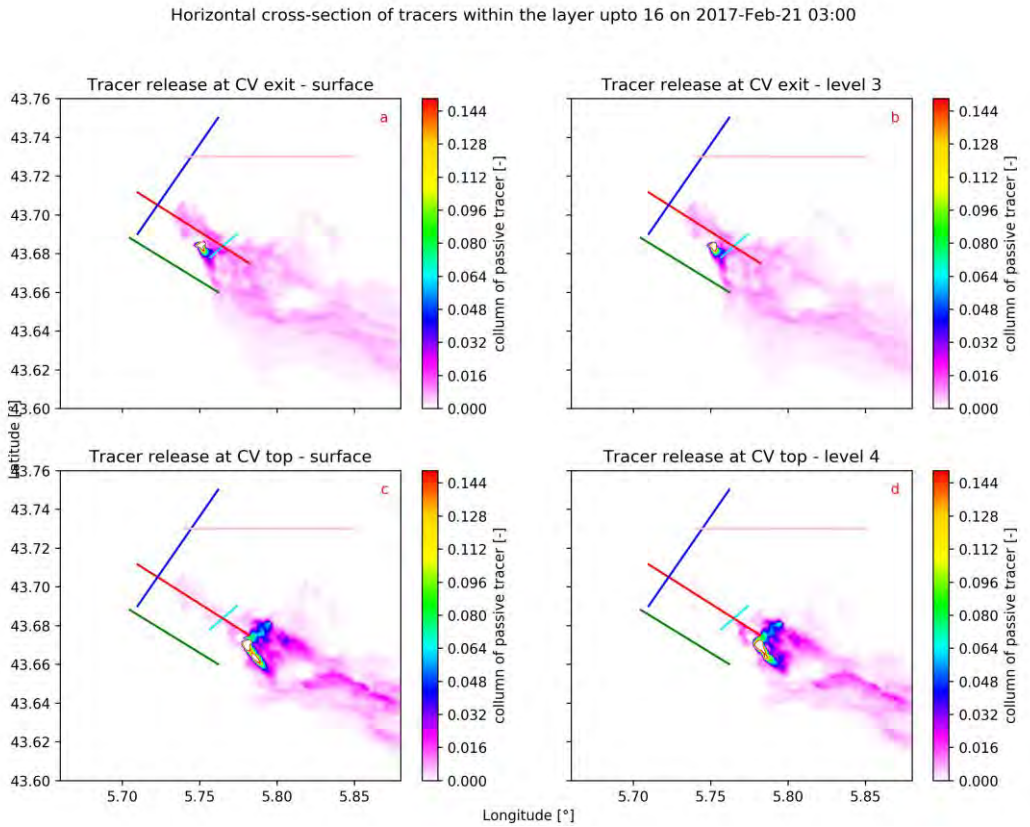

Figure A5.44: Similar to Figure A5.36 but at 03:00 UTC the day after.

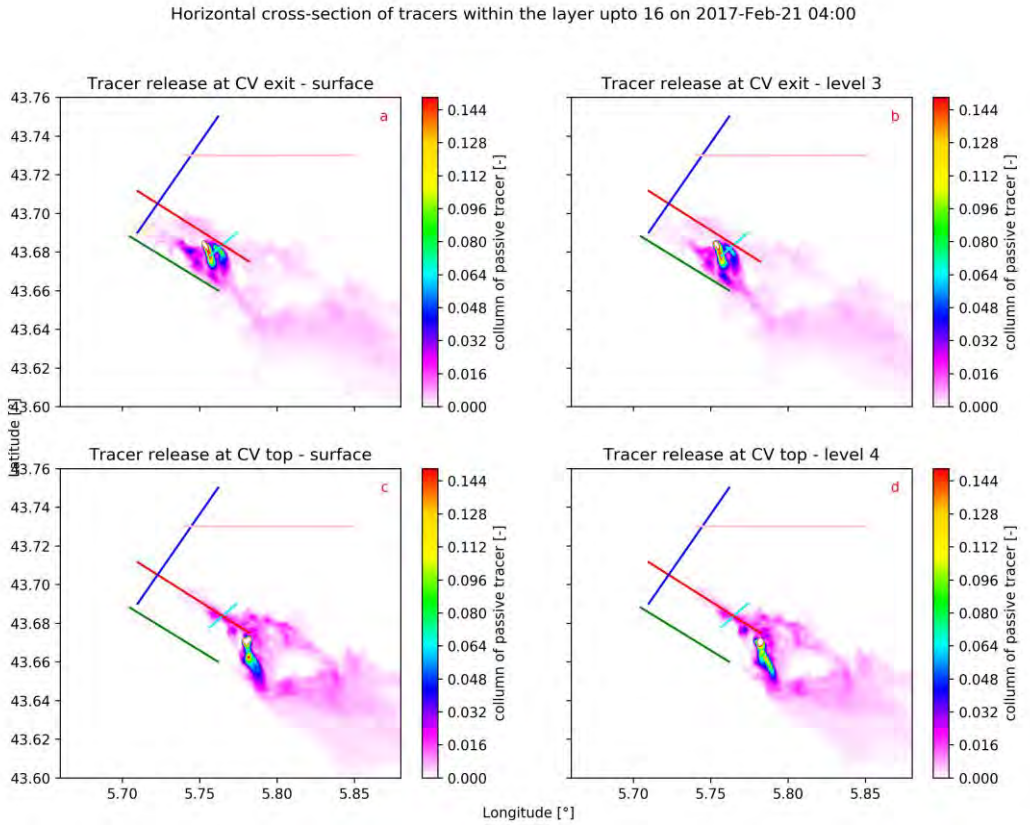

Figure A5.45: Similar to Figure A5.36 but at 04:00 UTC the day after.

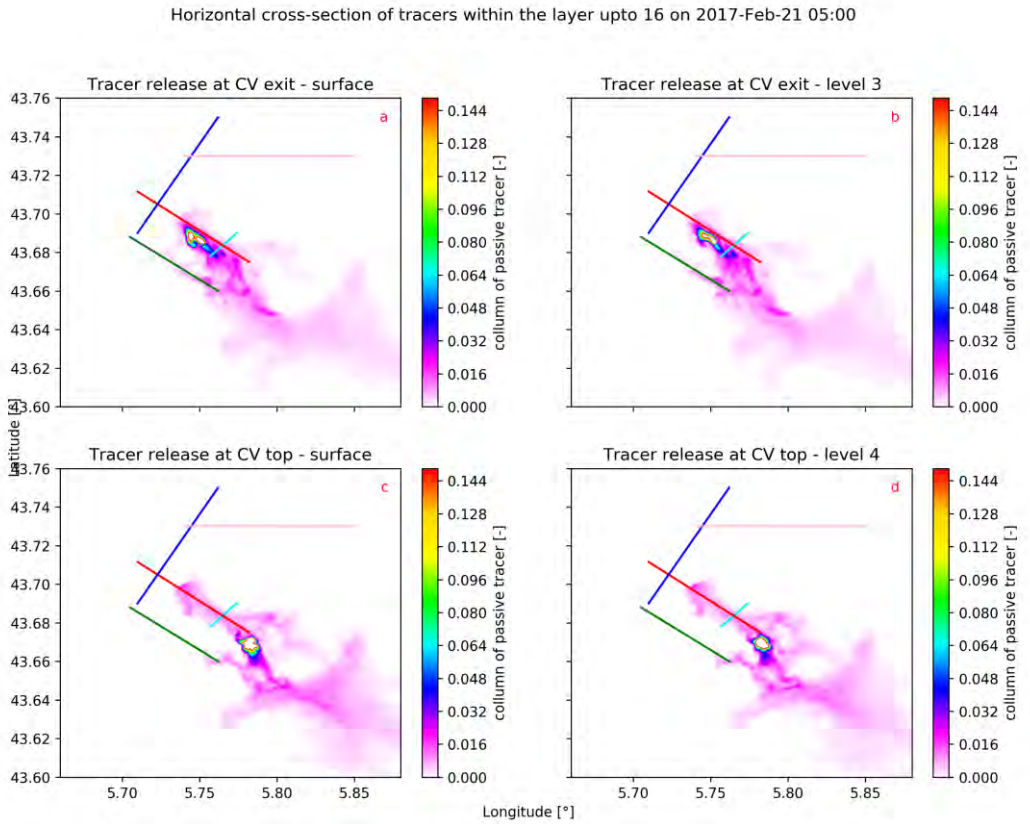

Figure A5.46: Similar to Figure A5.36 but at 05:00 UTC the day after.

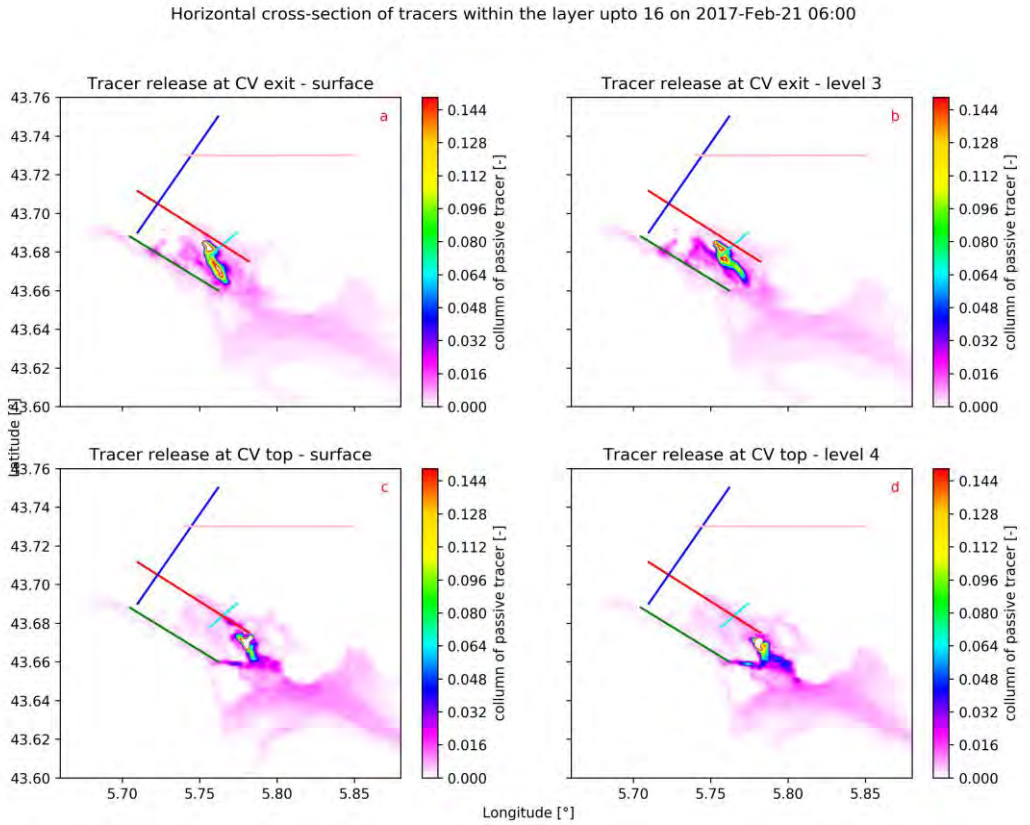

Figure A5.47: Similar to Figure A5.36 but at 06:00 UTC the day after.

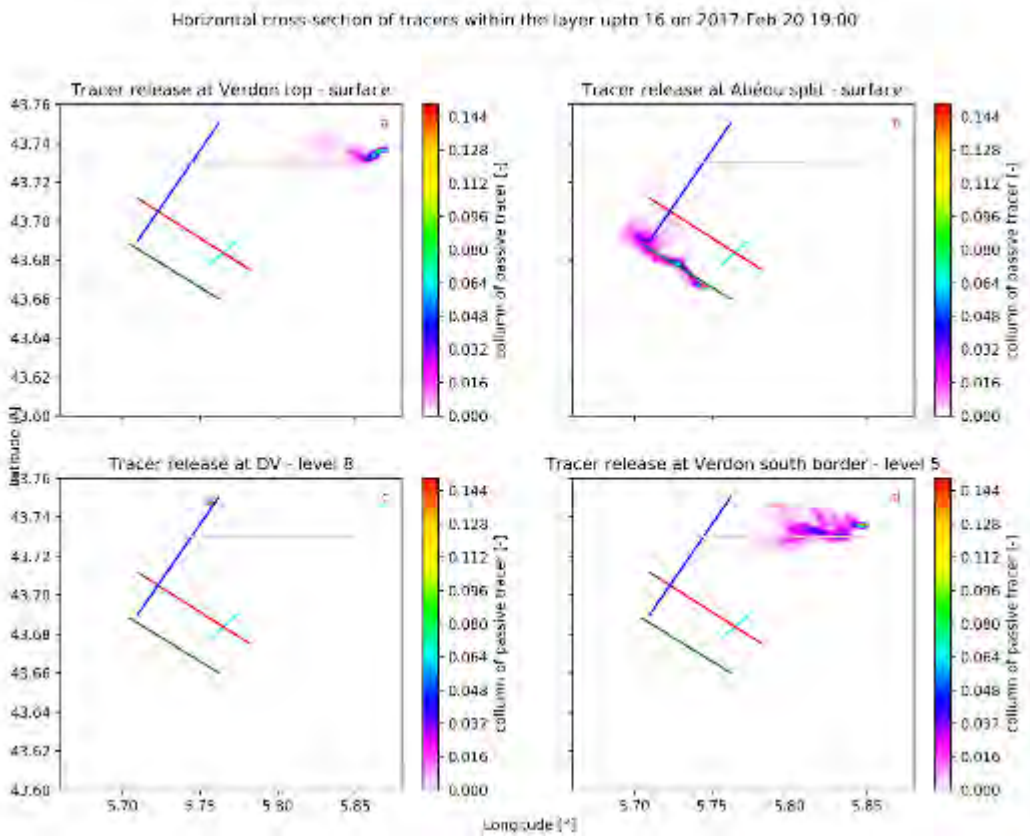

Figure A5.48: Tracer plumes of the four tracers released outside the CV at 19:00 UTC 20 February 2017. Plot (a) is the VV1, (b) AV, (c) DV, and (d) VV2.

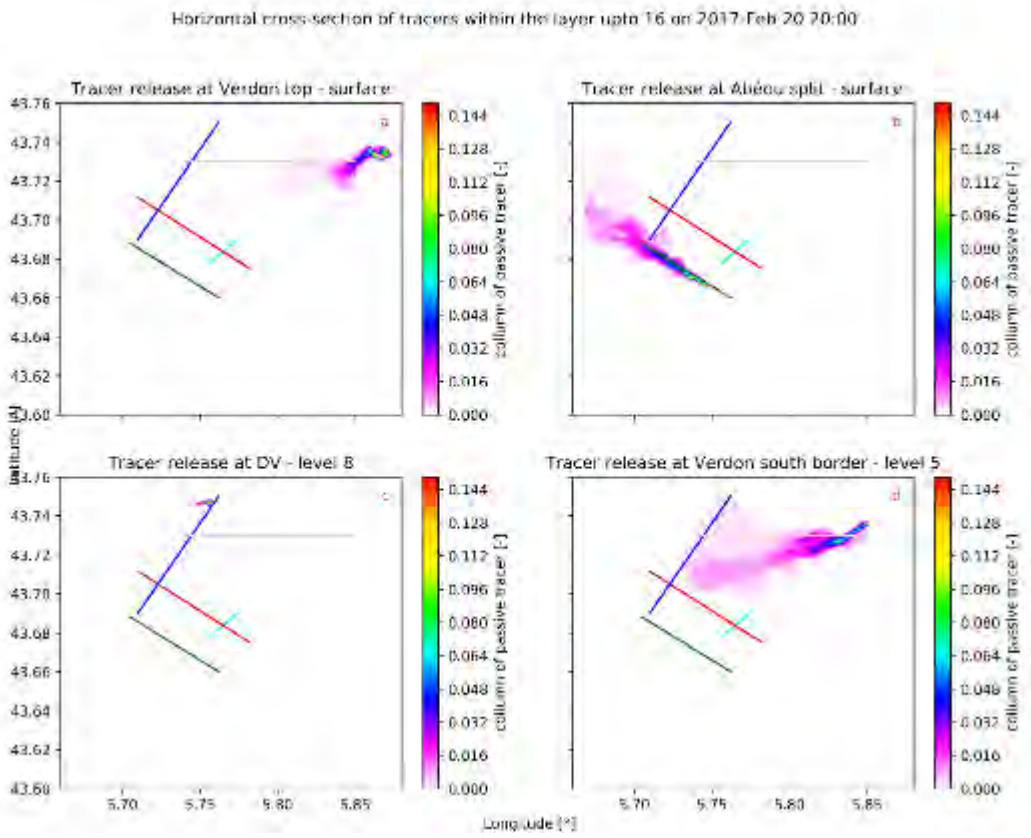

Figure A5.49: Similar to Figure A5.48 but at 20:00 UTC.

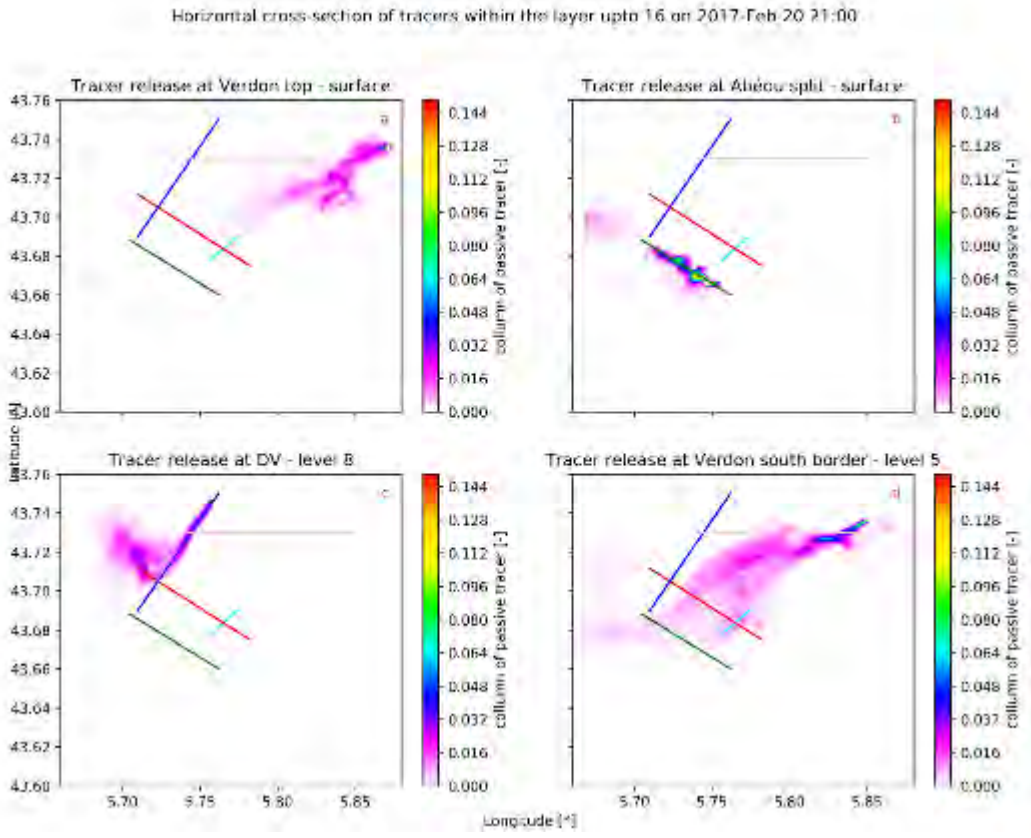

Figure A5.50: Similar to Figure A5.48 but at 21:00 UTC.

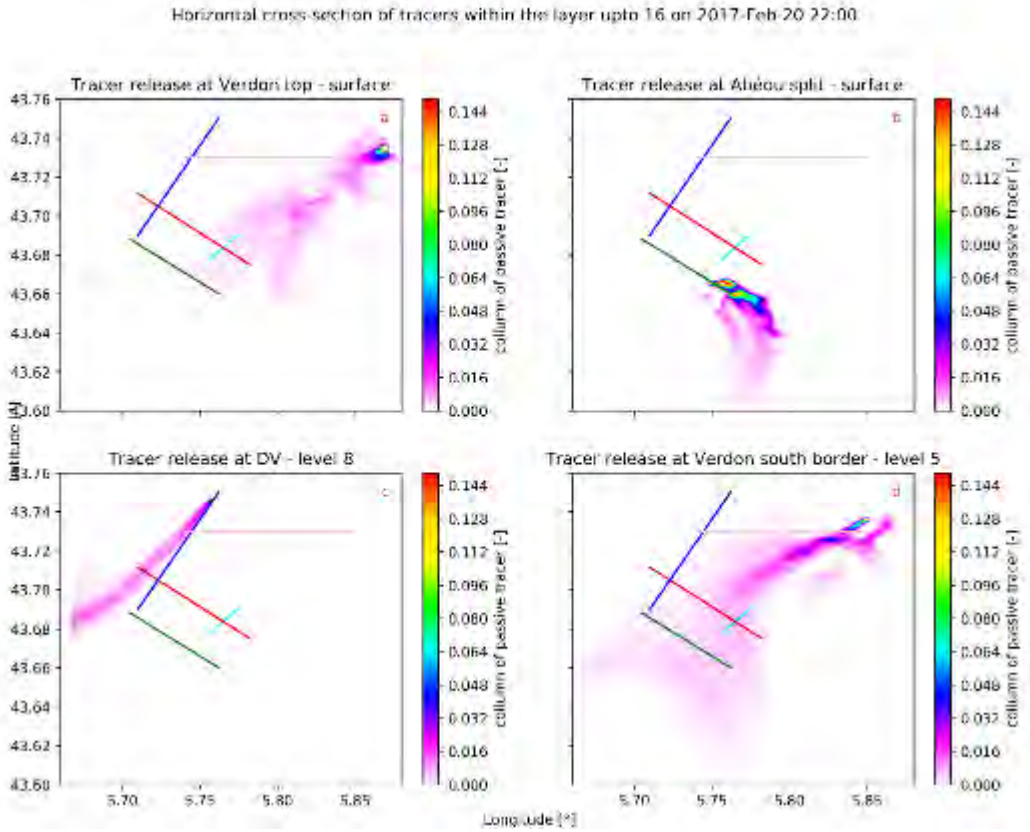

Figure A5.51: Similar to Figure A5.48 but at 22:00 UTC.

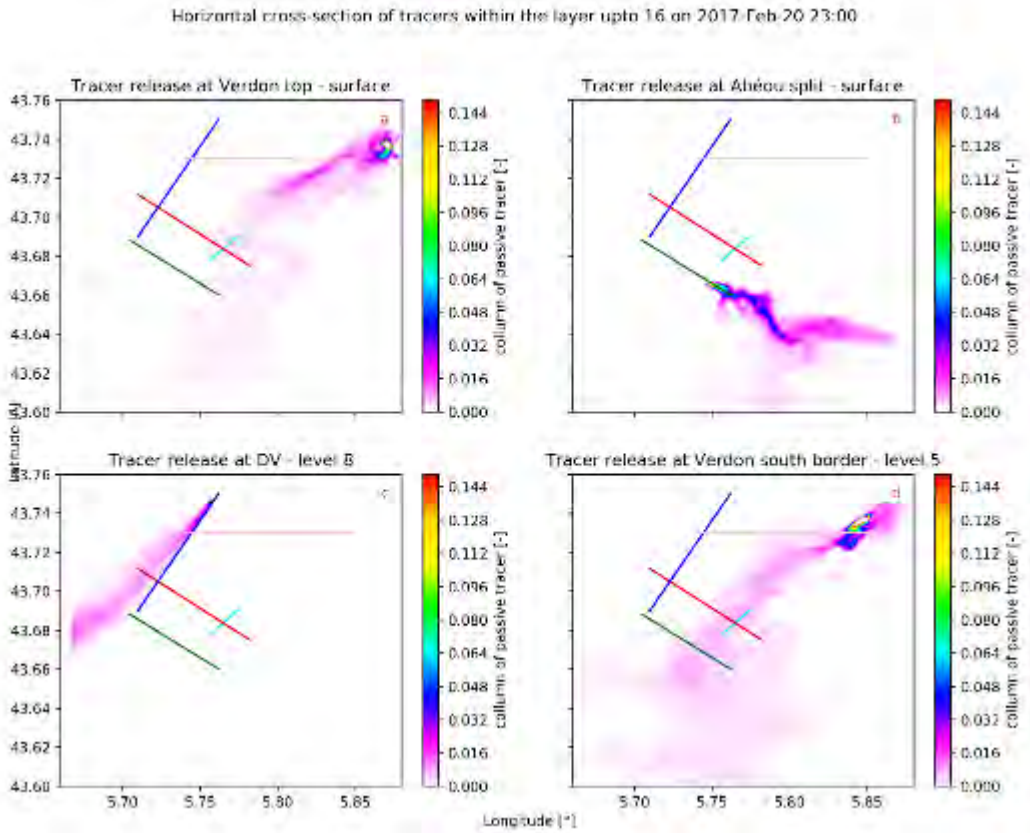

Figure A5.52: Similar to Figure A5.48 but at 23:00 UTC.

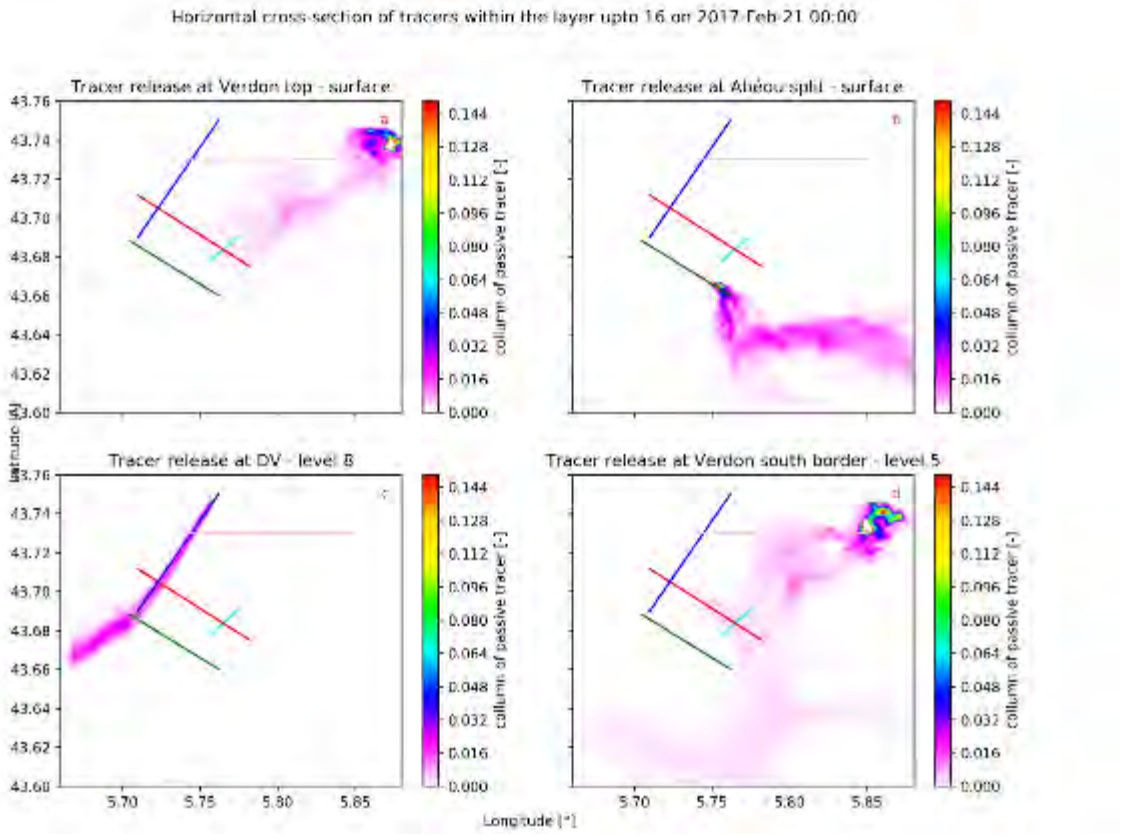

Figure A5.53: Similar to Figure A5.48 but at 00:00 UTC.

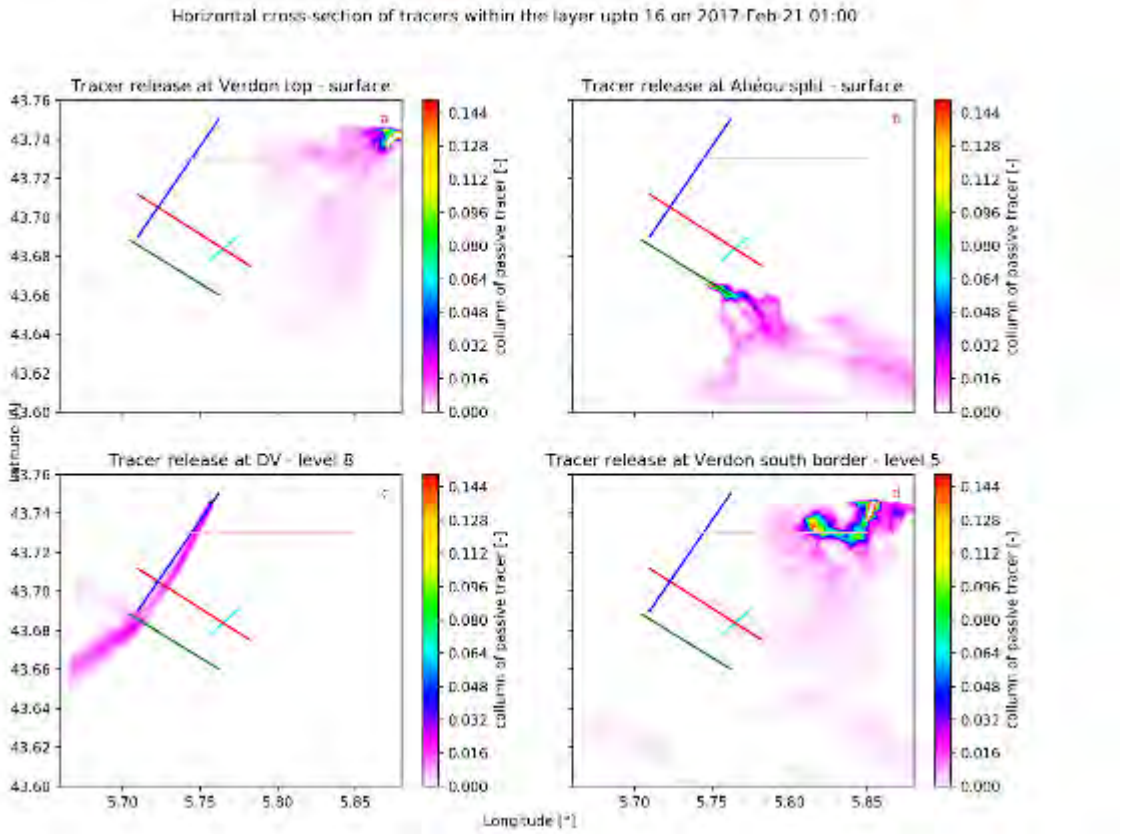

Figure A5.54: Similar to Figure A5.48 but at 01:00 UTC the day after.

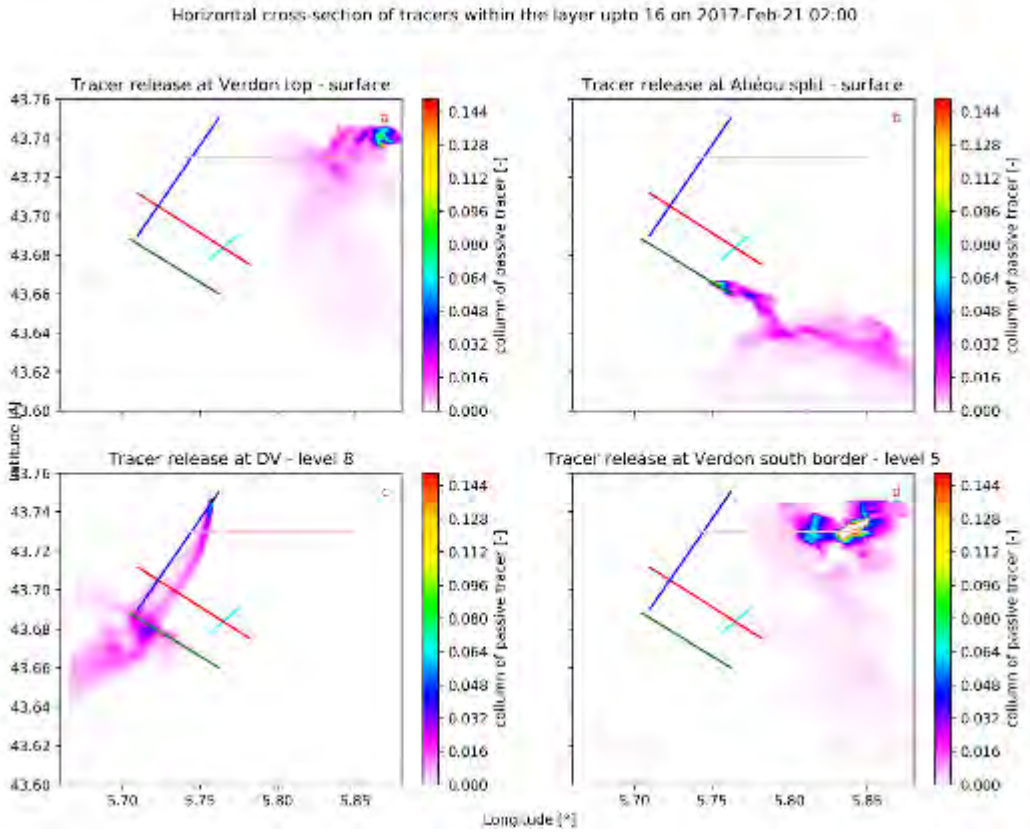

Figure A5.55: Similar to Figure A5.48 but at 02:00 UTC the day after.

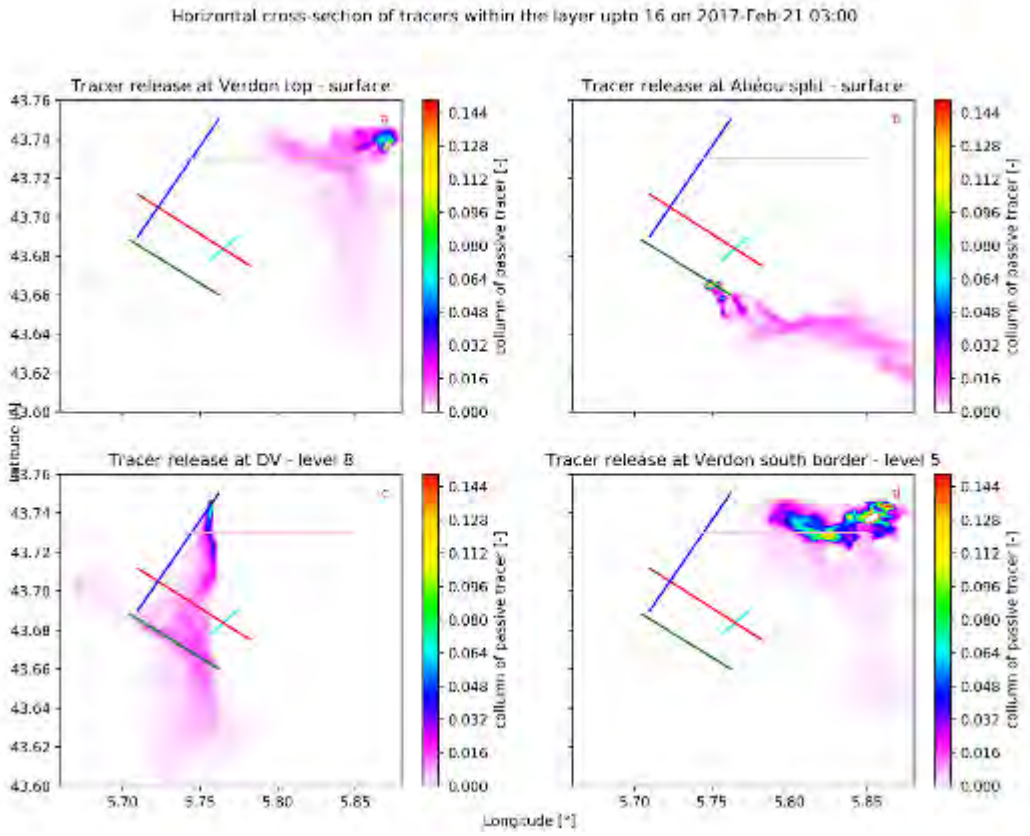

Figure A5.56: Similar to Figure A5.48 but at 03:00 UTC the day after.

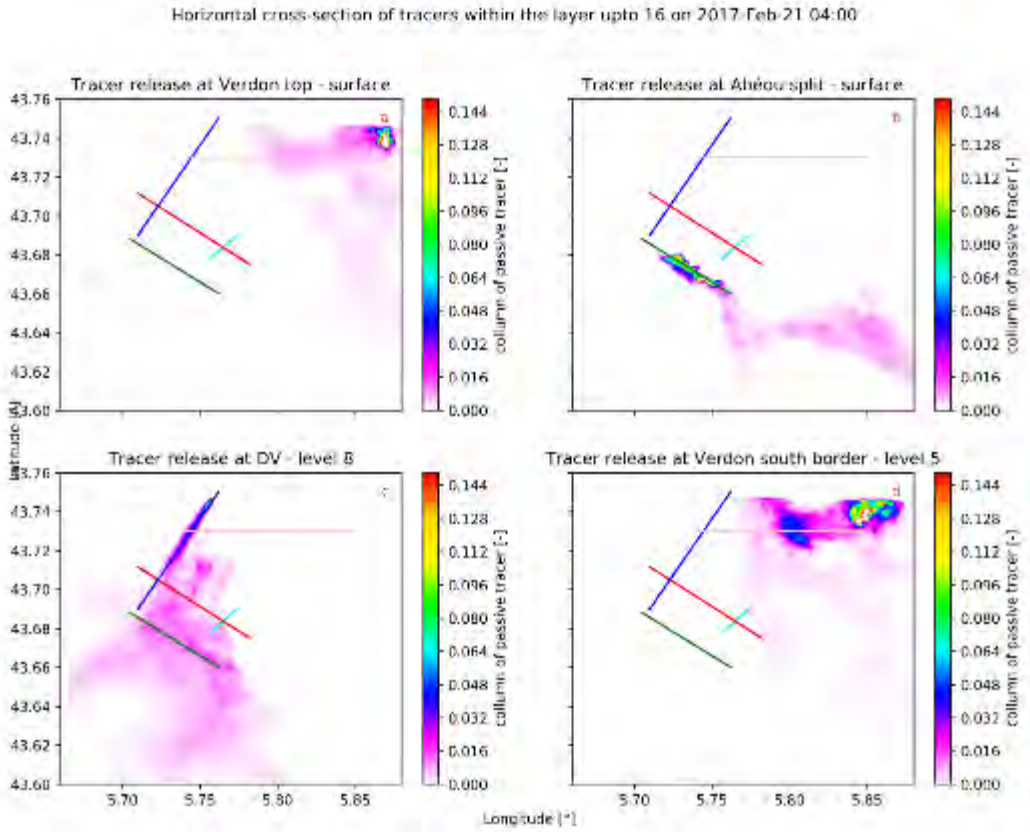

Figure A5.57 : Similar to Figure A5.48 but at 04:00 UTC the day after.

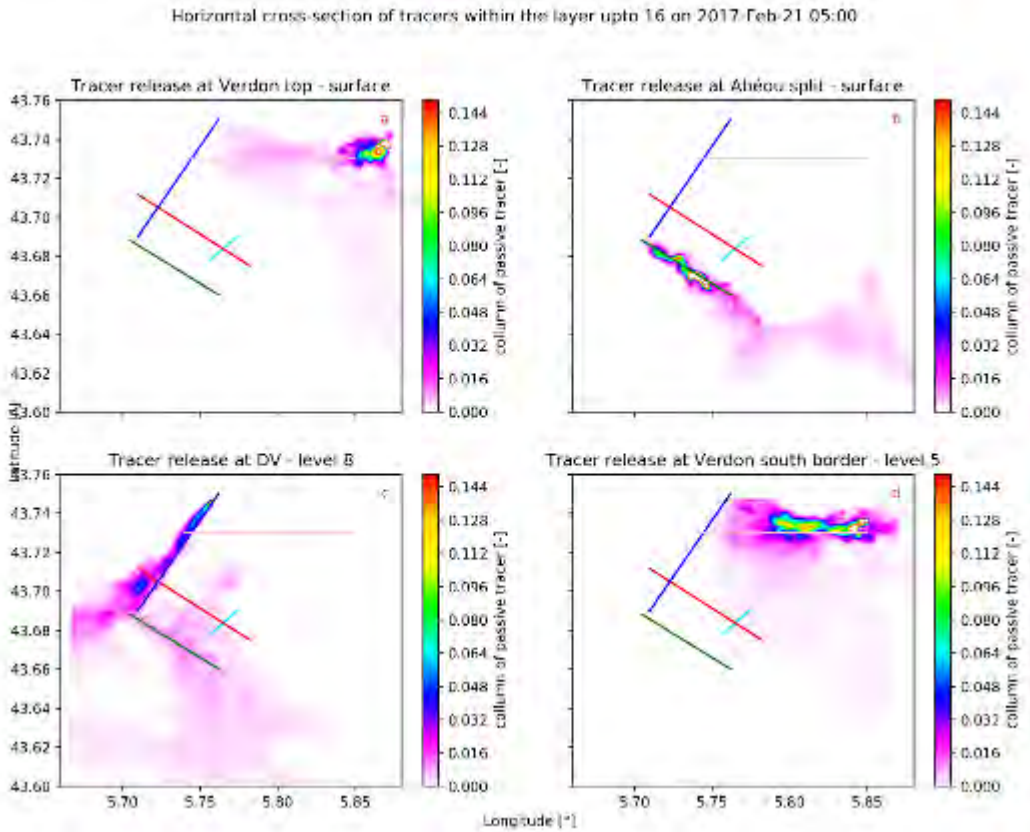

Figure A5.58: Similar to Figure A5.48 but at 05:00 UTC the day after.

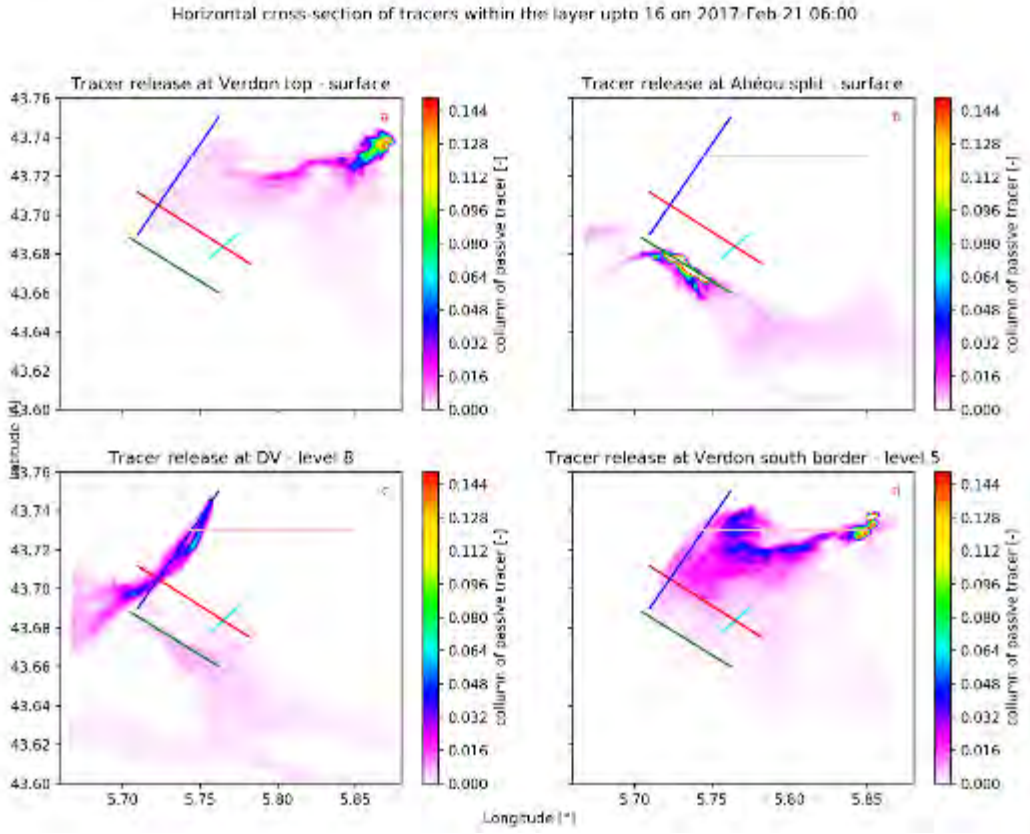

Figure A5.59: Similar to Figure A5.48 but at 06:00 UTC the day after.